DRAFT SF 298

1. Report Date (dd-mm-yy) 10 Oct 94	2. Report Type conference proceedings	3. Dates covered (from... to) 29 June - 2 July 1994	
4. Title & subtitle 4th International Symposium on Stratified Flows		5a. Contract or Grant # N00014-94-J-9018	
		5b. Program Element #	
6. Author(s) Emil Hopfinger, Bruno Voisin, Genevieve Chavand, editors		5c. Project # 5202	
		5d. Task # EUR	
		5e. Work Unit #	
7. Performing Organization Name & Address Laboratoire des Ecoulements Geophysiques et Industriels, Institut de Mecanique de Grenoble, B.P. 53 X - 38041 Grenoble Cedex 9 France		8. Performing Organization Report #	
9. Sponsoring/Monitoring Agency Name & Address Office of Naval Research Europe PSC 802 BOX 39 FPO AE 09499-0700		10. Monitor Acronym ONREUR	
		11. Monitor Report #	
12. Distribution/Availability Statement A			
13. Supplementary Notes 4 volumes			
14. Abstract			
15. Subject Terms stratified flows			

Security Classification of			19. Limitation of Abstract Unlimited	20. # of Pages	21. Responsible Person (Name and Telephone #) Mike Shear, 011-44-0171-514-4921
16. Report Unclassified	17. Abstract Unclassified	18. This Page Unclassified			

4th INTERNATIONAL SYMPOSIUM ON STRATIFIED FLOWS

Program

Wednesday – June 29 – Morning

7:45 – 9:00	**REGISTRATION AND COFFEE IN AMPHI. WEIL**
9:00 – 9:15	**Welcoming Address**
9:15 – 10:15	**Opening Lecture** Internal waves and related initial-value problems *Sir James Lighthill*
10:15 – 10:45	**COFFEE BREAK.**
	TRANSFER TO LECTURE HALLS E1 AND E2 IN D.S.U.

Session A1
SHEAR FLOW INSTABILITY

10:45 Wave packet critical layers in stratified shear flows – 83
S. A. Maslowe

11:00 Multiple instability in a laboratory stratified shear layer – 139
C. P. Caulfield, S. Yoshida. W. R. Peltier, M. Ohtani

11:15 Two-dimensional secondary instabilities in a stably-stratified shear layer – 240
C. Staquet

11:30 Secondary instability and three dimensionalization in a laboratory accelerating shear layer with varying density differences – 140
S. Yoshida, C. P. Caulfield, W. R. Peltier

11:45 Stability of nonlinear stratified flow over topography – 73
T. R. Akylas, J. Ramirez, D. Prasad

12:00 Observations and energetics of a naturally occurring shear instability in a stratified flow – 89
H. E. Seim, M. C. Gregg

12:15 The effect of non-symmetrical stratified shear layers on the development of Holmboe instabilities – 117
S. P. Haigh, G. A. Lawrence

12:30 Locked states, phase solitons and Holmboe waves in spatially forced mixing layers – 136
O. Pouliquen, J.-M. Chomaz, P. Huerre

Session B1
BAROCLINIC VORTICES

10:45 Nonlinear oscillatory evolution of a baroclinically unstable geostrophic vortex – 14
X. J. Carton

11:00 Intense vortex motion in a continuously stratified differentially rotating fluid – 77
G. Sutyrin

11:15 An experimental study of the effects of sloping topography and canyons on boundary currents in rotating, stratified fluids – 180
A. Folkard, P. Davies

11:30 On the energy flux from travelling hurricanes on a f-plane to the internal wave field – 91
J. Nilsson

11:45 Evolution of an exact, stratified eddy in a rotating, stratified Boussinesq fluid – 178
L. R. M. Maas, K. Zahariev

12:00 Cyclone-anticyclone asymmetry in the merging process – 93
S. Valcke, J. Verron

12:15 Advective and diffusive processes in baroclinic vortices – 104
J. Nycander, S. N. Aristov

12:30 Dynamics of internal solitary waves in a rotating fluid – 115
O. A. Gilman, R. Grimshaw, Yu. A. Stepanyants

12:45 – 2:00 **LUNCH**

2:00 – 3:30   **General Session**

Lagrangian dispersion in oceanic mesoscale turbulence
B. L. Hua

Large amplitude anomalies in baroclinic zonal flows
K. Helfrich, J. Pedlosky

3:30 – 4:00   **Poster Presentation GP1**

1. Characteristics of the instability in a surface boundary current – 251
   D. Obaton, G. Chabert d'Hières

2. Frontal phenomena observed in tidal estuaries – verification by 3-D baroclinic flow model – 146
   K. Nakatsuji, T. Sueyoshi, T. Fujiwara

3. Laboratory modelling of gravity currents on the slope in rotating fluid – 188
   A. G. Zatsepin, A. V. Semenov

4. Laboratory modeling of narrow current-topography interactions in a rotating stratified fluid – 247
   D. McGuinness, X. Zhang, D. L. Boyer

5. Experimental study of buoyant jet discharge in a rotating system – 176
   J. F. Atkinson, G. Lin

6. Development of boundary layers and transport processes effected by buoyancy – 239
   E. I. Nikiforovich, N. F. Yurchenko

7. The coupling of interfacial waves and turbulent convection in an annulus – 121
   A. P. Stamp, R. W. Griffiths

8 Convection from bounded body in rotating fluid – 27
   B. Boubnov

9. Simultaneous heat and mass transfers with or without evaporation in unsteady turbulent natural convection and application to a liquefied natural gas storage – 142
   C. T. Pham, J. P. Petit

10. Structure and dynamics of filaments in the canary and benguela upwelling regions – 189
   A. G. Kostianoy

4:00 – 4:30   **COFFEE BREAK AND POSTER VIEWING**

Session A2	**Session B2**
TURBULENT SHEAR FLOWS	**CONVECTION**

4:30 A study of a plane mixing layer with cross shear – 143
P. Atsavapranee, M. Gharib

4:30 Modelling deep ocean convection events – 78
G. N. Ivey, M. J. Coates, J. R. Taylor

4:45 Heat and mass transfer in stably stratified flow – 145
S. Komori, K. Nagata, Y. Murakami

4:45 Penetrative convection in rapidly rotating flows – 98
S. Legg, J. McWilliams

5:00 Some observations related to evolving Kelvin-Helmholtz billows – 249
I. P. D. De Silva, L. Montenegro, H. J. S. Fernando, A. Brandt

5:00 The interaction of convection and internal waves – 173
N. Kale, L. G. Redekopp

5:15 Three-dimensionalization of the stratified mixing layer – 199
W. R. Peltier, C. P. Caulfield, S. Yoshida

5:15 On the nature of multicell flow regimes observed in confined thermosolutal convection with lateral heating – 94
N. Tsitverblit

5:30 Model studies of atmospheric boundary-layer flow over topography – 74
P. Taylor, L. Chan, D. Xu, K. Ayotte

5:30 Boundary layer and scaling properties in turbulent thermal convection – 135
F. Chillà, S. Ciliberto, C. Innocenti, C. Laroche

5:45 Direct numerical simulations and experiments on a stably stratified turbulent boundary layer – 130
I. R. Cowan, R. E. Britter

5:45 Experimental study of high-Rayleigh-number convection in mercury and water – 234
S. Cioni, S. Ciliberto, J. Sommeria

6:00 Convection and internal waves in a stably stratified shear flow – 175
P. C. Gallacher, H. W. Wijesekera

6:00 Rayleigh-Taylor instability: perturbations, boundaries and growth – 192
S. B. Dalziel

6:15 Turbulent wakes in stratified fluids: results of numerical experiments – 103
G. G. Chernykh, N. P. Moshkin, O. F. Voropayeva

6:15 Rayleigh-Taylor stability in a two-fluid system under a general rotation field – 245
L. A. Dávalos-Orozco

7:00   **INFORMAL RECEPTION IN HALL OF D.S.U**

Internal waves and related initial-value problems

James Lighthill

Abstract

This paper gives a detailed account of how small disturbances to uniformly stratified fluid develop when the initial disturbances are confined to a limited region. Special stress is laid on properties of vorticity in stratified fluid, with horizontal (yet not vertical) components of vorticity being propagated away, alongside density variations, in any internal wave – an important difference from corresponding properties in homogeneous fluid.

The paper includes a comprehensive analysis of the waves which emanate from the initial disturbances, as well as of those residual motions that are left behind after all waves have been propagated away (those in each horizontal plane being determined from the initial distribution over that plane of the vorticity's vertical component). Some mathematical details are included in an Appendix, which outlines too an additional benefit from these studies by showing how the wave motion generated by any transient local forcing effect can always be identified as the solution of a well defined initial-value problem.

1 Introduction

This paper aims to treat comprehensively the development of small disturbances to a uniformly stratified fluid (on the Boussinesq approximation) in cases where the initial disturbances to uniform stratification occupy just a limited volume of fluid but are otherwise arbitrary. Particular attention is aid to the fact that, while certain elements of the initial disturbances are propagated outwards as internal waves, a residue may remain in the initial location as an (ultimately)steady horizontal motion. Relationships between the results obtained and general properties of vorticity are set out with care.

Also, attention is paid in an Appendix to outlining all the necessary mathematical analysis in the simplest possible (real-variable) form so that the mathe-

matical conclusions are easy to follow as well as having clear physical interpretations. Moreover the mathematical equivalence between initial-value problems and studies of the waves generated by purely transient local forcing effects is made clear by proving that the latter type of forcing generates the same waves as would arise from a certain (precisely related) initial-value problem.

In the body of the paper, however, emphasis is laid on physical aspects of how initial-value problems differ fundamentally for stratified and unstratified fluid. Without stratification there is no propagation of vorticity; which, on a linear theory, remains unchanged with time (evidently, the fully nonlinear conclusion that vortex lines move with the fluid assumes this limiting form for small disturbances). Physically, a familiar relationship (section 2) of vorticity to the angular momentum of a small fluid sphere allows this result to be interpreted in terms of all pressure forces on the sphere's surface acting through its centre and so having no power to change its angular momentum.

In stratified fluids, on the other hand, any vertical displacements can result in horizontal gradients of density. These shift such a sphere's centre of gravity from its centre of buoyancy (the geometric centre) and so lead to a horizontal couple or torque on the sphere and a rate of change of vorticity

$$\partial \omega / \partial t = (\nabla s) \times \mathbf{g}, \tag{1}$$

where s is the proportional change in density from its undisturbed value. Thus, density variations carried by internal waves carry also changes in vorticity — which, however, are confined to its horizontal components since $\mathbf{g}$ is directed vertically.

The science of aeroacoustics deals with questions of how turbulent flows in a homogeneous fluid generate sound waves. Vortex lines in the turbulence move with the fluid, and the only wave propagation that can carry disturbances away from the flow is an irrotational acoustic disturbance associated with a source term quadratic in the disturbance velocities.

By contrast, the study of how vortical disturbances in a stratified fluid generate internal waves involves no quadratic source terms. Already on a linear small-disturbance theory an initial distribution of vorticity generates internal waves which carry away changes in the relative density s along with associated fluctuations (1) in the horizontal components of vorticity. Ultimately, the waves have removed all variations in s so that, because by (1) ω is independent of time, the residual motion is a steady flow. It is specified on small-disturbance theory

2

by the fact that the vertical component of vorticity has never changed, This fixes the motions in each horizontal plane separately, with shear between planes determining horizontal components of vorticity; which, however, satisfy (1) because they are not varying with time.

In my book "Waves in Fluids" (Lighthill 1978) there is not much that, in 1994, I would wish to see altered except section 4.8. In this paper and its Appendix I welcome the change of indicating the physical and mathematical material which might (I believe) usefully replace the contents of that section.

2 Vorticity in internal waves

Classically, the vorticity ω is interpreted by analysing the motion of a small sphere of fluid into three components: (i) uniform translation at the velocity of its centre; (ii) rigid rotation with angular velocity $\frac{1}{2}\omega$; and (iii) a symmetrical straining motion. All of the sphere's angular momentum is in component (ii) and takes the form $\frac{1}{2}I\omega$ where I is the sphere's moment of inertia. In general motions of a fluid, the laws governing changes of ω can be deduced from a consideration of how forces acting on the sphere may be altering its angular momentum, provided that the effects of components (i) and (iii) are carefully taken into account.

On the other hand, these latter effects (a convective effect due to the sphere's translation and a stretching effect associated with changes in moments of inertia about principal axes of rate of strain) disappear from any studies where the squares of small disturbances from hydrostatic equilibrium are neglected; since, evidently, both convective velocity and rate of strain are small as well as the vorticity components on which they act. In such studies, then, the "small-sphere angular momentum" model of vorticity is specially easy to apply.

A sphere's buoyancy force, specified by Archimedes' Principle, balances its weight in hydrostatic equilibrium. On the other hand, these zero-order forces can generate a first-order rate of change of angular momentum if small disturbances displace the sphere's centre of gravity from its centre of buoyancy (the geometric centre). A gradient ∇s of relative density gives the sphere's centre of gravity a displacements $M^{-1}(\frac{1}{2}I\nabla s)$, where M is its mass while the second moment of the mass distribution in the direction of ∇s takes the simple form $\frac{1}{2}I\nabla s$. But the sphere's weight $M\mathbf{g}$, acting through this displaced centre of gravity, generates a rate of change of angular momentum

$$\frac{1}{2}I\partial\omega/\partial t = M^{-1}\left(\frac{1}{2}I\nabla s\right) \times M\mathbf{g} \tag{2}$$

from which equation (1) follows in any case where viscosity can be neglected (that is, where all forces acting on the sphere's surface are pressure forces which share

with the buoyancy the property of being directed through its centre).

Horizontal gradients of density, then, induce rates of change of horizontal vorticity components at right angles. For internal waves, this is well illustrated by the simple case of a plane wave.

On the Boussinesq approximation adopted in this paper, any vertical displacement h is resisted by a vertical force N^2h per unit mass where N is the Väisälä-Brunt frequency, here taken as uniform. Also, the velocity field is solenoidal, so that fluid motions must be perpendicular to the wavenumber vector; being directed up or down lines of steepest ascent in surfaces of constant phase under the combined action of the above vertical force and pressure gradients normal to those surfaces (WF,p.289). The resultant force along such a line, assumed at angle θ to the vertical, is $N^2h\cos\theta$ per unit mass; which, in opposing the acceleration of fluid $(\partial^2 h/\partial t^2)\sec\theta$, gives rise to oscillations with the familiar value

$$\sigma = N\cos\theta \qquad (3)$$

for the radian frequency σ (a letter used for frequency in this paper so that ω can be kept for vorticity).

But the oscillations in different surfaces of constant phase are by no means independent of each other. They take the form of a wave travelling in a direction n, normal to those surfaces, along which the phase of the oscillation changes at a rate 2π per wavelength. Thus, horizontal vorticity arises because the fluid velocity $(\partial h/\partial t)\sec\theta$ up the line of steepest ascent has a gradient $\partial/\partial n$ normal to the plane, so that the rate of change of horizontal vorticity is

$$\frac{\partial}{\partial n}\left(\frac{\partial^2 h}{\partial t^2}\sec\theta\right) = -N^2\cos\theta\frac{\partial h}{\partial n} \ ; \qquad (4)$$

which moreover does satisfy equation (1) because it is $(-g)$ times the horizontal gradient

$$\cos\theta\frac{\partial}{\partial n}(g^{-1}N^2h) \qquad (5)$$

of the relative excess density $s = g^{-1}N^2h$. Thus internal waves — even in the simple case of plane waves — involve shearing motions possessing horizontal vorticity, which in turn is always related to horizontal density gradients as indicated by equation (1).

Moreover, vorticity is important too for internal waves in general. For any solenoidal vector field (u, v, w) the relationship

$$curl\underline{\omega} = curl\,curl(u,v,w) = -(\nabla^2 u, \nabla^2 v, \nabla^2 w) \qquad (6)$$

4

is well known; here, its z-component (vertically upwards) gives

$$\frac{\partial}{\partial t}\nabla^2 w = -g\left(\frac{\partial^2 s}{\partial x^2} + \frac{\partial^2 s}{\partial y^2}\right) \qquad (7)$$

by equation (1). Now, since $\partial s/\partial t$ can be written as $g^{-1}N^2\partial h/\partial t$ or $g^{-1}N^2 w$, a second time-differentiation applied to (7) gives the full classical partial differential equation for internal waves:

$$\frac{\partial^2}{\partial t^2}\nabla^2 w = -N^2\left(\frac{\partial^2 w}{\partial x^2} + \frac{\partial^2 w}{\partial y^2}\right) . \qquad (8)$$

It is noteworthy, however, that equation (7) for the vertical component of $-\partial(curl\underset{\sim}{\omega})/\partial t$ included only the horizontal components ξ and η of $\underset{\sim}{\omega} = (\xi, \eta, \zeta)$. The propagation of these components, as was physically explained above, is intimately coupled to the propagation of velocities, densities and pressures in the wave. By contrast, the vertical component ζ does not propagate at all; rather, the vertical component of equation (1) gives

$$\partial\zeta/\partial t = 0 . \qquad (9)$$

We return in section 5 to some consequences of these different propagation properties for horizontal and vertical components of vorticity.

3   Group velocity in internal waves

Because in plane waves the fluid moves up and down the lines of steepest ascent in surfaces of constant phase, these are also the only possible directions of energy flux, specified as the mean product of fluid velocity and excess pressure. Another route to the same conclusion is based on viewing energy flux as the product of energy density with the group velocity U, defined as the gradient of the frequency σ in wavenumber space; thus, by equation (3), σ depends only on the direction and not on the magnitude of the wavenumber, so that its gradient U must be perpendicular to the wavenumber vector itself.

This is why crests of internal waves are observed (WF, figure 77) to stretch out radially from a source of wave energy. Actually, crests above the source appear to be travelling diagonally downwards (and crests below it diagonally upwards), reflecting the fact that the wavenumber vector and the group velocity always have vertical components of opposite sign.

Figure 1 makes this clear by showing how the direction of steepest ascent, specified in section 2 as making an angle θ to the vertical, represents the direction

of the group velocity for a wavenumber direction pointing along the downward normal to the surface of constant phase — simply because the frequency $\sigma = N \cos \theta$ increases in the direction θ decreasing. Also, the magnitude of U is $NK^{-1} \sin \theta$ in terms of θ and the magnitude K of the wavenumber.

In an initial-value problem, we may be interested in how different Fourier components in the initial disturbance (assumed confined to a limited volume) are subsequently propagated. Essentially, their energy moves a distance $\mathbf{U}t$ in time t. Therefore, in spherical polar coordinates (r, θ, ϕ), defined so that Cartesian coordinates (x, y, z) with z vertically upwards take the form

$$x = r \sin \theta \cos \phi, \; y = r \sin \theta \sin \phi, \; z = r \cos \theta, \qquad (10)$$

their position can be written

$$r = NK^{-1}t \sin \theta, \; \theta = \theta, \; \phi = \phi \qquad (11)$$

in terms of a definition of spherical polar coordinates (K, θ, ϕ) in wavenumber space such that the Cartesian form (k, l, m) of the wavenumber (with its direction diagonally downwards as in figure 1) is

$$k = K \cos \theta \cos \phi, \; \ell = K \cos \theta \sin \phi, \; m = -K \sin \theta. \qquad (12)$$

Equation (11) means that, at time t, two adjacent wave crests (a distance $2\pi K^{-1}$ apart) stretching out radially from the source region make an angle

$$(2\pi K^{-1})/r = 2\pi/(Nt \sin \theta); \qquad (13)$$

which, as observed experimentally (WF, figure 77), diminishes as t increases — and also as θ increases. For very small θ (near-vertical oscillations of fluid with frequency almost $=N$) the near-vertical energy propagation becomes very slow indeed; on the other hand, for θ near $\frac{1}{2}\pi$ (near-horizontal oscillations of fluid with frequency $\ll N$), the near-horizontal group velocity approaches the substantial value NK^{-1}.

As t increases, changes in the amplitude of waves of given wavenumber depend on changes in the volume $r^2 \sin \theta \, dr \, d\theta \, d\phi$ of physical space taken up by waves from a given elementary volume $K^2 \cos \theta \, dK \, d\theta \, d\phi$ of wavenumber space. By equation (11), this ratio is

$$\frac{r^2 \sin \theta}{K^2 \cos \theta} \left(\frac{\partial r}{\partial K} \right)_{\theta, \phi} = \frac{r^2 \sin \theta}{K^2 \cos \theta} \left(-\frac{Nt}{K^2} \sin \theta \right); \qquad (14)$$

6

where the minus sign, of course, just implies a reflection and does not affect the volume change itself, given by the modulus of expression (14).

This modulus can most usefully be expressed, either with r eliminated as $t^3 |J|$, with

$$J = -N^3 K^{-6} \sin^4 \theta \sec \theta \qquad (15)$$

as the Jacobian of the group velocity in wavenumber space (WF, p.358); or else with K eliminated as

$$r^6 (Nt)^{-3} \operatorname{cosec}^2 \theta \sec \theta . \qquad (16)$$

The first form, written $t^3 |\det A|$ in the Appendix (where initial-value problems are treated for general linear homogeneous dispersive systems), demonstrates now the volume occupied by waves from a given volume element of wavenumber space necessarily increases as t^3 — so that their energy density diminishes as t^{-3} and their amplitude as $t^{-3/2}$. At the same time the second form (16) will also be found (section 4) to offer useful information on amplitude distributions.

4 Waves excited by an initial local disturbance to uniform stratification

The initial-value problem for stratified fluid on the Boussinesq approximation, given that arbitrarily chosen small disturbances to uniform stratification initially occupy just a limited volume of fluid, is concerned first with identifying the waves generated (the subject of this section) and then with determining (see section 5) any residual motions that remain after the waves have been propagated away. Disturbances to uniform stratification may take the form of

(i) initial vertical displacements h of fluid; along with

(ii) an initial, necessarily solenoidal, distribution of fluid velocities (u, v, w).

We show first that the waves generated are uniquely determined given the initial distributions of h and of $\partial h / \partial t = w$. Then we study (section 5) to what extent this determination has solved the entire initial-value problem.

Both of the variables $w = \partial h / \partial t$ and h satisfy the same equation (8), with its dispersion relationship (3) linking the frequency σ to the polar angle θ in the definition (12) of wavenumber. Now section 2 of the Appendix obtains the solution of a general initial-value problem for a linear homogeneous system with a given dispersion relationship and with given initial values for a dependent variable

7

h and for its time derivative. Here – quite briefly– we apply this solution to internal waves and physically interpret it.

The analysis in section 2 of the Appendix supposes the frequency to be specified as a positive function $\sigma(\mathbf{k})$ which takes the same positive value for wavenumbers $\mathbf{k}$ and $-\mathbf{k}$. These conditions are satisfied by expression (3) for σ provided that the value of θ appearing in (12) is constrained to lie between $-\frac{1}{2}\pi$ and $\frac{1}{2}\pi$. Next, the functions $F(\mathbf{k})$ and $G(\mathbf{k})$ is wavenumber space are defined so that the initial values of h and $\partial h/\partial t$ have the Fourier Transforms given in equation (6) of the Appendix..

The waves then take, at any time $t > 0$, the exact form given in equation (4) of the Appendix – which moreover can be usefully approximated in an asymptotic procedure where t is allowed to become large while the ratio $\mathbf{x}/t$ remains constant. These asymptotics are based on the stationary-phase method (section 1 of the Appendix) and the conclusions are expressed in terms of the wavenumber $\mathbf{k}_s$ which for given $\mathbf{x}/t$ satisfies the condition of stationary phase (equation (8) of the Appendix). Physically, $\mathbf{k}_s$ is the wavenumber for which the group velocity $\mathbf{U}(\mathbf{k}_s)$ takes the value $\mathbf{x}/t$, so that energy associated with it has just reached the point $\mathbf{x}$ at time t. Then the asymptotic form of h is expressed in terms of $\mathbf{k}_s$ by expression (12) of the Appendix; here, A represents the matrix of second derivatives of $\sigma(\mathbf{k})$ at $\mathbf{k} = \mathbf{k}_s$, with $\det A$ as its determinant and S as its signature (the number of positive, minus the number of negative, eigenvalues).

In the special case of internal waves the relationship between $\mathbf{k}_s$ and $\mathbf{x}/t$ is precisely that which is embodied in equations (10), (11) and (12) above. Moreover, $\det A$ is the Jacobian (15), and the signature S can be shown to be 1 (the determinant's negative value being associated with the fact that just one of its three eigenvalues is negative).

But this special case of internal waves exhibits one very striking exceptional feature. The fact that the group velocity $\mathbf{U}$ is orthogonal to the wavenumber $\mathbf{k}$ means that $\mathbf{x} = \mathbf{U}(\mathbf{k}_s)t$ is itself orthogonal to $\mathbf{k}_s$ so that the term $\mathbf{k}_s \cdot \mathbf{x}$ which appears in the phase of the asymptotic expression (equation (12) of the Appendix) is everywhere zero! In short, the exponentials in it take the forms

$$e^{\pm iNt\cos\theta} , \tag{17}$$

8

which apparently describe mere oscillations at the frequency $\sigma = N \cos \theta$. What then has happened to the wavelike character of the disturbances?

The answer is that, although at any fixed position these exponentials rightly represent oscillations with frequency (3), nevertheless the wavelike nature of the disturbances is apparent from the spatial dependence of θ as defined in equation (8). Indeed a phase $Nt \cos \theta$ has a gradient in the direction (θ increasing, as figure 1 shows) of the wavenumber vector equal to

$$\frac{1}{r} \frac{\partial}{\partial \theta}(Nt \cos \theta) = -\frac{Nt \sin \theta}{r} ,$$ (18)

which by (11) takes the expected value of minus the wavenumber's magnitude K.

Against this background, expression (12) of the Appendix for the waves generated can now be written in two alternative forms. The first, with the Jacobian $J = \det A$ represented in terms of wavenumber as in (15), expresses the waves of given wavenumber $\pm \mathbf{k}$ at time t as

$$h \sim \left(\frac{2\pi}{Nt}\right)^{3/2} \frac{K^3 \cos^{1/2} \theta}{\sin^2 \theta} e^{i\pi/4} \left[F(\mathbf{k})e^{iNt \cos \theta} + G(-\mathbf{k})e^{-iNt \cos \theta} \right]$$ (19)

(with equations (12) defining K and θ). Expression (19) shows their expected decay as $t^{-3/2}$, associated with an increase like t^3 in the volume occupied by waves from a given element of wavenumber space. That increase is, of course slowest wherever the magnitude $NK^{-1} \sin \theta$ of the group velocity is smallest; as happens

(i) for waves of large wavenumber K — which, however, are subject to an additional viscous decay (WF, p.349) like

$$e^{(-1/2)\upsilon K^2 t}$$ (20)

in terms of the kinematic viscosity υ; and

(ii) for very small values of θ, corresponding to wavenumbers (12) with vertical component almost zero so that wave energy exhibits only very slow propagation (in the vertical direction).

9

Any such singularity around $\theta = 0$ disappears, however, when we adopt the more useful second alternative form for the wave asymptotics.

This represents $t^3 |\det A|$ in terms of position in space as in (16), and expresses the waves found at position (10) after time t as

$$h \sim \frac{(2\pi N t)^{3/2}}{r^3} (\sin\theta \cos^{1/2}\theta) e^{i\pi/4} \left[F(\mathbf{k}) e^{iNt\cos\theta} + G(-\mathbf{k}) e^{-iNt\cos\theta} \right] . \qquad (21)$$

where $\mathbf{k}$ is given by equations (12) with $K = N r^{-1} t \sin\theta$. Here, there is no singularity as $\theta \to 0$; moreover, any apparent growth for large t is suppressed by the viscous decay factor (20) – wherein K itself is increasing with t.

In summary, then, the initial-value problem for internal waves has this useful general asymptotic solution (21) as $t \to \infty$ for given r/t and θ. Moreover, the demonstration in section 3 of the Appendix that waves excited by any transient local forcing of the system taken an identical form (with $F(\mathbf{k})$ and $G(\mathbf{k})$ expressed rather simply in terms of the spatiotemporal Fourier Transform of the forcing function) adds to the utility of this very general result.

5 Residual motions left behind after waves have been propagated away

We return now to the question about initial-value problems posed in the first paragraph of section 4. Initial disturbances to uniform stratification may include a distribution of vertical displacements h and also a (solenoidal) distribution of fluid velocities (u, v, w); yet the initial distributions of h and w alone suffice to determine the waves generated.

Moreover the solenoidality condition

$$\partial u/\partial x + \partial v/\partial y = -\partial w/\partial z , \qquad (22)$$

taken together with the definition

$$\partial v/\partial x - \partial u/\partial y = \zeta \qquad (23)$$

of the vertical component of vorticity, imply that, in each horizontal plane $z = $ constant, knowledge of w fixes only the two-dimensional divergence – whereas both its value and that of ζ are needed to determine uniquely the velocity field (u, v), in that plane.

This conundrum's resolution comes from equation (1), and above all from its vertical component (9). We have just seen that general initial disturbances may

10

separately determine, not only those distributions of h and w which were shown in section 4 to excite waves, but also a distribution of the value (23) of ζ – while, conversely, the distributions of w and of ζ determine those of u and of v. But equation (9) assures us that the initial distribution of ζ remains unchanged as the waves propagate away.

Accordingly, when this propagation has reduced to zero the values of h and w in the limited region of the initial disturbance, equation (22) has zero on the right-hand side whereas the righthand side of equation (23) has never varied; so that the distribution of (u, v) in any plane $z =$ constant has become that vector field with zero two-dimensional divergence which is specified by the unchanging vorticity distribution (23). Moreover, since the density is uniform in that plane (because h has become zero), this steady horizontal velocity field feels no dynamic effects of fluid stratification.

It may seem paradoxical at first sight that the ultimate steady velocity distribution (u, v) is fixed quite separately in each plane $z =$ constant by the (unchanging) initial distribution of ζ in that plane. Clearly, between the different two-dimensional motions in adjacent horizontal planes, a shear must in general be present – which implies nonzero horizontal components ξ, η of the vorticity $\underline{\omega}$. Yet these are components which are coupled to the wave motions by equation (1) so that fluctuations in ξ and η must accompany propagation of the waves.

This paradox too can be finally resolved by observing that the ultimate motions in each horizontal plane are steady motions; thus, the associated shears, and the corresponding vorticity components ξ and η, show no variation with time. But it is only the time-variation of ξ or η which equation (1) couples to density variations. In the asymptotic state where all density variations have been propagated away, equation (1) allows nonzero distributions of ξ and η to remain in the region of the initial disturbance provided that – as has been found here– they do not change with time.

References
Jones, D.S. 1982 *The theory of generalised functions.* Cambridge University Press.

Lighthill, M.J. 1958 *An introduction to Fourier Analysis and Generalised Functions.* Cambridge University Press.

Lighthill, J. 1978 *Waves in Fluids* (referenced in this paper as WF). Cambridge University Press.

Appendix: general mathematical background on homogeneous linear dispersive-wave systems.

James Lighthill

In this Appendix, general initial-value problems for a homogeneous linear dispersive-wave system are solved expeditiously by an elegant method due to Jones (1982) for handling multidimensional stationary-phase problems. Afterwards, waves generated by given transient forcing effects are analysed, and proved equivalent to well defined initial-value problems.

1. Stationary phase in N dimensions

Asymptotic estimation by stationary phase is capable of rigorous validation by complex-variable methods as in WF, sections 3.7 (in one dimension) and 4.8 (in two or three dimensions), but the proofs become arduous in more than one dimension. Purely real-variable methods, as used by Jones (1982), are more transparent.

They start from the simple principles of Fourier Asymptotics which are set out for functions of a single real variable in chapter 4 of Lighthill (1958). These principles allow the asymptotic behaviour of a function's Fourier Transform to be deduced from the function's behaviour near its singularities by writing down directly the Fourier Transforms of expressions which represent that singular behaviour to a first approximation.

Then a one-dimensional stationary-phase integral such as

$$\int F(k) \exp\left[it\psi(k)\right] dk, \tag{1}$$

where neither the amplitude function $F(k)$ nor the phase function $\psi(k)$ has singularities, is readily estimated for large t by making the substitution $\psi(k) = y$. This converts it into a Fourier integral but introduces, of course, an additional singularity at every stationary point of $\psi(k)$; after which Fourier Asymptotics, as applied to the new integrand's singular behaviour near such points, yields directly the usual results of stationary-phase theory.

Correspondingly, the same integral (1) with k a vector in N-dimensional space is estimated asymptotically (Theorem 9.14 of Jones 1982) as a sum of contributions from stationary points k_s of $\psi(k)$. These, of course, are points where the

first derivatives of $\psi(k)$ all vanish so that the local behaviour of ψ is dominated by its matrix A of second derivatives. The contribution from every such point where the matrix A is nonsingular is found to be

$$(2\pi/t)^{N/2} F(k_s)\, |\det A|^{-1/2}\, e^{i[t\psi(k_s)+\pi S/4]} \tag{2}$$

in terms of the determinant, $\det A$, and the signature S of that matrix. (Conceptually, this result can be interpreted in terms of the corresponding one-dimensional result by rotating the axes so that the quadratic form representing the local behaviour of $\psi(k) - \psi(k_s)$ becomes a sum of squares of components of $k - k_s$ with coefficients whose product is $\det A$ while S is the number of positive minus the number of negative coefficients.)

2. Linear homogeneous dispersive systems

A linear homogeneous dispersive system is one where plane waves with vector wavenumber $k = (k_1, k_2, k_3)$ have radian frequency σ equal to a well defined function $\sigma(k)$; here, we always take σ as positive, and as having the same positive value for wavenumber k as for wavenumber $-k$. Its gradient, the group velocity

$$\partial\sigma/\partial k_j = U_j(k_1, k_2, k_3), \tag{3}$$

represents the velocity of energy propagation in these waves. Necessarily, it is an odd function of k (since σ is even); thus waves with wavenumbers k and $-k$, whose crests move in opposite directions, also have their energy travelling away from any source in diametrically opposite directions.

Now, a general linear combination

$$h = \int F('k) e^{i[\sigma(k)t - k.x]} dk + \int G(k) e^{-i[\sigma(k)t + k.x]} dk \tag{4}$$

of such plane waves (respectively, of wavenumbers k and $-k$) has initial values of h and $\partial h/\partial t$ equal to

$$\int [F(k)+G(k)] e^{-ik.x} dk \quad \text{and} \quad \int i\sigma(k)[F(k) - G(k)] e^{-ik.x} dk. \tag{5}$$

Accordingly, equation (4) gives the wave propagation resulting from arbitrarily chosen initial values of h and $\partial h/\partial t$ if these values' Fourier Transforms are, respectively, expressed as

$$F(k)+G(k) \quad \text{and} \quad i\sigma(k)[F(k)-G(k)]. \tag{6}$$

13

Moreover, the asymptotic behaviour for large t of each integral in (4) is obtained by the same method, which is set out here for just the first of them.

This assumes the form (1) with

$$\psi(\mathbf{k}) = \sigma(\mathbf{k}) - (\mathbf{k}.\mathbf{x})/t, \qquad (7)$$

and the required asymptotic estimate is made for fixed $\mathbf{x}/t$ as $t \rightarrow \infty$. The stationary points $\mathbf{k}_s$ of ψ are points where

$$\mathbf{U}(\mathbf{k}_s) = \mathbf{x}/t, \qquad (8)$$

so that the method identifies the waves appearing for $\mathbf{x}/t$ as those whose energy travels at velocity $\mathbf{U}$ given by equation (8). Also, the matrix A is simply the matrix of second derivatives of $\sigma(\mathbf{k})$ itself (since the last term in (7) is linear), and its determinant can be written as a Jacobian,

$$\det A = \frac{\partial(U_1, U_2, U_3)}{\partial(k_1, k_2, k_3)}, \qquad (9)$$

for the first derivatives (3) — which are the components of the group velocity vector.

Physically, this happens because equation (8) represents a mapping

$$k_j \rightarrow x_j = tU_j(\mathbf{k}) \qquad (10)$$

between the space of wavenumbers $\mathbf{k}$ and the physical locations $\mathbf{x}$ where such wavenumbers are found at time t. Accordingly, the volume element $d\mathbf{x}$ in physical space that is occupied by waves with wavenumber $\mathbf{k}$ lying in a volume element $d\mathbf{k}$ is given by the Jacobian of the mapping (10) as

$$d\mathbf{x} = \left| \frac{\partial(tU_1, tU_2, tU_3)}{\partial(k_1, k_2, k_3)} \right| d\mathbf{k} = t^3 |\det A| \, d\mathbf{k}, \qquad (11)$$

and the three-dimensional dependence (2) of amplitude on $t^{-3/2} |\det A|^{-1/2}$ reflects this spreading of the energy from these waves over an increasing volume (11).

The wavenumber $(-\mathbf{k})$ for the second integral in (4) is similarly identified as $\mathbf{k}_s$ by the stationary-phase condition $U(\mathbf{k}) = -\mathbf{x}/t$, and it follows that the asymptotic behaviour of (4) taken as a whole is

$$h \sim (2\pi/t)^{3/2} |\det A|^{-1/2} e^{\pi S/4} \left\{ F(\mathbf{k}_s) e^{i[\sigma(\mathbf{k}_s)t - \mathbf{k}_s.\mathbf{x}]} + G(-\mathbf{k}_s) e^{-i[\sigma(\mathbf{k}_s)t - \mathbf{k}_s.\mathbf{x}]} \right\}. (12)$$

Thus both terms in this solutions of the initial-value problem represent waves with the wavenumber $\mathbf{k}_s$ defined by equation (8), as expected on energy-propagation grounds.

14

3. Effects of transient forcing

Another interesting question related to a general linear homogeneous dispersive system concerns the waves produced by a purely transient local forcing of the system. The question is relevant to the subject of this paper because analysis of such waves identifies them as those arising in a certain precisely related initial-value problem.

An equation such as

$$B\left(-i\frac{\partial}{\partial t},\ i\frac{\partial}{\partial x_1},\ i\frac{\partial}{\partial x_2},\ i\frac{\partial}{\partial x_3}\right) h = q(\mathbf{x}, t) \tag{13}$$

may represent transient forcing of waves in a linear homogeneous dispersive system, for which the unforced system ($Bh = 0$) has the dispersion relationship

$$B(\sigma, k_1, k_2, k_3) = 0. \tag{14}$$

The forcing term $q(x, t)$ may be written as a four-dimensional Fourier integral

$$q(x, t) = \int_{-ia-\infty}^{-ia+\infty} e^{i\sigma t} d\sigma \int Q(\sigma, \mathbf{k}) e^{-i\mathbf{k}.\mathbf{x}} d\mathbf{k} \tag{15}$$

(for $a > 0$) where the inner integral is taken over the whole wavenumber space. The outer integral is taken along a line below the real axis in the complex plane so that the system is completely undisturbed for large negative t (when the modulus of $e^{i\sigma t}$ tends to zero).

We are interested in the solution of equation (13) for an initially undisturbed system, and the expression (15) for q allows this to be written down immediately as

$$h = \int_{-ia-\infty}^{-ia+\infty} e^{i\sigma t} d\sigma \int \frac{Q(\sigma, \mathbf{k})}{B(\sigma, \mathbf{k})} e^{-i\mathbf{k}.\mathbf{x}} d\mathbf{k}, \tag{16}$$

provided that the system is a stable one. (This condition implies that no poles of the integrand below the real axis can be present as a result of the dispersion relationship (14) possessing any solution for σ with negative imaginary part; therefore, the outer integral can be deformed into a path far below the real axis and must be initially zero.)

For large positive t, on the other hand, the integral with respect to σ (for each value of k), should be deformed into a path above the real axis — which may involve passing over any poles of the integrand on the real axis such as are identified by the dispersion relationship (14). When this defines a single positive

15

frequency $\sigma(\mathbf{k})$ for each $\mathbf{k}$, the poles are $\sigma(\mathbf{k})$ and $-\sigma(\mathbf{k})$, and each of them makes a contribution equal to $2\pi i$ times that residue of the integrand which is given when we replace the denominator by its derivative $\partial B/\partial \sigma$ (henceforth written as B_σ).

From this process, it follows that h takes the form (4) characteristic of initial-value problems, with the functions $F(\mathbf{k})$ and $G(\mathbf{k})$ defined as

$$F(\mathbf{k}) = 2\pi i \frac{Q(\sigma(\mathbf{k}), \mathbf{k})}{B_\sigma(\sigma(\mathbf{k}), \mathbf{k})}, \quad G(\mathbf{k}) = 2\pi i \frac{Q(-\sigma(\mathbf{k}), \mathbf{k})}{B_\sigma(-\sigma(\mathbf{k}), \mathbf{k})} \tag{17}$$

(Actually, the two denominators in (17) are identical but for a difference in sign if, as we assume, B is an even function of σ).

This reduction of the transient-forcing problem to a well defined initial-value problem means that it possesses the same asymptotic solution (12). From a physical viewpoint the interesting aspect of this conclusion is that, apart from factors which depend only on the wave system itself, the wave amplitudes are influenced by the actual forcing effect $q(\mathbf{x}, t)$ only through factors $Q(\pm\sigma(\mathbf{k}), \mathbf{k})$ which relate to "resonant" terms in the spatiotemporal Fourier Transform of $q(\mathbf{x}, t)$; that is, to terms with frequencies and wavenumbers in the precise dispersion relationship.
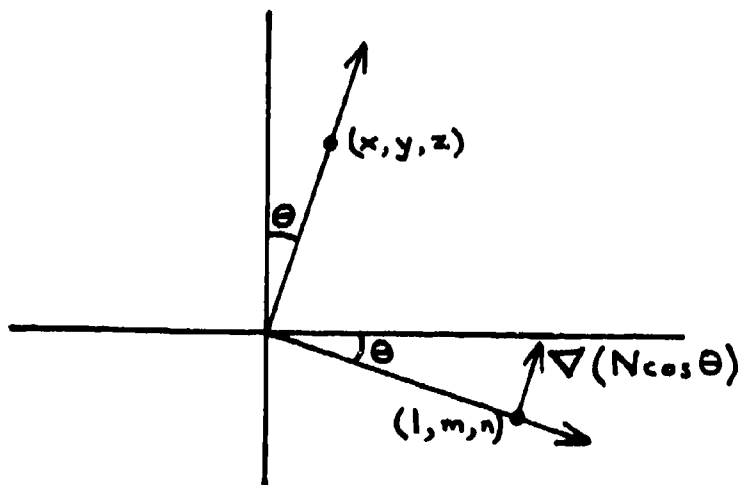
Figure 1. Wherever the vertical component m of a wavenumber vector (k, ℓ, m) with magnitude K takes the negative value $m = -K\sin\theta$, the group velocity given by the gradient of $\sigma = N\cos\theta$ points diagonally upwards (in the direction θ decreasing) through position vectors (x, y, z) with magnitude r for which the vertical component z takes the positive value $z = r\cos\theta$.

Wave Packet Critical Layers in Stratified Shear Flows

S.A. Maslowe

Institute of Geophysics and Planetary Physics
University of California, San Diego 92093-0225

Abstract

In the inviscid theory of shear flow stability, the eigenvalue problem for a neutral or weakly amplified mode revolves around possible discontinuities in the eigenfunction as the singular critical point is crossed. Extensions of the linear normal mode approach to include nonlinearity and/or wave packets lead to amplitude evolution equations whose coefficients generally involve singular integrals. In the past, viscosity, nonlinearity or time dependence has been introduced in a critical layer centered upon the singular point to resolve these integrals. The form of the amplitude evolution equation is greatly influenced by which choice is made. In this paper, a new approach is proposed in which wave packet effects are dominant in the critical layer and it is argued that in many applications this is the appropriate choice. The theory is applied here to two-dimensional wave propagation in stratified shear flows.

1. Introduction

The normal mode approach to investigating the stability of a stratified shear flow involves superimposing a small wavelike perturbation on the basic flow and determining its subsequent evolution with time. Because the Reynolds number is large in most geophysical applications, it is reasonable to employ inviscid theory. We consider perturbations to a locally parallel flow with velocity and density profiles $\overline{u}(y)$ and $\overline{\rho}(y)$, respectively.

The case of a disturbance that is periodic in space and time (i.e., a neutral mode) turns out to be quite significant. A characteristic feature of neutral modes in shear flows, as opposed to, say, Bénard convection is the presence of a critical point singularity which occurs at that value of y (the critical point y_c) where $\overline{u} = c$, the phase speed of the perturbation. The resolution of this difficulty in the classical theory consists of restoring viscosity within a thin 'critical layer' centered upon the point y_o. One consequence is that a discontinuity in Reynolds stress occurs across the critical layer, giving rise to the unstable oscillations known as Tollmien-Schlichting waves. The same mechanism was employed by Miles (1957) in a theory for the generation of water waves by wind.

A somewhat different class of problems responsible for much of the more recent interest in neutral modes consists of forced wave initial-value problems. These are not at all hydrodynamic stability problems in the traditional sense but the mathematics involved, as well as the language utilized, are similar. An example is the investigation by Booker and Bretherton (1967) of the upward propagation of gravity waves toward a critical level. The perturbation in this case is forced by a wavy boundary introduced at time $t = 0$. On the basis of a linear analysis, Booker and Bretherton argued that most of the wave energy would be absorbed in the critical layer. If this conclusion turns out to be correct, then critical layer absorption could serve as a significant mechanism to limit the propagation of wave energy into the upper atmosphere. However, for $t \gg 1$ the horizontal component of the perturbation velocity becomes infinite and, consequently, the linearization is no longer valid. Attempts to continue the analysis by introducing nonlinear terms in the critical layer are reviewed in a survey article by Stewartson (1981). Recent evidence suggests that some energy is transmitted beyond the critical level and more is reflected.

The absorption described above, as well as the Tollmien-Schlichting instability mechanism, is the result of a 'phase change' occurring across the critical layer. This so-called phase change is represented in the mathematical analysis by branch point singularities arising in the linear, inviscid solutions, as will be outlined below. Specifically, quantities written as $(y - y_c)$ for $y > y_c$, take the form $| y - y_c | \exp (-i\pi)$ for $y < y_c$. In linear initial-value problems, such as the one treated by Booker and Bretherton, this rule is arrived at by considering the long-time behavior of an inviscid flow, whereas in the classical theory the same result is obtained from an asymptotic large Reynolds number analysis of the Orr-Sommerfeld equation.

Any notion that the $-\pi$ phase change is a universal result was dispelled, however, by the recent development of a nonlinear critical layer theory. Benney and Bergeron (1969) showed that across a critical layer dominated by nonlinear effects, rather than viscosity, there is no phase change at all. One consequence is that the inviscid eigenvalue problem admits an entirely new class of waves which were computed for a number of shear flows by Benney and Bergeron. Such neutral modes are of particular interest in geophysical fluid dynamics because the Reynolds numbers in geophysical shear flows are typically very large and, therefore, a nonlinear critical layer is more appropriate than one in which diffusive effects dominate. Applications in geophysical fluid dynamics and other aspects of the theory, such as viscous effects, are reviewed in a survey article by Maslowe (1986).

The first attempt to introduce time dependence into the nonlinear critical layer theory is contained in the paper by Benney and Maslowe (1975). It was found advantageous in that work to generalize the monochromatic normal mode approach by considering wave packets. This, in any case, is consistent with a trend evident during the past 20 years in research on both stability and wave motion which is motivated by the observation that in nature, as well as in many experiments, disturbances are more likely to be packets than monochromatic waves.

Suppose that, instead of a single Fourier mode, we consider a disturbance in the form of a wave packet whose horizontal length scale is $O(1/\mu)$, with $\mu \ll 1$. The evolution of such a packet can be studied using the method of multiple scales by introducing an amplitude $A(X, T)$ which varies slowly in space and time; X and T are slow scales appropriate for describing the long-time evolution of an associated initial-value problem. The quantity $A(X, T)$ satisfies a partial differential equation which often turns out to be the Ginzburg-Landau equation in weakly nonlinear stability investigations. Let us consider only the linear portion of the amplitude equation and suppose that there is some parameter R in the problem (other than the wave number) such that instability occurs for R slightly greater than R_n, its neutral value. Under these circumstances, A satisfies the PDE

$$\mu\left(\frac{\partial A}{\partial T} + \frac{\partial \omega}{\partial \alpha}\frac{\partial A}{\partial X}\right) - \frac{1}{2}i\mu^2\frac{\partial^2\omega}{\partial\alpha^2}\frac{\partial^2 A}{\partial X^2} + \ldots = \frac{\partial\omega}{\partial R}(R - R_n)A, \tag{1}$$

where α, the wave number, is real and ω in stability problems is often complex with its real part being the frequency. The quantities $\partial^n\omega/\partial\alpha^n$ are given by expressions involving integrals which may be singular in the inviscid theories. The specific manner of computing these coefficients will vary from one problem to the next, but what is important is that the general form of (1) always applies provided that the dispersion relation is analytic.

This paper presents a new approach to dealing with critical layers arising from the propagation of wave packets satisfying (1). It will be shown that if $\mu \gg \epsilon^{1/2}$, where ϵ is an amplitude parameter, an inviscid linear critical layer theory can be developed which, in some sense, is related to the initial-value problem for a packet. After outlining the linear theory, it will be indicated how nonlinear effects can be incorporated into the critical layer analysis and the influence of nonlinearity on the outcome is discussed.

2. Waves in stratified shear flows

To illustrate the basic idea as simply as possible, we consider the equation stating that the density of a fluid particle remains constant in a stratified flow, viz., $D\rho/Dt = 0$. The perturbation $\hat{\rho}(x, y, t)$ to the mean density $\overline{\rho}(y)$, in linear inviscid theory, satisfies

$$\frac{\partial\hat{\rho}}{\partial t} + \overline{u}\frac{\partial\hat{\rho}}{\partial x} = \overline{\rho}'\frac{\partial\hat{\psi}}{\partial x}, \tag{2}$$

where $\hat{\psi}$ is the perturbation stream function. If we consider normal mode disturbances proportional to $\exp\{i\alpha(x - ct)\}$, then the y - dependent part of $\hat{\rho}$ satisfies

$$\rho(y) = \frac{\overline{\rho}'}{\overline{u} - c}\phi, \tag{3}$$

where $\phi(y)$ satisfies the Taylor-Goldstein equation. In the case of a neutral mode, c is real and has algebraic branch points where $\bar{u} = c$. Clearly, ρ is more singular than ϕ and it will now be shown how the notion of a wave packet can be used to eliminate the singularity.

We introduce the slow variables $X = \mu x$ and $T = \mu t$ and consider somewhat more general perturbations by writing

$$\hat{\psi} = \phi(X,y,T)e^{i\alpha(x-ct)} \text{ and } \hat{\rho} = \rho(X,y,T)e^{i\alpha(x-ct)}. \tag{4}$$

Multiple scaling transforms the x and t derivatives according to

$$\frac{\partial}{\partial x} \to i\alpha + \mu\frac{\partial}{\partial X} \text{ and } \frac{\partial}{\partial t} \to -i\alpha c + \mu\frac{\partial}{\partial T}$$

and introducing this transformation into (2) leads to the following partial differential equation (PDE) for ρ:

$$\left[(\bar{u} - c) - \frac{i\mu}{\alpha}\left(\bar{u}\frac{\partial}{\partial X} + \frac{\partial}{\partial T}\right)\right]\rho = \bar{\rho}'\left(1 - \frac{i\mu}{\alpha}\frac{\partial}{\partial X}\right)\psi. \tag{5}$$

Clearly, (5) reduces to the singular equation (3) in the limit $\mu = 0$; but for a finite bandwidth packet (i.e., $\mu > 0$) the singularity is no longer present. We seek a solution of (5) by expanding ρ in powers of μ and write

$$\rho = A(X,T)\rho_1(y) + \mu A_X\rho_2 + \mu^2 A_{XX}\rho_3 + \ldots, \tag{6}$$

where A satisfies the usual equation for a linear wave packet, namely,

$$A_T = c_g A_X + \frac{i\mu}{\alpha}dA_{XX} = 0. \tag{7}$$

Here, $c_g = \omega'$ is the group velocity and d is proportional to ω'' [cf.(1)]. The generalization of the Taylor-Goldstein equation for ϕ is accomplished in a similar manner. Due to its length, this PDE is not reproduced here, but for the interested reader it is equation (3.5) in the recent paper by Maslowe, Benney and Mahoney (1994).

Of course, the lowest-order terms in (6) and the corresponding expansion for ϕ will be singular at the critical point. However, Maslowe et al. have shown that the transition relations across the critical point can be determined by introducting a critical layer of thickness μ. Appropriate inner variables are

$$Y = (y - y_c)/\mu, \quad \Phi = \mu^{-\gamma}\phi \text{ and } P = \mu^{\gamma}\rho, \tag{8}$$

where γ is a function of J_c, the local Richardson number at the critical point in the case $J_c < 1/4$, whereas for $J_c \geq 1/4$, $\gamma = 1/2$.

Substituting the variables (8) into the inviscid, linearized Boussinesq equations leads to the inner equation

$$\left(Y + \frac{i}{p}\frac{\partial}{\partial X}\right)^2\Phi_{YY}^{(0)} + J_c\Phi^{(0)} = 0, \tag{9}$$

where $p = \alpha\bar{u}_c'/(c_g - c)$ and $\Phi^{(0)}$ is the leading term in an expansion of Φ. Note that the group velocity appears because, to lowest order, $A_T = -c_g A_X$ according to (7) and this result has been used to eliminate time-dependence.

Solving (9) is far from a trivial matter but the information of greatest interest, i.e., the phase change, can be determined by employing a Fourier transform in X followed by large $|Y|$ asymptotics. An interesting and subtle point has to do with the behavior of $\Phi^{(0)}$ as $X \to \infty$ in the case of a neutral mode. A singularity on the real axis in the wavenumber space arises after taking the Fourier transform of (9) and a radiation condition must then be imposed in order to decide which way to indent the contour when inverting the transform. This condition in the case $c_g > c$ is that upstream of the disturbance the presence of the packet is not sensed so that $\Phi^{(0)} \to 0$ as $X \to \infty$. (Note that (7) implies that we are in a frame of reference moving with the packet at the group velocity.) Conversely, when $c_g < c$, individual wave crests are moving faster than the packet and, as a result, $\Phi^{(0)} \to 0$ downstream of the packet, i.e., as $X \to -\infty$.

It develops that in both cases asymptotic matching of the critical layer solution to the outer expansion requires that we write $Y = e^{-i\pi}|Y|$ as $Y \to -\infty$, i.e., the phase change is $-\pi$. This assumes that $\bar{u}'_c > 0$; for $\bar{u}'_c < 0$ the phase change is π, exactly as in the classical theory. As a consequence, the theorems proved by Miles (1961) using Frobenius expansions of the Taylor-Goldstein equation are applicable to flows with a wave packet critical layer.

As mentioned in §1, there is a great deal of interest in the critical layer absorption problem with $J_c > 1/4$. The conclusions of Booker and Bretherton, based on the phase changes first derived by Miles, are not contradicted by the present analysis in the *linear* case. However, the solutions found by Booker and Bretherton break down as $t \to \infty$. Diffusive effects (viscosity and heat-conduction) can be introduced to deal with the singularity as shown by Hazel (1967).

The present approach, on the other hand, does not require the use of diffusive effects. Moreover, wave packets are probably a more appropriate choice than diffusion because disturbances in the real atmosphere and oceans are unlikely to be monochromatic. Wave packets have also been employed by Winters and Riley (1992) using ray theory and multiple scales. Their analysis, however, leads to critical point singularities as $t \to \infty$ which must be resolved by introducing diffusion. The present formulation avoids such breakdowns by using matched asymptotic expansions and scales appropriate to the long-time critical layer dynamics.

3. Nonlinear effects

The ultimate goal of the wave packet critical layer theory is to deal with situations where nonlinearity is present at the same time as packet dispersion. When J_c, the local Richardson number, is equal to or greater than 1/4 the nonlinear critical layer thickness is $\epsilon^{2/3}$ so the balance of interest is $\mu = \epsilon^{2/3}$ and we are discussing forced waves.

Brown and Stewartson (1980) have considered the inviscid initial-value problem with the early stage described by linear theory and the onset of nonlinearity is described by a quasi-steady nonlinear critical layer analysis. The initial breakdown of linear theory occurs when $t \sim O(\epsilon^{-2/3})$ and to go beyond this point an expansion in powers of $T = \epsilon^{2/3}t$ was employed to determine the first effects of nonlinearity. It was found that the latter consist of an exponentially small transmitted wave and a more significant reflected wave.

Troitskaya (1991), on the other hand, considered the steady problem for forced waves when both non-linearity and diffusive effects are present in the critical layer. While many of her findings are consistent with the results of Brown and Stewartson and others, a significant mean flow distortion is also revealed. For example, a jump in mean vorticity across the critical layer occurs which is larger in order of magnitude than the disturbance which produces it.

The present work is in the same spirit as the two papers cited in the preceding paragraphs except that we wish to determine how quantities such as wave reflection and transmission vary as a function of the parameter $\epsilon^{2/3}/\mu$. Based on the results of Brown and Stewartson and related studies of Rossby wave critical layers, it is likely that the amount of wave momentum absorbed decreases as this parameter increases owing to increased reflection and transmission. An interesting question in light of Troitskaya's analysis is how much mean flow distortion occurs in the wave packet critical layer when diffusive effects are ignored. These and related matters will be discussed in the talk, this aspect of the research being in its preliminary phase.

REFERENCES

Benney, D.J. and Bergeron, R.F. 1969 A new class of nonlinear waves in parallel flows. *Stud. Appl. Math.* **48**, 181-204.

Benney, D.J. and Maslowe, S.A. 1975 The evolution in space and time of nonlinear waves in parallel shear flows. *Stud. Appl. Math.* **54**, 181-205.

Booker, J.R. and Bretherton, F.P. 1967 The critical layer for internal gravity waves in a shear flow. *J. Fluid. Mech.* **27**, 513-539.

Brown, S.N. and Stewartson, K. 1980 On the nonlinear reflection of a gravity wave at a critical level, I. *J. Fluid Mech.* **100**, 577-595.

Hazel, P. 1967 The effect of viscosity and heat conduction on internal gravity waves at a critical level. *J. Fluid Mech.* **30**, 775-789.

Maslowe, S.A. 1986 Critical layers in shear flows. *Ann. Rev. Fluid. Mech.* **18**, 405-432.

Maslowe, S.A., Benney, D.J., and Mahoney, D.J. 1994 Wave packet critical layers in shear flows. *Stud. Appl. Math* **91**, 1-16.

Miles, J.W. 1957 On the generation of surface waves by shear flows. *J. Fluid. Mech.* **3**, 185-204.

Miles, J.W. 1961 On the stability of heterogeneous shear flows. *J. Fluid. Mech.* **10**, 496-508.

Stewartson, K. 1981 Marginally stable inviscid flows with critical layers. *IMA J. Appl. Math.* **27**, 133-175.

Troitskaya, Yu I. 1991 The viscous-diffusion nonlinear critical layer in a stratified flow. *J. Fluid. Mech.* **233**, 25-48.

Winters, K.B. and Riley, J.J. 1992 Instability of internal waves near a critical level. *Dyn. Atm. Oceans* **16**, 249-278.

Multiple Instability in a Laboratory Stratified Shear Layer

C. P. Caulfield[1], Shizuo Yoshida[2],
W. R. Peltier[1] and Morimasa Ohtani[2],
1: Department of Physics, University of Toronto
2: Department of Engineering Science, Hokkaido University

Abstract

We present observational evidence of the presence of a three layer density distribution, coupled with a sheared velocity profile, in the vicinity of a river mouth.
We discuss the subsequent evolution of such multi-layer shear flows both theoretically and experimentally. Three distinct types of instability are observed in accordance with the predictions of linear theory. In the laboratory, we measure the density profile and the velocity profile (using a seven point laser doppler velocimeter) continuously, and so are able to identify the flow characteristics that obtain when the flow is unstable to each of the different instabilities. The most important parameter responsible for the selection of the particular type of instability is found to be the ratio R of the depth of the intermediate density layer to the depth over which the velocity varies, though any asymmetry in the flow (either in the velocity or density fields) also plays a role.
The development of the various instabilities can be simply and intuitively interpreted in terms of interactions of interfacial waves, and at finite amplitude each type of instability has a different structure and mixes the flow in a qualitatively different manner. In particular, if R is close to 1, and hence the layer of intermediate density occupies a significant portion of the shear layer, overturnings appear in the intermediate layer, which are longlived, and strongly two dimensional. These overturnings are the three layer stratified generalisation of the Kelvin-Helmholtz instability first discussed by Taylor (1931). Surprisingly, these modes inefficiently mix the background flow, and the major mixing mechanisms are found to be overturnings in the lower fluid layer (and, to a lesser extent, the upper layer). These overturnings are manifestations of a three layer generalisation of the Holmboe (1962) instability, as discussed in Caulfield (1994). In general all three instabilities can be observed simultaneously at markedly different wavelengths and phase speeds for extended periods of time, even though linear theory may predict significantly different growthrates. The interaction between these various unstable waves markedly modifies the long-time evolution and mixing of the flow.

1: Theoretical introduction

In the immediate vicinity of a river mouth, much mixing takes place due to the sudden widening of the channel which the river flows along, which can lead to a three layer density structure which is then sheared by the salt wedge and river counterflow. This has been observed in field measurements of the Ishka river in Hokkaido, Japan.

The first theoretical investigation of a flow with a three layer density field was conducted by Taylor (1931), at the extreme of a three layer density field with the intermediate layer the same depth as the region of velocity variation. For all Ri_0, this flow exhibits overturnings in the intermediate layer, which propagate at the mean velocity of the background flow. As Taylor states, these overturnings can be thought of as arising from resonances of two gravity waves, one on each of the density interfaces. This instability has not been observed experimentally. Generalising his work, We wish to consider a flow with a three layer density distribution, but *a priori* we make no assumption about any symmetries between the density field and the velocity field. In particular, we do not assume that the intermediate layer has density equal to the mean of the other two layers. This generalises the results of Caulfield (1994). We consider a flow, which in an appropriate frame of reference, has a background velocity distribution $U(z)$ such

1

that

$$U(z) = \begin{cases} -\Delta U/2 , & z \le -d/2 , \\ \Delta U z/d , & -d/2 < z < d/2 , \\ \Delta U/2 , & z \ge d/2 , \end{cases} \qquad (1)$$

i.e. we consider a piecewise linear shear layer of depth d. We consider a piecewise constant three layer density distribution with intermediate layer depth δ, with a midpoint displaced an arbitrary distance h below the midpoint of the shear layer. Thus the flow has a background density profile $\rho(z)$ such that

$$\rho(z) = \begin{cases} \rho_3 & z \le -(\delta/2 + h) , \\ \rho_2 & -(\delta/2 + h) < z < \delta/2 - h , \\ \rho_1 & z \ge \delta/2 - h . \end{cases} \qquad (2)$$

Four non-dimensional parameters that describe the nature of the velocity and density distributions are defined as

$$Ri_0 \equiv \frac{g(\rho_3 - \rho_1)d}{\Delta U^2} , \qquad R \equiv \frac{\delta}{d} , \qquad \Theta \equiv \frac{\rho_2 - \rho_1}{\rho_3 - \rho_1} , \qquad \beta \equiv \frac{2h}{d} .$$

Ri_0 is the bulk Richardson number. R is a measure of the relative depths of the intermediate density layer to the depth of the shear layer (see Caulfield 1994). The parameter β is the three layer generalisation of the parameter ϵ used by Lawrence *et al.* (1991) to quantify the asymmetry in a two layer flow system. In our work, β is a measure of asymmetry in the *location* of the density field *relative* to the velocity field, while the parameter Θ is a measure of the asymmetry in the *distribution* of the density field. It is important to note that in general β can be negative (and thus the midpoint of the intermediate layer is *above* the midpoint of the shear layer), while R and Θ must be between 0 and 1.

In our calculations, we assume that $|\beta| + R \le 1$, and hence that the region of intermediate density is entirely contained within the region of varying velocity. This situation is thought to be the most physically likely. Relaxing this condition changes the governing equations slightly, but does not change the results significantly. By classical normal mode methods of matching pressure and vertical disturbance across interfaces, we may derive a sixth order eigenvalue equation for the phase speed c,

$$c^6 + a_1 c^5 + a_2 c^4 + a_3 c^3 + a_4 c^2 + a_5 c + a_6 = 0 , \qquad (3)$$

where the a_i are well defined functions of α, the non-dimensional wavenumber (i.e $\alpha \equiv kd/2$), Ri_0, R, β and Θ. The flow is unstable if $c_i > 0$, with growthrate αc_i.

As (3) is in general a sextic, we expect that, in general, the equation will have six complex roots. In figure 1a, the real parts of these roots (i.e. the phase speed c_r) are plotted with solid lines against α, for a typical experimental values of Ri_0, R, β and Θ, namely $Ri_0 = 1.5$, $R = 0.4$, $\beta = 0.2$ and $\Theta = 0.5$.

Regions of instability correspond to regions where two of the roots have the same phase speed and wavenumber. In this case, one of the roots is damped and the other one is predicted to grow. It is instructive to think of each of the instabilities as arising through an interaction of the (notional) marginally stable waves which would exist on each of the interfaces if the interfaces were totally isolated from each other, as discussed by Cairns (1979). To use the technique of Cairns, we must first consider each of the interfaces separately, which corresponds to the limit of large α, and hence short wavelength. In the large α limit, each of the interfaces is essentially decoupled from all of the others (provided that $|\beta| + R \ne 1$) and we can obtain equations for the phase speed of the disturbances on each of the interfaces *separately*. In figure 1a, we plot the phase speeds calculated for marginally stable waves on each interface as dashed lines. Now it is clear that each of the regions of instability can be identified with an interaction between

2

two of the interfacial waves, which occurs when the two waves have equal phase speeds and wavenumbers.

The small real phase instability occurs when there is an interaction between the gravity wave on the upper density interface which is travelling upstream relative to the background flow, and the gravity wave on the lower density interface which also is travelling upstream relative to the background flow. This corresponds to an asymmetric generalisation of the situation first considered by Taylor (1931), and for arbitrary R by Caulfield (1994), and we shall henceforth refer to this as a T mode.

The two regions of large (positive and negative) real phase speed instability correspond to the asymmetric three layer generalisation of the modes first considered by Holmboe (1962), and we shall refer to them as the HP and HM modes respectively. They are caused by interactions between upstream propagating Rayleigh waves (waves on vorticity interfaces) and downstream propagating gravity waves on the nearer density interface. Both are locally driven.

There is the possibility of two further regions of instability at small wavenumber, if the Rayleigh waves resonate with the gravity waves on the further density interface. These are non-local interactions, which we refer to as R modes.

For the parameters chosen for figure 1, the full calculations show that the R type modes are unstable at wavenumbers where the large α approximation used in the derivation of the expressions for the phase speeds of the interfacial waves is not valid. Indeed, there is a noticeable difference between the crossing of the interfacial waves, when their phase speed as a function of wavenumber is calculated separately for each interface, and the crossing for the roots of the full equation (3).
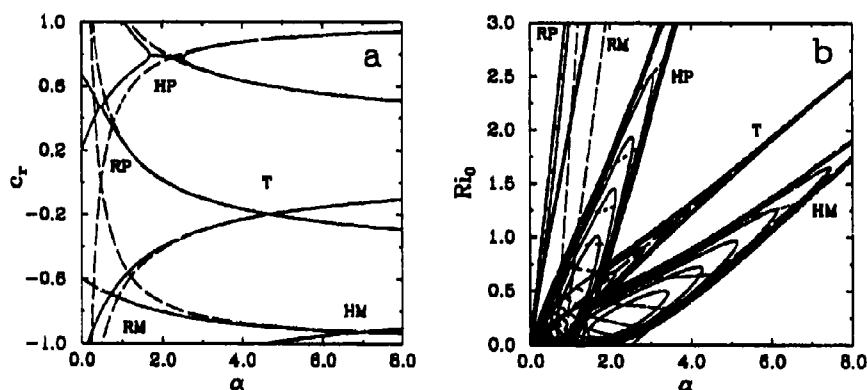
Figure 1: a) Variation of phase speed with wavenumber for solutions of (3) (solid lines) and marginally stable waves on the interfaces (dashed lines) for $Ri_0 = 1.5$, $R = 0.4$, $\beta = 0.2$ and $\Theta = 0.5$; b) Stability boundary with contours of growthrate (solid lines) and phase speed (dashed lines) for $R = 0.4$, $\beta = 0.2$ and $\Theta = 0.5$, asymptotes of marginally stable modes are shown as a long dashed line.

In figure 1b, we plot the regions of instability predicted by (3) in Ri_0–α space along with the resonance conditions for the various wave interactions for $\beta = 0.2$, $R = 0.4$, and $\Theta = 1/2$. Each branch ultimately asymptotes to the appropriate predicted resonance, as shown by the thick dashed lines, provided Ri_0 (and hence α) is sufficiently large.

Although not shown here, the relative significance of the various branches varies markedly as the various parameters change. The most significant effect is that the T mode moves to larger α and smaller growthrate as R decreases, while the Holmboe type modes start to dominate. Positive (negative) β, or $\Theta < (>)1/2$ decreases (increases) the wavenumber of the HP modes relative to that of the HM mode, and increases (decreases) the HP mode growthrate. The R modes are only significant at small R. Thus, a simple consideration of the various interfaces

3

separately sheds valuable insights on the growth mechanisms, phase speeds and wavelengths of the different types of instability predicted by the linear model.

2: Experimental procedure

A series of experiments were conducted in a flume 8 metres long by 50 cm wide with a terminal reservoir 2 metres long by 3 metres wide by 10 cm deep (see Yoshida 1986 for a description of the tank). The flume (modelling a river) was filled with a saline solution of density ρ_3 (typically $1.006 kgm^{-3}$) to a depth, d_3 of 4 or 6 cm. A less dense, though still salty layer of density ρ_2, dyed with Sodium Fluorescein (Uranine or $C_{20}H_{10}Na_2O_2$) was then introduced, until the total depth became 10 cm and the reservoir (representing the sea) overflowed. By variation of the density of this (intermediate) layer, the parameter Θ was varied between four values, namely $\Theta = 1/4$, 1/3, 1/2 and 2/3. A constant flux, Q, of fresh water was then introduced at the upstream end. A constant flux was also introduced to the flexible impermeable floor of the reservoir, and hence both the lower layer and upper layer had non-zero velocities, and an approximately linear velocity shear existed across the entirety of the intermediate dyed layer (see Yoshida 1986). It is important to note that, due to the experimental geometry, the absolute value of the upper layer flow in the laboratory frame is appreciably larger than the absolute value of the lower layer flow, and so the mean velocity of the flow was typically towards the downstream end.

Various values of flow rate, ρ_3 and ρ_2 were chosen to allow for variation in background flow parameter values. Due to the constant flow of the upper layer, the depth of the intermediate layer continually decreased with time. The density field was continually measured with a conductivity probe which slowly traversed the depth of the channel 58.8cm from its downstream end. In figure 2a we plot the density distribution at various times for a typical experiment. After initial transients, the interfacial width was found to be o(2 mm), and the depth δ of the intermediate layer can be seen to decrease as time passes.

The time evolution of the velocity field throughout the whole depth of the tank was tracked through time using image analysis of dye streaks, calibrated at seven points by a laser doppler velocimeter (LDV), located at 90.8cm from the end of the channel. Since the depth, δ, of the intermediate layer of fluid continually decreased with time due to entrainment, the mean upper layer velocity was not a constant throughout the experiment, but rather decreased, with a decay rate slow relative to the observed instability lifetimes. The range of values over which ΔU varied was a function, quite naturally of the lower layer depth d_3 and the volume flux, Q of fresh water.
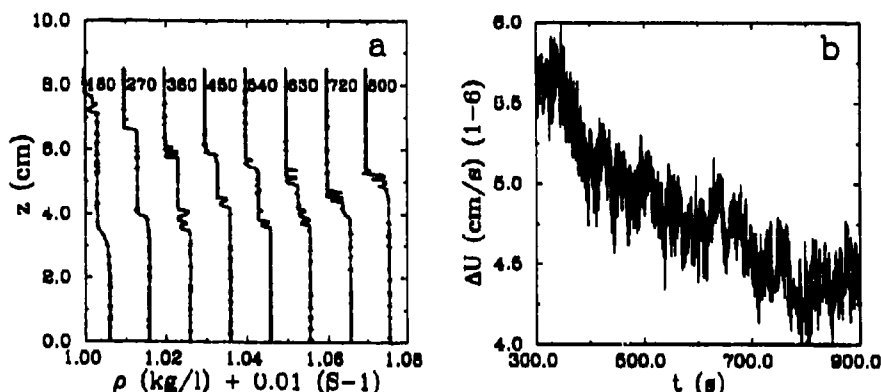
Figure 2: Evolution in a typical experiment of a) density profile, labelled with time in seconds (each reading is shifted by 0.01); b) velocity difference between two LDV measurements.

The time evolution of the velocity difference ΔU between two of the LDV signals, one located at a depth of 1.2cm from the bottom (and so definitely in the lower layer) and the

other at a depth of 8.05cm from the bottom (and so definitely in the upper layer) for a typical experiment is shown in figure 2b.

Another important (experimentally measured) quantity is d, the shear layer depth. Initially, as the flow develops, this depth increases, but a short time after shear is established across the entire width of the intermediate layer the shear layer depth d attains a maximum, and subsequently decreases with time. The rate of decrease of the depth, δ, of the intermediate layer was always faster than the rate of decrease of the shear layer depth, d, and so the value of the parameter R decreased as the experiment progressed. Another significant observation is though the depth of the intermediate layer decreases with time, the density does not vary appreciably until late in the experiment, which is consistent with the observation that little fluid is entrained into the intermediate layer due to the flow instabilities at large values of R, as can be seen in figure 2a.

The effect of a slow reduction in ΔU is to increase the bulk Richardson number Ri_0 of the flow, while the reduction in shear layer depth d tends to decrease the value of Ri_0. On balance, in general Ri_0 tends to decrease as the experiment continues, although not totally monotonically. Thus, large values of R, which pertain at the beginning of an experimental run before significant erosion of the intermediate layer, correspond in general to large values of Ri_0. The parameter β varied slowly and randomly within each experiment. Throughout our complete set of experiments, $1.03 \leq Ri_0 \leq 2.83$, $0.1 \leq R \leq 0.78$, $-0.34 \leq \beta \leq 0.2$ and $0.25 \leq \Theta \leq 0.75$. The flow structure experimentally imposed allowed us to observe the behaviour of flows at widely varying values of the parameter R, and thus allowed us to explore the effect of this new parameter on the behaviour of the flow.

3: Experimental Results

Qualitatively, all the experiments underwent similar transitions throughout their duration. The flow was visualised by means of a centrally located lightsheet, about 50 cm from the reservoir-flume channel junction. After an initial transient, the shear layer extended over the entire width of the intermediate density layer and the parameter R was close to 1, i.e. the intermediate layer was in some sense "thick". At this initial stage disturbances on the two density interfaces locked in phase in an approximately sinuous manner, the interfaces cusped inwards, and regions of overturning appeared within the intermediate density region (see figure 3a). These disturbances propagated at phase speeds close to the velocity of the background flow at the midpoint of the intermediate layer, and we identified these as T mode type disturbances. This instability caused large deflections in the location of the density interfaces (as can be seen from some of the profiles in figure 2a), but little entrainment. As discussed in section 2, the value of R slowly decreased throughout the experiment. Typically, as R decreased, the wavelength of the T mode type disturbances decreased (see figure 3b). Eventually, regions of overturning, propagating at speeds close to, but always less than the absolute value of the background flow appeared above and/or below the intermediate layer. T mode disturbances persisted for significant times after the appearance of the other two types of instability (see figure 3c). As observed by Lawrence et al. (1991) in the two layer case, asymmetry in the background flow has a profound effect on the wavelength and phase speed of the Holmboe type instabilities.

As the regions of overturning in the upper and/or lower layers passed by, we observed cusping upwards of the upper density interface and/or cusping downwards of the lower density interface, and thus we identified these disturbances with HP and HM mode type disturbances respectively.

Finally, as the intermediate layer became "narrow", the T mode type disturbances disappeared, and the flow became qualitatively similar to the previously studied two layer case (see figure 3d). Occasionally, particularly in the cases where Q the volume flux was small, and hence Ri_0 was large, extremely long wavelength disturbances, with relatively small absolute values of their phase speed appeared. These disturbances were suggestive of R mode type disturbances, though they were too infrequent to constitute conclusive evidence. Also, as the intermediate

layer became narrow, it became increasingly difficult to visualise the overturnings in the upper layer, as their associated upward cusping of the upper density interface became indistinct, and since they propagated at speeds of the order of centimetres per second in the laboratory frame, positive identification of these modes for R less than about $1/4$ became impossible. Since, within the laboratory frame, the overturnings in the lower layer were virtually stationary, we were able to identify this type of instability (i.e. HM modes) to smaller values of $R \sim 0.1$.
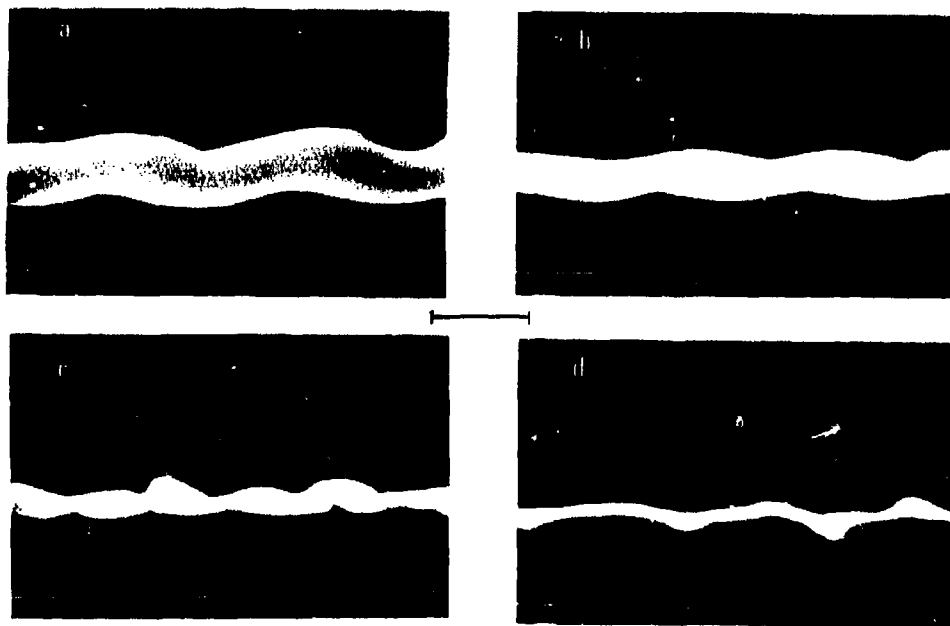
Figure 3: Experimental observations of: a) T modes for large R; b) T modes for smaller R; c) T modes and H modes; d) H modes alone. The scale is 5 cm.

In all, eighty nine well-defined unstable structures were observed, with, as discussed above, three qualitatively different finite amplitude structures, namely T, HP and HM mode type structures. Each experimental observation at a certain wavenumber with associated phase speed has associated with it five experimentally determined parameters, namely Ri_0, R, β, Θ and lower layer depth d_3. As discussed in section 1, Ri_0, R, β and Θ all affect the predicted properties of the linear instability. However, it was found that variation with R had the most pronounced effect, and so for each type of instability, we plot the observed wavenumber against R, to compare with predictions (shown as two points of the same symbol type connected with a line) of the linear theory developed in the section 1. In all cases the symbol type refers to a different combination of experimental values of Θ and d_3, as shown in the key. These were found to be insignificant.

In figure 4a, we see that there is a very close agreement for the wavenumber of the T mode type disturbances (as seen by the fact that most experimental observations lie on the line connecting the two extremal theoretical predictions). A similar result holds for the phase speed. Thus we have observed the T mode, and we also see the predicted transition to larger wavenumber as R decreases. The T mode overturnings were found to be strongly two dimensional, and though the overturnings were longlived within the intermediate layer, very little fluid was entrained from the other two layers, and hence the T mode did not contribute greatly to the mixing. This is not entirely a surprise, as Ri_0 is of order 1 here, and thus the mixing effects of Kelvin-Helmholtz type billows is thought to be severely suppressed. What is surprising is the continued observation of these modes to quite small values of $R \sim 0.25$, where linear theory predicts that the growthrate of the T mode is appreciably smaller (as little as 10% in extreme

6

cases) than the growthrates of the Holmboe type modes. As discussed in Caulfield (1994) for a symmetric flow, this may be due to the possibility of a resonant triad interaction between the Holmboe type instabilities and the T mode type instabilities An alternative hypothesis is that, since the critical layers of the various modes are so well separated, the growth and equilibration at finite amplitude of each mode proceeds in a manner essentially decoupled from the other modes, and thus the convential argument that the most unstable mode of linear theory eventually dominates is appropriate only within each branch.
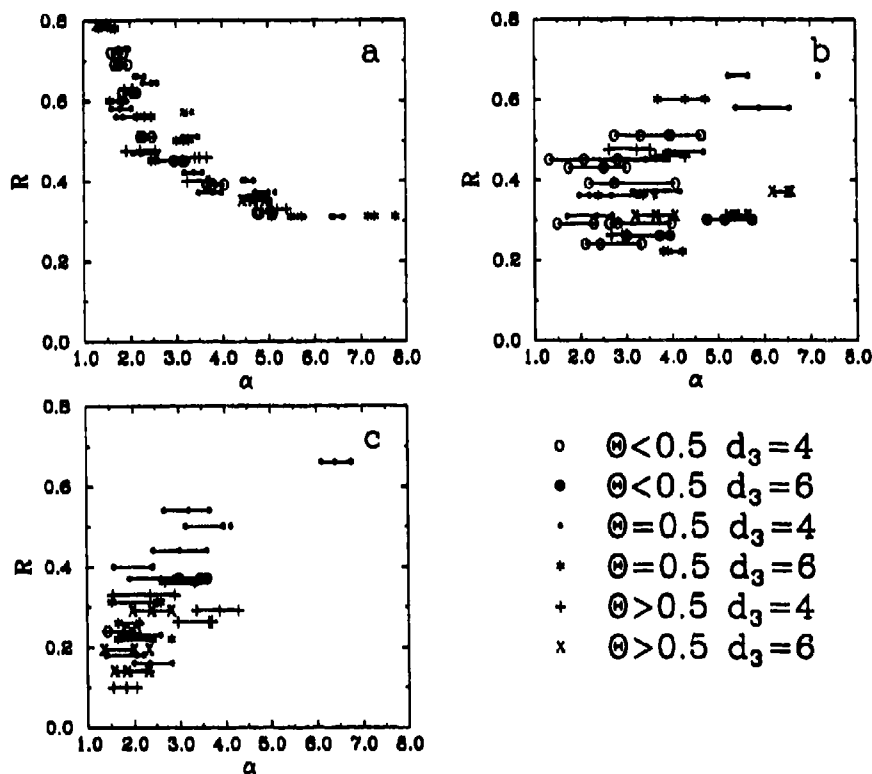
Figure 4: Experimentally measured wavenumbers plotted against linear predictions for a) T modes for large R; b) HP modes; c) HM modes alone.

Considering the Holmboe type instabilities, in figures 4b and 4c we plot observed wavenumber for HP type modes (i.e. upward cusping waves on the upper density interface associated with overturnings in the upper layer) and HM modes (i.e. downward cusping waves on the lower density interface associated with overturnings in the lower layer) with the regions predicted by the model to be unstable to HP and HM mode type disturbances. Once again, we see that there is a very close agreement. In these cases, no one of the parameters dominates the prediction and observation of the wavenumbers of the Holmboe type modes, and a knowledge of all the bulk properties of the flow is necessary to properly predict the observed instability, though there is some evidence of the predicted transition to larger wavenumber as R increases. Once again, the fact that other types of instabilitv were predicted to have greater linear growthrates than either of the Holmboe type modes does not preclude the development of said mode to finite amplitude.

The two Holmboe type modes were also two dimensional, and their wavefronts extended across most of the width of the tank, propagating parallel to the background flow. For significant

periods all three types of instability could be observed. Both Holmboe type modes, as shown in figures 3c and 3d, caused cusps to appear on the density interfaces, and were the major cause of mixing within the flow. It was difficult to quantify the effect of the HP modes since the upper layer fluid is continually being advected out of the observation area. However, due to the slow moving nature of the lower layer flow, it was possible to observe the mixing due to the HM modes at least qualitatively. This mixing associated with HM modes of the intermediate layer with the lower layer was often sufficiently vigorous for another, fourth, layer to appear with density intermediate between ρ_3 and ρ_2 (see figure 2a, the plot of the density profile at $t = 720$ seconds, late in the experiment).

4: Conclusions

A simple linear model well predicts the wavelengths and phase speeds of several forms of instability observed in a stratified shear flow, a simple idealisation of a flow which has been observed to occur at a river mouth.

In particular the linear mode first discussed by Taylor (1931), and herein referred to as the T mode, has been shown to be experimentally observable. Also, for multi-layer, and in general asymmetric flows, the bulk Richardson number is insufficient to describe the properties of the instability observed. It is necessary to know the relative depth of the intermediate layer as well as the extent of the asymmetry in the velocity and density fields to fully describe the flow and predict the properties of the instabilities. The T mode appears to have little effect on the amount of mixing within the flow, and the principal mechanism by which fluid is exchanged between the intermediate layer and the other two layers is through the cusping of the density interfaces due to the regions of overturning associated with the Holmboe type instabilities. This mixing can occur for bulk Richardson numbers in the range $1.03 \leq Ri_0 \leq 2.83$, and so it is necessary to be cautious in the parameterisation of mixing efficiencies of shear flows in terms of the bulk Richardson number alone, as the structure of the density field appears to have a significant qualitative effect on the mixing properties.

A three layer flow is susceptible to multiple simultaneous instabilities even when the predicted growthrates of the various observed modes vary by more than one order of magnitude. The ability of the various types of unstable structures to simultaneously grow to finite amplitude has been demonstrated, but as yet is not well understood.

We put forward two possible explanations which will be the subject of future work. Firstly, since the T modes and the Holmboe type modes appear simultaneously at times when typically the wavenumber of the T mode is appreciably larger than that of the two Holmboe type modes, there is the possibility, as mentioned in Caulfield (1994), of the three different types of instability forming a resonant triad (see Craik 1985 for a review). However this needs to be verified by direct calculation of not only the resonance conditions, (namely that the sums of the Holmboe type waves frequencies and wavenumbers are equal to the frequency and wavenumber of the T mode) but also of the interaction coefficients. Alternatively, since the modes develop finite amplitude structures in widely separated regions, it is possible that each mode can develop to finite amplitude in a manner largely independent of the other modes. However, a nonlinear analysis must be conducted to investigate properly the multiple modal structure at finite amplitude, as well as the (observed) different mixing effects of the instabilities.

5: References

Caulfield C. P., 1994: *J. Fluid Mech.* **258** 255-285.

Cairns R. A., 1979: *J. Fluid Mech.* **92** 1-14.

Craik A. D. D., 1985: "Wave Interactions and Fluid Flows," *C. U. P.*

Holmboe J., 1962: *Geofys. Publ.* **24** 67-113.

Lawrence G. A., Browand F. K. and Redekopp L. G., 1991: *Phys. Fluids* A **3** 2360-2370.

Taylor G. I., 1931: *Proc. Roy. Soc.* A **132** 499-523.

Yoshida S., 1986: Bull. Faculty Eng. Hokkaido U. **130** 127-135.

Two-dimensional secondary instabilities
in a stably-stratified shear layer

Chantal STAQUET

Laboratoire de Physique (CNRS, URA 1325), E.N.S. Lyon, 46 allée d'Italie, 69364 Lyon Cédex 07, France

I. Introduction

The buoyancy force in a stably-stratified fluid medium, if strong enough, compels the flow to organize into quasi-horizontal structures. Evidence of such a horizontal layering has been clearly shown in geophysical flows (e.g. Dalaudier et al. 1994 for the atmosphere, Gregg 1987, for the ocean), in laboratory experiments (e.g. Browand et al. 1987) and in numerical experiments (Herring and Metais 1989, Bouruet-Aubertot et al. 1994). These layers, which are only weakly correlated along the vertical, may slide the one over the other and thus generate velocity shears. If instability criteria are satisfied, these velocity shears may yield instabilities of the Kelvin-Helmholtz type and possibly trigger a turbulent behavior in the flow (Bouruet-Aubertot et al., 1994). Why and how do these layers become unstable is still an open question since they are embedded in a complicated flow and coexist with internal waves. The purpose of the present study is to analyse numerically on a simpler flow, a two-dimensional stably-stratified shear layer, the occurence of such secondary instabilities.

The two-dimensional homogeneous shear layer has been extensively studied (see Corcos and Sherman 1984 and Ho and Huerre 1984, for a review). Once the Kelvin-Helmholtz instability has developed and saturated, the initial vorticity, confined in a horizontal strip, has moved into equidistant vortices aligned along the streamwise direction, separated by quasi-irrotational flow (the braids). These vortices may then pair. When a stable stratification is present, the structure of the flow changes fundamentally as the instability develops. The reason is that a source of vorticity now exists, provided by the baroclinic torque of the flow. Our study will be conducted in the Boussinesq approximation. In this case, the baroclinic torque reduces to the curl of the buoyancy force and, therefore, solely involves gradients of the density field. As the Kelvin-Helmholtz instability develops, the horizontal density gradient generates vorticity of the same sign as the vorticity of the mean flow in the braids and partly destroys the vorticity of the cores. Consequently, thin tilted layers of intense vorticity form in the braid region, separared by weakened vortices. We shall refer to these thin layers as "baroclinic layers".

Such baroclinic layers have been observed in the atmosphere (Gossard et al. 1970), in the ocean (e.g. Woods 1969, Thorpe 1987), in laboratory experiments of stably-stratified shear layers (for instance Delisi and Corcos 1973, Koop and Browand 1979, Schowalter et al. 1993) and in two-dimensional numerical simulations of stably-stratified shear layers (Patnaik et al. 1976, Corcos and Sherman 1976, Klaassen and Peltier 1985a, 1985b, 1985c, 1989, 1991, Staquet 1991). All these authors have predicted, either with heuristic arguments or on a theoretical basis, that these layers could become unstable and bear a secondary Kelvin-Helmholtz instability. Such secondary instabilities have been clearly shown to occur in Staquet (1994a, 1994b). In these latter two papers, high resolution two-dimensional (as well as a few three-dimensional) numerical simulations of the Navier-Stokes equations in the Boussinesq approximation are presented, for a shear layer with either moderate or strong stratification. For the present extended abstract, we shall focus on strongly stratified two-dimensional flows. We shall show that the stability of the baroclinic layer is controlled by the large scale Kelvin-Helmholtz vortex, via the strain field that it induces in the stagnation point region of the layer. A consequence of this study, clearly illustrated here, is that, in a strongly stratified shear layer, secondary Kelvin-Helmholtz instabilities are fostered by the pairing of primary Kelvin-Helmholtz vortices.

II. Mathematical model and numerical method

The Navier-Stokes equations are solved in the Boussinesq approximation in the two-dimensional vertical (x,z) plane, with z directed along the vertical direction:

$$\frac{\partial \omega}{\partial t} + J(\omega, \psi) = \frac{g}{\rho_0} \frac{\partial \rho}{\partial x} + \nu \nabla^2 \omega \qquad \frac{\partial \rho}{\partial t} + J(\rho, \psi) = \kappa \nabla^2 \rho \qquad (2\text{-}1)$$

ψ is a stream function related to the velocity field by : $u=-\partial\psi/\partial z$, $w=\partial\psi/\partial x$. $\omega=(\nabla\times u).l_y$ is the spanwise vorticity component (l_y being the unit vector along the y direction); ω is related to ψ by: $\omega=-\Delta\psi$. g is the modulus of the acceleration of gravity and ν and κ are respectively the molecular viscosity and the diffusion coefficient for density changes. We decompose the density field as $\rho(x,z,t)=\bar{\rho}(z,t)+\rho'(x,z,t)$, where $\bar{\rho}(z,t)$ is the mean density and ρ' is the deviation from the mean; in the Boussinesq approximation, $\bar{\rho}+\rho'=\rho_0$, ρ_0 being the density of an hydrostatic basic state.

For boundary conditions we assume that the flow is periodic in the streamwise direction, and at the horizontally oriented boundaries take free-slip conditions on the velocity.

As in Patnaik et al. (1976), the mean velocity and mean density profiles at t=0 are defined as: $\overline{U_i}(z) = U\,\mathrm{erf}(\frac{\sqrt{\pi}}{2}\frac{z}{\delta_i})$ and $\bar{\rho_i}(z) = \rho_0 - \frac{\Delta\rho}{2}\,\mathrm{erf}(\frac{\sqrt{\pi}}{2}\frac{z}{\delta_i/\sqrt{Pr}})$. -U and U are the velocity

at the lower and upper boundaries respectively, while $\rho_0+\Delta\rho/2$ and $\rho_0-\Delta\rho/2$ (with $\Delta\rho>0$) denotes the corresponding densities. δ_i is half the initial vorticity thickness of the shear layer, defined by $U/(d\overline{U_i}/dz)_{max}$. $Pr=\nu/\kappa$ is the Prandtl number.

No density perturbation is superposed upon the mean density profile at t=0, while a deterministic perturbation is added to the mean velocity profile. Its vertical dependency is the eigenfunction of the Rayleigh equation (linear stability equation for J=0). Its streamwise dependency is sinusoidal, because of the periodic boundary conditions, with wavenumber equal to the fundamental (most unstable) wavenumber predicted by linear stability theory for J=0, k_f say. $k_f\delta_i=0.439$ in the present case.

Equations (2-1) are solved numerically in nondimensional form. The length and velocity scales are δ_i and U respectively and time is nondimensionalized by the advective time scale δ_i/U. The density is scaled by $\sqrt{Pr}\Delta\rho/2$. With this scaling, the nondimensional parameters which come into play in the equations are: Re, the Reynolds number, initially equal to $U\delta_i/\nu$; the minimum of the gradient Richardson number (or minimum Richardson number) , whose expression at t=0 is $J = \min_z -\frac{g}{\rho_0}[\frac{d\bar{\rho_i}}{dz}/(\frac{d\overline{U_i}}{dz})^2] = g\frac{\Delta\rho}{\rho_0}\frac{\sqrt{Pr}}{2}\frac{\delta_i}{U^2}$ and the Prandtl number. In the

calculations presented here, J and Pr are kept to a fixed value, equal to 0.167 and 0.7 respectively, while Re is varied between 400 to 3000.

Equations (2-1) are solved using a standard pseudo-spectral method (Canuto at al. 1988). Aliasing errors are removed by a truncation method. The viscous terms are computed explicitely while a third-order Adams-Bashforth scheme is employed to advance in time. More detail about the numerical method can be found in Staquet (1994a). Computations up to 1024^2 have been performed on a Cray C98, at the Computing Center of CNRS.

III. Formation of secondary instabilities in baroclinic layers

Visualizations of the shear layer at the time the vorticity has reached an absolute maximum is displayed in figure 1, for different Reynolds numbers. The structure of the Kelvin-Helmholtz vortex opposes that of the baroclinic layer. The vorticity varies smoothly inside the vortex and is associated with a complex density field, due to the roll-up of heavy and light fluid when the instability develops. Statically unstable situations then occur, with heavy fluid over light fluid. A consequence is that negative vorticity is produced, by the baroclinic torque, in the upper (and inner, by symmetry) boundaries of the Kelvin-Helmholtz vortex. By contrast, in the stagnation point region of the baroclinic layer, both vorticity and density fields exhibit sharp changes across the layer but almost no variation along the direction of the layer.

The behavior of the vortex when the Reynolds number is increased also opposes that of the baroclinic layer. The vertical extent of the vortex remains unchanged as Re is increased; it can be shown that this vertical extent is in very good agreement with a theoretical model proposed by Corcos and Sherman (1976) for the non linear development of the instability. As well, the

maximum vorticity of the vortex (reached at its center) hardly varies from one calculation to the other (≈0.7 for Re=400 and ≈1 for Re≥1000).

By contrast, the thickness and the vorticity of the baroclinic layer strongly varies as the Reynolds number increases. To understand this, it is first necessary to recall the physical mechanisms driving the evolution of the layer, a theoretical model of which was proposed by Corcos and Sherman (1976). Upon the layer, in the neighbourhood of its stagnation point, acts an outer velocity field induced by the large scale vortex, of the pure strain type. The advection perpendicular to the direction of the layer by this pure strain makes the thickness of the layer decrease exponentially. Diffusion by molecular effects however opposes this compression action and an equilibrium eventually sets in, which dictates the thickness of the layer. This strain field has a second effect upon the layer, now through its component along the direction of the layer: this component advects the vorticity of the layer toward the vortex cores. Here again, this effect is balanced by a mechanism of generation of vorticity, due to the baroclinic torque. An equilibrium eventually sets in, now along the direction of the layer, which yields a constant velocity difference across the layer.

It has been shown in Staquet (1994a) that the strain rate of the outer strain field acting upon the layer does not vary when the Reynolds number is increased (and is about constant in time). Hence, the thickness of the layer reflects the scale at which viscosity is acting; thus the larger Re is, the smaller the thickness, as illustrated by figure 1. (A $Re^{-1/2}$ dependency is predicted for the equilibrium thickness by the model of Corcos and Sherman, which agrees very well with the behavior computed numerically (Staquet 1994a, 1994b)). As the Reynolds number is increased, the vorticity of the layer at its stagnation point strongly increases. The baroclinic torque is solely responsible for this, since the vorticity is removed at the same rate whatever Re: as the thickness of the layer decreases, the streamwise gradient of the density field increases, which produces vorticity. (A $Re^{-1/2}$ dependency is predicted for the equilibrium vorticity by the model of Corcos and Sherman, which agrees again remarquably well with the numerical findings).

This behavior of the layer implies that the Richardson number at the stagnation point of the layer, Ri_s say, should decrease as Re is increased. Ri_s is plotted versus Re in figure 2 at the time the vorticity reaches an absolute maximum (attained at the stagnation point of the layer). As in Corcos and Sherman (1976), we define Ri_s as: $Ri_s = -J \left[\frac{\partial \rho}{\partial z} / \Omega^2 \right]_s$. Figure 2 shows that Ri_s reaches very small values, as low as 0.04 when Re≈2600. Supposing that the stability of an inclined shear layer is the same of that of a horizontal one, linear theory and calculations by Hazel (1972) predict that a secondary instability should occur if Ri_s becomes lower than 0.25. Nevertheless, in the present case, the stagnation point of the baroclinic layer remains stable.

In figure 1, an ondulation is visible for the highest Reynolds number case, in the part of the baroclinic layer that adjoins the region of the vortex where negative vorticity is produced. It is at this location that a secondary instability first amplifies. This instability is not of the Kelvin-Helmholtz type. Its subsequent development is visualized in figure 3, through constant contours of the vorticity field. It amplifies while propagating (or while being advected by the local shear). The origin of this instability seems to be clear: it grows where the positive vorticity of the baroclinic layer meets negative vorticity in the inner boundary of the Kelvin-Helmholtz vortex, that is, where a jet flow forms. It is not clear however, whether this instability is that of a jet flow, because it has a strongly asymmetric vorticity and is embedded in a complex flow. Moreover, the non linear development of this instability exhibits a strong resemblance with visualizations of critical layer experiments reported by Thorpe (1981). This instability is refered to as the "near-core" instability hereafter.

The advection of this instability toward the stagnation point of the baroclinic layer perturbs the whole flow. In particular, a strong disturbance is induced at the stagnation point of the layer, which triggers a secondary instability, now of the Kelvin-Helmholtz type (figure 3b).

IV. Influence of the outer strain field on the stability of the layer

We shall now examine the intriguing stability of the layer in the neighbourhood of its stagnation point, before the near-core instability develops. Two factors stabilize the layer there: the non zero value of the Richardson number, of course, but also the action of the pure strain field. Indeed, the strain field compresses any perturbation in the direction perpendicular to the layer, thereby reducing its growth rate; it also stretches any wavelength along the direction of the

3

layer, therefore making its growth rate eventually go to zero. These two effects of the outer strain field are at the basis of the model of Corcos and Sherman mentioned above for the non linear dynamics (and resulting structure) of the layer.

The stability of a uniform strip of vorticity in a perfect fluid, subjected to a constant strain rate, has been examined by Dritschel et al. (1991). The key parameter in this problem is the ratio of the strain rate γ over the vorticity of the layer Ω. Dritschel et al. have shown that even a value of γ/Ω as small as 0.065 leads to a three-fold amplification only of the perturbation. In this model flow, the perturbation always decays to zero, after a possible amplification, no stable stratification is present and the fluid is perfect. The situation examined here is somewhat different but it is still of interest to examine the behavior of γ/Ω at the stagnation point of the baroclinic layer.

This ratio is plotted in Figure 4 versus time. γ/Ω decays once the layer has formed (from $t \gtrsim 15$) and reaches very small values, equal to ≈ 0.03 for Re$\approx$2600 with Ri$_s \approx 0.045$. This suggests that critical values for the layer to become unstable, which have not been reached yet, would be even lower. The smallness of these values would be consistent with the findings of Dritschel et al.

If it is indeed the outer strain field that prevents the instability from occuring, then any event making the strain rate decrease should permit the development of the instability. A way to make this parameter decrease is to move the stagnation point of the baroclinic layer away from the Kelvin-Helmholtz vortex. Indeed, the strain rate is roughly proportional to the circulation of this vortex and inversely proportional to the distance squared between the vortex and the stagnation point of the layer. In Staquet (1994b), three calculations of a shear layer having J=0.0836 and Re=1000 have been performed, in which the wavelength of the initial perturbation is progressively increased from the fundamental wavelength up to twice this wavelength. The streamwise extent of the numerical domain is equal to 2π over this wavelength so that only one Kelvin-Helmholtz vortex develops. As the perturbation wavelength is increased, the baroclinic layer is shown to lengthen, progressively destabilize (bearing first the near-core instability) and eventually, for the longest wavelength, a secondary Kelvin-Helmholtz instability develops. We have computed the ratio γ/Ω for the three calculations. For the intermediate wavelength, where the baroclinic layer remains stable, γ/Ω is equal to 0.04, with Ri$_s$=0.55. For the longest wavelength calculation, $\gamma/\Omega \approx 0.02$ when the instability starts developing, with Ri$_s \approx 0.07$. These three calculations make clear the essential role of the outer strain field on the stability of the layer.

It follows that pairing should promote a secondary instability of the Kelvin-Helmholtz type in the baroclinic layer. Indeed, in moving the one toward the other, the vortices move away from the stagnation point of the layer. Their influence, and thus the induced strain rate, should decrease at this location. This argument is supported in figure 5 by visualizations of a strongly stratified shear layer with two primary Kelvin-Helmholtz vortices developing. A secondary instability is shown to develop spontaneously at the stagnation point of the baroclinic layer, without this part of the layer having been invaded by the propagating near-core secondary instability. At the very most does the secondary near-core instability provide the necessary perturbation, supposed to be small, to trigger the instability. The ratio γ/Ω for this calculation is plotted in figure 4 (curve e). γ/Ω is shown to have the smallest value, equal to 0.02 (with Ri$_s$=0.02, see figure 2). The same critical value for γ/Ω was found for an instability to develop in a J=0.0836 shear layer.

V. Analogy with three-dimensional turbulence

It is the non conservation of the local vorticity that makes possible the succession of secondary Kelvin-Helmholtz instabilities involving smaller and smaller scales observed in figure 5b: only because the stretched braid in between newly growing Kelvin-Helmholtz vortices is baroclinically regenerated with vorticity, can the instability mechanism continue. This non conservation of the vorticity is also a fundamental feature of three-dimensional turbulent flows, even without body force. We now examine whether this fundamental analogy may give rise to an analogous behavior. For this purpose, the dissipation rate of the total energy of the two-dimensional stably-stratified shear layer is examined as a function of the Reynolds number for

the series of one Kelvin-Helmholtz vortex calculations discussed above (J=0.167, Re varying between 400 and 3000).

For a shear layer in the Boussinesq approximation, the dissipation rate of the total energy can be written as: $\frac{dE}{dt} = -\frac{1}{Re}(Z + Re.\varepsilon_{EP})$ with $Re.\varepsilon_{EP} = -\frac{1}{L_z}\frac{1}{Pr}\Delta\rho$. $Z = \langle(\nabla\wedge u)^2\rangle$ is the volume-averaged enstrophy and L_z denotes the vertical length of the numerical domain. ε_{EP} is the dissipation rate of the potential energy, and is constant in the present case (supposing there is no mass flux across the horizontally oriented boundaries). It follows that dE/dt is of the form Z^*/Re, where $Z^*=Z+Re.\varepsilon_{EP}$ is the usual enstrophy with an additive constant. This additive constant is the same for all the calculations presented here.

Z^* is plotted in figure 6a. It exhibits a first maximum at about t≈48, whatever the initial value of the Reynolds number. Up to this time, the maximum vorticity (over the numerical domain) is always reached at the stagnation point of the baroclinic layer. It is thus this part of the flow that controls the evolution of the total enstrophy up to t≈48. Z^* continues to increase next for Re≥1500, when secondary instabilities develop in the baroclinic layer. A second maximum is reached at an instant independent of the Reynolds number. The value of this second maximum is strongly dependent on the Reynolds number however and it is thus of interest to examine the behavior of Z^*/Re for Re≥1500. This quantity, equal to minus the dissipation rate, is plotted in figure 6b. The second maximum of Z^*/Re, reached at a time the flow has become turbulent through secondary instabilities, seems to tend toward a constant value as the Reynolds number increases. Such a behavior is analogous to that found for instance by Brachet (1990) when studying numerically the temporal evolution of the enstrophy for the three-dimensional Taylor-Green vortex (with uniform density). This suggests that the dissipation rate of energy becomes independent of the viscosity in the limit of zero viscosity; in other words, this dissipation rate is controlled by non linear effects in this limit.

Finally, we note that the analogy between two-dimensional Boussinesq equations and three-dimensional equations for a fluid with uniform density has already been used by, e.g., Pumir and Siggia (1992) in their search for a singularity of the three-dimensional Euler equations.

VI. Conclusion

This study has focused on the development of secondary instabilities in the thin layers that appear in a two-dimensional stably-stratified shear flow, in between the primary Kelvin-Helmholtz vortices. We have shown that these large scale vortices control the stability of the layers, via the strain field that they induce in the stagnation point region of the layers. Consequently, pairing of primary vortices promotes the growth of a secondary Kelvin-Helmholtz instability. Because the baroclinic torque provides a source of vorticity, the vorticity is not materially conserved in this two-dimensional flow and analogy with three-dimensional turbulence can be drawn. We have shown that a deterministic mechanism is at the basis of this analogy, consisting of successive secondary Kelvin-Helmholtz instabilities transferring energy toward small scales. This view contrasts with the usual processes leading to energy transfers in three-dimensional turbulence.

This fundamental approach of the flow dynamics should be complemented by more applied studies, turned toward oceanography. The succession of secondary Kelvin-Helmholtz instabilities at different scales is supposed to be one of the mechanism by which mixing occurs in the ocean (Woods 1969, Thorpe 1987). It would thus be important to evaluate mixing in the present simulations. Also, the statistical properties of the flow would be of great interest, by comparison with spectra found either in the ocean or in the atmosphere.

Such a study is solely two-dimensional. In three-dimensional shear layers, intrinsically three-dimensional instabilities occur, which may deeply modify this view of the flow, if weakly stratified. It may be however that, for strong stratification, three-dimensional instability would be mostly convective and occuring in the cores of the primary Kelvin-Helmholtz vortices (Schowalter et al. 1993), thus inaffecting the dynamics of the baroclinic layers (except, possibly, for the "near-core" instability that we have found). This conjecture would need to be examined, by performing very high resolution three-dimensional numerical simulations.

References

BOURUET-AUBERTOT P., J. SOMMERIA & C. STAQUET 1994. Subm. to *J. Fluid Mech.*.

BRACHET M.-E. 1990. *C.R. Acad. Sci.*, t. 311-II, 775-780.

BROWAND F.K., D. GUYOMAR & S.-C. YOON 1987. *J. Geophys. Research*, 92-C5, 5329-5341.

CANUTO C., M.Y. HUSSAINI, A. QUARTERONI & T.A. ZANG 1988. *Springer series in computational physics*, Springer-Verlag.

CORCOS G.M. & F.S. SHERMAN 1976. *J. Fluid Mech.*, 73, 241-264.

CORCOS G.M. & F.S. SHERMAN 1984. *J. Fluid Mech.*, 139, 29-65.

DALAUDIER F., C. SIDI, M. CROCHET & J. VERNIN 1994.*J. Atmos. Sci.*, 51, 2, 237-248.

DELISI D. & G.M. CORCOS 1973. *Bound. Layer Met.*, 5, 121.

DRITSCHEL D.G., P.H. HAYNES, M.N. JUCKES & T.G. SHEPHERD 1991. *J. Fluid Mech.*, 230, 647-665.

GOSSARD E.E., J.H. RICHTER & D. ATLAS 1970. *J. Geophys. Research*, 75, 903-913.

GREGG M. 1987. *J. Geophys. Research*, 92-C5, 5249-5286.

HAZEL P. 1972. *J. Fluid Mech.*, 51, 39-61.

HERRING J.R. & O. METAIS 1989. *J. Fluid Mech.*, 202, 97-115.

HO C.M. & P. HUERRE 1984. *Ann. Rev. Fluid Mech.*, 16, 365-424.

KLAASSEN G. P. & W.R. PELTIER 1985a. *J. Atm. Sci.*, 42, 1321-1339.

KLAASSEN G. P. & W.R. PELTIER 1985b. *Geophys. Astrophys. Fluid Dyn.*, 32, 23-60.

KLAASSEN G. P. & W.R. PELTIER 1985c. *J. Fluid Mech.*, 155, 1-35.

KLAASSEN G. P. & W.R. PELTIER 1989. *J. Fluid Mech.*, 202, 367-402.

KLAASSEN G. P. & W.R. PELTIER 1991. *J. Fluid Mech.*, 227, 71-106.

KOOP C.G. & F.K. BROWAND 1979. *J. Fluid Mech.*, 93, 135-159.

LOMBARD P.N., D.D. STRETCH & J.J. RILEY 1990 . *Proceedings of the Ninth Symposium on Turbulence and Diffusion*, Roskilde, Denmark, 30 April-3 May.

PATNAIK P. C., F.S. SHERMAN & G.M. CORCOS 1976. *J. Fluid Mech.*, 73, 215-240.

PUMIR A. & E.D. SIGGIA 1992 . *Phys. Fluids* A, 4, 1472-1491.

SCHOWALTER D.G., C.W. Van ATTA & J.C. LASHERAS 1993. Subm. to *J. Fluid Mech.*

STAQUET C. 1991. O. Métais and M. Lesieur Eds. Kluwer Academic Publisher, 469-487.

STAQUET C. 1994a. Subm. to *J. Fluid Mech.*.

STAQUET C. 1994b. To appear in *Meccanica*.

THORPE S.A. 1981. *J. Fluid Mech.*, 103, 321-344.

THORPE S.A. 1987. *J. Geophys. Res.*, 92-C5, 5231-5248.

WOODS J.D. 1969. *Radio Science*, 4, 1289-1298.
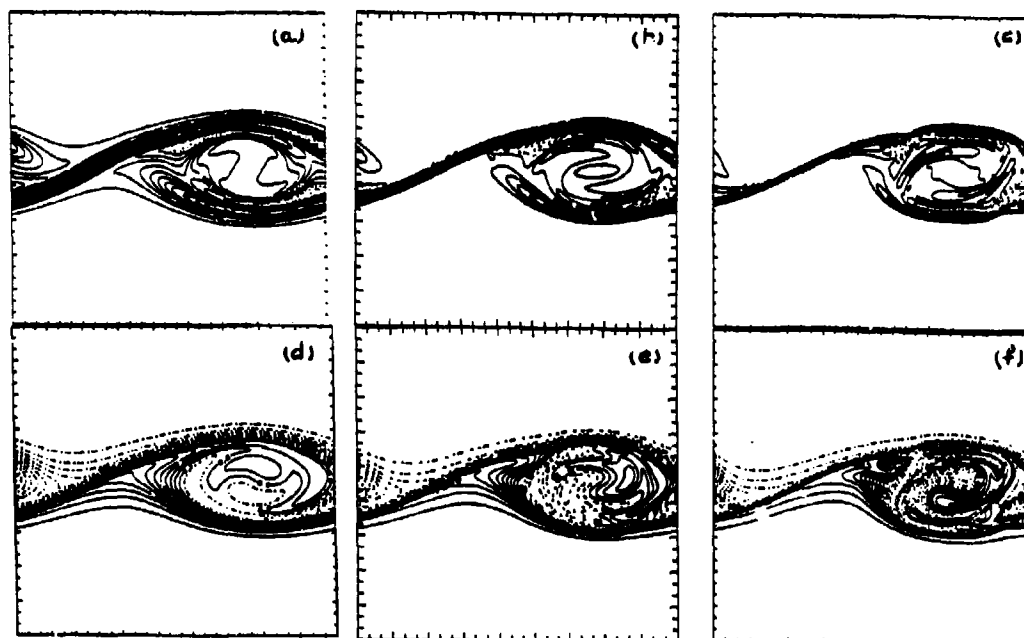
Figure 1: Influence of the initial Reynolds number Re upon the structure of the flow at the time the vorticity reaches an absolute maximum Ω_{max} (located at the stagnation point of the vorticity layer). d is the distance between contour levels. *Contours of constant vorticity.* (a) Re=400. Ω_{max}=2.3, d=0.1; (b) Re=1000, Ω_{max}=3.6, d=0.3; (c) Re=2600, Ω_{max}=6., d=0.5. *Associated contours of constant density:* (d) to (f), with d=0.1.
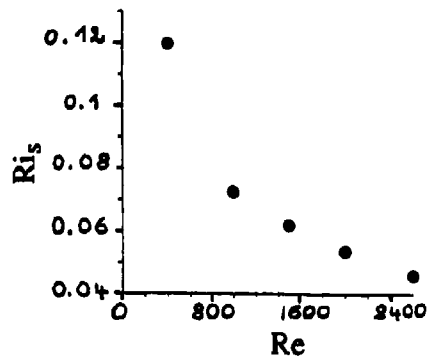
Figure 2: Richardson number at the stagnation point of the layer, Ri_S, versus Reynolds number.
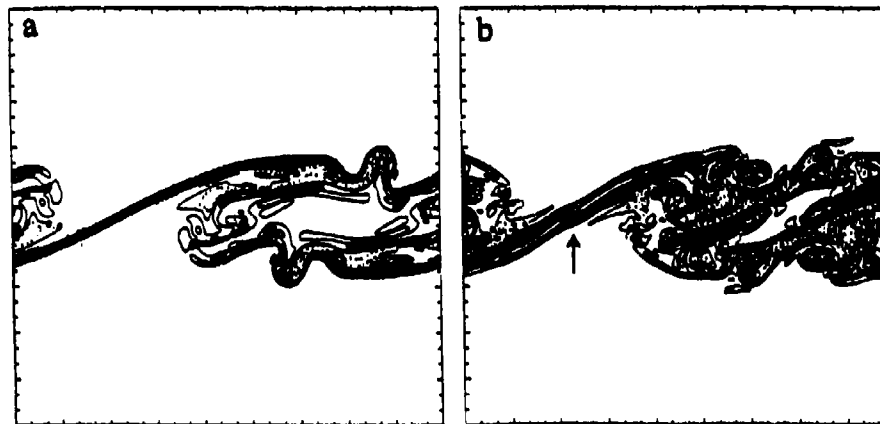
Figure 3: Development of secondary instabilities in a Re=2600 shear layer. Constant contours of the vorticity at (a) t=56.9; Ω_{max}= 6.; (b) t=73; Ω_{max}= 4.5. Ω_{max} is the vorticity maximum. d (distance between contour levels)=0.5. The arrow points toward a secondary Kelvin-Helmholtz vortex developing at the stagnation point of the baroclinic layer.
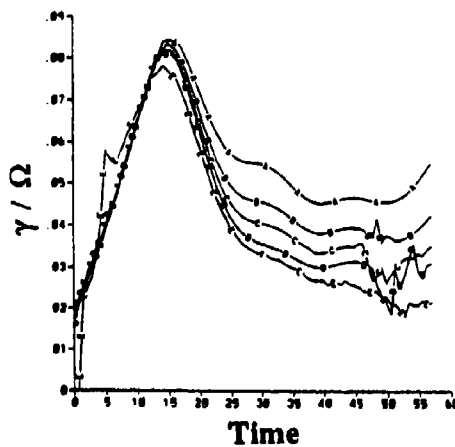
Figure 4: Temporal evolution of γ/Ω at the stagnation point of the baroclinic layer. γ is the (uniform) strain rate of the strain field induced by the large scale Kelvin-Helmholtz vortex in the stagnation point region of the baroclinic layer. Ω is the vorticity of the layer. In all calculations except for curve (e), only one Kelvin-Helmholtz structure develops. (a) Re=1000; (b) Re=1500; (c) Re=2000; (d) Re=2600; (e) Re=2000, but two Kelvin-Helmholtz structures develop.

7
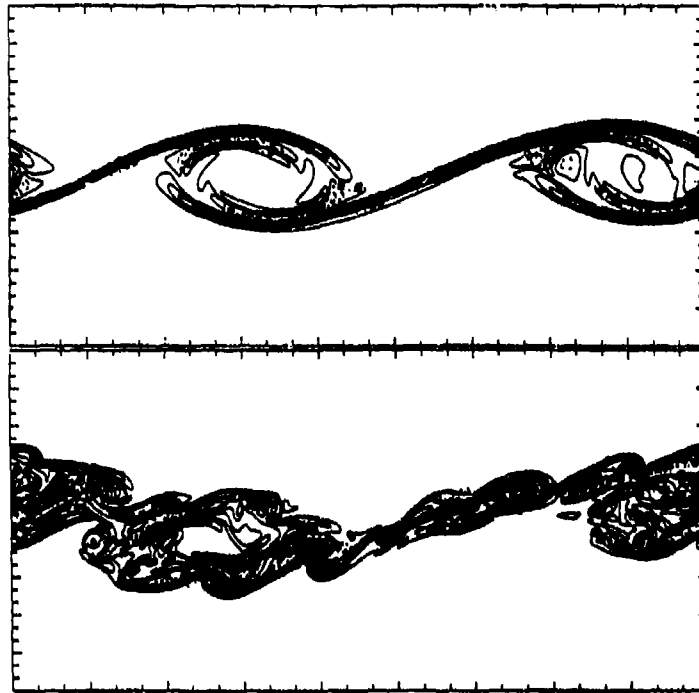
Figure 5: Development of secondary instabilities in a Re=2000 shear layer with two Kelvin-Helmholtz vortices developing and pairing. *Constant contours of vorticity* : (a) t=42.7; Ω_{max}=4.8; (b) t=74; Ω_{max}=4.4. Ω_{max} is the vorticity maximum. The distance between contour levels is d=0.4.
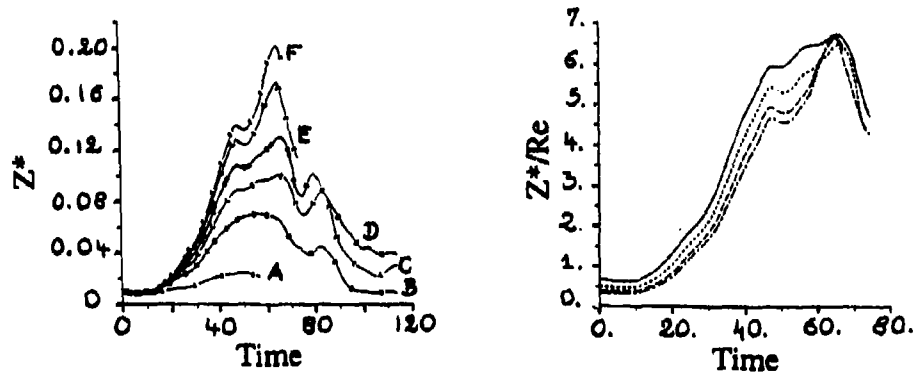
Figure 6: Strongly stratified shear layer with one Kelvin-Helmholtz structure developing. (a) Z^* defined in section V, versus time. (a) Re=400; (b) Re=1000; (c) Re=1500; (d) Re=2000; (e) Re=2600; (f) Re=3000. (b) Z^*/Re, equal to minus the dissipation rate of the total energy, is plotted versus time for Re≥1500. *Full line:* Re=1500; *Dash line:* Re=2000; *Long dash line:* Re=2600; *Short dash-long dash line:* Re=3000.

8

Secondary Instability and Three Dimensionalization in a Laboratory Accelerating Shear Layer with Varying Density Differences

Shizuo Yoshida[1], C. P. Caulfield[2]
and W. R. Peltier[2]
1: Department of Engineering Science, Hokkaido University
2: Department of Physics, University of Toronto

Abstract

We investigate the processes by which an accelerating stratified shear flow undergoes the transition to turbulence in a sequence of experiments in a tilted tank. Using direct measurements of the velocity and density profiles we observe that the Richardson number at onset of Kelvin-Helmholtz type instability varies only slightly with the total density difference, or the Reynolds number, if this is sufficiently high. However, we observe that the mechanisms by which the flow undergoes breakdown are both complex and diverse, and suggest that the (non-dimensional) total density difference and /or the ratio of the depth of the shear layer to the total tank depth are important parameters in the determination of the dominant secondary structures.

In general, inherently three dimensional, and relatively large scale, flow structures strongly suppress the formation of larger scale vortices through simple pairing. Also, these large scale three dimensional structures appear to totally dominate the transiton to turbulence, and appear to be much more significant in the breakdown of the flow than the small scale transverse convective rolls theoretically predicted by Klaassen and Peltier (1985b), and subsequently oberved by Thorpe (1985).

Subharmonic, quasi-two dimensional vortex transitions are observed, but these appear not to occur just as simple pairings. For example, three vortices are observed to merge into a single secondary billow, or two merge and the other persists, as predicted theoretically by Klaassen and Peltier (1989). Three dimensional vortex merging (knots) of initially quasi-two dimensional billows are also observed. Such knots are observed not only as pairwise transitions, as discussed by Thorpe (1985), but also single billows are observed to knot with both adjacent neighbours. Also, billows are observed to bow during merging events.

Narrow streamwise vortices (tubes) are also observed, and they appear to have two distinct generation mechanisms. Firstly, they are observed to develop as secondary structures between quasi-two dimensional billows subsequent to billow roll-up. Also, particularly at larger density differences, or when the shear layer is sufficiently narrow compared to the total tank depth, we also observe billows that never fully develop across the tank, but rather bifurcate into a "Y" shaped structure. The two arms of the "Y" align in a streamwise direction, and wrap around neighbouring billows in a similar manner to secondary tubes, however we postulate that in a fundamental sense these "Y" shaped structures are a primary instability of the flow.

1: Introduction

Stably stratified shear flows occur in many geophysical flows of interest, and the processes by which such flows become unstable, break down and (potentially) mix the fluid has been a topic of much research (see Thorpe 1987 for a review). It is well known, from a theorem due to Miles (1961) and Howard (1961) that if the gradient Richardson number, Ri, (a measure of relative importance of the buoyancy forces to the inertial forces) defined as

$$Ri = -\frac{(g d\rho/dz)}{\rho_0 \left(d\bar{U}/dz\right)^2} \, ,$$
(1)

where ρ and $\hat{U}$ are the background distributions of density and velocity respectively and ρ_0 is some reference density, is greater than 1/4 throughout the flow, then the flow is stable to linear, normal mode type perturbations.

Theoretical analyses (see Drazin and Reid 1981 for a review) have concentrated until recently on the linear, two dimensional, instability of inherently two dimensional background states which violate this condition. This approach can be motivated by a theorem due to Yih (1955), which is essentially a generalisation of Squire's Theorem (1933) to stratified flow. A potentially unstable mode whose wavenumber vector is oriented at an angle to the mean flow can be identified with an equivalent mode with wavenumber vector parallel to a mean flow with a higher Richardson number. Thus if the maximal (at given Ri) growthrate of a mode increases at a sufficient (well-defined) rate with Ri, Yih's theorem predicts that the mode travelling at an angle will, within linear theory, have a larger growthrate than all modes travelling parallel to a given flow. In this case, the flow may be *primarily unstable* to three dimensional disturbances. Since, in most flows (though not all, see e.g. Caulfield 1994) the effect of increasing stable stratification (and thus Ri) is stabilising on the flow instability, the reasonable expectation is that the primary instability of a parallel stratified shear layer will be largely two dimensional.

Many experiments (e.g Thorpe 1968, Yoshida 1977, Koop and Browand 1979, Lawrence *et al.* 1991) have demonstrated that various flows with sufficiently small Ri somewhere within the flow do indeed exhibit primary two dimensional instabilities of varying kinds, predicted relatively well by linear theories. An important parameter in the character of the instability appears to be the ratio of the characteristic lengthscale of velocity variation to the characteristic lengthscale of density variation. If the depth of the region of density variation is very much smaller than the depth of the region of velocity variation then the primary instability is of Holmboe type, with counter-propagating cusped waves appearing on the density interface, manifestations of the existence of a regions of concentrated spanwise vorticity regions above and below the interface. This instability has no analogue in the unstratified shear layer, and is not as well understood as the instability which appears when the velocity and density distributions are approximately matched. In this case, analogously to the unstratified flow, the shear layer rolls up into spanwise tubes of vorticity (the so-called Kelvin-Helmholtz billows).

Two dimensional numerical simulations of such flows exhibit well-defined vortex roll-up, and after the vortex has equilibrated, some mixing onsets in the core due to the statically unstable density field which developes (see e.g. Klaassen and Peltier 1985a). However, a single Kelvin-Helmholtz billow does not appear to break down vigorously. In two dimensions, much more mixing appears to take place during secondary subharmonic transitions, when billows merge (see Klaassen and Peltier 1989). Though this is usually referred to as vortex pairing, other transitions (e.g. $3 \to 2$ or $3 \to 1$) were predicted and numerically simulated, and so we prefer to use the term vortex merging to describe this process.

Nevertheless, as discussed in Klaassen and Peltier (1985b), any attempt to characterise the onset of turbulence purely in terms two dimensional theoretical and numerical calculations must be treated with extreme caution, as the evidence from the laboratory is that the onset of mixing is inherently linked to the onset of three dimensional motions within, and between, several billows which have developed across a streamwise extent significantly larger (and in a real sense less constrained) than a typical numerical domain.

Billows, as discussed by Thorpe (1987) are subject to a variety of secondary instabilities. On a small scale, there is the convective shear aligned instability predicted in Klaassen and Peltier (1985b). However, as mentioned by Thorpe,

"the appearance of (these) secondary patterns in the billows does not signal an immediate transition to turbulence."

Also observed by Thorpe in his now classic tilted tank experiments are "tubes", thin streamwise tubes of vorticity communicating between two billows, and "knots", which he described as three dimensional pairing events, in the sense that the billows do not pair simultaneously across their

2

whole width.

An understanding of these transitions both in their efficiency for mixing, and their dependence on the background parameters is extremely important. Thorpe identified the Reynolds number, which we shall define as

$$Re = \frac{Ud}{\nu} , \qquad (2)$$

where U is half the total velocity difference within the flow, d is half the shear layer depth, and ν is as usual the kinematic vorticity of the fluid under question, and the bulk Richardson number, Ri_0 defined as

$$Ri_0 = \frac{g \Delta d}{U^2} , \qquad (3)$$

at onset of the instability as being important parameters, as one expects of course that for small Re, the effect of viscosity will be to inhibit the development of the small scales necessary for the full development of the turbulence, or even inhibit the growth of primary and secondary instabilities. Here, Δ is defined as

$$\Delta = \frac{(\rho_1 - \rho_0)}{(\rho_1 + \rho_0)} , \qquad (4)$$

where ρ_1 is the maximal density within the flow, and ρ_0 is the minimal density within the flow. We note that, in a sense, Δ is a nondimensional expression for *half* the total density difference within the flow.

In this paper, we attempt to investigate further the routes by which a stratified shear layer undergoes mixing in a three dimensional manner, by means of discussion of a sequence of new tilted tank experiments, largely in the region of parameter space suggested by Thorpe to be susceptible to a wide range of three dimensional instabilities. We wish to investigate the possible importance of other nondimensional parameters which naturally arise in these experiments. In particular, two parameters which a careful consideration of theory suggests may be important are the above mentioned Δ, and the ratio, D of the shear layer depth to the total tank depth. The reason that we are interested in the nondimensional density difference is that it appears, not only in the definition of the bulk Richardson number Ri_0, but also in the definition of the Rayleigh number associated with the convectively unstable regions in the billow core (see Klaassen and Peltier 1985b). We are also interested in the effect of variation in the ratio D because of the effect that that variation in the shear layer depth has on the *dimensional* wavelength, and core diameter of the billows which appear. Clearly, if the primary billows which appear are too large, the boundaries will suppress merging mechanisms which are characterised by large vertical displacements of the billow cores. Of course, variation in D, all things being equal, unavoidably causes a variation in Re too, so one must be extremely careful in the interpretation of the effect in variation of any one parameter.

2: Experimental procedure

We conducted several series of laboratory experiments using a tilting tank, similar to those used by Thorpe (see e.g. Thorpe 1968, Thorpe 1985). The tank is 3 metres long, 30cm wide and 15 cm deep. Our visualisation and filling procedures were different from Thorpes however, and we thus describe them here. First we filled the tank to depth of 7.25cm with a precisely measured volume of salty water with varying amounts of salt added by volume (we conducted experiments in the range of 2 g l^{-1} $\rightarrow$ 200 g l^{-1}). For these values, we thus were able to scan values in Δ in the range:

$$7.914 \times 10^{-4} \leq \Delta \leq 4.776 \times 10^{-2} .$$

For the visualisation experiments, we then added a small quantity of Fluorescein (Uranine or $C_{20}H_{10}Na_2O_2$), and then vigorously and repetitively tilted the tank until such time as the contents of the tank were well-mixed to a density ρ_1. A small ($\sim$ 20ml) sample was then taken,

3

which was used to subsequently calibrate the conductivity probe measurements, and to obtain a highly accurate value for Δ.

We then tilted the tank at an angle of approximately 25° and introduced, at a very slow rate, a volume (4.5l) of salty water, which was dyed blue for the visualisation experiments, at a density, ρ_2, where

$$\rho_2 = (\rho_1 + \rho_0)/2 \ ,$$

i.e. the mean of ρ_1, the lower layer density and ρ_0 the density of fresh water. This volume of blue salty water is equivalent to a depth of 0.5cm of the tank. The filling rate was controlled to be sufficiently slow to suppress visible mixing between the fluid of density ρ_2 and the fluid of density ρ_1.

Finally, we filled the tank with fresh water at room temperature with density ρ_0, initially at a slow rate to once again suppress visible mixing between the fluid with density ρ_0 and the fluid with density ρ_2. Since the density differences, especially with the low salt concentrations, were extremely small, the temperature of the fresh water used in the upper layer was carefully monitored. Once the tank was filled, it was slowly tilted back to the horizontal, once again every effort being made to minimise mixing.

The fluid in the tank was then left for varying amounts of time, to allow the region over which the density varied to take on different values. Just before the experiment a profile of density was taken using a conductivity probe, and a profile of temperature was taken at the midpoint of the tank. The temperature was measured to an accuracy of $0.1°C$, and the variation from top to bottom ranged from a few tenths of a degree for the experiments with small values of Δ to about one degree for the experiments with larger values of Δ. Density and temperature profiles for a typical experiment are shown in figure 1.
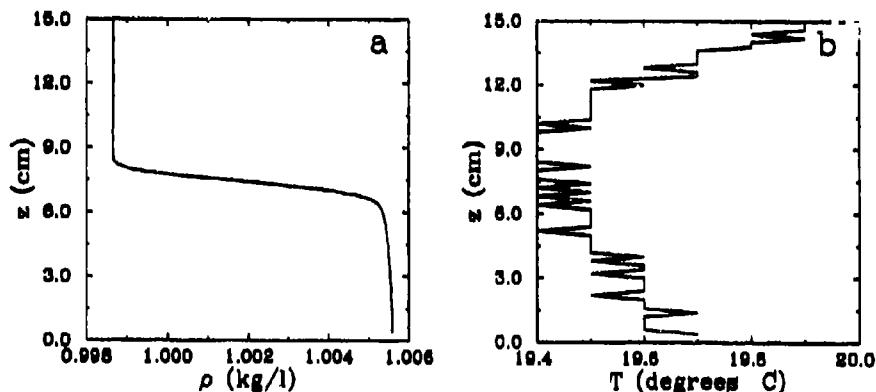
Figure 1: a) Density profile and b) temperature profile for a typical experiment (here $\Delta = 3.4129 \times 10^{-3}$).

Note that the density varies in a very smooth, and approximately linear fashion from ρ_1 to ρ_0, and no record can be seen of the intermediate layer in the density field, though it is still very clear in the flow visualisations. This is not at all surprising, since the entire filling process took several hours typically. Fitting a line, matched to the density gradient at the midpoint of the tank, we were able to define a characteristic scale of density variation h defined by

$$\frac{d\rho}{dz}(z = \text{midpoint}) = \frac{(\rho_0 - \rho_1)}{2h} \ , \tag{5}$$

and so h is equal to the half depth of the region of significant density variation. We also note that this profile is close to the error function profile assumed by Thorpe (see e.g. Thorpe 1985). We conducted a series of experiments to test the postulated velocity distribution discussed at length

4

by Thorpe in the appendix of his 1985 paper (essentially the viscous velocity profile arising from the density driven flow), by particle tracking aluminium particles by means of photographic streaks. Good agreement was found, and so we feel confident in using his expressions for the various flow parameters, namely R, the ratio of the velocity scales to the density scale, D the ratio of the shear layer depth to the tank depth, Re and Ri_0 at instability onset. In figure 2, we plot experimental values of R, D, Δ and Ri_0 against Re. Experiments with tilt angle $\alpha_0 = 7.5°$ are denoted by a cross, and experiments with $\alpha_0 = 10.8°$ with a circle. Note that Re increases with Δ, but not uniformly. Several values of very similar Δ have quite different Re, which can be attributed to the fact that these experiments were started at different times after the filling was complete, and thus had varying values of h and D.
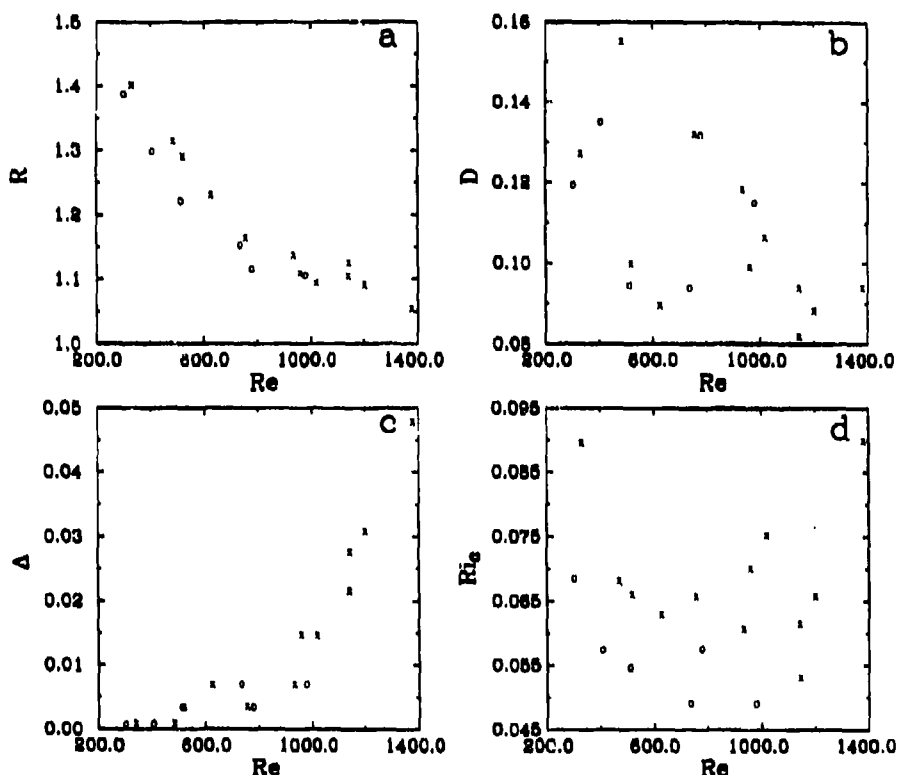
Figure 2: Experimentally measured values of a) R; b) D; c) Δ; and d) Ri_0 plotted against Re. Experiments with $\alpha_0 = 7.5°$ are denoted by a cross, and experiments with $\alpha_0 = 10.8°$ with a circle.

The ratio R of velocity scale to density scale is equal to

$$R = \frac{1 + \sqrt{1 + \pi \nu t_0 / h^2}}{2} \,, \qquad (6)$$

where t_0 is the time from tilt to instability onset. For our experiments t_0 varied from 3.2 to 41 seconds, while R varied from 1.05 to 1.4. In general R decreased as Δ increased. We note that this implies that the shear layer depth is typically larger then the density layer depth, but of the same order, and so Holmboe type instabilities are not expected, nor are they observed. Thus the ratio D of the shear layer depth $2d$ to the total tank depth L in terms of measurable quantities is

$$D = 2Rh/L \,. \qquad (7)$$

5

The Reynolds number at onset is

$$Re = \frac{g\Delta R h t_0 \sin \alpha_0}{\nu} ,$$ (8)

where α_0, as mentioned above, is the tilt angle. In all the experiments, for simplicity we tilted the tank, and then left it at that angle. Though this means that the flow continues to be accelerated, we believe that the values of the angle α_0 which we chose were sufficiently small (in general $\alpha_0 = 7.5°$, though some of the experiments at smaller Δ had $\alpha_0 = 10.8°$) so that the acceleration was sufficiently small for the flow unsteadiness to not invalidate our results, yet sufficiently large so that secondary instabilities onset before end effects intruded. The final parameter of interest is the bulk Richardson number Ri_0 at onset, defined as

$$Ri_0 = \frac{R^2 h \cos \alpha_0}{g \Delta t_0^2 \sin^2 \alpha_0} .$$ (9)

As can be seen in figure 2, onset values of Ri_0 and Re were in the ranges

$$0.049 \leq Ri_0 \leq 0.09 ,$$
$$300 \leq Re \leq 1400 ,$$

respectively. There did not appear to be any trend in the relationship between Ri_0 and Δ, though Ri_0 was smaller for approximately the same $\angle$ for the experiments with larger tilt angle α_0. Also Ri_0 seemed to be largely de-correlated from Re

3: Experimental results

Since we are principally interested in the processes by which large scale breakdown of the flow occurs, we designed the experiments to highlight the processes by which the billows broke down, and so we did not concern ourself with the visualisation of the small scale streamwise convective rolls predicted by Klaassen and Peltier (1985b). Using a camera mounted above the tank, on the supporting frame which tilted with the tank, we videotaped the visualisation experiments. A mirror was aligned so that both top and side views of the central 70cm of tank were recorded.

Also, since we were interested in the mixing efficiency of the various instabilities we also measured the density of the fluid using the conductivity probe after the experiments. As a control, we also measured the density profile after an experiment which did not become unstable before end effects were clearly significant. The characteristics of the profiles for both stable and unstable tilted tank experiments were largely similar, and thus we believe that mixing efficiencies extracted from experiments of this type should be treated with extreme caution, as the final profile appears to be totally dominated by the sloshing overturning at the end of the experiment.

Within each experiment, in general we observed the development of billow type structures, perhaps some process of three dimensionalisation, and, if so, then rapid breakdown. For the smaller values of Δ and Re, and thus larger values of D and R, we observed relatively long wavelength billows which paired in a largely two dimensional manner, and indeed in some extreme cases, did not pair at all. However, as D decreased, and Δ increased, the behaviour changed markedly, even between experiments with very similar transition Re and Ri_0. As the wavelength of the billows decreased, billows ceased to be aligned perpendicularly to the background flow. For intermediate values of Δ and/or D, typically the billows would develop across the entire width of the tank, but be bent. A thin tube of streamwise vorticity would develop between the points of greatest curvature on two billows, which clearly was associated with the rapid breakdown of the billows. Typically this secondary instability did not suppress pairing, and it would only become apparent some time after the primary billows had become well-developed. We believe this is the secondary "tube" discussed by Thorpe.

6

As Δ increased, for the smaller values of D, the bends in the billows became more pro-
nounced, and a new phenomenon occured. Over a certain extent near the middle of the tank,
one side N billows would start to form, while on the other side $N + 1$ billows would appear with
a very similar wavelength. We would suggest two possible causes for this new phenomenon.
Firstly, unavoidably the velocity and density fields are not uniform throughout the tank, and so
the particular background conditions susceptible to shear flow instability vary within the tank.
Thus slight variations in the conditions would suggest that even for the same nondimensional
wavenumber predicted by linear theory, the wavelength of that instability, when manifested at
finite amplitude would vary from place to place. Alternatively, as is well known, the variation
of growthrate for Kelvin-Helmholtz instability with wavenumber is relatively weak, and so, in a
long tank a competition between two close wavelengths which both are commensurate with the
length of the tank is, at least theoretically, possible.

Whatever the cause, (and slight imperfections at the sidewalls cannot be discounted) a billow
structure would appear which did not extend across the entire width of the tank. Sometimes
this fragmentary billow would rapidly merge with the nearest portion of a fully developed billow.
Alternatively, as mentioned in the abstract, the billow would form a "Y" shaped structure. The
two arms of the "Y" align in a streamwise direction, and wrap around neighbouring billows in a
similar manner to secondary tubes. However the "Y" type structure appeared to onset earlier in
the flow, before the billows were very well developed, and so we postulate that in a fundamental
sense these "Y" shaped structures are a primary instability of the flow.

Of course, with both these structures (namely the tubes and the "Y" shaped billows), billow
merging typically did not proceed in an orderly two dimensional fashion. As discussed by Thorpe
(1985), "knots" appeared in the sense that billows did not merge uniformly across the entire
tank width. Unlike Thorpe, we were not able to identify a decrease in the likelihood of knots
with increasing Re, and indeed it appeared to become more prevalent as D decreased. This may
be because as D decreases, and hence the lengthscale of the billows decreases relative to the tank
depth, it is reasonable to assume that the sidewall effects are becoming less significant. Because
we varied Δ, reduction in the depth $2h$ of the region of density variation did not necessarily
mean that the Reynolds number Re was also reduced. The "Y" shaped structures would rapidly
cause the neighbouring billows to break down.

Another observed knot structure involved a three billow interaction. The middle billow
would start to merge with the two outer billows simultaneously, and thus would be aligned
diagonally between the two outer billows. The two outer billows would start to merge, with
the middle billow being engulfed by the process. This process appeared to occur for small
wavelength billows (i.e. when D was small or Δ was large). This merger event appeared to
require quite large vertical deflections of the billow cores, and since the billow core diameter
is generally proportional to the wavelength, small wavelength billows appeared to have enough
"room" to undergo this transition. Finally, it is important to mention that knotting not only
occured through merger being initiated near to the sides of the tank, but also on occasion two
neighbouring billows would bend towards each other and merge in the middle of the tank with
widely separated ends.

These three dimensional merging events appeared to preclude the formation of well or-
ganised quasi-two dimensional vortices which were observed to appear during the quasi-two
dimensional merging events. Even in two dimensional merger however, it would not, in general
be correct to describe the observed behaviour as pairing, as three billows merging simultaneously
in a quasi-two dimensional manner was observed as well, as theoretically predicted (Klaassen
and Peltier 1989).

4: Conclusions

An attempt has been made to investigate and describe qualitatively the possible large scale three
dimensional instabilities. Provided the scale of the billows is sufficiently small relative to the tank
depth a rich variety of three dimensional structures appear which do not appear to be a strong

function of Re or Ri_0 at onset. Of particular interest is the formation at the first apparent stage of onset of imperfect billows which do not extend across the entire width of the tank. The rich variety of three dimensional transitions preclude the efficient formation of subharmonic larger scale vortices, and in our experiments the simple primary development of two dimensional billows which "pair" was one, rather special, possibility amongst many for the transition of a shear layer to vigorous mixing. Further experimentation and numerical simulation are necessary, for we still are an extremely long way from being able to plot a transition diagram for stratified shear flows analogous to that drawn by Busse (1981) for Rayleigh-Bernard convection (see Thorpe 1987 for a fuller discussion). We seemed to observe the importance of a further parameter of importance, namely the ratio of the shear layer depth to the tank depth, or alternatively the nondimensional density difference, further complicating our task. To make matters worse, throughout we have not concerned ourseleves with the Prandtl number, which in real geophysical applications is likely to be important.

5: References

Busse, F. H., 1981: in "Transition and Turbulence," ed. Meyer R. E., *Academic*.
Caulfield C. P., *J. Fluid Mech.* **258** 255–285 (1994).
Drazin P. G. and Reid W. H., 1981: "Hydrodynamic Stability, " *C. U. P.*
Howard L. N., 1961: *J. Fluid Mech.* **10** 509–512.
Klaassen G. P. and Peltier W. R., 1985a: *J. Atmos. Sci.* **42** 1321–1339.
Klaassen G. P. and Peltier W. R., 1985b: *J. Fluid Mech.* **155** 1–35.
Klaassen G. P. and Peltier W. R., 1989: *J. Fluid Mech.* **202** 367–402.
Koop C. G. and Browand F. K., 1979: *J. Fluid Mech.* **93** 135–159.
Lawrence G. A., Browand F. K. and Redekopp L. G., 1991: *Phys. Fluids* A **3** 2360–2370.
Miles J. W., 1961: *J. Fluid Mech.* **10** 496–508.
Squire H. B., 1933: *Proc. Roy. Soc.* A **142** 621–628.
Thorpe S. A., 1968: *J. Fluid Mech.* **32** 693–704.
Thorpe S. A., 1985: *Geophys. Astrophys Fluid Dyn.* **34** 175–199.
Thorpe S. A., 1987: *J. Geophys. Res.* **92** C 5231–5248.
Yih C-S., 1955: *Quart. Appl. Math.* **12** 434–435.

Stability of nonlinear stratified flow over topography

T.R. Akylas, J. Ramirez & D. Prasad

Department of Mechanical Engineering
Massachusetts Institute of Technology
Cambridge, Massachusetts 02139, USA

Summary

We examine the stability to small perturbations of Long's steady, finite-amplitude internal-wave patterns generated by stratified flow of large depth over topography. Figure 1 is a schematic of the flow configuration. Far upstream ($x \to -\infty$), the flow is uniform and the Brunt-Väisälä frequency is constant. Above the obstacle, the flow is disturbed, and the higher the obstacle steepness, ϵ, the more severe this disturbance is. In fact, Long's steady-state theory predicts that for $\epsilon > 0.85$ the streamlines overturn ('break') and the flow is expected to be statically unstable. We examined the stability of these steady states for $\epsilon < 0.85$, using the asymptotic theory of Kantzios & Akylas (1993). A small localized perturbation to the steady state was assumed, and its development in time was followed by solving the governing evolution equations numerically. Figure 2a shows the disturbed (dotted) streamlines for $\epsilon = 0.5$ at time $T = 0.5$, while Figure 2b shows the disturbed streamlines for the same value of ϵ at a later time, $T = 2.0$. Clearly, the disturbance is spreading out (dispersing); the flow relaxes to the steady-state streamlines (continuous line), and there is no instability. On the other hand, for $\epsilon = 0.75$ (see Figures 3a,b) the disturbance grows and instability is present. The conclusion is consistent with the disturbance kinetic energy shown in Figure 4 as a function of time for various values of ϵ. The kinetic energy grows for small time, owing to the interaction of the disturbance with the basic flow, but later this interaction ceases and the kinetic energy approaches a constant value when $\epsilon \leq 0.7$. However, when $\epsilon \geq 0.7$ the kinetic energy keeps growing as energy is continually transferred from the basic flow to the disturbance. This instability is due to the steepening of streamlines of the basic flow as ϵ is increased (shear-flow instability); it occurs below the critical steepness for overturning predicted by the steady-state theory and appears to be new.

References

Kantzios, Y.D. & Akylas, T.R., An Asymptotic Theory of Nonlinear Stratified Flow of Large Depth Over Topography, *Proceedings of the Royal Society of London A*, **440**:639 653, 1993.
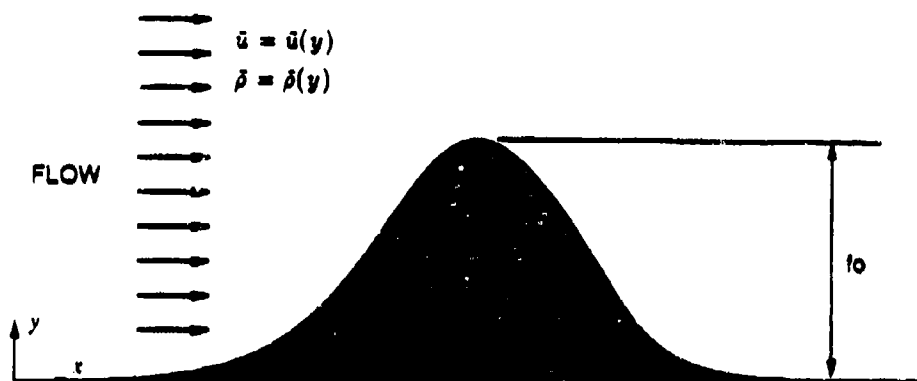
Figure 1
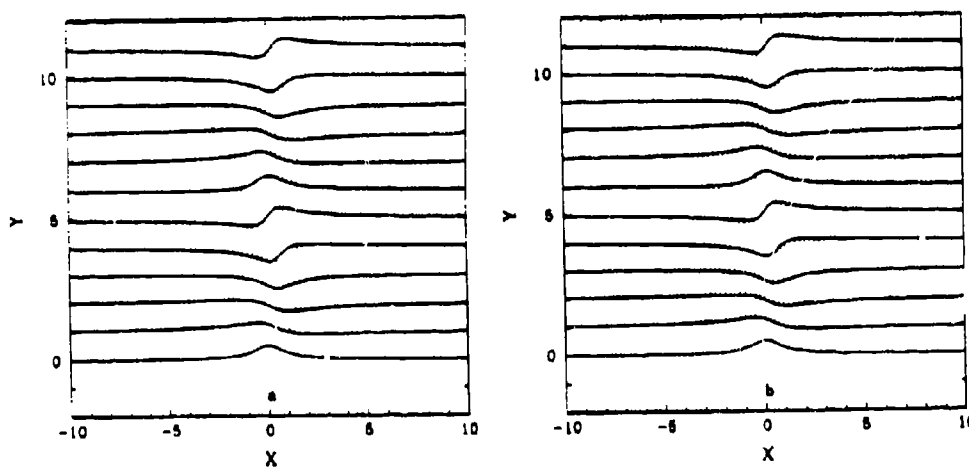
Figure 2a,b
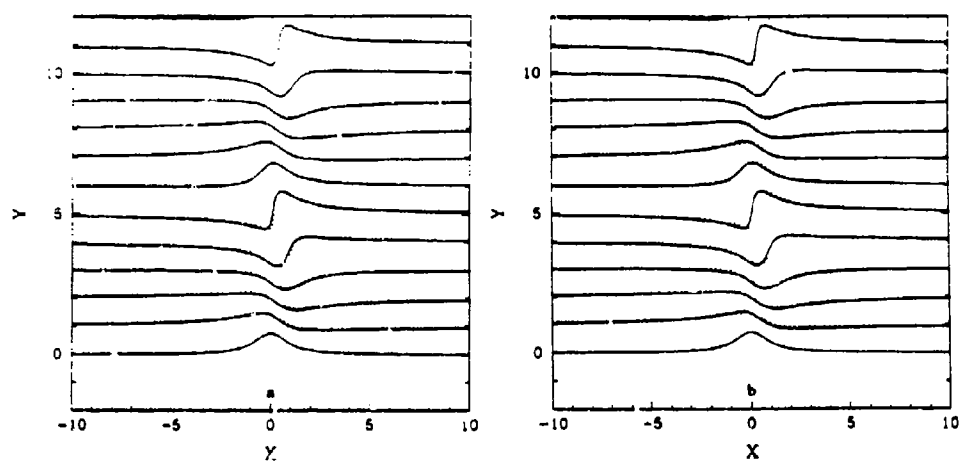
Figure 3a,b
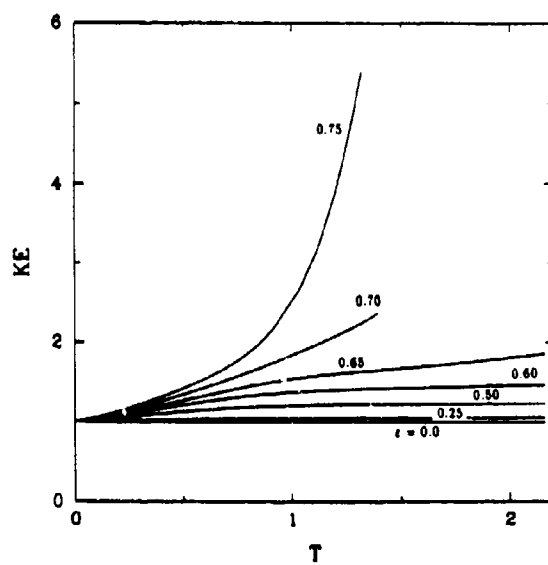
Figure 4

Observations and energetics of a naturally occurring shear instability in a stratified flow

HARVEY E. SEIM AND MICHAEL C. GREGG

Applied Physics Laboratory, College of Ocean and Fishery Sciences, University of Washington

Simultaneous profiles of microstructure, horizontal velocity, and acoustic backscatter are used to describe a naturally occurring shear instability. A kilometer-long set of 20 m tall billows formed downstream of the constriction in a tidal channel at the mid-depth interface of the approximately two-layered flow. The billows generate large density overturns and dissipation rates greater than 10^{-5} W kg^{-1} within the first large overturn. The billows produce an actively turbulent well-mixed layer which persists for more than 6 buoyancy periods. Using data from the large overturns within the shear layer, we find that $\epsilon/\nu N^2 \approx 3 \times 10^4$. In addition, the root-mean-square overturn scale, $L_{rms} = 2.6$ m, and buoyancy scale, $L_b = 2.7$ m, are about equal. The decrease in mean kinetic energy is approximately locally balanced by turbulent production. This implies no net radiation of energy into the surrounding fluid, but the large uncertainties in turbulent production make this result tenuous. The flux Richardson number averages 0.25, and the average momentum flux is 0.22 Pa.

INTRODUCTION

Though shear instabilities in stratified flows are thought to play a significant role in generating turbulence and vertical mixing in the ocean and atmosphere [*Gregg*, 1987; *Fritts and Rastogi*, 1985], few detailed measurements in a natural setting exist. A number of radar images, sometimes supplemented with radiosonde or aircraft data [e.g. *Browning et al.*, 1973] gave an initial description of clear air turbulence in the atmosphere, and dye studies in the ocean thermocline [*Woods*, 1968] revealed their presence in the ocean, but comprehensive observations of instabilities, over a range of scales and which follow their evolution, do not exist. We present simultaneous profiles of microstructure, horizontal velocity, and acoustic backscatter collected over an hour in an evolving shear instability. Though not comprehensive, the observations permit an examination of the initial formation of billows, their transition to turbulence, and a realization of the vertical mixing they produce. We also examine the energetics of the turbulent event by comparing profiles collected soon after the formation of the billows with profiles collected several buoyancy periods later.

BACKGROUND

This study took place in Admiralty Inlet, a 30 km long, 70 m deep tidal channel connecting the fjord-like estuary of Puget Sound to the Strait of Juan de Fuca (Figure 1). Owing to considerable river runoff into Puget Sound, a strong mean exchange flow exists in Admiralty Inlet, riverine water flowing seaward in the surface layer with a compensating inflow of denser water at depth. Two factors complicate this exchange flow in Admiralty Inlet: first, the 2 m tides of the northeast Pacific Ocean make the flow strongly time-dependent, and second, the rough bathymetry of Admiralty Inlet generates internal hydraulic controls. Both effects localize intense mixing in space and time within the Inlet.

The formation of the shear instability presented here was intimately linked to a transient hydraulic control off Bush Point (Figure 1).
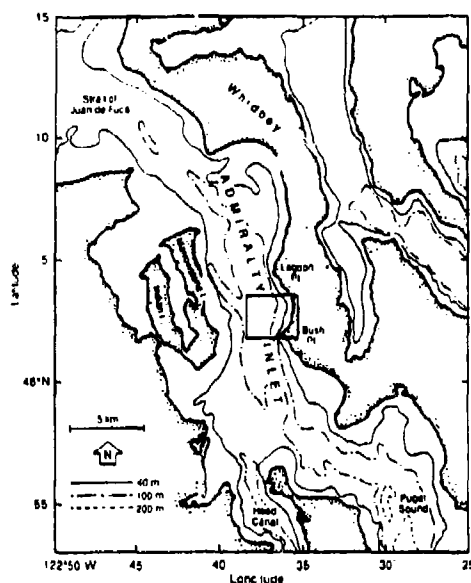
Fig. 1. Bathymetry of Admiralty Inlet. The box shows were intensive measurements of the billows were collected. Note that Bush and and Marrowstone Island for a pronounced constriction to northward (ebbing) flow.

Northward (ebbing) flow experiences a rapid contraction as it passes by this location: if the flow speed is large enough to rai~~ ~he iternal Froude number above 1 _ ~~re u is the flow speed and c_i is t ⌐ d of the gravest internal mode), the.. ? h⌐⌐⌐aulic control will exist at this ⌐⌐ ⌐r. ⌐ ~bservations span the time whe:) ⌐e flcw ⌐⌐ceierated from speeds insufficient to produc⌐ $Fr = 1$ to speeds well above this threshold [Seim and Gregg, 1994a].

The observations consist of measurements collected with three instruments. An acoustic Doppler current profiler (ADCP) measured the horizontal currents with 4 m vertical resolution and horizontal resolution of roughly 60 m. The advanced microstructure profiler (AMP), a free-falling loosely tethered platform, measured conductivity-temperature-depth profiles with 0.1 m resolution and 0.5 m resolution profiles of ϵ, the dissipation rate of turbulent kinetic energy, and χ, the dissipation rate of temperature variance (based on microscale shear and

temperature gradient measurements). A high-frequency echosounder measured profiles of volume scattering strength every second. Echosounder images proved invaluable in identifying processes sampled with the other instruments. Details of the instrumentation and processing are given in Seim and Gregg [1994a]; Seim et al. [1994].

OBSERVATIONS

Soon after high tide on March 28, 1988, we began AMP profiling steaming north with the current past Bush Point (Figure 2). A series of wave-like features centered at 0.5 MPa appeared on the echosounder roughly a kilometer downstream of the constriction (Figure 3). We continued 2 km downstream until billows were no longer obvious on the echosounder, then turned the ship into the current to steam upstream past Bush Point. The AMP could not be recovered while making headway so we instead maintained our position while collecting 10 more AMP profiles. Fortuitously, the tidal currents advected the billows beneath the ship, allowing us to collect a second set of profiles through the billows later in their evolution. This is most easily seen by integrating the velocity difference between the ship and 0.5 MPa, the pressure at which the billows were centered. The resulting ship track relative to the billows is shown in Figure 2c and demonstrates that profiles 53-56 and 63-66 were collected in approximately the same positions in the billows. We later compare these two sets of profiles (from the downstream and upstream legs) to assess the energetics of the shear instability.

AMP profile 5852 (Figure 4a) shows conditions just before the billows form (Figure 3 shows the location of this profile relative to the billows). The flow is two-layered with the weakly-stratified layers separated by a strong pycnocline. The upper layering moved 0.5 ms^{-1} faster than the lower layer. The vorticity thickness of the velocity interface is $h \approx 10$ m. Though large, ϵ is not associated with large overturns of the density field near the pycnocline. This is apparent in the displacement profiles (L_t), which show how far water parcels in
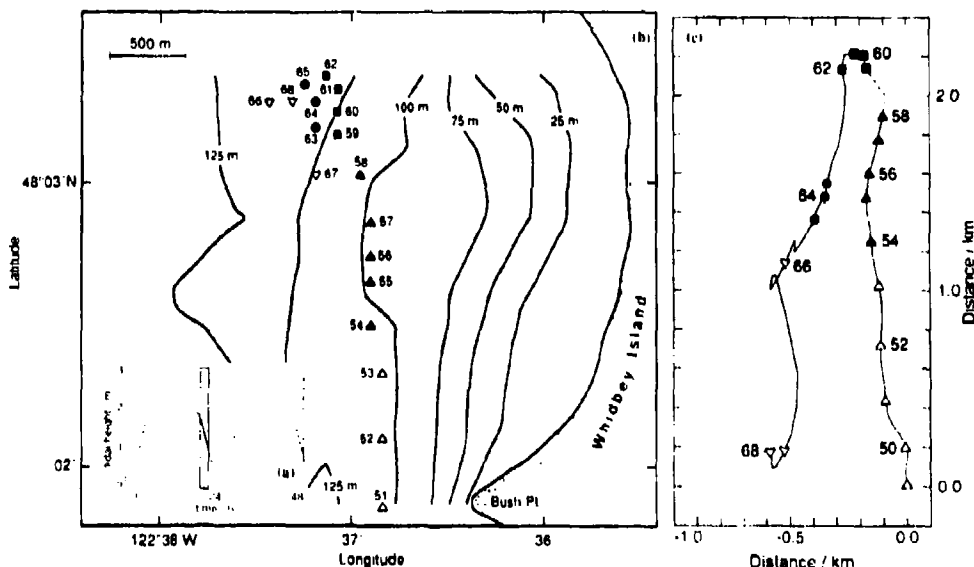
Fig. 2. a) Shading marks the sampling time on the tidal height curve. b) Location of AMP profiles within the intensive sampling area. Shaded symbols denote profiles through billows or a mid-depth mixed layer, and numbering indicates AMP profile. b) Ship track relative to 0.5 MPa. In this coordinate system profile 53-56 and 63-66 sample roughly the same position.

the observed density profile must be moved vertically to produce a gravitationally-stable density profile [Thorpe, 1977].

Conditions change dramatically by AMP profile 5854 (Figure 4b). This profile, which passes through the first large billow on the echosounder image (Figure 3), finds 20 m of the density field overturned, and $\epsilon > 10^{-5}$ W kg^{-1} over the same depth range. Vertical motions within the overturn strongly perturb the fallrate (w) of the profiler, and their form closely matches the displacement profile.

Outer scales of the billows are similar to those in laboratory flows. From the acoustic image we estimate a billow wavelength of 70 m, which with $h = 10$ m yields a non-dimensional wavenumber $\alpha \equiv k(h/2) \approx 0.49$. Similar α's are predicted for the most unstable mode by linear theory [Thorpe, 1971] and have been observed in the atmosphere [Fritts and Rastogi, 1985]. Thorpe [1973] found the aspect ratio of billows to decrease with increasing initial gradient Richardson number (Ri_o). Forming a bulk Richardson number as $Ri \equiv g\Delta\rho h / \rho(\Delta U)^2$, we estimate an initial $Ri_o = 0.2$ using $\Delta\rho = 0.5$ kg m^{-3} and $\Delta U = 0.5$ m s^{-1}. Given the

aspect ratio of the billows is 0.14 using a billow amplitude of 10 m, the macroscopic character of the billows is similar to laboratory and atmospheric observations.

Downstream continuation of the billows is apparent in Figure 3, but there is a substantial difference in the density of the billows. Figure 5 compares contours of density with profiles of L_t on the downstream leg. The pycnocline rises until billows form and large overturns occur. It then thickens and falls. Overturning, however, remains at the same pressure and therefore occurs in progressively less dense fluid, such that the large overturn in AMP 5857 is in weakly stratified water above the pycnocline. The variations in height of the pycnocline are related to the changing hydraulic conditions. The pycnocline movement changes the average density at the billows: Figure 5c shows ρ_p, the average density 0.3 and 0.65 MPa, changes by 0.3 kg m^{-3} over the section. This time-dependence prohibits interpreting the section as a statistically steady realization.

The upstream leg resampled the billows at a later stage of their evolution. Using the event-averaged density profile to determine $N^2 \approx$
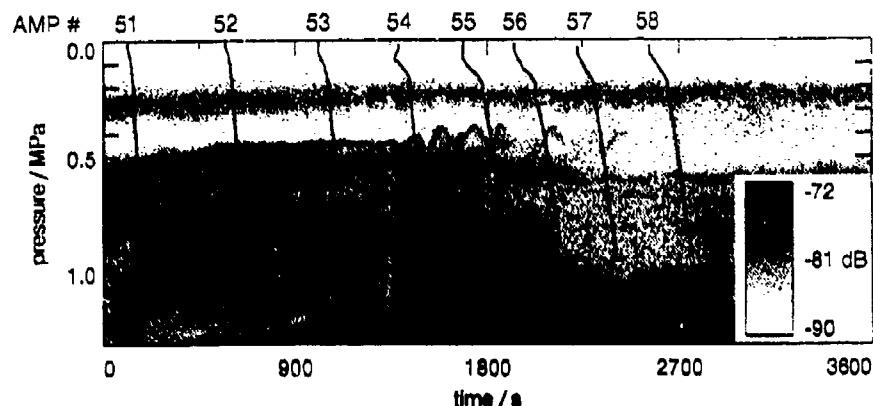
Fig. 3. Acoustic image of the water column during the hour the billows were observaed. Shading is proprotional to the volume scattering strength, in decibels relative to 1 μPa at 1 m. The dark nearly vertical lines are the estimated trajectories of AMP profiles.

10^{-4} s^{-2}, the upstream leg resamples the billows 4-8 buoyancy periods later. Surprisingly, the billows are still actively turbulent. The buoyancy Reynolds number, $Re_b \equiv \epsilon/\nu N^2$, is greater than 10^4, well above 2000 when an inertial subrange of isotropic velocities is to be expected [Gargett et al., 1984]. The impact the shear instability on the density field is clearly seen in Figure 4c: a 20 m thick well-mixed layer now splits the pycnocline and is associated with intense dissipation.

Some generalizations about the character of the turbulence and mixing generated by the billows are possible. Shear spectra from meters scales to dissipative scales are fit well by the universal spectrum [Panchev and Kesich, 1969], indicating that simple theories of isotropic turbulence are applicable within the actively mixing billows. The billows produces a mixed-layer of a single composition rather 'ian a distribution of densities (Figure 6). This is consistent with the phenomonological model of Broadwell and Breidenthal [1982] of high Reynolds-number mixing layers and clearly points out that the process cannot be represented by gradient diffusion. Variations in L_{rms}, the rms overturn scale, and $L_b \equiv (\epsilon/N^3)^{1/2}$, the buoyancy scale, track each other throughout the event, their ratio remaining near one over approximately six buoyancy periods [Seim and Gregg, 1994a]. Thus, contrary to the development of turbulence generated by grids [e.g.

Rohr et al., 1988] there is no indication the ratio of turbulent length scales provides a measure of the stage of evolution of a shear instability.

ENERGETICS

By comparing mean conditions on the downstream and upstream passes through the billows we can quantify the the amount of energy released by the instability. Comparing changes in the mean fields with the measured dissipation rates estimates the mixing efficiency.

Because the flow is time-dependence we cannot treat our data sections as snapshots of a statistically-steady process. (The event varies with time because of pycnocline movement associated with establishing hydraulic control as the ebb tide strengthens.) We instead adopt a coordinate system moving with the billows, as defined in Figure 2c, and compute changes at specific along-channel positions between the two passes. By making our coordinate system nearly Lagrangian we minimize the importance of advection in the energy balances, and by repeating the comparison for a number of along-channel positions we accumulate estimates to improve our statistics.

Cecreasing ρ_p toward the nort (see Figure 5) is also apparent in the upstream leg (Figure 7). The repeatability of the density structure between the two passes lends confidence that the coordinate system follows the mean motion

Fig. 5. a) Contours of σ_θ derived from the AMP profile (aliased for scales $\leq$ 300 m); b) Profiles of displacement, L_t; and c) average density between 0.3 and 0.65 MPa. The pycnocline rises steeply after the control and before billows, then thickens and falls after billows form.
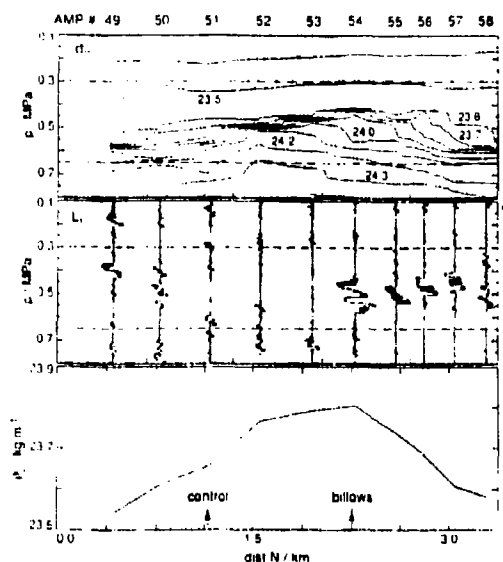
of the billows. The increased thickness of the density interface in the upstream leg (figure 7) is also consistent with the expected impact of the billows on the density field. Having established the consistency of the observations, we use a simple set of balance equations to q·antify the observed changes.

The energy balance of an arbitrarily stratified, incompressible flow is described by equations relating volume integrals [*Winters et al.*, 1994]. Approximations of these equations in one dimension, suited to the profile observations, are (see *Seim and Gregg* [1994b])

$$\frac{\partial}{\partial t} KE = -\nabla \cdot J_k - P \quad [\text{W kg}^{-1}] \quad (1)$$

$$\frac{\partial}{\partial t} TKE = P - <\epsilon> + J_b \quad [\text{W kg}^{-1}] \quad (2)$$

$$\frac{\partial}{\partial t} BPE = -\nabla \cdot J_p + 0.5\lambda_{pe} \quad [\text{W kg}^{-1}] \quad (3)$$

$$\frac{\partial}{\partial t} APEF = -0.5 * \lambda_{pe} - J_b \quad [\text{W kg}^{-1}] \quad (4)$$

Fig. 4. AMP profiles just upstream of the billows (a, AMP 5852), through the first large billows (b, AMP 5854), and 6 buoyancy periods later (c, AMP 5863). The flow is initially two-layered (a) but develops a 20 m thick unstable and highly dissipative layer where the echosounder reveals billows. This eventually becomes well-mixed (c).
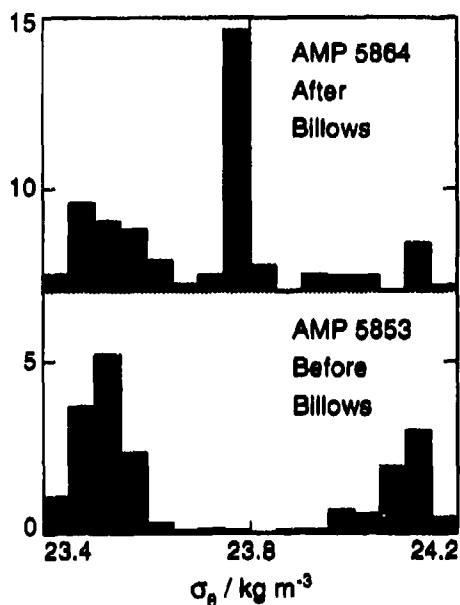
Fig. 6. Probability distribution of density in the pycnocline before the billows form and 6 buoyancy periods after they form. The distribution is bimodal before the instability, characteristic of an interface. The action of the billows forms a single mode of water at an intermediate density, not a range of density values, and cannot be modeled as a gradient diffusion process.

Fig. 7. AMP density profiles, arranged by location in the billows-following coordinate system, collected on the downstream leg (a) and upstream leg (b). The decrease in σ_θ from south to north at 0.5 MPa is obvious in both sets. The pycnocline changes from a single sharp interface to two smaller interfaces, separated by a well-mixed layer, between passes.

where

$$TKE \equiv < 0.5(3q^2) > \qquad (5)$$

$$P \equiv < -\overline{u'w'}(\partial u/\partial z) - \overline{v'w'}(\partial v/\partial z) > \qquad (6)$$

$$APEF \equiv < (1/2)[g/\rho N]^2\overline{\rho'^2} > \qquad (7)$$

$$\chi_{pe} \equiv < [g\alpha/N]^2(1 + 1/R_\rho^2)\chi > \qquad (8)$$

$$J_b \equiv -(g/\rho_0) < w'\rho' > \qquad (9)$$

and

$$<> \equiv \frac{1}{V}\int_V dV \qquad (10)$$

Here KE is mean kinetic energy due to shear; TKE is turbulent kinetic energy; BPE is background potential energy; $APEF$ is available potential energy of fluctuations; P is turbulent production, coupling equations (1) and (2); and J_b is the buoyancy flux, coupling equations (2) and (4). Turbulent fluctuations are denoted with primes ('); q is the turbulent velocity scale; χ_{pe} is an estimate of the dissipation rate of potential energy, based on χ;

α is the thermal expansion coefficient; $R_\rho \equiv \alpha(\partial T/\partial z)/\beta(\partial S/\partial z) \approx -0.05$ is the stability ratio; β is the haline contraction coefficient; ρ_0 is a reference density; and g is gravitational acceleration. The divergence of the energy-flux density vector in (1), $\nabla \cdot J_k$, accounts for unresolved energy-flux divergences, due to advection of KE or pressure work (diffusion is assumed negligible). A similar term appears in (3). This divergence can be a dominant term in the equations if non-local processes are important to the dynamics. In (1) we make the standard assumptions that the viscous dissipation by the mean currents and the buoyancy flux due to the mean currents are negligible, and in (2) and (4) we assume a local, time-dependent balance.

Equations (1) and (2) are standard forms for the kinetic energy balance equations assuming a Reynolds decomposition. Equations (4) and (3) are motivated by balance equations for potential energy suggested by *Winters et al.* [1994] which rely on a three-dimensional sort-

ing of the density field to define the components of the potential energy. This decomposition clearly identifies BPE as the only component that changes due to diabatic processes. *Winters and D'Asaro* [1994] have shown that the conversion of available potential energy to BPE is equal to the volume-integrated value of χ_{pe}. Further, (3) demonstrates that χ_{pe} is always directly related to the change in BPE, whereas (4) shows that the buoyancy flux is indirectly related to changes in BFE. Only when the available potential energy is steady does the buoyancy flux equal χ_{pe}.

Together, (1, 2, 3, and 4) form a set of consistent relations that describe the energy budget, i.e. when summed they show that energy changes of a baroclinic flow are due to either flux divergence or viscous dissipation. These equations describe the energy balance during an instability. Energy accumulates in the volume by flux convergence until KE exceeds the work needed to overturn the density field. Energy is then lost to turbulent production, with P being the source term for (2); energy is then either stored as TKE, dissipated via ϵ, or converted to available potential energy through J_b. Finally, $APEF$ may be converted to BPE through χ_{pe}. We estimate the magnitude of the various terms with our observations

We intentionally do not address the energy budget of the barotropic flow. We assume that the kinetic energy due to the vertically averaged flow and potential energy due to the vertically averaged density do not directly act as sources or sinks for the shear instability and therefore exclude them from the energy balance. Though these components are important to understanding the forcing of the billows our observations are inadequate to address the full energetics of the barotropic flow because we have not measured the free-surface gradient.

With our observations we estimate ϵ, TKE, KE, χ_{pe}, $APEF$ and BPE between 0.3 and 0.65 MPa for each AMP profile. These pressure correspond to minima in average profiles of turbulent intensity and justify a local balance of turbulent energy. Plotting in a billows-following coordinate system reveals some simple trends (Figure 8). On the downstream leg
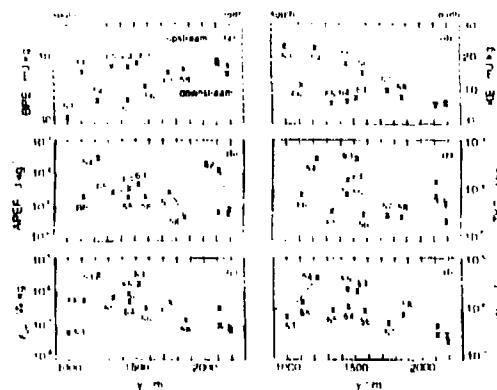
Fig. 8. Measured energy quantities as a function of along-channel position in the billows-following coordinate system. Variations of (a) BPE and (d) KE are nearly mirror images, as expected if KE is the energy source and BPE the energy sink. The instantaneous estimates of (b) $APEF$ and (e) TKE vary widely with no obvious pattern remain much smaller than the variations in KE. The dissipation rates (c) χ_{pe} and (f) ϵ are largest at the south end of the set, reflecting increased available potential energy when overturns are centered on the density interface.

KE (BPE) steadily decreases (increases) after the billows form, consistent with it being a source (sink) of energy for the instability. The estimates of $APEF$ and TKE display no obvious trend, though *Seim and Gregg* [1994b] note the maxima correspond to likely pairing events, but are uniformly small, remaining an order of magnitude smaller than the changes in KE. The dissipation rates tend to be greater to the south, where overturning was centered on the density interface. This suggests that ϵ and χ_{pe} reflect the increased available potential energy in these billows.

Equations (1) – (4) are solved for J_b, P, $\nabla \cdot J_k$ and $\nabla \cdot J_p$ at each of the seven locations where AMP profiles were collected. The averages and deviations of all the terms are presented in Table 1. The changes in TKE and $APEF$ are negligible compared to ϵ and χ_{pe} and (2) and (4) collapse to steady, local balances. The change in KE is approximately balanced by P, indicating that little of the KE released by the instability was radiated away as internal waves. It is surprising, then, that $\chi_{pe}/2$ is only 25%

TABLE 1. Averages, in $\mu W\ kg^{-1}$ (except R_f), ±
one standard deviation

Term	Value
$\partial KE/\partial t$	-2.9 ± 0.7
P	2.4 ± 0.5
$\nabla \cdot J_k$	0.5 ± 0.6
$\partial BPE/\partial t$	2.5 ± 0.5
J_b	-0.6 ± 0.2
$\nabla \cdot J_p$	-1.9 ± 0.6
ϵ	1.9 ± 0.4
χ_{pe}	1.1 ± 0.4
R_f	0.22 ± 0.04
$\partial TKE/\partial t$	0.04 ± 0.09
$\partial APEF/\partial t$	-0.01 ± 0.03

of the change in BPE. Two points should be made: first, using χ to estimate χ_{pe} in a dominantly salt-stratified fluid is untested and may be a biased estimator; second, confidence limits of the estimates are large owing to the lognormal distributions of the dissipation rates. We present a likely alternative. Within the range defined by the confidence limits is a solution with a flux convergence of both KE and BPE of equal size. This solution assumes the dissipation rates are underestimated by a factor of 1.7. Because we collected a limited number of profiles, a moderate underestimation of ϵ and χ_{pe} is reasonable.

Lastly, we find the flux Richardson number $R_f \equiv J_b/P \approx 0.22$, and that the interfacial stress, or momentum flux, through 0.5 MPa is 0.25 Pa within the control volume (600 m x 1000 m x 35 m) over an hour. Both values indicate the billows have a singificant impact on the mean flow.

REFERENCES

Broadwell, J. E., and R. E. Breidenthal, A simple model of mixing and chemical reaction in a turbulent shear layer, *J. Fluid Mech.*, *125*, 397–410, 1982.

Browning, K., G. Bryant, J. Starr, and D. Axford, Air motion within kelvin-helmholtz billllows determined from simultaneous doppler radar and aircraft measurements, *Quart. J. R. Meteor. Soc.*, *99*, 608–618, 1973.

Fritts, D., and P. Rastogi, Convective and dynamical instabilities due to gravity wave motions in the lower and middle atmosphere: Theory and observations, *Radio Science*, *20(6)*, 1247–1277, 1985.

Gargett, A. E., T. R. Osborn, and P. W. Nasmyth, Local isotropy and the decay of turbulence in a stratified fluid, *J. Fluid Mech.*, *144*, 231–280, 1984.

Gregg, M. C., Diapycnal mixing in the thermocline: A review, *J. Geopys. Res.*, *92*, 5249–5286, 1987.

Panchev, S., and D. Kesich, Energy spectrum of isotropic turbulence at large wavenumbers, *Comptes rendu de l'Académie bulgare des Sciences*, *22(6)*, 627–630, 1969.

Rohr, J., E. Itsweire, K. Helland, and C. VanAtta, Growth and decay of turbulence in a stably stratified shear flow, *J. Fluid Mech.*, *195*, 77–111, 1988.

Seim, H., and M. Gregg, Detailed observations of a naturally-occurring shear instability, *J. Geopys. Res.*, in press, 1994a.

Seim, H., and M. Gregg, Energetics of a naturally-occurring shear instability, *J. Geopys. Res.*, submitted, 1994b.

Seim, H., M. Gregg, and R. Miyamoto, Acoustic backscatter from turbulent microstructure, *J. of Atmos. and Ocean Tech.*, submitted, 1994.

Thorpe, S. A., Experiments on the instability of stratified shear flows: miscible fluids, *J. Fluid Mech.*, *46(2)*, 299–319, 1971.

Thorpe, S. A., Experiments on instability and turbulence in a stratified shear flow, *J. Fluid Mech.*, *61(4)*, 731–751, 1973.

Thorpe, S. A., Turbulence and mixing in a scottish loch, *Phil. Trans. R. Soc.*, *A286*, 125–181, 1977.

Winters, K. B., and E. A. D'Asaro, Diapycnal density fluxes in a stratified flow, *J. Fluid Mech.*, submitted, 1994.

Winters, K. B., P. N. Lombard, J. J. Riley, and E. D'Asaro, Available potential energy and mixing in density stratified fluids, *J. Fluid Mech.*, submitted, 1994.

Woods, J., Wave-induced shear instability in the summer thermocline, *J. Fluid Mech.*, *32*, 791–800, 1968.

THE EFFECT OF NON-SYMMETRICAL STRATIFIED SHEAR LAYERS ON THE DEVELOPMENT OF HOLMBOE INSTABILITIES

S.P. Haigh[1] and G.A. Lawrence[2]

[1] Department of Mathematics, University of British Columbia
[2] Department of Civil Engineering, University of British Columbia

Abstract

For two layer flows, linear stability analysis predicts two types of instabilities: Kelvin-Helmholtz instabilities which occur at small Richardson numbers and Holmboe instabilities which occur at larger Richardson numbers. Although growth rates of Holmboe instabilities are much smaller than those of Kelvin-Helmholtz instabilities, Kelvin-Helmholtz instabilities only occur for a small range of Richardson numbers and thus we would expect Holmboe type instabilities to occur more frequently. Here we study the effect of displacing the density interface with respect to the velocity interface on the development of a Holmboe type instability. In particular, we wish to determine how large this displacement must be before we only expect to see one mode of the Holmboe instability. Results are compared to recent experiments where Holmboe instabilities have been observed.

1 Introduction

We are interested in stratified shear flows for which the density interface thickness is much thinner than the shear layer thickness. Holmboe[2] was the first to study such a flow. He examined an inviscid flow with a discontinuous mean density profile (zero thickness layer) and a piecewise continuous mean velocity profile. For small values of the bulk Richardson number, J, linear stability analysis predicts a Kelvin-Helmholtz type of instability, characterized by zero phase speed. For sufficiently large values of J, however, there are two unstable modes of equal growth rate and equal but opposite phase speeds. These are usually called Holmboe instabilities.

Since Holmboe instabilities occur at larger values of J than the well known Kelvin-Helmholtz instabilities, one would expect these types of instabilities to occur more frequently in nature. Smyth[5] and Smyth et. al.[6] have numerically computed the nonlinear evolution of a Holmboe instability giving us a good idea how the instability may look. Also, Holmboe waves have been observed by Koop[3] (reproduced in part in Tritton and Davies[7] Fig 8.8), and Zhu and Lawrence[10]. Experimentalists have found, however, that Holmboe instabilities are, in general, difficult to observe in the laboratory. Lawrence et. al.[4] have put forth a possible explanation for this. Holmboe's work assumed that the flow is symmetric. This means that in order for one to observe a Holmboe type instability the center of the density interface must coincide with the center of the shear layer. In many experimental situations this is difficult to achieve. Lawrence et. al.[4] studied the effect of displacing the density interface with respect to the center of the shear layer, using the same profiles as in Holmboe's original work. This displacement is characterized by the nondimensional parameter ϵ which is the ratio of the displacement over half the shear layer thickness. As ϵ increases, the two Holmboe modes split. The growth rate of one mode gets larger while the growth rate of the other gets smaller. For $\epsilon = 1.0$ only one unstable mode is present. Yonemitsu[8] and Yonemitsu et. al.[9] studied the same effect for a viscous flow with hyperbolic tangent mean velocity profile and discontinuous mean density. Similar splitting behaviour with increasing ϵ was observed.

Linear stability analysis indicates that a non-symmetric profile ($\epsilon \neq 0$) is one possible explanation for why Holmboe waves are not always observed for large values of J. Unfortunately, the value of ϵ in a given experiment is difficult to measure[4] Also, linear stability analysis does not give a clear indication of how the value of ϵ affects the development of the flow. For this reason we will compute the nonlinear evolution of a flow for various values of ϵ and compare our results with the experimental results of Lawrence et. al.[4], and Zhu and Lawrence[10](see figure 1).

2   Linear Stability Analysis

Since our eventual goal is to compute the nonlinear evolution of a non-symmetric Holmboe instability, we require smooth profiles. Thus we assume, as in Smyth[5], that the nondimensional mean velocity, U, and the nondimensional mean density, ρ_n, can be described in terms of the hyperbolic tangent function.

$$
\left.
\begin{aligned}
U(z) &= \tanh z \\
\rho_a(z) &= -\tfrac{1}{h}\tanh R(z + \epsilon)
\end{aligned}
\right\}
\tag{1}
$$

Here R is ratio of the shear layer thickness to the density interface thickness and, as above, ϵ is a measure of the distance of the center of the density interface from the center of the shear layer (see figure 2). Since we wish to model flows for which the shear layer thickness is much larger than the density interface thickness, we want to choose R as large as possible, but small enough to be able to compute without requiring too high a resolution. We have found $R = 6$ to be a reasonable choice.

In the simulation, dissipation is required for numerical stability. For this reason, we include the effects of viscosity and thermal dissipation in the linear stability analysis. The important flow parameters are the bulk Richardson number, J, the Reynolds number, Re, and the Prandtl number, Pr.

$$
Pr = \frac{\nu}{\kappa}, \qquad Re = \frac{\Delta U h}{2\nu}, \qquad J = \frac{\Delta \rho h}{2(\Delta U)^2 \bar{\rho}}
$$

Here ν is the kinematic viscosity, κ is the thermal diffusivity, and the other parameters are as in figure 2. Smyth et. al.[6] have shown that the influence of diffusion tends to drive flows as described by (1) towards a state in which $R = \sqrt{Pr}$. For this reason, we choose $Pr = R^2$. Also, in order to compare our results with the experimental results in [4] we use $Re = 25$.

Results of the linear stability analysis are shown in figure 3. We see that for $\epsilon = 0$ there are, for a fixed value of J, two modes with equal growth rates. As ϵ increases, the modes split into two. The growth rate of the right-moving mode increases while the growth rate of the left-moving mode decreases. This is consistent with previous findings[4, 8, 9]. One important difference, however, is that the wavenumber at which the largest growth rate occurs gets larger for the right-moving wave and smaller for the left-moving wave as ϵ increases. This is opposite of what happens when the mean density interface has zero thickness. We have found that this behaviour depends on both the value of the ratio R and the Reynolds number Re.

3   Nonlinear Simulations

In order to examine how a non-symmetric mean flow affects the development of a Holmboe wave we numerically compute the evolution of such a flow. To this end, the nonlinear equations

of the perturbations are used with the Boussinesq approximation. We assume that the flow is two-dimensional, allowing us to use a streamfunction representation.

$$\begin{aligned}
(\Delta\psi')_t + (U+u')(\Delta\psi')_x + w'U_{zz} + w'(\Delta\psi')_z &= RJ\rho'_x + \tfrac{1}{Re}\Delta\Delta\psi' \\
\rho'_t + (U+u')\rho'_x + w'(\rho_a + \rho')_z &= \tfrac{1}{Re\,Pr}\Delta\rho'
\end{aligned}\right\} \qquad (2)$$

In (2), the primes denote the perturbed quantities. It is assumed that the flow is periodic in the direction of the flow (x-direction) and that the perturbations are zero at the vertical boundaries $z = \pm H/2$ where H is the total depth of the flow. Bearing in mind the results of Hazel[1] we choose $H = 10$. Thus the computational domain is $0 \le x \le P$ and $-5 \le z \le 5$ where P is the length of the period in the x-direction.

The perturbations are initially given by the linear solution. As we see in figure 3 the most unstable modes for the right and left moving waves occur at different wave numbers when $\varepsilon \ne 0$. If these modes were used to initialize the flow, the computational domain would have to be very large in order to maintain periodicity in the x-direction. For this reason, the wave number, α^*, at which the most unstable mode occurs (here it is the right moving wave) is used. Thus the flow has period $2\pi/\alpha^*$ and is initialized with the two most unstable linear perturbations that occur at the wave number α^*, one with positive phase speed (moving to the left) and one with negative phase speed. We see from figure 2 that this implies a larger difference between the two growth rates for a given value of ε than predicted by the linear analysis. Thus we are over-emphasizing the effect of ε.

Figures 4, 5 and 6 show the results of the nonlinear simulations for $J = 0.3$, $J = 0.12$ and $J = 0.09$. We see that for $\varepsilon = 0$ there are two waves: one wave which protrudes into the upper layer and moves to the right and a second wave which protrudes into the lower layer and moves to the left. We also see that the instabilities get larger with decreasing J. This indicates that although the linear growth rate for $J = 0.12$ is larger than for $J = 0.09$ (see figure 3), the effect of stratification on the nonlinear development of the flow tends to damp the linear growth more for larger values of the bulk Richardson number.

In figures 5 and 6, the solid contour represents zero density separating regions of lower density in the upper layer and higher density in the lower layer. This allows us to make an analogy with a two-layer flow. We see as ε increases, the right moving wave which protrudes into the upper layer starts to dominate while the effect of the left moving wave becomes negligeable. This is particularly evident for the case where $J = 0.12$. Also, for $J = 0.12$, as ε increases, the lower layer starts to billow into the upper layer, as can be seen be observing how the contour of zero density changes with changing ε. This can be explained by observing that the linear growth rate of the right moving wave increases with ε.

4 Comparison with Experiments

We now compare the results shown in figures 4, 5 and 6 with the experimental results shown in figure 1. We start with the experimental results of Lawrence et. al.[4] (figure 1a). First consider the case $J = 0.12$. We see from the experiments that there are only disturbances protruding into the upper layer. This indicates that the value of ε must be sufficiently large so that only the right moving wave is present. In this case, however, there is no billowing into the upper layer, thus ε must be sufficiently small so that the growth rate of the right-moving wave is small enough to prohibit any billowing. On careful examination of figure 5 we conclude that the value of ε in the shown experiment is approximately 0.1. As for the flow when $J = 0.09$, we see once again that there are only disturbances protruding into the upper layer present, but here there is billowing. From figure 6 we see that although there is billowing for all values

of ϵ, it is only when ϵ has reached 0.25 that the effect of the left moving wave is no longer noticeable. The experimental results of Zhu and Lawrence[10] (figure 1b) look similar to the computations shown in figure 4. Thus the value of ϵ is close to zero. It should be noted that the differences between the experimental and computed results can be attributed to the fact that the measured values of the bulk Richardson number in the experiments are approximate and the effect of ϵ in the computations is indicative of the behaviour, but not exact.

5   Conclusions

Nonlinear simulations show that non-symmetric profiles can be used to explain the "one-sidedness" often observed in experiments with larger values of J. We see that in order to observe a "true" Holmboe instability (two waves moving in opposite directions) as in figure 1b, the mean profiles must be almost symmetric ($\epsilon \ll 0.1$). When Holmboe instabilities are not observed in an experiment, the results of the simulations can be used to determine a rough approximation of the value of ϵ required in order to observe the given flow.

References

[1] Hazel, P., "Numerical studies of the stability of inviscid stratified shear flow", *J. Fluid Mech.*, **51**, 39-61 (1972).

[2] Holmboe, J., "On the behavior of Symmetric Waves in Stratified Shear Layers", *Geof. Publ.*, **24**, 67-113 (1962).

[3] Koop, C.G., *Instability and Turbulence in a Stratified Shear Layer*, Univ. Southern Calif., Dept. Aerospace Eng. Rep. USCAE 134 (1976).

[4] Lawrence, G.A., F.K. Browand & L.G. Redekopp "The stability of a sheared density interface", *Physics of Fluids A: Fluid Dynamics*, **3**(10).2360-2370 (1991).

[5] Smyth, W.D., *Hölmboe Waves*, M. Sc. Thesis, Department of Physics, University of Toronto, Toronto (1986).

[6] Smyth, W.D., G.P. Klassen, and W.R. Peltier, "Finite Amplitude Holmboe Waves", *Geophys. Astrophys. Fluid Dynamics*, **43**, 181-222 (1988).

[7] Tritton, D.J., P.A. Davies, "Instabilities in Geophysical Fluid Dynamics" in *Hydrodynamic Instabilities and the Transition to Turbulence*, 2nd ed., (eds. H.L. Swinney and J.P. Gollub) Springer-Verlag (1985).

[8] Yonemitsu, N., *The Stability and Interfacial Wave Phenomena of a Salt Wedge Flow*, Ph.D. Thesis, University of Alberta, Edmonton (1991).

[9] Yonemitsu, N., G.E. Swaters, N. Rajaratnam, and G.A. Lawrence, "Shear Instabilities in Arrested Salt-Wedge Flows", *Fourth International Symposium on Stratified Flow*, Grenoble, France, June 29-July 2, 1994.

[10] Zhu, Z. and G.A. Lawrence, "Exchange Flow Through a Channel with Underwater Sill", *Fourth International Symposium on Stratified Flows*, Grenoble, France, June 29 - July 2, 1994.

Figure 1: a) Experimental results from Lawrence *et. al.* for $J = 0.12$ and 0.09. In both these cases linear stability analysis predicts Holmboe type instabilities, but we see that there only disturbances protruding into the upper layer; b) results from Zhu and Lawrence, here Holmboe type instabilities are observed. All values of J are approximate.
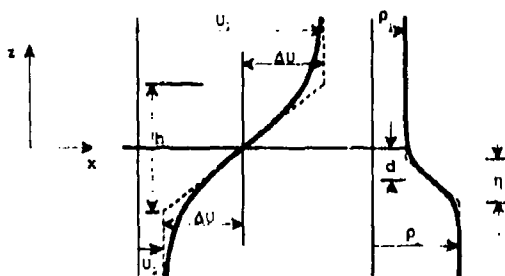
Figure 2: Diagram of the mean velocity and density profiles with $\Delta U = \dfrac{U_1 - U_2}{2}$, $\Delta \rho = \dfrac{\rho_2 - \rho_1}{2}$, $\bar{\rho} = \dfrac{\rho_1 + \rho_2}{2}$, $R = \dfrac{h}{\eta}$, and $\epsilon = \dfrac{2d}{h}$
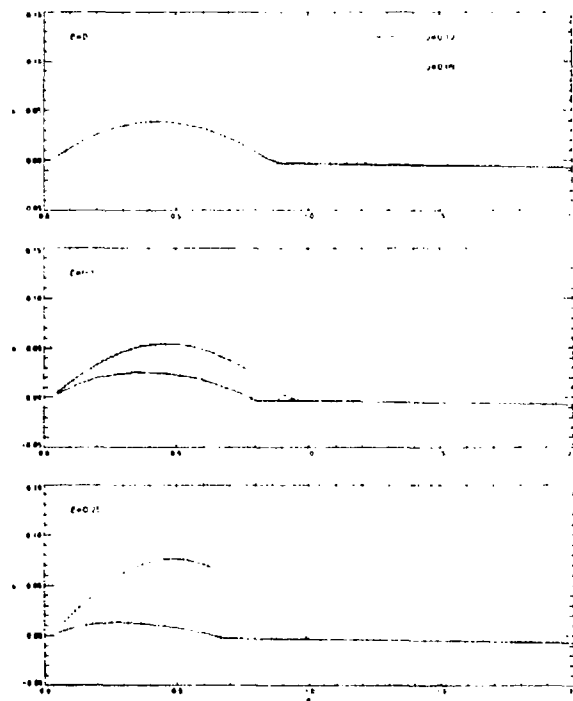
Figure 3: Results of linear stability analysis for $J = 0.12$ and 0.09 with $Re = 25$, $Pr = 36$, and $R = 6$. Here σ_r is the growthrate and α is the wavenumber. When $\epsilon = 0$ there are two unstable wave with the same growth rate and opposite phase speeds. For $\epsilon \neq 0$, the faster growing mode corresponds to the right-moving wave and the slower growing mode to the left-moving wave.
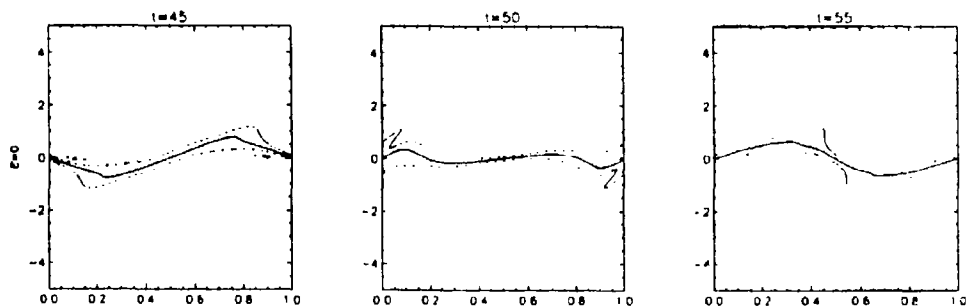
Figure 4: Results of nonlinear simulations with $J = 0.3$, $R = 6$, $Re = 25$, and $Pr = 36$ for $\epsilon = 0$. Here contours are of constant density $\rho = \rho_0(z) + \rho'$ in the $x - z$ plane. x has been scaled with respect to its period $2\pi/\alpha^*$ where $\alpha^* = 0.6$.
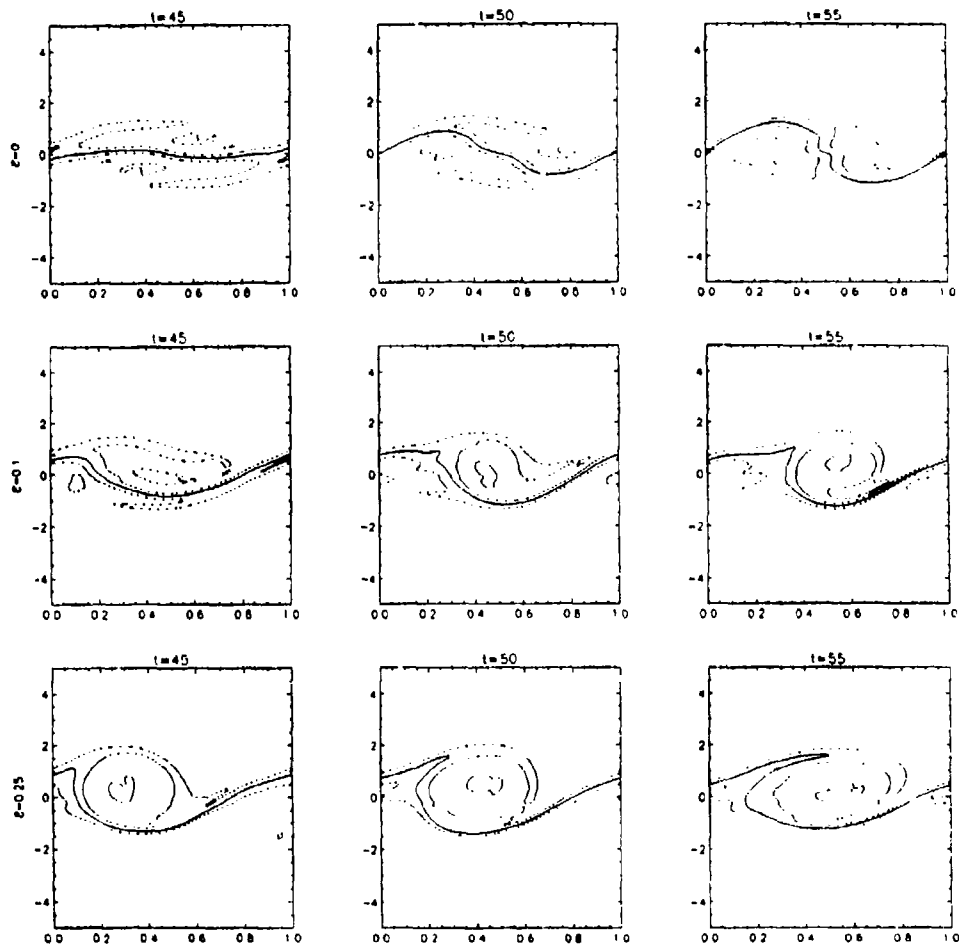
Figure 5: Results of nonlinear simulations with $J = 0.12$, $R = 6$, $Re = 25$, and $Pr = 36$ for $\varepsilon = 0$, 0.1 and 0.25. Here contours are of constant density $\rho = \rho_a(z) + \rho'$ in the $x - z$ plane where x has been scaled with respect to its period $2\pi/\alpha^*$.
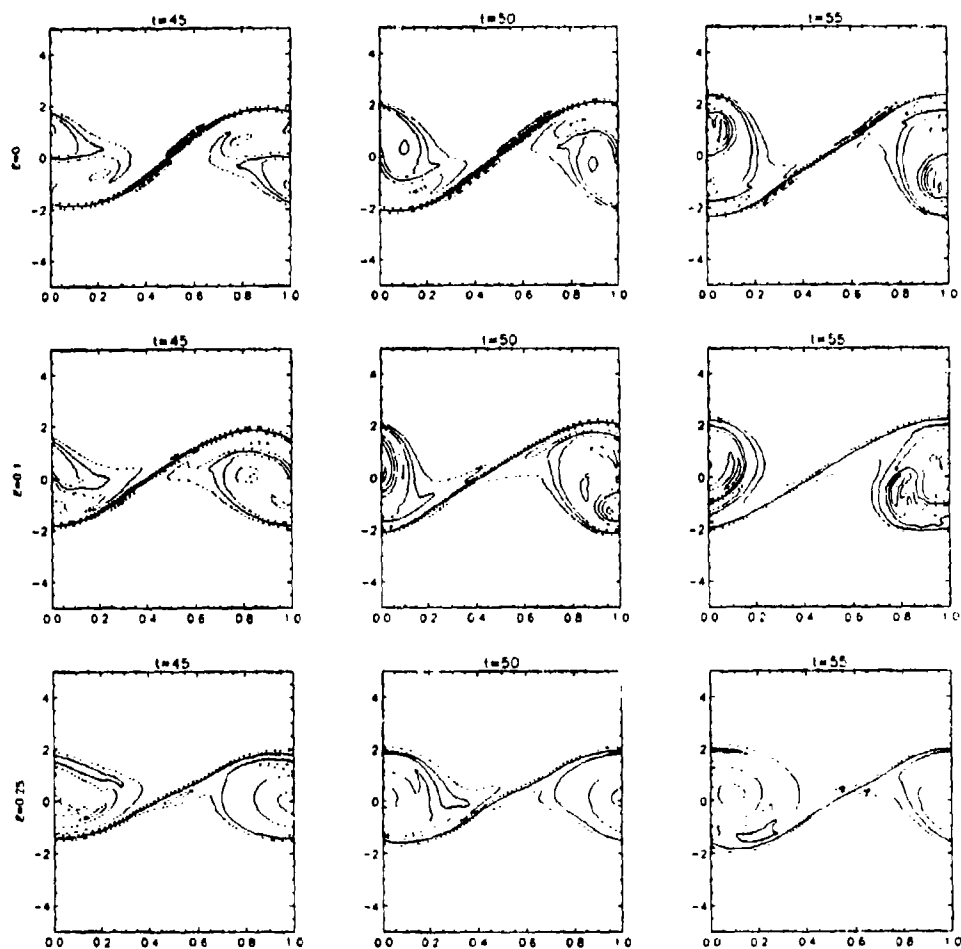
Figure 6: Results of nonlinear simulations with $J = 0.09$, $R = 6$, $Re = 25$, and $Pr = 36$ for $\varepsilon = 0$, 0.1, and 0.25. Here contours of constant density $\rho = \rho_a(z) + \rho'$ in the $x - z$ plane where x has been scaled with respect to its period $2\pi/\alpha^*$.

LOCKED STATES, PHASE SOLITONS AND HOLMBOE WAVES IN SPATIALLY FORCED MIXING LAYERS

Olivier Pouliquen, Jean-Marc Chomaz & Patrick Huerre
Laboratoire d'Hydrodynamique (LadHyX)
Ecole polytechnique
F-91128 Palaiseau Cédex France

A comprehensive experimental and theoretical study of finite-amplitude Kelvin-Helmholtz and Holmboe waves at the interface separating two immiscible fluids has been undertaken. The experimental set-up consists in generating an accelerating shear flow by tilting a tube filled with two liquids of different density (Reynolds 1883, Thorpe 1969). As soon as the shear exceeds a critical value, interfacial waves are produced at an intrinsic wavelength that can be predicted by linear stability theory. The evolution of the interface can be synchronized by spatially forcing the flow with the help of small obstacles periodically distributed along the horizontal walls. When the tube is maintained tilted so as to produce an accelerating shear flow, the competition between the forcing wavenumber and the intrinsic wavenumber gives rise to a variety of locked states at superharmonics of the imposed wavenumber (Figure 1). As the forcing wavenumber is increased above the natural wavenumber, stationary phase solitons are observed that are indicative of the existence of incommensurate states (Pouliquen et al. 1992).
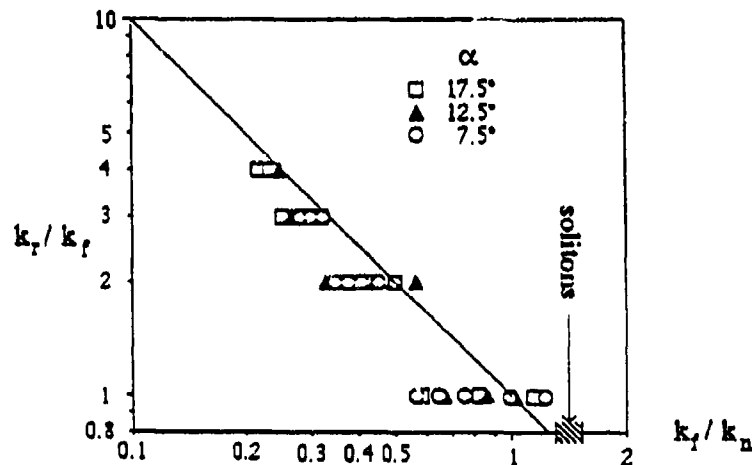
Figure 1. Mode diagram of accelerating shear layer under spatially forced conditions. The ratio of the response wave number k_r to the forcing wave number k_f is plotted as a function of the ratio of the forcing wave number k_f to the natural wave number k_n. The symbols refer to different inclination angles as indicated.

In concurrent theoretical studies (Pouliquen et al. 1994b), the spatio-temporal evolution of the vortex sheet separating two finite depth layers of immiscible fluids has been examined in the vicinity of threshold (Weissman 1979) in the presence of spatially periodic forcing. As a result of Galilean invariance, the interface deformation has been shown to satisfy a coupled system of evolution equations involving not only the usual "short wave" at the critical wavenumber but also a shallow-water "long wave" associated with the mean elevation of the interface. In the Boussinesq approximation this model reduces to a forced Klein-

Gordon equation. Forcing is shown to lead to one-dimensional propagating Sine-Gordon phase solitons in agreement with numerical simulations of the Klein-Gordon amplitude equation.
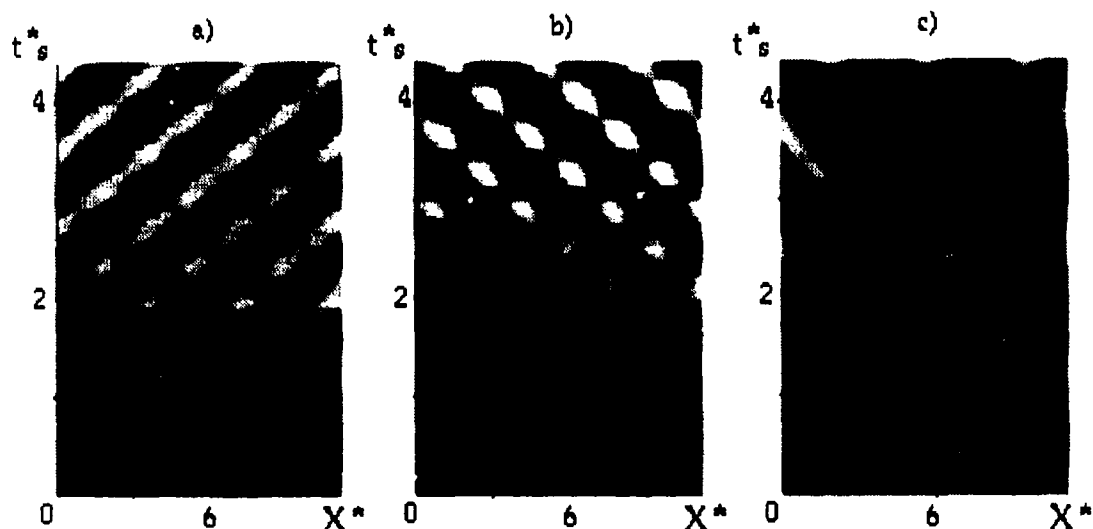
Figure 2. Spatio-temporal x*-t* diagram of interface elevation in the case of constant shear. Following the viscosities of the two fluids the bifurcating wave propagates either to the right (a), or in both directions (b) or to the left (c).

In order to test the predictions of this weakly nonlinear analysis, constant-shear experiments have been performed near onset by bringing the tube back to its initially horizontal position (Pouliquen *et al.* 1994a). The nature of the instability is then observed to change : whereas stationary perturbations prevailed in the accelerating case, counterpropagating waves are now produced which cannot be accounted for by the vortex sheet model. A linear stability analysis of a density discontinuity embedded within a piecewise linear velocity profile has demonstrated that such waves are Holmboe modes (Holmboe 1962, Koop & Browand 1991, Lawrence *et al.* 1991 and Smyth & Peltier 1991) associated with the formation of diffusive layers above and below the interface. Good agreement is then obtained between measured and predicted values of the critical velocity difference, propagating velocity and growth rates of the waves. The instability analysis of asymmetric velocity profiles further reveals that the breaking of reflectional symmetry gives rise to a single propagating wave near onset in complete agreement with experiments (Figure 2.).

REFERENCES
HOLMBOE, J. 1962 *Geofys. Publ.* **24**, 67.
KOOP, C.G. & BROWAND, F.K. 1979 *J.Fluid Mech.* **93**, 135.
LAWRENCE, G.A., BROWAND, F.K. & REDEKOPP, L.G. 1991 *Phys. Fluids* A. **3**, 2360.
POULIQUEN, O., CHOMAZ, J.M., HUERRE, P. & TABELING, P. 1992 *Phys. Rev. Lett.* **68**, 2596.
POULIQUEN, O., CHOMAZ, J.M. & HUERRE, P. 1994a *J.Fluid Mech.* **226**, 277.
POULIQUEN, O., HUERRE, P. & CHOMAZ, J.M. 1994b *preprint.*
REYNOLDS, O. 1883 *Phil. Trans. R. Soc. Lond.* **174**, 935.
SMYTH, W.D. & PELTIER, W.R. 1991 *J.Fluid Mech.* **228**, 387.
THORPE, S.A. 1969 *J.Fluid Mech.* **39**, 25-48.
WEISSMAN, M.A. 1979 *Phil. Trans. R. Soc. Lond.* **A290**, 639.

Nonlinear oscillatory evolution of a baroclinically unstable geostrophic vortex

Xavier J. Carton

EPSHOM/CMO, Brest, France 29275

April 1994

Abstract

In a two-layer quasi-geostrophic model, we investigate the nonlinear evolution of a linearly unstable baroclinic vortex. For moderate growth rate, weak perturbation amplitude and very little hyperviscosity, a regime of regular oscillation is attained which is accounted for in physical space by a quasi-periodic reversal of the vertical phase shift, and in an integral manner, by a corresponding back-and-forth potential energy transfer between the mean flow and the perturbation. In a rotating frame, the disturbance varies around an elliptical mean state, which has a biunivocal relation between potential vorticity and the corotating streamfunction with the layerwise angular velocity. Simulations with weaker Burger or Reynolds numbers show less regularity in the flow and eventual vortex breaking.

1 Introduction

Vortices are long-lived and robust features which play a major role in the dynamics of ocean flows. They often originate in the instability of large-scale or of coastal currents, but they can propagate far away from their region of formation thus contributing to the global budgets of heat and momentum. It is therefore of great importance to determine the vortices' resistance to external perturbations. Hereafter only geostrophic vortices with low Rossby numbers are considered, to retain mathematical simplicity.

Vortex stability has already been investigated at great length in the context of two-dimensional incompressible flows (Gent and Mc Williams, 86; Carton *et al.*, 89; van Heijst it et al., 91; Orlandi and van Heijst, 92; Carton and Legras, 94). It has been proved that multipolar structures could stem from barotropically unstable vortices (Carnevale and Kloosterziel, 94; Morel and Carton, 94) and that tripoles were stable forms (Polvani and Carton, 90). Vortex stability in stratified fluids has received less attention due to complexity of the problem (Griffiths and Linden, 81; Ikeda, 81; Flierl, 88; Helfrich and Send, 88; Flor et

1

al., 93). There, the dimension of the parameter space renders a comprehensive sensitivity study not tractable, even for a two-layer flow.

After setting the mathematical framework (section 2), we present the linear instability of a baroclinic gaussian vortex and the diversity of finite-amplitude regimes (section 3). We then concentrate on an elliptically perturbed vortex: we detail the vortex evolution during the nonlinear stage of the instability and relate it to vertical phase shifts and energy transfers. We determine the underlying baroclinic ellipse in a layerwise rotating frame and finally evoke possible extensions of the study.

2 Mathematical and physical framework

In oceanic flows, the Earth rotation and thermohaline stratification often render motions quasi two-dimensional and non divergent. These influences, of comparable strength, then dominate advective effects, so that the Burger number $B = (\frac{Nh}{fL})^2$ is order unity and the Rossby number $Ro = \frac{U}{fL}$ is small, with U, L, h, f, H typical measures of horizontal velocity, scale, vertical scale, Coriolis parameter and Brunt-Vaisala frequency. It is reasonable to assume weak diffusion, so that the Reynolds number $Re = \frac{UL}{\nu}$ is extremely large (ν is the fluid viscosity). Under these assumptions, f-plane approximation and constant total depth (flat bottom, rigid lid), a two-layer quasi-geostrophic model is used, and is sufficient to represent baroclinic instability.

In dimensionless form, the potential vorticity conservation in each layer is:

$$\frac{dq_j}{dt} = \partial_t q_j + \frac{1}{r}(\partial_r \psi_j \partial_\theta q_j - \partial_\theta \psi_j \partial_r q_j) = -Re^{-1}\nabla^6 \psi_j \qquad (1)$$

in polar coordinates, where $j = 1$ and 2 represent the upper and lower layers, and for which we have used the well-known hyperviscosity. The potential vorticities are defined by

$$q_j = \nabla^2 \psi_j - B^{-1} h_k (\psi_j - \psi_k), \qquad (2)$$

where $k = 3 - j$, h_j is the dimensionless thickness of layer j and B is the squared deformation radius. Our choice is $h_1 = h_2 = 1/2$, though this suppresses the baroclinic triad (Carton and McWilliams, 89, section 2.2). It has been checked that this does not qualitatively alter the following results. Our nonlinear numerical model is based on a spectral Galerkin method, assumes biperiodic boundary conditions and is resolved on 128 gridpoints in both horizontal directions. The Re^{-1} values varies between zero and $8\,10^{-9}$.

2

The initial conditions are composed of an axisymmetric vortex and a superimposed monochromatic normal mode perturbation:

$$\psi_j(r, \theta) = \bar{\psi}_j(r) + \psi'_j(r, \theta, t),$$ (3)

for which the mean flow has a gaussian density interface

$$\bar{\psi}_1 = -\bar{\psi}_2 = \psi_0 e^{-r^2}$$ (4)

and the disturbance has the form

$$\psi'_j = Real[\,\varphi_j(r)\, exp(i\ell(\theta - ct))\,]$$ (5)

where ℓ is the azimuthal wavenumber, $\omega = \ell\, Real(c)$ the angular rotation rate, and $\sigma = \ell\, Im(c)$ the growth rate.

3 Vortex instability and nonlinear evolution

3.1 Linear instability and nonlinear regimes

Introducing the formulae (3) and (5) into the linearized form of equation (1) with (2) yields a generalized eigenvalue/eigenvector problem in c, $\varphi(r)$, which can be solved only numerically for the vortex (4). This is done by means of a matrix method which has previously been checked against a shooting method. Figure 1 shows the variation of σ versus B^{-1} for $\ell = 2$ and $Re^{-1} = 0$. Increasing the vortex size with respect to the deformation radius depletes the kinetic energy source for barotropic instability and enhances potential energy conversion, hence baroclinic instability. Beyond $B_t^{-1} = 0.8$ and below the threshold $B_c^{-1} = 2.0$, disturbances cannot extract energy from the mean vortex and thus decay. Beyond $B_s^{-1} = 3.6$, the baroclinic instability is explosive and nonlinear interactions generate vertical vortex breaking into two tilted dipoles. Finally for $B_c^{-1} < B^{-1} < B_s^{-1}$, moderate initial perturbation amplitudes and little viscosity ($Re < 8\,10^{-9}$), nonlinear interactions result in a finite-amplitude oscillation of the disturbance (see Fig. 2a for $B^{-1} = 2.4$ and $Re^{-1} = 2\,10^{-9}$). Larger Re^{-1} values bring a slow growing trend on the oscillation, eventually resulting in asymmetric breaking. Finally, a similar phenomenology has been observed for different wavenumbers (Carton and McWilliams, 89), for other depth ratios or mean relative vorticity profiles.

3.2 Finite-amplitude oscillation

Figure 2b shows the time series of the phase of the perturbation in both layers, for our reference experiment ($B^{-1} = 2.4$ and $Re^{-1} = 2\,10^{-9}$). Originally, they

3

vary accordingly to (5), maintaining a vertical shift opposite to the mean shear. Therefore the disturbance extracts potential energy from the mean vortex (Pedlosky, 79). This conversion can be computed; if $\varphi_j(r) = A_j(r)e^{i\phi_j(r)}$:

$$ T_p \;=\; \frac{\psi_0 f}{2BR} \int_0^R [A_1 A_2 sin(\phi_2 - \phi_1)] r e^{-r^2} dr \qquad (6) $$

where R is a radius large enough for the A_j to decay significantly. At $t \sim 500$, a phase reversal occurs in the lower layer, followed by a periodic but opposite variation to that in the upper layer. This evolution corresponds to a regular back-and-forth energy exchange between the vortex and the disturbance and thus a finite-amplitude oscillation.

During the oscillation, a decomposition into azimuthal modes shows that odd-wavenumber components have vanishing intensity; moreover, the alteration of the axisymmetric part of the flow from the initial shape is not sufficient to render the mean vortex neutral to its mode-2 perturbation; finally the intensity of higher even-wavenumber components is too weak to intervene in the nonlinear equilibration process (contrary to barotropic flows). A low-order projection model and amplitude equation have not been derived here as the radial profiles of the modes vary much in time. Power, cross-modal and cross-layer spectra have been computed for this experiment, and show well-defined frequencies for the dominant modal components. These observations point to a radically different equilibration mechanism to that occuring for barotropic vortices: filament shedding is not striking, the shield in relative vorticity has a minor role, nonlinearities are weak in the finite-amplitude regime, few modes are involved, no steady state is attained but a counter-rotating, oscillating ellipse, for which the ellipticity does not reach large values. All this suggests to compare this experiment with a contour surgery simulation (Dritschel, 88) of a baroclinic Kirchoff ellipse with the same vertical structure and average ellipticity. Time series of the deviation and frequency spectra for the surgery run show a surprising similarity with the spectral simulation. This supports our analysis of a simple dynamical system. Finally, temporal regularity is lost in both cases (spectral code or contour surgery), when the initial perturbation amplitude or the viscosity are larger or for shallow upper layers ($h_1 = 0.2$ representative of the ocean thermocline).

3.3 The underlying baroclinic ellipse

In a frame of reference rotating with the layerwise angular velocity of the mode-2 component, the vortex appears in both layers as a pulsating ellipse. Its time-average over 18 periods of oscillation yields a slightly elliptical baroclinic vortex (Fig.3a), with a simple relation between the potential vorticity and

4

the corotating streamfunction (see fig.3b). When inserted in equation (1), this form corresponds to a layerwise steady state, which has nevertheless no meaning as a vertically coherent structure, because of the vertical counter-rotation. Moreover, this average vortex is unstable and evolves to the pulsating ellipse when used as an initial condition for a rerun of the model. This ellipse is a limit cycle, a non chaotic attractor (with little sensitivity to noise in the initial conditions).

4 Conclusions

Baroclinically unstable geostrophic vortices with a gaussian interface and a mode-2 deformation can evolve to a vertically counter-rotating, pulsating ellipse for moderate growth rates, weak perturbation amplitudes and little viscosity. The time evolution of this ellipse is regular, showing a periodic reversal of the vertical phase shift and of the corresponding potential energy conversion. Few modes are involved in this process and there is a significant regularity in time of the evolution. In a layer projection, the oscillation occurs around a slightly elliptical state, unstable but not chaotic, with a simple relation between potential vorticity and streamfunction, and there is a limit cycle. To better assess the influence of the interaction between the upper and lower layer mode-2 components, we plan to run a equivalent-barotropic simulation of the same case, with a periodic forcing generated by a rotating, but non pulsating shear corresponding to a fixed aspect ratio (lower layer) ellipse.

Acknowledgements

References

Carnevale, G.F. and R.C. Kloosterziel, 1994: Emergence and evolution of triangular vortices. *J. Fluid Mech.*, **259**, 305-331.

Carton, X.J., and J.C. McWilliams, 1989: Barotropic and baroclinic instabilities of axisymmetric vortices in a quasigeostrophic model. *Proceedings of the XXth Liége Colloquium on ocean hydrodynamics, Elsevier*, **50**, 225-244.

Carton, X.J., and B. Legras, 1994: The life-cycle of tripoles in two-dimensional incompressible flows. *J. Fluid Mech.*, **267**, 53-82.

Dritschel, D.G., 1988: Contour surgery: a topological reconnection scheme for extended integrations using contour dynamics. *J. Comput. Phys.*, **10**, 77.

Flierl, G.R., 1988: On the instability of geostrophic vortices, *J. Fluid Mech.*, **197**, 349-388.

Flor, J.B., Govers, W.S.S., van Heijst, G.J.F. and R. van Sluis, 1993: Formation of a tripolar vortex in a stratified fluid. *Appl. Sci. Res.*, **51**, 405-409.

Gent, P.R., and J.C. McWilliams, 1986: The instability of barotropic circular vortices. *Geophys. Astrophys. Fluid Dyn.*, **35**, 209-233.

Griffiths, R.W., and P.F. Linden, 1981 : The stability of vortices in a rotating stratified fluid, *J. Fluid Mech.*, **105**, 283-316.

Helfrich, K.R., and U. Send, 1988: Finite-amplitude evolution of two-layer geostrophic vortices, *J. Fluid Mech.*, **197**, 331-348.

Ikeda, M., 1981: Instability and splitting of mesoscale rings using a quasi-geostrophic model on a f-plane. *J. Phys. Oceanogr.*, **11**, 987-998.

Morel, Y.G., and X.J. Carton, 1994: Multipolar vortices in 2D incompressible flows. *J. Fluid Mech.*, **267**, 28-52.

Orlandi, P., and G.J.F. van Heijst, 1992: Numerical simulation of tripolar vortices in 2D flows. *Fluid Dyn. Res.*, **9**, 179-206.

Pedlosky, J., 1979: *Geophysical Fluid Dynamics*, Springer Verlag, 624 pp.

Polvani, L.M., and X.J. Carton, 1990: The tripole: a new coherent vortex structure of incompressible two-dimensional flows. *Geophys. Astrophys. Fluid Dyn.*, **51**, 87-102.

van Heijst, G.J.F., Kloosterziel, R.C. and C.W.M. Williams, 1991: Laboratory experiments on the tripolar vortex in a rotating fluid. *J. Fluid Mech.*, **225**, 301-331.

6
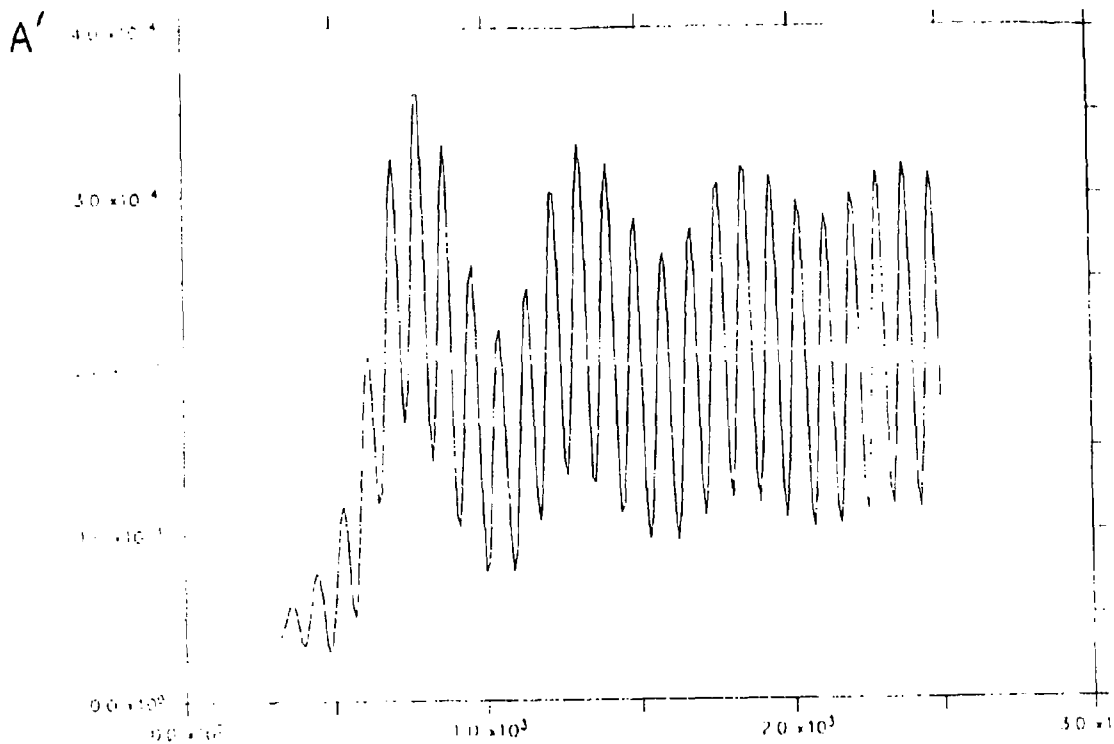
2a. Nonlinear evolution of the perturbation amplitude for the reference simulation
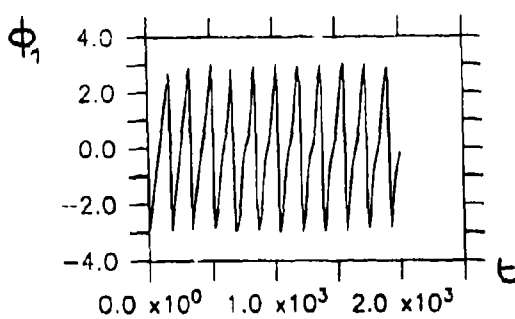
phase mode 2 versus time, upper layer   phase mode 2 versus time, lowe
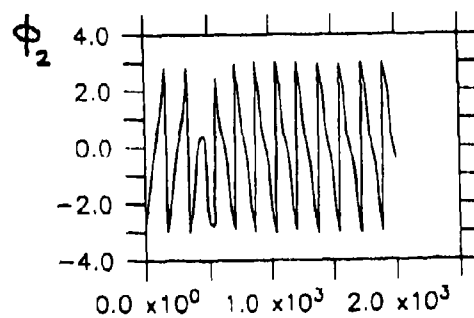
2b. Nonlinear evolution of the perturbation phase for the reference simulation
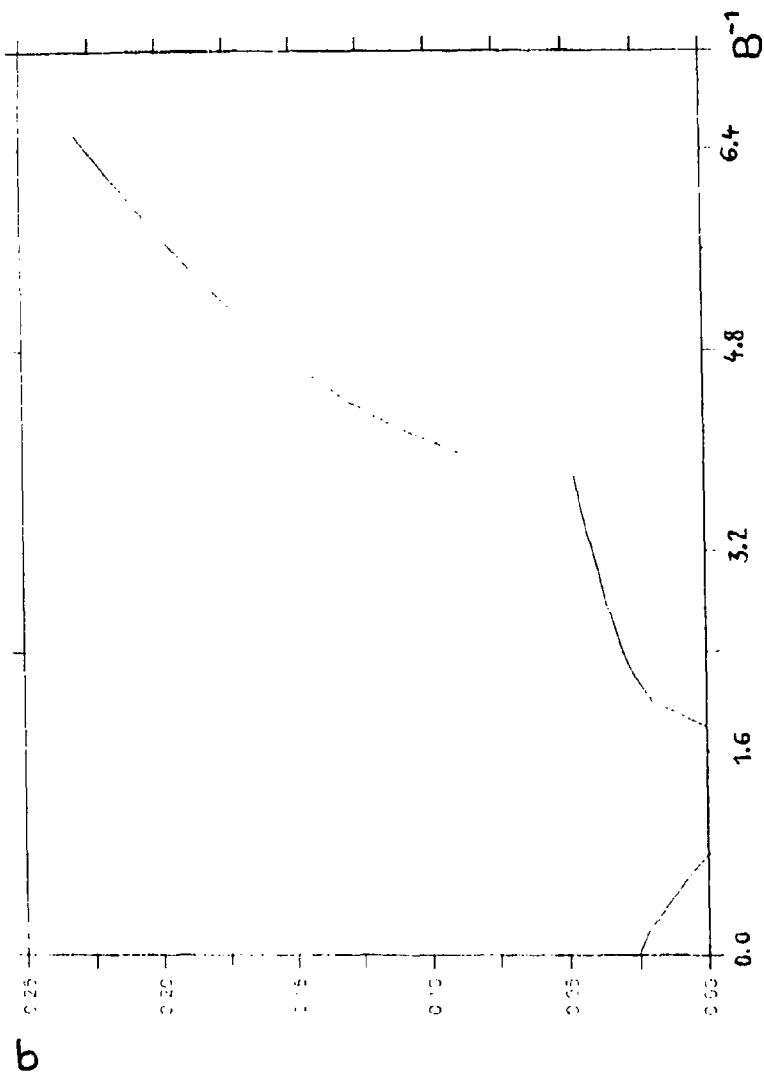
1 Maximum growth rate σ as a function of the inverse Burger number. for $\iota = 2$.
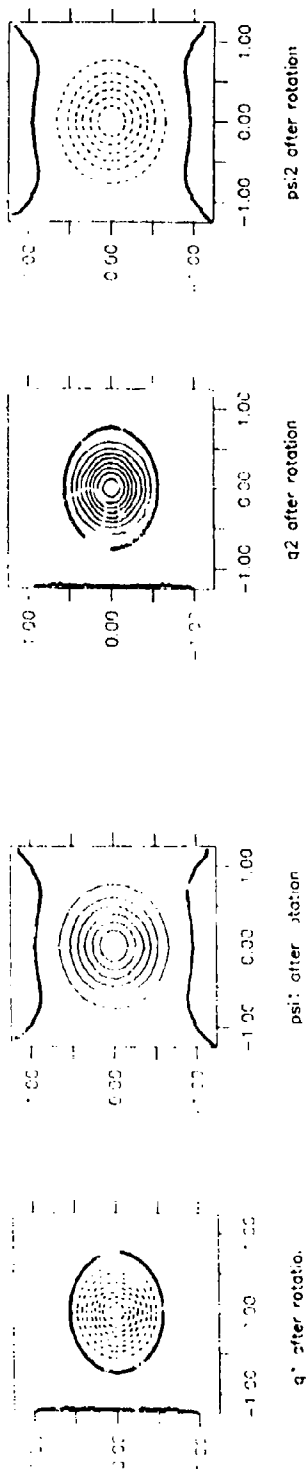
3a. Upper potential vorticity $q_j(x,y)$ and streamfunction $\psi_j(x,y), j = 1, 2$ fields for the phase-averaged state of the reference simulation with layerwise angular velocity
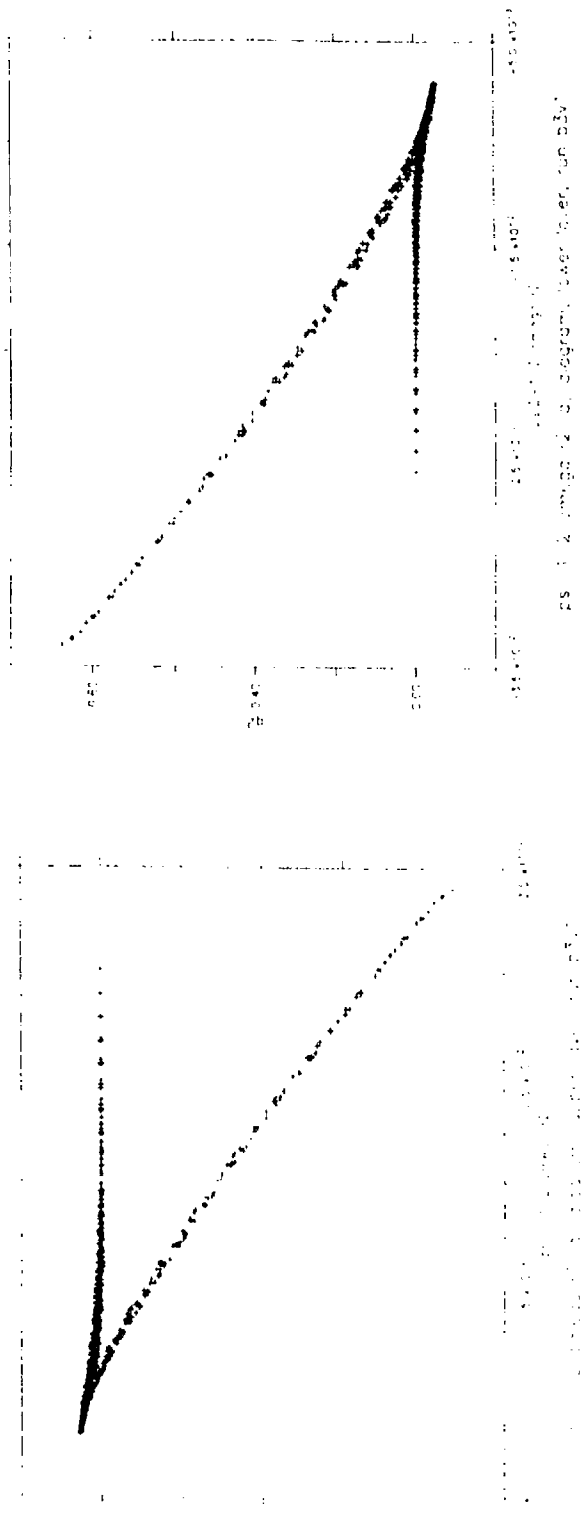
3b. Scatter-plot diagram of the potential vorticity versus the co-rotating streamfunction for the phase-averaged state

INTENSE VORTEX MOTION IN A CONTINUOUSLY STRATIFIED DIFFERENTIALLY ROTATING FLUID

Georgi Sutyrin

Russian Academy of Sciences
P.P. Shirshov Institute of Oceanology
23 Krasikova Street, Moscow 117259, Russia

ABSTRACT

An analytic expression is obtained for the β-induced meridionally-westward acceleration of a monopolar geostrophic vortex with a localized core of the potential vorticity perturbation in a continuously stratified fluid. For a singular vortex with the point core the asymmetric flow has a self-similar dipolar structure producing the vortex motion in the direction 120^0 from the east with the velocity increasing as $t^{2/3}$. Effects of asymmetric distortion of the finite vortex core are considered.

1. Abundant intense vortices in the atmospheres and the oceans are strongly influenced by the variation of the Coriolis parameter with the latitude, the so-called "β-effect". An asymmetric circulation around a monopolar vortex which is mainly responsible for the β-induced vortex drift has been intensively studied during the last decade, both analytically, numerically and in laboratory experiments. The development of the asymmetric perturbation with modenumber $l = 1$ (l is the azimuthal wavenumber) and corresponding meridionally-westward acceleration of the intense vortex during many turnaround times have been analyzed in details using the equivalent-barotropic quasigeostrophic model [1-5].

In the present work, the development of the asymmetric circulation around an intense vortex in a continuously stratified fluid is analyzed using a baroclinic geostrophic monopole model with the potential vorticity perturbation localized in a disk-shaped vortex core. Outside the core the azimuthal velocity and the density perturbation decrease with increasing a distance from the core in agreement with observed structure of long-lived oceanic rings and lenses [6]. At large distances from the core the vortex structure is described by a singular solution corresponding to a point "vortex charge" [7]. In particular, a self-similar dipolar structure of the β-induced asymmetric flow for a singular vortex with a point core, is revealed. Effects of vertical distortion of finite vortex core are considered by splitting the core into a set of thin disk-shaped subcores.

2. We start from the equation describing material conservation of the potential vorticity in fluid particles

$$\frac{Dq}{Dt} = \frac{\partial q}{\partial t} + u\frac{\partial q}{\partial x} + v\frac{\partial q}{\partial x} = 0. \tag{1}$$

Within the quasigeostrophic approximation at the β-plane for a continuously stratified fluid in terms of the geopotential, p, the geostrophic velocity, (u,v), and the potential vorticity, q, are

$$u = -\frac{\partial p}{\partial y}, \qquad v = \frac{\partial p}{\partial x} \tag{2}$$

$$q = \nabla^2 p + \frac{\partial}{\partial z}\left(\frac{1}{N^2}\frac{\partial p}{\partial z}\right) + \beta y \tag{3}$$

Here we adopt local Cartesian coordinates, (x, y, z), non-dimensionalizing by the horizontal scale, L, velocity scale, U, time scale, L/U, and the vertical scale, $H = Lf_0/N_0$, where f_0 and N_0 are the characteristic Coriolis and Brunt-Vaisala frequencies, thus $N^2(z)$ is the nondimensional vertical gradient of the mean density profile, $\beta = Lf'/U$ and f' is the meridional gradient of the Coriolis frequency.

Eq. (1) obeys the symmetry relation $p(x, y, z, t) = -p(x, -y, z, t)$. Thus, regarding monopolar vortices, we consider only the evolution of geostrophic cyclones, i.e. structures with positive amplitude of the fluid potential vorticity $q - \beta y$.

By solving Eq.(3), the geopotential can be expressed in terms of the Green function $G(\sigma, z, z')$, $2\sigma = (x - x')^2 + (y - y')^2$, of the boundary-value problem for this three-dimensional elliptic operator

$$p(x, y, z, t) = \int G(\sigma, z, z')[q(x', y', z') - \beta y']dx'dy'dz' \tag{4}$$

Besides material conservation of the potential vorticity in fluid particles, there are two quadratic invariants of Eq. (1), the total energy and potential enstrophy,

$$E = \frac{1}{2}\int [(\nabla p)^2 + \frac{1}{N^2}\left(\frac{\partial p}{\partial z}\right)^2]dxdydz, \qquad V = \frac{1}{2}\int (q - \beta y)^2 dxdydz \tag{5}$$

3. To consider the evolution of M vortices with initially compact cores of the fluid potential vorticity $q - \beta y$, we introduce M *local* cylindric coordinates (r, θ, z) relative to horizontal position $(x_k(t), y_k(t))$ of the center of the kth structure. In a co-moving reference frame the flow field is described by the streamfunction

$$\psi_k = p + \dot{x}_k r \sin\theta - \dot{y}_k r \cos\theta, \qquad \dot{x}_k = \frac{dx_k}{dt}, \qquad \dot{y}_k = \frac{dy_k}{dt} \tag{6}$$

where $(\dot{x}_k(t), \dot{y}_k(t))$ is the instantaneous propagation velocity of the kth vortex. Thus, in translating coordinates Eq.(1) becomes

$$\frac{\partial q_k}{\partial t} = \frac{1}{r}\frac{\partial(q_k, \psi_k)}{\partial(r, \theta)} = J(q_k, \psi_k) \tag{7}$$

where J denotes the horizontal Jacobian.

Defining the propagation velocity of the kth vortex center as the flow velocity at the center $r = 0, z = z_k$, from (6) we obtain

$$\dot{r}_k = \dot{x}_k + i\dot{y}_k = \frac{i}{\pi} \int_0^{2\pi} \left(\frac{\partial p}{\partial r} \right)_k \exp(i\theta) d\theta \qquad (8)$$

Thus, the vortex propagation is defined only by the azimuthal mode $l = 1$ of the asymmetric geopotential p relative the kth center.

For every vortex we may separate the streamfunction and potential vorticity into symmetric and asymmetric parts

$$\psi_k = P_k(r, z, t) + \phi_k(r, \theta, z, t), \quad q_k = Q_k(r, z, t) + \xi_k(r, \theta, z, t) \qquad (9)$$

Thus, from Eq.(5) we obtain that the evolution of the symmetric and asymmetric circulations obeys

$$\frac{\partial Q_k}{\partial t} = \langle J(\xi_k, \phi_k) \rangle, \qquad (10)$$

$$\frac{\partial \xi_k}{\partial t} + \frac{\delta}{\partial \theta}(\Omega_k \xi_k - \Gamma_k \phi_k) = J(\xi_k, \phi_k) - \langle J(\xi_k, \phi_k) \rangle, \qquad (11)$$

$$\Omega_k = \frac{1}{r} \frac{\partial P_k}{\partial r}, \qquad \Gamma_k = \frac{1}{r} \frac{\partial Q_k}{\partial r} \qquad (12)$$

Here $\langle \ \rangle$ denotes an azimuthally average relative to the kth center, $\Omega_k(r, z, t)$ is the rotational frequency and $\Gamma_k(r, z, t)$ is defined from the radial gradient of the kth vortex potential velocity. Note, that P_k and ϕ_k describe the flow induced by the potential vorticity of all vortices according to Eq. (4)

$$P_k + \phi_k = \sum_{m=1}^{m=M} \int G(\sigma_{km}, z, z')(Q_m + \xi_m - \beta y_m - \beta r' \sin\theta') r' dr' d\theta' dz' \qquad (13)$$

where

$$2\sigma_{km} = (r\cos\theta - r'\cos\theta' + x_k - x_m)^2 + (r\sin\theta - r'\sin\theta' + y_k - y_m)^2 \qquad (14)$$

Thus, the evolution of every vortex is influenced by all others.

4. First we consider the evolution of a single initially axisymmetric vortex on the β-plane. Focusing our attention on the evolution of strong monopolar vortex assuming $\beta \ll 1$, we describe developing of the asymmetric potential vorticity ξ_1, which is proportional to β, by neglecting the right-hand sides in Eqs (10)-(11) which are proportional to β^2

$$\frac{\partial \xi_1}{\partial t} + \Omega_1 \frac{\partial \xi_1}{\partial \theta} = \Gamma_1 \frac{\partial \phi_1}{\partial \theta} \qquad (15)$$

Here $\Omega_1(r, z)$ and $\Gamma_1(r, z)$ are defined by (12) for the initial axisymmetric vortex because its structure does not change in the leading order according to (10).

For an axisymmetric vortex with an extremum of the fluid potential vorticity at the level $z = z_1$ on the axis of symmetry, initially

$$\xi_1(r, z, 0) = \beta r \sin\theta \left(1 - \frac{\Gamma_1(r, z)}{\Gamma_1(0, z_1)} \right) \tag{16}$$

describing small shift of the axis of symmetry relative to the potential vorticity extremum which is defined as the vortex center, where $\xi_1 = 0$.

As follows from Eqs (15)-(16), the asymmetric circulation generated by the β-effect around the vortex is represented by the azimuthal $l = 1$ perturbation in the form

$$\xi_1 = \mathrm{Re}[r(a + i\beta)\exp(-i\theta)], \qquad \phi_1 = \mathrm{Re}[r(b + i\dot{r}_1)\exp(-i\theta)] \tag{17}$$

$$\frac{\partial a}{\partial t} - i\Omega_1(a + i\beta) = -i\Gamma_1(b + i\dot{r}_1) \tag{18}$$

$$b = \int G'(r, r', z, z')a(r', z', t)r'^3 dr' dz' \tag{19}$$

$$G' = \frac{1}{rr'} \int_0^{2\pi} G(\sigma, z, z') \cos\theta'' d\theta'' = -\frac{1}{2} \int_0^{2\pi} \frac{\partial G}{\partial \sigma} d\theta'', \qquad \theta'' = \theta' - \theta \tag{20}$$

where $a(r, z, t)$ and $b(r, z, t)$ are complex functions, describing the radial-vertical structure of the azimuthal $l = 1$ perturbation of the fluid potential vorticity and geopotential, correspondingly.

When defining the vortex center as an extremum in the potential vorticity q, we must in Eq. (18), set $a = -i\beta$ at $r = 0$, $z = z_1$. Using (19)-(20) and integrating by θ'', we obtain an expression for propagation velocity as follows

$$\dot{r}_1 = ib(0, z_1, t) = -i\pi \int \left(\frac{\partial G}{\partial \sigma} \right)_0 a(r', z', t)r'^3 dr' dz' \tag{21}$$

As follows from Eqs (16) and (19), initially

$$a = -i\beta \frac{\Gamma_1(r, z)}{\Gamma_1(0, z_1)} \qquad b = -i\beta \frac{\Omega_1(r, z)}{\Gamma_1(0, z_1)} \tag{22}$$

implying that the monopolar vortex starts by drifting westward

$$\dot{x}_1 = \beta \frac{\Omega_1(0, z_1)}{\Gamma_1(0, z_1)} < 0 \tag{23}$$

The differential rotation of the asymmetric potential vorticity (the term $\Omega_1 \partial\xi_1/\partial\theta$ in Eq.(15)) and the distortion in the vortex shape caused by the asymmetric flow relative

to the vortex center (the right-hand side of Eq.(15)) produces a west-meridional accelera-
tion of the vortex center.

Quasilinear system (18)-(21) allows for calculating the vortex motion in the differen-
tially rotating fluid during many turnaround times. Similar approach has been used for
describing the self-propelled propagation of a strong vortex due to the β-effect within the
equivalent-barotropic model.[1-5]

5. The solution of (18) consists of two parts. The first one develops due to the
differential advection of the asymmetric potential vorticity (the term $\Omega_1 \partial \xi_1 / \partial \theta$ in Eq.(15)).
It is described by a simple expression obtained while neglecting the right-hand side in
Eqs.(15), (18)

$$\xi_1' = \beta r \left(1 - \frac{\Gamma_1(r,z)}{\Gamma_1(0,z_1)} \right) \sin(\theta - \Omega_1 t), \qquad a' = i\beta \left(1 - \frac{\Gamma(r,z)}{\Gamma_1(0,z_1)} \right) \exp(-i\Omega_1 t) - i\beta \quad (24)$$

and produces a west-meridional acceleration of the vortex center.

The residual $\xi_1 - \xi_1'$ is generated by the advection of the potential vorticity of the
symmetric vortex by the asymmetric flow relative to the vortex center (the right-hand side
in Eq.(15)) then produces additional motion of the vortex center due to such a distortion
of the vortex core. Note, in the equivalent-barotropic model the effect of a distortion of the
vortex shape on the vortex motion can be expressed in an explicit analytical form either
for a piece-wise constant potential thickness of the initial axisymmetric vortex[4], or for a
distributed axisymmetric vortex within the barotropic non-divergent model.[5]

For a singular vortex with the point core of the potential vorticity, $\Gamma_1 = 0$ everywhere
except the vortex center and the asymmetric circulation is described only by (24) in the
simple form

$$\xi_1' = \beta r \sin(\theta - \Omega_1 t), \qquad a' = i\beta(\exp(-i\Omega_1 t) - 1) \qquad (25)$$

and inserting (25) into (21) we obtain the explicit expression for acceleration of such
singular vortex.

In particular, for constant $N = 1$ and far from boundaries, the Green function and
the vortex flow are prescribed in the form[7]

$$G = -\frac{1}{4\pi} [2\sigma + (z - z')^2]^{-1/2}, \qquad P_1 = -\frac{1}{R}, \qquad R^2 = r^2 + (z_1 - z)^2 \qquad (26)$$

Correspondingly,

$$\left(\frac{\partial G}{\partial \sigma} \right)_0 = \frac{\Omega_1}{4\pi}, \qquad \Omega_1 = \frac{1}{R^3} \qquad (27)$$

if we normalize the rotational frequency $\Omega_1 = 1$ at the distance $R = 1$.

In this case the asymmetric flow induced by the β-effect has a self-similar dipolar
structure depending only on $\tau = tR^{-3}$. For the vortex propagation from (21) and (25) we
obtain

$$\dot{r}_1 = \frac{\beta}{4} \int (\exp(i\Omega_1 t) - 1)\Omega_1 r^3 dr dz = \frac{\beta t^{2/3}}{18} \int_0^\infty (\exp(i\tau) - 1)\frac{d\tau}{\tau^{5/3}} \qquad (28)$$

Thus, the singular vortex with the point core moves west-poleward with the velocity increasing as $t^{2/3}$ in the direction 120^0 from the east.

The distortion of the vortex core is negligible also for thin disk-shaped core with constant potential vorticity because again $\Gamma_1 = 0$ everywhere except at the core boundary $r = r_c$. Thus, the solution of (18) has the form (25) if we eliminate singularity at the core boundary in (18) setting

$$\dot{r}_1 = ib(r_c, z_1, t) = -i\pi \int \left(\frac{\partial G}{\partial \sigma}\right)_c a(r', z', t) r'^3 dr' dz' \qquad (29)$$

The rotational frequency Ω_1 for the a disk-shaped core is expressed by elliptic integrals[6] as well as the vortex propagation according to (25) and (29).

6. To take into account the vertical distortion of the vortex core if it is not thin, we consider vertically grouped set of thin vortex subcores, assuming their centers are slightly displaced from the axisymmetric state.

Introducing the small parameter $\epsilon^2 = \max(x_k^2 + y_k^2) \ll 1$, we see that the asymmetric flow is proportional to ϵ so that in the leading order we again can neglect the right-hand sides of (10)-(11) which are proportional to ϵ^2, to obtain $Q_k(r, z) = Q_{init}$ and

$$\frac{\partial \xi_k}{\partial t} + \Omega_k \frac{\partial \xi_k}{\partial \theta} = \Gamma_k \frac{\partial \phi_k}{\partial \theta} \qquad (30)$$

where the rotational frequency Ω_k and Γ_k are prescribed by unperturbed state according to (12), while according to (13) the asymmetric streamfunction ϕ_k relative to the kth center is induced by the asymmetric potential vorticity ξ_m induced directly by the β-effect around every subcore as well as by the symmetric circulation of all subcores due to horizontal shift of their centers which represents the distortion of the vortex core

$$\psi_k = \sum_{m=1}^{m=M} (\phi_{km} + \Phi_{km}) + r(\dot{x}_k \sin\theta - \dot{y}_k \cos\theta) \qquad (31)$$

$$\phi_{km} = \int G(\sigma_{km}, z, z')(\xi_m - \beta r' \sin\theta') r' dr' d\theta' dz \qquad (32)$$

$$\Phi_{km} = \int [G(\sigma_{km}, z, z') - G(\sigma, z, z')] Q_m(r', z') r' dr' d\theta'' dz' = P_{km}(R_{km}, z) - P_{km}(r, z) \qquad (33)$$

where

$$2\sigma = r^2 + r'^2 - 2rr' \cos(\theta - \theta'), \qquad R_{km}^2 = (r\cos\theta + x_k - x_m)^2 + (r\sin\theta + y_k - y_m)^2 \qquad (34)$$

Expanding (32)-(33) for small ϵ we obtain

$$\varphi_{km} = \int G(\sigma, z, z')(\xi_m - \beta r' \sin\theta') r' dr' d\theta' dz \qquad (35)$$

$$\Phi_{km} = r\Omega_{km}[(x_k - x_m)\cos\theta + (y_k - y_m)\sin\theta] + O(\epsilon^2), \qquad \Omega_{km} = \frac{1}{r}\frac{\partial P_{km}}{\partial r} \qquad (36)$$

Following (30)-(36), the asymmetric flow around vortex centers can be again represented by the azimuthal $l = 1$ perturbation in the form

$$\xi_k = \mathrm{Re}[r(a_k + i\beta)\exp(-i\theta)], \qquad \phi_{km} = \mathrm{Re}[rb_{km}(r,t)\exp(-i\theta)] \qquad (37)$$

$$\frac{\partial a_k}{\partial t} - i\Omega_k(a_k + i\beta) = -i\Gamma_k[\sum_{m=1}^{m=M}(\Omega_{km}r_{km} + b_{km}) + i\dot{x}_k - \dot{y}_k] \qquad (38)$$

$$b_{km} = \int G'_k(r,r',z,z')a_m(r',z',t)r'^3 dr' dz' \qquad (39)$$

where $a_m(r,z,t)$ and $b_{km}(r,z,t)$ are complex functions, describing the radial-vertical structure of the mth asymmetric fluid potential vorticity and corresponding flow induced around kth subcore, while $r_{km} = x_k - x_m + iy_k - iy_m$.

Eliminating singularities by setting $a_k(r_{kc}, z_k, t) = 0$ in (38) gives M equations for the propagation velocities of subcore centers

$$\dot{x}_k + i\dot{y}_k = i\sum_{m=1}^{m=M}(\Omega_{kmc}r_{km} + b_{kmc}), \qquad (40)$$

where according to (20) and (39)

$$b_{kmc} = -\pi\int\left(\frac{\partial G}{\partial\sigma}\right)_{kc} a_m(r',z',t)r'^3 dr' dz' \qquad (41)$$

Here Ω_{kmc} is the rotational frequency induced by the mth subcore at the boundary of the kth subcore and M is the total number of all subcores.

Without the β-effect, there is no asymmetric deformation of vortex cores, $b_{kmc} = 0$, and Eq. (40) is reduced into

$$\dot{x}_k + i\dot{y}_k = i\sum_{m=1}^{m=M}\Omega_{kmc}r_{km} \qquad (42)$$

Instead of (40), this linear system of ODE (42) describe mutual rotation of thin subcores simulating the asymmetric deformation of vortex cores by such kind of vertical discretization. Note, that the system (42) can be written in the Hamiltonian form

$$\dot{x}_k = -\frac{\partial H}{\partial y_k}, \qquad \dot{y}_k = \frac{\partial H}{\partial x_k} \qquad (43)$$

where the Hamiltonian H

$$H = \frac{1}{2}\sum_{k=1}^{M}\sum_{m=1}^{M}\Omega_{km}[(x_k - x_m)^2 + (y_k - y_m)^2] \qquad (44)$$

is conserved as a consequence of the angular momentum conservation.

In general case, the solution of (38) for a_m has the same form as (25) so that all b_{kmc} expressed by integrals (41) are explicit functions of time. The system (42) can be rewritten in terms of relative distance between subcores

$$\dot{r}_{km} = i \sum_{l=1}^{M} (\Omega_{klc} r_{kl} - \Omega_{mlc} r_{ml} + b_{klc}(t) - b_{mlc}(t)) \tag{45}$$

and solved in terms of eigenvalues and eigenvectors of matrix Ω.

The system (45) allows for taking into account asymmetric deformation of vortex core and corresponding modification of the vortex propagation during many turnaround times.

References

[1] G. G. Sutyrin, "The beta-effect and the evolution of a localized vortex," Sov. Phys. Dokl. **32**, 791 (1987).

[2] G.G. Sutyrin, "Motion of an intense vortex on a rotating globe," Fluid Dyn. **23**, 215 (1988).

[3] G. M. Reznik, "Dynamics of singular vortices on a beta-plane," J. Fluid Mech. **240**, 405 (1992).

[4] G. G. Sutyrin and G. R. Flierl, "Intense vortex motion on the beta-plane. Development of the beta-gyres," J. Atmos. Sci. **51**, 773 (1994).

[5] G. M. Reznik and W. K. Dewar, "An analytical theory of distributed axisymmetric barotropic vortices on the β-plane", J. Fluid Mech., in press (1994).

[6] G. G. Sutyrin, "The structure of a monopolar baroclinic eddy," Oceanology **29**, 139 (1990).

[7] V. M. Gryanik, "Dynamics of localized vortex perturbations - "vortex charges" in a baroclinic fluid," Izvestiya, Atmos. Oceanic. Phys. **19**, 347 (1983).

AN EXPERIMENTAL STUDY OF THE EFFECTS OF SLOPING TOPOGRAPHY AND CANYONS ON BOUNDARY CURRENTS IN ROTATING, STRATIFIED FLUIDS

Andrew Folkard and Peter Davies
Department of Civil Engineering,
The University, Dundee DD1 4HN U.K.

ABSTRACT

A series of experiments is described in which an oscillating grid, positioned at one end and mid-depth of a rotating channel filled initially with a linearly-stratified fluid, produces an intermediate depth boundary current. In the first set of experiments, the bottom of the channel slopes away from the side on which the boundary current is formed, although it is wholly below the boundary current flowing along the vertical sidewall. In the second configuration, the bottom once again slopes away from the boundary current sidewall, but in this case the currents impinges wholly along the sloping bottom. Gaps of varying lengths are placed in the sloping bottom, and their interactions with the boundary current are observed. In the first configuration, the presence of a sloping bottom is found to destabilize the flow. In the second configuration, the gap causes an eddy to be trapped against its upstream side. The ratio of the gap width to the flow deformation radius is found to be the dominant parameter in determining the nature and persistence of the eddy. The experiments are discussed in relation to similar experiments using rectilinear boundaries, and to the suggested formation of meddies at canyons in the Spanish continental slope.

INTRODUCTION

This work has both general and specific motivations. The former is a desire to understand the interaction of intermediate-depth boundary currents (IDBCs herein) with non-rectilinear boundaries. In this sense, the work is an extension of previous, counterpart experiments with a vertical wall/flat bottom boundary geometry (Besley, 1989). The previous work found that the boundary current became unstable to mesoscale, lateral intrusions when $N_0/\Omega \leq 3.5$ (where N_0 is the ambient buoyancy frequency and Ω is the channel rotation rate). These instabilities always formed at the cross-channel front of the mixed patch at the grid, and not on the boundary current itself. Examples of these results are shown in Figure 1. In the present work, instabilities were always observed forming on the boundary current, even though $N_0/\Omega > 3.5$ for all runs. The specific motivation of the experiments was to investigate the possibility of meddy formation at sites where the Mediterranean outflow encounters submarine canyons in the continental slope, since there exists strong circumstantial evidence for the occurrence of such a process (Prater and Sanford, 1991).

APPARATUS AND PROCEDURE

A perspex channel (2.1 m long × 0.46 m wide × 0.31 m deep) was fitted with a rigid lid to form an enclosed space ~0.24 m deep into which the stratified fluid was placed. At one end of the channel a grid suspended at an intermediate depth could be oscillated vertically with an amplitude of ~1.5 cm, at a variable rate (5 - 35 rad/s). The grid consisted of a 6×4 array of square elements made up of perspex limbs separated by a mesh width of 6 cm.

Side slopes of two different gradients were employed (Figure 2). Two sections of sloping bottom were used, the gap between them forming the interruption in the slope described above. Plan views of the three gap configurations are shown in Figure 3. The channel and all the attendant instrumentation were mounted on a rotating table, which had an adjustable rotation speed in the range 0.05 - 0.6 rad s⁻¹. An array of three cameras positi ned
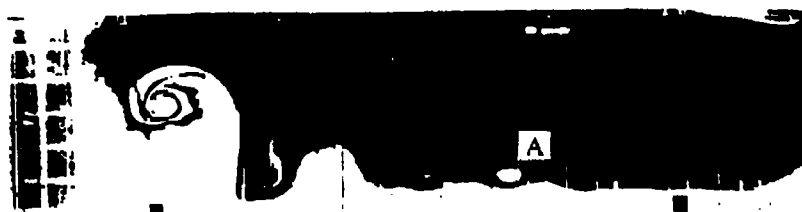
Figure 1 Plan view of typical intrusions observed by Besley (1989). The small feature (A) corresponds to that measured in these experiments. All these features form on the cross-channel front near the grid at the left hand end of the figure

above the channel was used to record the passage of the flow. The channel was illuminated by a horizontal sheet of light, so that only events occurring near the grid depth were recorded. The flow was visualized in two ways. Firstly, runs were carried out in which clouds of tin particles were electrochemically released from solder attached to the grid, giving the mixed fluid a cloudy-white appearance and indicating the overall shape of the flow. These runs were then repeated using particles which were neutrally buoyant at the depth of the grid, providing details of the internal structure of the flow, thus complementing the solder method.

The channel was filled and its initial buoyancy frequency (N_0 - a value of 1.0 rad s^{-1} was used in all runs) measured. The rotation rate of the apparatus was then gradually increased from rest to within $\pm 1\%$ of an operator-specified value. Once the required rotation rate had been reached the system was left until the fluid had

Figure 2 Views of the channel from the grid end showing the relative positions of the slope and boundary current for (i, top) Case I and (ii, bottom) Case II flows

reached a state of solid-body rotation. The grid was then turned on and the experiment commenced (the grid oscillation rate was 20 rad s^{-1} in all runs). In all runs a series of 20 photographs were recorded 15 seconds apart. Each experimen therefore lasted for five minutes, after which the intrusive flow had traversed the perimete of the channel and began to re-enter the mixed patch. Since this indicated a change in the initial conditions, results were not recorded beyond this stage.

RESULTS

Case I Flows

This section describes the results obtained from experimental runs in which the configuration in Figure 2 (i) was used. Variations of the gap width, G, and the rotation rate, Ω, were investigated. A gap width of ∞ indicates that no downstream sloping section was used. Examples of the flows observed are shown in Figure 4. Figure 4 (i) shows a typical

boundary current configuration for the slower rotation rate, $\Omega=0.13$ rad/s. At least two laterally-growing, vortical features such as those shown were observed in every run for this rotation rate. These began to develop as soon as the boundary current was formed, apparently growing from perturbations caused when the mixed patch impinged on the side wall. When the rotation rate was higher (e.g. Figure 4 ii), although no change in the along-channel sense was noted, the lateral growth appeared to be concentrated into only one or

Figure 3 Plan views of the slope configurations used for (i) $G = \infty$ (ii) $G = 0.40$ m (iii) $G = 0.15$ m

two, much larger, vortical features. In both cases, the advection rate of the intrusions was somewhat slower than the nose speed of the boundary current proper. Very similar features were observed in the identically-parameterized runs using the particle-tracking method.

Figure 4 Typical flows in Case I runs for (i. top) $\Omega = 0.13$ rad s^{-1} (ii. bottom) $\Omega = 0.26$ rad s^{-1}. Note that the intrusions here originate on the along-channel front of the boundary current (c.f. Figure 1).

Length measurements were scaled by the first internal deformation radius, $R_d = (g'H)^{1/2}/f$, where $g' = g\Delta\rho/\rho_0$ is the reduced gravity ($\Delta\rho$ being the density jump at the top and bottom of the mixed layer, and ρ_0 the density of the mixed layer), H is a typical depth of the current and $f = 2\Omega$. Although no measurements of depths were made, the depth of the current was observed to be of the order of a few centimetres. Using $H \sim (K/N)^{1/2}$, where K is the grid action (Long, 1978), gives a value of ~0.03 m, which is consistent with observations.

Vertical density profiles of mixed patches measured in another context (Folkard *et al.*, 1994) suggest that $\Delta\rho \sim 10$ kg m^{-3}, giving $g' \sim 0.1$ ms^{-2}. These estimates give $R_d \sim 0.2$ and 0.1 m for $\Omega = 0.13$ and 0.26 rad s^{-1} respectively.

The speed, v_{nose}, of the nose (defined as the point furthest downstream reached by the cloud of tin particles) was found to be $\sim 0.30(g'H)^{1/2}$ for all six values of (G,Ω), using the values of g' and H defined above.

Current widths were measured at Point A on Figure 3 during each run, and were found to have values in the range 0.5-$1.0R_d$ at most times, implying that the current is essentially geostrophic. The only exceptions occurred in the $\Omega = 0.26$ rad s^{-1} runs, when features such as that shown in Figure 4 (ii) passed the measurement point, appearing at the same time for all values of G. In the $G = 0.15$ m runs, a second such feature was also observed.

The along-channel position of the first lateral intrusion to form in each run was shown in Figure 6 (the position of this feature is defined in Figure 5). In the case of low rotation, the data show very little variation with gap width, especially at low Ωt, when $v/v_{nose} \sim$

Figure 5 Definitions of the instability amplitude (*y*) and position (*x*) measurements

0.5. At higher Ωt, the advection rate decreased with increasing G. The data for the $\Omega = 0.26$ rad s^{-1} cases have initial values very close to $v/v_{nose} \sim 0.25$. The divergence observed in the $\Omega = 0.13$ rad s^{-1} case is much more marked here. the $G=\infty$ and 0.40 m intrusions becoming almost stagnant, implying that the presence of a flat bottom had a retarding effect. Note that the positions at which this happened were not coincident with changes in the topography over which they occurred.

Figure 6 Development of the position (*x* in Figure 5) of the first lateral intrusion to form on the boundary current. Symbols as in Fig. 7

Figure 7 Development of the amplitude (*y* in Figure 5) of the first lateral intrusion to form on the boundary current
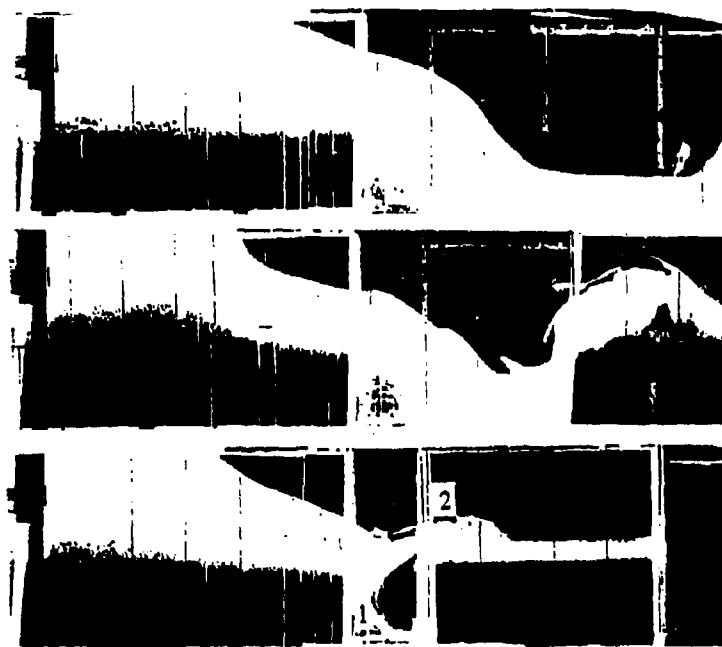
Figure 8 Photographs showing typical flow patterns for Case II runs, for (i, top) $G = \infty$ (ii, middle) $G = 0.40$ m (iii, bottom) $G = 0.15$ m

Figure 7 shows the variation of the amplitude of these features. In the $\Omega = 0.13$ rad s^{-1} cases, a wider gap corresponds to more rapid growth. All these intrusions had amplitudes in the range 0.5-$1.5R_d$. The $\Omega = 0.26$ rad s^{-1} cases show evidence of the large intrusions exemplified in Figure 4 (ii), the amplitudes growing to $-4R_d$. Once again, growth rate increased with increasing G, the variation being observed at all times, rather than appearing suddenly when the intrusions pass over a change in the bottom topography.

Case II Flows

This section presents results from the runs using the configuration in Figure 2 ii. Examples of typical flows for each of the three gap sizes used are shown in Figure 8. In all these runs, the boundary current separated from the side slope at the upstream edge of the gap, forming an eddy that remained in contact with the upstream side of the gap, in contrast to the separation observed by Stern and Whitehead (1990), and postulated by D'Asaro (1988). Klinger (1993) observed that separation is suppressed when the current is baroclinic and when it is flowing along a sloping bottom, both of which pertain to these experiments. Vertical oscillations in the current, caused by the relaxation of the sloping boundary condition, were observed in every run at the point of separation.

Once the flow reached the vertical sidewall within the gap in the $G=\infty$ and 0.40 m cases (Figure 8 i & ii), the boundary current reformed. When $G = 0.40$ m, this boundary current then encountered the downstream side of the gap and was forced away from the wall. When it emerged from the gap in the bottom slope, it turned to the right once again. A period of adjustment then followed in which the current was not attached to the wall. There was, however, no counter-current formation here, and an eddy was not observed in any of the runs. After the adjustment period, the flow resumed its passage along the sloping bottom.

The $G=0.15$ m cases (e.g. Figure 8 iii) differed qualitatively from the other cases, in

that the flow appeared to separate, one vein (*I*) forming an eddy within the gap, and the other (*2*) rejoining the sloping bottom downstream of the gap. The flow in the gap appeared to stagnate eventually, and the boundary current simply flowed across the top of it, relatively undisturbed. In Figure 8 (i) & (ii), there is evidence of cyclonic vortices in the upstream corner of the gap, closer to the wall than the main eddy centre and with cores of ambient (clear) water. This suggests that these features are "counter-eddies" formed by the action of the main eddy on the fluid between itself and the gap corner. $v_{bot}/(g'H)^{1/2}$ is found to be ~0.15 in all of these runs i.e. half that found in the Case I runs for otherwise identical conditions. The current was observed to adopt a width of approximately R_d when flowing along a vertical sidewall above a flat bottom. Elsewhere, the flow is controlled primarily by the constraints of the boundary geometry.

Eddy Measurements

Measurements were made of velocity profiles along lines parallel and perpendicular to the channel sides and passing through the centre of each eddy that was observed in the particle-seeded runs. The position of the eddy centre was judged subjectively, since it was found to be unambiguous. The notation used in describing these measurements is shown in Figure 9. The velocity maximum was measured for the two counter-flow components at 15 s intervals. Each such pair of data was averaged, and these combined data were plotted against Ωt, having first been smoothed using a 5-point running average, and normalized by their maximum values. These plots (Figures 10 and 11) show the expected tendency of the counter-flows to decay most rapidly in the $G =$ 0.15 m cases, due to the constrictive presence of a narrow gap. A more surprising result is the significantly higher decay rate in the $G = \infty$ case, than in the $G = 0.40$ m case.
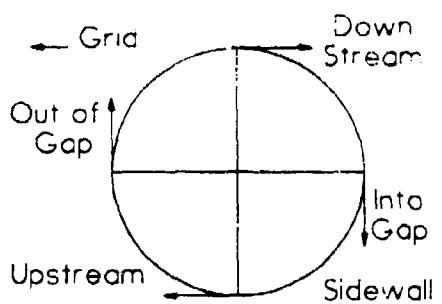
Figure 9 Definitions of the flow directions within the eddies. The "upstream" and "out of gap" flows are collectively referred to as "counter-flows"

DISCUSSION

Case I Flows

The introduction of a sloping bottom is observed to have very significant effects on the boundary current (c.f. Figure 1, showing the behaviour above a flat bottom, from Besley, 1989), most obviously the appearance on it of unstable lateral intrusions. The size and advection rate of these features is strongly dependent on the background rotation rate, and to a lesser extent on the size of the gap in the sloping bottom. This may be partially due to the reduction in volume caused by the introduction of the sloping bottom. However, the constancy of the nose speed in all runs, and the differences observed between the $G = 0.40$ m and 0.15 m cases, which use the same fluid volume, suggest that this effect is not important. Although lateral intrusions are apparent in Besley's results, the initial intrusion, measured here, remains very small in all his cases. Furthermore, the parameters used here in runs in which channel-width intrusions were formed are well within Besley's range for a stable boundary current. These comparisons imply very strongly that the presence of a sloping bottom topography destabilizes the boundary current. However, the features here have growth rates and advection velocities that vary continuously, rather than changing suddenly

at changes in the topography. Thus, it is evident that the effects of the topography variations are transmitted up and/or downstream.
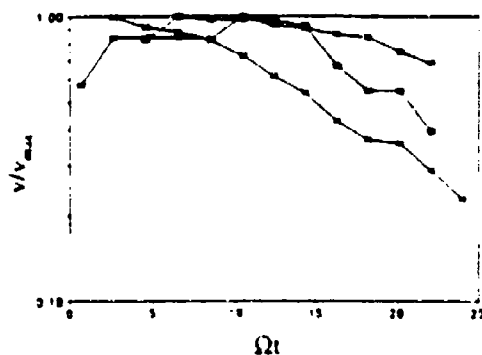
Figure 10 Speed decay for $\Omega=0.13$ rad/s. Symbols here and in Fig. 11 as for Fig. 7
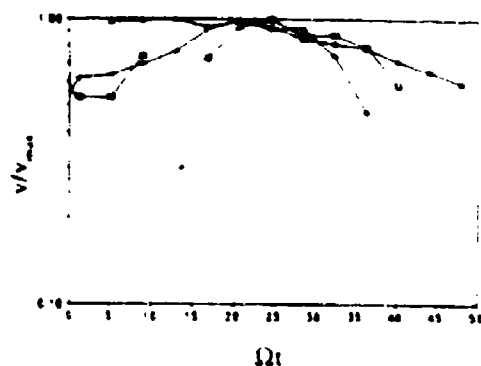
Figure 11 Speed decay for $\Omega=0.26$ rad/s

The increase in size of the intrusions with increased rotation rate suggests that the role of potential vorticity conservation should be considered in their development. The following mechanism is suggested as a model of how this may occur: an initial, perturbative, lateral intrusion of the boundary current away from the sidewall is compensated for by a movement of vortex columns beneath the current towards the wall, and therefore up the bottom slope This causes squashing of the columns, and their vorticity decreases correspondingly, producing vertical shear between them and the boundary current. The resultant deceleration of the flow reduces the Coriolis force into the wall, and the current spreads further from the wall, enhancing the intrusion.

Case II Flows

The results obtained in these runs show that anticyclonic eddies are formed at the upstream end of a gap in a sloping bottom. The persistence of these eddies is found to be strongly dependent on the ratio of the flow deformation radius to the width of the gap. At high values of R_d/G, the narrowness of the gap causes the eddy to decay rapidly. A critical value of R_d/G, below which the decay rate of the eddy decreases, is found to be in the range 0.5-0.7 (since the eddy for $(R_d/G) = (0.2,0.4)$ is relatively persistent, but that for $(R_d/G) = (0.1,0.15)$ decays relatively rapidly). Below $R_d/G \sim 0.25$, the decay rate increases again. Observations (e.g. Ambar and Howe, 1979), of tongues of Mediterranean outflow that sometimes follow contours into canyons and sometimes flow across them unaffected may be explained in terms of the ratio of the canyon width and the deformation radius. Such a description certainly has strong similarities with the results observed here.

It is possible that the decay of the eddies observed in all cases here is due to boundary friction that is much higher than that found in nature. Evidence of this discrepancy is provided by offshore excursions of fluid particles observed at some canyons by Ambar and Howe (1979) and in a model of such a flow by Hughes *et al.* (1990) for canyons of width less than the internal deformation radius of the current. These authors claim that this phenomenon is due to rotational motion within the canyon that is evidently suppressed in the present experiments by boundary friction. Despite this, the difference in eddy decay rates

observed in the present study shows that upstream transmittance of the effect of the downstream end of the gap is very important for this configuration as well as in the Case I configuration.

These results are relevant to the question of meddy formation mainly in relation to the theories of D'Asaro (1988) and Prater and Sanford (1991). These authors claim that the very high anticyclonic vorticity observed at the centres of meddies is only present in the boundary layer of boundary currents. Therefore to form such features, flow separation must occur. The present work raises the question of how the eddies propagate away from the separation site once they have been formed, since in all the runs carried out here, the eddy became trapped as the boundary current flowed over it and reattached to the boundary downstream of the sharp corner in the topography, in a fashion similar to that observed by Klinger (1993). Prater and Sanford suggest that the interaction of a baroclinically unstable lateral intrusion on the boundary current with the canyon may allow the eddy to propagate away. Nof's (1991) mechanism of eddy formation due to the intermittency of the boundary current, although apparently insufficient in itself to explain meddy formation, is another possible cause of eddy propagation.

CONCLUSIONS

(i) The presence of a sloping bottom below an IDBC which is flowing along a vertical sidewall was observed to induce unstable lateral intrusions of the boundary current not observed when the boundary current flowed above a flat bottom. Increasing the background rotation rate sharply increased the growth rate of such features. The presence of sharp changes in the topography between a sloping and a flat bottom had effects on the features that were transmitted up and downstream of their position.

(ii) An IDBC flowing along a sloping bottom which encountered a sharp corner in the topography was observed to form an anticyclonic eddy that became trapped at the corner by the flow past it of the boundary current. This eddy was found to be most persistent when the size of the gap in the sloping bottom, G, was in the range $2.0 - 4.0R_d$.

REFERENCES

Ambar, I. and Howe. M.R., 1979. Observations of the Mediterranean outflow - I deep circulation in the vicinity of the Gulf of Cadiz. Deep-Sea Res., 26A, 535-554

Besley, P., 1989. Eddies and turbulence in stratified fluids; an experimental investigation. Ph.D. thesis University of Dundee, U.K., 203pp

D'Asaro, E., 1988. Generation of submesoscale vortices: a new mechanism, J. Geophys. Res., 93, C4, 6685-6693

Folkard, A.M., Davies, P.A., and Fernando, H.J.S., 1994. Measurements of a turbulent patch in a rotating, linearly stratified fluid, (these proceedings)

Hughes, R.L., Ofusu, K.N., and Hickey, B., 1990, On the behaviour of boundary undercurrents near canyons, J. Geophys. Res., 95, 20259-20266

Klinger, B.A., 1993. Gyre formation at a corner by rotating barotropic coastal flows along a slope. Dyn. Atmos. Oceans, 19, 27-63

Long, R.R., 1978. A theory of mixing in stably stratified fluids. J. Fluid Mech., 84, 113-124

Nof, D., 1991. Lenses generated by intermittent currents. Deep-Sea Res., 38, 325-345

Prater, M., and Sanford, T.B., 1991, Dynamical aspects of the Cadiz meddy and hypotheses of generation, in Proceedings of the International Workshop on outflows and overflows in the Atlantic. Lisbon, Portugal, October 1-4, 1991 30-35

Stern, M.E. and Whitehead, J.A., 1990. ation of a boundary jet in a rotating fluid. J. Fluid Mech., 217, 41-69

On the energy flux from travelling hurricanes on a f-plane to the internal wave field

Johan Nilsson, Department of Oceanography,
University of Göteborg, Box 4038, S-40040 Göteborg, Sweden

1. Internal waves generated by moving hurricanes

Tropical storms with surface wind in excess of 33 ms^{-1} are termed hurricanes in the Atlantic ocean, in the Pacific they are known as typhoons. These storms move over the tropical oceans at an average speed of about 6 ms^{-1}. Hurricanes have approximately axi-symmetric wind fields with a radial extent of about 200-300 km. The radius of maximum wind is usually found 20-30 km from the storm centre. In the open ocean the wind stress at the sea surface is the dominating forcing mechanism and the oceanic response is essentially baroclinic (Geisler 1970). The wind stress accelerates currents in the sea surface mixed layer. These currents are generally divergent and induce vertical motion in the thermocline. The resulting perturbation on the stratification excites internal waves.

Internal wave generation by hurricanes can be studied with a model that describes the oceanic response to a steady axi-symmetric wind stress pattern, which moves at an uniform velocity. Even though the velocity and the intensity of a hurricane may change in time this simple model contains the most important ingredients. In this study the response of a continuously stratified ocean to a moving wind stress pattern is analysed with linear theory on a f-plane. The Boussinesq and the hydrostatic approximations are applied. The wind forcing, say $X=(X,Y)$, is represented as a body force distributed evenly in the sea surface mixed layer. The magnitude of the body force is

given by the wind stress divided by the mixed layer depth. When
the hydrostatic approximation is made the dependent variables
can be resolved in an infinite set of normal modes. Each mode
has a vertical structure that is determined by the
stratication alone (Gill 1982 $,9.10). The time evolution of
the horizontal structure mode is governed by the shallow water
equations

$$\frac{\partial \tilde{u}_n}{\partial t} - f\tilde{v}_n = g\frac{\partial \tilde{h}_n}{\partial x} + \sigma_n X \qquad (1a)$$

$$\frac{\partial \tilde{v}_n}{\partial t} + f\tilde{u}_n = g\frac{\partial \tilde{h}_n}{\partial y} + \sigma_n Y \qquad (1b)$$

$$\frac{\partial \tilde{h}_n}{\partial t} = H_n\left(\frac{\partial \tilde{u}_n}{\partial x} + \frac{\partial \tilde{v}_n}{\partial y}\right) \qquad (1c)$$

where σ_n is the projection of the wind forcing on the n-th mode.
This set of equations supports free waves that satisfy the
dispersion relation (Gill 1982,$7.3)

$$\omega^2 = f^2 + c_n^2(k^2 + l^2) \qquad (2)$$

where $k=(k,l)$ is the horizontal wave vector and c_n is the wave
speed of mode n.

   In the present application waves are forced by a steady but
moving stress pattern. A steady forcing field can only excite
waves that appear stationary in a frame of reference following
the wave source. A ship in uniform motion is a well known wave
source of this type. In a fixed frame of reference the
frequencies of the waves are given by (the storm moves at the

velocity U in the negative x-direction)

$$\omega = -Uk \qquad (3)$$

The Eqs.(2) and (3) defines a curve, say S_n, in the k-l plane that specifies the excitable waves. The wave number curve S_n is determined by

$$k^2 - (l^2 + c_n^2 l^2)(U^2 - c_n^2)^{-1} = 0 \qquad (4)$$

Eq.(4) describes a family of hyperbolic curves for $U>c_n$. When $U<c_n$ no waves are excited, which is explained by the fact that the phase velocity, C_p, always exceeds c_n.

$$|C_p| = c_n (1 + l^2/(c_n k)^2)^{1/2} \quad , \quad |C_g| = c_n^2 |C_p|^{-1} \qquad (5a,b)$$

When $U>c_n$ waves are excited and an internal wave wake trails behind the storm. No waves are found ahead of the storm since the group velocity, C_g, is always smaller than the phase velocity. This wave wake has many features in common with the more well known surface gravity wave wake excited by a ship in uniform motion. The wave energy, which propagates at the group velocity, lags behind the storm. The waves are thus continuously radiating energy away from the storm.

2. The internal wave power generated by a moving storm

The wave energy flux relative to the moving wave source may for each mode be expressed as (Lighthill 1978, §4.12)

$$I_n = W_n (U + C_g) \qquad (6)$$

where W_n is the contribution to the wave energy per unit area from mode n. The wave power, $P_w(n)$, is obtained by integrating the energy flux across a curve that encloses the forcing region. The wave power is the fraction of the rate of work performed by

the wind stress that is absorbed by the internal wave field. A powerful technique for performing such calculations for a general wave system has been presented by Lighthill (1978, §4.12). The result in the present case is given by (see Nilsson 1993 for details)

$$P_w(n)_{Div} = \rho_1 H_{mix} \sigma_n (1 - c_n^2/U) \frac{1}{2} \frac{\pi}{2} \int_{S_n} |\hat{\mathbf{X}}(\mathbf{k})|^2 \cos^2(\alpha(\mathbf{k})) \, dl \qquad (7)$$

$$P_w(n)_{Curl} = \rho_1 H_{mix} \sigma_n (1 - c_n^2/U) \frac{1}{2} \frac{\pi}{2} \int_{S_n} (f/Uk)^2 |\hat{\mathbf{X}}(\mathbf{k})|^2 \sin^2(\alpha(\mathbf{k})) \, dl \qquad (8)$$

Here the wave power has been divided in one part associated with the divergence and one part associated with the curl of the wind stress, i.e $P_w(n) = P_w(n)_{Div} + P_w(n)_{Curl}$. The quantity $|\mathbf{X}(\mathbf{k})|^2$ (the square of the Fourier transform of the wind forcing) may be called the spectrum of the wind forcing. $\alpha(\mathbf{k})$, the angle between the wave vector $\mathbf{k}$ and the forcing $\mathbf{X}(\mathbf{k})$, determines the relative magnitude of the divergence and the curl of the wind stress. The integral in Eq.(7) is a simple integral along the wave number curve S_n of the divergent part of the wind forcing spectrum. Similarly, the integral i· Eq.(8) involves the rotational part of the wind forcing spectrum, modified by the factor $(f/Uk)^2$. This factor, the ratio between f and the frequency of the waves on S_n, never exceeds unity.

3. Application to hurricanes

From observations it is known the that the radial wind
distribution varies between different hurricanes and also may
change during the life span of a single hurricane (Weatherford
and Gray 1988). The following simple wind stress distribution is
used here

$$|\tau| = \tau_{max} \left(\frac{r}{L}\right) \exp\left(1 - \left(\frac{r}{L}\right)\right) \qquad (9)$$

This pattern gives a reasonable description of hurricane stress
fields in many cases. A constant inflow angle of $\varphi = 18.43°$ is
used, which means that the wave power is dominated by the
contribution from the the curl of the wind stress (note that
$\alpha(k) = \pi/2 + \varphi$). The radius of maximum wind, L, is chosen to 30 km
and the maximum wind speed is 35 ms^{-1}, which yields:
$\tau_{max} = 3.4 \times 10^{-3}$ m^{2}s^{-2}. The stratification is chosen to represent
the western Atlantic at 30° north (f=7,3x10^{-5} s^{-1}). The wave
speeds of the first three modes are: 2.8, 1.5 and 1 ms^{-1} and the
mixed layer depth is 50 m.

The stress pattern used here admits a solution on closed
form of Eqs.(7) and (8) (Nilsson 1993). The total internal wave
power, P_w, is obtained by adding the contribution from each
baroclinic mode. In figure 1. P_w is shown as a function of the
storm speed, U, for the case described above. The result is
based on a summation over the first 400 modes. The wave power in
the limit of a vanishing stratification ($c_n = 0$), P_i, is
illustrated as well. A striking feature is that P_w peaks for a
certain storm speed, say U_r. This occurs when the wave numbers
of the free waves match those of the forcing. In the vicinity of
U_r a resonant coupling between the forcing and the waves is
achieved.

When U is increased above U_r, the wave numbers of the excited waves have to diminish in order to keep up with the storm. This decouples the forcing and the waves, and wave power declines. For speeds much larger than U_r the wave lengths of the excited waves exceed the dimension of the storm. The wave power is then essentially determined by the time that a fixed cross section is exposed to the stress. In this regime P_w scales as $1/U$.

When U is reduced below U_r shorter and slower waves are excited. As U is further decreased the wave numbers of the excited waves become so large that they are absent in the spectrum of the forcing. P_w approaches zero, for decreasing U, in a manner determined by the form of the forcing spectrum at high wave numbers. It should also be noted that as U falls below the value of c_n for a given mode that mode ceases to contribute to the wave power.

There are to differences between P_w and P_i that deserves attention. Firstly, non zero c_n increase the phase speed, which implies that the storm moves at a higher speed when waves with resonant wave numbers are excited. P_w will thus peak at a higher storm speed than P_i. Secondly the amplitude of P_w is diminished when the stratification gets stronger. In the present case the P_w is mainly generated by the curl of the stress pattern, i.e. by Eq.(8). The decrease in amplitude is attributed to the factor $(f/Uk)^2$, which is reduced when the strength of the stratification is increased. Since $P_w(n)_{Curl}$ vanish when f approaches zero it is not surprising that the curl of the stress is most effective of generating waves when rotation is the main restoring force.

Generally U_r may be estimated as

$$U_1 = l_0 \, f \qquad\qquad (10)$$

where L_0 is the relevant length scale of the stress field. For the stress pattern used here: $L_0 \approx 1.6L$, i.e. about 48 km.

The internal wave power generated by a moving storm have many similarities with the wave power generated by a ship in motion. The dependence of the wave power on the speed of the wave source are analogous in the two cases. The explanation is that the phase speed decreases with increasing wave numbers for both wave systems.

References:

Geisler, J.E., 1970: Linear theory of the response of a two layer ocean to a moving hurricane. Geophys. Fluid Dyn., 1, 249-272.

Gill, A.E., 1982: Atmosphere-Ocean Dynamics. Academic Press, 662pp.

Lighthill, M.J., 1978: Waves in fluids. Cambridge University Press. 504 pp.

Nilsson, J., 1993: On the energy flux from travelling hurricanes to the oceanic internal wave field. Submitted to J. Phys. Oceanogr.

Weatherford, C.L. and W.M. Gray, 1988: Thypoon structure as revealed by aircraft reconnaissance. Part 2: Structural variability., Mon. Wea. Rev., 116., 1044-1056.

Figure caption: The internal wave power, P_w, (in Watts) generated by a moving hurricane at 30° latitude over a stratified ocean. P_w is the rate of energy supply from the storm to the internal wave field. The wave power in the limit of vanishing stratification, P_i, is also shown.
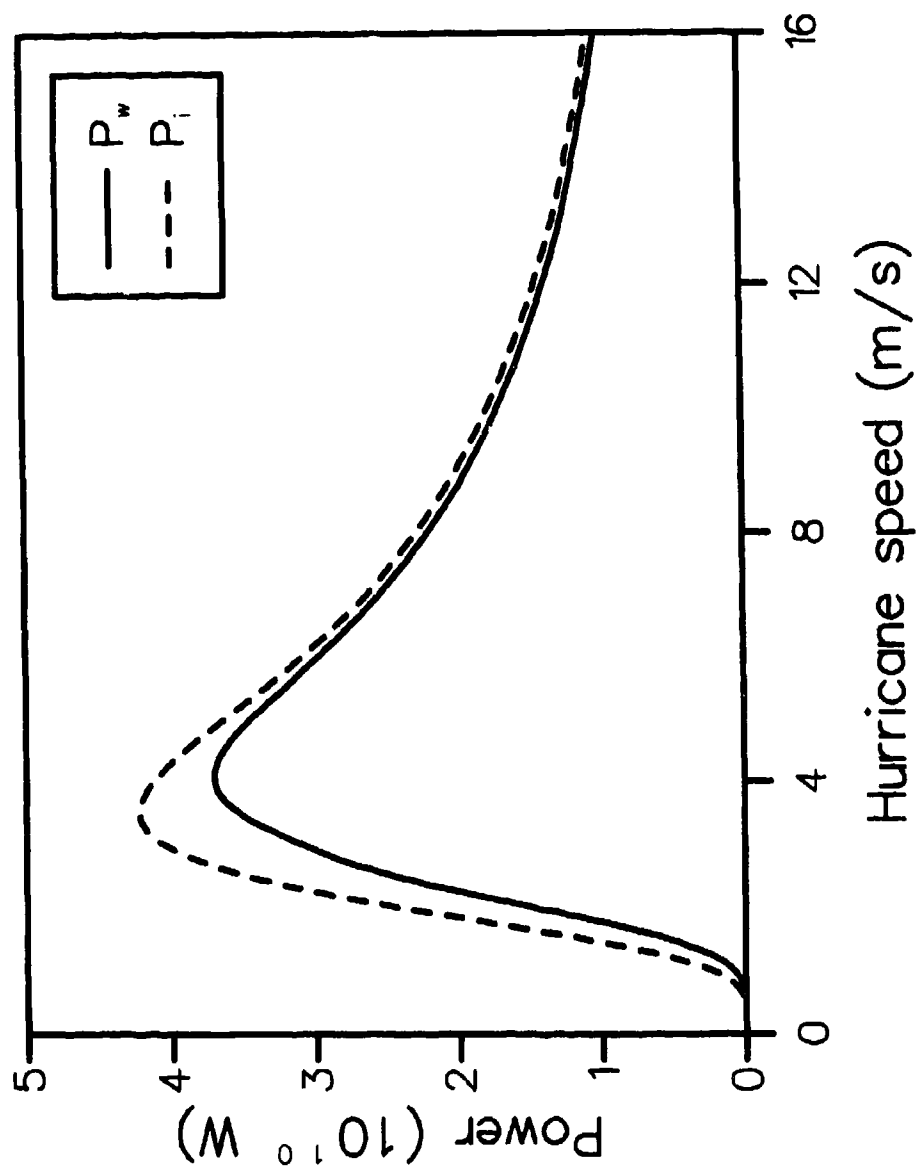
Evolution of an exact, stratified eddy in a rotating, stratified Boussinesq fluid

Leo R. M. Maas
Netherlands Institute for Sea Research
P.O. Box 59, 1790 AB Texel, The Netherlands
and
Konstantin Zahariev
Centre for Earth and Ocean Research
University of Victoria, Victoria, B.C., Canada

Abstract

An exact model to describe submesoscale, coherent vortices in a uniformly stratified fluid is presented. The model allows for stratification of the eddy interior, so as to agree with observations. The closed set of equations governing the evolution of the eddy on the f-plane is derived. In the case that the interior isopycnal surfaces remain horizontal the set reduces, for small Burger number, to the "lens equations" that govern the evolution of uniform-density, warm-core eddies.

1 Introduction

Observations of a Meddy (Mediterranean eddy) by Armi *et al.* (1989) have revealed the following features: It consists of an anticyclonically rotating lens of salt water (angular velocity $\approx -f/3$) situated at a depth of about $1000m$. The Meddy has a radial extent of approximately $25km$ and a depth of about $300m$. The density field within the Meddy is stably stratified, albeit weaker than the exterior stratification. The isopycnals within the meddy typically slope in a consistent fashion and change height dramatically at the edge.

Meddies are one particular class of submesoscale, coherent vortices, observations and models of which are reviewed in McWilliams (1985). In particular he introduced a simple model of a steady circular vortex that may be stratified in the interior. The model is underdetermined — there is one more unknown than there are equations — and one is free to prescribe an "eddy-like", monopolar pressure field, from which the azimuthal velocity and stratification follow. The boundary of the eddy in this model is, however, ill-defined. Other models assume the interior of the eddy to have either constant density (Gill, 1981; Dugan *et al*, 1982; Ruddick, 1987), or the same density gradient as the exterior (Zhmur and Pankratov, 1990, Meacham, 1992). Gill's (1981) study determines the shape and exterior velocity structure of a (basically 2D) elliptical eddy based on quasigeostrophy and hydrostacy assuming the potential vorticity to be constant in the exterior. This approach is extended by Zhmur and Pankratov (1990) and Meacham (1992) by considering 3D ellipsoidal regions with different but uniform potential vorticity in the interior and by matching interior and exterior solutions. In Ruddick's (1987) study the eddy is residing at the interface of two infinitely deep and therefore motionless layers. Attention is consequently concentrated solely on the interior dynamics. Dugan *et al.*'s (1982) model also concentrates on the interior dynamics, assuming somewhat

unrealistically that the velocities in the exterior, stratified region vanish. In our model a similar approach is taken, except that the exterior fields are instead considered to be unresolved (and solvable by e.g. the approach taken by Zhmur and Pankratov, 1990).

In order to describe the observed interior stratification a simple, exact model of an ellipsoidal, stratified eddy in a rotating stratified sea is proposed below. In this model the eddy is enclosed by a surface of vanishing perturbation pressure, and the velocity and density fields are linear, and perturbation pressure field quadratic functions of the spatial coordinates. These have time-dependent coefficients whose time evolution is determined by a closed set of ordinary different.al equations, that can be solved explicitly in particular circumstances.

2 Exact stratified eddy model

Consider the inviscid Navier-Stokes equations on the f-plane, scaled with 'external' scales: reference density ρ_0, Coriolis parameter f and reduced gravity $g' = g\epsilon$, where g denotes the acceleration of gravity and ϵ the scale of the overall density perturbation relative to ρ_0. Regular perturbation expansion in ϵ leads, in lowest order, to the following dimensionless equations for a Boussinesq fluid:

$$\frac{Du}{Dt} - v = -\frac{\partial p}{\partial x}, \tag{1a}$$

$$\frac{Dv}{Dt} + u = -\frac{\partial p}{\partial y}, \tag{1b}$$

$$\frac{Dw}{Dt} = -(\frac{\partial p}{\partial z} + \rho), \tag{1c}$$

where D/Dt denotes the material derivative. Because both particle and phase speeds of disturbances are much smaller than the speed of sound, and also because the vertical scales of motion are much smaller than the scale height of the ocean (which exceeds its depth), the ocean is an incompressible fluid:

$$\nabla \cdot \mathbf{u} = 0. \tag{1d}$$

and hence

$$\frac{D\rho}{Dt} = 0, \tag{1e}$$

Here u, v, w are the velocity components along x, y, z directions in a Cartesian frame of reference whose origin is located at the center of the eddy; ρ and p are the density and pressure fields expanded about the uniform and linearly varying reference state respectively. The eddy is considered to exist within an enclosed region exterior of which the fluid is assumed to be linearly stratified: $\rho_e(z) = -zN^2/f^2$, to which the exterior pressure field $p_e(z)$ is hydrostatically related. Here N denotes the Brunt-Väisälä frequency, defined as $N = -g/\rho_0 d\rho/dz$. It is usefull to define perturbation pressure and density:

$$p'(x, t) = p(\mathbf{x}, t) - p_e(z), \tag{2a}$$

$$\rho'(\mathbf{x}, t) = \rho(\mathbf{x}, t) - \rho_e(z), \tag{2b}$$

which are nonzero in the interior only. The edge of the eddy is enclosed by a surface on which the perturbation pressure vanishes: $p' = 0$.

While considering the motion of a homogeneous water mass in a paraboloidal basin Ball (1963) showed that the centre of gravity may execute inertial oscillations, independent of any changes in shape of the free surface. His analysis was reinterpreted in a reduced gravity context and applied to model (uniform-density) warm-core, surface eddies by Cushman-Roisin *et al.* (1985), Young (1986), Cushman-Roisin (1987) and others. It can be shown that the subsurface, stratified eddy considered presently may likewise execute inertio-buoyancy oscillations as a whole, independent of any changes in shape, orientation and size that it may exhibit. These motions of the geometric centre are here ignored however. Ball's (1963) result was based upon integral considerations. Young (1986), aiming to give a complete description of the motion of the warm-core eddy in terms of integral quantities like the centre of gravity and moments of inertia, concluded that not enough such integral relations exist. Rather, by specifying the velocity and height fields to consist of low order polynomials with time-dependent coefficients the internal structure of the eddy turns out to be describable by eight coupled ordinary differential equations, termed the lens equations by Ruddick (1987). Young (1986) solved these, up to a final quadrature; a last integration that can be accomplished in terms of elliptic integrals.

Several conserved quantities can be formulated for the equations governing a Boussinesq fluid, Eqs. (1):

1) volume V

$$V \equiv \int_D d\mathbf{x}, \tag{3a}$$

2) potential vorticity Π

$$(\omega + \hat{\mathbf{k}}) \cdot \nabla \rho,$$

where $\omega = \nabla \times \mathbf{u}$ is the vorticity and $\hat{\mathbf{k}}$ a vertical unit vector. This quantity is materially conserved and therefore, in view of the commutativity of the time-derivative and global integration operators which the Boussinesq fluid exhibits, also its integral over the eddy domain D is conserved:

$$\Pi = \int_D (\omega + \hat{\mathbf{k}}) \cdot \nabla \rho \, d\mathbf{x}. \tag{3b}$$

3) Energy E

$$E \equiv \int_D \left[\frac{1}{2} \mathbf{u} \cdot \mathbf{u} + z\rho + p_e \right] d\mathbf{x}, \tag{3c}$$

4) the vertical component of the absolute angular momentum vector $L_a^{(z)}$

$$L_a^{(z)} = \int_D xv - yu + \frac{1}{2}(x^2 + y^2) d\mathbf{x}. \tag{3d}$$

As in Young's (1986) analysis this does not suffice to determine the complete internal evolution of the eddy however.

Therefore we also employ a low order polynomial expansion of the velocity, density and pressure field:

$$u_i(\mathbf{x}, t) = u_{ij}(t) \ x_j, \tag{4a}$$

$$\rho(\mathbf{x}, t) = \rho_i(t) x_i, \tag{4b}$$

$$p'(\mathbf{x}, t) = p_0(t) + \frac{1}{2} p'_{ij}(t) x_i x_j, \tag{4c}$$

3

where indices $i, j \in \{1, 2, 3\}$ and matrix p'_{ij} is symmetric. Substituting these expressions with nineteen unknown functions of time in (1), we obtain:

$$\frac{du_{ij}}{dt} + u_{ik}u_{kj} + \epsilon_{i3k}u_{kj} + p'_{ij} + \delta_{i3}\rho_j = 0, \tag{5a}$$

$$\frac{d\rho_i}{dt} + u_{ki}\rho_k = 0, \tag{5b}$$

and

$$u_{kk} = 0, \tag{5c}$$

where summation over repeated indices is implied and ϵ_{ijk} and δ_{ij} are the anti-symmetric and Dirac-delta tensors respectively. These constitute a total of thirteen equations. The six missing follow from the boundary condition expressing that a particle once residing on the boundary remains on the boundary:

$$\frac{Dp'(\mathbf{x}, t)}{Dt} = 0 \quad at \quad p'(\mathbf{x}, t) = 0.$$

Inserting expression (4c) in both the boundary condition (employing (4a) in the material derivative) as well as the description of the boundary itself leads to two polynomial expressions with seven independently varying, spatial fields. When eliminating the spatially uniform term between these two and subsequently requiring the separate vanishing of each of the coefficients of the resulting polynomial with six spatially dependent terms leads to

$$\left(\frac{d}{dt} - \frac{1}{p_0}\frac{dp_0}{dt} \right) p'_{ij} + p'_{ik}u_{kj} + p'_{jk}u_{ki} = 0. \tag{5d}$$

This leaves us with a closed set of nineteen nonlinearly-coupled, ordinary differential equations for as many unknowns, describing the evolution of an eddy in a uniformly stratified, rotating medium having a different internal stratification.

No notion of applying the model to oceanic eddies (except the arguments to validate the Boussinesq approximation) has been introduced up to now. The model equally applies to laboratory eddies. However, if we intend to apply the model to oceanic eddies, the observed disparity in horizontal and vertical scales L and H has to be brought into the description. In such a case it is usefull to rescale the horizontal and vertical scales and velocities separately and equations (5) change only by the appearance of the square of the aspect ratio $a = H/L \ll 1$ in front of the acceleration terms in the vertical momentum equation. For $i = 3$ Eq. (5a) simplifies to:

$$p'_{3j} = -\rho'_j,$$

where perturbation density $\rho' = \rho'_i x_i$. Since the interior is less stratified than the exterior (Dugan et al. 1982, Armi et al. 1989) $\rho'_3 > 0$. The exterior density field is in this case given by $\rho_e(z) = -Sz$, with $S = (NH)^2/(fL)^2$ denoting the Burger number. This implies $\rho_i = \rho'_i - S\delta_{3i}$.

3 Special cases

3.1 Steadily rotating stratified eddy

4

A solution of (5) is given by the disc shaped perturbation pressure field

$$p' = \frac{1}{2}\rho'_3(H^2 - z^2) + \frac{1}{2}\Omega(\Omega + 1)(x^2 + y^2).$$

where $u_{21} = -u_{12} \equiv \Omega$ and the central pressure p_0 has been determined by assuming that the vertical scale H of the eddy is known. If also horizontal scale L and interior stratification ρ'_3 are given the angular velocity Ω can be obtained from

$$\Omega(\Omega + 1) = -\rho'_3 \frac{H^2}{L^2}$$

Recall that $\rho'_3 > 0$. As ρ'_3 is a sizeable part of N^2/f^2 the right-hand side can be expressed as a fraction of S. The vortex is necessarily a high pressure, anticyclonic eddy with $\Omega \in (-1,0)$.

3.2 Oscillating planar eddy

Consider the case that isopycnal surfaces stay flat: $\rho_1 = \rho_2 = 0$. From (5b) this implies $u_{31} = u_{32} = 0$ and $u_{33} = -1/\rho_3 d\rho_3/dt$: horizontal uniformity of the vertical velocity field. With the hydrostatic assumption, equation (5d), for p'_{13} and p'_{23} implies that the horizontal velocities have no shear in the vertical $u_{13} = u_{23} = 0$. Consequently, again from (5d), $p'_{33} = c_0 p_0 \rho_3^2$, where c_0 is a constant. However, because of hydrostacy, $p'_{33} = -\rho'_3$, and thus

$$\frac{1}{p_0}\frac{dp_0}{dt} = -\frac{1}{\rho_3}\frac{d\rho_3}{dt}\left(2 - \frac{\rho_3}{\rho'_3}\right).$$

For vanishingly small Burger number the right-hand side equals $u_{33} = -u_{11} - u_{22}$ and the equations for $u_{11}, u_{12}, u_{21}, u_{22}, p'_{11}, p'_{12}, p'_{22}$ and p_0 become identical to the Lens equations (see Cushman-Roisin et al 1985, 1987; and Young ,1986, correcting some misprints in their equations).

4 Discussion and Conclusions

A complete set of equations, (5), describing the evolution of an interiorly stratified eddy in a uniformly stratified, rotating medium has been derived. The set has been shown to reduce to the lens equations in the limit that the aspect ratio and Burger number are small. For this set, derived to describe constant density warm-core eddies, solutions have been obtained, which show that the eddy executes simultaneous shape, size and orientation changes that occur superinertial, inertial and either sub- or superinertial respectively (Young, 1986). In the present application, where the surroundings is uniformly stratified, inertial and superinertial oscillations are subject to radiative damping. Hence, it is likely that only orientation changes will remain.

More detailed analysis of the equations needs to be performed. In particular the case with sloping isopycnal surfaces needs to be addressed as this feature is suggested in the observations of a Meddy (Armi et al, 1989).

5 Acknowledgements

References

Armi, L. ,D. Hebert, N. Oakey, J.F. Price, P.L. Richardson, H.T. Rossby and B. Ruddick, 1989, Two years in the life of a Mediterranean salt lens, *J. Phys. Oc.* *19*, 354-370.

Ball, F.K., 1963, Some general theorems concerning the finite motion of a shallow rotating liquid lying on a paraboloid. *J. Fluid Mech.* *17*, 240-256.

Cushman-Roisin, B., 1987, Exact analytical solutions for elliptical vortices of the shallow-water equations. *Tellus 39A*, 235-244.

Cushman-Roisin, B., W.H. Heil and D. Nof, 1985, Oscillations and rotations of elliptical warm-core rings. *J. Geophys. Res. 90*, 11,756-11,764.

Dugan, J.P. R.P. Mied, P.C. Mignerey, and A.F. Schuetz, 1982, Compact, Intrathermocline eddies in the Sargasso Sea. *J. Geophys. Res. 87*, 385-393.

Gill, A.E., 1981, Homogeneous intrusions in a rotating stratified fluid, *J. Fluid Mech. 103*, 275-295.

McWilliams, J.C., 1985, Submesoscale, coherent vortices in the ocean. *Rev. of Geophys. 23*, 165-182.

Meacham, S.P., 1992, Quasigeostrophic, ellipsoidal vortices in a stratified fluid. *Dyn. Atm. Oc. 16*, 189-223.

Ruddick, B.R., 1987, Anticyclonic lenses in large-scal strain and shear. *J. Phys. Ocean. 17*, 741-749.

Young, W. R., 1986, Elliptical vortices in shallow water. *J. Fluid Mech. 171*, 101-119.

Zhmur, V.V. and K.K. Pankratov, 1990, Dynamics of mesoscale eddy structure in the flow field of a large, strong eddy. *Oceanology 30*, 124-129.

CYCLONE-ANTICYCLONE ASYMMETRY IN THE MERGING PROCESS

S. VALCKE and J. VERRON

URA 1509 CNRS, L.E.G.I. - Institut de Mécanique de Grenoble
BP 53X, 38041 Grenoble Cédex, France

1- Introduction

Cyclone-anticyclone asymmetry is a striking feature which emerges from the observations of geophysical flows. Long-lived vortices in the atmosphere of large planets and intrathermocline eddies of the earth ocean show a predominance of anticyclones. Rather differently, oceanic rings created in the Gulf-Stream or Kuro-Shio regions exhibit a large proportion of cyclones. Many dynamical differences between cyclones and anticyclones are not, up to now, well understood. This is in particular the case with regard to a basic eddy interaction process such as merging.

In their laboratory experiments in rotating tanks, Griffiths and Hopfinger (1987) observed that, in an unstratified fluid, cyclones merged from all initial separation distances while a stability boundary was found for anticyclones. However, as they studied geostrophic (weak) vortices, they expected to find no difference between cyclones and anticyclones. The asymmetry observed was therefore attributed to a differential effect of the bottom Ekman layer which caused cyclones to diffuse more rapidly than anticyclones. Their additional experiments in the two-layer stratified case supported this hypothesis as they found no major difference between the merging of upper-layer geostrophic cyclones and anticyclones.

Concerning theoretical and numerical investigations, the merging process has already received considerable attention in the purely two-dimensional situation (Overman & Zabusky 1982, Melander *et al.* 1988, Dritschel & Waugh 1992). For the rotating case, Carton and Bertrand (1993) recently studied the effect of ageostrophy and found that in a flow with finite Rossby number, anticyclones merge more easily than cyclones. As far as rotating stratified flows are concerned, there has been only few studies, mostly based on the quasigeostrophic (QG) approximation (Polvani *et al.* 1989, Masina & Pinardi 1993, Meacham 1994). In this framework, the work by Verron and Valcke (1994), hereafter VV, showed that the merging process may be strongly influenced by the stratification. However, in the QG approximation, no difference can be found between cyclones and anticyclones. Pavia and Cushman-Roisin (1990) went further by considering frontal eddies in the shallow-water reduced-gravity case. In particular, they found that cyclones and zero-potential-vorticity anticyclones were resistant to merging.

In the present paper, a two-layer shallow-water (isopycnic) model is used to generalize the study of the QG baroclinic merging by VV. This model allows the numerical simulation of a larger range of eddies without restriction on the Rossby number and include the cyclone-anticyclone asymmetry. The general objective is to try to understand how stratification can selectively affect the merging process of ageostrophic cyclones and anticyclones. The layout of the paper is as follows. In section 2, the physical system under study is presented, and VV's results in the QG case are recalled. In section 3, the present model characteristics and the initialization of the numerical experiments are described. The results are presented in section 4. The discussion in section 5 considers an interpretation of these results based on the interface deviation. The last section summarizes the results and conclusions.

2- The physical problem and previous quasigeostrophic results

The physical system in which the merging problem is considered is a two-layer rotating fluid. The undisturbed depths of the two layers are supposed to be equal ($H_1 = H_2 = H$) and of different densities ρ_1 and ρ_2. (The subscript 1 indicates the upper layer, 2 the bottom layer.) The radius of deformation, representative of the stratification, writes $\lambda = \sqrt{g'H}/\sqrt{2}f_0$ where the Coriolis parameter f_0 is assumed to be constant and $g' = g\Delta\rho/\rho$ measures the density jump, $\Delta\rho$, between the two layers. The bottom layer is initially at rest and the vortices are defined in the upper layer as two circular patches of relative vorticity, ω, of radius R (Rankine profiles denoted R_a^k). In our case, the Rankine profile is approximated by:

$$R_a^k \approx \Omega\left[1 - 0.5(tanh\,4(r/R - 1) + 1)\right] \tag{1}$$

where Ω is the maximum value of the vorticity in the core and r the radial distance from the centre of the vortex k. The initial upper-layer velocities, assumed to be nondivergent, are then related to the streamfunction ψ_{10} by $u = -\partial\psi_{10}/\partial y$ and $v = \partial\psi_{10}/\partial x$ with ψ_{10} given by

$$\nabla^2\psi_{10} = \sum_{k=1,2} R_a^k \tag{2}$$

In the QG approximation studied by VV, the evolution of this physical system can be modelled by the following set of equations written for Q_1, the potential vorticity (PV):

$$\frac{DQ_1}{Dt} = \frac{D}{Dt}\left[\omega_1 + \frac{1}{2}\lambda^{-2}(\psi_2 - \psi_1)\right] = V_1 \tag{3a}$$

$$\frac{DQ_2}{Dt} = \frac{D}{Dt}\left[\omega_2 - \frac{1}{2}\lambda^{-2}(\psi_2 - \psi_1)\right] = V_2 \tag{3b}$$

Dissipative terms of the form $V_i = -A_4\nabla^4\omega_i$ were needed, in the finite-difference code used in the numerical simulations, to dissipate the enstrophy which tends to accumulate at the small scales.

2

For the physical system described above, the initial PV in the two layers is:

$$Q_{10} = \sum_{k=1,2} R_a^k - \frac{1}{2}\lambda^{-2}\psi_{10} \qquad (4a)$$

$$Q_{20} = +\frac{1}{2}\lambda^{-2}\psi_{10} \qquad (4b)$$

This was denoted as the Relative Vorticity Initialization (RVI).

Because of the small numerical viscosity A_4 introduced in the model, it was observed that the vortices eventually merge for all d, the initial distance centre to centre. For this reason, t_c/T, the time required for merging nondimensionalized by the vortex turnover period $T = 2\pi/\Omega$, was considered to be the relevant vortex interaction factor.

In the RVI case, the merging was found to be strongly dependent on the background stratification. In fact, for any fixed d, the merging time t_c/T was found to vary a lot with the stratification parameter λ/R. For example, for an initial distance d/R as large as 5.5, merging is obtained for $t_c/T \simeq 65$ when $\lambda/R = 3.2$ while it is 4 times shorter when $\lambda/R = 1.7$. On the other hand, for $\lambda/R \leq 1.5$, the vortices never merge. Globally, the merging was observed to be very much favoured for a restricted range of λ/R, between around 1.5 and 3.

Interpretation for this scale-dependency of the merging was proposed which involves competing effects between an attracting vortex shape effect and a repulsing hetonic interaction. As λ/R is decreased from ∞ to $O(1)$ values, the stratification weakens and the term $1/2 \cdot \lambda^{-2}\psi_{10}$ increases. This corresponds to an increasing "skirt" shape for the PV of the upper-layer vortices Q_{10}, i.e. a PV more and more important beyond the core region. Equivalently, the interface is initially more and more deviated. Consequently, the tendency to merge increases and t_c/T gets smaller. This enhanced tendency for the vortices to merge as λ/R decreases was called the "barotropic attracting shape" effect.

Concurrently, as the stratification gets weaker, the layers become very much coupled. The PV of the lower layer, $Q_{20} = +1/2 \cdot \lambda^{-2}\psi_{10}$, becomes important and influences the upper-layer dynamics. In fact, the RVI case corresponds to two PV vortices of one sign in the upper layer and to two PV vortices of opposite sign in the lower layer. This is analogous to a configuration of two hetons as described by Hogg and Stommel (1985). In the RVI case, the hetons have a finite core and Valcke and Verron(1993) showed that for a weak stratification, the dynamical effect of the lower-layer vortices is to make the upper-layer vortices diverge from each other, thereby inhibiting their merging. This effect was called the "baroclinic repulsing hetonic" effect. In conclusion, the restricted range of λ/R of promoted merging is the result of the two competing effects.

3

3- The model and the initialization of the numerical experiments

The numerical model used in this paper is the Miami isopycnic coordinate, primitive equation model (Bleck and Boudra 1981) in an adiabatic two-layer flat-bottom formulation. In the present case, the equations reduce to the shallow-water equations for each layer of uniform density ρ_i and of varying thickness h_i. This model employs an Arakawa C-grid configuration and the version used in our experiments incorporates the rigid-lid approximation. We assumed no bottom friction, thereby removing an eventual Ekman layer effect. The numerical dissipation terms, $A_4\nabla^4 u$ or $A_4\nabla^4 v$, are of the biharmonic type on the velocity.

The physical system described in section 2 can be studied in this model by initializing the corresponding velocity fields. Rest is imposed initially in the bottom layer and the upper-layer velocities are given by (2). However, in the isopycnic model, the interface deviation η has also to be determined and this makes a problem to arise. If the interface deviation is not in balance with the velocity field, it undergoes strong adjustements generating gravity waves and disturbing the initial conditions in which we want to study the merging process. Moreover, an initial interface deviation totally in balance is dynamically inconsistent with our problem: the initial state would then be stationary and would not undergo any evolution in time. In the previous QG simulations, this difficulty did not emerge as η was a diagnostic variable given by $\eta = f_0/g'(\psi_2 - \psi_1)$ which comes from the geostrophic equilibrium (the development of the shallow-water equations at the $O(0)$ in the Rossby number $Ro = U/f_0 L$).

The interface chosen stems from a "balance model" developed, in this case, from the shallow-water equations and considering the terms up to the $O(1)$ in Ro. Taking the divergence of these equations, the expression for $\nabla^2 p$, where p is the pressure, can be written. The nondimensionalization of this equation makes the Rossby number Ro and Burger number, $Bu = N_0^2 H^2 / f_0^2 L^2$, to appear. U, L, H and $N_0^2 = -g\partial_z \rho/\rho$ are respectively the scales for the horizontal velocity, the horizontal distance, the vertical distance and the vertical stratification. If $Bu \geq 1$, the dimensionless equation can be written:

$$\nabla^2 p = \omega + 2RoJ(u,v) + O(Ro^2) \tag{5}$$

where J is the Jacobian operator.

When the lower-layer velocities are negligible compared to the upper-layer velocities, p and η are linked by $\nabla^2 p = -\rho g'\nabla^2\eta$. Using this relation and keeping the terms up to the $O(1)$ in Ro, we get (in a dimensional form):

$$\nabla^2\eta = -\frac{1}{g'}(f_0\omega + 2J(u,v)) \tag{6}$$

Preliminary experiments with only one vortex using the interface given by (6) were made. They showed that for ageostrophic vortices with Ro as large as $Ro = 0.5$ the adjustement of the interface deviation was always less than 4% (for $1 \leq \lambda/R \leq \infty$).

4

For the strong cyclones (anticyclones), the initial interface was slightly underestimate (overestimate). In the numerical experiments described in the next section. we used the interface given by (5), being aware that it is uncertain. at this stage. how the slight residual adjustement could influence the merging dynamics.
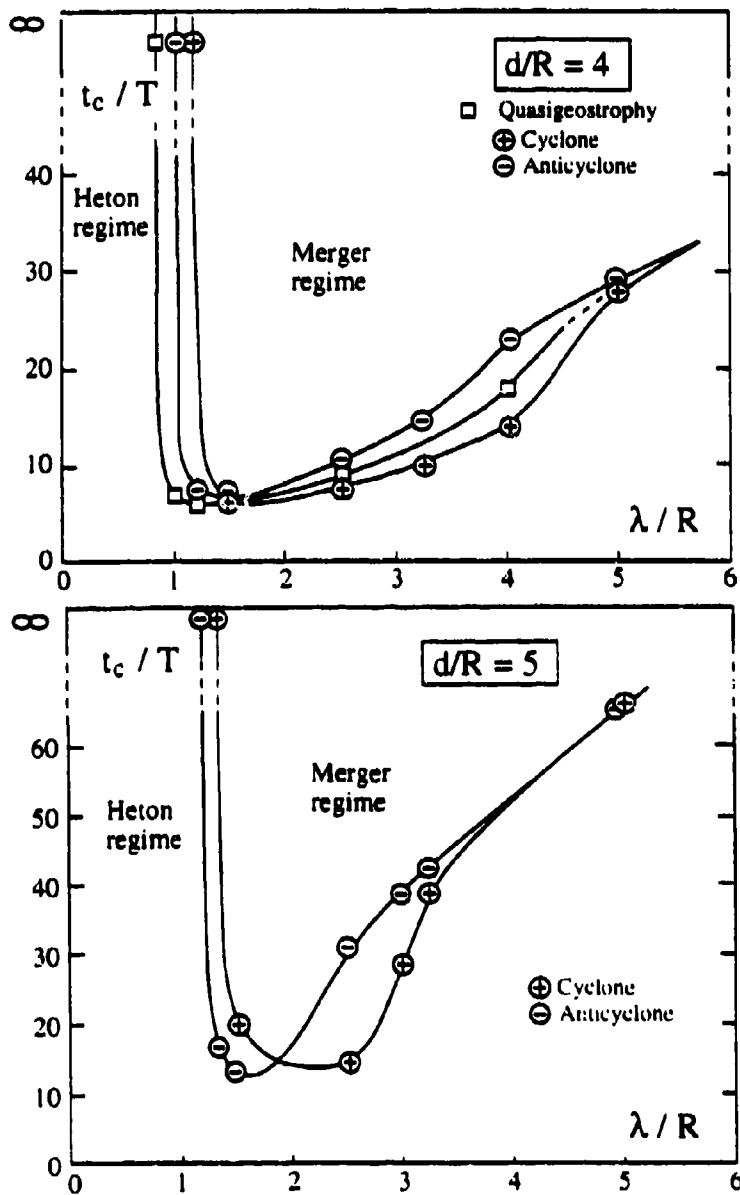
Fig.1 t_c/T vs λ/R in the two-layer case for cyclones ($\Omega/2f_0 = 0.5$). anticyclones ($\Omega/2f_0 = -0.5$) and for QG vortices ($\Omega/2f_0 \ll 1$).

5

4- Results of the numerical experiments

We processed to several merging experiments for strong cyclones ($\Omega/2f_0 = 0.5$) and strong anticyclones ($\Omega/2f_0 = -0.5$) in a range of the stratification parameter $1 \leq \lambda/R \leq 5$. The results are presented on Figure 1. It shows the merging time t_c/T as a function of λ/R for two initial distances d/R. These experiments used a numerical viscosity of $A_4/\Omega R^4 = 10^{-5}$.

Qualitatively, the same dependency of the merging on the stratification as in the QG experiments of VV is recovered. As a reference, the QG case is shown on the figure for $d/R = 4$. As λ/R decreases, the interface is initially more and more deviated, the tendency to merge increases and t_c/T decreases. Concurrently, as the stratification weakens, the layers become very much coupled and around $\lambda/R = 1$ to 1.5, the repulsing hetonic effect takes place; the vortices never merge and t_c/T was set to ∞.

However, appreciable differences appear between strong cyclones and anticyclones. In the merger regime, the cyclones merge much faster than the anticyclones. For example, for $d/R = 5$ and $\lambda/R = 2.5$, the t_c/T for cyclones is as low as half the t_c/T for anticyclones. Moreover, the hetonic effect is more important for cyclones than for anticyclones appearing for greater λ/R. It is interesting to note that these results can be interpreted in terms of stability of cyclones and anticyclones with respect to merging. In short, three stratification regimes can then be identified: (i) for strong stratification, the cyclones and the anticyclones are equivalently stable; (ii) for intermediate stratification, anticyclones are more stable than cyclones; (iii) for weak stratification, the cyclones become more resistant to merging because the repulsing hetonic effect is stronger.

5- Discussion

The behaviours of the cyclones and anticyclones and their differences can be related to the initial interface deviation. In the QG case, the promoted tendency to merge as the stratification weakens was interpreted by an interface initially more and more deviated. This interpretation is still valid for ageostrophic cyclones and anticyclones. We argue that this phenomenon is therefore due to the dynamics of the interface and of the upper layer only. To test this hypothesis, we proceeded to merging experiments in the "equivalent barotropic" situation which is the limiting case when the bottom layer gets infinitely deep. In that case, we get rid of the dynamical influence of the lower layer. The results are shown on Figure 2. Note that λ is then written as $\lambda = \sqrt{g'H_1}/f_0$.

Comparing Fig. 2 with Fig. 1 for $d/R = 5$, we see that the behaviours of ageostrophic cyclones and anticyclones coincide exactly in the two-layer and in the equivalent barotropic cases for $2.5 \leq \lambda/R \leq 6$. For $\lambda/R \leq 2.5$, the curves differ because no baroclinic counter effect of the hetonic type can be present in the equivalent barotropic case. The hypothesis that the dynamics of the interface can explain the promoted merging tendency for a decreasing λ/R is then confirmed.

Furthermore, the differences in t_c/T between the QG case, strong cyclones and strong anticyclones can also be interpreted in terms of the initial interface deviation η. In the expression for η given by the balance model (6), the ageostrophic term $J(u,v)$ makes the interface deviation (scaled by the vorticity Ω) slightly more important for a strong cyclone, and slightly less important for a strong anticyclone, than in the QG case . This can explain why the cyclones merge more easily than QG vortices which themselves merge more easily than anticyclones.
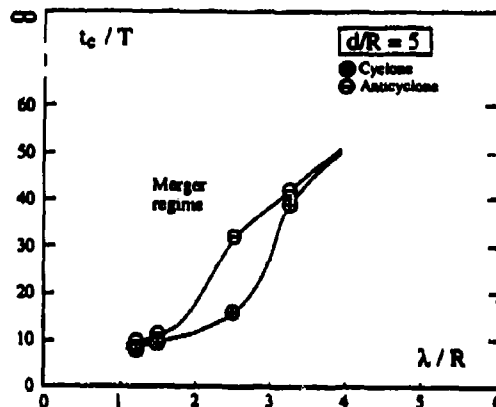
Fig.2 t_c/T as a function of λ/R in the equivalent barotropic case for cyclones ($\Omega/2f_0 = 0.5$), anticyclones ($\Omega/2f_0 = -0.5$).

Similarly, we can give a tentative explanation of the differences arising between strong cyclones and anticyclones in the heton regime by considering these differences in η. In the QG case, the hetonic effect was related to the dynamics of Q_{20} for small λ/R. The lower-layer potential vorticity Q_{20}, given by (4b), is in fact directly related to η by $Q_{20} = 1/2\lambda^{-2}\psi_{10} = \eta f_0/H$. The more the interface is deviated, the more important is Q_{20}, and the stronger the hetonic repulsing effect is. This could explain why the hetonic effect for the strong cyclones is greater than for strong anticyclones.

Considering η, the QG curve in the hetonic regime should be between the strong cyclone and the strong anticyclone curves, but this is not the case. However, it is important to note that, at these small values of λ/R, in addition of breaking the QG restriction of small Ro number, ageostrophic vortices violate also the QG hypothesis of small interface deformation with respect to layer thickness. This could be why the effect of the interface deviation in QG case and in the ageostrophic cases are no longer directly comparable.

6- Summary

This paper presented numerical experiments on the merging of ageostrophic cyclones and anticyclones, using an isopycnic shallow-water model. The vortices were initialized by determining the initial velocity fields, and the interface deformation stemmed from a balance model accurate to the first order in Ro. Qualitatively, the same dependency of the merging on the stratification as in QG experiments was recovered; it was interpreted

7

in terms of competing effects between an interface deformation effect and a repulsing hetonic effect. However, noticeable differences appeared between strong cyclones and anticyclones. In a weakly-stratified regime, the cyclones were observed to be more stable than anticyclones with regard to merging but the opposite was true for a stronger stratification. These differences were related to the initial interface deviation which is always greater for ageostrophic cyclones than for ageostrophic anticyclones.

Acknowledgements

REFERENCES

Bleck R. and D. B. Boudra, 1981: Initial testing of a numerical ocean circulation model using an hybrid (quasi-isopycnic) vertical coordinate. *J. of Phys. Ocean.*, **11**, 755-770.

Carton, X.J. and C. Bertrand, 1993: The influence of environmental parameters on two-dimensional vortex merger. *Proceedings of the Colloquium on the Modelling of Oceanic Vortices*, to appear.

Dritschel, D.G. and D.W. Waugh, 1992: Quantification of the inelastic interaction of unequal vortices in two-dimensional vortex dynamics. *Phys. Fluids*, **A 4**, 1737-1744.

Griffiths R.W. and E.J. Hopfinger, 1987: Coalescing of geostrophic vortices. *J. of Fluid Mechanics*, **178**, 73-97.

Hogg N. and H. Stommel, 1985: The heton, an elementary interaction between discrete baroclinic geostrophic vortices and its implications concerning eddy heat flow. *Proc. R. Soc. Lond.*, **A 397**, 1-20.

Masina, S. and N. Pinardi, 1993: The halting effect of baroclinicity in vortex merging. *J. of Phys. Ocean.*, **23**, No. 8, 1618-1637.

Meacham, S.P. 1994: The merger of three-dimensional, quasigeostrophic vortices in a stratified fluid. Submitted to *Physics of Fluids A*.

Melander M.V., Zabusky N.J. and J.C.McWilliams, 1988: Symmetric vortex merger in two dimensions : causes and conditions. *J. of Fluid Mechanics*, **195**, 303-340.

Overman E.A. and N.J. Zabusky, 1982: Evolution and merger of isolated vortex structures. *Phys. Fluids*, **25**, 1297-1305.

Pavia, E.G. and B. Cushman-Roisin, 1990: Merging of frontal-eddies. *J. of Phys. Ocean.*, **20**, 1886-1906.

Polvani L.M., Zabusky N.J. and G.R. Flierl, 1989: Two-layer geostrophic vortex dynamics. Part 1. Upper layer V-states and merger. *J. of Fluid Mechanics*, **205**, 215-242.

Valcke S. and J. Verron, 1993: On interactions between two finite-core hetons. *Phys. Fluids*, **A5**, 2058-2060.

Verron, J. and S. Valcke, 1994: Scale-dependent merging of baroclinic vortices. *J. of Fluid Mechanics*, **264**, 81-106.

Advective and diffusive processes in baroclinic vortices

J. Nycander (Dept. of Technology, Uppsala University, Box 534, 751 21 Uppsala, Sweden)

S. N. Aristov (Institute of Continuum Mechanics, Korolev St. 1, Perm 614061, Russia)

ABSTRACT

Baroclinic vortices are studied analytically, taking viscosity v and thermal diffusivity κ into account. The direction of the meridional circulation depends on the Prandtl number $Pr = v/\kappa$. If $Pr > 1$ there is upwelling in the interior of the vortex, and the vertical heat diffusion is therefore inhibited by advection. The radial flow is inward in most of the vortex, which is compensated by outward flow in a viscous boundary layer just below the surface. We particularly study the strongly nonlinear regime, when the background stratification is much weaker that that of the vortex. In the limit $Pr \gg 1$ we find that the nonlinear equation governing the flow has a class of exact time-dependent solutions. In this class the evolution of the vertical temperature profile is determined by the Burgers equation, while the horizontal profile is determined by the Liouville equation. Both these equations can be solved analytically.

I. INTRODUCTION

Isolated circular vortices with a life-time up to several years are very common in the oceans. In this work we study the slow convective meridional flow driven by viscosity and diffusion in a warm-core baroclinic vortex.

The most important parameter determining the character of the meridional circulation is the Prandtl number, $Pr = v/\kappa$, where v is the viscosity and κ the thermal diffusivity. In water $Pr \approx 6$. (The corresponding Schmidt number $Sc = v/\kappa_c$, where κ_c is the salt diffusivity, is about 5000 in the ocean.) However, in a realistic model one should use the effective turbulent transport coefficients, which are not very well-defined, but certainly much larger than the laminar values. The correct value of Pr is then not known.

The previous study most closely related to the present work is the one by Flierl & Mied (1985). They performed analytic calculations and numerical simulations of the meridional circulation and gradual decay of a warm core ring, using both large and small Prandtl number ($Pr = 10$ and 0.1, respectively). In the analytic calculations they used a simplified linear model, i.e. the stratification of the density anomaly in the vortex was assumed to be much weaker than the background stratification, so that the advection of the perturbed temperature field could be neglected, while the advection of the background field was included. The found that the direction of the meridional circulation depends on whether Pr is larger or smaller than unity.

In their numerical simulations Flierl & Mied used fully nonlinear balance equations, and the nonlinearity (i.e. the ratio between the stratification of the density anomaly in the vortex and the background stratification) was of the order 10^2. This may be unrealistically large, but the nonlinearity in real vortices can clearly exceed unity (Monin & Fedorov, 1983). The simulations confirmed that the direction of the meridional circulation depends on the Prandtl number. They also showed that the vortex decays much faster if $Pr = 0.1$ than if $Pr = 10$, which can not be explained from the linear model.

These results indicate that a particularly interesting case is when both the nonlinearity and the

Prandtl number are large. The meridional circulation is then inward and upward in the vortex core, hence the advection opposes the diffusion, prolonging the life-time of the vortex. In the present work we will derive some analytic results for this regime. Assuming the Rossby number Ro to be small and Pr $>>$ 1, the dynamics can be described by a relatively simple nonlinear equation earlier obtained by Giil (1981) and Garrett (1982). We find that this equation has a class of nonstationary exact solutions. In this class the vertical dynamics is determined by Burger's equation, which is integrable. The horizontal temperature profile is independent of time and depth, and determined by the Liouville equation, which can also be solved exactly. The solution can have the form of an isolated vortex with no background stratification, which corresponds to a large nonlinearity, as in the numerical simulations by Flierl & Mied.

II. DERIVATION OF THE DYNAMIC EQUATION

We start the considerations from the three-dimensional Boussinesque equations. Using the shallow-water approximation we replace the vertical component of the equation of motion by the hydrostatic approximation:

$$\frac{dp}{dz} = g\rho_0 \alpha T, \tag{1}$$

where p and T are the pressure and temperature deviations from a basic state assumed to have constant temperature and density, and α is the volume expansion coefficient defined by $\rho = \rho_0(1 - \alpha T)$, where ρ is the total density. We assume that the Rossby number is small, and the flow circularly symmetric. Substituting the horizontal component of the equation of motion into the incompressibility condition, we obtain

$$\frac{\partial w}{\partial z} = \frac{1}{\rho_0 f^2} \frac{\partial}{\partial t} \nabla^2 p - \frac{v}{\rho_0 f^2} \frac{\partial^2}{\partial z^2} \nabla^2 p, \tag{2}$$

where w is the vertical velocity, f is the Coriolis parameter, and the Laplacian here and below only contains horizontal derivatives, i.e. $\nabla^2 = r^{-1}\partial/\partial r + \partial^2/\partial r^2$. The ageostrophic terms in the divergence of the horizontal velocity on the right-hand side of eq. (2) are caused by inertia and vertical viscosity, respectively. (The horizontal viscosity is neglected since the vertical length scale is much smaller than the horizontal one.) The same ageostrophic terms also appear in the heat equation:

$$\frac{\partial T}{\partial t} + w\frac{\partial T}{\partial z} + \left(\frac{v}{\rho_0 f^2}\frac{\partial^3 p}{\partial z^2 \partial r} - \frac{1}{\rho_0 f^2}\frac{\partial^2 p}{\partial t \partial r}\right)\frac{\partial T}{\partial r} = \kappa\frac{\partial^2 T}{\partial z^2}. \tag{3}$$

These equations must be supplemented by appropriate boundary conditions. Taking the lower boundary of the domain to lie just above the Ekman layer on the bottom, we obtain

$$w = w_E = \frac{h_E}{2\rho_0 f}\nabla^2 p \quad \text{at} \quad z = -H_0, \tag{4}$$

where $h_E = (2v/f)^{1/2}$ is the thickness of the Ekman layer. The surface is regarded as rigid, so that

the barotropic Rossby radius is infinite, which is a good approximation in the cases of interest. However, we can not use a no-slip condition as at the bottom. Instead, the appropriate condition at a free surface of a viscous fluid is that the normal derivative of the tangential velocity vanishes. If there is a horizontal temperature gradient this condition is violated by the thermal wind relation (i.e. by the geostrophic velocity), which is obtained by differentiating eq. (1) with respect to r. A viscous boundary layer is therefore formed. The flow in this layer can be obtained by the same method as in the usual Ekman layer (cf. Aristov & Nycander, 1994, for details). It is found that the appropriate boundary condition is

$$w = -\frac{g\alpha h_E^2}{2f} \nabla^2 T = -\frac{h_E^2}{2\rho_0 f} \nabla^2 \frac{\partial p}{\partial z} \quad \text{at} \quad z = 0, \tag{5}$$

where $z = 0$ is just below the boundary layer. This condition was also used by Flierl & Mied (1985).

The temperature changes very little across the boundary layer at the surface, hence if the temperature is held fixed at the surface, the same condition applies at the boundary of the domain, just below the boundary layer. (This is not true for the heat flux: there is a jump condition for the vertical temperature gradient across the boundary layer.)

Equations (1)-(5) describe two kinds of processes with different time scales. The first one is spin-down of the barotropic component, and the second one is baroclinic diffusion and advection, which is the main subject of the present work. The main assumption we make in order to separate these processes and derive a simplified equation is $\text{Pr} \gg 1$.

The typical time scale of barotropic spin-down is $\tau_E \sim 2H_0/(fh_E)$, while the time scale for baroclinic diffusion and advection obtained from eq. (3) is $\tau_\kappa \sim 2H^2\text{Pr}/(fh_E^2)$, where H is the vertical scale of the baroclinic vortex (which may be much smaller than the total depth H_0). We find $\tau_\kappa/\tau_E \sim H^2\text{Pr}/(h_E H_0)$, so that unless the vortex is very shallow (i.e. H/H_0 very small), spin-down is much faster than the diffusive processes. This means that the pressure perturbation decreases approximately uniformly at all depths during spin-down, until it is zero at the bottom and the Ekman pumping ceases. We can then consider the baroclinic component in isolation.

The next step is to estimate the bottom pressure generated by the baroclinic circulation. It may be found that this is much smaller than the direct pressure perturbation obtained from eq. (1), and also that the vertical velocity from the Ekman pumping caused by this bottom pressure can be neglected, provided that $\text{Pr} \gg 1$ (Aristov & Nycander, 1994). Thus, we may set $p = 0$ at $z = -H_0$. Finally, the two terms on the right-hand side of eq. (2) are compared, using the time scale τ_E. It is found that the viscous term dominates if $\text{Pr} \gg 1$. Equation (2) can then be integrated, using eq. (1), which gives

$$w = -\frac{g\alpha v}{f^2} \nabla^2 T. \tag{6}$$

This result is then substituted into eq. (3). In that equation we may neglect the term $\partial^2 p/\partial t \partial r$, since it is one order smaller than the first term in the Rossby number. The result is

$$\frac{\partial T}{\partial t} = -\frac{vg\alpha}{f^2}\left[\frac{\partial^2 T}{\partial z \partial r}\frac{\partial T}{\partial r} - \frac{1}{r}\frac{\partial}{\partial r}\left(r\frac{\partial T}{\partial r}\right)\frac{\partial T}{\partial z}\right] + \kappa\frac{\partial^2 T}{\partial z^2}. \tag{7}$$

which is our final dynamic equation. In the planar case (for a straight front) it has earlier been obtained by Gill (1981) and Garrett (1982). The first and second terms on the right-hand side describe the temperature change caused by horizontal and vertical advection, respectively. Assuming these terms to be of the same order as the diffusion term (the last term), we obtain the estimate $Ro \sim Pr^{-1}$, confirming the consistency of the approximations.

We finally summarize the scaling region in which eq. (7) is valid: $Ro \sim Pr^{-1} \ll 1$, $\partial/\partial t \sim \kappa/H^2$ and $Ek \ll 1$, where $Ek \sim v/fH^2$. The ratio between Ro and Ek is arbitrary.

III. EXACT SOLUTIONS

We will now find a class of exact solutions to eq. (7) by separation of variables:

$$T = \Theta(r) F(t,z). \tag{8}$$

Substituting (8) into (7), and setting the separations constant equal to r_0^{-2}, where r_0 is an arbitrary length that will be chosen as the vortex radius, we obtain

$$\frac{\partial F}{\partial t} + \frac{vg\alpha}{r_0^2 f^2} F \frac{\partial F}{\partial z} = \kappa \frac{\partial^2 F}{\partial z^2}, \tag{9}$$

$$\left(\frac{\partial \Theta}{\partial r}\right)^2 = \Theta\left(\frac{1}{r_0^2} + \frac{1}{r}\frac{\partial}{\partial r} r \frac{\partial \Theta}{\partial r}\right) \tag{10}$$

Equation (9) is Burger's equation, which is known to be integrable. Equation (10) can be transformed to the onedimensional Liouville equation (Aristov & Nycander, 1994), which can also be integrated. We will here use the solution

$$\Theta = \frac{1}{8}\left[1 - \left(\frac{r}{r_0}\right)^2\right]^2, \quad r < r_0,$$

$$\Theta = 0, \quad r > r_0, \tag{11}$$

cf. Fig. 1. The solution is continuous up to the first derivative, while the second derivative is discontinuous at r_0. This means that the heat flux and the radial velocity are continuous, while the vertical velocity is discontinuous, according to eq. (6). This is permissible since we have neglected the horizontal viscosity. In reality it will presumably lead to the formation of a boundary layer whose width is of the same magnitude as the height H of the vortex, and much smaller than the horizontal scale.

For a baroclinic vortex with the horizontal temperature profile given by eq. (11), the vertical evolution is determined by Burger's equation. Qualitatively, a solution of this equation sharpens its profile at places where $\partial F/\partial z$ is negative, until a chock wave appears that propagates steadily upward. However, $\partial F/\partial z < 0$ means that the fluid is unstably stratified, since Θ is positive, and such a flow will therefore be quickly disrupted by Rayleigh-Taylor type instabilities. Physically realizable flows must have $\partial F/\partial z > 0$ everywhere, and the vertical profile will then in general tend to become smoother.

Burger's equation can be solved by introducing the function $\phi = \exp(-p'/2)$, where p' is defined by $\partial p'/\partial z = (v\alpha g/\kappa f^2)F$. We assume that $p' \to 0$ as $z \to -\infty$. Using this substitution, eq. (9) is transformed to the linear diffusion equation,

$$\frac{\partial\phi}{\partial t} = \kappa\frac{\partial^2\phi}{\partial z^2},$$
(12)

which can be solved by standard methods. For illustration, we have done this with the initial condition $F(z) = 0$ at $t = 0$, and the boundary condition $F = F_0$ at $z = 0$. The corresponding conditions for ϕ are $\phi(z) = 1$ at $t = 0$, and $\partial\phi/\partial z + C\phi = 0$ at $z = 0$, where

$$C = v g \alpha F_0/(2\kappa\tau_0^2 f^2).$$
(13)

Solving eq. (12) by Fourier transformation, we obtain after some calculations

$$F = F_0\left[1 - \frac{\mathrm{erf}\left(\frac{z}{2\sqrt{\kappa t}}\right)\exp\left(Cz - C^2\kappa t\right)}{1 + \mathrm{erf}\left(\frac{z - 2C\kappa t}{2\sqrt{\kappa t}}\right)}\right]^{-1},$$
(14)

where erf is the error function. This solution describes how a vortex is excited by heating the surface. Its behaviour in various asymptotic regimes can easily be understood. There is a characteristic time $t_c = 1/(\kappa C^2)$, and for $t \ll t_c$ the solution is approximately

$$F = F_0\left[1 + \mathrm{erf}\left(\frac{z}{2\sqrt{\kappa t}}\right)\right].$$
(15)

This is the solution of the linearized version of eq. (9), with the same boundary and initial conditions. Thus, before t_c the meridional circulation is still too weak to affect the development, and the heat is simply diffusing downward.

For $t \gg t_c$ the heat advection is very important. There are then two different asymptotic depth regions. At $z \gg -(\kappa t)^{1/2}$ (i.e. small depth), we obtain

$$F \cong \frac{F_0}{1 - Cz}.$$
(16)

Thus, the upper part of the vortex is stationary, and heat advection and diffusion almost exactly balance. At $z \ll -(\kappa t)^{1/2}$ we obtain, using the asymptotic expansion of the error function,

$$F \cong \frac{2F_0}{2C\kappa t - z}\left(\frac{\kappa t}{\pi}\right)^{1/2}\exp\left(-\frac{z^2}{4\kappa t}\right).$$
(17)

This represents a diffusive front, where advection is not yet important.

In Fig. 2 we have plotted the solution (14), both before and after t_c. We also show the linear, purely diffusive solution (15) and the stationary solution (16). The general development is that the full solution (14) follows the linear solution until this crosses the stationary curve. After that (14) is approximately equal to the smallest of the linear and the stationary solutions, and everywhere smaller than both.

The pressure perturbation at the surface increases logarithmically with the depth of the stationary region, as can be seen by integrating eq. (16). Thus, in the initial stage of the solution (14), before t_c, the pressure increases as $\sqrt{t}$. After t_c it grows more slowly, as $\log(t)$, but without bound (unless the depth of the ocean is finite). At some time the azimuthal velocity and the Rossby number therefore become too large for the model to be valid. The reason for this is of course that the surface is heated in this problem. If there is no heat flux into the vortex, the surface pressure can only decrease.

The meridional flow and the isotherms in the baroclinic vortices studied here are shown qualitatively in Fig. 3. Notice that the radial velocity is inward (toward the centre of the vortex) everywhere in the interior of the fluid. This is compensated by an outward flow in the boundary layer near the surface, where the velocity is larger than the interior ageostrophic velocity by the factor H/h_E. (On the other hand, it is smaller than the azimuthal geostrophic velocity by the same factor.)

IV. DISCUSSION

In this paper we have studied dissipational processes and the induced meridional flow in circular baroclinic vortices. This is one of the main candidates for an explanation of their gradual decay. (The other one is radiation of Rossby waves.) These processes also determine the evolution of the three-dimensional structure of the vortices, e.g. the profile of the thermocline and the relative importance of the barotropic and baroclinic modes.

The main simplifying assumption of our analysis was that the Prandtl number is large. It was found that unless the vortex is extremely shallow, the spin-down of the barotropic component is then much faster than the diffusion time for the baroclinic mode, and that the bottom pressure excited by the baroclinic mode has a negligible effect on the meridional circulation. Thus, the diffusive processes drive the vertical structure toward compensation, with negligible flow below the thermocline.

The meridional flow in the vortex core is upward and inward, so that the advection opposes the diffusion. If the nonlinearity (i.e. the ratio between the stratification of the density anomaly in the vortex and the background stratification) and the Prandtl number are both large, this can result in a substantially longer life-time of the vortex, as seen in the simulations by Flierl & Mied (1985). We here particularly studied this regime, and found that in the limiting case (with zero background stratification) there exists a class of exact, nonlinear time-dependent solutions. The horizontal profile of the vortex is then given by eq. (11), while the evolution of the vertical profile is determined by Burger's equation, eq. (9), which is integrable. We have also shown an explicit example of such an exact, time-dependent solution.

Although the simplifying assumptions are perhaps not entirely realistic, this result should serve as a valuable reference point for future modelling. It also has intrinsic interest, being perhaps the first case where the profile of the thermocline can be determined analytically and self-consistently in a nonlinear convection problem.

ACKNOWLEDGEMENT

REFERENCES

Aristov, S.N. & Nycander, J., 1994. Convective flow in baroclinic vortices. J. Phys. Oceanogr., in press.

Flierl, G.R. & Mied, R.P., 1985. Frictionally induced circulations and spin down of a warm-core ring. J. Geophys. Res. **90**, 8917-8927.

Garrett, C., 1982. On spindown in the ocean interior. J. Phys. Oceanogr. **12**, 989-993.

Gill, A.E., 1981. Homogeneous intrusions in a rotating stratified fluid. J. Fluid Mech. **103**, 275-295.

Monin, A.S. & Fedorov, K.N., 1983. Poloidal circulation in rings. Dokl. Akad. Nauk SSSR **270**, 1213-1216.
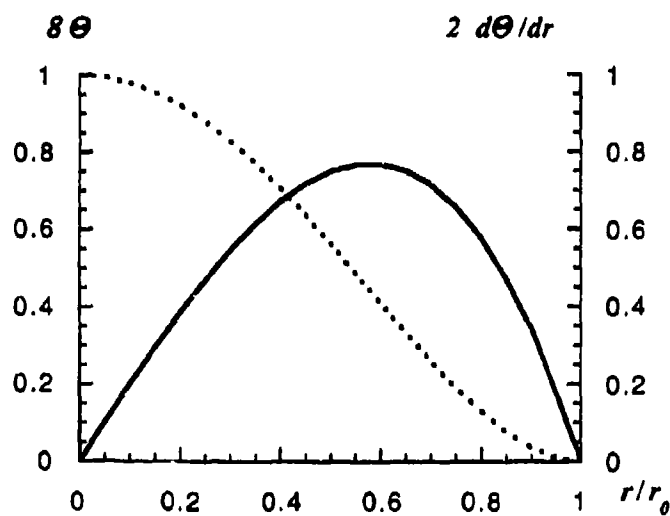
Fig. 1

Radial profile of the temperature and the azimuthal velocity, from eq. (11). $\Theta(r)$ (dotted) is proportional to the temperature, and $\Theta'(r)$ (solid) to the velocity. r_0 is the vortex radius.
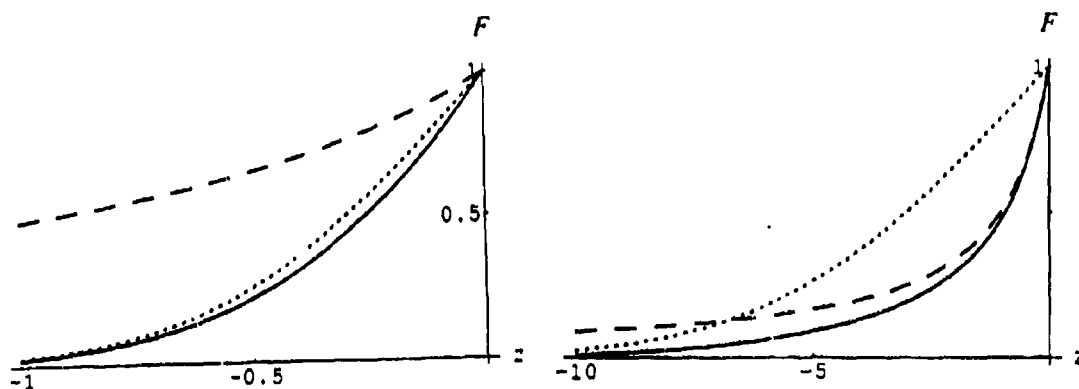
Fig. 2
Plot of the exact solution (14) (solid curve). We also show the linear, purely diffusive solution (15) (dotted) and the stationary solution (16) (dashed). The values used are $C = F_0 = \kappa = 1$, which gives $t_c = 1$.
a) $t = 0.1\, t_c$
b) $t = 10\, t_c$
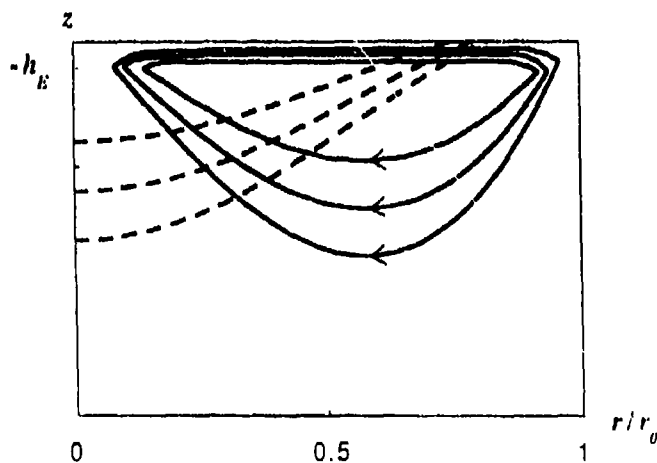
Fig. 3
Qualitative structure of the vortex. h_E is the thickness of the Ekman layer at the surface and H the vortex depth (i.e. the depth of the thermocline). Solid curves are streamlines of the meridional flow and dashed curves isotherms.

Dynamics of internal solitary waves in a rotating fluid

O.A.Gilman

Department of Applied Mathematics

Nizhny Novgorod State Technical University

24 Minin Str., Nizhny Novgorod, Russia

R.Grimshaw

Department of Mathematics, Monash University

Clayton, Victoria 3168, Melbourne, Australia

Yu.A.Stepanyants

Institute of Applied Physics, Russian Academy of Science

46 Uljanov Str., 603600 Nizhny Novgorod, Russia

1. In investigations of long internal and surface waves in the ocean with characteristic scales of the order of tens of kilometers one needs to take into consideration the effect of Earth's rotation. Such wave processes may be described in the shallow water approximation because an average depth of the ocean h is 4 to 5 km. If the perturbation amplitude is not too high, as is usually the case, then such waves may be described, as was first shown in [1], by a generalized Korteweg–de Vries (KdV) equation that is also often referred to as the Ostrovsky equation

$$(u_t + C_0 u_x + \alpha u u_x + \beta u_{xxx})_x = f^2 u / 2C_0, \qquad (1)$$

where the parameters for surface waves are: $C_0 = \sqrt{gh}$, h is the total depth of the basin, $\alpha = 3C_0/2h$, $\beta = C_0 h^2/6$, and f is the Coriolis parameter, $u(x,t)$ being the perturbation of free surface. (The expressions for internal wave coefficients can be found, for example, in [1].)

Equation (1) and its generalizations to the case of deep ocean as well as to two-dimensional perturbations were considered in [2, 3]. The basic properties of solutions to (1) are surveyed in [4]. It should be noted that, as shown in [2, 5], eq. (1) has no solitary stationary solutions with zero asymptotic forms at the infinity for negative-dispersion waves, for example, surface gravity and internal waves in the ocean. Besides, no periodic analytical solutions have been found

yet. Some numerical solutions were constructed in [4]. These include a family of solutions which can be interpreted as a periodic sequence of pulses (whose form resembles KdV solitons) between which the wave has a parabolic profile.

In this paper we show that solutions of this type may be constructed by means of an approximate asymptotic procedure that is valid for both negative and positive dispersion waves. The constructed solutions are verified by numerical computation of their evolution within the frames of eq. (1). The conditions of the existence of stable and unstable stationary periodic solutions are also revealed.

In conclusion we analyse some typical features of nonstationary dynamics of spatially periodic perturbations with solitary pulses.

2. We now consider stationary solutions of the Ostrovsky equation mentioned above. It is convenient to rewrite it in dimensionless form

$$\left(u_t + 3uu_x - \frac{\beta}{4}u_{xxx}\right)_x = \frac{\varepsilon^2}{2}u, \tag{2}$$

where $\beta = \pm 1$ is the dimensionless parameter determining the type of disperison ($\beta = -1$ for negative-dispersion surface and internal waves in the ocean and $\beta = 1$ for positive-dispersion capillary waves on the surface of a liquid or for oblique magneto-acoustic waves in a plasma) and ε is the dimensionless parameter which is assumed to be small. Under the restriction of stationary progressive waves we put $u(x,t) = u(x-ct)$ where c is the now unknown wave velocity. For this class of solutions, we obtain instead of (1) a nonlinear ordinary differential equation

$$\left(-cu + \frac{3}{2}u^2 - \frac{\beta}{4}u''\right)'' = \frac{\varepsilon^2}{2}u, \tag{3}$$

where the prime denotes differentiation with respect to the "travelling coordinate" $\xi = x - ct$.

Let us represent the internal solution of this equation as an asymptotic series expansion

$$u(\xi) = u_0(\xi) + \varepsilon^2 u_1(\xi) + \ldots$$
$$c = c_0 + \varepsilon^2 c_1 + \ldots \tag{4}$$

This solution transforms, at $\varepsilon = 0$, to the exact solution of a KdV equation that follows from (2) with a zero right-hand side. We take as a "zero approximation" the soliton solution of a KdV equation:

$$u_0(\xi) = -\beta\gamma^2 \mathrm{sech}^2\gamma\xi + d$$
$$c_0 = -\beta\gamma^2 + 3d \tag{5}$$

The substitution of the series expansion (4) into eq. (3) yields an equation to the first approximation in leading order with respect to ε:

$$\left(\beta\gamma^2 u_1 + 3u_0 u_1 - \frac{\beta}{4}u_1''\right)'' = \frac{1}{2}u_0 + c_1 u_0'' \tag{6}$$

2

By integrating this expression twice we obtain

$$\beta\gamma^2 u_1 + 3u_0 u_1 - \frac{\beta}{4}u_1'' =$$

$$= -c_1\beta\gamma^2\mathrm{sech}^2\gamma\xi + A\xi + B_1 + \frac{d}{4}\xi^2 - \frac{\beta}{2}\ln(\cosh\gamma\xi). \tag{7}$$

where A and B_1 are integration constants. This equation is simplified far from the soliton crest for sufficiently large ξ thanks to the fact that the function $\mathrm{sech}\gamma\xi$ is rapidly vanishing to zero. As a result we obtain a simple second-order linear equation with a polynomial right-hand side:

$$\frac{\beta}{4}u_1'' - \beta\gamma^2 u_1 = -\frac{d}{4}\xi^2 + \frac{\beta\gamma}{2}\xi - A\xi - B. \tag{8}$$

where B is a new integration constant. A forced solution of this equation is readily written in the form

$$u_1(\xi) = \frac{d\xi^2}{4\beta\gamma^2} - \frac{\xi}{\gamma^2}\left(\frac{\gamma}{2} - \frac{A}{\beta}\right) + \frac{1}{\beta\gamma^2}\left(\frac{d}{8\gamma^2} + B\right) \tag{9}$$

Thus, with the "zero approximation" far from the soliton crest taken into account, we can write the sought solution to an accuracy of ε^2:

$$u \approx d + \varepsilon^2\left[\frac{d\xi^2}{4\beta\gamma^2} - \frac{\xi}{\gamma^2}\left(\frac{\gamma}{2} - \frac{A}{\beta}\right) + \frac{1}{\beta\gamma^2}\left(\frac{d}{8\gamma^2} + B\right)\right] \tag{10}$$

We now consider an external solution of eq. (3) which is sought in the form

$$u = \alpha(\xi - \xi_0)^2 + \delta \tag{11}$$

The substitution of this expression into eq. (3) verifies that it is its exact solution for $\alpha = \varepsilon^2/36$ and $\delta = -c/6$, ξ_0 being an arbitrary parameter associated with the choice of the coordinate origin.

Consider a periodic sequence of arcs of parabolas described by (11) with the values found for α and δ and period λ. The "amplitude" a, i.e., the distance between the trough and the crest of the wave, is expressed through wavelength: $a = (\varepsilon^2\lambda^2)/144$. By choosing the reference point along the ξ-axis at one of the crests, we can also express ξ_0 through λ: $\xi_0 = \lambda/2$.

Thus we obtain a remarkable result: The approximate solution (4) of eq. (3) constructed to an accuracy of ε^2 far from the soliton crest is a wave with a parabolic profile (10). At the same time, a wave having such a profile is an exact solution of eq. (3). In other words, the approximate solution (4) transforms, at large ξ, from the asymptotic form to the exact solution (11) if the free parameters

3

contained in (10) are determined correctly. By equating the expressions (10) and (11) to the known values of α and δ we find

$$d = \frac{\beta\gamma^2}{9}; \quad c_0 = -\frac{2}{3}\beta\gamma^2;$$

$$A = \frac{\beta\gamma^2}{2}\left(\frac{1}{\gamma} - \frac{\lambda}{18}\right); \quad B = \frac{\beta}{6}\left(\frac{\gamma^2\lambda^2}{24} - \frac{1}{12} - \gamma^2 c_1\right)$$

Then, the approximate equation (3), to an accuracy of ε^2, has the form

$$u(\xi) = -\beta\gamma^2\text{sech}^2\gamma\xi + \frac{\beta\gamma^2}{9} + \frac{\varepsilon^2}{36}\left[\left(\xi - \frac{\lambda}{2}\right)^2 - 6c_1\right] \qquad (12)$$

and the wave velocity is expressed by

$$c = -\frac{2}{3}\beta\gamma^2 + \varepsilon^2 c_1 \qquad (13)$$

At this stage, the solution (12)–(13) contains three free parameters: γ, λ and c_1. It is necessary, however, to take into consideration the restrictions following from eq. (2) for periodic solutions:

$$\int_0^\lambda u(x, t)dx = 0 \qquad (14)$$

The substitution of (12) yields

$$c_1 = \frac{\lambda^2}{72} + \frac{2\beta\gamma^2}{3\varepsilon^2}\left(1 - \frac{18}{\gamma\lambda}\right) \qquad (15)$$

(we proceeded from the fact that the wavelength λ is much greater than the characteristic size of the soliton $1/\gamma$ so that $\tanh(\gamma\lambda/2) \approx 1$). Then, finally, the wave profile and velocity are given by the formulas

$$u(\xi) = -\beta\gamma^2\text{sech}^2\gamma\xi + 2\beta\frac{\gamma}{\lambda} + \frac{\varepsilon^2}{36}\left[\left(\xi - \frac{\lambda}{2}\right)^2 - \frac{\lambda^2}{12}\right] \qquad (16)$$

$$c = -12\beta\frac{\gamma}{\lambda} + \varepsilon^2\frac{\lambda^2}{72}$$

Thus, the constructed solution contains two independent parameters γ and λ that are related only by the condition $\gamma\lambda \gg 1$. However, if we demand that the condition (14) should be fulfilled in the zero-th order with respect to ε then these two parameters will be related by $\gamma\lambda = 18$, which gives to a good accuracy $\tanh(\gamma\lambda/2) \approx 1$.

4

3. Our results show that the constructed solutions are described by even functions that are symmetric both with respect to the soliton crests and to parabola troughs. The latter circumstance enables us to suppose that there exist more complicated stationary solutions with solitons both at the wave crests and troughs. In constructing such an approximate solution we proceed from the formulas (12) and (13) which describe a periodic sequence of arcs of parabolas (exact solutions to (3)) and of solitons at their crests. The fields of the nearest solitons are infinitesimal near parabola troughs and may be neglected. Consequently, a local solution is sought near parabola troughs in the form (12), again, but for other values of γ:

$$u(\xi) = -\beta\gamma_1^2 \operatorname{sech}^2 \gamma_1 \left(\xi - \frac{\lambda}{2} \right) + \frac{\beta\gamma^2}{9} + \frac{\varepsilon^2}{36} \left[\left(\xi - \frac{\lambda}{2} \right)^2 - 6c_1 \right] \qquad (17)$$

The soliton velocity determined by the parameter γ_1 and the local displacement d_1 at the point $\xi = \lambda/2$ must then coincide (the stationarity condition) with (13) that was found earlier. As a result we have

$$c \equiv -\beta\gamma_1^2 + 3d_1 = -\beta\gamma_1^2 + \frac{\beta\gamma^2}{3} - \varepsilon^2 \frac{c_1}{2} = \frac{2}{3}\beta\gamma^2 + \varepsilon^2 c_1$$

¿From this we find the relationship between γ_1 and γ:

$$\gamma_1^2 = \gamma^2 - \frac{3}{2}\varepsilon^2 \frac{c_1}{\beta} \qquad (18)$$

We now again regard the restriction (14) that follows from the properties of eq. (2). Taking into consideration that the complete solution contains two solitons of different amplitudes on a period, from (14) we find

$$-2\beta\gamma - 2\beta\gamma_1 + \left[\frac{\beta\gamma^2}{9} + \frac{\varepsilon^2}{36} \left(\frac{\lambda^2}{4} - 6c_1 \right) \right] \lambda - \frac{\varepsilon^2 \lambda^2}{216} = 0$$

In the zero approximation with respect to ε, from this follows

$$\lambda = 18(\gamma + \gamma_1)/\gamma^2 \qquad (19)$$

And, in the next order with respect to ε, we find $c_1 = \lambda^2/72$.

Removing, by means of the found expression, c_1 from (18) and combining the latter with (19) we get a system of two equations for three parameters γ, γ_1 and λ. Supposing one of them, for instance λ, to be independent we express through it two other parameters (to an accuracy of ε^2 including):

$$\gamma \approx \frac{36}{\lambda} \left(1 - \frac{2\varepsilon^2 \lambda^4}{\beta 12^5} \right), \quad \gamma_1 \approx \frac{36}{\lambda} \left(1 - \frac{4\varepsilon^2 \lambda^4}{\beta 12^5} \right) \qquad (20)$$

5

4. For verification of the constructed asymptotic theory we performed direct numerical computations of the evolution of the found approximate solutions within the frames of the basic Ostrovsky equation (2). For this purpose we elaborated a Turbo Pascal program. Conservation of the total energy of perturbations defined as

$$E = \frac{1}{2} \int_0^\lambda u^2(x,t)dx, \tag{21}$$

where λ is the wave period, was checked in the course of calculations. Directly from (2) follows that the quantity E is the integral of motion; it was conserved in our calculations to an accuracy of about 10^{-4}.

Our calculations confirm that the solutions described by the formula (16) for $\beta = -1$ and arbitrary ε (up to rather high values, for example, 0.7) are stable in the course of calculations and are in a good agreement with analytical theory. They remained stationary to a high accuracy in calculations for longer than twenty periods and no tendency to destruction was observed. However, the velocity of wave propagation slightly differed from the theoretical values.

The calculations indicate that the shape of the wave, evidently, depends weakly on the value of the parameter ε, while the wave velocity is a more sensitive quantity which is determined the more precisely, the smaller this parameter.

The approximate solutions evolved differently for $\beta = 1$ and sufficiently large ε (greater than ~ 0.3). In this case, the initial perturbations did not remain stationary, instead, they were destroyed in the course of calculations demonstrating a complicated dynamics. This fact may, evidently, be treated as the instability of stationary solutions of interest with respect to small perturbations at $\beta = 1$. (The constructed approximate solutions may, obviously, be regarded as some perturbed exact stationary solutions.) It is also confirmed by the fact that the time of destruction of initial perturbations increased with decreasing ε.

A similar picture of destruction of initial perturbations was observed for the solutions with two pulses on a period described by the formulas (17) and (20). The solutions proved to be unstable for any sign of β and for arbitrary ε.

As has been mentioned, eq. (2) describes, in particular, surface and internal waves in a rotating ocean with the dispersion such that $\beta = -1$ corresponds to them in dimensional variables. Thus, the solutions which were found as stable ones actually refer to this type of waves.

5. Besides the stationary solutions considered above we also investigated spatially periodic perturbations with nonstationary pulses on each period. In spite of the "anti-soliton" restriction [2,5], we found that soliton-type quasi-stationary solitary waves may exist within the frames of eq. (2) with periodic boundary conditions. We revealed at least two different regimes of dynamics of solitary waves. The first of them is slow interaction of a KdV soliton with a very long

quasi-sinusoidal wave of a relatively small amplitude. The soliton moves a little faster than the sinusoid due to the nonlinear correction to its velocity and passes consecutively through its crests and troughs. The soliton's amplitude increases as it is drifting from the crest to the trough of the sinusoid and decreases in motion from the trough to the crest. This regime is described adequately by an approximate adiabatic theory of the interaction of a KdV soliton with a smooth external disturbance.

The other regime is dynamics of an initial KdV soliton at periodic boundary conditions under the action of the right-hand side of eq. (2). If the right-hand side of the equation is sufficiently small and the period is much greater than the characteristic size of the soliton, then the soliton amplitude decreases in the evolution, and a long trail having the polarity opposite to that of the soliton is formed behind it. The original soliton eventually disappears and a new one, whose parameters are almost identical to the parameters of the original soliton, is born at one of the trail slopes. Still further, this process is repeated periodically so that a phenomenon that greatly resembles recurrency in the KdV model [6] and in other related systems [7] is observed.

Thus, long-lived solitary patterns interacting with periodic perturbations may exist in the real ocean, with Earth's rotation taken into account. The energy supply in such perturbations may be rather significant compared with the quasi-periodic background. Further investigation of solitary patterns and their modelling in laboratory conditions appear to be of considerable interest.

References

1. L.A.Ostrovsky. "Nonlinear internal waves in a rotating ocean". Oceanology **18**, N 2 (1978) [English translation of the Russian Journal].

2. A.I.Leonov. "The effect of Earth rotation on the propagation of weak non-linear surface and internal long oceanic waves", Annals of the New York Acad. Sci. **373** (1981) 150–159.

3. R.G.Grimshaw. "Evolution equations for weakly nonlinear long internal waves in a rotating fluid". Stud. Appl. Math. **73** (1985) 1–33.

4. L.A.Ostrovsky and Yu.A.Stepanyants. "Nonlinear surface and internal waves in rotating fluids", Nonlinear Waves 3. Proc. of the Gorky School 1989. ed. by A.V.Gaponov–Grekhov, M.I.Rabinovich, & J.Engelbrecht, Springer-Verlag, Berlin Heidelberg, 1990. p.106-128.

5. V.M.Galkin, Yu.A.Stepanyants. "On the existence of stationary solitary waves in a rotating fluid", J. Appl. Maths. Mechs. **55**, N 6 (1991) 939–943 [English translation of the Russian journal].

6. A.C.Scott, F.Y.F.Chu, and D.W.McLaughlin. "The soliton: a new concept in applied science", Proc. **IEEE 61**, N 10 (1973) 1443–1483.

7. H.C.Yuen and B.M.Lake. Nonlinear Dynamics of Deep-Water Gravity Waves, Academic Press. New York, 1982.

Lagrangian dispersion in oceanic mesoscale turbulence

Bach Lien Hua [*]

May 4, 1994

Turbulent dispersion in oceanic mesoscale turbulence is addressed in this paper, specifically its relation with the stratified aspect of the dynamics. It is often observed that stratification induces a substantial variation with depth of the characteristics of the turbulence of the flow. For instance, measurements of either eddy kinetic energy or particle diffusivity in oceanic mesoscale turbulence exhibit large variations with depth (Price, 1983, Owens, 1991). Yet a surprising observation of single-particle dispersion from subsurface floats is that the Lagrangian integral time scale T_L exhibits rather small spatial variations, both in the horizontal and vertical directions (Price, 1983; Rossby et al, 1986). Can these observations be explained dynamically in the framework of stratified geostrophic turbulence which appears to adequately capture many aspects of observed geophysical turbulence (e.g. Hua and Haidvogel,1986; McWilliams, 1989)? This question is the primary focus of the present work.

A key idea is that, because of the steepness of Lagrangian velocity spectra which is associated with the inverse cascade in geostrophic turbulence, T_L is mostly controlled by the variance of lagrangian accelerations $< | \vec{\gamma} |^2 >$, whenever intermittency is not too large. Using familiar ideas of balanced dynamics, we can derive an expression relating $< | \vec{\gamma} |^2 >$ to the variance of gradients of ageostrophic pressure p and divergent velocity field potential χ, which constitute the two modes of dispersion of geostrophic turbulence. Fields of p and χ are statistically orthogonal at a given horizontal level while their depth variations are anticorrelated because of the incompressibility constraint. This is reflected in physical space by spatial patterns of both quantities which have comparable horizontal scales and which are likely to be oriented at right angles with respect to each other at a given level, while their variations with depth tend to compensate. Fig.1 presents fields of p and χ at a given level in direct numerical simulations (DNS) of geostrophic turbulence forced by the baroclinic instability of a mean shear (Hua and McWilliams, 1994). Depth profiles of both modes of dispersion and of eddy kinetic energy from DNS are given in Fig.2, illustrating the compensation tendencies between the two modes of dispersion.

Using an idealized statistical model for the spectrum of geostrophic streamfunction, which is isotropic, stationary, non-intermittent (quasi-normal) and assuming an analytical shape which is consistent with direct numerical simulations of forced/damped geostrophic turbulence, we can relate $< | \vec{\gamma} |^2 >$ and hence T_L to a depth-dependent

[*]Laboratoire de Physique des Oceans,UMR 127 CNRS. IFREMER 29280 Plouzané France

combination of the variances of relative vorticity and stretching vorticity at a given level,

$$T_L \approx [\, a\,\mathcal{S} + b\,Z\,]^{-1/2}, \tag{1}$$

where a and b are depth-dependent constants, $\mathcal{S}$ is the vortex stretching variance and Z is the variance of relative vorticity. This relation illustrates the respective time scales for the horizontal and pseudo-vertical Lagrangian accelerations. It is interesting to note that the two components of potential vorticity contribute to the total dispersion through combination of their respective variances, rather than through potential enstrophy, that is the variance of their sum.

The above expression for T_L does not imply a spatial uniformity of its distribution with depth, nor do we find it in numerical simulations of horizontally homogeneous geostrophic turbulence. Our simulatons reveal that a variety of depth profiles of T_L can be observed which strongly depend upon the way the geostrophic turbulence is forced/damped. However, we have a square root dependence in (1) and since distributions of vorticity and stretching variances tend to be anticorrelated with depth, their combination is much more uniform than either one taken alone. Although the issue of potential vorticity homogenization (Hoskins et al, 1985) is not our main point, in conditions where the large-scale potential vorticity is observerved to be uniform, such as in gyre-scale oceanic observations (Keffer et al, 1982) and in numerical simulations of wind-driven gyres (Barnier et al, 1991), we also have found numerically that the corresponding spatial distribution of T_L also tends to be more uniform both in the horizontal and vertical (Hua, 1994).

The analytical predictions of our statistical model have ben assessed with a reasonable degree of confirmation by numerical quasi-geostrophic turbulent solutions. For instance, Fig.2 also displays the intercomparison between the analytical results and DNS of the depth profiles of the two modes of dispersion, showing an overall agreement between both approaches which confirm the compensating tendencies with depth of the two modes of dispersion. Fig. 3 provides the probability distribution functions (PDF) of the quantity $W = \sigma^2 - \omega^2$, where σ^2 is squared strain and ω^2 is squared relative vorticity (Hua, 1994). The quantity W has been shown by Weiss (1991) to play a central role in turbulent tracer transport and the analytical prediction (continuous curve) captures well the enveloppe behaviour of the PDF observed in the DNS. Both are significantly disctinct from a gaussian distribution (dashed line).

Intermittency seems to present the largest source of discrepancy with our analytical approach, but one can argue that oceanic mesoscale turbulence, which is primarily forced by baroclinic instability in presence of differential rotation (β effect), involve intermittency levels which are significantly less than those usually observed in f-plane turbulent decay (Bartello and Holloway, 1991).

Thus the main result of this work is that for a moderate intermittency of the geostrophic turbulence forced by baroclinic instability, the effective dispersion results from both horizontal turbulent transport and from divergent transport effects due to the stratified nature of the flow. These effects constitute the two modes of dispersion of geostrophic turbulence.

References

Babiano, A., C. Basdevant, P. LeRoy and R. Sadourny, 1987. Single particle dispersion, lagrangian structure function ans lagrangian energy spectrum in two-dimensional turbulence, J. Mar. Research, 45, 107-131.

Barnier B., B.L. Hua and C. Leprovost, 1991. On the catalytic role of high baroclinic modes in eddy-driven large-scale circulations. J. Phys. Oceanog., 21, 976-997.

Bartello P. and G. Holloway, 1991. Passive scalar transport in β—plane turbulence, J. Fluid Mech., 223, 521-536.

Hoskins, B.J., M.E. McIntyre and A.W. Robertson, 1985. On the use and significance of isentropic potential vorticity maps. Quart. J. Roy. Meteor. Soc., 111, 817-946.

Hua B.L. and J.C. McWilliams, 1994. Lagrangian acceleration and dispersion in geostrophic turbulence. (submitted to J. Fluid Mech.)

Hua, B.L., 1994. Skewness of the generalized centrifugal force divergence for a joint normal distribution of strain and vorticity components, Physics of Fluids, A, in press.

Hua, B.L., 1994. The conservation of potential vorticity along lagrangian trajectories in simulations of eddy-driven flows. J. Phys. Oceanog., 24, 498-508.

Keffer, T., P. Rhines and S. McDowell, 1982. North Atlantic potential vorticity and its relation to the general circulation. J. Phys. Oceanog., 12, 1417-1436.

McWilliams, J. C., 1989: Statistical properties of decaying geostrophic turbulence. J. Fluid Mech., 198, 199-230.

Owens, B.W., 1991. A statistical description of the mean circulation and eddy variability in the Northwestern Atlanti using SOFAR floats, Prog. in Oceanography, 28, 257-303.

Price, J.F., 1984. Particle dispersion in the North West Atlantic, Unpublished manuscript.

Rossby, T., J. Price and D. Webb, 1986. The spatial and temporal evolution of a cluster of SOFAR floats in POLYMODE Local Dynamics Experiment (LDE). J. Phys. Oceanog., 16, 428-44

Weiss, J., 1991. The dynamics of enstrophy transfer in two-dimensional hydrodynamics. Physica D, 1991, 48, 273-294.

Captions

Fig.1. Fields of ageostrophic pressure p (a) and divergent potential χ (b) at the top of the water column for an exponential stratification profile. The spectra of their respective gradients correspond to Fig.3b.

Fig. 2. Vertical profiles for a constant stratification profile of (a) kinetic energy $E(z)$; (b)$< |\nabla p|^2 > /E$ (continuous line) and $< |\nabla \chi|^2 > /E$ (dash-dotted line) and their respective quasi-normal estimates (dotted line) and (dash-star line).

Fig.3. Pdf's of the generalized centrifugal force divergence $W = -\nabla^2 p$: (a) as observed in a numerical simulation with small intermittency (continuous line); (b) as given by analytical results (dash-dotted line); (c) for a Gaussian distribution with equal variance (dotted line).
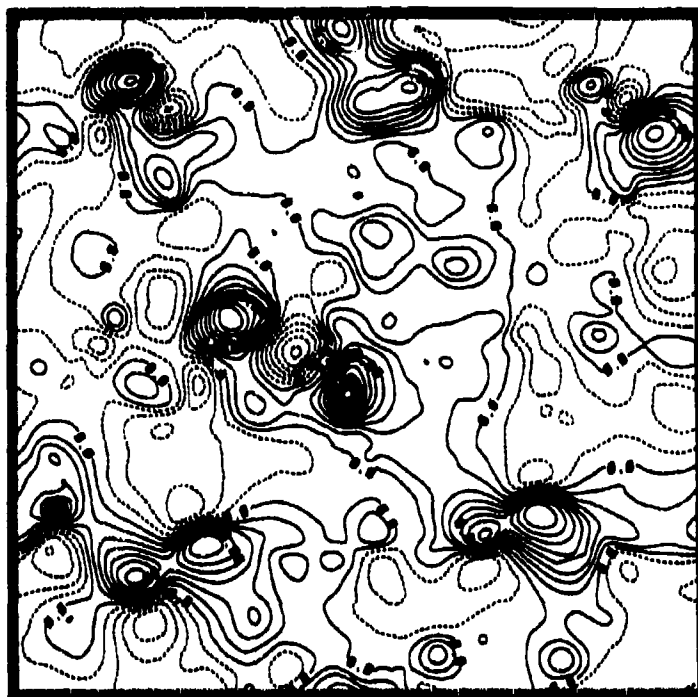
(a)
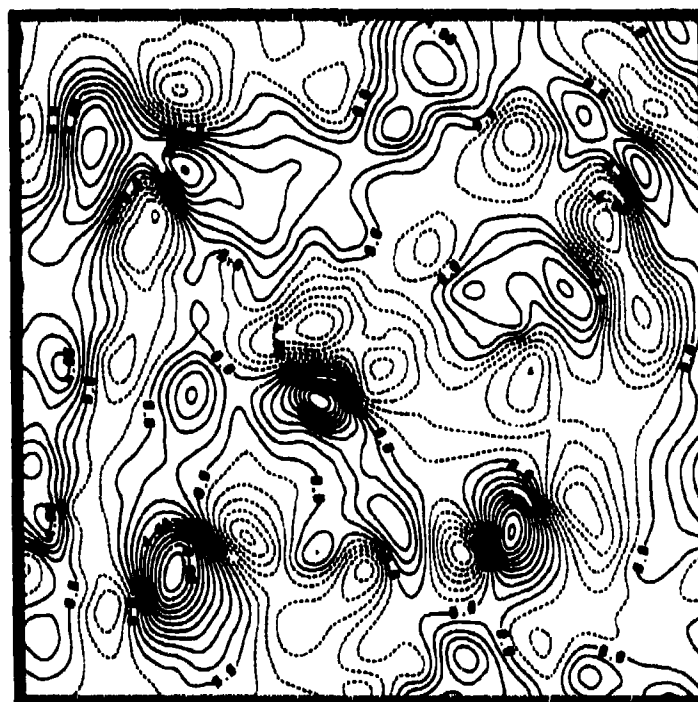
(b)

Fig 1
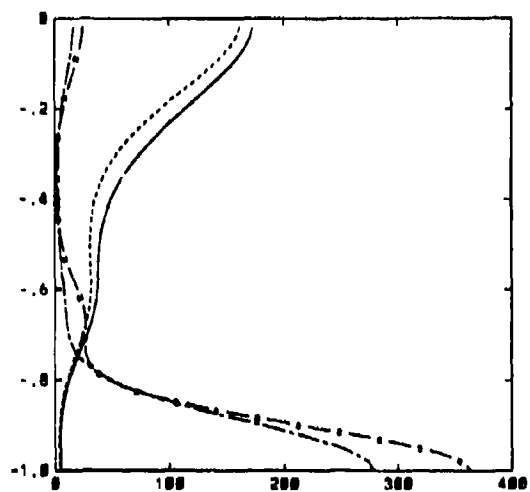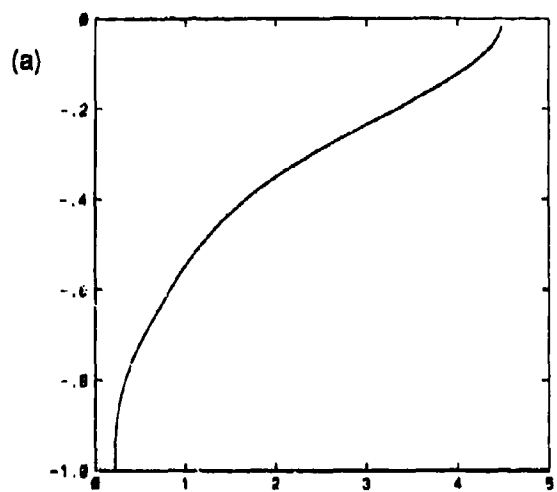
Fig 2
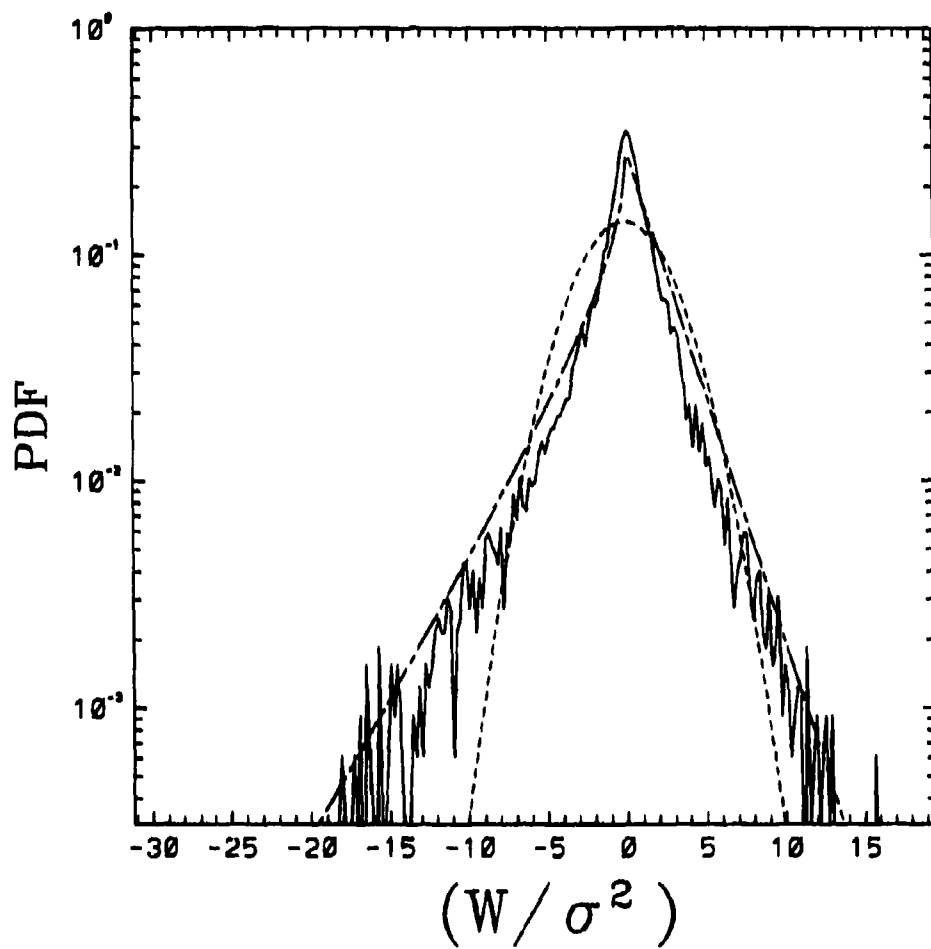
Fig 3

LARGE AMPLITUDE ANOMALIES IN
BAROCLINIC ZONAL FLOWS
By
K. Helfrich and J. Pedlosky

A new manifestation of baroclinic instability is obtained by examining the dynamics of long waves in a baroclinic zonal current when the current is marginally *subcritical* to long waves and when the long waves are the most unstable waves in the spectrum. This can occur when the width of the current is less than the Rossby radius of deformation.

We employ the classic two layer baroclinic model on the β plane in which the basic state is a jet-like shear flow initially limited to the upper layer.

The investigation of the weakly nonlinear formulation of the problem[1] leads to an amplitude evolution equation for the amplitude of a " long" anomaly, A, as a function of development time, T, and long zonal space scale ξ, and when appropriately scaled it becomes

$$\frac{\partial^2 A}{\partial T^2} - \frac{\partial^2 A}{\partial \xi^2} + \frac{\partial^4 A}{\partial \xi^4} + \frac{1}{2}\frac{\partial^2 A^2}{\partial \xi^2} = 0 \qquad (1)$$

The meridional structure of the anomaly is given by the solution of an eigenvalue problem in which the eigenvalue is the phase speed, co, of the propagating anomaly. In particular the eigenvalue is a double root for co which explains the second order in time form of the evolution equation.

Solutions of (1) in the form of solitary waves can be found. We have been able to interpret the solitary wave as a propagating region of enhanced instability. When the amplitude of the solitary wave exceeds a critical value the combined flow (solitary wave plus jet) becomes locally unstable. The instability manifests itself either as a splitting of the solitary wave, emitting two daughter solitary waves, or as an explosive instability which does not equilibrate within the asymptotic theory. This nonlinear instability suggests a subcritical bifurcation of the original flow.

Direct numerical calculations of the full quasi geostrophic equations reveal that the explosive instability is captured by a new state in which a domain of strongly altered zonal flow is embedded within the original basic flow. In the lower layer where the basic flow is weak, this new state contains a latitude band of recirculation with uniform potential vorticity, q_2, see figure 1 and 2. The initial value problem shows that this zone emerges from a narrow layer along the boundary of the jet within the channel domain of the problem. This fluid then fills the zonally limited region of uniform q.

In agreement with our view of the process as a subcritical bifurcation the structure of the new state has been successfully reproduced by finding conjugate solutions of the equation

$$q_n = Q(\psi_n), \qquad\qquad n=1,2 \quad (2)$$

The functional forms for Q_n are taken to be the original potential vorticity/streamfunction relations except in a domain in y, determined by the calculation, in which q_2 is uniform for $y > y_o$. The solutions agree well with the results of our complete numerical calculations.

These conjugate solutions representing the locally altered zonal state appear to be attractors in the sense that any locally supercritical perturbation, not only the solitary wave, will produce the final local flow described by (2).

We suggest that these large amplitude states may be candidates for atmospheric and oceanic persistent anomalies.

[1] Helfrich, Karl R. and J. Pedlosky 1993 Time-Dependent isolated anomalies in zonal flows. *Journ.Fluid Mech* vol. **251** 377-409

ψ_2

$t = 0$

$t = 120$

$t = 200$

$t = 320$
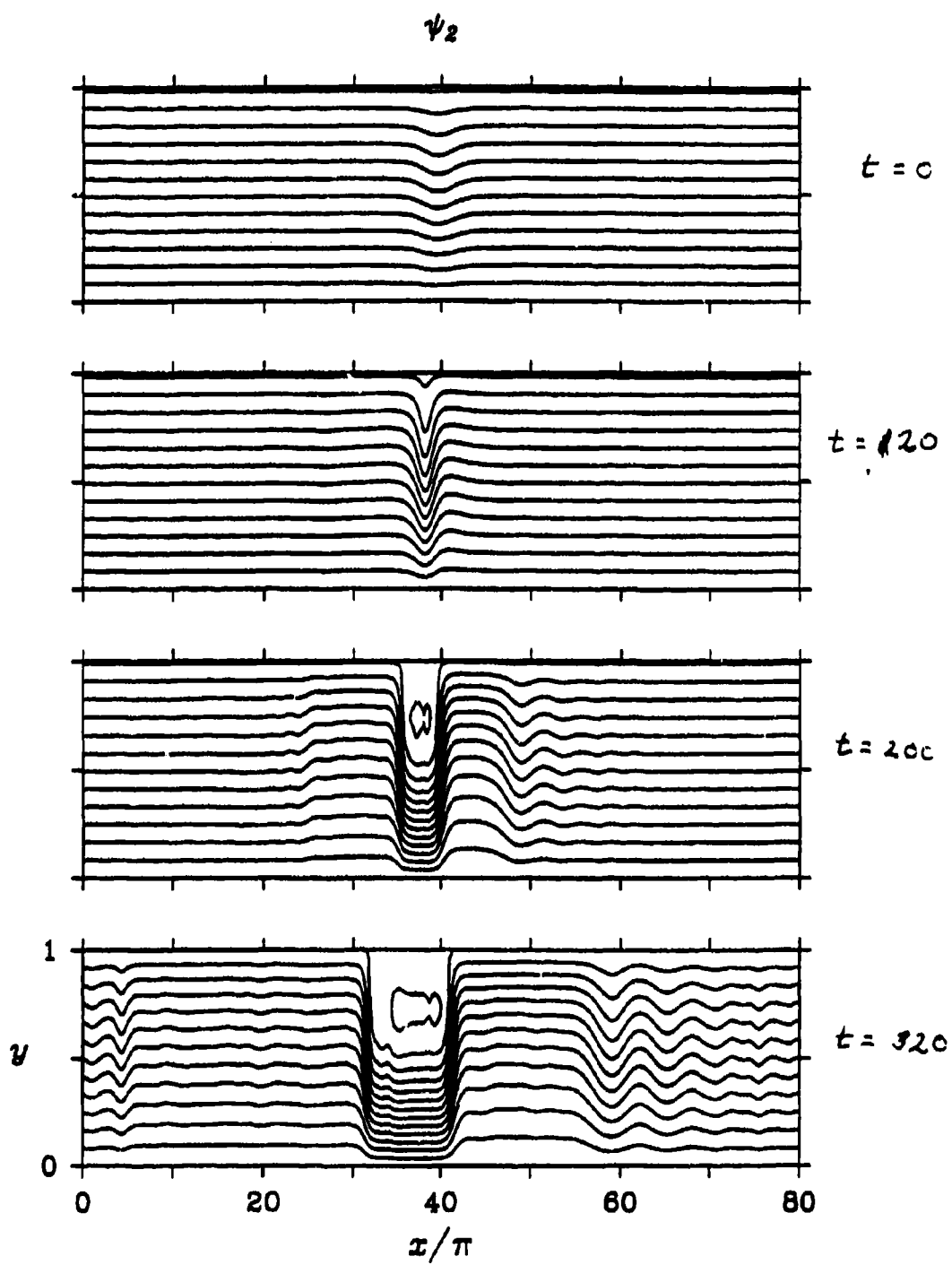
fig 1

q_2
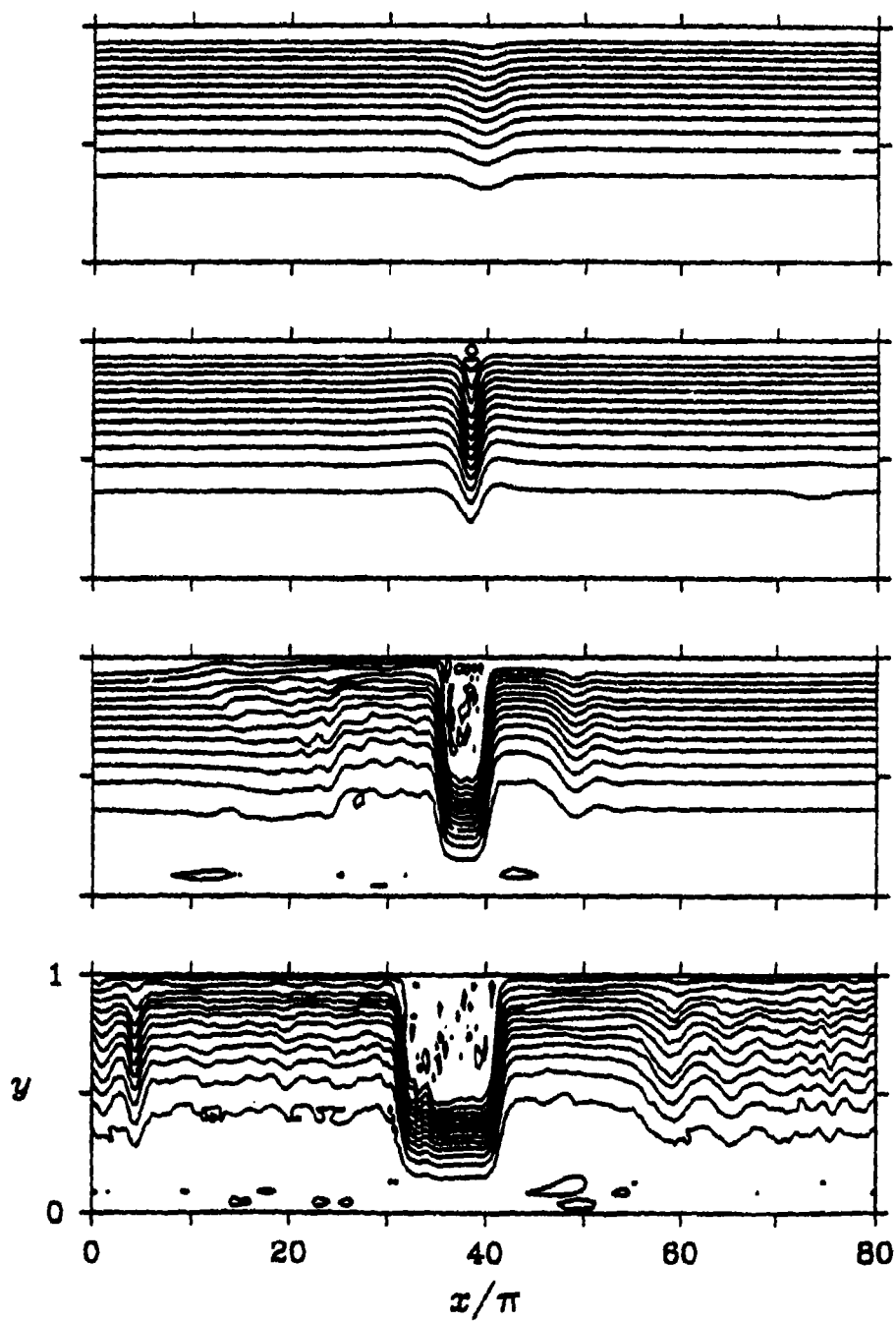
Fig 2

Characteristics of the instability in a surface boundary current

D. Obaton G. Chabert d'Hières
Equipe Coriolis, LEGI-IMG, BP 53, 38041 Grenoble cedex 9, France

1. Description of the flow

The stability of a surface boundary current is studied in the laboratory with background rotation. The buoyant current propagates under the action of gravity other a deep passive dense water. It is deviated by the Coriolis force and then follows the wall of the tank letting it on the right. Under certain circumstances it becomes unstable.

Experiments are conducted on the big rotating platform of the LEGI-IMG, Grenoble. Salted water filling the tank is first driven in body rotation, then the current of fresh water is initiated. The source of the current is located by the surface, perpendicularly to the wall. It has a triangular section to allow the fluid to be in geostrophic equilibrium, considering that the initial velocity is uniform (figure 1). As a consequence, potential vorticity is well defined and not uniform, it increases away from the wall due to decreasing current thickness. A sink is located downstream of the source and removes the current before it starts a second circuit. Therefore the current is of constant volume and constant flow rate. It is mainly laminar, expect for the nose not considered here.

The ratio of the two layers depth h_0/H is typically 0.1 (H is the total depth). Dimensional quantities that can be varied are the flow rate Q_0, the current width L_0 and the thickness of the light fluid at the wall h_0, all three taken at the source. The rotation of the tank, then the Coriolis parameter f, and the density difference $g' = g (\rho_2 - \rho_1)/\rho_1$ are also changed. The molecular viscosity of the water v is added to those quantities.

Taking account of the viscosity, the current is governing by three non dimensional parameters. Because a baroclinic instability is expecting, the Burger number is considered

$$B_u = g'h_0 / f^2L^2 \qquad\qquad 0.10 < B_u < 0.89.$$

The viscosity is introduced by the vertical Ekman number

$$E_k = v / fh_0^2 \qquad\qquad 0.2\ 10^{-3} < E_k < 8.1\ 10^{-3}.$$

The aspect ratio of the current at the source is added to those two parameters

$$h_0/L_0 \qquad\qquad 0.05 < h_0 < 0.64.$$
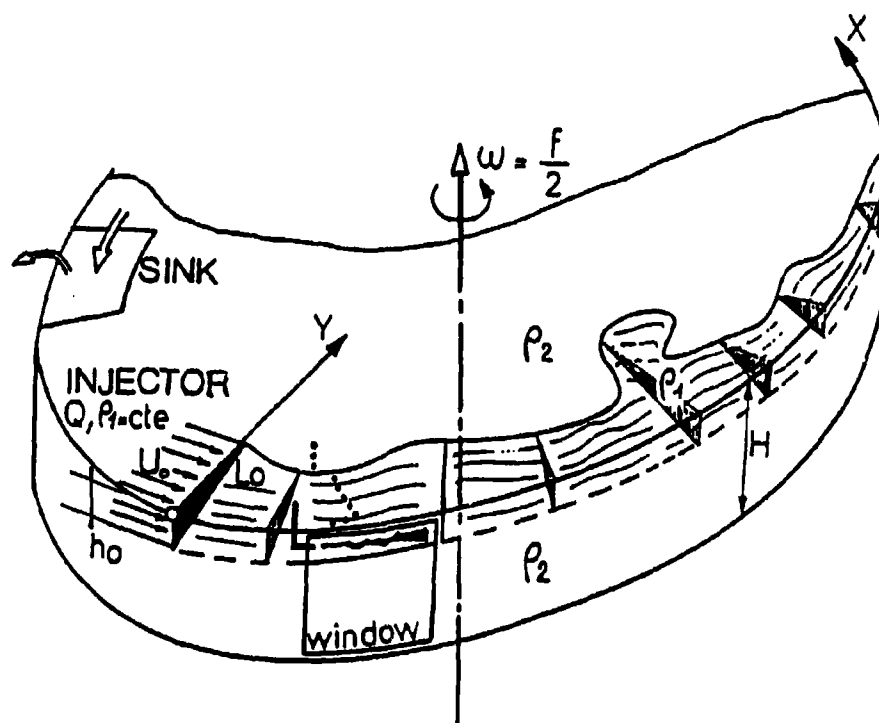
Figure 1. Experimental apparatus and dimensional quantities of the flow.

When the flow becomes unstable, there is a local increase of the width of the current at some distance from the source. At the front, a cyclonic eddy appears due to the horizontal shear with the dense passive water. At the same time and the same place, the current thickness increases near the wall. Then an anticyclonic eddy appears inside the flow. The lower layer is little affected by any movement: velocities are naught or negligeable. As the anticyclone develops, the interface increases below. And progressively, the lower layer is rotating with that eddy. At the front the cyclone may disappear. The dipole cyclone-anticyclone and the main current going around the anticyclonic eddy is called a meander in the experiments. When the first meander exists, many others can appeared in the flow. They are all observed downstream of the first meander i.e. further from the source. They usually appear nearly at the same time, but after the first one has been formed. Their development is similar to the development of the first meander.

As all these meanders increase in size and depth, they move within the flow in the same direction, with a speed equals to 1/10 of that of the mean velocity. The stable flow and the regular flow outside the meanders have streamlines parallel to the wall and are in geostrophic equilibrium. In the meanders, this state is no longer checked.

These dipoles cyclone-anticyclones are very similar to those found by Griffiths and Linden (1981, 1982) in their periodic coastal current. Vinger and McClimans (1980) and McClimans and Green (1982) also observed that kind of structures in an experiment close to the present one except for the ratio of layers depth that is 4-5 times greater than the one studied here.

2. Results

It is shown that the stability of the flow depends on the Ekman number, and that there is only one type of instability. For $E_k < 1.5 \ 10^{-3}$ all flows are unstable and for $E_k > 3.0 \ 10^{-3}$ they are all stable. This is true whatever the value of the Burger number is. Despite the fact the ratio of the layers depth ho/H has not been much varied, it is possible that this parameter has also a significant role.

Destabilisation of the flow is linked to a minimum value of the local Burger number. (The local Burger number is calculated over a section of the current.) This minimum varies with the type of flow, therefore the Burger number has not to reach a critical value to destabilise the current. Later and further from the source the formation of the first meander, larger the Burger number. The destabilisation is also slowed when the Ekman number increases. This instability is not due to a wave either coming directly from the source or reflected by the nose of the current or by the sink. It can be due to the detachment of the wall boundary layer. Formation and increase of the first meander can afterwards create a wave which degenerate to the other meanders. These two last results are only suggestions and have not been proved.

To characterise the instability, tranfers of energy are analysed across different sections of the flow. These measurements are made, at nearly the same time, in the regular parts of the current and the meander. These measurements are repeated from time to time when the size of the meander increase and before the velocity in the lower layer is significant. measurements of the mean vertical velocity of the flow (by the means of floats) and of the layer thickness (using a light absorption technique) are made. These two quantities are made along the width of the current. Kinetic and potential energies are next calculated a section of the current ahead of a meander and in a structure. Then the ratio of the two energies and its evolution with time, when instability occurs, is studied.
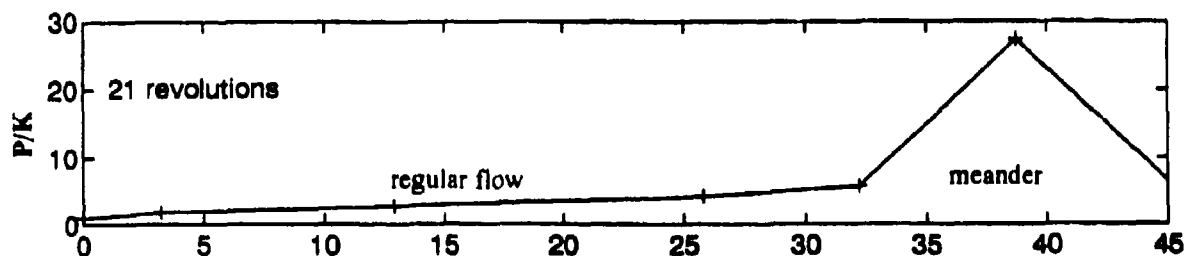
Figure 2. Ratio of potential energy P to kinetic energy K at different sections in the flow.

Between the regular flow and a part of the flow containing a meander, the potential energy increases (figure 2). This means that there is some kinetic energy that transfers to potential energy. This result and the facts that 1) the thickness of the current increases into a meander, 2) the Burger number taken either at the source or at some various sections in the flow has not an important role on the stability of the flow, give a good indication that the instability is essentially barotropic.

Griffiths R.W., Linden P.F., 1981. The stability of buoyancy-driven costal currents. Dyn. Atmos. Oceans, 5, 281-306.

Griffiths R.W., Linden P.F., 1982. Laboratory experiments on fronts. Part 1: density-driven boundary currents. Geophys. Astrophys. Fluid Dyn., 19, 159-187.

McClimans T.A., Green T., 1982. Phase speed and growth of whirls in a baroclinic coastal current. River and Harbour Laboratory Report. STF60 A82108, Norway.

Vinger A., McClimans T.A., 1980. Laboratory studies of baroclinic coastal currents along a straight, vertical coastline. River and Harbour Laboratory Report. STF60 A80081, Norway.

FRONTAL PHENOMENA OBSERVED IN TIDAL ESTUARIES
- VERIFICATION BY 3-D BAROCLINIC FLOW MODEL -

K. Nakatsuji*, T. Sueyoshi* and T. Fujiwara**

*) Dept. of Civil Eng. Osaka University, Osaka 565, Japan
**) Dept. of Fishery, Kyoto University, Kyoto 610-10, Japan

ABSTRACT : Two cases study of frontal phenomena observed in Osaka Bay, Japan is presented using a three-dimensional, time-dependent baroclinic flow model. The first case study involves an estuarine front of the Yodo River flood flow, in which buoyancy and earth's rotation are the main force to lead strong geostrophic along-front jet. The second case study involves a tidal front observed along the line connecting 20m depth points in Osaka Bay. Stratified waters developed in the shallow basin and vertically well-mixed ones due to a strong tidal flow through narrow straits meet with each other to make a remarkable front.

INTRODUCTION

Fronts are well-defined boundaries between water masses where horizontal gradients in density and other fluid properties are large. These gradients are generated by buoyancy according to river discharges and heat fluxes through the water surface. Recent development of remote sensing techniques have enabled one to clarify the existence of frontal phenomena in coastal seas; an estuarine river-forced front, a tidal front and a thermohaline front. Among them, the thermohaline front appears between water masses of low temperature and low salinity and those of high temperature and high salinity. It is characterized by a little difference in density. (Yanagi, 1980) The former two frontal phenomena depend not only on the source of river discharges, but also on the acceleration, friction and the rotation of the earth. Onishi (1990) and Nakatsuji et al. (1992) pointed out on the basis of remote sensing by satellite that lots of effluent from rivers deflect anticyclonically in the Northern Hemisphere and form a baroclinic boundary current that keeps the coastline on its right-hand side. In regard to the tidal front across Osaka Bay from north to south, there are a large number of f .d surveys conducted by Ueshima et al. (1987), Yanagi and Takahashi (1988), and Fujiwara et al. (1989).

In the present study, the dynamics of frontal phenomena observed in Osaka Bay is examined using a three-dimensional, time-dependent baroclinic flow model. In the first half, the spreading of the Yodo River flood flows is examined in relation to the Rossby deformation radius. In the second half, the mechanism of tidal front is made clear in a strait-basin system. (Fujiwara et al., 1994)

RIVER-FORCED ESTUARINE FRONT

Behaviour of Yodo River Flood Flow in Osaka Bay During High Discharge

Osaka Bay is an oval shaped bay with a 60 km major axis and a 25 km minor axis as shown in Fig. 1. Osaka Bay has two-openings: Akashi Strait and Kitan Strait and the Yodo
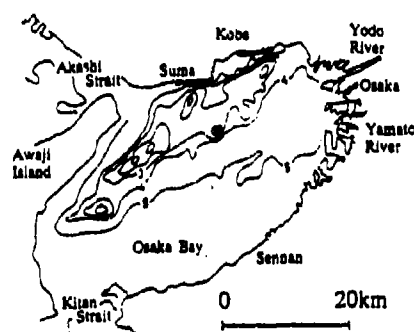
Fig. 1 Infra-red image of surface
temperature taken at 14:24
August 2 1982 from NOAA.
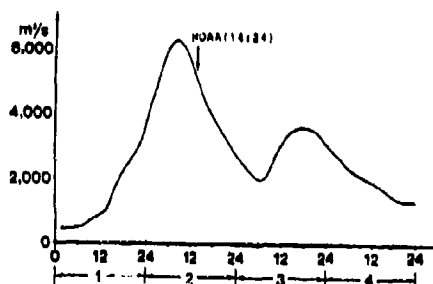
Fig. 2 Hydrograph of The Yodo River
measured during Typhoon 8210.
6270 m^3/s was recorded.

and Yamato Rivers are located at the head of bay. Osaka Bay, therefore, is a typical semi-enclosed bay. The eastern bay is shallow than 20 m due to long term sedimentation from rivers, while the western bay is 40 m- and 70 m- deep valley, because it is subject to strong tidal flows through two straits.

Figure 1 shows the surface temperature distribution of Osaka Bay obtained by NOAA at 14:24, August 2, 1982 during typhoon 8210 which was followed by a low pressure. The maximum flow rate was 6,270 m^3/s. The contours indicate relative temperature distribution every 0.5°C with a resolution of 0.12°C. The infrared image was taken 6 hours 20 minutes after the maximum discharge as shown in Fig. 2. Figure 1 indicates that the Yodo River outflow advanced from the river mouth westward off Kobe and then turned southward along Awaji Island. The longer axis extends some 55 km from the river mouth and the shorter axis is 14 km maximum. The infrared image makes clear that the Yodo River flood outflow behaves in a completely different manner from the behaviour of the Yodo River water at nominal discharge rates. Most of Yodo River water has been consiuered to flow southward on the basis of field surveys.

The horizontal scale of interest is the Rossby deformation radius $r_d = \sqrt{(\Delta\rho/\rho_s)gh(D-h)D}$ × f^{-1} in which f is Coriolis parameter. As there is no measured value for river water thickness at the river mouth h_0 during high discharge, we assume it to be 2 or 4 meters; hence the Rossby deformation radius roughly estimated is $r_d = 7.3$ km for $h_0 = 2$ m, or $r_d = 9.5$ km for $h_0 = 4$ m. The area occupied by the Yodo River outflow is 55 km × 20 km as shown in Fig. 1 and it is larger than the radius r_d. This leads us to believe that the outflow is considerably influenced by the rotation of the earth.

The Three-Dimensional Flow Model

The numerical model uses the hydrostatic and Boussinesq approximations and solves for three-dimensional velocities (U, V, W) and buoyancy (B). Details are given in Murota et al. (1988) and Nakatsuji et al. (1989). The stratification-dependent turbulent transfer is modelled by the vertical eddy viscosity coefficient ϵ_z and eddy diffusivity K_z in due consideration of stratification functions. The neutral value of ϵ_{zN} is used 0.005 m^2/s. A horizontal eddy viscosity or diffusivity is used 20 m^2/s. Freshwater of zero salinity flows near the surface from rivers into the model basin initially filled with saline sea water of $\sigma_t = 22$. At the river mouth, the time-variation of river discharges is given according to the observed hydrographs of Typhoon 8210 as shown in Fig. 2. The water elevation is assumed to be zero and tidal

flows are not taken into account in the computation. The model ocean of Osaka Bay is 58 km long and 54 km wide and a maximum of 52 m deep as shown in Fig. 3. The model's resolutions are 2 km in the horizontal plane with eight vertical levels each between 0.4 m and 20 m thick. The time increment is 6 seconds.

Numerical Results on Estuarine Front
(1) Coriolis deflected coastal jet

Figure 3 shows the horizontal velocity and density fields in the 0.4 m thick surface layer at 20 hours after the beginning of flood flow for the cases with and without the earth's rotation. Contours of the density difference normalized by the initial difference, $\sigma_i = 22$ are denoted by broken lines with intervals of 10%. In the case without rotation the Yodo River plume spreads out over the sea water radially accompanied by a thinning in its vertical extent. That is a typical plume-like flow. The isopycnal contours tend to fan out in a concentric circle and the velocity vectors cross at right angles to the isopycnal contours.

On the other hand, in the case with the earth's rotation, the velocity vectors turn to the right so alongshore velocities become dominant. The isopycnal contours are stretched out parallel to the coastline and even the outermost 10% contour is confined within about 10 km of the shore. It is a clear indication of the river plume being a geostrophic current, since the Rossby deformation radius may be 10 km or less. The plume reattaches to the right-hand side coast forming a coastal current, which is affected by the earth's rotation. Such a flow is often visible in the river water effluent from the air due to colour contrasts in the different water masses.

Figure 4 demonstrates the Yodo River plume spreading at the surface layer of 0.4 m after 35, 40 and 45 hours in consideration of the earth's rotation. The computed result at 35 hours just corresponds to the time when the infrared image was taken from the NOAA satellite. The Yodo River plume at this point behaves basically in the same manner as observed in Fig. 3. It indicates that the Coriolis force may significantly affect the Yodo River plume spreading. The point of interest here is that the isopycnal contours are close to each other at the tip of river plume. Because of the geostrophic adjustment, the rotation may suppress offshore spreading but accelerate alongshore spreading that leads to the formation of the frontal structure discussed later. The front can be seen to propagate southwestward along the coast of Awaji Island as a narrow current with a width of 8 km. The river plume continues to propagate along the coast while maintaining a frontal structure even after he lapse of 50 hours, although the speed slows down slightly with distance. It is about 12 km wide and has a speed of about 0.4 m/s. Such an alongshore Coriolis-deflected current is called "a coastal jet".
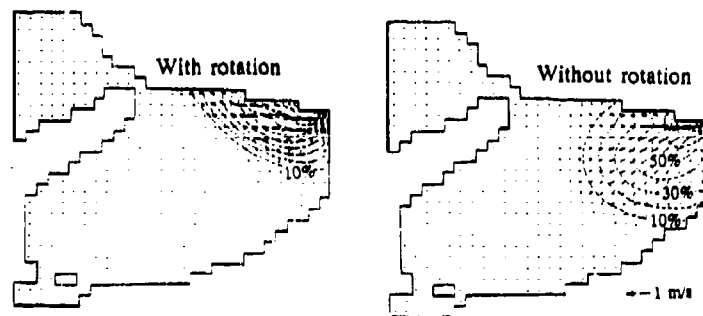
Fig. 3 Surface velocity and density fields of Yodo River flood flow with and without earth's rotation after 20 hours of typhoon 8210.
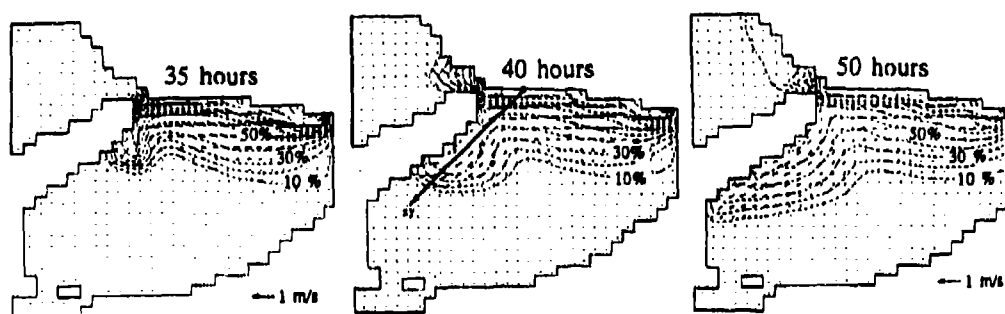
Fig. 4 Horizontal flow and density fields of Yodo River plume spreading
after 35, 40 and 50 hours at surface layer of 0.4 m thickness.

(2) Three-dimensional structure of estuarine front

To better illustrate the three-dimensional structure of the intruding current, Fig. 5 shows
the vertical sections of alongshore current and isopycnals at 35 hours and 40 hours.
Isopycnals are drawn at intervals of 5% of $\sigma_t = 22$ in this figure. This section is taken 2 km
off and in parallel to the coast of Awaji Island, which is shown by a solid line in Fig. 4(b).
The origin of xy = 0 corresponds to the coastline near Akashi side and values of xy increases
in the southwest direction. The river water transported by the westward baroclinic current
along the Kobe coast stays in the left-hand bulge of Fig. 5 where alongshore velocities
become very small. Because of the horizontal pressure gradients due to density gradients
(baroclinic mode) and surface gradients (barotropic mode) as well as the geostrophic
adjustment, the accumulated water forms an intruding current once more and flows along the
coastline. The velocity inside the current first accelerates away from the bulge and then slows
down near the head of intruding current. Judging from the velocity vector, its head may form
an advancing front often observed in gravity currents. The thickness of current is about 2 m
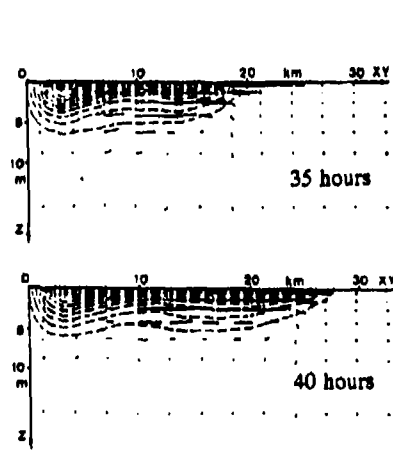
Fig. 5 Velocity vector and isopycnals
at alongshore vertical sections
showing vertical structure.
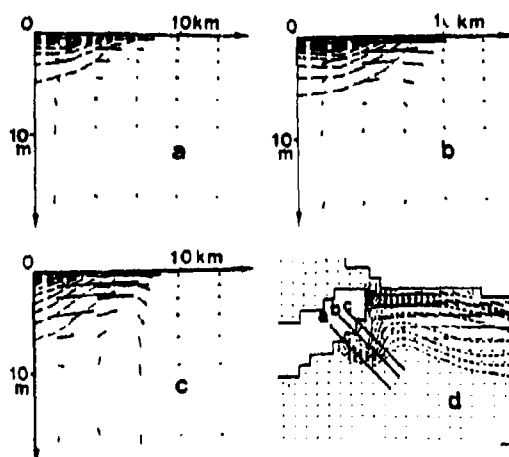
Fig. 6 Transverse velocity vector and
isopycnals at cross-sections of
intruding current at 35 hours.

when estimated on the basis of 5% isopycnal contour and about 3 m on the basis of zero-velocity contour. The intrusion speed of the head between 35 and 40 hours can be estimated by the distance travelled during 5 hours. It is about 0.42 m/s which is equivalent to 1.5 × $\sqrt{(\Delta\rho/\rho_o)gh}$ (= 1.5 × C). The value is somewhat larger compared with the theoretical one of 1.4 × C and the experimental one of (1.09 − 1.16) × C which were obtained for a density current overlying a lower layer with rotation by Stern et al. (1982).

Figure 6 shows velocity vectors and isopycnals at 5% intervals at the cross sections marked in Fig.6(d) which shows the horizontal flows and density fields at the surface layer after 35 hours. The spreading ranges from 6 km to 8 km horizontally and from 5 m to 6 m vertically; its velocity is about 0.6 m/s. Figure 6(a) which corresponds to the tip of the front shows the existence of a sinking current formed by an external fluid body as the spreading advances. In Figs. 6(b) and 6(c), a current that expands offshore can be seen inside the front. The experiments conducted by Stern et al. (1982) clarified the width of the current to be 0.4 to 0.5 times the Rossby deformation radius, which agrees with the present computed results.

As mentioned above, the river water spreading is characterized by the formation of a coastal current through geostrophic adjustment. Figure 7 shows the variations of the propagation speed of the Yodo River flood flow plotted against the alongshore distance measured from the river mouth. The intrusion speed tends to accelerate with distance before the river water reaches the Akashi Strait. After staying at that region of s = 38 km, the accumulated water begins to flow again and turn southwest. It is surprising that the maximum speed attained is about 0.4 m/s even 53 km from the river mouth. After that, the intrusion speed drops because the density difference between flood water and sea water is reduced. Its speed averages 0.35 m/s. Consequently, the flood water of the Yodo River reaches the Kitan Strait after only 60 hours after the beginning of flood.

In the present computation, the effects of tidal flow are not taken into account. It is of course an important factor to determine the river plume spreading patterns. The tidal modulation effects are discussed in another paper. (Nakatsuji et al., 1992)

TIDAL FRONT

Tidal Front Observed in Osaka Bay

Figure 8 demonstrates surface temperature distribution taken by MSS loaded in airplane by Ueshima et al. (1987). The tidal flow at Akashi Strait is a final stage of eastward flow. There is clearly a surface temperature contrast of almost 0.5 °C between the two sides of the
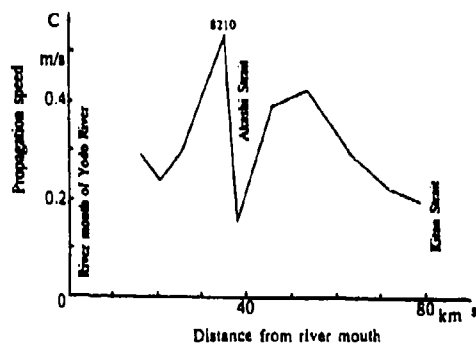
Fig. 7 Propagation speed along the center-line of Yodo River flood flow.
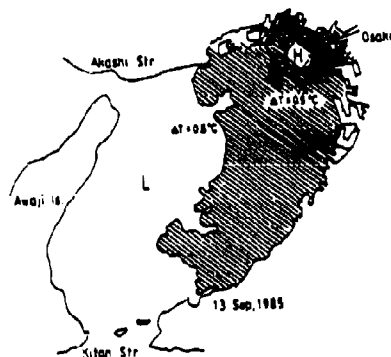
Fig. 8 Tidal front appeared in Osaka Bay (from Ueshima et al., 1987)

front across the center area of Osaka bay from north to south. The tidal front develops along the line connecting 20 m depth points. One side of the front remains strongly stratified in shallow basin affected by lots of river water effluent and heat flux through sea surface especially in summer, while another side is vertically well-mixed due to a strong tidal flow through narrow and deep straits. Yanagi and Takahashi (1988) reported on the basis of field observation in summer that the differences in temperature, salinity and density are 1.5 °C, 4.0 ‰ and σ_t = 3 at 5 km intervals across the tidal front, respectively.

The Baroclinic Flow Model

In order to clarifying the tidal front, it is necessary to improve the precision of movement and turbulent transfer in vertical direction. Therefore, the three-dimensional baroclinic flow model used in the computation of estuarine front is reorganized. Main points of modification are as follows; (a) model resolution of 1 km in the horizontal plane with 7 vertical layers having thickness of 2, 4, 6, 8, 10, 15 and 15 m from surface to bottom and (b) the tidal flow computation in which a cosine wave with a 12-hour cycle and amplitude of 38 – c at open boundaries, and (c) flow rate of Yodo River, 205 m^3/s and heat transfer through sea surface, 29.7 cal//s/m^2 in summer.

Numerical Results of Tidal Front
(1) Baroclinic flow pattern and tidal front

The computation results to be discussed here are those on the t tidal cycle, in which the change in the density distribution during one tidal cycle becomes negligible small as compared with that of the previous tidal cycle.

Figure 9 shows the velocity and the density fields of the surface layer (1 m deep from the surface) when the eastward or westward flow through Akashi Strait reaches its maximum. The contours of density are marked at every 10 % of the density difference between the river and sea water where σ_t = 23. When the eastward flow at Akashi Strait is at its maximum, the flow into Osaka Bay spreads in a jet-like form toward the southeast. The flow makes its way in clockwise circular arcs along a 20 m-deep contour line toward the Kitan Strait. Meanwhile the discharge from the Yodo River spreads southwest, running southward to cross the 20% density contour line at a right angle. The jet-like tidal flow from the Akashi Strait combines with this river discharge at the 20 m-deep point and continues southward.
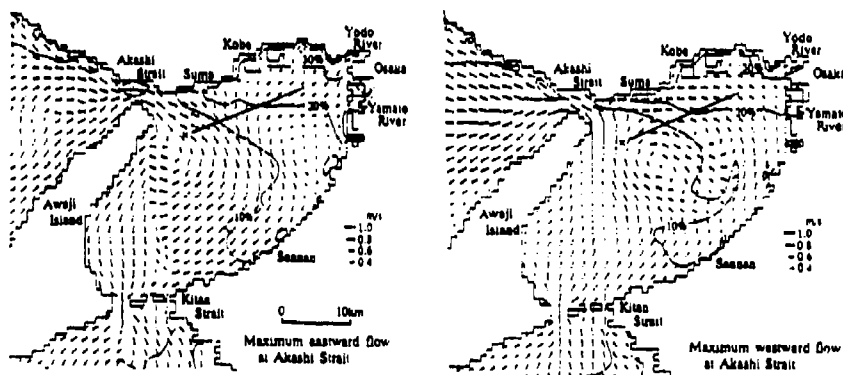
Fig. 9 Surface flow vectors and density distribution when
the maximum eastward/westward at the Akashi Strait.
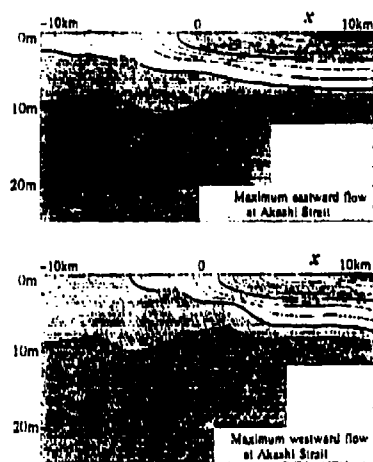
Fig. 10 Density distribution on the cross
section of tidal front correspond-
Fig. 9 by a solid line.
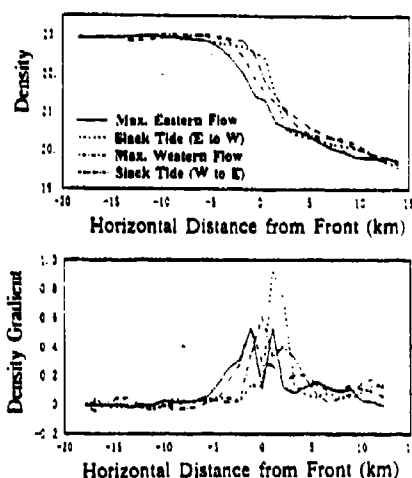
Fig. 11 Surface density and density
gradient distribution every
three hours.

When the westward flow is at its maximum, the water flow can roughly be divided into
two: one running from the Kitan Strait northward along the east coast of Awaji Island, and
the other that flows northward, off the coast of Sennan. Water from the Yodo River is carried
by the tidal flow toward Kobe, a part of which flows into the Akashi Strait. It is worth noting
that the southeastward flow at Kino-se persists even when the tidal flow direction changes.
Kino-se is the shallowest point in the western bay which is indicated by the cross mark in
Fig. 9. Between this southeastward flow and the flow in the inner bay, a discontinuous flow
is observed. If the density distribution in Fig. 9 is represented in finer contour lines, the
discontinuous boundary can be shown to be bands of different densities, that is a tidal front.

Figure 10 shows the density distribution at the cross-section of the tidal front, which is
indicated by the solid line in Fig. 9. The horizontal 0 point corresponds to the 20 m-deep
sea bed. The direction toward the inner bay (toward Osaka) is positive, while the direction
toward the outer bay (toward Awaji Island) is negative. In the inner bay, approximately 5 m-
thick stratification with $\sigma_t = 22$ or lower can be observed. The stratification is stable, rarely
affected by the change in the tidal flow. The area where the sea bed is deeper than 20 m (x
< 0) is exposed to stronger tidal flows and, as a result, vertical mixing occurs. In this area
σ_t is 22.5 or higher. Between these two areas, where σ_t is more than 20 and less than 22,
density contours are almost perpendicular to the water surface.

Figure 11 shows the horizontal distribution of surface density and its gradient every three
hours. The gradient indicates the sharpness of the front. This figure shows that the tidal front
on this cross section is located at the location where the sea bed is about 20 m deep. The
density changes by $\sigma_t = 2$ over 7 km on this plane. The density gradient is the greatest when
the eastward tidal flow through Akashi Strait reverses westward. At this time the front is 2
km wide and σ_t rises from the head to the center of the bay by $\sigma_t = 2$. It is because the
eastward flow through Akashi Strait spread deep into the head of bay. Field data obtained
by Yanagi and Takahashi (1988) indicated the density change of $\sigma_t = 3$ over 5 km width of
the tidal front. From these comparison, the computation results overestimate a little larger
than observation ones.

CONCLUSION

The river-forced front and the tidal front observed in Osaka Bay are examined using a three-dimensional, time-dependent baroclinic flow model. Frontal phenomena are accompanied by the convergence of surface water to make well-defined discontinuity in density and other fluid properties such as temperature, salinity and so on. In cases of an estuarine front, on a larger scale than the Rossby deformation radius, the earth's rotation in addition to the buoyancy are the major forces to make a strong geostrophic along-shore current. Since contamination such as industrial and domestic waste products is discharged in large quantities, the behaviour of estuarine fronts is very important to the environment of coastal seas and estuaries. On the other hand, the appearance of tidal front is dependent of stratification developed in shallow basin and vertically well-mixed water due to strong tidal flows through straits. It plays an important role in formation of the baroclinic residual current system, estuarine circulation system and also water qualities transfer in enclosed coastal seas and bays. The research for clarifying the dynamics of frontal phenomena is, therefore, necessary to understand the physical and bio-chemical processes and their economic implications for good management.

REFERENCES

Fujiwara, T., T. Higo and Y. Takasugi (1989): Proc. Coastal Eng., JSCE. 36, 209-213 (in Japanese)

Fujiwara, T., H. Nakata and K. Nakatsuji (1994): Continental Shelf Res., 14, 9, 1025-1038.

Murota, A., K. Nakatsuji and T.Y. Huh (1988): Proc. 6th Congress APRD, IAHR, 3, 33-40.

Nakatsuji, K., J.Y. Huh and A. Murota (1989): *Hydraulic Environmental Modelling of Coastal, Estuarine and River Waters*, Ed. R.A. Falconer, Gower Technical., 310-321.

Nakatsuji, K., K. Muraoka and S. Aburatani (1992): *Hydraulic and Environmental Modelling: Estuarine and River Waters*, Ed. R.A. Falconer et al., Ashgate, 299-309.

Onishi, S. (1990): *Remote Sensing of Shelf Sea Hydrodynamics*, Ed. J.C.J. Nihoul, Elsevier Oceanography Series, 38, 107-132.

Stern, M.E., J.A. Whitehead and B.L. Hua (1982): J. Fluid Math., 123, 237-265.

Ueshima, H., I. Yuasa, M. Takarada, H. Hashimoto, M. Yamazaki and H. Tanabe (1987): Proc. Coastal Eng., JSCE. 34, 661-665. (in Japanese).

Yanagi, T. (1980): J. Oceanogr. Soc. Japan, 35, 253-260.

Yanagi, T. and Takahashi (1988): Dynamics Atmosphere and Ocean, 12, 191-206.

LABORATORY MODELLING OF GRAVITY CURRENTS ON THE SLOPE IN ROTATING FLUID

A.G.Zatsepin and A.V.Semenov
(P.P.Shirshov Institute of Oceanology, Moscow)

The sinking of dense water along inclined oceanic bottom (shelves, slopes) is remarkable process responsible for the formation of oceanic bottom water masses and ventilation of the deep ocean. The dynamics and other specific details of this process are poorly known, because of the complexity of its investigation in natural conditions. In this short report we present the main results of preliminary laboratory studies and accompaining theoretical analysis of the basic dynamical features of the above-mentioned dense water flows. The influence of Earth rotation on the sloping gravity currents is simulated with the help of rotating table. The significance of proposed studies is conditioned by the important role of Earth rotation on the dynamics and structure of mesoscale and large scale oceanic dense water flows. To our knowledge there is no comprehensive study of gravity currents along sloping bottom in rotating fluid. Nevertheless we would like to mention the papers and reports by Griffiths (1983), Davey and Killworth (1989), Whitehead et al (1990) dealing with some aspects of the problem involved.

In 1993 we performed a series of experiments with gravity currents on the sloping bottom (angle of the slope - 39 deg.) in the rectangular organic glass tank 50*50*20 cubic cm. filled by salted water and positioned in the center of the rotating table. Sloping bottom was simulated by the surface of the conical body which peaked up just in the center of the tank. Gravity currents were produced by one of two local constant flux sources of more saline water. One of such sources was placed on the peak of the conical body (central source) and the other - on its sloping side (lateral source). In case of experiments with the central source nearly axysimmetric gravity current was formed with a front propagating down the slope. Distance L of the front from the source was measured as a function of time t, volume flux Q = 0.8 - 6.2 cm^3/c, reduced gravity g* = 0.4 - 4.8 cm/c^2 and Coriolis parameter f = 0.83 - 2.0 1/c. The results confirmed the self-similar theoretical solution which was obtained by Dr.A.G.Zatsepin for one-layer model approximation. In this model the balance between three main forces (downslope gravity, Coriolis and friction forces) was taken into account. The success of one-layer approximation was due to the small thickness (3-8 Eckman lengthscale) of the gravity current compared to the depth of the upper layer.

In case of experiments with lateral source gravity current was spreading predominantly anticyclonically (to the west) and down the slope because of friction. Three different regimes of the current were observed: a) "train" of quasi-isolated vorticies (large Q and small g* values), b) train of fronts (small Q and large g* values) c) quasi-monolith current (moderate Q and g* values). In case a) there was strong mesoscale interaction between the thick gravity current and the upper layer fluid, and the vortical structures in both layers had predominantly cyclonical sign. In the case b) gravity

current was thin and the wavelength of observed frontal structure was close to that of Eckman layer instability (Whitehead et al.,1990).

One of the aims of the future study of sloping gravity currents in the rotating fluid is to clarify the conditions under which the flow produced by local constant flux source breaks down to a series of discrete vortical or frontal structures and to describe physical mechanisms of their formation.

LITERATURE

1. Davey,M. and P.D.Killworth. Flows produced by discrete sources of buoyancy // J. Phys. Oceanogr., 1989, V.19, N.9, 1279-1290.
2. Griffiths R.W. Internal wave drag and the production of intense vorticies by turbulent gravity current with implications for sinking of bottom waters // Ocean modelling, 1983, N.50, 9-12.
3. Whitehead J.A., et al. Experimental observations of baroclinic eddies on a sloping bottom//J.G.R., 1990, V.95, N.C6, 9585-9610

LABORATORY MODELING OF NARROW CURRENT-TOPOGRAPHY INTERACTIONS IN A ROTATING STRATIFIED FLUID

D.S. MCGUINNESS
X. ZHANG
D.L. BOYER
Arizona State University
Department of Mechanical and Aerospace Engineering
Tempe, AZ 85287-6106
USA

Abstract

This communication outlines laboratory work performed in modeling narrow current-topography interactions under the influence of rotation and stratification. The experiments employed a surface-driven source-sink technique in an annular geometry, and used a single cosine-squared topography of revolution. The currents generated possessed a Gaussian-like horizontal profile decreasing linearly with depth. Owing to stratification effects, the current quickly developed instabilities characterized by cross-stream meanders and evenly-distributed azimuthal cyclonic vortices. Particle-streak photographs showed overall qualitative features of the fluid motion in a 120° test section, both with and without the presence of topography. Particle-imaging techniques provided velocity and vorticity fields. Interaction with the topography demonstrated the presence of both a cyclonic vortex and accompanying anticyclonic region in the obstacle lee, decreasing in strength with elevation. Comparison with data collected from field observations is also discussed.

1. Introduction

Motivated by recent field studies at Fieberling Guyot, an isolated seamount in the North Pacific, the present communication outlines laboratory modeling of current-topography interaction under rotation and stratification. For the most part, past physical modeling of current-topography systems has dealt primarily with broad, uniform currents. The reader is referred to work by Baines and Davies (1980), and Boyer et al. (1987), dealing with stratification effects, and Boyer and Zhang (1990) and Zhang and Boyer (1993) concerning time-dependent flows. Currently, some numerical work has been performed relating to jets and topography. Examples include Spall and Robinson (1990) and Haidvogel et al. (1991), both involving jets along coastal regions, and Bannon (1980), focusing on barotropic jet-like flows near an isolated obstacle. As narrow or "jet-like" currents are quite common in nature, the modeling of jet-topography interaction in a laboratory setting is of interest.

2. Physical System and Parameters

The experimental facility is a large circular test cell (Figure 1) measuring 180 cm in diameter and 20 cm in height, filled with fluid to a level H. Supported above the floor of the tank rest two concentric structures: an inner Plexiglas disk, r_2, and outer Plexiglas ring, r_3. Given the geometry, a free-surface annular region is formed between the two features. Fixed to the inner wall of the tank are 16 inlet tubes, by which fluid is introduced into the facility at the same level as the disk and ring. A thin strip of sponge material aids in producing a radially uniform flow along the surface of the ring. A circular array of elliptical holes is cut in the disk at a radius r_1, to draw this fluid from the tank, via a central tube, and recirculate it using a micro-gear pump. In this manner, a source-sink arrangement is established within the test cell. This same facility was used by Zhang et al. (1994). Further, the entire system is placed upon a turntable, capable of solid body rotation (Ω) at a Coriolis parameter $f = 2\Omega$. Under rotation, the fluid entering the annulus is deflected under Coriolis forces, thereby creating a Gaussian-like azimuthal velocity distribution within the free-surface region. Effectively, this approach simulates a wind-shear forcing

possessing a particular cross-stream profile (Chen et al., 1992 and Boyer et al., 1993) A cosine-squared topography of revolution can be placed in the annular region to study its effects on the current so generated.

Given the above facility, a set of dimensionless parameters can be defined to characterize the resulting flow field. These are listed, along with laboratory ranges, as

$$Ro = \frac{u_{max}}{fD} = 0.02 \sim 0.08, \qquad \text{Rossby number,}$$

$$E = \frac{\nu}{fH^2} = 2.4(10)^{-4}, \qquad \text{Ekman number,}$$

$$S = \frac{N^2 H^2}{f^2 D^2} = 0.20 \sim 0.95, \qquad \text{Burger number,}$$

$$\frac{h_o}{H}, \frac{D}{H} = 0.81, 2.15, \qquad \text{normalized topography width and height,}$$

$$\frac{W_y}{D} = 1.5, \qquad \text{normalized width of the current,}$$

$$\frac{y_1}{D} = -0.5 \sim 0.5, \qquad \text{normalized topography position relative to}$$

the annular centerline.

where u_{max} is the maximum strength of the current, h_o and D the characteristic vertical and horizontal dimensions of the axisymmetric topography, ν the kinematic viscosity of water, $N = (g\Delta\rho/\rho_o H)^{1/2}$ the Brünt-Viäsälä frequency, g the acceleration due to gravity, $\Delta\rho$ the density difference between the top and bottom of the fluid, ρ_o the mean density of the fluid. W_y the characteristic width of the current and y_T the position of the topography relative to the annular centerline. Note that the topography aspect ratio, h_o/D was not matched in the present work. Assuming appropriate values for Ro, E, and S (see Pedlosky, 1987), the flow can be shown to be hydrostatic, hence neglecting this requirement. It can be shown that such a system simulates oceanic currents in the vicinity of a tall topography with the Ekman number based on an eddy viscosity (Zhang and Boyer, 1993).

3. Experimental Techniques

The fluid employed was linearly stratified with saltwater using the two-tank method described by Oster and Vamamoto (1963). Following this, the tank was slowly spun-up to solid body rotation (an increase on-the-order of $8.3(10)^{-3}$ rads^{-1} every minute) to prevent mixing. To be conservative, four hours elapsed prior to initiating the pumping system to allow the facility to reach the state of solid body rotation. This done, the current took approximately two additional hours to reach a state of quasi-equilibrium. For the experiments, f, H, D, h_o, and D were held fixed, forcing E, S, h_o/D and D/h to remain constant. The flow rate and position of the topography was varied. i.e., changes in the flow with variable Rossby number and y_T/D values were investigated. W_y/D was approximately constant.

The flow was visualized by employing neutrally buoyant polystyrene beads of diameter 0.5 mm and mean density $\rho_o = 1.043$ kgcm^{-3}. Given a small density difference approximating $\Delta\rho$, a uniform distribution of particles with height was achieved. The beads, in turn, were illuminated with either vertical or horizontal light sheets of thickness ~0.5 cm. In the first case, time-exposed photographs were taken with a 35 mm camera mounted in the rotating frame. A computer control mechanism allowed simultaneous light and camera control. Commanding the lights to follow a "on-off-on" pattern during a   are produced a set of "dot-dash" particle-streaks in each image. This provided a means to record both the direction and speed of each particle. A video camera, mounted in the rotating frame was also used to record real-time portions of the velocity field.

Using Digimage, a particle-image processing system developed at Cambridge University, these recordings were digitized frame-by-frame in an effort to particle-track the flow during each video frame. Using a two-dimensional interpolation scheme, velocity values are collapsed onto a predetermined grid. Files were then produced which generated real-time "snap-shots" of both the velocity and vorticity fields. The reader is referred to McGuinness (1994) for a more detailed explanation.

4. Experimental Results

4.1 Homogeneous Fluids: A Summary

As a precursor, homogeneous fluid tests were conducted. Parameters adjusted included the flowrate, rotation speed, current width, and position of the topography relative to the current. As a function of the external parameters, findings showed the generation of both a stable and unstable current which was vertically uniform, but possessed horizontal shear. An analytical model of the current was developed which provided an accurate scaling for the profiles of the azimuthal velocity. In the presence of topography, the characteristic flow-field possessed a large anticyclonic deflection in the obstacle lee which was a function of the upstream local vorticity. This feature was altered by moving the topography within the annular region, relative to the current centerline. Some numerical work was performed, providing a satisfactory comparison with laboratory findings. Zhang et al. (1994) provides a detailed description of this work.

4.2 Stratified Fluids

4.2.1 *Narrow current generation without topography*

After initiating the source-sink forcing, the motion along the free-surface develops a Gaussian-like azimuthal profile. Gradually, the entire fluid column accelerates due to rotation and stratification, producing an unstable current, with the strongest speed being found at the surface and decreasing with depth. Characteristic in all of these flows are cross-stream instabilities. These wave-like meanders eventually reached a quasi-steady state, combined with approximate equally distributed cyclonic vortex cells arranged azimuthally, but concentrated left of the main flow, facing downstream. Possessing a speed on-the-order of 1/3 that of the current, these features advected in a cyclonic manner within the tank annulus. Shown schematically in Figure 2 (for a set of five vortices), the number of vortices decreasing with increasing Ro, (see also, Chen et al., 1992). Further, Figure 3 displays a particle-streak photograph of the test section taken at a fluid level of $z/H = 0.53$, z being the vertical coordinate with the origin fixed to the floor of the test cell. In the caption, the subscript "c" denotes the use of W_s as the characteristic lengthscale, for topography is absent. Note the disk and ring edge, along with the two vortex cells (see arrows). The current can be seen meandering in a cross-stream fashion. Flow is from right to left.

To further understand the current, data recorded with the particle-image processing system was performed. The schematic in Figure 4 shows the size and position of the particle-tracking window in relation to the test section. Figures 5a,b show two consecutive flow fields, taken at $z/H = 0.53$, for parameters identical to those in Figure 3. In this case, the dimensions of the test section approximate 40 cm by 30 cm, over which a 32 by 24 point grid was imposed. The flow field was averaged over 30 video frames (one second), collapsing the velocity, based on approximately 500 particles to the grid points. Both the velocity field (indicated by the arrows) and the corresponding vorticity (shown as color contours) are shown. For reference, the color scale for vorticity (s^{-1}) is presented. The images indicate the advection of a cyclonic vortex cell into the test section during the 90 second time interval.

By investigating such images at different elevations, it was demonstrated that the current had a vertical shear with similar horizontal structure at various depths, but with vorticity decreasing with depth. Adjustment of the flowrate served to increase the overall strength of the current, and decrease the number of vortex cells observed.

4.2.2 *Narrow current-topography interaction*

Experimentation with the presence of topography involved adjustment of the flowrate as well as the position of the obstacle relative to the centerline of the annulus.

Figure 6 is a particle-streak photograph showing the formation of a cyclonic vortex in the lee of the obstacle (see arrow) at z/H = 0.53. The dashed line indicates the base of the topography, while the bright are patterns outline the reflection from two juxtaposed light sheets. Also seen is the presence of a vortex cell. Flow is again from right to left. In this case, the topography rests at a position y_T/D = -0.25. Owing to stratification effects the flow above the obstacle does not generate a lee-side vortex. Due to the meandering nature of the current, no profound differences are seen with adjustment of the topography to other y_T/D positions.

Digimage was also employed to study the current-topography interaction. Figures 7a,b are the velocity and vorticity fields obtained from particle-imaging for the identical experiment as in Figure 6. The white circle outlines the base of the obstacle. At this observation level, the topography interacts with the fluid and thus, the velocity and vorticity fields directly above the center portion of the obstacle must be ignored. First, note the approach of a cyclonic vortex-cell prior to its interaction with the obstacle. Also, two structures in the lee of the topography can clearly be seen. This includes both a cyclonic vortex (white-cored feature to the right, facing downstream), and accompanying anticyclonic region (black-cored, to the left) formed due to the high localized value of shear. Unlike Figure 7a, 7b (105 seconds later in time) shows a flow structure dominated by the presence of the large cyclonic vortex-cell, as it has fully impinged upon the obstacle. The patterns depicted were observed to be approximately periodic, with the cyclonic eddy, and accompanying anticyclonic region returning to their original strengths and positions. In addition, similar qualitative results are seen at a level z/H = 0.7 (just below the peak of the obstacle), with the two structures possessing a corresponding decrease in strength. Additional experimentation is described in more detail by McGuinness (1994).

5. Conclusions

Using a surface-driven source-sink technique, a vertically sheared narrow current, possessing a Gaussian-like horizontal profile, is generated within an annular facility and allowed to interact with topography in the presence of background rotation. Important parameters include the Rossby, Ekman, and Burger numbers, normalized topographic lengths, and normalized positions of the obstacle within the annulus.

The present preliminary experiments focus on stratified fluids with and without the presence of topography. Particle-streak photographs outlined the qualitative flow structure within a 120° test section, while particle-imaging techniques provided more quantitative details of the velocity and vorticity fields within a smaller area. Both showed a horizontally and vertically sheared current possessing cross-stream instabilities, combined with azimuthally distributed cyclonic vortex structures. These were quasi-steady, and advected around the facility annulus with a speed 1/3 that of the current. Cases with topography outlined a complex interaction between the current and obstacle. Specifically, a cyclonic vortex and accompanying anticyclonic region were generated in the obstacle lee, decreasing in strength with increasing fluid elevation. Similar qualitative results ensued when the obstacle was repositioned within the annulus.

Scant laboratory, and only selected numerical, modeling has been performed in the area of horizontally and vertically sheared currents in the presence of topography. Field observations have shown similar features in the vicinity of Fieberling Guyot. In two studies of Fieberling, Roden (1991, 1993) observed "jet-like" currents in the vicinity of the seamount which possessed both horizontal and vertical shear. The lateral lengthscale of the features showed all to be "narrow currents," i.e., having a horizontal dimension on-the-order of the characteristic width of the topography. Further, a weak mean current with intermittent cyclonic and anticyclonic eddy fields were also discovered. These preliminary experimental results are in consonance with the field observations. Through the present work, the feasibility of modeling current-topography interaction has been shown. Employing the same source-sink approach, other current-topographic feature interactions, such as continental shelf breaks and multiple obstacles, could be studied. Further, the use of recently developed particle-imaging software has also proved itself in applications dealing with geometry, rotation, and background stratification.

Acknowledgments

References

BAINES, P.G. & DAVIES, P.A. 1980 Laboratory studies of topographic effects in rotating and/or stratified fluids. *Orographic Effects in Planetary Flows* , GARP Publication Series No. 23, 233-299.

BANNON, P.R. 1980 Rotating barotropic flow over finite isolated topography. *J. Fluid Mech.*, **101**, 281-306.

BOYER, D.L., CHEN, R., TAO, L. & DAVIES, P.A. 1993 Physical model of bathymetric effects of the Antarctic Circumpolar Current. *J. Geophys. Res.* **98**, 2587-2608.

BOYER, D.L., DAVIES, P.A., HOLLAND, W.R., BIOLLEY, F. & HONJI, H. 1987 Stratified rotating flow over and around isolated three-dimensional topography. *Phil. Trans. R. Soc., Lond.* **A322**, 213-241.

BOYER, D.L. & ZHANG, X. 1990 The interaction of time-dependent rotating and stratified flow with isolated topography. *Dyn. Atmos. Oceans*, **14**, 543-575.

CHEN, R., BOYER, D.L. & TAO, L. 1992 Stability characteristics of jets in linearly-stratified, rotating fluids. *J. Geophys., Astrophys. Fluid Dyn.* **65**, 1-29.

HAIDVOGEL, D.B., BECKMAN, A. & HEDSTRÖM, K.S. 1991 Dynamical simulations of filament formation and evolution in the coastal transition zone. *J. Geophys. Res.* **96** (C8), 15017-15040.

McGUINNESS, D.S. 1994 Physical modeling of narrow current-topography interaction in a rotating and stratified environment. M.S. Thesis, Arizona State University.

OSTER, G. & VAMAMOTO, M. 1963 Density gradient techniques. *Chem. Rev.* **63**, 257-268.

PEDLOSKY, J. 1987 Geophysical Fluid Dynamics, Springer-Verlag. New York, 2nd. ed.

RODEN, G.I. 1991 Mesoscale flow and thermohaline structure around Fieberling seamount. *J. Geophys. Res.* **96**, 16653-16672.

RODEN, G.I. 1993 Effects of the Fieberling seamounts group upon flow and thermohaline structure in the Spring of 1991. *J. Geophys. Res.*, in press.

SPALL, M.A. & ROBINSON, A.R. 1990 Regional primitive equation of the Gulf Stream meander and ring formation region. *J. Phys. Oceanogr.* **20** (7), 985-1016.

ZHANG, X. & BOYER, D.L. 1993 Laboratory study of rotating, stratified, oscillatory flow over a seamount. *J. Phys. Oceanogr.* **23**, 1122-1141.

ZHANG, X., McGUINNESS, D.S. & BOYER, D.L. 1994 Narrow barotropic currents impinging on an isolated seamount. *J. Geophys. Res.*, in press.
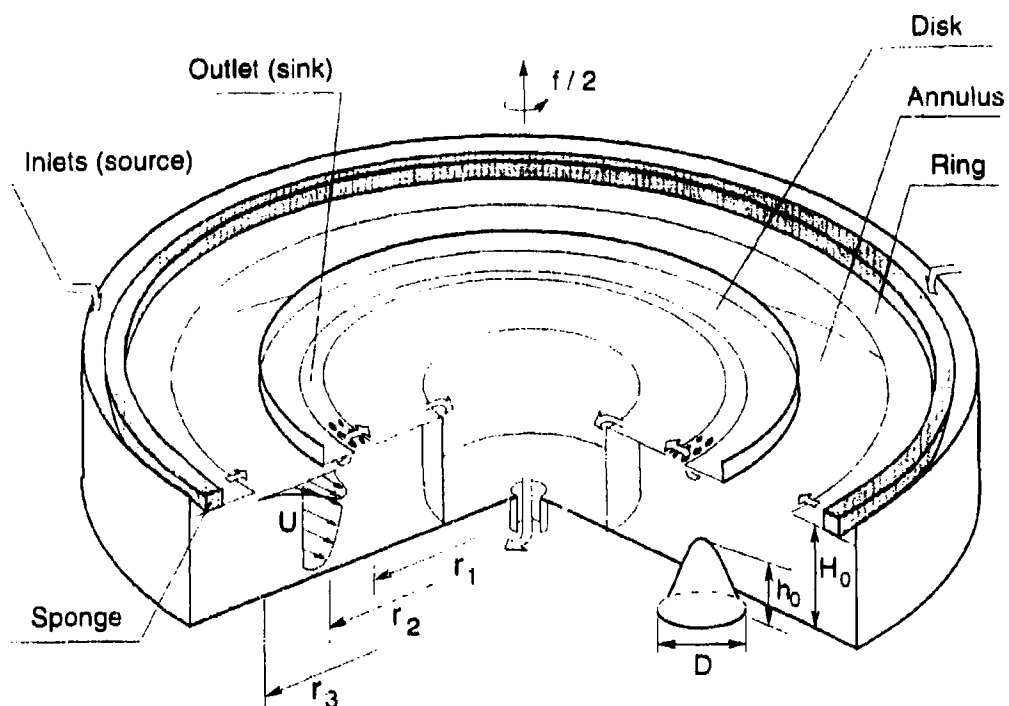
Figure 1. Schematic diagram of test cell and generation of narrow current.
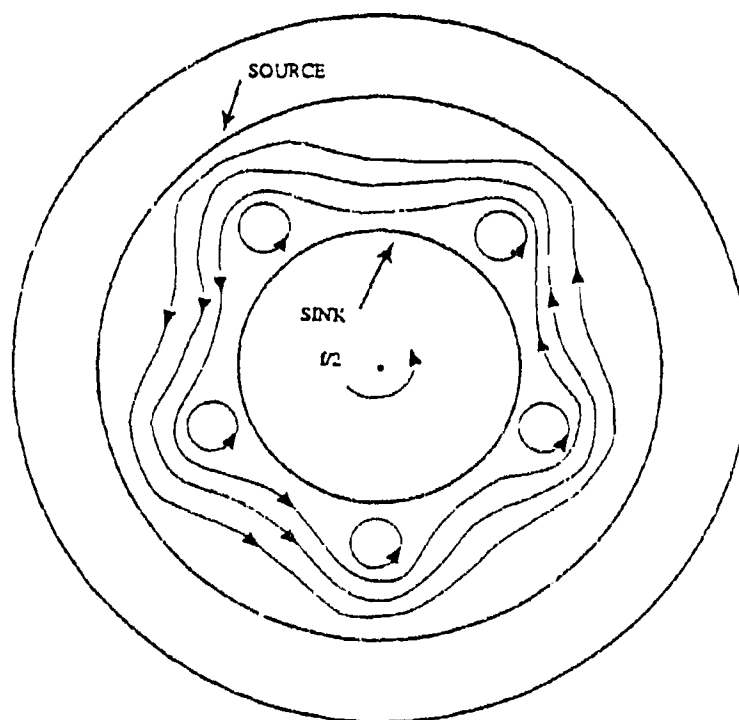
Figure 2. Schematic representation of an unstable current possessing 5 cyclonic vortices.

Figure 4. Schematic representation of particle-imaging geometry.
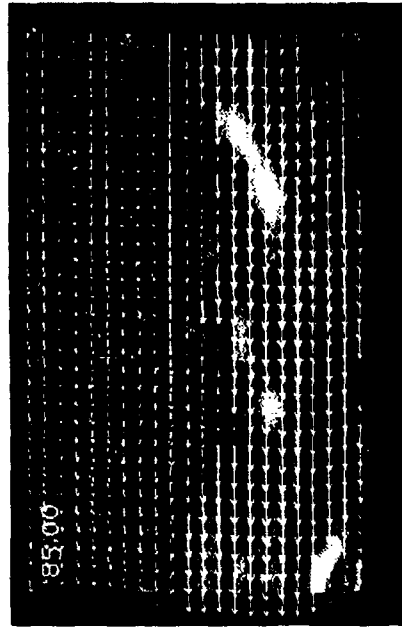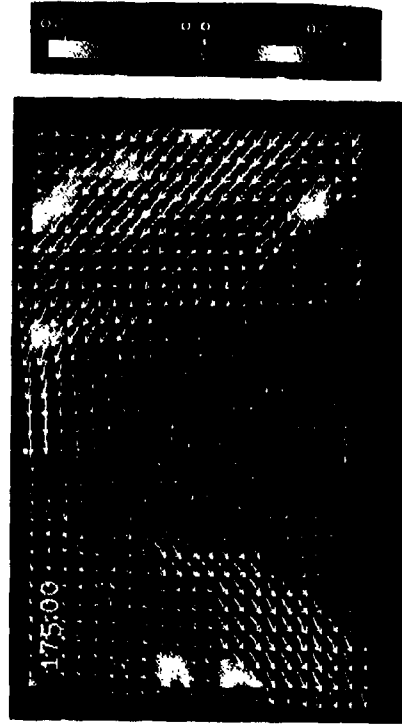
(b)

Figure 5. Successive velocity and vorticity fields over a 90 second interval for $Ro_c = 0.05$, $E = 2.3(10)^{-4}$, $S_c = 0.22$ and $z/H = 0.54$

Figure 3. Particle-streak photograph for $Ro_c = 0.03$, $E = 2.3(10)^{-4}$, $S_c = 0.34$ and $z/H = 0.54$.

(a)
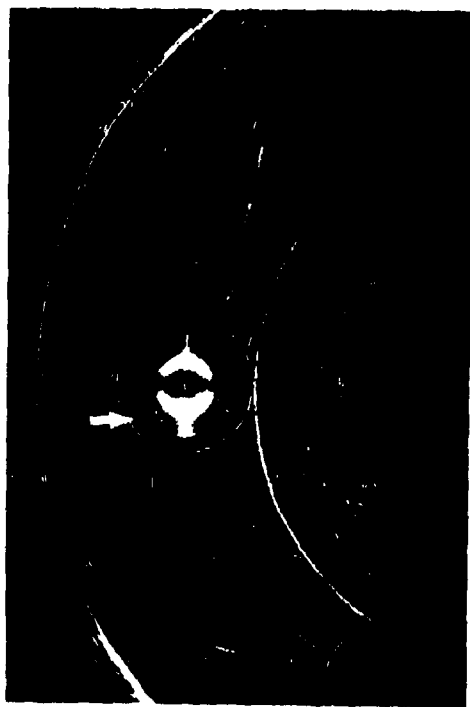
Figure 6. Particle-streak photograph of narrow current-topography interaction for $Ro = 0.04$, $E = 2.3(10)^{-4}$, $S = 0.76$, $y_T/D = -0.25$ and $z/H = 0.54$.

(b)

(a)
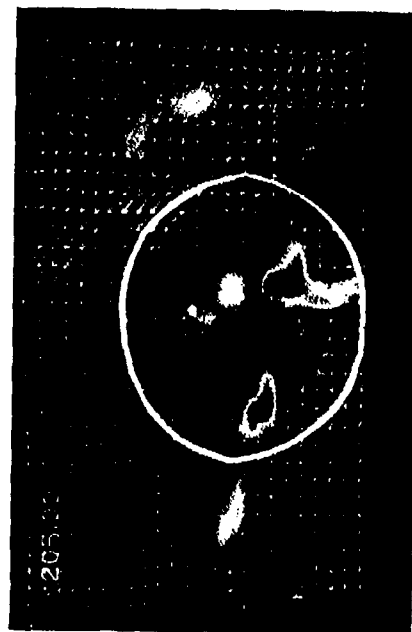
Figure 7. Successive velocity and vorticity fields, over a 105 second interval, of narrow current-topography interaction from particle-imaging for $Ro = 0.05$, $E = 2.3(10)^{-4}$, $S = 0.63$, $y_T/D = -0.25$ and $z/H = 0.43$.

Experimental Study of Buoyant Jet Discharge

In a Rotating System

J.F. Atkinson and G. Lin

Department of Civil Engineering
State University of New York at Buffalo
Buffalo, New York 14260 (USA)

Abstract

An experimental study is described in which a buoyant jet is discharged at the surface of a rotating tank of water. This setup is meant to simulate the discharge of rivers or estuaries into large lakes or coastal areas. The present experiments are performed with initial discharge densimetric Froude number greater than one, so that a "surface-to-bottom" discharge is obtained. The width of the discharge is also smaller than the Rossby radius, so that flow extends across the entire width of the opening. The overall objective of this research is to develop a model to predict the behavior of these flows as functions of rotation rate, bottom friction, and discharge buoyancy, momentum and aspect ratio. These results are to be used along with numerical studies so that other effects might be incorporated such as ambient cross-flow or wind stress. The present results concern the importance of rotation on the plume trajectory in the near-field region where there is still bottom attachment. Experiments are performed for discharge without a bottom (i.e., discharge on a step) and with a bottom of constant slope. The experimental results are consistent with a scaling analysis which shows the relative importance of the Coriolis term in the momentum equations for this region, depending on discharge and bottom conditions.

Introduction

The marginal band in which land and sea (including large lakes) meet represents an important and complicated system. Human activities tend to be concentrated in such areas, which support intense economic development, particularly where large rivers empty into seas (see, for example, discussion by Land-Margin Ecosystems Research Coordinating Committee, 1992). These regions are typically rich in nutrients, though contaminants may also be transported from inland, having various adverse effects. The fate of these nutrients and contaminants, as well as sediments, depends on the interacting factors which determine the trajectory and mixing of the discharged water. The basic physical behavior of these systems, particularly the interaction between rivers or estuaries and the seas into which they discharge, provides a number of interesting fluid mechanics problems, but it is also interesting because of its implications for waste management and future economic development. The present work is aimed at developing a greater understanding of these important flows.

When fresh water from rivers or less salty water from estuaries enters the sea an interface forms due to the density difference between the flowing and receiving waters. This effect is also associated with thermal discharges from power plants into colder lake or coastal waters. Buoyant discharges have been extensively studied, being important for a number of applications in both natural and engineered systems.

These discharges often dominate local physical and biological processes. The near-field processes also have implications for the vertical structure of the ocean interior (Garrett et al., 1993) or for the general circulation on a shelf (Chapman and Lentz, 1994). Studies of these discharges must consider a broad range of spatial scales, from about 10^0 - 10^3 km. For the present study, interest is primarily for flows which have a characteristic length scale large enough that effects of the earth's rotation are significant. In addition to rotation, these flows are influenced by buoyancy, initial momentum, entrainment and frictional stresses.

Due to their importance in environmental hydraulics, buoyant jets discharged near the water surface have been examined in a large number of studies in the engineering literature. Physical modeling of smaller-scale flows (i.e., without rotation) has been successful in developing predictions of entrainment and subsequent dilution (Jirka, 1982). Many of the earlier studies in this area are reviewed by Jirka (1982) and Chu and Jirka (1986). Experimental studies of large-scale buoyant discharges are less common, though several important dynamical features have been demonstrated. These include the formation of an anticyclonic turning region near the source and the subsequent formation of a right-bounded (northern hemisphere) coastal current (McClimans, 1986; Atkinson and Masse, 1990). Although the estimation of initial entrainment and mixing is thought to be fairly well understood, it should be noted that most of these studies have considered discharges over a sharp drop-off. A significant difference between this situation and the conditions of a coastal jet is that entrainment may occur immediately from underneath in the former case, while for the latter case bottom attachment initially prevents vertical entrainment. Atkinson (1993) reviewed the problem of estimating the position of the point of detachment from the bottom and developed a model to calculate this position based on a numerical integration of the longitudinal momentum equation. However, like the experiments used to generate data for model comparison, the model did not consider rotation and it is unclear how this might affect the calculations for the separation point.

A number of field studies have been performed to document buoyant plumes and their frontal and mixing characteristics (e.g., Garvine, 1974; Wright and Coleman, 1977; Luketina and Imberger, 1987; Boicourt, 1973; Masse and Murthy, 1990). However, only a few experimental studies have been performed for rotating buoyant discharges. One example is the study by Whitehead (1987), who carried out experiments to examine steady, barotropic, inviscid flow through a rectangular opening in a rotating frame, with the intent of simulating flows through straights in the oceans. He showed that it was not necessary for the channel width, W, to be greater than the Rossby radius, $r_i = (g'h)^{1/2}/f$, in order for rotation effects to be seen within the channel. In this definition $g' = g\Delta\rho/\rho_0$ is reduced gravity, where $\Delta\rho$ is the density difference between the buoyant discharge and the receiving water, ρ_0 is the jet density, g is gravitational acceleration, h is discharge depth and f is the Coriolis parameter. Other researchers have used the Kelvin number, $K = W/r_i$ to determine when rotation should be important (e.g., Masse and Murthy, 1990). For $K >> 1$, the channel flow will tend to concentrate along the left-hand (viewed facing upstream) bank and a reverse flow (upstream) may even occur on the right bank. Unfortunately, the physical dimensions of these flows usually preclude the gathering of very detailed synoptic data sets. Physical modeling experiments, where various features can be controlled, can add significantly to our knowledge of these flows.

Experimental Apparatus and Procedures

The apparatus, sketched in Figure 1, consists of a rectangular tank, approximately 2 m x 3 m in surface area, installed within a rotating room capable of speeds up to 6 revolutions per minute. The inlet is a rectangular channel with adjustable width, up to 30 cm. A broad overflow weir installed at the opposite end is used to maintain constant depth during an experiment. The tank has clear side walls for viewing. Experiments may be done either with or without an adjustable-slope bottom in place. Salinity is used to

provide the required buoyancy. Because of plumbing problems associated with the rotation of the room, the apparatus is designed to hold all the water, both inflow and discharge, needed for a given test. The test section (the uppermost of three compartments) has a depth of 25 cm and has clear plexiglass sides for viewing. The rotating room is supported by a single thrust bearing with a 100-ton capacity. It has been checked with surveying instruments to insure rotation is in the horizontal plane only, and tests have shown that the rotation is nearly perfectly smooth (i.e., a water surface remains smooth while being rotated).

An experiment is performed by filling the test section with water of desired salinity and, for rotating tests, "spinning up" the tank for a period of about an hour to establish a steady rotating system. Fresh water is then pumped at a given flow rate from the lower compartment up through a "stilling" box and onto the inlet channel, from which it discharges into the test section. A separate tank holds additional salt water which can be pumped into the test section through a diffuser plate during the course of an experiment to make up water entrained into the jet. The water which passes over the downstream weir falls into the middle compartment of the apparatus and can either be stored for disposal after the experiment or recycled through the lower compartment to allow longer test runs. One potential disadvantage of this latter procedure is that the inflow salinity does not remain perfectly constant. However, tests performed so far have shown that the change in density of the jet water is negligible over a typical test run. The discharge of water over the downstream weir creates a small net flow (and possible associated circulation) in the test section, but experience has indicated that this effect is negligible.

The primary goal of the present set of experiments was to document the overall trajectory of the discharge under different bottom conditions and rotation rates. Flow visualization was used as the primary instrumentation. The bottom of the test section was marked with a 10 cm square grid. Dye is added to the inflowing water and an overhead video camera records the basic motions. Test conditions for the present experiments are summarized in Table 1. This series of tests evaluates flow trajectories for three different bottom conditions, with and without buoyancy and with and without rotation. The three bottom conditions were (1) discharge on a *step*; (2) shallow water, or *flat* discharge (depth of receiving water was equal to depth of discharge); and (3) discharge on a shelf with constant *slope*, $S = 10\%$. For all cases reported here the inflow discharge rate and geometry were kept constant at 1.0 l/s, and 20.0 cm wide by 1.5 cm deep, respectively. This gives a discharge velocity, $U_0 = 33.3$ cm/sec.

For the stratified tests, Tests 4 and 13, the Rossby radius is calculated as $r_i = 6.5$ cm and 10.3 cm, respectively, resulting in values for the Kelvin number, K, around 2 - 3. This implies that rotation effects are probably present in the discharge channel, although observations indicated that there was still approximately uniform flow across the mouth of the discharge. In addition, the depth of flow was only 1.5 cm, so that detection of a possible lateral tilting of the water surface is difficult. The parameters for the present tests were chosen to evaluate the general behavior of the discharge after entering the test section, but future tests will have to be conducted with smaller K. Tests with rotation were conducted until there was an apparent effect of the side walls on the observed flow patterns and a return flow was generated along the upstream wall. Tests without rotation could be run for longer periods without a significant side-wall effect. In either case, however, it is not possible to simulate far-field conditions with this setup.
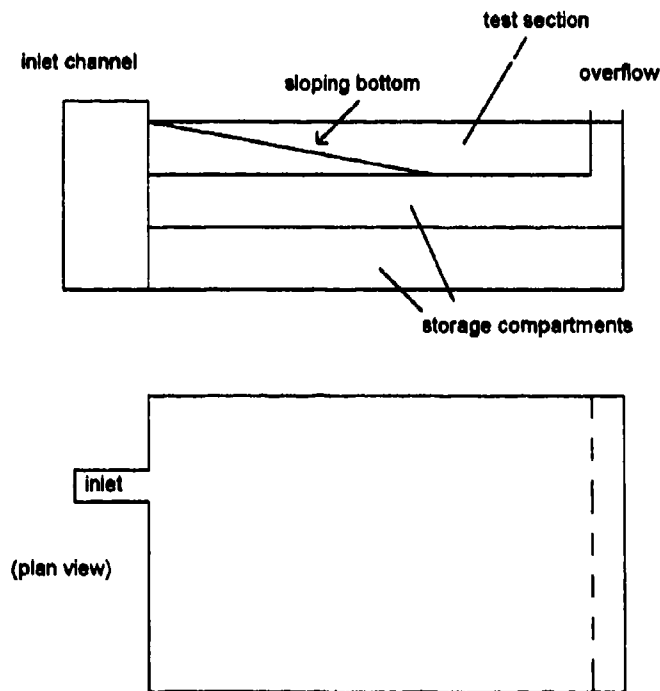
Figure 1. Experimental apparatus.

Run Conditions				Observations		
Test No.	Bottom	ω (sec^{-1})	g' (cm/sec^2)	L_1 (cm)	L_2 (cm)	R (cm)
2	step	0.262	0.0	100	30	55
3	step	0.262	0.0	150	35	55
4	step	0.262	7.75	145	20	115
5	flat	0.0	0.0	---	---	---
6	flat	0.262	0.0	180 *	30	130
7	flat	0.419	0.0	140	10	90
8	slope	0.0	0.0	---	---	---
9	slope	0.262	0.0	220 *	25	115
10	slope	0.0	0.0	---	---	---
11	slope	0.262	0.0	250 *	25	135
12	slope	0.0	19.6	---	---	---
13	slope	0.262	19.6	110	30	70

notes: ω = rotation rate = f/2; * values outside range of camera, but are at least 200 cm

Table 1. Test data and observations.

4

Results and Analysis

The last three columns in Table 1 list observed lengths describing the geometry of the discharge flow trajectory, as shown in Figure 2. Here, L_1 is the maximum horizontal distance from the discharge wall reached by the plume, L_2 is the distance reached before the plume starts to turn and R is the radius of curvature of the turning plume. Of course, these values are developed from observations on videotapes and are therefore subject to a certain degree of uncertainty, estimated at ± 5 - 10 cm. However, there are some trends which are indicated. For example, a comparison of Tests 6 and 7 shows the expected result that the discharge turns on a tighter curve (i.e., smaller R) when ω is larger, with all other conditions the same.

It is also interesting to compare Tests 2 (or 3) and 6, which concern a neutral discharge on either a step or into a shallow receiving water (flat bottom). In both cases the plume starts turning at about the same location, but the discharge on a step is not able to penetrate into the receiving water as much as the shallow water flow, and turns more sharply. This loss of forward motion is apparently due to entrainment and vertical spreading; the shallow water discharge maintains stronger momentum into the receiving water. This effect can also be seen by looking at Test 9 or 11, which considered similar conditions, except with a sloping shelf in place. The initial turning point is again about the same, but the curvature was intermediate between the values for the step and shallow water discharges. This result is to be expected, since the limitation on vertical spreading and entrainment is less than for the flat bottom, but greater than for the step discharge. The plume in this case was observed to maintain contact with the shelf until it reached the bottom of the tank (the shelf slope was less than the observed vertical slope of the spreading step discharge). Bottom friction will also affect the plume and slow its forward progress, but this effect is not as strong as entrainment. Future studies should examine this process more closely.

The effect of density stratification is seen by comparing Tests 4 and 2 (or 3) and Tests 13 and 9 (or 11). Buoyancy works in much the same way as the shallow bottom or slope, in terms of limiting vertical spreading. In Test 4, which considers a salinity difference of less than 1% (by weight), the flow characteristics were very similar to the discharge in Test 6, though the turning was slightly sharper and the maximum penetration into the tank was somewhat less. This is to be expected because entrainment is reduced, but not as much as with the solid bottom. A similar result is see in Test 13, which had a salinity difference more than twice the difference in Test 4 (see Table 1). In this case the plume started turning at about the same location and had about the same R, but L_1 was larger. This is believed to be related to the additional reduction in vertical entrainment associated with the stronger stratification, and is also consistent with a larger calculated value for Rossby radius (see below), but further tests are needed to quantify this effect.

One additional length scale of interest is the distance over which the jet remains attached to the bottom, for tests with a sloping bottom, or the distance at which the jet reaches the bottom, for tests with a step discharge. This point was easier to identify with step discharges because the sloping shelf did not interfere with observation. For Tests 2 and 3 the flow extended throughout the depth within about 1 m offshore. With the shelf in place it was easier to observe the separation point in tests without rotation. For example, in Test 12 the separation point was observed approximately 80 cm offshore. In Test 13, however, it was not possible to identify the exact location of this point, due to the turning of the plume, although it was in the same region. An initial approach for analyzing this problem may be obtained from Atkinson (1993), who developed a model based on a numerical integration of the longitudinal momentum equation in order to determine the point of bottom detachment for a buoyant discharge on a slope. However, that analysis did not consider possible effects of rotation. It is not clear, for instance, whether total depth or total distance along the trajectory is more important in controlling bottom separation (note

that depth is less along an equal distance in rotating cases, due to the curvature of the jet trajectory), and on-going tests are being conducted to evaluate this question.
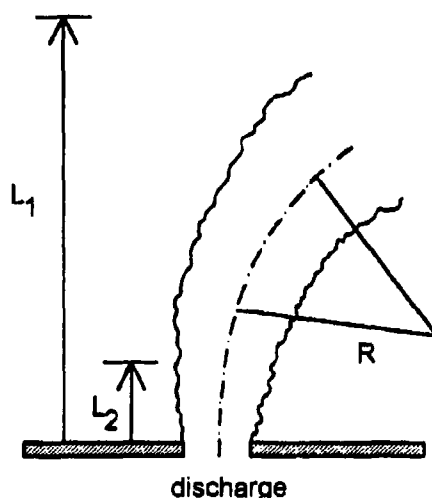

Figure 2. Definition sketch for length variables describing plume geometry.

In addition to observations of the bottom separation point, tests without rotation provide a comparison of observations of the front produced when the fresh water flow was started. For all cases the front was observed to spread radially (or laterally) more quickly in tests without rotation. With rotation this spreading was reduced and a typical "mushroom" head would appear. Vortices generated at the sides of the advancing front tended not to drift significantly from the main trajectory of the jet and became engulfed into the head, while lateral spreading of the front was much stronger without rotation. This restriction of horizontal spreading is consistent with other studies in rotating systems (see, for example, Helfrich and Battisti, 1991) and is a feature that must be recognized in developing models of large-scale buoyant discharges.

In order to evaluate the trajectory of a buoyant discharge on a slope a number of variables may be defined. The variables which determine basic flow characteristics include discharge velocity U_0 and depth h_0, g', f, W and r_i. In general, ambient cross-flow velocity should also be considered (e.g., Chu and Jirka, 1986), but the present experimental apparatus cannot simulate this feature and it is assumed zero for this discussion. There are several important dimensionless parameters which may be formed from the above variables. As previously mentioned, the Kelvin number indicates the extent of rotational effects expected within the channel itself, before discharge. The densimetric Froude number, $Fr_0 = U_0/(g'h_0)^{1/2}$, controls the extent of bottom attachment. Classic arrested wedge analysis (e.g., Turner, 1973) shows that $Fr_0 > 1$ is a necessary condition for bottom attachment at the discharge point (i.e., a "surface-to-bottom" discharge). In fact, experiments on jets in non-rotating systems have shown that Fr_0 must be greater than about 2.5 for there to be bottom attachment on the slope (Safaie, 1979). Values for Fr_0 were 9.8 (Test 4) and 6.1 (Tests 12 and 13). Reynolds number, $Re = U_0L/v$, where L is a horizontal length scale and v is kinematic viscosity, may be important to describe turbulent mixing effects, but according to McClimans and Saegrov (1982) the actual value is not critical as long as it is well above 500. The only imposed horizontal length

6

scale is the width, W, though r_i is also important for rotating tests. Values for Re are all well above 500 for the tests reported here. The Rossby number, Ro = U_o/fL, indicates the relative importance of rotation in the equations of motion. Using L = W, values for Ro were 3.2 for all rotating tests except Test 7, which had Ro = 2.0. These values are of order O(1), signifying that rotation should be important, as indeed the observations support.

A far-field flow may be defined after the point at which the discharge starts to show significant curvature (L_2 in Fig. 2). If a geostrophic balance is in place then it can be shown that $Fr^2 \approx Ro$ (Fr is the local value for Froude number) and since Fr should be approximately of order O(1) (Atkinson et al., 1994), then the far-field may be defined as starting at the point where the local value of Ro approaches 1. The length scale in the definition for Ro then becomes equal to the Rossby radius, r_i. In other words, the plume would be expected to turn over a distance r_i. This interpretation is consistent with previous discussions of r_i (Garvine, 1987). Atkinson et al. (1994) also showed that this conclusion was consistent with observations of the Niagara River plume in Lake Ontario. Alternatively, if a geostrophic balance is not in place then other factors must be taken into consideration. For example, the present observations indicate that L_2 is about three times greater than r_i, based on initial discharge depth and relative buoyancy, and also that the plume turns before it separates from the bottom. Therefore, bottom friction should still be important and the above analysis will not be valid.

Conclusions

Experiments have been performed to study buoyant discharges in a rotating system. The data set is still limited to a relatively small number of tests, but the general behavior of the flow in response to changes in rotation, bottom conditions and buoyancy has been outlined. On-going experiments are using more detailed instrumentation to evaluate specific questions, such as the effect of rotation on the bottom separation point on a slope, and the effect of larger Kelvin numbers on the characteristics of the discharge itself. Some preliminary scaling arguments have been presented which appear to describe the general behavior, but these need to be refined as more data become available.

Acknowledgment

References

Atkinson, J.F. and A M. Masse (1990), "Physical Modeling Study of the Niagara River Plume", ASCE Hydraulics Division Specialty Conf., San Diego.

Atkinson, Joseph F. (1993), "Detachment of Buoyant Surface Jets Discharged on a Slope", Journal of Hydraulic Engineering, 119, 878-894.

Atkinson, J.F., G. Lin and M. Joshi (1994), "Physical Model of Niagara River Plume", tentatively accepted, Journal of Great Lakes Research.

Boicourt, W.C. (1973), "The Circulation f Water on the Continental Shelf from Chesapeake Bay to Cape Hatteras", Ph.D. dissertation, Johns Hopkins Univ., Baltimore, MD.

Chapman, David C. and Steven J. Lentz (1993), "Trapping of a Coastal Density Front by the Bottom Boundary Layer", to appear in J. Phys. Oceanog.

Chu, V.H. and G.H. Jirka (1986), "Surface Buoyant Jets and Plumes", in *Encyclopedia of Fluid Mech.* 6, ed. N. Chermisinoff, Gulf Publ. Co., Houston, TX.

Garrett, Chris, Parker MacCready and Peter Rhines (1993), "Boundary Mixing and Arrested Ekman Layers: Rotating Stratified Flow Near a Sloping Boundary", *Ann. Rev. Fluid Mech.* 25, 291-323.

Garvine, Richard W. (1974), "Physical Features of the Connecticut River Outflow During High Discharge", *J. Geophys. Res.* 79, 831-846.

Garvine, Richard W. (1987), "Estuary Plumes and Fronts in Shelf Waters: A Layer Model", *J. Phys. Oceanog.* 17, 1877-1896.

Helfrich, Karl R. and Thomas M. Battisti (1991), "Experiments on Baroclinic Vortex Shedding from Hydrothermal Plumes", J. Geophys. Res. 96, (C7), 12,511-12,518.

Jirka, G.H. (1982), "Turbulent Buoyant Jets in Shallow Fluid Layers", in *Turbulent Jets and Plumes*, ed. W. Rodi, Pergammon Press, Oxford.

Land-Margin Ecosystems Research Coordinating Committee (1992), "Understanding Changes in Coastal Environments: The LMER Program", EOS 73 (45), Nov. 10.

Luketina, D.A. and J. Imberger (1987), "Characteristics of a Buoyant Surface Jet", *J. Geophys. Res.* 92, 5435-5447.

Masse, Ann K. and C.R. Murthy (1990), "Observations of the Niagara River Plume", *J. Geophys. Res.* 25 (C9), 16097-16109.

McClimans, T.A. (1986), "Laboratory Modeling of Dynamic Processes in Fjords and Shelf Waters", in *The Role of Freshwater Outflow in Coastal Marine Ecosystems*, ed. S. Skreslet, NATO ASI series G7, 67-84.

McClimans, T.A. and S. Saegrov (1982), "River Plume Studies in Distorted Froude Models", *J. Hydraulic Res.* 20, 15-27.

Safaie, Bijan (1979), "Mixing of Buoyant Surface Jet Over Sloping Bottom", *J. Waterway Port Coastal Div. ASCE* 105, 357-373.

Turner, J. Stewart (1973), *Buoyancy Effects in Fluids*, Cambridge Univ. Press.

Whitehead, J.A. (1987), "Flow of a Homogeneous Rotating Fluid through Straights", *Geophys. Astrophys. Fluid Dynamics* 36, 187-205.

Wright, L.D. and J.M. Coleman (1977), "Mississippi River Mouth Processes: Effluent Dynamics and Morphologic Development", *J. Geology* 82, 751-778.

DEVELOPMENT OF BOUNDARY LAYERS
AND TRANSPORT PROCESSES EFFECTED BY BUOYANCY

E.I.Nikiforovich, N.F.Yurchenko

Institute of Hydromechanics, Ukrainian Academy of Sciences
ul. Zheliabova,8/4,252057 Kiev, UKRAINE

The model of a stratified fluid was shown [Nikiforovich, Maderich] to have the proper spatio-temporal scales depending on the extent of its thermodynamical nonequilibrium. Then in the frame of this concept, the model of a homogeneous fluid is a singularly degenerated one.

Physically it means that bulk vorticity sources appear in a fluid due to available thermodynamic nonequilibrium (that is due to stratification), their intensity having been proportional to the value of this nonequilibrium. In a general case nonlinear interaction between vorticity sources of thermodynamical and fluid dynamical nature (the second one corresponding to the homogeneous fluid flow) defines a flow field in a stratified fluid. Stratification degeneration results in the degeneration of the bulk vorticity sources which should qualitatively change the flow field pattern.

The typical case of the above mentioned interaction represents the development of a temperature stratified boundary layer (SBL) over a flat plate. This problem investigation must give the most clear insight into the mechanisms controlling the behaviour of flows with various types of vorticity.

There are two aspects of the problem which were studied practically independent from each other. The first one deals with the buoyancy effect on the 2D boundary layer structure and heat transfer. The second one concerns the boundary layer stability, transition to 3D motion, its structure and heat transfer peculiarities. Experimentaly 3D motion of the longitudinal vortical type was found to be certainly preferable in boundary layers over heated surfaces; space scales of this structure and its downstream observed positions were estimated but not determined through the basic flow parameters. Numerous theoretical works [G.Wichern.1991;W.Schneider,1979] represent attempts to find a solution of boundary layer equations in a form of expansions of a parameter discounting buoyancy using numerical methods and the idea of local self-similarity or nonsimilarity. However the solutions were found only for a narrow range of the expansion parameter values. Besides, the expansion convergence is not evident.

Thus the purpose of this work is as follows:

(i) to construct SBL equations, to analyze the nonlinear interaction of bulk and surface vorticity sources;

(ii) to study physical mechanisms of 3D vortex structures development in SBL;

(iii) to analyze spatio-temporal characteristics of vortical structures arising due to buoyancy; to verify the developed approach using the comparison of theoretical estimates and experimental results.

PROBLEM FORMULATION

Homogeneous, viscous and heat conducting flow with velocity U_0 and temperature T_0 over a horisontal (for simplicity) flat plate with temperature T, is considered (fig. 1). Viscosity ι

and heat conductivity coefficients are supposed to be constant. Navier-Stokes, continuity and heat conductivity equations in a coordinate system related to the plate have a form of

$$\frac{\partial w}{\partial t} + \vec{u}\nabla w = -\frac{1}{\rho_0}\frac{\partial p}{\partial z} + \nu\Delta w + F_z, \quad (1)$$

$$\frac{\partial u}{\partial t} + \vec{u}\nabla u = \frac{1}{\rho_0}\frac{\partial p}{\partial x} + \nu\Delta u + F_x, \quad (2)$$

$$\frac{\partial v}{\partial t} + \vec{u}\nabla v = -\frac{1}{\rho_0}\frac{\partial p}{\partial y} + \nu\Delta V + F_y, \quad (3)$$

$$\frac{\partial u}{\partial x} + \frac{\partial v}{\partial y} + \frac{\partial w}{\partial z} = 0, \quad (4)$$

$$\frac{\partial T}{\partial t} + \vec{u}\nabla T = \nu Pr^{-1}\Delta T \quad (5)$$
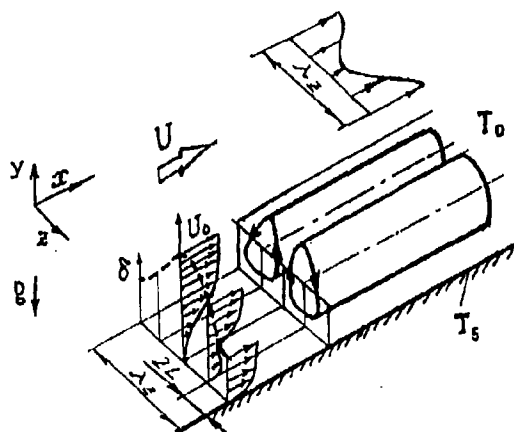
Figure 1. Schematic view of the boundary layer structure of the longitudinal vortical type with corresponding velocity distributions and shown space scales.

here $\vec{F} = \frac{\rho}{\rho_0}\vec{g} = \{F_x, F_y, F_z\}$ is a gravity force, $\vec{u}\nabla = u\frac{\partial}{\partial x} + v\frac{\partial}{\partial y} + w\frac{\partial}{\partial z}$ is a convective operator, $\Delta = \frac{\partial^2}{\partial x^2} + \frac{\partial^2}{\partial y^2} - \frac{\partial^2}{\partial z^2}$ is a Laplasian operator, Pr is the Prandtl number, $\vec{g} = g\vec{\gamma}$, g – gravity acceleration.

The most important role in the stratified fluid dynamics belongs to a form of the state equation which just defines the stratification. Here density is accepted to be linearly dependent on temperature

$$\rho = \rho_0[1 - \beta(T - T_0)], \quad (6)$$

$\beta = -\frac{1}{\rho_0}\left(\frac{\partial\rho}{\partial T}\right)_{T_0}$ being the coefficient of volumetric thermal expansion. The form of the state equation (6) naturally defines the nondimensional parameter $\varepsilon = \beta(T_s - T_0)$ which characterizes the degree of fluid thermodynamic nonequilibrium (for definiteness $T_s > T_0$). It is evident that the case of $\varepsilon = 0$ corresponds to the homogeneous fluid, for ordinary fluids and conditions $\varepsilon \ll 1$. The gravity force has a form of $\vec{F} = (1 - \varepsilon\theta)\vec{g} = \{0; -(1 - \varepsilon\theta)g; 0\}$, here $\theta = \frac{T - T_0}{T_s - T_0}$. If the dynamic pressure is introduced

$$p_d = p - \rho_0 g y \quad (7)$$

then the buoyancy force takes a form of

$$\vec{F}_b = \{0; \varepsilon g \theta; 0\} \quad (8)$$

and it follows from the eqs. (1) - (3) that in a general case the buoyancy force (8) defines the bulk vorticity source with the intensity proportional to the degree of fluid thermodynamic nonequilibrium. Now in addition the gravity acceleration g should be included in a set of defining parameters. In its turn it results in nonequilibrium space scales of $f_1(\varepsilon)(\nu^2/g)^{1/3}$, $f_2(\varepsilon)u_0^2/g$ and $f_3(\varepsilon)u_0^5/g\nu$ type, f_i being certain functions of parameter ε degenerating at $\varepsilon \to 0$. Just available nonequilibrium scales define the main difference between boundary layers in homogeneous and stratified fluid.

ON THE SELF-SIMILARITY OF SBL

As mentioned above, the limiting case of $\epsilon = 0$ corresponds to the flat plate boundary layer developing in a homogeneous fluid flow which is described by Prandtl equations. The influence of buoyancy may seem to be taken into account by introducing disturbances into solutions of Prandtl equations which are proportional to ϵ parameter. This approach was realized in [G.Wickern,1991;W.Schneider,1979]. However the situation appears to be much more complicated. Solutions of Prandtl equations are known to be self-similar. It results from the only space scale equal to ν/U_0. Thermodynamic nonequilibrium ($\epsilon \neq 0$) results in the occurence of space scales explicitly dependent on ϵ. Hence boundary layer self-similarity should not take place in a general case, i.e. the degeneration of SBL equations is singular [Nikiforovich,1993]. Thus deriving SBL equations, one can naturally suppose that the velocity field depends on the small parameter ϵ and that there exist nonequilibrium space scales different in streamwise and spanwise directions.

Asymptotic analysis of 2-D Navier-Stokes equations results in two basic conclusions:

(i) boundary layer approximation always requires the consideration of bouyancy;

(ii) stratification degeneration law for the existance of Blasius flow should have a form: $\epsilon Re^{1/2} \to 0$ as $\epsilon \to 0$ and $Re \to \infty$.

THREE-DIMENSIONAL VORTEX STRUCTURES IN SBL

Vorticity generation in a fluid body is a consequence of the potential energy transition into the kinetic one. This transition may acquire various forms of vortical motion. The widespread form of the vortical motion in boundary layers with body forces is the 3D motion of the longitudinal vortices kind. The experimental evidence of such flow structure development results from typical velocity distributions in boundary layers over heated surfaces displaying periodic velocity variations along a spanwise axis [e.g., see Akiyama et al, Gilpin et al]. In addition, heat transfer measurements along a heated horisontal bottom of an air tube [Yurchenko, Pedishius] showed a significant growth of heat transfer factors beginning from the downstream positions where the development of longitudinal vortices was observed (curve 1, fig.2).

Figure 2. Heat transfer factors for a horisontal flat plate heated from below and maximum fluctuating velocities along the boundary layer thickness depending on the length Reynolds number: 1, 3 - respectively (Re) and $u/U(Re)$ for the natural transition development; 2 - (Re) for the tripped boundary layer; 4 - respectively $u/U(Re)$ and (Re) for the case of generated longitudinal vortices

This process is in a good agreement with the growing intensity of velocity fluctuations (curve 3). The initiation of the development of longitudinal vortices with a certain space scale results in the augmentation of heat transfer near the heated wall (curve 5) even compared to the artificially turbulized boundary layer (curve 2).

Thus the understanding of mechanisms and prediction of spacio-temporal properties of 3D vortical structure in boundary layers depending on the defining flow parameters is important both in basic, and applied aspects. The most general approach and insight into the problem is provided by the development of theoretical analysis of SBL.

SPATIO-TEMPORAL PROPERTIES OF 3D SBL

As was mentioned above, 3D vortical structures in SBL arise due to buoyancy forces. Therefore it can be supposed that their spatio-temporal characteristics and the equation solution depend explicitly on the small parameter ϵ. In other words, it is supposed that the solution in the domain of a 3D boundary layer has a form of

$$U_* = U/U_0 = U_0^*(t^*, x^*, y^*, z^*) + \ldots \tag{9}$$

$$V_* = V/V_0 = \epsilon^q V_0^*(t^*, x^*, y^*, z^*) + \ldots \tag{10}$$

$$W_* = W/W_0 = \epsilon^p W_0^*(t^*, x^*, y^*, z^*) + \ldots \tag{11}$$

$$\theta = \theta_0(t^*, x^*, \ldots) + \ldots \tag{12}$$

$$p_d^* = p_d/\rho_0 U_0^2 = \epsilon^r p_{d_0}^* \tag{13}$$

here $U_0^*, V_0^*, W_0^*, p_{d_0}, \theta_0$ by the definition are the values of a unit order and nondimensional variables are given by

$$x^* = \epsilon^{-m} x/l_{0x}, \; y^* = \epsilon^{-n} y/l_{0y}, \; z^* = \epsilon^{-l} z/l_{0z}, \; t^* = \epsilon^{-k} t U_0/l_{0x}, \tag{14}$$

$l_{0x}, l_{0y}, l_{0z}, V_0, W_0$ are constant in value with dimensions corresponding to length and velocity (their magnitudes will be determined below); index of ϵ power is an arbitrary value which should be found. Substituting (9) – (12) expansions into the equation system (1) – (5) and taking the limit of $\epsilon \to 0$ one can get

$$m = -2/3, \, n = -1/3, \, q = 1/3, \, p = 1/3, \, l = -1/3, \, k = -2/3, \, r = 2/3 \tag{15}$$

$$V_0 = W_0 = (g\nu)^{1/3}, \; l_{0x} = U_0(\nu/g^2)^{1/3}, \; l_{0y} = l_{0z} = (\nu^2/g)^{1/3} \tag{16}$$

The set of ϵ power index and the certain scales of $V_0, W_0, l_{0x}, l_{0y}, l_{0z}$ provide a simultaneous account of inertious, viscous and buoyancy forces in the equations of 3D SBL.

The equation system for the nonstationary 3D SBL at the zero approximation in ϵ takes a form of

$$\frac{\partial U_0}{\partial x} + \frac{\partial V_0}{\partial y} + \frac{\partial W_0}{\partial z} = 0, \tag{17}$$

$$\frac{\partial U_0}{\partial t} + \vec{U}_0 \nabla U_0 = \frac{\partial^2 U_0}{\partial y^2} + \frac{\partial^2 U_0}{\partial z^2}, \tag{18}$$

$$\frac{\partial V_0}{\partial t} + \vec{U}_0 \nabla V_0 = -\frac{\partial r_{d_0}}{\partial y} \pm +\theta_0 + \frac{\partial^2 V_0}{\partial y^2} + \frac{\partial^2 V_0}{\partial z^2}, \tag{19}$$

$$\frac{\partial W_0}{\partial t} + \vec{U}_0 \nabla W_0 = -\frac{\partial p_{d_0}}{\partial z} + \frac{\partial^2 W_0}{\partial y^2} + \frac{\partial^2 W_0}{\partial z^2}, \tag{20}$$

$$\frac{\partial \theta_0}{\partial t} + \vec{U}_0 \nabla \theta_0 = Pr^{-1} \left[\frac{\partial^2 \theta_0}{\partial y^2} + \frac{\partial^2 \theta_0}{\partial z^2} \right], \tag{21}$$

here $\vec{U}_0 = \{U_0, V_0, W_0\}$ and astericks are omitted for convinience at nondimensional values. The plus sign in the bouyancy force corresponds to the heated surface case and the minus corresponds to the cooled wall.

Taking into account (14) - (16), spatio-temporal scales of 3D SBL take a form of

$$\{L_{x_0} = \varepsilon^{-2/3}(\nu/g^2)^{1/3}U_0; \; L_{y_0} = L_{z_0} = L_0 = \varepsilon^{-1/3}(\nu^2/g)^{1/3}; \; T_0 = \varepsilon^{-2/3}(\nu/g^2)^{1/3}\}. \qquad (22)$$

So far as these scales appear due to buoyancy forces responsible for the bulk vorticity sources, the obtained scales can be easily interpreted physically - L_{x0}, L_{y0}, L_{z0} represent characteristic space scales along the downstream, spanwise and normal axes of considered vortical structures. It means that fluid-thermodynamical structure of 3D SBL is developing as a result of the nonlinear interaction of viscous and bulk vorticity sources. It follows from (22) that these developed vortical structures are elongated downstream, the ratio between their lateral and longitudinal scales having an order of $\varepsilon^{1/3}$. Estimation of corresponding velocities in SBL gives

$$U_0 \sim O(1), \quad V_0 \sim W_0 \sim \varepsilon^{1/3}. \qquad (23)$$

Corrections to the zero approximation in ε to the 3D SBL solutions can be shown to be of the order of $\varepsilon^{2/3}$ for velocities, of $\varepsilon^{4/3}$ for pressure, and of $\varepsilon^{2/3}$ for temperature.

To get more clear physical understanding of obtained scales, experimental results should be considered dealt with the development of 3D boundary layer structure over a heated surface.

Physically L_0 scale accurate to the function of the Prandtl number corresponds to a minimum vortex scale arising due to the buoyancy. That is the longitudinal vortex wave number λ_s and L_0 scale must be related by a universal dependence of the kind of

$$\lambda_s = f_0(Pr)L_0 \sim \beta^{-1/3}(T_s - T_0)^{-1/3}\nu^{2/3}g^{-1/3}, \qquad (24)$$

here $f_0(Pr)$ is a universal function dependent only on the Prandtl number. Experimental results are in a good agreement with this relationship.

Using the expression for the lateral L_0 scale, one can get the downstream distance L_0 of existing 2D SBL. The 2D SBL thickness δ_2 grows along L_2 according to $\delta_2 = L_2 Re_{L_2}^{-1/2}$ It was shown that this thickness can not exceed L_0 scale. Hence its streamwise extent (or the downstream position where 3D vortices appear) can be estimated depending on the basic flow parameters as

$$L_2 = f_2(Pr)L_0 Re_{L_0} \sim U_0\beta^{-2/3}(T_s - T_0)^{-2/3}g^{-4/3}\nu^{1/3} \qquad (25)$$

here $f_1(Pr)$ is the universal function of the Prandtl number values of which can be obtained experimentally.

CONCLUSIONS

- Nonpotential body forces in a boundary layer result in the development of the flow structure space scales characterizing the intensity of bulk vorticity sources. In a general case the interaction of bulk and surface vorticities does not permit a self-similar solution for a 2D boundary layer and essentially effects the flow strucure.

- Two types of space-time scales for vortical structures in boundary layers effected by buoyancy were established using the asymptotic analysis of 3D nonstationary equations.

Theoretical estimates were found out to be in a good agreement with experimental results related to the boundary layer structure developing in a boundary layer over a flat heated surface.

- Applied aspect of this investigation is demonstrated concerning experimentally obtained growth of heat transfer in a boundary layer with embedded longitudinal vortices.

References

E.Nikiforovich and V.Maderich, "Asymptotic analysis of the Navier-Stokes equations in problems of free convection", Sov. Phys. Dokl., 34 (9), September, p.p. 767-769, 1989

G.Wickern, "Mixed convection from an arbitrary inclined semi-infinite flat plate " - 1,2; J. Heat & Mass Transfer, vol. 34, No.8, p.p. 1935-1957, 1991

W.Schneider, "A similarity solution for combined forced and free convection flow over a horizontal plate", Int. J.Heat and Mass Transfer, v.22, p.p. 1401-1406,1979

E.Nikiforovich, "Barocline mechanism of vorticity generation in a boudary layer", Abstr. of Euromech 300, Istanbul, Turkey, 1993

N.Yurchenko, G.Pedishius, "Generation of longitudinal vortices in boudary layers effected by body forces", Eng. - Phys. J., v. 57, No.3, p.p.392-398, 1989

M.Akiyama, G.J.Hwang, K.C.Cheng, "Experiments on the onset of longitudinal vortices in laminar forced convection between horizontal plates", TASME, Ser. C, v. 93, No.4, p.p. 15-22, 1971

R.R.Gilpin, H.Imura, K.C.Cheng, "Experiments on the onset of longitudinal vortices in horizontal Blasius flow heated from below", TASME, Ser.C, v.101, No.1, p.p. 31-37, 1978

THE COUPLING OF INTERFACIAL WAVES AND TURBULENT CONVECTION IN AN ANNULUS

Andrew P. Stamp and Ross W. Griffiths

Research School of Earth Sciences, Australian National University,
Canberra, A.C.T. 0200, Australia

Abstract

When layers of salt and sugar solution are separated by a diffusive interface, in-terfacial waves are spontaneously generated by the turbulent convection once the system evolves to a critical value of the density-anomaly ratio $R_\rho \equiv \beta \Delta S / \alpha \Delta T$ (Stamp *et al.*, 1994). The waves modulate the interfacial fluxes by modifying the interface thickness and thereby organize the otherwise random convective motions into coherent large-scale circulations. In long rectangular channels a wide range of conditions gives rise to a single wave which propagates back-and-forth, resulting in quasi-periodic reversals of tank-scale circulations. Here it is shown that in an annulus this same coupling phenomenon gives rise to turbulent convection cells of a travelling-wave nature, coupled to large-amplitude solitary waves on the interface.

1 Introduction

Double-diffusive convection occurs when a fluid contains two or more components which diffuse at different rates and make opposing contributions to the vertical density gradient. When the faster diffusing component is unstably stratified, a thin 'diffusive' density inter-face forms and the diffusive buoyancy flux through this interface drives convection in the adjacent layers (Turner, 1965). Subsequent studies have focused on the interfacial fluxes so as to understand mixing in geophysical and industrial settings (Turner 1974; 1985).

An intriguing property of the two-layer convecting system is a systematic interfacial wavemotion coupled to large-scale convection in the layers first observed by Turner & Chen (1974) when a diffusive interface was formed by placing salt solution above sugar solution. Although Linden & Shirtcliffe (1978) noted that the presence of waves could increase the fluxes through a diffusive interface, little further attention has been given to the generation of these long-lived waves and they have gone unexplained until recently. Stamp *et al.* (1994) studied the coupling of waves and convection in this double-diffusive system as an example of the organization of coherent motions in turbulent flows, and as a possible analog to the coupling across the air-sea interface of fluctuations in atmospheric circulation with long waves on the equatorial ocean thermocline.

Stamp *et al.* found that the convection spontaneously generates large-amplitude waves on the interface. The waves correspond to a local thickening of the interface and produce horizontal variations in the interfacial buoyancy flux, which in turn force circulations on the scale of the distance between waves. For a wide range of conditions a single wave propagates back-and-forth along the channel, organizing the convection into two cells which oscillate in length from zero to the full length of the channel. This oscillation begins when the interface is thick enough to support waves of sufficient amplitude and speed to match the convective velocities, and continues until the property gradients have run down to a point where the interfacial fluxes and convective velocities are too small to match interfacial wavespeeds.

Here we report experiments which show that coupling occurs in a narrow annular gap. In this case, a small number of equally-spaced waves propagated in a continuous

circular path, with each wave organizing the surrounding convection in each layer into two large-scale travelling cells. As a rule, all waves (and convection cells) propagated in the same direction. However, occasionally one wave propagated in the opposite direction, and during the ensuing head-on collisions the entire leftward and rightward travelling flow patterns passed though each other unchanged.

2 Rectangular channels

The experiments in narrow channels carried out by Stamp *et al.* were set up with an aqueous salt–sugar interface separating two layers of depth $H = 11.5$ cm. Three independent dimensionless parameters govern the flow: the density-anomaly ratio $(R_\rho \equiv \beta \Delta S / \alpha \Delta T)$, the total fractional density difference across the interface $(\Delta \rho / \rho_0 \equiv \beta \Delta S - \alpha \Delta T)$, and the channel aspect ratio (L/H). Here L is the channel length, ΔT and ΔS are the concentration differences of salt and sugar across the interface, α and β are the expansion coefficients appropriate for the linearized equation of state

$$\rho = \rho_0(1 + \alpha T + \beta S), \tag{1}$$

and ρ_0 is a reference density.

At the start of each experiment the interfacial fluxes and resulting convective velocities were large because the interface was thin. However, as salt moved from the upper to the lower layer and sugar moved from the lower to the upper layer, the concentration differences across the interface decreased, both R_ρ and $\Delta \rho$ increased, and the fluxes decreased. As a result, the convection became weaker and the interface thickened by diffusion. This evolution began with the convective motions becoming progressively more two-dimensional and organizing the interface into thick and thin regions. The thick regions propagated as mode 2 (varicose) solitary waves but were too small and slow to couple with the vigorous convection. However, as the interface thickened, the waves became larger and faster, while the buoyancy flux and convective velocities decreased. Once the system evolved to a critical value of the density-anomaly ratio, which increased with channel length, the wavespeeds and horizontal convective velocities became comparable, strong coupling ensued, and a single thick region of interface developed. This region propagated back-and-forth along the channel as a solitary wave followed by a region of thickened interface which was acted upon by gravity and the stress exerted by the convection. The resulting horizontal differences in buoyancy flux organized the convection into large-scale circulations which reversed direction quasi-periodically (figure 1).

The waves persisted for about 4 hours and travelled 20 m. In contrast, solitary waves propagating along a density interface between two deep motionless layers of constant density persist only for about 2 minutes and travel 3 m (Stamp & Jacka, 1994). Hence the waves propagating along the diffusive interface gained energy from the organized convection. Whilst the qualitative behaviour of the flow remained unchanged during run-down, the average thickness of the interface increased and the buoyancy flux, convective velocities and wavespeed decreased. However, the wavespeed did not decrease monotonically. Instead the nonlinear coupling gave rise to large deviations from average values (figure 2).

The wavespeed was largest when the interfacial density difference $(\Delta \rho / \rho_0)$ was large and the interface close to static stability $(R_\rho \to 1)$, that is, when the fluxes were largest (figure 3a). Stamp *et al.* argued that the horizontal convective velocities are given by

$$u \sim (BL)^{\frac{1}{3}}, \tag{2}$$

2
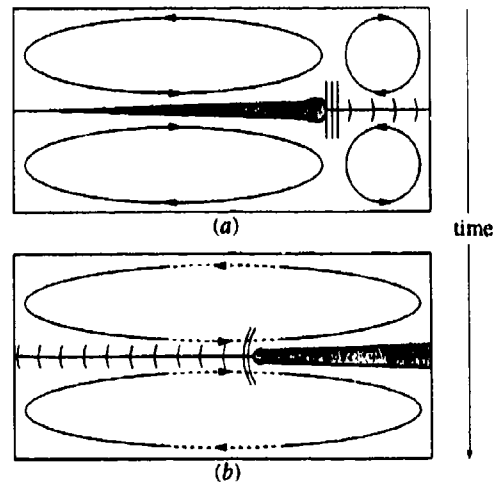
Figure 1: Waves in a narrow channel consist of a long thin tail following a short thick nose. Most of the unstable fluid is produced in the boundary layers along the thin interface ahead of the wave. However, the organized convection swept much of this fluid to near the nose. (a) As the wave approached an endwall, the size and strength of the cells along the wave increased at the expense of the cells ahead of the wave, and this accelerated the wave. (b) After collision with the endwall, the nose propagated back through the tail against the convective motion. Convection from the interface near the nose then broke the single cell in two, and the cycle repeated with the interfacial fluid trapped against the endwall collapsing under gravity.
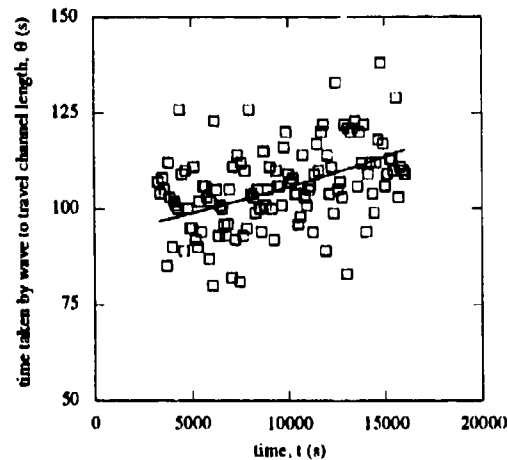
Figure 2: Time taken by the wave to travel the length of a 15 cm channel vs. time since the start of the experiment. The decrease in convective activity due to run-down produced a slow decrease in wavespeed, while the nonlinear coupling produced large fluctuations between successive transits.

3
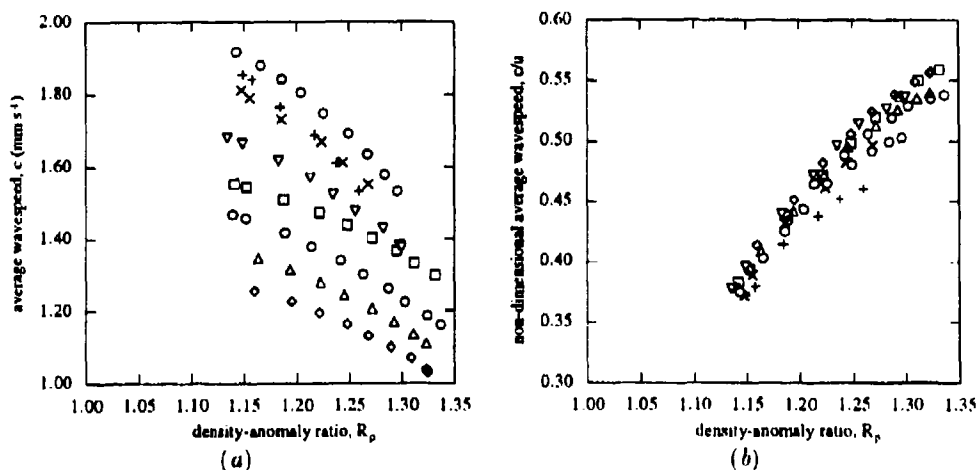
Figure 3: Wavespeeds for experiments in a 15×5 cm channel. (a) c vs. R_ρ. Larger initial wavespeeds correspond to larger starting values of $\Delta\rho/\rho_0$. (b) c/u vs. R_ρ. The normalized wavespeed increases with R_ρ because the nature of coupling depends on the structure of the interface.

where B is the interfacial buoyancy flux (units $m^2 s^{-3}$). Using the measured buoyancy fluxes the normalized wavespeeds, c/u, collapse onto a single curve (figure 3b)

$$c \sim f(R_\rho)u, \qquad (3)$$

where the additional dependence on R_ρ suggests that the exact nature of the coupling depends on the structure of the interface.

3   Annular geometry

Further experiments have been carried out in an acrylic annulus with an inner diameter of 25 cm and outer diameter of 35 cm. Each experiment was started by placing the upper (salt) layer in the annular gap and then feeding in the denser lower (sugar) layer through inlets at the base of the tank. For flow visualization a 50 Watt fluorescent lamp was placed on the axis of the annulus and tracing paper attached to the inner and outer sidewalls.

After about an hour a stable configuration of three or four large thick regions of interface formed. These regions consisted of a long thin tail attached to a short thick nose, and all propagated in a wavelike manner around the annulus in the same direction. The convection in each layer surrounding each wave was organized into two large-scale counter-rotating cells (figure 4). In this manner, the interfacial waves and convection cells travelled in a continuous circular path without reflection. At first the waves were equally-spaced, but with time the waves of larger amplitude caught up with those of lesser amplitude. During the ensuing overtaking collisions the waves merged and the number of convection cells decreased. As a rule, the number of waves decreased to two about 30 minutes after waves first appeared. In the rare cases when the system evolved to support a single wave (with two convection cells in each layer), its tail and each convection cell extended half way around the annulus.

4
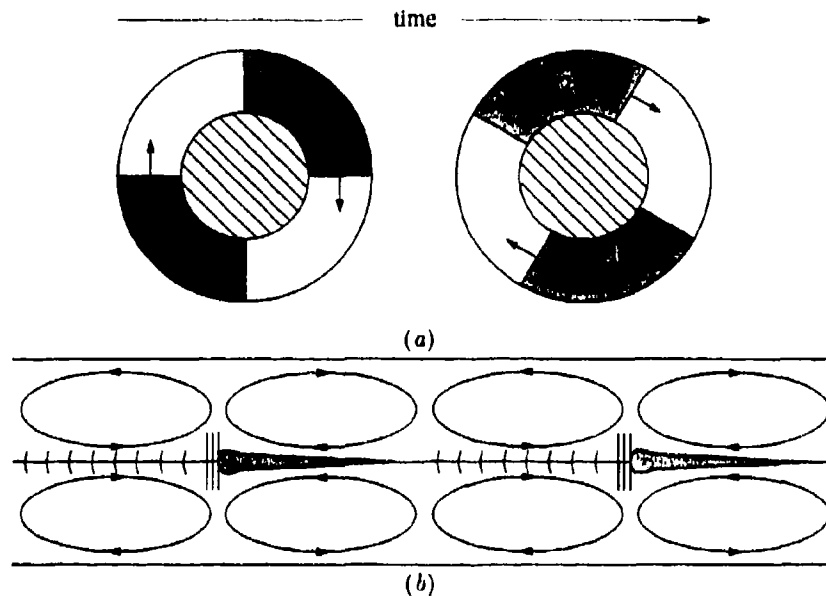
Figure 4: Illustration of the flow in an annulus. (*a*) Top and (*b*) side views of the 2-wave regime. The two waves and four convection cells in each layer travelled in a continuous circular path without reflection.

Sometimes the pattern of co-rotating waves was disrupted by generation of a new wave. This process began with a thickening of a small patch of interface ahead of an existing wave. The lump was swept towards the wave by the large-scale convective circulations and grew in size as it engulfed other small interfacial lumps in its path. In this manner, the lump became large enough to organize the surrounding convection and disrupt the existing convection pattern. This new interfacial wave and its associated cells propagated around the annulus in the opposite direction to the older waves. In general, the entire leftward and rightward travelling flow patterns passed through each other unchanged during the ensuing head-on collisions. However, when the colliding waves were of significantly different amplitudes, the larger wave engulfed the smaller wave and the convection pattern changed accordingly.

4 Onset of coherent motion and wavespeed measurements

Measurements of the flow in the annulus were made to determine the conditions for onset of coherent motions due to wave-convection coupling, and to test the dependence of the wavespeed on R_ρ and $\Delta\rho/\rho_0$ (table 1). The data indicated that strong coupling occurred when the density-anomaly ratio exceeded the critical value

$$R_\rho^c = 1.17 \pm 0.01 \quad \text{for} \quad 0.0005 \leq \Delta\rho/\rho_0 \leq 0.0020. \tag{4}$$

This value is close to the critical value for flows in a rectangular channel of horizontal cross-section 15×5 cm. The similarity occurs because in both cases the convection cells were about 15 cm long (three equally-spaced waves in the annulus organized the

		initial conditions		onset of coupling			final measurements		
run	symbol	$\Delta\rho/\rho_0$	R_ρ	t (h:m:s)	$\Delta\rho/\rho_0$	R_ρ	t (h:m:s)	$\Delta\rho/\rho_0$	R_ρ
1	□	0.0005	1.02	1:10:24	0.0030	1.17	2:22:21	0.0037	1.24
2a	×	0.0014	1.03	1:08:24	0.0058	1.18	2:47:01	0.0074	1.27
2b	+	0.0014	1.03	1:00:39	0.0056	1.17	2:48:38	0.0075	1.28
3	○	0.0020	1.02	1:04:40	0.0118	1.17	2:51:00	0.0157	1.26

Table 1: Experimental parameters and results for annulus experiments. The final measurements correspond to the time at which waves and organized convection became undetectable.

convection in each layer into six cells of length $2\pi\bar{r}/2 \times 3 \approx 15$ cm, where $\bar{r}$ is the mean radius), and hence the horizontal convective velocities were similar.

Wave position was measured as a function of time. However, it was not possible to obtain a complete record for every wave because of the complicated wave-wave interactions and the practical difficulties associated with monitoring several waves at once.

The evolution of experiment $2a$ is shown in figure 5. A stable configuration of three waves formed about an hour after the start of the experiment, and 20 minutes later the number of waves decreased to two. These waves were on opposite sides of the annulus and propagated in the same direction. However, wave $2a.2$ was larger and faster than wave $2a.1$ and, after a further 40 minutes, the waves merged to form wave $2a.3$. This wave and its associated convection cells extended half way around the annulus. The increase in the horizontal scale of the convection resulted in larger horizontal convective velocities and a corresponding increase in the wavespeed. Meanwhile, a new wave formed and propagated in the opposite direction to wave $2a.3$, rapidly decreasing in amplitude during the ensuing head-on collisions.

As in rectangular channels, the wavespeed in the annulus was largest when the interfacial density difference $\Delta\rho/\rho_0$ was large and the interface close to static stability ($R_\rho \to 1$). That is, when the buoyancy flux was largest. For example, there was a two-fold difference in the fluxes between experiments $2b$ and 3, and the wavespeed in the latter flow was about 25% faster than that in $2b$. In addition, for flows having similar layer properties the wavespeeds were larger for a smaller number of waves because the convection was organized over different horizontal lengths and therefore the horizontal convective velocities were different.

Figure 6 shows the normalized wavespeed for each of the waves that were monitored in detail. Because each wave organized the surrounding convection into two large-scale convection cells the length scale used in calculating the convective velocities from (2) was taken as the mean circumference of the annulus divided by twice the number of waves:

$$L = 2\pi\bar{r}/2n. \tag{5}$$

Measurements for the different experiments collapse onto a single curve, indicating that the wavespeed varied approximately as the horizontal convective velocity. The collapse is not perfect, with waves 1.1 and 1.2 decaying more rapidly than the other waves. However, this anomalous behaviour was probably an artefact of the poorly constrained wave position measurements in the case with the weakest convection.
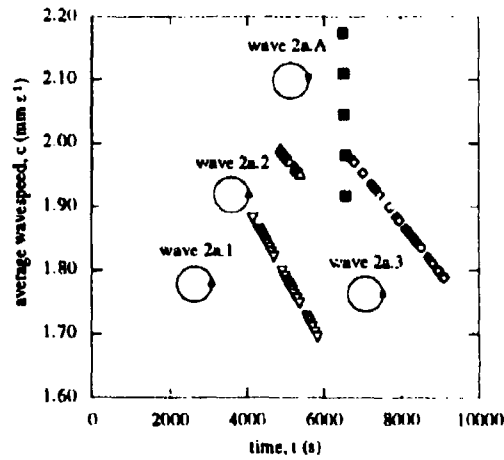
Figure 5: Evolution of experiment 2a. After about 80 minutes the flow consisted of two waves (2a.1 and 2a.2) propagating around the annulus in a counter-clockwise direction. Small differences in the amplitude and speed of these waves gave rise to an overtaking collision and merge to form wave 2a.3. This faster wave extended half way around the annulus. Meanwhile, a new wave (■) formed and propagated in a clockwise direction before being destroyed.
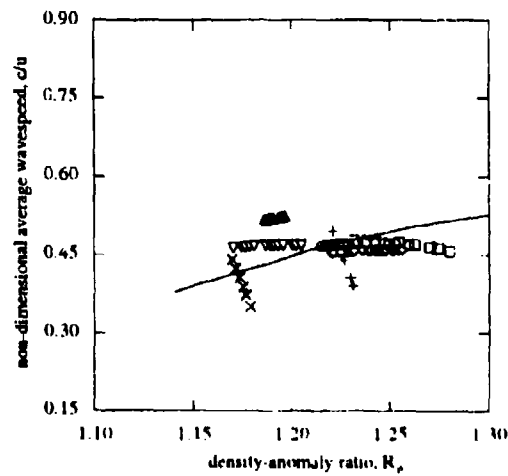
Figure 6: Wavespeeds for the annulus waves normalized by the horizontal convective velocity calculated from (2) using the measured buoyancy fluxes. The wavespeeds for each wave were smoothed by differentiating the polynomial that best fits the displacement time measurements. The solid line shows the results for an experiment under similar conditions in a rectangular channel.

7

After the number of waves in the annulus had decreased to two the wavespeeds were much larger than those for flows with the same layer properties in a 15 × 5 cm rectangular channel. However, the ratio of wavespeed to convective velocity was similar ($c/u \approx 0.5$) in both cases because annulus convection was at this stage characterized by a larger horizontal length scale. Similarly, the scaling (2) and resonance assumption (3) correctly predict the changes of wavespeed when there was a change in the number of interfacial waves and convection cells travelling around the annulus.

5 Summary and Conclusions

Coupling of large-amplitude waves and turbulent convection driven by the buoyancy flux through a diffusive interface is readily established in the laboratory. The spontaneous generation of interfacial waves and their interaction with convection gives rise to coherent convective motions on the scale of the box length or annulus perimeter. In a rectangular channel a large amplitude interfacial wave reflects back and forth between the endwalls whereas in an annulus both interfacial waves and convection cells travel continuously each being maintained by the other. The coupling of waves and convection in the double-diffusive system at very large Rayleigh numbers may provide an appropriate laboratory analog for other systems such as atmospheric squall lines and equatorial ocean-atmosphere interactions.

References

LINDEN, P. F., & SHIRTCLIFFE, T. G. L. 1978. The diffusive interface in double-diffusive convection. *J. Fluid Mech.* **87**, 417–432.

STAMP, A. P., & JACKA, M. 1995. Deep water internal solitary waves. In press, *J. Fluid Mech.*

STAMP, A. P., HUGHES, G. O., GRIFFITHS, R. W. & NOKES, R. I. 1994. The coupling of waves and convection in rectangular channels. In preparation for *J. Fluid Mech.*

TURNER, J. S. 1965. The coupled turbulent transports of salt and heat across a sharp density interface. *Int. J. Heat Mass Trans.* **8**, 759–767.

TURNER, J. S. 1974. Double-diffusive convection. *Ann. Rev. Fluid Mech.* **6**, 37–56.

TURNER, J. S. 1985. Multicomponent convection. *Ann. Rev. Fluid Mech.* **17**, 11–44.

TURNER, J. S. & CHEN, C. F. 1974. Two-dimensional effects in double-diffusive convection. *J. Fluid Mech.* **63**, 577–592.

Convection from bounded body in rotating fluid

B. Boubnov

Institute of Atmospheric Physics,109017,Moscow,Russia

For many geophysical and astrophysical objects the rotation together with spatial inhomogeneity of energy sources distribution in the gravity field determines the origin and character of the fluid motion. Two main cases of the convective motions in rotating fluids are usually considered: the infinite plane layer with the temperature difference on the horizontal boundaries [1,2] and rotating annuli with the temperature differences on the vertical walls [3]. In nature more often the case of simultaneous non-uniform horizontally and vertically temperature gradient, which, of course, is much more complicated from theoretical and experimental point of view. Some examples of the mixing influence of the vertical and horizontal temperature gradients in rotating fluid one can find in [4,5], where mostly the external temperature distributions define these gradients.

Convection from the bounded body is the another example of simultaneous influence both temperature gradient, but in this case these gradients usually are defined mostly by the geometrical parameters. One temperature differences ΔT between the temperature of body and the temperature fluid far from body and additional with compare to the infinite plane space scale the horizontal size of the heating body D will significant change the motion of the fluid as in nonrotating as in rotating cases.

The main determining non-dimensional parameters for localized convection in a plane horizontal infinite layer (we consider that horizontal scale of the fluid layer is much more than D) in non-rotating fluid are Rayleigh, Ra, Prandtl, Pr numbers and aspect ratio, $\delta = D/h$, where h is the depth of the fluid layer. The choice of the proper length scale in the determination of the Rayleigh number h or D, depends on the values of δ. We define two related values of the Rayleigh number

$$Ra_D = \delta^3 Ra_h = \frac{\alpha g D^3 \Delta T}{k \nu},$$

Different regimes of convection without rotation for the different Ra and δ from [6] are presented on Figure 1. There are three main regimes: I - laminar toroidal cell, which is usual for the small h, II - thermal plume, III - turbulent convection (region IV on Figure 1 - transition region between the main regimes). The main diference between the regimes I and II are in the space close to the heated body; at some distance from which due to the turbulent entrainment of the thermal plume we could not differ this regimes.

Total rotation of the layer changes the flow patterns significantly. Far from the heated body only this influence for both regimes II and III can be similar to the influence of the rotation to a turbulent convection in the plane fluid layer. In this case the vortex structure origin and some vortices due to baroclinic instability propagate away from the upper worm (or down cold) flow [1,2,6,7,8]. Near the heated body in regime III the influence of the Coriolis force to the flow from the edge of the disk will change this flow and intensive singular vortex (or number of vortices) can be origin. Example of two tipe of this vortices are prezented in Figure 2. The main additional non-dimensional parameter which usually is used in convection with rotation

Taylor number $Ta = 4\Omega^2 h^4 / \nu^2$ (where Ω -is the constant rotation) not so convinient for the convection from bounded body. Very important role in this case will play the Rossby number Ro $Ro = V/(\Omega D)$, where the velocity scale V can be defined as characteristic geostrophic

velocity. which was obtained [9] from the assumption that all dissipation of the kinetic energy
ε produced in the Ekman boundary layer $V = (\frac{ε}{2\Omega})^{1/2}$.

Usual critical value of Rossby number $Ro = 1$ will define the role of rotation. When $Ro >> 1$ convection in turbulent regimes near the heated body will not differ from the non-rotating case, but far from the body due to the turbulent entrainment horizontal scale of motion increases and suitable Rossby number (defined by this scale) can be compare or less than 1, and influence of rotation will be significant. The same effect will be and in regime II of thermal plume, where near the small heated body Rossby number usually is very large.
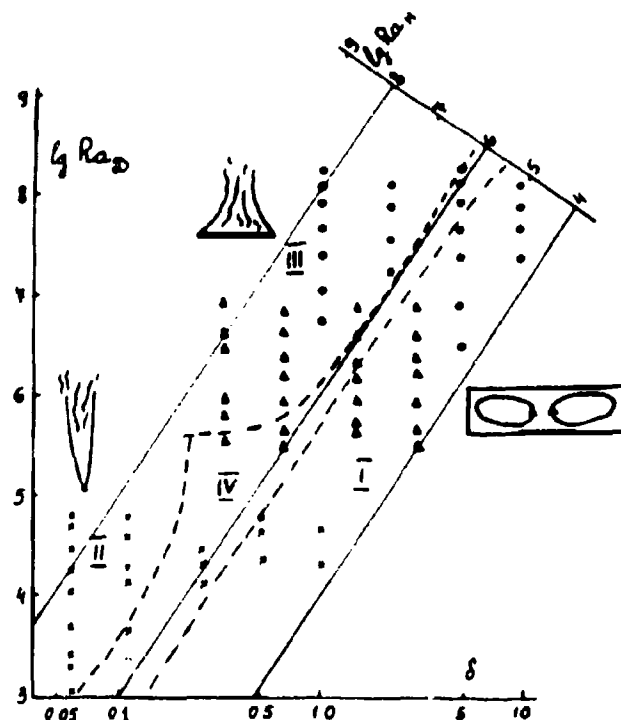
Figure 1.

When $Ro << 1$ due to a geostrophic balance convection motions above the disk differ slightly from the convection motion in the infinite fluid layer [1,2], and near the boundaries the baroclinic vortices are propagated away from the body [7]. The case $Ro \approx 1$ is more comlicated. and singular intensive vortices (Fig.2) can developed in this case. These vortices are usual for experiment on tornado-like motions, and the main conditions for the origin of this vorices is updown flow and non-uniform rotation of this flow. Review of laboratory experiments on this problem one can find in [10]. Main differences of our experiments from the previous one are, from one side, that this situation is more closed to the natural conditions and, from the other side, that we have a simple possibility to simulate not only a origin of the vortex, but also its propagation from the place of origin. The additional goal of these experiments - a possibility to study transitions from the different convective regimes: from the singular intensive vortex to the system of the less intens.ve vortices.

First experiments [6,11] were conducted in rotation or non-rotational fluid with some small non-gomogeneity of the rotation (in spin-down regime). Two type of vortices were found: lam-

inar and oscillating (two stage of this oscillating vortex are presented in Fig.2). This situation is usual and similar to a case of the convection from the bounded body for non-rotating cases. The most important consequence of this transitions from laminar convection to the turbulent one is the change of a heat flux which comes from the heated body to the fluid. For non-rotating case the value of q in the dependence of non-dimensional heat flux - Nusselt number on a Rayleigh number $Nu = CRa^q$ changes from $1/5$ for laminar convection to the $1/3$ for the turbulent one.

Figure 2.

For oscillating vortices two stage of vortex structure are suitable: spiral vortex, when is very intensive heat flux from the body, and toroidal vortex when heat flux is much less. The frequency of oscillation of a process is appropriated to the Howard frequency in turbulent convection, and the process is very similar to the Howard's process. In first stage toroidal vortex keep a heat near the body and after some critical value of Rayleigh number due to instability the process come to intensive spiral vortex, in which a heat flux is much more intensive and after some time when it is not enough a heat energy to supply the motion in spiral vortex, the system comes to the toroidal vortex and process repeat again. Frequency of oscillation is very close to the Howard frequency for non-rotating fluids, depends mostly from the Rayleight number and change in the limit of 3-10 sec. In this stage of the experimental study there more questions than answers, but we would like to put attentions for questions which is very important for the understanding the basic vortex formation and can have geophysical applications as to the origin of intensive vortices as a flow above the heating places in the regime of turbulent convection with the influence of the flow from the sides and rotation.

References

[1] Boubnov B.M.& Golitsyn G.S. 1986 Experimental study of convective structures in rotating fluids. J. Fluid Mech. V.167, p.p.503-531.

[2] Boubnov B.M. & Golitsyn G.S. 1990 Temperature and velocity field regimes of convective motions in a rotating plane fluid layer. J. Fluid Mech. V.219, p.p. 215-239.

[3] Hide R. & Mason P.J. 1975 Sloping convection in a rotating liquid. Adv. Physics, V.24, No1, p.p.47-100.

[4] Hignett P., Ibberson A. & Kilworth P 1981 On rotating thermal convection driven by non-uniform heating from below. J. Fluid Mech., V. 109, p.p.161-187.

[5] Boubnov B.M. & Golitsyn G.S. 1988 Influence of vertical stratification on the motion patterns in differentially heated rotating annulus. Geophys. Astrophys. Fluid Dyn., V. 42, p.p.1-35.

[6] Boubnov B.M. & Heijst van G.J.F. 1994 Experiments on convection from horizontal plate with and without rotation. Experiments in Fluid. (to be published).

[7] Maxworthy T. & Narimosa S. 1991 Vortex generation by convection in a rotating fluid. Ocean Moddeling, V. 92, p.p.1037-1040.

[8] Maxworthy T. 1992 Convection and shear turbulence with rotation. In: Rotating Fluids in Geophysical and Industrial Applications, (Hopfinger E.J., ed.), Springer-Verlag, Wien -New York, p.p.339-357.

[9] Golitsyn G.S. 1980 Geostrophic convection. Dokl. AN SSSR, V.261, No 2, p.p.317-320.

[10] Bengtsson L. & Lighthill J. (Ed) 1982 Intensive Atmospheric Vortices. Springer-Verlag, New York, 368p.

[11] Dmitrienko A.V. 1993 Laboratory study of tornado-like vortices on convection from the bounded body; Thesis of M.D. Moscow. Phys. Tech. Inst.

SIMULTANEOUS HEAT AND MASS TRANSFERS WITH OR WITHOUT EVAPORATION IN UNSTEADY TURBULENT NATURAL CONVECTION AND APPLICATION TO A LIQUEFIED NATURAL GAS STORAGE.

C.T. Pham and J.P. Petit

Laboratoire E.M2.C., U.PR. 288 du C.N.R.S. et de l'E.C.P.,
Ecole Centrale Paris, 92295 Chatenay-Malabry Cedex, France.

ABSTRACT

A destratification by double-diffusive natural convection is numerically studied in a 2D cavity containing a fluid which is initially stratified in temperature and in concentration. the upper surface of storage is either adiabatic or with evaporation. The fluid motion, linked to the opposite mass and thermal buoyancy forces, are obtained by resolution of the unsteady balance equations, written with the stream function-vorticity formalism using the Boussinesq approximation. The turbulence is introduced by a k-ε standard model in LRN (low Reynolds number) form. A finite-difference technique using the A.D.I. method is implemented. The convection term is discretized using a hybrid scheme based on the mesh Reynolds number and adapted to a non uniform grid. The time step is determined to ensure stability and to optimize the computation time. The results are obtained for $Gr_{th} \leq 10^{14}$ and $|Gr_m| \leq 10^{15}$ in the case of liquefied natural gas (LNG). The evolution of significant problem variables (temperature, concentration, velocity, turbulent kinetic energy and turbulent dissipation) allow one to follow the fluid destratification.

1. INTRODUCTION

The present paper reports a study of destratification by turbulent natural convection of a fluid contained in a 2D cavity which is initially stratified in temperature and in concentration. The flow is driven by density variations caused by simultaneous heat and mass transfer. Many free convection flows which occur in nature and in industry originate from these density variations: drying processes, solar energy storage, storage of LNG, crystal growth, atmospheric flows. Howover, there is a lack of literature concerning flows driven by multiple buoyancy forces, because of the complexity of the phenomena. The problem of combined temperature and concentration gradient in enclosures has been little studied (Bejan 1985, Ostrach 1982a, Sévéléder and Petit 1989a, Trevisan and Bejan 1987) and authors have tried to solve steady problems. Unsteady natural convection flows have received considerable attention when density variations are due only to temperature gradients (Patterson and Imberger 1980, Wang 1987). The unsteady state of simultaneous heat and mass transfer is mostly studied in the case of differentially heated lateral walls (Kamakura and Ozoe 1993, Lee and Hyun 1991). The case of a fluid which is simultaneously stratified in concentration and in temperature whose the destratification is caused by lateral inflow of heat and bottom fluxes, is considered by Sévéléder and Petit (1989b). This study concerns only the laminar flow, with thermal and mass Grashof numbers $< 10^7$ in absolute values. The transfers at the interface are more particularly studied by Bergman et al (1985), but the considered case corresponds to a slow development of the lower layer, the heating is only at the bottom.

Our study approaches a real case of LNG storage: in terms of the Grashof numbers (10^{14}), wall heat fluxes and free surface evaporation.

2. MATHEMATICAL FORMULATION

Consider a 2D rectangular cavity with a height-to-width ratio $A1 = H/L$. The cavity is closed or with a free surface evaporation. The initial and boundary conditions for temperature and concentration in the last case are shown in Figure 1. These conditions correspond to those which occur at the time of storage of LNG and although they present a case of important practical interest, studies of this type are very rare (Sévéléder 1990). The cavity is filled with a fluid composed of a single diffusing chemical species (of small concentration) diffusing in a solvent. The mass evaporation is expressed as inflow of the solution.
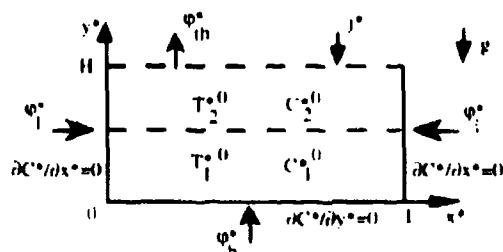
Fig.1 Initial and boudary conditions

The fluxes φ^*_{th}, j^* at the free surface are computed by a Hashemi and Wesson model (1971), adapted to the storage of LNG:

For $T^* > T^*_{sat}$: $\varphi^*_{th} = c_1 \lambda (\frac{g\beta_{th}}{a\nu})^{1/3}(T^* - T^*_{sat})^{4/3}$ where $c_1 = 0.13$; T^*_{sat} being the saturation temperature   (1)

$$j^* = -\varphi^*_{th}/(h_{lg}\rho) \tag{2}$$

For $T^* \leq T^*_{sat}$: $j^* = \varphi^*_{th} = 0$ (3)

The dimensionless equations of momentum, energy, species, turbulent kinetic energy and turbulent energy dissipation conservation are written with constant fluid physical properties and using the Boussinesq approximation:

$$\frac{\partial \Psi}{\partial t} = \Omega + \Delta\Psi \tag{4}$$

$$\frac{D\Omega}{Dt} = ((Gr_{th} + |Gr_m|)^{0.5} + \frac{\nu_t}{\sigma_k})\Delta\Omega + 2\frac{\partial \nu_t}{\partial x}\frac{\partial \Omega}{\partial x} + 2\frac{\partial \nu_t}{\partial y}\frac{\partial \Omega}{\partial y} + S_\Omega \tag{5}$$

$$\frac{DT}{Dt} = (\frac{(Gr_{th} + |Gr_m|)^{0.5}}{Pr} + \frac{\nu_t}{Pr_t})\Delta T + \frac{1}{Pr_t}\frac{\partial \nu_t}{\partial x}\frac{\partial T}{\partial x} + \frac{1}{Pr_t}\frac{\partial \nu_t}{\partial y}\frac{\partial T}{\partial y} \tag{6}$$

$$\frac{DC}{Dt} = (\frac{(Gr_{th} + |Gr_m|)^{0.5}}{Sc} + \frac{\nu_t}{Sc_t})\Delta C + \frac{1}{Sc_t}\frac{\partial \nu_t}{\partial x}\frac{\partial C}{\partial x} + \frac{1}{Sc_t}\frac{\partial \nu_t}{\partial y}\frac{\partial C}{\partial y} \tag{7}$$

$$\frac{Dk}{Dt} = ((Gr_{th} + |Gr_m|)^{0.5} + \frac{\nu_t}{\sigma_k})\Delta k + \frac{1}{\sigma_k}\frac{\partial \nu_t}{\partial x}\frac{\partial k}{\partial x} + \frac{1}{\sigma_k}\frac{\partial \nu_t}{\partial y}\frac{\partial k}{\partial y} + S_k \tag{8}$$

$$\frac{D\varepsilon}{Dt} = ((Gr_{th} + |Gr_m|)^{0.5} + \frac{\nu_t}{\sigma_\varepsilon})\Delta\varepsilon + \frac{1}{\sigma_\varepsilon}\frac{\partial \nu_t}{\partial x}\frac{\partial \varepsilon}{\partial x} + \frac{1}{\sigma_\varepsilon}\frac{\partial \nu_t}{\partial y}\frac{\partial \varepsilon}{\partial y} + S_\varepsilon \tag{9}$$

where $S_\Omega = (Gr_{th} + |Gr_m|)^{0.5}(Gr_{th}\frac{\partial T}{\partial x} + Gr_m\frac{\partial C}{\partial x}) + 2\frac{\partial^2 \nu_t}{\partial y\partial x}(\frac{\partial \nu}{\partial y} - \frac{\partial u}{\partial x}) + (\frac{\partial^2 \nu_t}{\partial x^2} - \frac{\partial^2 \nu_t}{\partial y^2})(\frac{\partial u}{\partial y} + \frac{\partial \nu}{\partial x})$ (10)

$$S_k = \nu_t\{2(\frac{\partial u}{\partial x})^2 + 2(\frac{\partial \nu}{\partial y})^2 + (\frac{\partial u}{\partial y} + \frac{\partial \nu}{\partial x})^2\} - \nu_t(Gr_{th} + |Gr_m|)^{0.5}(\frac{Gr_{th}}{Pr_t}\frac{\partial T}{\partial y} + \frac{Gr_m}{Sc_t}\frac{\partial C}{\partial y}) - \varepsilon \tag{11}$$

$$S_\varepsilon = C_1 \varepsilon \nu_t \frac{\varepsilon}{k}\{2(\frac{\partial u}{\partial x})^2 + 2(\frac{\partial \nu}{\partial y})^2 + (\frac{\partial u}{\partial y} + \frac{\partial \nu}{\partial x})^2\} - C_2 \varepsilon \frac{\varepsilon^2}{k} - C_3 \varepsilon \nu_t (Gr_{th} + |Gr_m|)^{0.5}\frac{\varepsilon}{k}(\frac{Gr_{th}}{Pr_t}\frac{\partial T}{\partial y} + \frac{Gr_m}{Sc_t}\frac{\partial C}{\partial y}) \tag{12}$$

$$\nu_t = C_\mu k^2/\varepsilon \tag{13}$$

In the turbulent kinetic energy equation, the term of transport by diffusion is approximated by the expression of Launder and Spalding (1974), whereas the buoyancy force effects in the terms of production and of viscous damping of the turbulent dissipation equation are written introducing the approximation of Hanjalic and Launder (1976). The values taken for different coefficients of these equations are those generally recommended for natural convection and LRN modeling (Ahluwalia and Chan 1989, Antonia and K m 1991, Ozoe et al 1985, Patel et al 1985, Yang and Aung 1985): $Pr_t = Sc_t = 1.0$, $\sigma_k = 1.0$, $\sigma_\varepsilon = 1.3$, $C_{1\varepsilon} = 1.44$, $C_{2\varepsilon} = 1.92$, $C_{3\varepsilon} = 0.7$, $C_\mu = 0.09$.

The thermal and mass Grashof numbers (Gr_{th}, Gr_m) are based on the height and, respectively, on the initial temperature and concentration differences between two layers. We consider here only the case of a negative mass expansion coefficient, which means that the body forces due to heat and mass transfer are in opposite directions ($Gr_{th} > 0$, $Gr_m < 0$).

3 NUMERICAL SOLUTION

3.1 Integration

The equations (4-9) have the same general form $\frac{\partial F}{\partial t} = B + AF + A_x\frac{\partial F}{\partial x} + A_y\frac{\partial F}{\partial y} + A_{xy}(\frac{\partial^2 F}{\partial x^2} + \frac{\partial^2 F}{\partial y^2})$ (14)

2

The stream function Ψ and turbulent kinetic energy k are zero at the walls. Wall vorticity Ω is computed by considering a Taylor series expansion for the stream function in the wall vicinity. The turbulent energy dissipation ϵ is computed at a first point in the vicinity of the wall (situated in the turbulent inertial sublayer) supposing universal equilibrium :

$$\epsilon = -\overline{uv}\frac{\partial u}{\partial y} = \frac{C_\mu^{3/4}k^{3/2}}{\kappa \Delta y_0} \tag{15}$$

where $\kappa = 0.42$ (Von Karman constant). This value is attributed to ϵ at the wall (Ozoe et al 1985). At the free surface, $\Psi = \partial\Psi/\partial x = 0$, with the hypothesis that the free surface remains even and horizontal; for the vorticity, the boundary condition is reduced to $\Omega = 0$ using the balance between the surface shear stress and the gradient of surface tension (Ostrach 1982b, Villers and Platten 1985) while considering the case where the horizontal gradients of concentration and temperature are small (Sévéléder 1990); the surface tension gradient is expressed with the same gradients and with the thermal and mass Marangoni numbers (Bergmann 1986). In a first approach, k = 0 and ϵ is computed by the method used at the wall.

The interior initial dimensionless values of the cavity are

$$T_1^0 = 0.5 ; \quad T_2^0 = -0.5 ; \quad C_1^0 = 0.5 ; \quad C_2^0 = -0.5; \quad \Psi^0 = \Omega^0 = 0 ; \quad k^0 = 10^{-23} ; \quad \epsilon^0 = 10^{-24} \tag{16}$$

A finite-difference technique using the A.D.I. method (Beam and Warming 1979, Roache 1976) is applied. The grid is non uniform and Cartesian. The computational code which evolved from this method is an extension of the code developed for the laminar regime with a semi-implicit method and a uniform grid (Sévéléder 1990). The equation (14), written in the form $\partial F/\partial t = f(F)$, has f(F) expressed by:

$$f(F) = B + (S_x + S_y)F \tag{17}$$

where $$S_x = \eta A + A_x \partial/\partial x + A_{xy}\partial^2/\partial x^2 \quad \text{and} \quad S_y = (1-\eta)A + A_y\partial/\partial y + A_{xy}\partial^2/\partial y^2 \tag{18}$$

Equation (14) is discretized in time and space by A.D.I. method using (17) and one has thus:

$$(1 - \frac{\Delta t}{2}S_x)F^{n+1/2} = \frac{\Delta t}{2}B + (1 + \frac{\Delta t}{2}S_y)F^n \tag{19}$$

$$(1 - \frac{\Delta t}{2}S_y)F^{n+1} = \frac{\Delta t}{2}B + (1 + \frac{\Delta t}{2}S_x)F^{n+1/2} \tag{20}$$

where $(1 - \frac{\Delta t}{2}S_x)$ and $(1 - \frac{\Delta t}{2}S_y)$ are the tridiagonal matrixes. The solution is obtained by a Gaussian elimination method for a vectorial computation or by application of Thomas algorithm (Roache 1976) for a scalar one.

For an optimal solution, a non uniform grid (71*61) is continuously generated by a function based on $\tan^{-1}$. The finest mesh is obtained in the vicinity of the walls and of the interface between the two layers, the first mesh is of the order of five thousandths of the cavity height.

For the discretization of diffusive terms, a centered scheme is used, whereas convection terms are discretized by a hybrid scheme based on the mesh Reynolds number ($Re_x = A_x max(\Delta x_i, \Delta x_{i-1})/A_{xy}$) : the centered scheme is used when $Re_{x(y)} \leq 2$ and an upwind scheme when $Re_{x(y)} > 2$, in order to have both advantages of a small numerical viscosity of the centered scheme and of a less strict limitation of the time step of an upwind (Sévéléder 1990).

3.2. Determination of Δt, η

As our purpose is to simulate unsteady phenomena, the time step has to be very small. It is important to choose an optimum value of the time step. This choice is based on two conditions:

a) "Pseudo Courant-Friedrich-Levy" condition: $\Delta t_1^n = e.min(\frac{\Delta x_{min}}{u_{max}}, \frac{\Delta y_{min}}{v_{max}})$

where e is a security factor that can be taken equal to 0.8.

b) Diagonal dominance condition which imposes: $\Delta t_2^n = min(\frac{2}{\eta A}, \frac{2}{(1-\eta) A})$

where $\eta = 0.5$ yields more possibilities for Δt. This condition has only to be proved with the coefficient A of equation (9) because A=0 in other equations.

In practice, to limit the accrued errors, the initial time step is chosen very small. It is thus necessary to raise the time step in the course of the computation : $\Delta t^{n+1} = min (\Delta t_1^n, \Delta t_2^n, \delta\Delta t^n)$

where δ is an evolution coefficient, equal to 1.002 for first thousand iterations and is later adjusted as a function of the evolution of computed quantities.
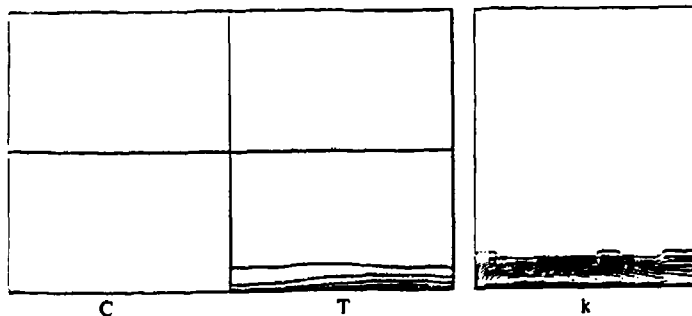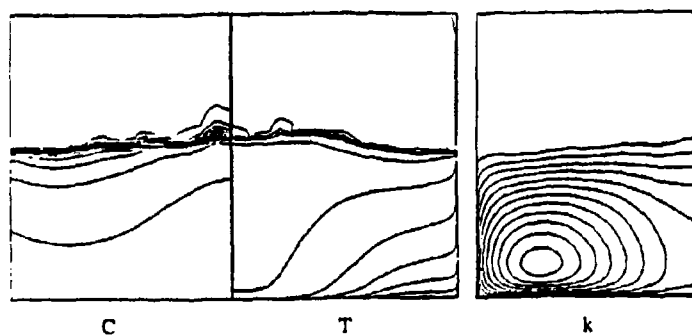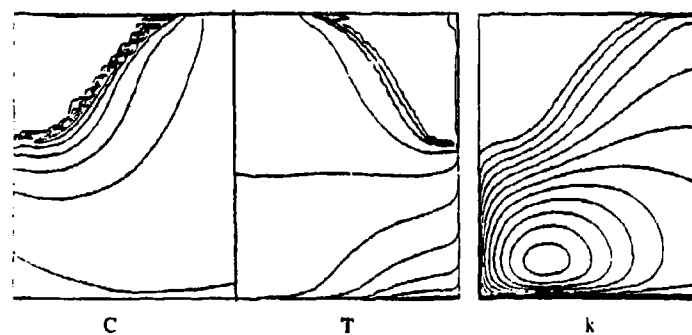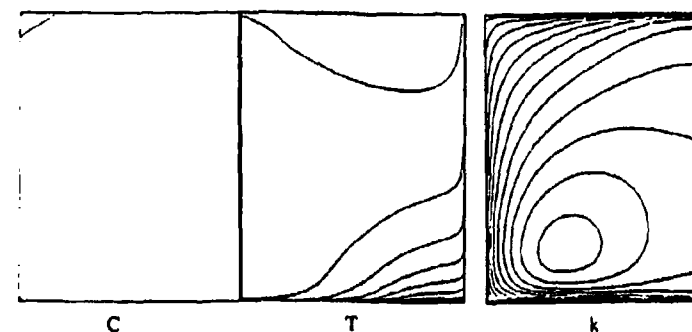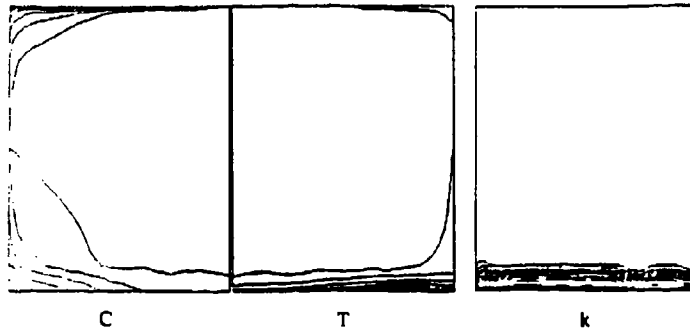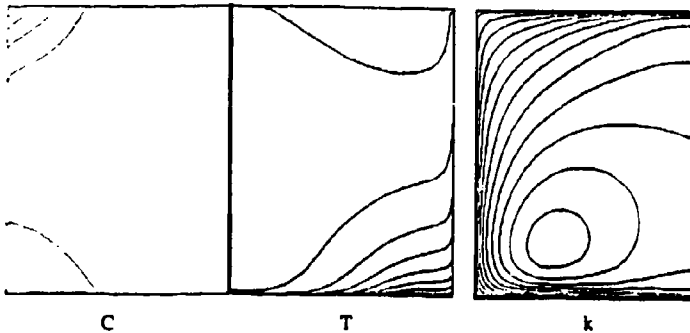
4. RESULTS

Fig. 2. Isovalues of concentration, temperature and kinetic turbulent energy: $Gr_{th} = 10^{14}$, $Gr_m = -10^{15}$, closed cavity, $t = 16$

	C	T	k
Max	0.5	2.8	1.8e-3
Min	-0.5	-0.5	0.
Δ	0.09	0.30	1.6e-4

Fig. 3. Isovalues of concentration, temperature and kinetic turbulent energy: $Gr_{th} = 10^{14}$, $Gr_m = -10^{15}$, closed cavity, $t = 75$

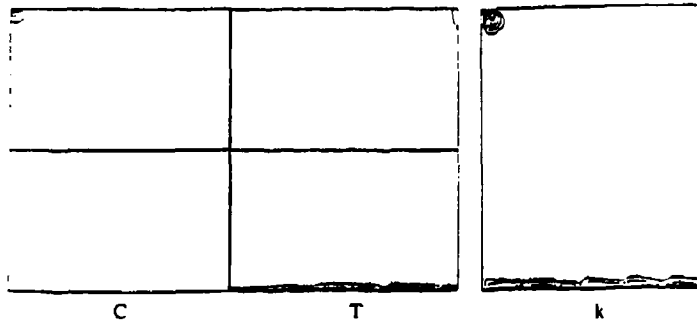|	C	T	k
Max	0.4	8.5	1.0e-2
Min	-0.5	-0.5	0.
Δ	0.08	0.82	9.5e-4

Fig. 4. Isovalues of concentration, temperature and kinetic turbulent energy: $Gr_{th} = 10^{14}$, $Gr_m = -10^{15}$, closed cavity, $t = 99$

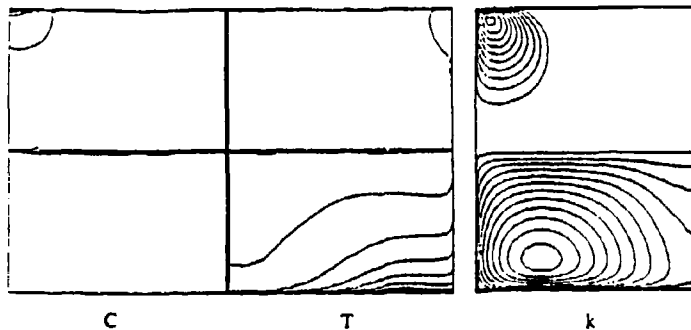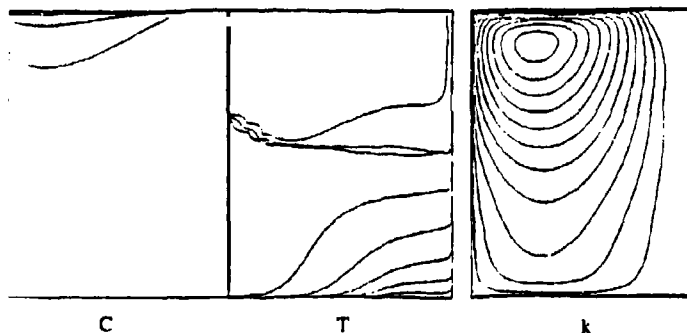|	C	T	k
Max	0.3	9.5	1.2e-2
Min	-0.5	-0.5	0.
Δ	0.07	0.91	1.1e-3

Fig. 5. Isovalues of concentration, temperature and kinetic turbulent energy: $Gr_{th} = 10^{14}$, $Gr_m = -10^{15}$, closed cavity, $t = 171$

	C	T	k
Max	3.2e-3	10.9	1.6e-2
Min	-3.2e-3	5.9	0.
Δ	5.9e-4	0.45	1.4e-3

We consider a rectangular cavity with a height-to-width ratio equal to 2/3, filled by the liquefied natural gas (Pr = 2.1, Sc = 121.0, β_{th} = 3.12 10^{-3} K^{-1}, β_m = -1.34 10^{-3} kg^{-1} m^3). Both initial layers have the same thickness, the lower layer is hoter and more concentrated ($T_1^{*0} > T_2^{*0}$, $C_1^{*0} > C_2^{*0}$). The fluxes at the lateral and bottom wall:$\varphi_l = 10$ W/m², $\varphi_b = 15$ W/m² . The movement which is developed in the cavity depends on the initial and boundary conditions, on the thermal and mass Grashof numbers and also on their relative importance:

$$N = \frac{Gr_m}{Gr_{th}} = \frac{\beta_m(C^{*0}_1 - C^{*0}_2)}{\beta_{th}(T^{*0}_1 - T^{*0}_2)}$$

We are interested only in the negative values of the N, this is in the case where the Archimède mass and thermal forces are in opposite directions that is the case generally occurred in the LNG storage. The Grashof numbers values actually used, considering the physical conditions of the LNG storage, correspond to the 10m diameter tanks with a 7m filling height. As the problem has an axis of symmetry, the isovalues figures are presented by a left half domain for C, k and one right for T.

The Figures 2 to 5 present the concentration, temperature and turbulent energy (k) at the different destratification times for N = -10 and for a upper adiabatic surface. The complete destratification has some phases and is obtained after about a quarter hour on order. On the first phase, either of two layers remains visible (Fig. 2 and 3), the thermal and mass diffusion develops essentially at the interface level where the temperature and concentration gradients are most important. The turbulent energy develops preferentially at the bottom level and invades afterwards all the cavity, remaining always being preponderate at the bottom. There, the thermal fluxes are most important ($\varphi_b/\varphi_l = 1.5$). The second phase presents very clearly the interface that bursts at the cavity center (Fig.4) and that leads to the complete destratification: the concentration is practically constant at the all tank (Fig.5), there is an unhomogeneity in the isotherms by the wall heating.

The ratio N has a very important role for the destratification: the interface "bursting" is driven when this ratio is near -1. The Figures 6 and 7 correspond to the same case that precedes, but with N^0 = -1, all others conditions being identical. Thus, one has: the first phase is inexisting, the destratification is achieved after a extremely small time (about 2 min.).

Fig. 6. Isovalues of concentration, temperature and kinetic turbulent energy: Gr_{th} =10^{14}, Gr_m = -10^{14}, closed cavity, t = 4

	C	T	k
Max	0.4	2.4	7.6e-3
Min	-0.4	-0.4	0.
Δ	0.08	0.26	6.9e-4

C   T   k

Fig. 7. Isovalues of concentration, temperature and kinetic turbulent energy: Gr_{th} =10^{14}, Gr_m = -10^{14}, closed cavity, t = 33

	C	T	k
Max	4.6e-3	7.0	8.8e-2
Min	-7.2e-3	2.0	0
Δ	1.1e-4	0.45	8.0e-3

C   T   k

The Figures 8 to 10 present the concentration, temperature and turbulent energy at the different times of the destratification while there is an evaporation at the free surface. All others conditions are same as the first case. This evaporation is modeled by the law of Hashemi-Wesson (1971) that is modified for LNG because in this case, there is a part of the solvent being evaporated, but the solution.

Fig. 8. Isovalues of concentration, temperature and kinetic turbulent energy: $Gr_{th} = 10^{14}$, $Gr_m = -10^{15}$, evaporation, $t = 9$

	C	T	k
Max	0.5	1.8	2.3e-3
Min	-0.5	-0.5	0.
Δ	0.09	0.21	2.1e-4

C   T   k

Fig. 9. Isovalues of concentration, temperature and kinetic turbulent energy: $Gr_{th} = 10^{14}$, $Gr_m = -10^{15}$, evaporation, $t = 24$

	C	T	k
Max	0.9	4.5	9.3e-3
Min	-0.5	-0.6	0.
Δ	0.1	0.46	8.5e-4

C   T   k

Fig. 10. Isovalues of concentration, temperature and kinetic turbulent energy: $Gr_{th} = 10^{14}$, $Gr_m = -10^{15}$, evaporation, $t = 71$

	C	T	k
Max	4.1	8.4	1.1e-1
Min	-0.48	-0.49	0
Δ	0.4	0.81	9.9e-3

C   T   k

The destratification is clearly faster (about 4 min.). During the first phase when all two layers persist, the thermal and mass diffusion at the interface level is not pratically existing: the cooling of the upper layer by evaporation is exactly compensated by wall thermal supply at the upper layer level. The lower layer presents a very important superheat. The interface vanishing is nearly instantaneous, freeing accumulated energy in the lower layer and producing a very important evaporation peak (rollover). In the next, the concentration is homogeneous in the most of the tank excepting at the free surface level where it subsists a small evaporation.

5 CONCLUSION

A numerical method has been developed to solve the non linear parabolic equations governing the turbulent motions induced by double-diffusive transfer in the rectangular cavities of large dimensions. This numerical method is stable with the high Grashof number because the thermal and mass body forces are opposed. The results obtained for an initial stratification of the LNG allow one to follow the fluid destratification until the rollover phenomena.

NOMENCLATURE

Subscript   1 = Lower layer
                     2 = Upper layer

Superscript   n = Time step number
                     * = Dimensional
                     0 = Initial condition

a = Thermal diffusivity (m^2/s)

C = Species concentration = $(C^* - C^{*0})/\Delta C^{*0}$, where $C^{*n} = 0.5(C^{*n}_1 + C^{*n}_2)$, $\Delta C^{*n} = C^{*n}_1 - C^{*n}_2$

D = Binary diffusion coefficient (m^2/s)

g = Acceleration due to gravity (m/s^2)

Gr_m = Mass Grashof number = $\beta_m g H^3 \Delta C^{*n}/v^2$

Gr_{th} = Thermal Grashof number = $\beta_{th} g H^3 \Delta T^{*n}/v^2$

h_{lg} = Enthalpy of evaporation (J/kg)

H = Height (m)

j = Mass flux = $j^* H/(D \Delta C^{*n})$

L = Width of the cavity (m)

k = Turbulent kinetic energy = $k^*(v/H)^{-2}(Gr_{th} + Gr_m)^{-1}$

Pr = Prandtl number = v/a

φ = Heat flux = $\varphi^* H/(\lambda \Delta T^{*n})$

Sc = Schmidt number = v/D

t = Time = $t^*(v/H^2)(Gr_{th} + Gr_m)^{0.5}$

T = Temperature = $(T^* - T^{*n})/\Delta T^{*n}$, where $T^{*n} = 0.5(T^{*n}_1 + T^{*n}_2)$, $\Delta T^{*n} = T^{*n}_1 - T^{*n}_2$

$u[v]$ = Velocity in $x[y]$ direction = $u^*[v^*](H/v)(Gr_{th} + Gr_m)^{-0.5}$

u', v' = Velocity fluctuations (m/s)

$x[y]$ = Cartesian coordinates = $x^*[y^*]/H$

β_m = Volumetric coefficient of expansion with concentration = $-(1/\rho)(d\rho/dC^*)_{T^*}$ ($kg^{-1} m^3$)

β_{th} = Volumetric coefficient of expansion with temperature = $-(1/\rho)(d\rho/dT^*)_{C^*}$ (K^{-1})

ε = Turbulent energy dissipation = $\varepsilon^* H^3 v^{-3}(Gr_{th} + Gr_m)^{-1.5}$

η_l = Zeroth order coefficient in x dependence equation (19)

λ = Thermal conductivity (W/mK)

v = Kinematic viscosity of the fluid (m^2/s)

v_t = Turbulent viscosity = $v_t^* v^{-1}(Gr_{th} + Gr_m)^{-0.5}$

ρ = Fluid density (kg/m^3)

Ω = Vorticity = $\Omega^* H^2 v^{-1}(Gr_{th} + Gr_m)^{-0.5}$

Ψ = Stream function = $\Psi^* v^{-1}(Gr_{th} + Gr_m)^{-0.5}$

REFERENCES

Ahluwalia, A.K. & Chan, A.M.C. 1989, Numerical simulation of laminar and turbulent heat and mass transfer in natural convection, Num. Methods in Laminar and Turbulent Flows - 6, pp. 2019-2028.

Antonia, R.A. & Kim, J. 1991, Turbulent Prandtl number in the near wall region of a turbulent channel flow, Int. J. Heat Mass Transfer, vol. 34, no. 7, pp. 1905-1908.

7

Beam, R.M. & Warming, R.F. 1979. Alternating direction implicit method for parabolic equations with a mixed derivative. SIAM. J. Sci. Comput., vol. 1.

Bejan, A. 1985. Mass and heat transfer by natural convection in a vertical cavity. Int. J. Heat Fluid Flow. no. 6. pp. 149-159

Bergman, T.L., Incropera, F.P. & Viskanta, R. 1985. A differential model for salt-stratified, double-diffusive systems heated from below. Int. J. Heat Mass Transfer, vol. 28, no. 4, pp. 779-788.

Bergman, T.L., Numerical simulation of double-diffusive Marangoni convection, Phys. Fluids, vol. 29, n°7, pp. 2103-2108, 1986

Hanjalic, K. & Launder, B.E. 1976. Contribution towards a Reynolds Stress Closure for Low Reynolds Number Turbulence. J. Fluid Mech., vol. 74, pt. 4, pp. 593-610.

Hashmi H.T. and Wesson H.R. 1971, Cut LNG storage costs, Hydrocarbon Processing, vol. 50, p.117

Kamakura, K. & Ozoe, H. 1993. Numerical analyses of transien formation and degradation process of multilayered roll cells with double-diffusive natural convection in an enclosure. Num. Heat Transfer. pt. A, vol. 23, pp. 61-77.

Launder, B.E. & Spalding, D.B. 1974. The Numerical Computation of Turbulent Flows. Comput. Methods in Applied Mechanics and Engineering, vol. 3, pp. 269-289.

Lee, J.W. & Hyun, J.M. 1991. Time-dependant double-diffusion in a stably stratified fluid under lateral heating. Int. J. Heat and Mass Transfer, vol. 34, no. 9, pp. 2409-2421.

Ozoe, H., Mouri, A., Ohmuro, M., Churchil, S.W. & Lior, N. 1985. Numerical Calculations of Laminar and Turbulent Natural Convection in Water in Rectangular Channels Heated and Cooled Isothermally on the Opposing Vertical Walls. Int. J. Heat Mass Transfer, vol. 28, no. 1, pp.125-138.

Ostrach, S. 1982a. Natural convection heat transfer in cavities and cells. Proc. 7th Int. Heat Transfer Conf., vol. 1. pp. 365-379.

Ostrach, S. 1982b. Low gravity fluid flows. Ann. Rev. Fluid Mech., vol. 14. pp.313-345.

Patel, V.C., Rodi, W. & Scheuerer, G. 1985. Turbulence models for near-wall and low Reynolds number flows: a review. AIAA Journal. vol. 23, no. 9.

Patterson, J. & Imberger, J. 1980. Unsteady natural convection in a rectangular cavity. J. Fluid Mech., vol. 100, pp. 65-86.

Roache, P.J. 1976. Computational Fluid Dynamics. pp. 91-94, Hermosa, Albuquerque, New Mexico.

Seveleder, V. 1990. Convection naturelle doublement diffusive dans des fluides stratifiés. Application au cas du Gaz Naturel Liquéfié. Thèse de Doctorat, Ecole Centrale Paris.

Seveleder, V. & Petit, J.P. 1989a. Flow structures induced by opposing forces in double-diffusive natural convection in a cavity. Num. Heat Transfer, pt. A, vol. 15, pp. 431-444.

Seveleder, V. & Petit, J.P. 1989b. Simultaneous heat and mass transfer in unsteady natural convection. Proc. 6th Num. Methods in Laminar and Turbulent Flows. pp. 999-1009.

Trevisan, O.V. & Bejan, A. 1987. Combined Heat and Mass Transfer by Natural Convection in a Vertical Enclosure. Trans ASME J. Heat Transfer, vol. 109, pp. 104-112.

Villers D. and Platten J.K. 1985. Marangoni convection in systems presenting a minimum in surface tension. Physico-Chemical Hydrodynamics, vol. 6, n°4, pp. 435-451.

Wang, P. 1987. Spline method of fractional steps in numerical model of unsteady natural convection flow at high Rayleigh number. Num. Heat Transfer, vol. 11, pp. 95-108.

Yang, R.J. & Aung, W. 1985. Equations and Coefficients for Turbulence Modeling. Natural Convection. Fundamentals and Applications, ed. Kakac, S., Aung, W. & Viskanta, R., pp. 259-300. Hemisphere, New York.

STRUCTURE AND DYNAMICS OF FILAMENTS IN THE CANARY AND BENGUELA UPWELLING REGIONS

A.G.Kostianoy (P.P.Shirshov Institute of Oceanology, 23, Krasikova str., Moscow, Russia).

Satellite data (thermal and colour imagery) has changed our view on the mesoscale structure of coastal upwellings after relatively recent discovery of cold, chlorophyll-rich, narrow (<50 km wide) offshore flowing filaments off the west coasts of North America, North and South Africa. On the base of archive satellite IR images and oceanographic data we investigated structure and dynamics of surface filaments in the Canary (15-25"N) and Benguela (15"-32"S) upwelling regions.

The data used in the study of the Canary upwelling region has been collected between 1984 and 1987. Besides the system of cold filaments (51 jets), which extend off-shore and beyond the coastal zone, cold filaments extending along the Banc d'Arguin border and warm filaments (9 jets) spreading from the ocean towards the coast were discovered. Cold filaments were concentrated near 23", 20"30', 19" and 18"N. The seasonal variability shows that 30% of them were observed in May-June and 58% in November-December. The maximal length of cold filaments lies in the range 50-250 km, the width 10-75 km, the temperature anomaly -0.8...-2.4"C, the maximal velocity 35-218 cm/s. Three-dimensional velocity structure of filaments is shown on the base of ADCP ship data. The most striking is the observation of large vertical velocities in filaments.

The data used in the study of the Benguela upwelling region has been collected during January-February 1986 and April-June 1988. Besides the system of cold filaments, large warm filaments (jets) spreading from the open ocean towards the coast were observed also. Cold filaments were concentrated near 18"-19", 22"-23"30' and 26"-27"30'S without any correlation with bottom topography irregularities. The length of cold filaments lies in the range 80-370 km, the width 10-80 km, the temperature anomaly -0.8...-2.4"C. The estimates of the velocity of filaments development give values up to 1-2 m/s. Warm jets were as long as 140-320 km with positive temperature anomalies up to 2.4"C.

It was found that seasonal variability of the filaments location in both upwelling regions depends on general upwelling intensity motion along the coast of North-West and South-West Africa during a year. A comparison between two system of filaments was made.

Estimates of cross-frontal water exchange due to filamentation show that these coherent structures play a major role in the water and particle exchange between coastal zone and the open ocean. Using the statistical data on filaments, it is possible to estimate the value of the velocity of cross-frontal water exchange, which equals to $Ue = 0.5 - 1.5$ cm/s. This value may underestimate the real one, because the water transport due eddies, subsurface lens-like eddies, subsurface jets and some other mesoscale structures was not taken into account because of the lack of information.

Recently, we introduced a new non-dimensioanl parameter P in order to estimate the "permeability" of fronts to water exchange (Zatsepin, Kostianoy, 1992). $P = Ue/U$, where Ue is the ve-

locity of cross frontal water exchange, and U is the r.m.s. velocity of mesoscale motion in the frontal zone. This parameter characterizes the relative part of mesoscale kinetic energy which produces cross-frontal water exchange. The estimated values of Ue and P for the Canary and Benguela upwelling regions are approximately the same. A comparison with Gulf Stream frontal zone was made, which shows that its permeability P due to ring exchange is lower than in the upwelling regions. It means that the Gulf Stream front is a more stronger barrier to water exchange than the Canary and Benguela upwelling front.

A Study of a Plane Mixing Layer With Cross Shear

Paisan Atsavapranee and Mory Gharib, *Graduate Aeronautical Laboratories, California Institute of Technology, Pasadena, CA 91125*

It is widely recognized that stratified mixing layers play a major role in both natural and industrial flows. Their understanding poses a challenging problem involving vorticity generation by baroclinicity, set in a complex coexistence and interaction of 2-D and 3-D structures on route to turbulence. The central goal of our current paper is to understand the nature of instabilities and turbulence in a plane stratified mixing layer complicated by the presence of cross shear. It is our speculation that the interaction of cross shear with plane mixing layers offers a unique turbulence control technique in industrial flows, and that it is widespread in nature because one important characteristics of natural mixing layers is the freedom of the mean shear to change direction in a transient way during the development of the mixing layer. In a jet stream or an oceanic shear layer, for example, the mean flow could easily shift direction during the development of a mixing layer. In an estuary flow, the river channel could expand or contract in a way as to introduce cross shear. Such an added complexity could change the characteristics of the instabilities and turbulence in very profound ways, resulting in different routes to transition and different turbulent states.

An apparatus similar to that used by S.A. Thorpe is constructed for the purpose of this study. In his 1968 paper, he describes how a temporally-developing stratified mixing layer can be generated without the presence of a splitter plate, using an enclosed horizontal tank filled with a layer of salt water and a layer of fresh water of equal depths. The tank is tilted off the horizon generating the potentials for the two layers to accelerate in opposite directions, resulting in a velocity shear at the interface. A similar tilting tank is constructed for this study, but with the allowance for the tank to be rotated around a secondary axis. The tank, 5 in. x 30 in. x 96 in. in dimensions, is first tilted around the first axis; and a certain time later, while the resulting shear layer is still developing, we tilt the tank around the second axis, generating the cross shear. The second tilt essentially allows us to control the overall mean shear by imposing cross shear on the developing primary shear layer. This is equivalent to realistic situations, in which the mean shear is not fixed in one direction but rather can change direction in a way that introduces cross shear to the initial mixing layer. The flow generated in such an apparatus well represents a generic temporal and complex turbulent flow in a non-equilibrium state, found in nature and industry. The novelty of our approach are the control of an added degree of complexity (cross shear) that other experiments have so far ignored and the lack of some flaws that are inherent in another type of apparatus. Traditionally, a shear tunnel with a straight splitter plate partitioning a low and a high speed flow is used (Koop & Browand, 1980), but it falls short in many ways. The presence of the flow-manipulating screens and the splitter plate can seriously alter the flow characteristics by introducing disturbances and artifacts into an otherwise clean and free mixing layer. The presence of a wake component is undesirable. And the flow generated in a shear tunnel exhibits an elliptic nature to a certain degree: downstream processes can create finite disturbances

upstream in a feedback mechanism, whereas a natural mixing layer, like ours, is temporal and purely parabolic in nature: dynamics of the flow obviously cannot influence processes that have already happened. The schematics of our experimental apparatus is presented in Fig. 1.

Preliminary flow visualizations and experiments have been carried out, using laser-induced fluorescence (LIF) technique and digital particle image velocimetry (DPIV, Willert & Gharib, 1991). The specific gravities of the top and bottom layers are 0.998 and 1.085, respectively, giving a density stratification of about 8%, normalized by the average density of the two layers. Flow visualization from the top (Fig. 2 and 3), using a technique to make the bottom layer opaque in order to visualize the interface, reveals many interesting features. Fig. 2 shows a plan-view photograph of the flow developed from a two-dimensional shear. The dark lines represent the edges of vortical structures that form shadows when the interface is illuminated from the top. Observations reveal that although the flow is generated in a very low-disturbance environment, the resulting Kelvin-Helmholtz instability is most often time not perfectly two-dimensional. The Kelvin-Helmholtz instability tends to develop into different regions of Kelvin-Helmholtz rollers, and it is possible to have slight amplitude and phase discrepancies among these regions. Each of these regions would eventually grow large enough in amplitude to interact with its neighbors. The consequence of these amplitude variations and phase shifts are complex interaction of the rollers reminiscent of patterns in desert sand dunes. The resulting rollers would generally be spanwise but exhibit defects or dislocations where the end of one roller can connect to the midspan of another. This observation seems to indicate that stratified mixing layers have finite spanwise coherence scales which are in the order of a few Kelvin-Helmholtz wavelengths. Observations of similar dislocations of Kelvin-Helmholtz rollers have also been recorded in a homogeneous mixing layer (Browand & Trout, 1980).

Fig. 3 illustrates the top view of the flow patterns in a shear layer to which cross shear is introduced a few seconds after the primary shear. As expected, the usual Kelvin-Helmholtz instabilities develop as a result of the main shear, with the main rollers aligned along the spanwise direction (z-axis). In addition streamwise streaks which are roughly perpendicular to the main rollers develop along the braid (Fig. 3a). The length scale of these streaks, after they first appear, is initially about 0.3 in., an order of magnitude lower than that of the main rollers which have a wavelength of about 3 in. As the mixing layer develops, the length scale of the streamwise streaks increases, seemingly going through successive doublings in scale (Fig. 3b.), and eventually, the mixing layer goes through turbulent transition. The y-z view or a cross-cut view of these small structures (Fig. 4) reveals that they seem to be structures of concentrated streamwise vorticity, and they are of the same sign everywhere. In fact they behave very much like Kelvin-Helmholtz rollers in that they roll up and pair. Fig. 5 is a sequence of pictures showing the pairing of two streamwise vortices. It is normal for these streamwise vortices to pair twice or three times, eventually making their sizes comparable to those of the main rollers which pair much slower. Fig. 6 shows a schematics of such a situation: the sketch on the left is the overall view of the mixing layer, and the sketch on the right shows what an y-z view would look like. These streamwise vortices are co-rotating and obviously of a different type of streamwise vortices from the counter-rotating type as described by Bernal &

Roshko (1986), because counter-rotating streamwise vortices would reveal "mushroom" shapes in the y-z plane, like that depicted in Fig. 7.

It is clear from these observations that the streamwise streaks are in fact concentrated streamwise vortical structures and that they are direct consequences of the cross shear. Deep understanding of the nature of these streamwise vortices is still a long way away, but a rudimentary picture of the dynamics can be derived from the clues available. The introduction of cross shear to a developing plane mixing layer essentially has the effect of imposing uniform streamwise vorticity everywhere in the mixing layer. This streamwise vortex sheet feels the presence of the flow field of the main mixing layer, and as a result becomes unstable giving rise to the concentrated streamwise vortices. The stability problem of the streamwise vortices can be qualitatively explained. In the braid region of the main rollers around the stagnation point, the local flow field looks like that of Hiemenz flow. This flow field creates a strain field that would magnify by stretching any streamwise vorticity present. With a uniform streamwise vortex sheet imposed upon the mixing layer, the stretching action in the braid region would magnify the streamwise vorticity there and make it very likely for the sheet to go unstable in a Kelvin-Helmholtz-like manner. The braid flow field would further stretch these Kelvin-Helmholtz-like streamwise vortices, which would go through pairings similar to normal Kelvin-Helmholtz rollers. The fact that the streamwise vortices are so perpendicular to the spanwise ones are most likely due to the fact that the main Kelvin-Helmholtz roll-up depletes the braid of the spanwise vorticity and concentrates most of it in the rollers. The vorticity in the braid, after the introduction of cross shear, is therefore mainly in the streamwise direction. One would expect the length scale of the streamwise vortices to scale on the thickness of the layer in the braid where they originate. Since the braid is continually being stretched thinner and thinner, it is expected and in fact observed in our experiments that the length scale of the streamwise vortices would be lower than that of the main rollers and would depend on how thick the braid is when the cross shear is introduced.

We believe these co-rotating streamwise vortices to have great significance in determining the nature of the mixing layer. Not only would the characteristics of the turbulence be different but also the degree of mixing would be greater as well. Measurements of the mixing layer thickness, before and after the tank tilting, shows that mixing layers with cross shear get 1.6-2.0 times as thick as the mixing layers without cross shear. In a simple two-dimensional mixing layer, it is the main rollers that do most of the entrainment and mixing, with the braid contributing little to the process. The presence of these streamwise vortices in the braid, which seemingly behave much like the main rollers themselves, would greatly enhance mixing, not only by entraining and mixing fluid themselves but also by interacting with the main rollers, creating more small scale turbulence. Since the streamwise vortices grow to a size comparable to that of the main rollers, the interaction between the two perpendicular structures can be expected to be significant, resulting in more mixing and earlier transition. The complete study of the interaction of a mixing layer with cross shear and the resulting turbulence characteristics is therefore of immense significance for a better understanding of natural and complex industrial turbulence.

REFERENCES

Bernal, L.P. & Roshko, A. 1986 Streamwise vortex structures in plane mixing layers. *J. Fluid Mech.* **170**, 499.

Browand, F.K. & Trout, T.R. 1980 A note on spanwise structure in the two-dimensional mixing layer. *J. Fluid Mech.* **97**, 771.

Koop, C.G. & Browand, F.K. 1980 Instabilities and turbulence in a stratified fluid with shear. *J. Fluid Mech.* **93**, 135.

Thorpe, S.A. 1968 A method of producing a shear flow in a stratified fluid. *J. Fluid Mech.* **32**, 693.

Willert, C.E. & Gharib, M. 1991 Digital particle image velocimetry. *Experiments in Fluids.* **10**, 181.
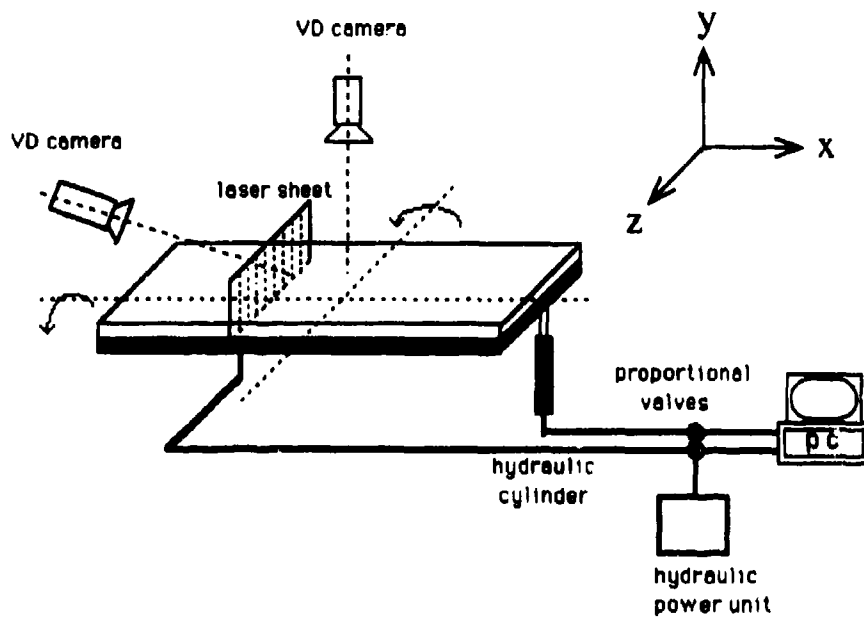
Fig. 1 Tank Schematics.

Fig. 2. Top view of a plane mixing layer showing dislocations of the rollers during early rollup.

a)

b)

Fig. 3 Top view of a mixing layer to which a weak cross shear is imposed.
Streamwise streaks develop in the braid and increase in scale as they evolve. The times
of a) and b) are 5.1 and 5.5 seconds after initiation of main tilt. Cross shear is introduced
at 5 secs, shortly after the onset of the main Kelvin-Helmholtz instabilities (at 3.9 sec.).
The Reynolds number of the main shear is 2800. The Richardson number is 0.03 for the
main shear and 0.5 for the cross shear. The cross shear is about 20% of the main shear.
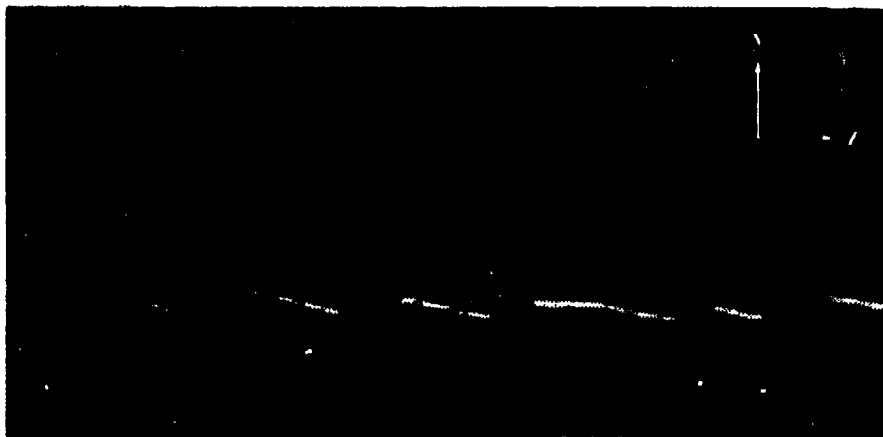
Fig. 4 A cross-sectional view of the streamwise streaks showing the "co-rotating" streamwise vortices. The image is taken 5.6 seconds after the initiation of the main tilt. Cross shear is introduced at 4 secs, about the same time as the onset of the main Kelvin-Helmholtz instabilities (at 4.1 sec.). The Reynolds number of the main shear is 1600. The Richardson number is 0.07 for the main shear and 0.15 for the cross shear. The cross shear is approximately 50% of the main shear.

a)   b)   c)
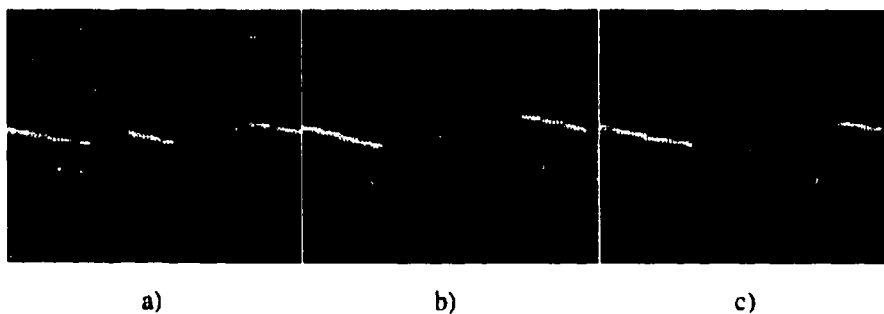
Fig. 5 A sequence of pictures showing two "co-rotating" streamwise vortices in the process of pairing. The conditions are the same as in Fig. 4. The times of the sequence are 5.60, 5.73, and 5.85 seconds after the inition of the main tilt.

cross shear

primary shear

overall view   cross-cut view

Fig. 6 Schematics for structures in a mixing layer with cross shear.

primary shear

overall! view   cross-cut view
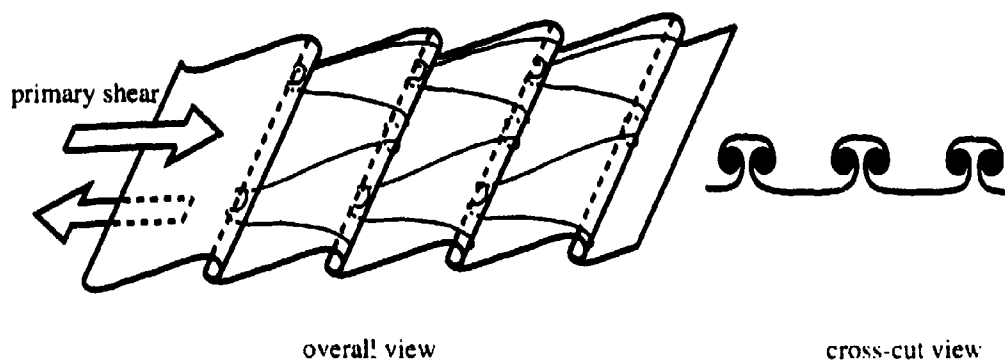
Fig. 7 Schematics for structures in a mixing layer w/o cross shear, as observed by Bernal & Roshko, 1986. A mixing layer with cross shear does not give rise to counter-rotating streamwise vortices as illustrated here.

Heat and mass transfer in stably stratified flow

SATORU KOMORI, KOUJI NAGATA AND YASUHIRO MURAKAMI
*Department of Chemical Engineering, Kyushu University,
Hakozaki, Fukuoka 812, Japan*

Abstract. Heat and mass transfer mechanism in strong stable thermal-stratification is experimentally investigated in unsheared water flows downstream of turbulence-generation grids, where both active scalar (heat) and passive scalar (mass) are diffused. Instantaneous velocity, temperature and concentration are simultaneously measured using a laser Doppler velocimeter, a resistance thermometer and a laser-induced fluorescence technique, and turbulence quantities such as turbulent scalar fluxes, joint probability density functions and cospectra are calculated. The results show that the difference of turbulent diffusion between heat (active scar) and mass (passive scalar) in strongly-stratified water flows appears in the high-frequency region and it results in a little larger turbulent mass flux than heat flux. The dissipation rate is rather different between heat and mass, and therefore the temperature fluctuation more rapidly decays than the concentration fluctuation. The counter-gradient scalar transfer occurs in strongly stably-stratified conditions, and the counter-gradient transfer mechanism is explained from the relationship between buoyancy and turbulent motions. The counter-gradient scalar transfer is initiated by the buoyancy-induced small-scale finger-like motions and then the contribution of the large-scale motions pushed back by buoyancy to the counter-gradient scalar transfer becomes dominant. The contributions of the small- and large-scale motions in the present thermally-stratified water flows are quite contrastive to the measurements in previously investigated thermally-stratified air flows where the counter-gradient heat transfer is generated mainly by large-scale motions.

1. Introduction

Thermally-stratified turbulent flows occur in the ocean, the atmospheric boundary layer, and in many industrial operations, and there turbulent diffusion of scalar quantities such as heat and mass is strongly affected by buoyancy. It is, therefore, of great practical interest to investigate the heat and mass transfer mechanism in stratified flows in modeling the turbulent diffusion of scalar quantities in the environment and in designing industrial equipments with stratified flows.

Extensive studies on the turbulence structure and scalar transfer have been performed in stably stratified flows. Though most of fundamental phenomena appearing in stably stratified flows seem to have been investigated up, several problems to be experimentally clarified still remain. One of the problems is the counter-gradient scalar transfer in strong stable stratification. Komori et al. [1] have found the counter-gradient heat and momentum transfer in a thermally-stratified open-channel water flow with weak shear, and Rohr et al. [2] have also investigated the counter-gradient mass transfer in density-stratified open-channel flows. However, these studies on stratified water flows have not clarified the details of the counter-gradient scalar transfer mechanism. Especially the contribution of small-scale motions to the counter-gradient transfer has not been fully discussed [2]. For stably-stratified air flows, Lienhard and Van Atta [3] and Yoon and Warhaft [4] have observed the counter-gradient heat flux (CGHF). Their studies have showed which scale motion contributes to the CGHF, and they also have suggested that it is of interest to investigate the effects of the Prandtl number on the CGHF.

On the other hand, Deissler [5] have discussed the effects of the Prandtl number on the CGHF in weak turbulence by solving the linearized two-point correlation equations, and he have predicted that the contributions of large- and small-scale motions to the CGHF are quite

different between high and low Prandtl numbers. Recently, Gerz et al.[6] and Holt et al. [7] have carried out direct numerical simulations (DNS) for homogeneous stratified flows, and they have predicted the effects of the Prandtl and Reynolds numbers. However, the results of the DNS with high Prandtl and Reynolds numbers are still controversial, and therefore more reliable measurements of the counter-gradient scalar flux in stratified water flows with high Prandtl numbers are required.

Another problem is the difference of turbulent diffusion between active scalar (heat) and passive scalar (mass) in thermally-stratified water flows. The difference may be generated by different molecular diffusivities between heat and mass, and it may be significant in strongly stratified flows where turbulent motions are much suppressed by buoyancy. However, this problem has not been experimentally investigated in stratified flows where both heat and mass are simultaneously diffused.

The purpose of this study is, therefore, to experimentally investigate both the counter-gradient scalar transfer mechanism in unsheared thermally-stratified water flows and the effects of the Prandtl number on the counter-gradient scalar transfer. This study also aims to experimentally clarify the difference of turbulent diffusion between heat (active scalar) and mass (passive scalar).

2. Experiments

Figure 1 shows the measuring system and test apparatus. The test apparatus used was the water tunnel which was made of polymethylemethacrylate (PMMA), 1m in length and 0.1x 0.1m in cross section. The waters with high and low temperatures were pumped up from two big storage tanks to the head tanks, and they passed the contraction, which was separated by a splitter plate into upper and lower sections. The high-temperature water in the upper stream was heated by a boiler in a storage tank and the temperature was regulated by an electric heater connected to a thermometer. A turbulence grid was installed at the entrance of a test section, and it was of round-rod, square-mesh, single-biplane construction. The mesh size M and the diameter of the rod d were 0.02 and 0.003m, respectively. Both mean
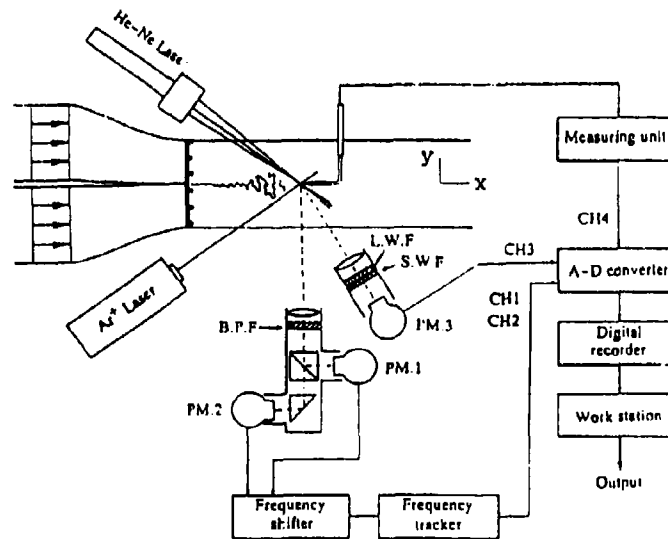
Fig.1. Measuring system and test apparatus.

2

velocities of upper high-temperature and lower low-temperature streams, $\overline{U}$, were set to the same value of 0.125m/s, so that a shear-free (unsheared) mixing layer was developed downstream of a turbulence grid. The Reynolds number based on the mesh size was 2,500 and the turbulence Reynolds number based on the integral scale was estimated to be about 20 at x/M=6. Three stably-stratified conditions were used and the temperature difference between upper and lower streams was set to 3K, 7K and 15K, respectively. The temperature difference corresponded to the Brunt-Väisälä frequencies of N= 0.67, 1.17 and 1.75Hz at x/M=6. The sodium fluorescein dye ($C_{20}H_{10}Na_2O_5$) was homogeneously premixed into the upper stream to investigate turbulent diffusion of the mass (passive scalar) which is diffused with heat.

Instantaneous velocity, temperature and concentration were measured using a two-component laser-Doppler velocimeter, a resistance thermometer connected to a cold film I-probe of 10μm diameter and a laser-induced fluorescence method. The details of the simultaneous measuring techniques for velocity, temperature and concentration are described in Komori et al.[1, 8].

The measurements were made on the centerline in the region of 6≤x/M≤20.   The sampling interval and the sample size were 0.00025 sec and 240,000, respectively. Statistical processing of the digitized data was made by a computer (SONY NWS-3860).

3. Results and discussion

3.1 Mechanism of counter-gradient scalar transfer

Figures 2 and 3 show the streamwise variations of vertical heat and mass fluxes, $-\overline{v\theta}$ and $-\overline{v\gamma}$. Here the vertical heat and mass fluxes are normalized by the product of the mean velocity $\overline{U}$ and the initial temperature- or concentration-difference. For all stratified conditions, the distributions of the heat (active scalar) flux are quite similar to the mass (passive scalar) flux distributions. Both heat and mass fluxes decrease with increasing the stability (the Brunt-Väisälä frequency N). In the strongest stratification case of N=1.75Hz, the fluxes change their signs in the region of 10<x/M<20 though the mean temperature and concentration gradients
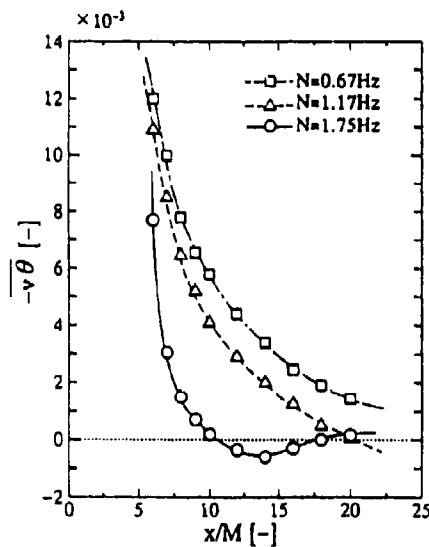
Fig.2. Streamwise variations of
vertical heat flux $-\overline{v\theta}$.
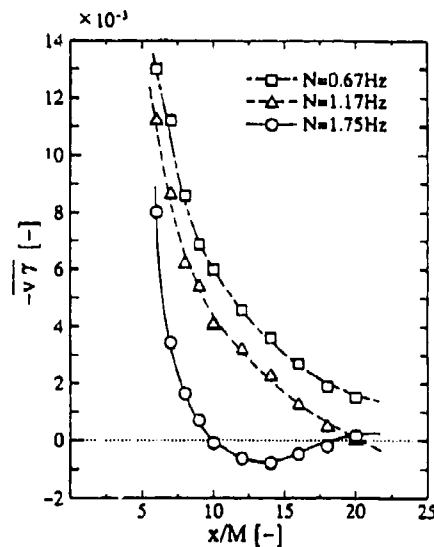
Fig.3. Streamwise variations of
vertical mass flux $-\overline{v\gamma}$.

3

are always positive in the upward direction. The counter-gradient heat and mass fluxes are generated by two combinations of positive v and θ and negative v and θ or positive v and γ and negative v and γ. In fact, the joint probability density function of v and θ in Fig.4 shows that in strong stratification of $N=1.75Hz$ the large positive and negative v are mainly associated with large positive and negative θ, respectively, (Fig.4b) whereas the joint probability function in weak stratification prevails into the second and fourth quadrants (Fig.4a). The behavior of the joint probability function of v and γ was similar to that of v and θ. Thus, it is found that the counter-gradient heat (active scalar) and mass (passive scalar) transfer in strong stratification is generated by both upward motion of hot eddies with high concentration and downward motion of cold eddies with low concentration.
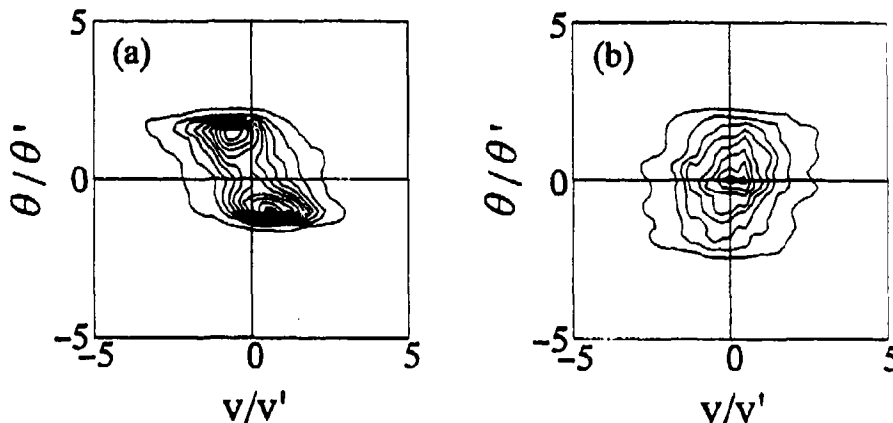
Fig.4. Joint probability density function of v and θ;
(a) in weak stratification; (b) in strong stratification

Figures 5 and 6 show the cospectra of v and θ, $Cs_{v\theta}$, at three locations of $x/M=6$, 10 and 14 under two stratified conditions of $N=0.67$ and $1.75Hz$, and the magnified cospectra of $N=1.75Hz$ at $x/M=10$ and 14 are shown in Fig.7. The area of the cospectra multiplied by the frequency f indicates the quantity of the heat flux, and the negative and positive values of $Cs_{v\theta}$ correspond to down-gradient heat flux (DGHF) and counter-gradient heat flux (CGHF), respectively. In weak stratification the cospectra at all locations are always negative in the whole frequency region (Fig.5). The distributions of the cospectra show that all turbulent eddies contribute to the DGHF in weak stratification. In strong stratification of $N=1.75Hz$, the cospectrum starts to change the sign from the higher frequency range and the cospectrum at $x/M=14$ becomes positive in the whole frequency range (Figs.6 and 7). This means that in strongly stratified water flows the small-scale motions first contribute to the CGHF and the large-scale motions follow the small-scale motions. In fact the flow visualization based on the laser-induced fluorescence technique shows that the buoyancy-induced upward and downward small-scale finger-like motions intruding into the original levels appear in the downstream region near $x/M=10$ and the large-scale eddies are pushed back by buoyancy toward the original levels in the region near $x/M=14$. The contributions of the turbulent eddies to the counter-gradient heat transfer are quite different in air flows [3,4]. The buoyancy-induced small-scale finger-like motions will never be observed in stratified air flows, since the relative molecular diffusion of heat is rather faster in air flows than in water flows. The difference between stratified water and air flows supports the predictions by Deissler [5], Gerz et al.[6] and Holt et al. [7]. Stronger buoyancy effect on the counter-gradient heat transfer in water flows can easily be seen when we compare the correlation coefficient between v and θ

4

plotted against the dimensionless time $Nx/\bar{U}$ with the previous measurements in air flows [3,4].
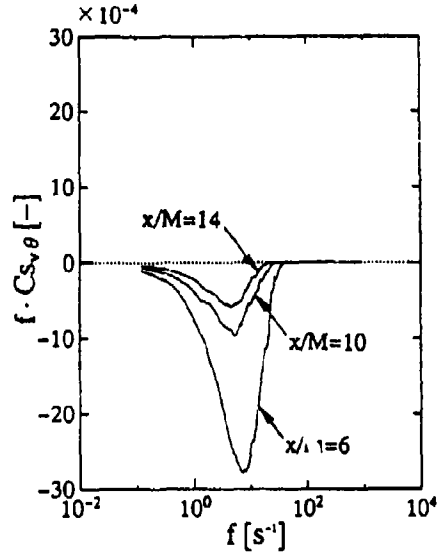
Fig.5. Cospectra of v and θ at three
        locations of x/M=6, 10 and 14
        in weak stratification of N=0.67Hz.
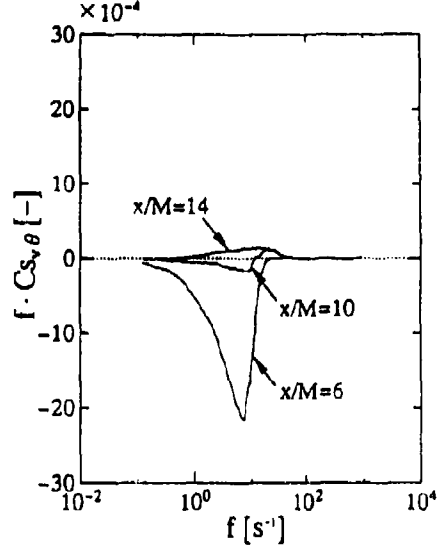
Fig.6. Cospectra of v and θ at three
        locations of x/M=6, 10 and 14
        in strong stratification of N=1.75Hz.
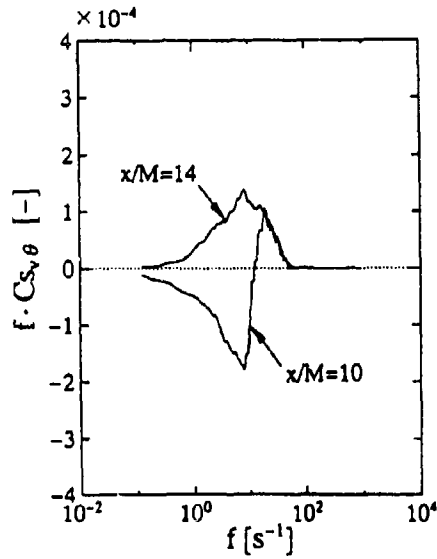
Fig.7. Magnified distributions of the cospectra
        of v and θ at two locations of x/M=10
        and 14 in strong stratification of N=1.75Hz.
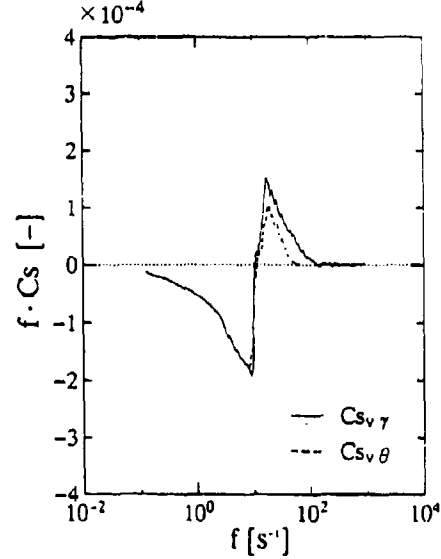
Fig.8. Comparison between the cospectra
        Cs$_{vy}$ and Cs$_{vθ}$ at x/M=10 in
        strong stratification of N=1.75Hz.

3.2 Difference of turbulent diffusion of heat (active scalar) and mass (passive scalar)

When the heat flux (Fig.2) is compared with the mass flux (Fig.3), the absolute value of the mass flux is a little larger than that of the heat flux. Especially in strong stratification of N=1.75Hz the difference reaches about 10% of the mean flux in the region of 10<x/M<20. The difference between the heat and mass fluxes is due to the difference between the molecular diffusivities of heat and mass. As shown in Figs.8 and 9, the comparisons between the cospectra $Cs_{V\gamma}$ and $Cs_{V\theta}$ at two locations of x/M=10 and 14 in strong stratification of N=1.75Hz show that the contribution of higher-frequency motions to the counter-gradient mass flux is larger than that to the counter-gradient heat transfer. Of course, the effect of the molecular diffusivity on the dissipation rate becomes significant, and therefore the mean squared temperature fluctuation more rapidly decays in the downstream region than the mean squared concentration fluctuation as shown in Fig.10. These effects of the molecular diffusion on heat and mass transfer will not be observed in stratified air flows since the Prandtl number is very close to the Schmidt number.
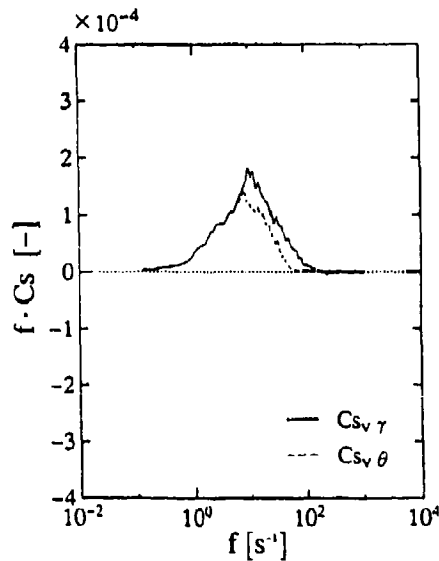
Fig.9. Comparison between the cospectra $Cs_{V\gamma}$ and $Cs_{V\theta}$ at x/M=14 in strong stratification of N=1.75Hz.
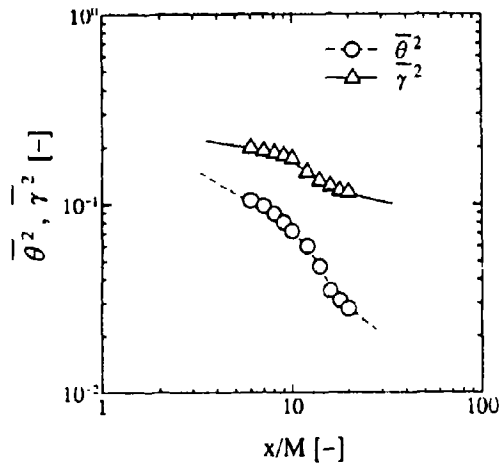
Fig.10. Streamwise variations of the mean squared temperature and concentration fluctuations in strong stratification of N=1.75Hz.

4. Conclusions

Heat and mass transfer mechanism in strong stable thermal-stratification was experimentally investigated in unsheared water flows downstream of turbulence-generation grids. The main results from this study can be summarized as follows.

1. The counter-gradient scalar transfer occurs in strongly stably-stratified conditions. The counter-gradient scalar transfer is initiated by the buoyancy-induced small-scale finger-like motions and then the counter-gradient transfer by the large-scale motions pushed back by buoyancy becomes dominant in the downstream region. The contributions of small- and large-scale motions to the counter-gradient scalar transfer is quite contrastive to previously

investigated thermally-stratified air flows where the counter-gradient heat transfer is generated mainly by large-scale motions.

2. The difference of turbulent diffusion between heat (active scalar) and mass (passive scalar) is induced by the difference between the molecular diffusivities of heat and mass in the higher frequency region, and the absolute value of the mass flux is a little larger than that of the heat flux. Though the effect of the molecular diffusion on the mean heat and mass fluxes is not so large, the decay of the scalar fluctuation in the downstream direction is strongly affected by the molecular diffusion.

References
1. Komori, S., Ueda, H., Ogino, F. and Mizushina T., *J. Fluid Mech.*, **130**, 13-26 (1983).
2. Rohr, J.J., Itsweire, E.C., Helland, K.N. and Van Atta, C.W., *J. Fluid Mech.*, **155**, 77-111 (1988).
3. Lienhard, V. and Van Atta, C.W., *J. Fluid Mech.*, **210**, 57-112 (1990).
4. Yoon, K. and Warhaft, Z., *J. Fluid Mech.*, **215**, 601-638 (1991)
5. Deissler, R.G., *J. Geophys. Res.*, **67**, 3049-3062 (1962).
6. Gerz, T., Schumann, U. and Elghobashi, S.E., *J. Fluid Mech.*, **200**, 563-594 (1989).
7. Holt, S.E., Koseff, J.R. and Ferziger, J.H., *J. Fluid Mech.*, **237**, 499-539 (1992).
8. Komori, S., Nagata, K, Kanzaki, T. and Murakami, Y., *AIChE J.*, **39**, 1611-1620 (1993).

Some Observations Related to Evolving Kelvin-Helmholtz Billows

De Silva, IPD, Montenegro, L and Fernando, HJS. Department of Mechanical & Aerospace Engineering, Arizona State University, Tempe, AZ 85287-6106.
Brandt, A. Applied Physics Laboratory, The Johns Hopkins University, Laurel, MD 20723-6099.

Abstract

Laboratory experiments were carried out to investigate the effects of relative thicknesses of velocity and density profiles and their displacements with respect to each other on the characteristics of Kelvin-Helmholtz (K-H) billows that are developed in stratified shear flows. Two experimental facilities were used. First, a two-layer stably stratified shear flow was employed to obtain a time series of the local Richardson number, $Ri = \Delta b \Delta z / \Delta u^2$, where Δb is the local buoyancy difference, Δu is the local shear and $\Delta z = 2.7$ mm is the scale over which the measurements were made. Second, a tilting tube was used to obtain standing K-H billows in an accelerating shear flow. The results illustrated the development of local overturning motions (convective instabilities), as K-H billows advect past an Eulerian measuring point. The results showed that the local Richardson number can be small compared to the global Richardson number based on bulk flow parameters, and hence suggest that inferences should not be made solely based on global Richardson-number measurements. Laser-induced fluorescence technique was used to obtain both quantitative and qualitative results concerning the internal temporal and spatial density structures within K-H billows. Digitized images show that mixing begins to appear at the core area of evolving billows, long before their collapse. Thorpe displacements evaluated from the images were used to delineate the locations where convective instabilities occur within billows.

1 Introduction

Kelvin-Helmholtz instability has been considered as a possible cause of clear-air turbulence in the atmosphere. The turbulence generated due to shear instabilities has been identified in atmosphere (Gossard 1962; Scorer 1969), in oceans (Woods 1968; Hebert et al 1992; Marmorino 1987) and in lakes (Thorpe & Hall 1974). Comprehensive reports on theoretical considerations pertinent to stability of parallel shear flows are given, for example, by Drazin & Howard (1966) and Thorpe (1969a). Scorer (1969, and also in a series of preceding papers) shows striking photographs of atmospheric occurrences of billowing. K-H instabilities may also be responsible for much of the vertical transport of buoyancy and heat in the ocean. Although the mixing events due to K-H billows are dictated by the local gradient Richardson number, $N^2/(dU/dz)^2$, not much related field measurements are available. According to the measurements of Kundu & Beardsley (1991), in oceans, K-H type instabilities are more common in coastal areas with stronger currents than in the open ocean where the instabilities mostly occur due to superposition of internal waves.

Thorpe (1971, 1973) observed that in a two-layer system the Richardson number at the interface after the evolution of billows is a constant, about 0.33, regardless of the initial Richardson number; this suggests a self-adjustment of the flow field. On the other hand, the vertical lengthscales of the mean velocity and density profiles were found to depend on the Richardson number. Thorpe (1968) reported the development of small-scale secondary instabilities on the braids that connect adjoining billows; nonetheless, the three dimensional motions that lead to turbulence are known to start within the billows. The onset of small-scale irregularities on the wave spirals is first observed when the wave slope assumes values between 1.2 and 1.4; these instabilities finally tend to develop into turbulence and mixed regions. The mechanism for such a transition, although not known precisely, is thought to be due to convective instabilities. Numerical simulations show that most

unstable disturbances are convectively driven and, small-scale rolls in the billows are oriented in the direction of mean flow. Increase of Prandtl number tends to destabilize the rolls (Klaassen & Peltier 1985, 1991; for experimental evidence see Thorpe 1985). In a recent paper, Lawrence et al. (1991) studied the stability of stratified shear flows when the density interface (of thickness δ) is much thinner than, and is displaced by an amount d with respect to, the velocity interface (of thickness h). In practice both these scales grow with time (or with the downstream distance). The difference in h and δ results in preferential entrainment of the fluid from one layer to the other. The ratio of h/δ is an important factor in the stability of the flow field. In general, when h/$\delta \sim 1$, the flow could be stabilized by choosing a sufficiently larger density step. On the other hand when, h/δ >> 1, such stabilization is not always possible. It was shown that, for h/$\delta \rightarrow \infty$, and Re $\rightarrow \infty$ some wave numbers are always unstable irrespective of the value of Ri.

2 Experiments

The experiments were conducted using two different configurations. The first was an annular closed-circuit water channel and the second was a tilting tank. A schematic diagram of the water channel is shown in Figure 1; it is a modified version of the Odell & Kovasznay (1971) apparatus and a disk pump was used to drive the less dense upper fluid over an almost stagnant heavier salt solution. To minimize mixing between the two layers, the fluids were physically separated by a thin horizontal sheet of Plexiglas, except over a test section of about 100 cm long, over which the experimental data were taken. The top fluid layer enters the test section following its passage over the splitter plate, which is an integral part of Plexiglas separation sheets. The stainless steel splitter plate was 1 mm thick and has a taper of 20:1 at the trailing edge. The initial Richardson number, $Ri_0 = \Delta bh/\Delta U^2$, based on the buoyancy difference (Δb), the velocity difference (ΔU) and the thickness of the velocity interface h, was varied in the range 0.4 to 72.

The tilting tank has dimensions of 0.15 x 0.15 x 4 m. The tank was initially filled with the heavier (salty) fluid and the lighter fluid was slowly added from the top to avoid mixing. In experiments where the laser-induced fluorescence (LIF) technique was used, the bottom heavy salty layer was seeded with Rhodamine-6G dye, and 200-proof Ethyl alcohol was added to the top layer to match the refractive indices. The vertical mid plane along the longest axis of the tank was illuminated with a vertical sheet of Argon-ion laser (2 W). The experiments were initiated by momentarily tilting the tube from its horizontal position to a specified inclination. The velocity shear generated at the interface by the ascending motion of the lighter layer and vice versa leads to the development of a well-defined series of K-H instabilities, as was reported by Thorpe (1968,1969b, 1971, 1973). The depths of two fluid layers in the tilting tank were the same and hence the billows are stationary. A billow, near the center of the tank, where wall and end effects are minimal, was selected and analyzed in detail.

3 Results

Figure 2 shows a series of (LIF) photographs of a temporally evolving K-H billow captured using the LIF technique. As seen in the Figure 2a, the initial thickness of the density interface due to molecular diffusion is thin; and it remains thin during the initial evolution of the billow. The latter observation suggests that not much mixing occurs at the interface nor at the braids, and most of the mixing was found to betide at the eye of the billow. Figure 2b shows the billow at a later time where well-defined spiraling motions can be seen. Figure 2c depicts the billow just prior to its collapse and Figure 2d shows a highly turbulent billow during mature stages of the evolution. As a result, the core of the billow undergoes small-scale mixing. This turbulent mixing activity is further enhanced by

the presence of gravitationally unstable shearing motions during the roll-up. However, the billows are expected to gain some stability and longevity by the stabilizing Coriolis forces that are induced due to the vigorous spin within the "eye". According to a theory proposed by Gibson & Imberger (1994), maximum dissipation within a billow occurs at the density interface during the initial growth of instabilities; in general, the interior of the billows are gravitationally unstable. A different scenario of K-H evolution has been put forward by Thorpe (1987) and Gregg (1987); accordingly the maximum dissipation occurs in small viscous-dissipative scales that are present in secondary convective rolls that appear during the roll-up motion.

The magnitude of the local gradient Richardson number Ri is of prime interest in predicting the K-H billow occurrences, but the problem is to determine over what scales the Ri should be measured so that the results are of some practical use. It is clear that, in a flow field with non-uniform density and velocity profiles, the measured Ri depends on the lengthscale of measurement, and the largest scale that can be employed with some consequence is of interest. A noteworthy achievement of the present work is the measurement of the local gradient Richardson number Ri, via the measurement of the local velocity shear and the local buoyancy difference at a separation of $\Delta z = 0.27$ cm. The measurement locations were well within the region of maximum density and velocity shear (The experiments by Scotti & Corcos (1972) on a heat-stratified air shear-layer showed that the minimum local Ri occurs near the center of the shear layer). The results show that the local Ri tends to change with time as the waves pass by the measurement point. This is due to the change of the local velocity and density structure in the vicinity of waves. The properties of the waves are determined by the initial vertical profiles of velocity and density as well as background disturbances. Continuous changes occurring in local density and velocity profiles, as well as the secondary instabilities of three-dimensional nature, tend to change Ri in an irregular manner. In the measurements, Ri was defined as the minimum absolute averaged Ri over a period of half a second. Such averaging was necessary in order to eliminate the possibility of having $\Delta u = 0$, which gives unrealistic data. Since the time scale of the instability waves is much longer than the averaging time, the results are expected to give an idea on the local instantaneous values (note that the averaging does not exclude situations with Ri < 0). Figure 3(a) shows the variation of Ri with time for $Ri_0 \approx$ 72 and $\varepsilon \approx d/h \approx 1.8$; here no K-H instabilities were observed, because of the large magnitudes of Ri. Figure 3(b) shows the variation of Ri with $Ri_0 \approx 10.6$, $\varepsilon \approx 1.2$. During this experiment a recurrent sequence of K-H waves was observed. Note that the magnitude of the instantaneous local gradient Ri remains low compared to that of the high initial Ri_0 experiment described in Figure 3(a). Also note that Ri becomes negative, which indicates overturning motions.

4 Conclusions

The local gradient Richardson number was measured by finite differencing the time traces of velocity and density records taken in a stably stratified two-layer shear flow, at a vertical separation of 0.27 cm. The measurements showed that, at a fixed point, Ri fluctuates with time as a result of continuous distortions that occur in vertical density and velocity profiles with the passage of instability waves. It was found that the averaged Ri depends on the initial bulk Ri_0, as was pointed out by Sullivan (1992) and Fernando & Stephenson (1991). LIF photographs clearly indicate that much of the mixing occurs in the vicinity of the eye of the billows.

References

Drazin, P.G. & Howard, L.N. *Adv. Applied Mech.*, **9**, 1-89(1966).

Fernando, H.J.S & Stephenson, P. *Environmental Hydraulics*, Balkema Publishing, The Netherlands (1991).

Gibson, C.H. & Imberger, J. Submitted to *J. Fluid Mech.*(1994).

Gossard, G.E. *J. Geophys. Res.*, **67**, 745-757(1962).

Gregg, M.C. *J. Geophys. Res.*, **92**, 5249-5286(1987).

Herbert, D., Moum, J.N., Paulson, C.A. & Caldwell, D.R. *J. Phys. Oceanogr.* **22**, 1346-1356(1992).

Klaassen, G.P. & Peltier, W.R. *Geophys. Astrophys. Fluid Dyn.*, **32**, 23-60(1985).

Klaassen, G.P. & Peltier, W.R. *J. Fluid Mech.*, **227**, 71-106(1991).

Kundu, P.K. & Beardsley, R.C. *J. Geophys. Res.*, **96**, 4855-4868(1991).

Lawrence, G.A., Browand, F.K. & Redekopp, L.G. *Phys. Fluids*, **3, 10**, 2360-2370(1991).

Marmorino, G.O. *J. Phys. Oceanogr.*, **17**, 1348-1355(1987).

Odell, G.M. & Kovasznay, L.S.G. *J. Fluid Mech.*, **50**, 535-543(1971).

Scorer, R.S. *Radio Science*, **4, 12**, 1299-1308(1969).

Scotti, R.S. & Corcos, G.M. *J. Fluid Mech.*, **52**, 499-528(1972).

Sullivan, G.D. *Ph.D. Dissertation.* California Institute of Technology, 1992.

Thorpe, S.A. *J. Fluid Mech.*, **32**, 693-704(1968).

Thorpe, S.A. *J. Fluid Mech.*, **36**, 673-683(1969a).

Thorpe, S.A. *Radio Sci.*, **12**, 1327-1331(1969b).

Thorpe, S.A. *J. Fluid Mech.*, **46**, 299-319(1971).

Thorpe, S.A. *J. Fluid Mech.*, **61**, 731-751(1973).

Thorpe, S.A. *Geophys. Astrophys. Fluid Dyn.*, **34**, 175-199(1985)

Thorpe, S.A. *J. Geophys. Res.*, **92**, 5231-5248(1987).

Thorpe, S.A. & Hall A.J. *Limnology and Oceanogr.*, **19**, 973-976(1974).

Woods, J.D. *J. Fluid Mech.*, **32**, 791-800(1968).
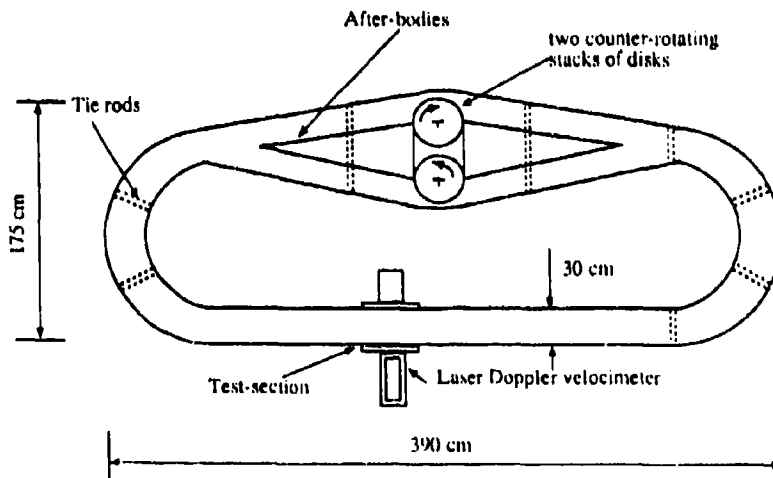
Figure 1   Schematic diagram of the closed-circuit water channel.
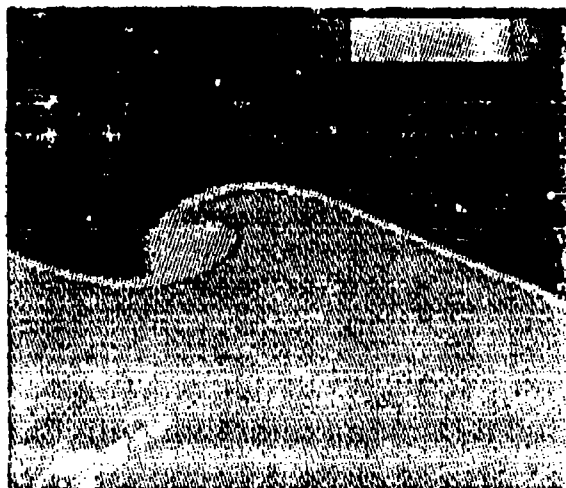
(a)
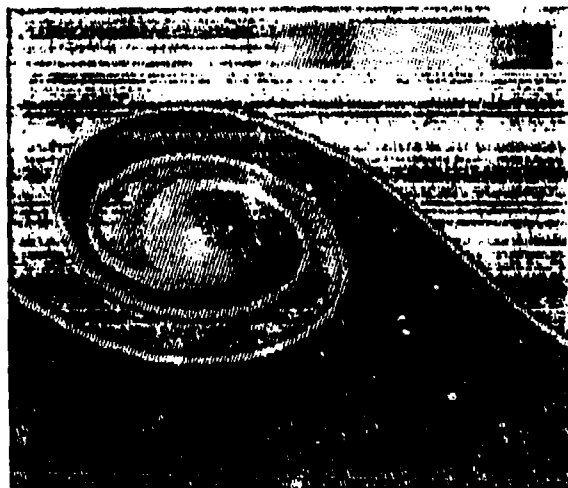
(b)

Figure 2   A series of LIF photographs that show the time evolution of K-H billows. Figures (a), (b), (c) and (d) represent the state of the billow after 0.7, 1.9, 3.3 and 3.8 seconds, respectively. The densities of the upper and lower layers are 0.983 gm/cm^3 and 1.015 gm/cm^3, respectively. The tilt angle is 4°.
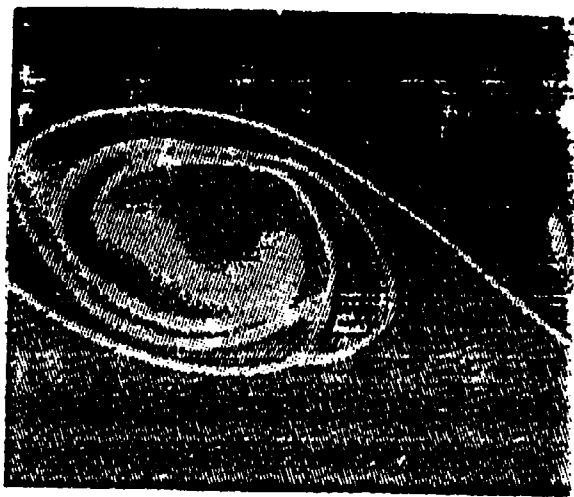
(c)

(d)
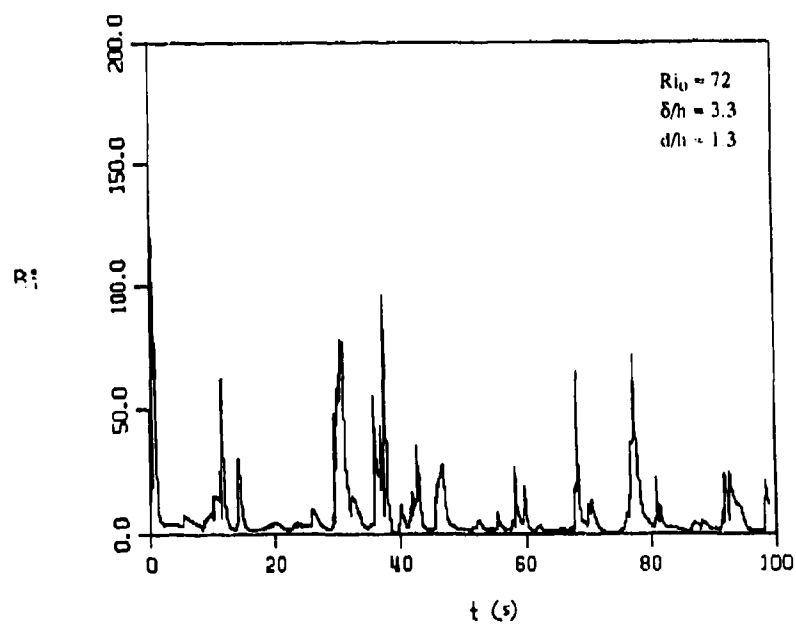
(a)
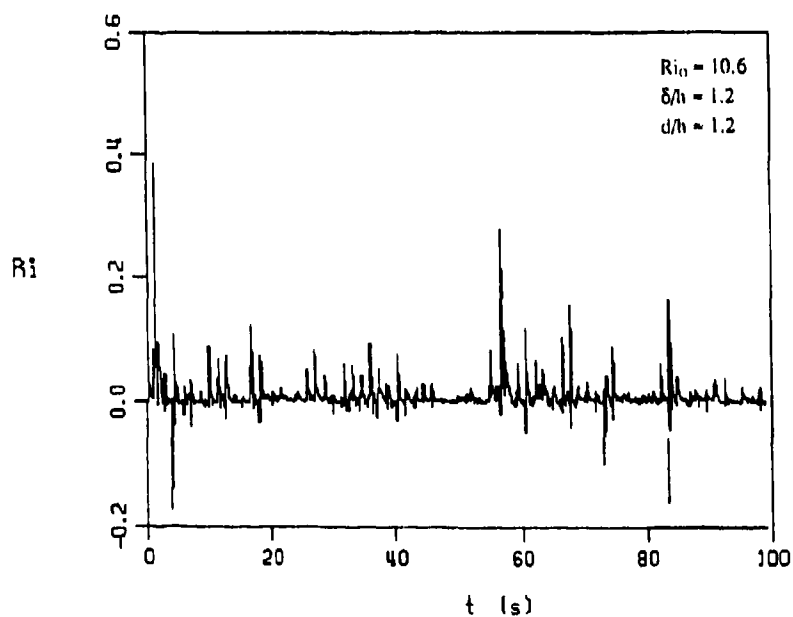
(b)

Figure 3   Time variation of the local gradient Richardson number.

Three Dimensionalization of the Stratified Mixing Layer

W.R. Peltier[1], C.P. Caulfield[1] and Shizuo Yoshida[2]
1: Department of Physics, University of Toronto
2: Department of Engineering Science, Hokkaido University

Abstract

We present a detailed analysis of the processes through which three dimensional motions arise in the free stratified mixing layer. Previously published Floquet analyses of the governing instabilities, both for stratified and unstratified flows, have suggested a wide range of mechanisms to be possible candidates for the origins of the streamwise vortex streaks that are observed to be precursory to fully developed turbulent flow. We employ very high resolution LES methods to reveal which of these candidate mechanisms is dominant.

1: Introduction

The issue of the origin of three dimensional motions in the free mixing layer is clearly central to the understanding of transition in such flows. Recent reviews of this problem have been presented by Ho and Huerre (1984) and Bayly et al. (1988) for the homogeneous problem and by Thorpe (1987) for the stratified case. Laboratory investigations by Breidenthal (1981), Bernal and Roshko (1986), Lasheras et al. (1986) and Lasheras and Choi (1988) have documented, for the unstratified case, the appearance of "mushroom-shaped" streamwise vortices as being precursory to turbulent collapse. Metcalfe et al. (1978) performed detailed three dimensional numerical simulations of merging KH vortices and showed that the initially realized three dimensional motions consisted primarily of such streamwise 'ribs' of vorticity that appeared to develop in the strained region between the initially two dimensional large vortices. Metcalfe et al., however, assert that they were unable to determine whether the streamwise vortex ribs that appeared in their simulations were generated through a flow transition that originated in the vortex cores or in the braids themselves. This is an important point because Corcos and Lin (1984) and Lin and Corcos (1984) have attributed the appearance of streamwise vortex streaks to the so-called translative instability of Pierrehumbert and Widnall (1982) a mode that was later associated (Pierrehumbert 1986; see also Bayly 1986) with a non-scale selective instability (the *elliptical* instability) that is supported by any vortex with non-zero ellipticity. The analyses to be presented herein are rather definitive, we believe, in demonstrating that the appearance of streamwise streaks in the unstratified mixing layer has nothing to do with the elliptical instability but rather is caused by an instability that is energized locally in the braids that was first documented by Klaassen and Peltier (1991). These analyses are therefore discordant with the recent numerical analyses of Rogers and Moser (1992).

In the case of the considerably more complicated stratified mixing layer problem the theoretical analyses of Klaassen and Peltier (1985) suggested that streamwise vortex streaks should also arise in this case but that they might be expected to originate through a shear aligned convective instability of the kind first (apparently) analysed by Kelly (1977). The possible importance of this dynamical mechanism was first suggested on physical grounds by Peltier et al. (1978) and Davis and Peltier (1979) later demonstrated that supercritical Rayleigh numbers were in fact delivered by two dimensional KH billows in super-adiabatic sub-layers within (and especially surrounding) the overturning vortex cores. The Floquet analysis of stability presented in Klaassen and Peltier (1985) and more fully elaborated in Klaassen and Peltier (1991) suggested that the cross-stream scale of the vortex streaks that would be generated by this mechanism would be approximately .1 λ_{KH} where λ_{KH} is the wavelength of the two-dimensional Kelvin-Helmholtz wave. Thorpe (1985) subsequently performed a new sequence of tilted tube experiments in order to search for the shear aligned convective rolls predicted by the Klaassen and Peltier analyses, experiments that did in fact reveal some evidence of the predicted mechanism prior to turbulent collapse. No unambiguous identification

of the observed cross-stream structures with the theoretical prediction was possible, however, so that in the case of the stratified fre : mixing layer the current state of understanding is as incomplete as it is in the unstratified case previously discussed.

In this paper our goal will be to summarize a new sequence of very high resolution numerical ι .periments that we have recently performed in an effort to provide definitive answers to the above questions. Following a brief review of the Floquet theory and its predictions in the following section, we will proceed to discuss the new numerical simulations of mixed layer collapse that have been performed. Our conclusions are presented in the final section of the paper.

2: The linear stability of two dimensional nonlinear dependent flows

It follows from Squire's (1933) theorem that the initial instability of a stratified parallel flow with horizontal velocity $u_x(z)$ and potential temperature (in the compressible case) $\theta(z)$ will be two dimensional in most circumstances (e.g. Smyth and Peltier 1990. A typical basic state that is employed in the investigation of the structures that develop from such instability is:

$$u_x(x,z;t=o) = u_o \tanh((z-H/2)/h) \tag{1a}$$

$$\theta(x,z;t=o) = \Theta + \theta_o \tanh((z-H/2)h) \tag{1b}$$

A numerical model is typically required to investigate the evolution of the two dimensional time dependent flows that develop from the initial instability of such a basic state (see the following section for a brief discussion of the model that we employ). Since the temporal instability has a well defined streamwise scale determined by the wavelength of the fastest growing mode of linear instability it is natural to assume that the flow remains spatially periodic in the streamwise direction as it evolves and most previous analyses of the maturation of the initially two dimensional linear instability have been based upon this assumption (e.g. Peltier et al. 1978). Note that this assumption does not preclude vortex pairing if the numerical domain is taken to be at least two wavelengths long. Although we will not discuss vortex merging instabilities here it should be noted that such process are rather well understood theoretically (Kelly 1967; Klaassen and Peltier 1989; Smyth and Peltier 1992).

Klaassen and Peltier (1985, 1991) show that the issue of the local in time stability of the evolving nonlinear 2-D Kelvin-Helmholtz wave may be reduced using Galerkin methods to solution of the following eigensystem:

$$s\, a_{\kappa\mu} = \left(I^{(1)}_{\kappa\mu\lambda\nu} - \frac{A_{\lambda\nu}}{Re}\, \delta_{\kappa\lambda}\delta_{\mu\nu} \right) a_{\lambda\nu} = I^{(2)}_{\kappa\mu\lambda\nu} b_{\lambda\nu} + Ri \left(i\, \frac{B_\kappa D_\mu}{A_{\kappa\mu}} \right) c_{\kappa\mu} \tag{2a}$$

$$s\, b_{\kappa\mu} = I^{(3)}_{\kappa\mu\lambda\nu} a_{\lambda\nu} = \left(I^{(4)}_{\kappa\mu\lambda\nu} - \frac{A_{\lambda\nu}}{Re}\, \delta_{\kappa\nu}\delta_{\mu\nu} \right) b_{\lambda\nu} + Ri \left(\frac{1-D^2_\mu}{A_{\kappa\mu}} \right) c_{\kappa\mu} \tag{2b}$$

$$s\, c_{\kappa\mu} = I^{(5)}_{\kappa\mu\lambda\nu} a_{\lambda\nu} + I^{(6)}_{\kappa\mu\lambda\nu} b_{\lambda\nu} \cdot \left(I^{(7)}_{\kappa\mu\lambda\nu} - \frac{A_{\lambda\nu}}{RePr}\, \delta_{\kappa\lambda}\delta_{\mu\nu} \right) c_{\lambda\nu} \tag{2c}$$

in which $B_\lambda = \lambda a + b$, $D_\nu = \nu\pi/H$, $A_{\lambda\nu} = B^2_\lambda + D^2_\nu + d^2$ and $a_{\kappa\mu}$, $b_{\kappa\mu}$, $c_{\kappa\mu}$ are the coefficients in the Galerkin expansions for the streamwise and vertical components of velocity and the potential temperature respectively. The interaction integrals $I^{(i)}_{\kappa\mu\lambda\nu}$ consist of projections of the non-linear two dimensional KH wave fields onto the Galerkin basis. The Reynolds number in the problem is Re = $u_o h/\nu$, the Prandtl number is Pr = ν/κ and the bulk Richardson number is Ri=gh $\Delta\theta/(\theta_o u_o^2)$. By concatenating the Galerkin coefficients $a_{\kappa\mu}$, $b_{\kappa\mu}$, $c_{\kappa\mu}$ into a single vector $\underline{V}$ (say) with a single running subscript we may clearly re-write (2) in standard matrix eigenvalue form as $E_{ij} V_j = s V_j$.

A useful diagnostic procedure for evaluation of the results that are obtained from the solution of this eigenvalue problem is to construct an energy budget for the eigensolutions $\underline{V}$ following Laprise and Peltier (1989) as:

$$\sigma <K'> \ = \ <Sh> \ + \ <St> \ + \ <H> \ - \ <D> \tag{3}$$

in which $s=\sigma+i\omega$ so that σ is the real part of the eigenvalue (the growth rate of the mode) and ω is it's temporal frequency. In (3) $<K'>$ is the perturbation kinetic energy of the instability averaged over the domain. $<Sh>$ is the integrated shear production of perturbation KE, $<St>$ is production by "stretching", $<H>$ is the production through convective instability and $<D>$ is the (negative definite) loss due to viscous dissipation.

For the purposes of the present paper we will first compare solutions of (2) via (3) for two evolving Kelvin-Helmholtz waves at comparable times in their life-cycles. The two wave-states will be those for $R_i = 0$ and $Ri = 0.04$ respectively and in each case we shall assume PR=1 and Re=300 for the purpose of evolving the two dimensional non-linear wave from the initial instability of the parallel flow. In Figure 1a we show the growth rate σ andin Figure 1b the wave frequency ω as a function of the cross-stream wave number d for the unstratified case with Ri=0 at the time of maximum perturbation kinetic energy in the KH wave. Figure 2 illustrates the main components of the budget in (8) for the fastest growing mode of instability denoted by the diamond symbol in Figure 1a which occurs at d=1.8. Inspection of Figure 2 demonstrates that this fastest growing mode is located in the braids of the nonlinear wave. In the more accurate version of this stability analysis for the unstratified case recently presented by Smyth and Peltier (1994) it is demonstrated that modes on the low side of the inflection in the curve of highest growth rate are, however, core centred and "elliptical" (see Smyth and Peltier 1994, Figure 2). Since the growth rate varies slowly as a function of wavenumber from braid centred to core centred it clearly is an important issue as to which would be most fully realized in nature and most strongly control transition.

In Figure 3a,b and 4 we show similar data to that for the unstratified case. Inspection of the results for this example which differs from the unstratified case only in that Ri=0.04 demonstrates that a profound modification of the fastest growing instability has been introduced by the stratification. Firstly the wavenumber of the fastest growing mode has been shifted to d=2.6 from d=1.8 while secondly (Figure 4) the mode has ceased to be braid centred. Rather it has come to be quite strongly confined into the outermost superadiabatic sublayer (visible in the $<H>$ field). In this case the fastest growing elliptical mode is found at the considerably lower cross-stream wavenumber of d=1, somewhat higher than in the unstratified case where it was found near d=0.7. In what follows we shall attempt to determine whether and which of these predictions concerning the mechanism of transition are correct.

3: Large eddy simulations of transition in free shear layers

In support of our experimental and theoretical program on free shear layer transition we have undertaken the investigation, by numerical means, of the competition between the above described modal instability mechanisms that could mediate transition. In both the unstratified and stratified cases there exist braid centred and core centred mechanisms while in the stratified case the shear aligned convective mechanism may also contribute. Our numerical simulations have been performed with a model modified from the anelastic model described in Clark (1977) which solves the governing equations in the Boussinesq approximation as:

$$\underline{\nabla} \cdot (\underline{u}) = 0 \tag{4a}$$

$$\frac{D\underline{u}}{Dt} = -\underline{\nabla}p^* + R_i \theta^* \delta_i \frac{1}{Re} \nabla^2 \underline{u} \tag{4b}$$

$$\frac{D\theta^*}{Dt} = \frac{1}{Re\,Pr} \nabla^2 \theta^* \tag{4c}$$

in which the potential temperature deviation is $\theta^* = (\theta - \Theta)/\theta$. The numerical methods employed
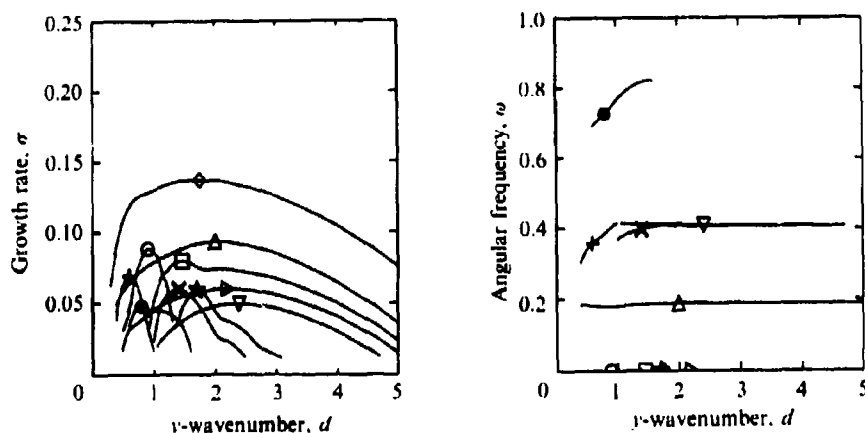
3

Figure 1. Growth rate σ and angular frequency ω vs. spanwise (y) wavenumber d for the maximum-amplitude state of a nonlinear KH wave with bulk Richardson number Ri=0. (For b=0). The symbols on each σ vs. d curve denote the fastest growing mode, and the same symbol is used to label the corresponding ω vs. d curve. Note that only the non-negative eigenfrequencies are shown.
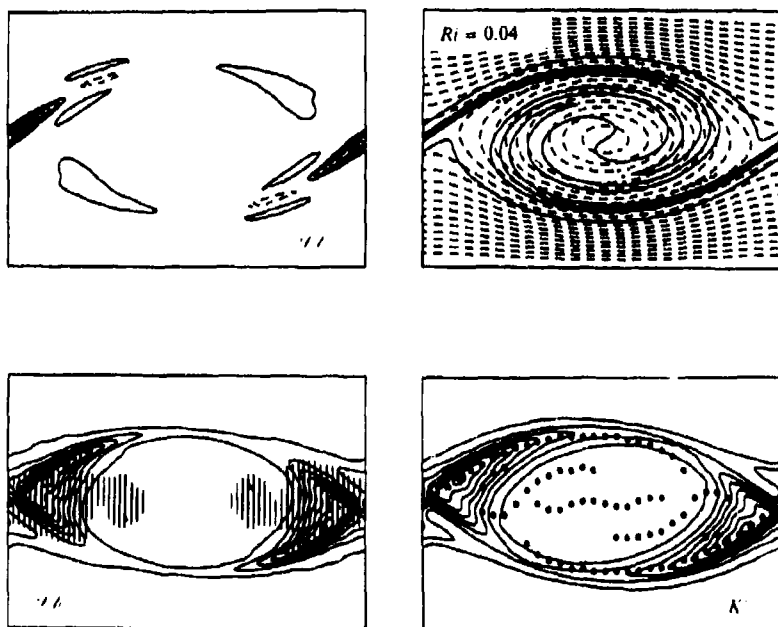

Figure 2. Eigenfunction correlations depicting the spatial dependence of the kinetic energy and the energy transfers for the most unstable ω_b mode (labelled ◇ in figure 13) of the maximum-amplitude KH wave with Ri = 0. Here t = 26, b = 0, d = 1.8, σ = 0.137, ω ≈ 0, <Sh> = 0.145, <St> = 0.012, <H> ≈ 0, <D> = -0.020 in units of <K'>. The shearing conversion SH(x,z) and the stretching conversion St(x,z) are given by the integrands in equations (3.29)-(3.30) respectively, while the perturbation kinetic energy density K' is given by (3.25). the vertical lines superimposed on the Sh field represent the regions of the nonlinear KH wave where the shearing deformation exceeds 0.43 of its maximum value. This fraction was chosen so as to reveal the detailed structure of the deformation field on the wave core. The dot superimposed on the K' field mark the position of vertical line maxima in the vorticity field, which mark the location of the braids and the vorticity ridges in the core. The domain length and height are respectively 14 and 10 in units of h). The top right-hand panel shows an overlay of streamfunction and potential temperature for the stratified case Ri = 0.04 in order to demonstrate the position of the vortex core within the frame.

4
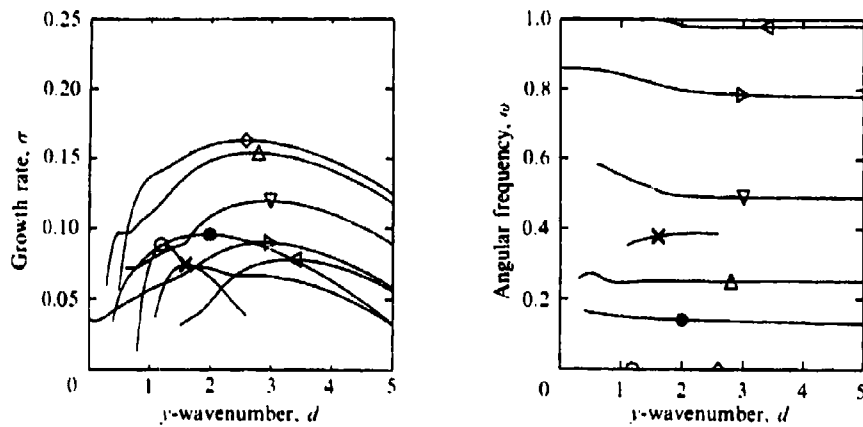
Figure 3. As for figure 1, except Ri = 0.04.
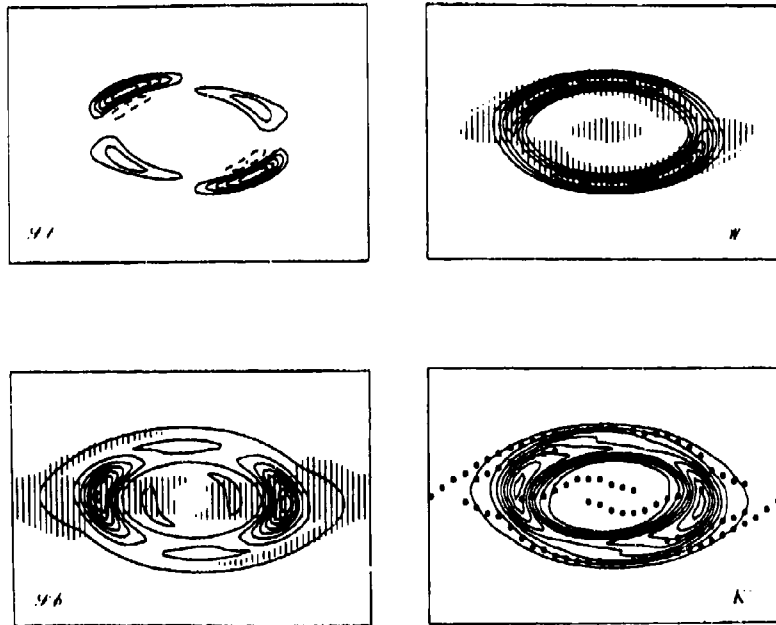
Figure 4. Eigenfunction correlations for the most unstable ω_r mode (labelled ◇ in figure 3) of the maximum amplitude KH wave with Ri = 0.04. Here t = 32, b = 0, d = 2.6, σ = 0.163, ω = 0. <Sh> = 0.110, <Si> = 0.010, <H> = 0.079, <D> = 0.036 in units of <K'>. The vertical heat flux H (x,z) is given by the integrand in (3.31). The superadiabatic region associated with the overturning fluid in the vortex core is marked with vertical lines superimposed on the H field. See Figure 2 for further details.

consist of centred second order accurate finite differences on a staggered mesh for the spatial derivates while the time stepping is achieved using a leap frog scheme coupled with a Euler backwards step every 10 Δt in order to reduce splitting errors. For the two simulation to be described here we have employed 100 grid points in the streamwise direction, 100 grid points in the vertical direction and 200 grid points in the cross-stream direction. In each case the domain length has been set equal to 2 wavelengths of the fundamental mode of KH instability (λ_{KH}) while the width of the box has been taken equal to 40 h. Since the wavelength of the fastest growing mode is typically about 14 h this means that the width of the model in the cross-stream direction is just under 3 λ_{KH}. The height of the model domain has been taken to be equal to 20 h and the shear layer to be centred within the region.

5

Ri(0) = 0.00   Ri(0) = 0.05
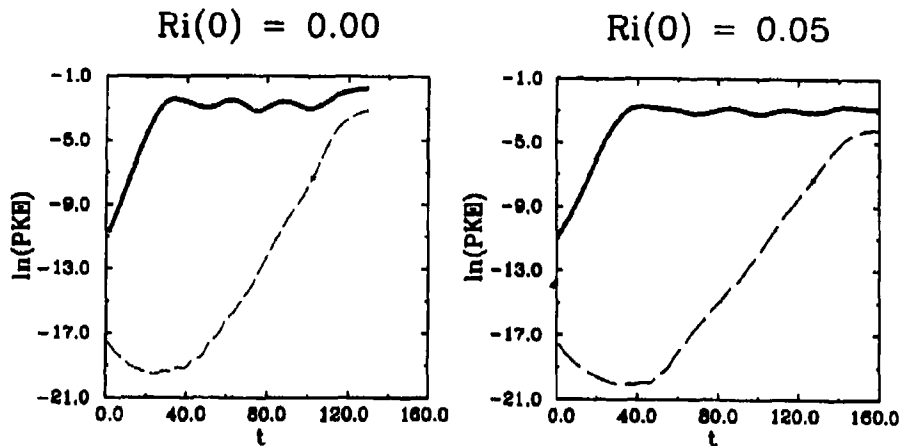
Figure 5. Total perturbation kinetic energy (PKE) vs. time (solid line) and cross-stream component of PKE vs. time (dashed line) for the three dimensional simulations with Ri = 0.0 and Ri = 0.05.

Figure 5 shows perturbation kinetic energy time series for both the unstratified simulation (a) and the stratified simulation (b). Both were initialized with a purely modal fluctuation in the along stream direction and a white noise perturbation of smaller amplitude in the cross-stream direction. The latter aspect of the initialization procedure is especially important as we did not wish to bias in any way the cross stream length scales that would develop in the course of transition. Inspection of Figure 5 demonstrates that perturbation kinetic energy grows exponentially initially and at a rate that agrees quite closely with the predictions of linear stability theory. Eventually wave kinetic energy saturates leading to the development of a slow quasi-periodic nutation thereafter. The cross-stream component of the perturbation kinetic energy is shown separately on plates a and b of Figure 5 and inspection reveals that it decays until after the linear growth phase has ceased, this being an expected consequence of the lack of a timescale separation between the two dimensional wave and the incipient instabilities to which it becomes subject. On both plates a and b of this Figure we have marked the times for which full three dimensional images revealing the spatial structure of the instabilities controlling transition will be shown. These times have been chosen to be "comparable" in the sense that $<ux^2/2>$ is the same fraction of total perturbation kinetic energy for each.

Figures 6 and 7 respectively show three dimensional grey scale images of streamwise vorticity for the unstratified and stratified free mixing layers respectively at these model times. In both simulations complete turbulent collapse occurs within a relatively short period following the development of the structures shown. Inspection of Figure 6 very clearly demonstrates that the streamwise vortex streaks that appear as the dominant structures in the unstratified case are braid centred and possess a cross-stream length scale that is accurately predicted by the results of the Floquet analysis shown in Figure 1a. Therefore the streamwise streaks are not connected in any way to the translative instability of Pierrehumbert and Widnall (1982) nor, by extension, to the elliptical instability of Pierrehumbert (1986) and Bayly (1986). They develop from the insitu instability captured in the Floquet analysis.

Similar inspection of Figure 7 shows that the streamwise vortex streaks that develop in the stratified case have no expression in the braids that lie between distinct vortex cores. Rather they are confined to a ring around the dominant central vortex as predicted for the shear aligned convective instability of Peltier et al. (1978), Davis and Peltier (1979) and Klaassen and Peltier (1985, 1991). That the streamwise streaks that appear in the stratified case also have a characteristic length scale that is shorter than the braid centred mode of the unstratified case is also clear by inspection and comparison of the two Figures.
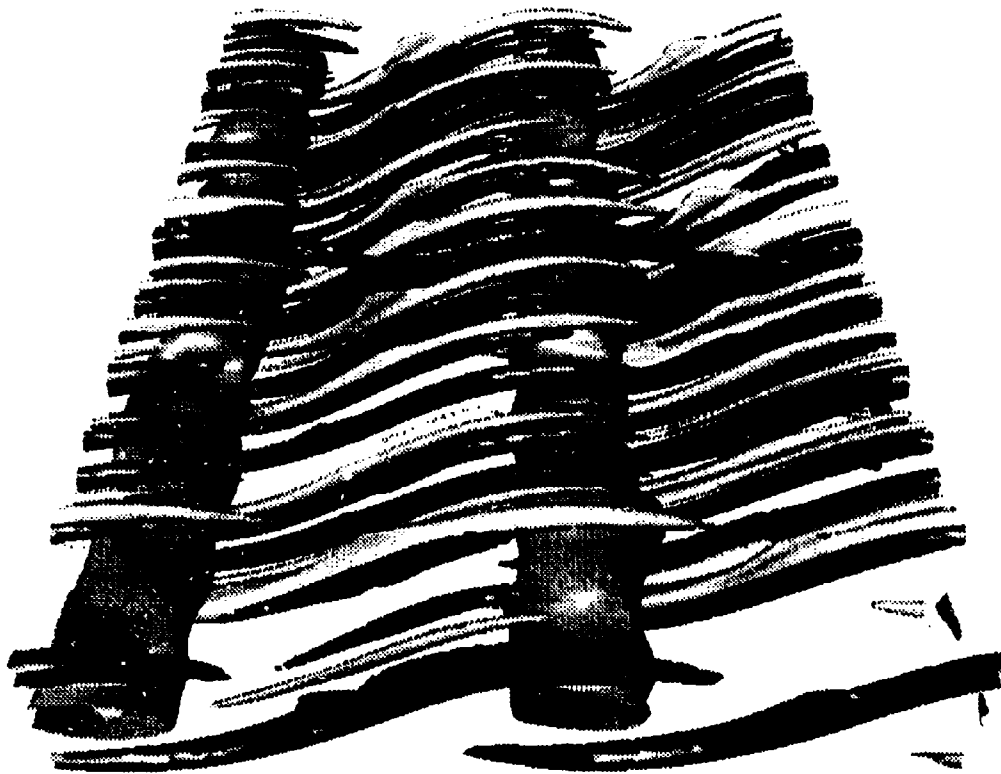
6

Figure 6. Positive (dark) and negative (light) streamwise vorticity isosurfaces with a spanwise vorticity isosurface that dilineates the vortex cores for the unstratified simulation with Ri = 0.0.

4: Discussion and conclusions

We have described a sequence of new analyses of transition in the free stratified mixing layer focused upon the problem of accurately isolating the mechanism responsible for the generation of streamwise vortex streaks. These analyses have established, rather definitively in our view, that these streamwise streaks, which are precursory to the onset of fully developed turbulent flow, are not produced by elliptical instability of the vortex cores. Rather they are caused by an insitu braid centred instability when the fluid is instratified and a shear aligned convective instability when the fluid is stratified. Both of these fundamental mechanisms have been well explained and in fact were originally predicted by the three dimensional non-separable stability analyses of Klaassen and Peltier (1991). In this paper we have not addressed the issue of the competition of vortex merging instability mechanisms, which are essentially two dimensional, with the three dimensional modes upon which we have focused here. This aspect of transition in the mixing layer will be discussed elsewhere.

5: References

Bayly, B.J., Phys. Rev. Lett. **57**, 2160-2163 (1986).
Bayly, B.J., Orszag, S.A. and Herbert, T., Ann. Rev. Fluid Mech. **20**, 359-391 (1988).
Bernal, A.P. and Roshko, A. J. Fluid Mech. **10**, 499-525 (1986).
Breidenthal, R.E., J. Fluid Mech. **109**, 1-24 (1981).
Clark, T.L., J. Comput. Phys. **24**, 186-215 (1977).
Corcos, G.M. and Lin, J.S., J. Fluid Mech. **139**, 67-95 (1984).
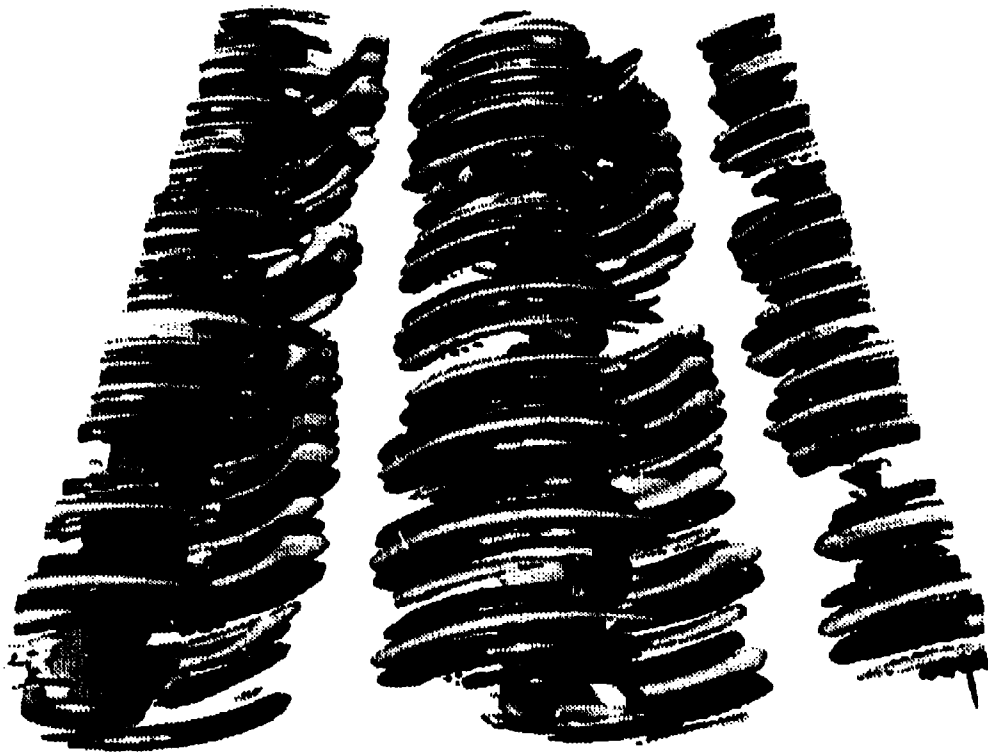
Figure 7. Same as figure 6 but for the stratified simulation with Ri = 0.05.

Davis, P.A. and Peltier, W.R., J. Atmos. Sci. 36, 2395-242 (1979).

Ho, C.-M. and Huerre, P., Ann. Rev. Fluid Mech. 16, 365-424 (1984).

Kelly, R.E., J. Fluid Mech. 27, 657-689 (1967).

Kelly, R.E., In Physicochemical Hydrodynamics vol. 1 (ed. V.G. Levich), Advance (1977).

Klaassen, G.P. and Peltier, W.R., J. Fluid Mech. 155, 1-35 (1985).

Klaassen, G.P. and Peltier, W.R., J. Fluid Mech. 202, 367-402 (1989).

Klaassen, G.P. and Peltier, W.R., J. Fluid Mech. 2277, 71-106 (1991).

Laprise, R. and Peltier, W.R., J. Atmos. Sci. 46, 545-564 (1989).

Lasheras, J.C., Cho, J.S. and Maxworthy, T., J. Fluid Mech. 172, 231-258 (1986).

Lasheras, J.C. and Choi, H., J. Fluid Mech. 189, 53-86 (1988).

Lin, S.J. and Corcos, G.M., J. Fluid Mech. 141, 139-178 (1984).

Metcalfe, R.W., Orszag, S.A., Brachet, M.E., Menon, S. and Riley, J.J., J. Fluid Mech. 184, 2077-2143 (1967).

Pierrehumbert, R.T., Phys. Rev. Lett. 57, 215-2159 (1986).

Pierrehumbert, R.T. and Widnall, S.E., J. Fluid Mech. 114, 59-82 (1982).

Peltier, W.R., Hallé, J. and Clark, T.L., Geophys. Astrophys. Fluid Dyn. 10, 53-80 (1978).

Rogers, M.M. and Moser, R.D., J. Fluid Mech. 243, 183-226 (1992).

Smyth, W.D. and Peltier, W.R., Geophys. Astrophys. Fluid Dyn. 52, 249-261 (1990).

Smyth, W.D. and Peltier, W.R., Geophys. Astrophys. Fluid Dyn. 69, 1-32 (1993).

Smyth, W.D. and Peltier, W.R., J. Fluid Mech., 265, 25-64 (1994).

Squire, H.B., Proc. Roy. Soc. Lond. A142, 621-628 (1933).

Thorpe, S.A., Geophys. Astrophys. Fluid Dyn. 34, 175-199 (1985).

Model Studies of Atmospheric Boundary-Layer Flow over Topography

Peter Taylor, Lucilla Chan, Dapeng Xu and Keith Ayotte

Dept of Earth and Atmospheric Science, York University, North York, Ontario, Canada, M3J 1P3

Abstract

Two models of stably stratified, two-dimensional, turbulent boundary-layer flow over periodic sinusoidal topography are being developed. One uses a finite-difference numerical scheme and integrates the time dependent, Reynolds averaged equations of motion with a specified initial state until a steady-state is reached. The other obtains a steady state solution directly using a mixed spectral finite difference approach. This is based on the MSFD and NLMSFD models of Beljaars et al (1987) and Xu and Taylor (1992). Both models are being used with considerable success to study neutrally stratified flow over topography, and various levels of turbulence closure can be invoked. Initial work on stratified boundary-layer flow over topography will be described.

Introduction

For neutrally stratified flows, a number of non-linear, finite difference models of turbulent boundary-layer flow over hills have been published (e.g Taylor, 1977) while Jackson and Hunt (1975 - JH) proposed a linear model. This proved very successful and spawned a number of developments. Among them were the Mixed Spectral Finite Difference (MSFD) model of Beljaars et al (1987) and the generalisation by Hunt et al (1988a). Other authors developed finite difference models with second order closures.

Inviscid stably stratified flow over topography has been studied for many years and the theory, at least for small amplitude waves and especially for constant buoyancy frequency, N, and background velocity, U_0, are well established for both rotating and non-rotating frames of reference. For the relatively small scale topography that we are concerned with here (length scales of order 1km) rotation effects are secondary, although they may cause directional shear in the basic flow. There are a number of models of non-linear, hydrostatic and non-hydrostatic, stationary and non-stationary mountain waves, with typical horizontal scales of order 10 to 100 km in the literature. In general however the treatment of boundary layer turbulence is highly simplified and the models are often run without surface friction or heat flux.

Hunt et al (1988b) have used developments of the JH model to study inversion capped and stably stratified flow over low hills. The outer layer flow is assumed inviscid and approximate, analytic solutions are obtained for an inner layer. With our

1

numerical models we hope to allow a more detailed representation of the effects of turbulence and to enable the study of a broader range of flows. The distinction between the present work and most other studies of stratified flow over topography lies in the representation of turbulent fluxes of heat and momentum. In the atmospheric flow context, we believe that these will be important for topography with horizontal scales of order 1km or less.

The NLMSFD model and results for neutrally stratified flows

One of the models that we are working with is a Non-Linear extension of Beljaars et al's (1989) Mixed Spectral, Finite-Difference model. Within this NLMSFD model we assume that the mean flow is steady and that both the Coriolis force and molecular diffusion are negligible because we are interested in small scale topography and aerodynamically rough surfaces. For neutral stratification, the momentum and continuity equations are

$$U_k \frac{\partial U_i}{\partial x_k} = -\frac{1}{\rho} \frac{\partial P}{\partial x_i} - \frac{\partial \overline{u_i u_k}}{\partial x_k} \qquad (1)$$

$$\frac{\partial U_k}{\partial x_k} = 0 \qquad (2)$$

where uppercase U and P express mean velocity and pressure respectively, lowercase u represents turbulent fluctuations and the overbar indicates an ensemble average. Summation is implied whenever an index repeats in the same term. The Reynolds stress, Turbulent Kinetic Energy (TKE), TKE dissipation rate (ε) or turbulence length scale equations and the boundary conditions are discussed in Xu et al (1994). Periodic conditions are applied at the lateral boundaries. The model is 3D and is implemented with several different turbulence closures including LRR models 1 and 2 (Launder, Reece and Rodi, 1975). In this paper, we shall limit discussion to 2D results with E-κz and LRR closures (κ = 0.4 is the von Karman constant). Details of results with other forms of closure and 3D results are included in Xu et al (1994).

Figure 1 shows some sample velocity perturbation (ΔU) results for flow over 2D and 3D sinusoidal wavy surfaces with maximum slopes (ak) of 0.157. The surfaces are defined by, z_s = -acos kx and z_s = a coskx cosky, where k = $2\pi/\lambda$ and λ is the wavelenth of the topography. Figure 1a shows profiles over the summits while Figure 1b shows velocity perturbations as contours in the (x,ζ) plane for the 2D case [ζ = ln($(z+z_0)/z_0$) is a stretched vertical coordinate]. The upper boundary condition used for these runs was ΔU = 0 on z = λ. Velocity perturbations, pressure and surface shear stress perturbations for 3D topography are all

2

slightly lower than for flow over 2D terrain.

In addition to other applications the model can be applied to problems of boundary-layer parameterization in regional and global NWP and climate models. Moderately steep topography will cause an additional pressure drag in a shear flow, even in neutral stratification. Fig 2 shows form drag results (A_D is the x component of form drag per unit surface area normalised by upstream shear stress, ρu_{*0}^2, and by the square of the hill slope $(ak)^2$) for modestly sloped topography as a function of λ/z_0. Two dimensional topography clearly produces more drag than three dimensional topography. We also find that the predicted form drag coefficients are affected by dimension and by turbulence closure. In general the discrepancies between models with lower order closure and higher order closure and between 2D and 3D results are both of order 100%. Non-linear effects on form drag are slope dependent, but, at moderate slopes, appear to be rather weak. The strong dependence of form drag on turbulence closure indicates that accurate prediction of form drag by numerical models may prove difficult. This is discussed in more detail in Xu et al (1994) and Xu and Taylor (1994).

Preliminary Finite Difference Model Results for weakly stratified constant flux layer flows

The finite difference model used is an extension, for stratified flows and non-orthogonal coordinates, of the one presented by Gent and Taylor (1976). Equation (1) above is modified to include buoyancy forces, making the Boussinesq approximation. The vertical component then becomes,

$$\frac{\partial W}{\partial t}+U\frac{\partial W}{\partial x}+W\frac{\partial W}{\partial z}=\frac{g}{\theta_0}\theta_1-\frac{1}{\rho_0}\frac{\partial P_1}{\partial z}-\left(\frac{\partial \overline{u'w'}}{\partial x}+\frac{\partial \overline{w'^2}}{\partial z}\right) \qquad (3)$$

We also solve the thermodynamic equation and buoyancy forces give rise to terms in the Reynolds stress equations. The turbulent kinetic energy equation, used in the E-kz model, then becomes,

$$\frac{\partial E}{\partial t}+U\frac{\partial E}{\partial x}+W\frac{\partial E}{\partial z}=\frac{g}{\theta_0}\overline{\theta'w'}-\frac{\partial}{\partial x}\left(\overline{u'e'}+\frac{1}{\rho_0}\overline{u'P_1'}\right)-\frac{\partial}{\partial z}\left(\overline{w'e'}+\frac{1}{\rho_0}\overline{w'P_1'}\right)$$
$$-\overline{u'^2}\frac{\partial U}{\partial x}-\overline{u'w'}\left(\frac{\partial U}{\partial z}+\frac{\partial W}{\partial x}\right)-\overline{w'^2}\frac{\partial W}{\partial z}-\epsilon \qquad (4)$$

In addition, for models with a turbulence closure requiring them, we must modify the mixing and dissipation length scales to account for stability effects. Within the E-kz model we use

$$l = \kappa(z+z_0)/(1 + 5(z+z_0)/L) \qquad (5)$$

and

$$l_d = \kappa(z+z_0)/(1 + 4(z+z_0)/L) \qquad (6)$$

The, local, Monin-Obukhov length, L is given by,

$$L = u_*{}^2\theta_0/(\kappa g\theta_*) \qquad (7)$$

where $u_* = (\tau/\rho)^{1/2}$ and the downward heat flux, $-H = \rho c_p\theta_*u_*$. Additional adjustments are made to account for the non-orthogonal coordinate system (see Taylor, 1977 for details). The models have initially been tested for constant flux layers using various stabilities and surface wave amplitudes with rigid lid upper boundary conditions. These equations are transformed from the (x,z) to a stretched, terrain-following (x,ζ) coordinate system, where the stretching is performed to reflect the near surface logarithmic and far surface linear characteristics of the horizontal velocity profile of a stably stratified constant flux layer. A staggered grid is imposed on the domain in (x,ζ) space and an implicit, forward in time, centered in space, finite-difference numerical scheme based on the equations of motion is implemented to find the steady-state solution. Pressures are treated via the method of artificial compressibility.

In the simplest stratified case the flow is assumed to be driven by a horizontal shear stress and vertical heat flux applied at the top of the computational domain and the stable stratification is described by a real, positive Monin-Obukhov length L determined from these turbulent fluxes. However this idealised, constant flux layer approach gives unrealistic temperature gradients and velocity shears in the upper part of the domain which trap upwardly propagating waves and severely limit the range of atmospheric flow situations that can be modelled.

In order to provide realistic, specified initial or undisturbed profiles of buoyancy frequency, N, and mean velocity, U, as well as permit steady state, spatially periodic, boundary-generated wave solutions, we are now introducing artificial source functions for heat and momentum. We justify this on the basis of a separation between $1/N$ and the time scale for the evolution of the boundary layer profiles. The appropriate source functions S_m, S_h can be found from the equations of motion for horizontal homogenous flow with the specified velocity and buoyancy frequency profiles. After specifying $U(z)$ and $N(z)$, the TKE equation is integrated in time until a steady-state is achieved. The stress and heat flux can then be computed within the momentum and heat equations to obtained the source functions S_m and S_h. Since the near surface flow situation is that of a constant flux layer, $U(z)$ and the mean potential temperature, $\theta(z)$, specified by $N(z)$, should be near logarithmic as z approaches 0. The source functions are introduced into our two-dimensional model by substituting $z-z_s$ for z in the terrain-following coordinate

4

system. Similarly, the U, θ and E profiles are used to specify the initial flow.

The finite-difference model has been tested following the constant flux layer approach, with $S_m = S_h = 0$. The results point to the disadvantages of this approach as described earlier. The model achieved steady-state results only for weak stratification represented by relatively large Monin-Obukhov lengths. As expected, the steady-state results for weak stratifications reveal a total absence of internal gravity waves. The near surface streamlines and the corresponding Froude numbers are shown for flow over a sinusoidal hill of amplitude $a=250z_0$ and wavelength $\lambda = 10000z_0$ with $L = 5000z_0$ in Figure 3. The Froude numbers are comparable to those at similar heights calculated from a constant flux layer flow over a flat surface under the same stratification. Even if the flow is altered so that the Froude number ($F = U/N\lambda$) is restricted to less than unity, internal gravity waves would still be absent since the numerical solution would be distorted by waves reflected downward from the rigid lid upper boundary used in these simulations, as indicated in Fig 4a.

We therefore require upper boundary conditions which would allow upward propagating waves to radiate out of the computational domain. In order to adapt the model for use at strong stratification and to satisfy the Froude number constraint, the initial velocity profile U(z) is modified using source functions so that it remains unchanged from the constant flux profile in the lower portions and asymptotically approaches a constant value U_0 far above, while the temperature profile is essentially the same as before (see Fig 4b). As a result of the stable stratification and reduced shear the flow far above the surface is now non-turbulent. A wave transmitting upper boundary conditions can be found by considering the steady-state periodic solution to the equations of motion in this non-turbulent region, as in the method proposed by Klemp and Durran (1983). At present, a suitable set of upper boundary conditions has been found, which we are in the process of testing.

It is anticipated that results with specified U and N profiles will be available in the near future.

Acknowledgements

5

References

Beljaars, A. C. M., Walmsley, J. L. and Taylor, P. A., 1987, A
mixed spectral finite difference model for neutrally
stratified boundary-layer flow over roughness changes and
topography, boundary-layer meteorol., 38, 273-303.

Gent, P.R and Taylor, 1976, A numerical model of the airflow
above water waves. J. Fluid. Mech., 77, 105-128.

Hunt, J. C. R., Leibovich, S. and Richards, K. J., 1988a,
Turbulent shear flows over low hills, Q. J. R. Meteorol. Soc.,
114, 1435-1470.

Hunt, J. C. R., Richards, K. J. and Brighton, P.W.M., 1988b,
Stably stratified flow over low hills, Q. J. R. Meteorol. Soc.,
114, 859-886.

Jackson, P. S. and Hunt, J. C. R., 1975, Turbulent wind flow over
a hill, Quart. J. R. Met. Soc., 101, 929-955.

Klemp, J.B. and Durran D.R., 1983, An upper boundary condition
permitting internal gravity wave radiation in numerical mesoscale
models, Monthly Weather Review, 111, 430-444.

Launder, B. E., Reece, G. J. and Rodi, W., 1975, Progress in the
development of a Reynolds-stress turbulence closure, J. Fluid
Mech., 68, 537-566.

Taylor, P. A., 1977, Some numerical studies of surface boundary-
layer flow above gentle topography, Boundary-Layer Meteorol.,
11, 439-465.

Xu, D. and Taylor, P. A., 1992, A non-linear extension of the
mixed spectral finite-difference model for neutrally
stratified turbulent flow over topography, Boundary-Layer
Meteorol., 59, 177-186.

Xu, D. and Taylor, P. A., 1994, Boundary-Layer Parameterization
of Drag over Small Scale Topography, submitted to Quart. J. R.
Meteorol. Soc.

Xu, D., Ayotte, K. W. and Taylor, P. A., 1994, Development of a
Non-Linear Mixed Spectral Finite Difference Model for turbulent
boundary-layer flow over topography, in press, Boundary-Layer
Meteorology.
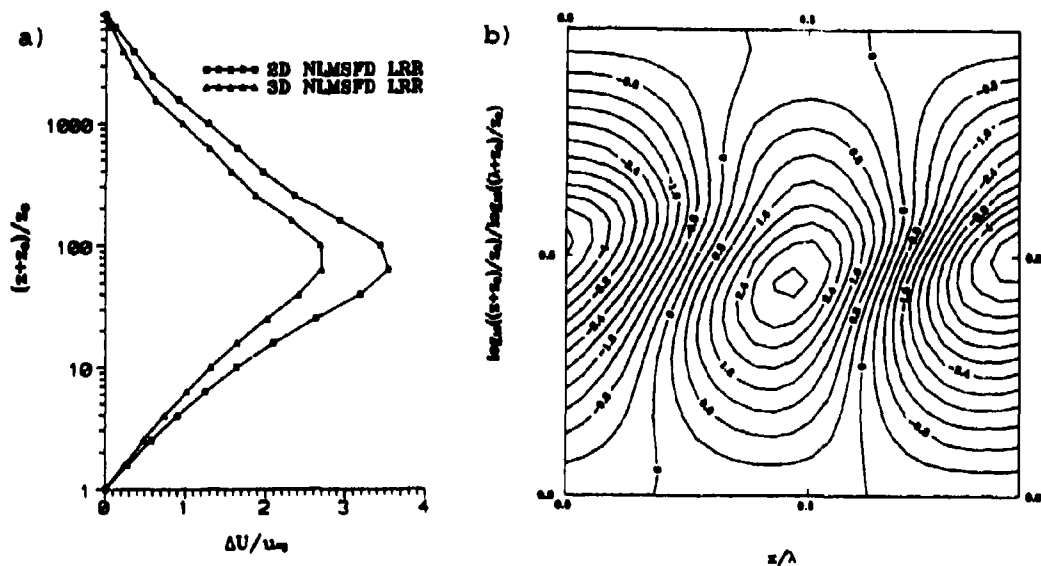
Figure 1 Velocity perturbations for flow over 2D and 3D waves, ak=0.157, $\lambda/z_0=10^4$. a) at the summit from 2D and 3D models, b) contours in (x,ζ) space from the 2D model.
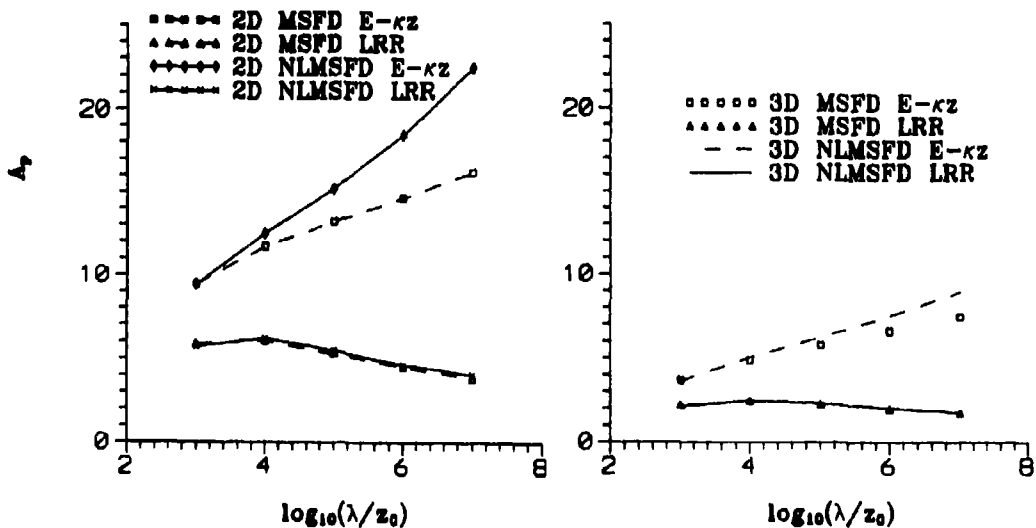
Fig 2   Form drag coefficients (A_p) for flow over 2D and 3D sinusoidal terrain. E-kz and LRR closures, ak = 0.157.
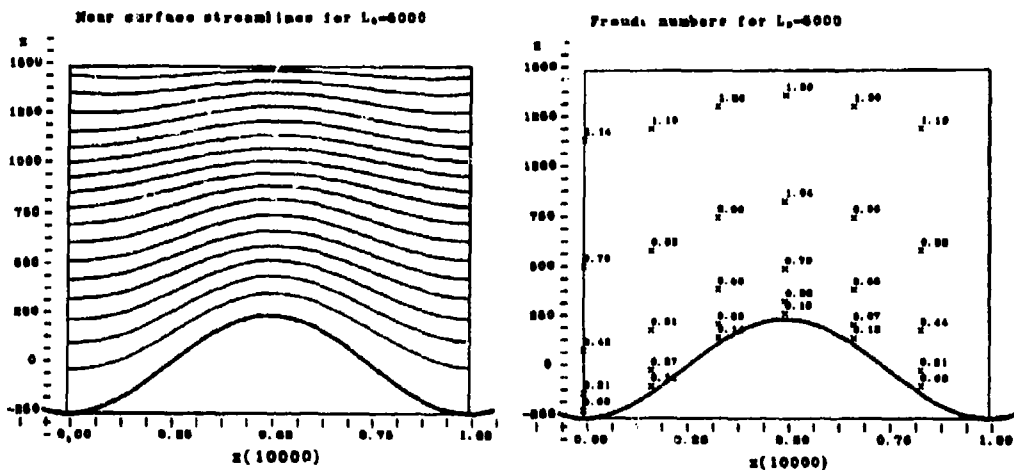
Fig 3   Finite difference model results for flow over sinusoidal
terrain.   Basic flow is a constant flux boundary-layer.   Froude
numbers are numerical values at selected gridpoints.   Note that
all lengths are scaled by the constant roughness length z_0.
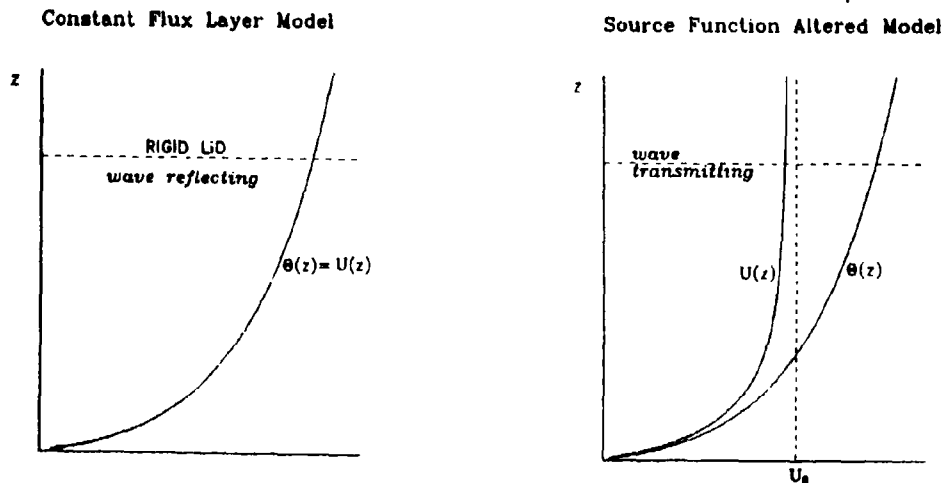
Fig 4   Schematic diagram of temperature and velocity profiles in
models with and without source functions.

8

Direct Numerical Simulations and Experiments on a Stably Stratified Turbulent Boundary Layer

I.R. COWAN AND R.E. BRITTER
Department of Engineering, University of Cambridge. Trumpington Street,
Cambridge, CB2 1PZ, UK.

Abstract. Direct numerical simulations (DNS) and wind-tunnel experiments have been undertaken on an incompressible, smooth-walled, low Reynolds number turbulent boundary layer ($Re_\theta < 900$) over a flat plate, with injection of fluid through a slot in the upstream end of the plate. The injection of a mixture of ambient and dense gas served to trip the boundary layer as well as providing a stable density stratification. A finite difference/volume code with *no* turbulence model was used for the simulations, and the number of grid cells employed ($255\times96\times96$) was found to be adequate to resolve most of the turbulence scales. Experimental measurements were made in a low-speed wind-tunnel of the velocity and concentration field. Examined here are the effects of a stable stratification upon the boundary layer entrainment and upon the large-scale turbulence structure.

1 Introduction

A number of studies have been made of stably stratified wall shear flows, with various methods for introducing the buoyancy into the flow — see Cowan & Britter (1994) for a summary. A novel technique for the buoyancy injection was suggested by Britter (1988), and has been investigated by Cowan (1994). This is drawn schematically in figure 1. The buoyancy was introduced into the flow at the *start* of the turbulent boundary layer — a mixture of ambient and dense gas was injected through a slot in the wall, just downstream of a boundary layer trip. The injection served to mix the source fluid throughout the boundary layer, so that a stratified boundary layer developed downstream.

$$Ri_b = \frac{g'_s q_s}{U^{\prime 3}_{\infty}}$$
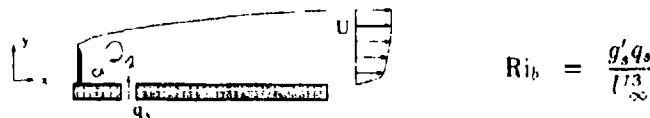
Figure 1: Schematic of the injection of buoyancy into the boundary layer flow.

This model flow has two main advantages over previous studies: firstly, the stratification effects can be parameterised by a bulk Richardson number, Ri_b, dependent only upon the source conditions; secondly, the buoyancy and the boundary layer develop downstream under the same turbulence scales, in contrast to the situation of a dense plume growing inside a boundary layer. The bulk Richardson number is defined in figure 1, where q_s is the volume flow rate per unit span of injected (source) fluid, ρ the

fluid density, $g'_s = g(\rho_s - \rho_0)/\rho_0$ the reduced gravity and U_∞ the free-stream velocity.

The practic elevance of this study is in meteorology and industrial hazard assessment, where redu. d turbulence levels can have a significant effect on the atmospheric conditions, and upon the rate of dilution of a conventional pollutant or accidental release.

2   The computational code

The finite volume code used for the simulations was a modified version of that used by Voke & Gavrilakis (1993), and integrated the instantaneous, Boussinesq equations for momentum and concentration (see Cowan, 1994, for further details):

$$\frac{\partial U_i}{\partial t} + \frac{\partial U_i U_j}{\partial x_j} = -\frac{1}{\rho_0}\frac{\partial p}{\partial x_i} + \nu\frac{\partial^2 U_i}{\partial x_j^2} - \frac{\rho}{\rho_0}g\delta_{i2}$$

$$\frac{\partial}{\partial t}(\rho C) + \frac{\partial}{\partial x_i}(\rho C U_i) = \frac{\partial}{\partial x_i}(\nu\rho\frac{\partial C}{\partial x_i})$$
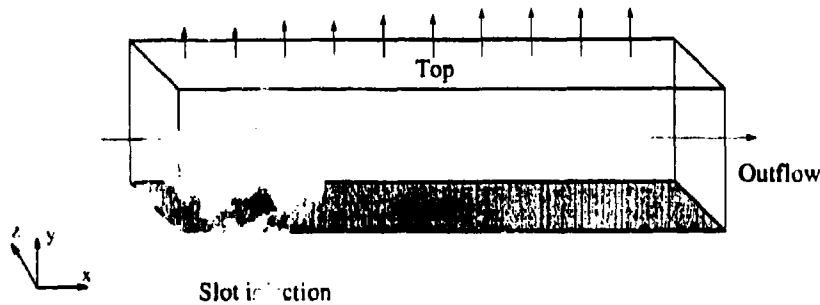
Figure 2: Simulation domain.

This paper uses the notation $U = \bar{U} + u$, where the bar denotes a time-average, for the Reynolds decomposition of quantities.

Some of the boundary conditions on the simulation domain (see figure 2) were: a Blasius laminar velocity profile at inflow; a periodic boundary on the side walls (homogeneity assumed in the spanwise direction); a fixed vertical velocity distribution on the top wall (to ensure a constant free-stream velocity, U_∞); the "advective" boundary condition of Gao et al. (1991) at outflow. A turbulent boundary layer was formed from the laminar inflow profile using a numerical "trip", aided by the slot injection. An injection velocity of $0.05\,\mathrm{ms}^{-1}$, or 5% U_∞, was used for all the simulations. The slot position (measured from the inflow plane, $x = 0$) was $x = 0.71 \rightarrow 0.80$m.

A stretched vertical mesh was employed, giving improved resolution near the wall, whilst the spanwise and longitudinal meshes were uniform. The domain size was

(3.0m, 0.3m, 0.3m), with (255, 96, 96) gridcells in the (x, y, z) directions, giving mesh resolutions of $(39\ell^+, 10\ell^+ \to 39\ell^+, 10\ell^+)$, where $\ell^+ = \nu/u_*$ is one viscous unit. Profiles of mean velocity $etc.$ were taken at a distance of $x_m = 2.59m$ downstream of the inflow plane. Table 1 lists the Reynolds numbers, based upon momentum thickness, at this position (Re_θ) and the bulk Richardson numbers (Ri_b) for the three simulations performed. The runs each required 210Mb of memory, and were performed on the Cray YMP8 at the Rutherford Appleton Laboratories, UK. Full resolution of all the turbulent scales proved not to be possible with the available resources, and the minor effects this had on the velocity field are discussed in Cowan (1994).

LABEL	Ri_b	$(Re_\theta)_m$
R1n	0	870
R2s	0.025	800
R3S	0.035	790

Table 1: Simulation details.

3　Simulation data

A stable stratification generally damps vertical motions since these require work against gravity. These vertical motions, however, are highly important to the entrainment and mixing of the boundary layer, and both these aspects will be shown to have been significantly affected by stability in this study. A full consideration of all the simulation data is not possible here, and so focus is restricted to this one aspect of the effect of stability.

Figures 3a and 3b plot two boundary layer integral parameters against downstream distance: the skin friction coefficient, $c_f = \tau_w / \frac{1}{2}\rho_0 U_\infty^2$, and the "entrainment" thickness, $\delta_e = \delta - \delta^*$, which is defined as the difference between the boundary layer thickness, δ, and the displacement thickness, $\delta^* = \int_0^\infty \left(1 - U/U_\infty\right) dy$. An entrainment velocity, representing the rate of increase of volume flow rate in the boundary layer, can be derived as: $u_e/U_\infty = d\delta_e/dx$.

Reductions in the downstream growth rate of the entrainment thickness (figure 3b) demonstrate that entrainment of free-stream fluid into the boundary layer is inhibited by stable stratification (u_e/U_∞ is reduced), and suggest that large-scale turbulent mixing is suppressed. This reduces the ability of the boundary layer to transport momentum from the free-stream to the wall region, causing a reduction in mean velocity shear at the wall, and thus in c_f (figure 3a).

Figure 3c plots the downstream development of the maximum mean concentration of the injected fluid, C_m, normalised by the source concentration, C_s. Note that for this type of flow, C_m occurs at the wall: $C_m = (\bar{C})_{max} = \bar{C}|_{y=0}$. After the initial mixing and rapid dilution near the source ($x < 1.5$), the rates of decrease in C_m/C_s
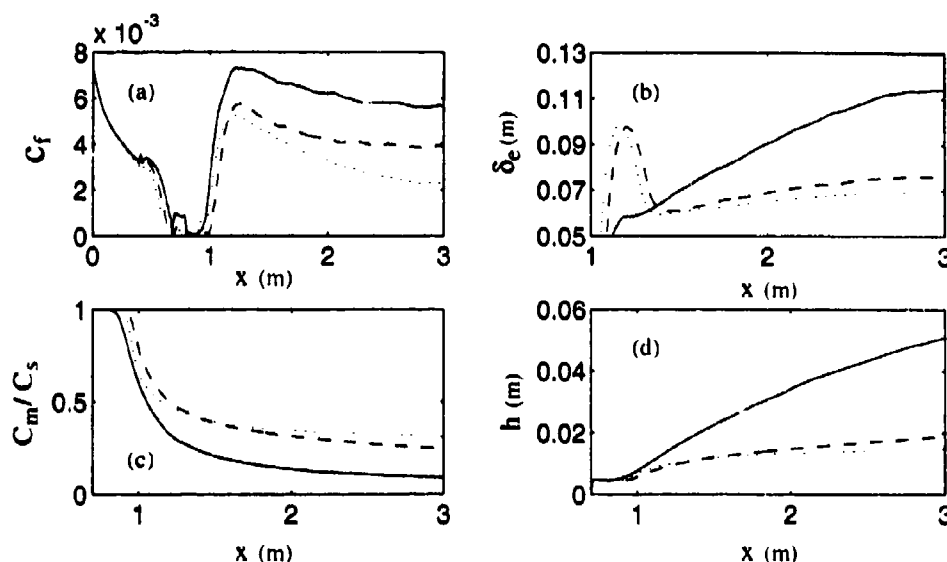
Figure 3: Integral parameters: (a) skin friction coefficient, c_f; (b) entrainment thickness, δ_e; (c) normalised ground level concentration, C_m/C_s; (d) concentration thickness, h.   Key: R1n(—); R2s(- - -); R3S(· · ·)

become small and thus difficult to compare. Figure 3d improves on this by plotting the "concentration thickness", defined as $h = C_s q_s/C_m U_\infty$. Concentration profiles are roughly similar, hence the downstream decrease in C_m is due to entrainment of ambient. free-stream fluid into the boundary layer. The observed large reductions in dh/dx thus imply large reductions in the entrainment for the stable cases.

These changes in the integral parameters are symptoms of changes in the turbulence structure. This is evident in figure 4, which plots profiles of the vertical turbulent intensity and the turbulent shear stress: both are significantly reduced by stable stratification. Vertical fluxes of concentration. $\overline{wc}$, are similarly affected.

The suppression of turbulent shear stress may be linked to the inhibition of large-scale vertical motions. since most of the shear stress production arises from the near-wall bursting process — an event that is associated with large vertical ejections of fluid from the near-wall region. Reductions in the shear stress cause a decrease in the turbulent kinetic energy. and lead to a relaminarisation of the boundary layer at high levels of stratification. An analysis of the terms in the shear stress and the kinetic energy budgets found that this collapse in turbulence energy was due to an inability to maintain a shear stress, rather than due to an inability to supply (potential) energy to the buoyancy sink term in the kinetic energy budget. This is in agreement with the hypothesis of Arya (1975).
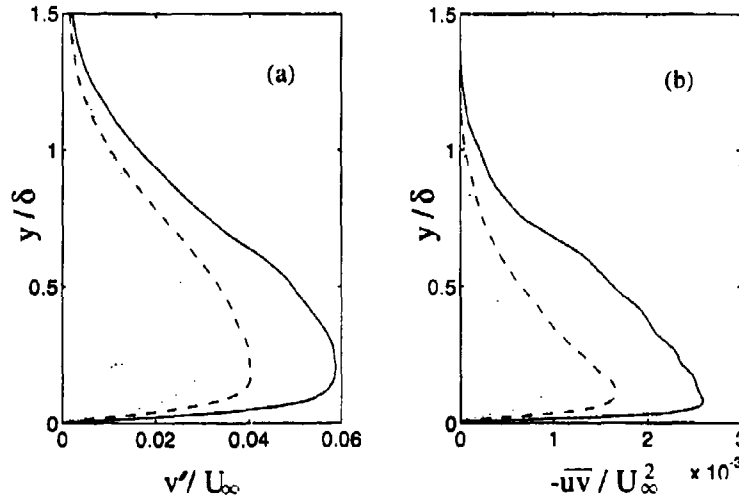
Figure 4: Simulation data. (a) vertical turbulent intensity, v'/U_∞; (b) turbulent shear stress, $-\overline{uv}/U_\infty^2$.   Key: R1n(—); R2s(- - -); R3S($\cdots$)

4   Experimental data

Flow visualisation was undertaken initially. injecting smoke into the boundary layer and using a laser sheet to illuminate either a longitudinal or a spanwise slice of the flow (see Cowan, 1994). For neutral conditions. this demonstrated the high degree of intermittency in the outer part of the boundary layer, and confirmed the presence of large-scale vertical motions. The effects of stability upon these motions and upon the turbulence levels were obvious and in accordance with the comments of the previous section.

Experimental velocity and concentration data were taken with a single hot-wire anemometer and a flame-ionising detector (FID). The hot-wire was run at high temperature, rendering it insensitive to fluctuations in the concentration of the secondary gas, carbon dioxide (after McQuaid & Wright. 1973). Trace quantities of propane were pre-mixed with the injected source fluid, allowing the FID to indirectly measure the source fluid concentration.

The experimental data was broadly in agreement with the extensive results from the simulations (see Cowan, 1994). Hence, instead of repeating the above analysis. we present here time series of instantaneous concentration at three positions in the boundary layer. for neutrally and stably stratified cases — figure 5. These are similar to those recorded by Stretch (1986), and demonstrate the large changes in the probability distribution of the concentration with height in the boundary layer (see figure 6). Note that this data can also be extracted from the DNS simulations.

Consider the neutral data first: it is interesting to note that the maximum instantaneous concentration is roughly constant throughout the boundary layer. at a value
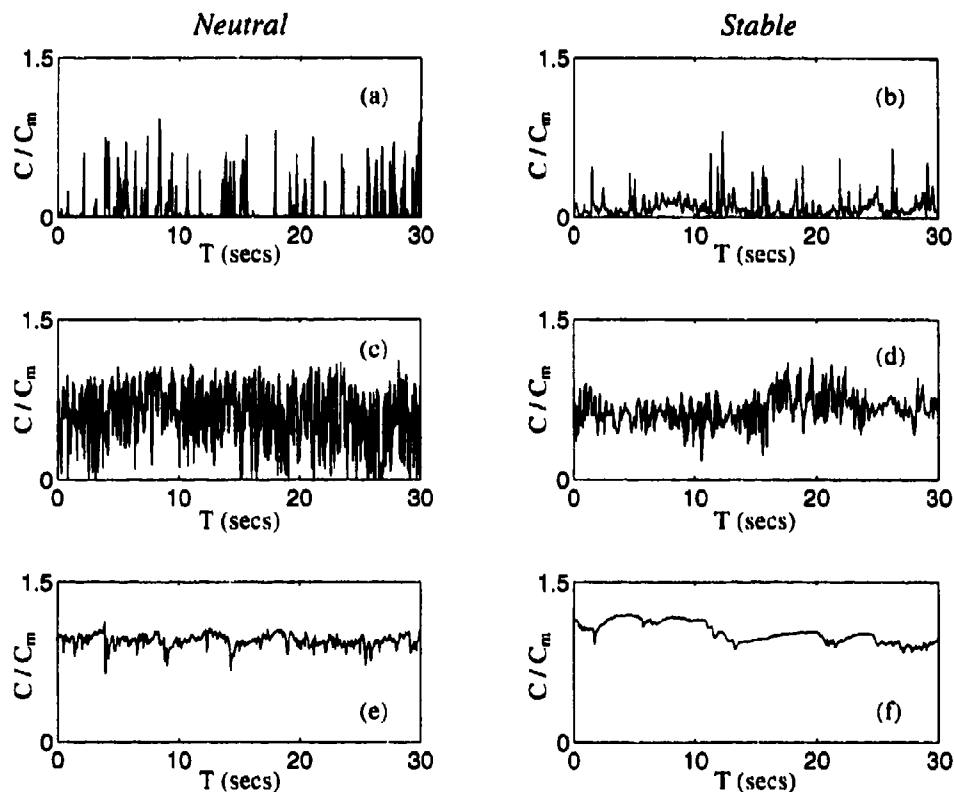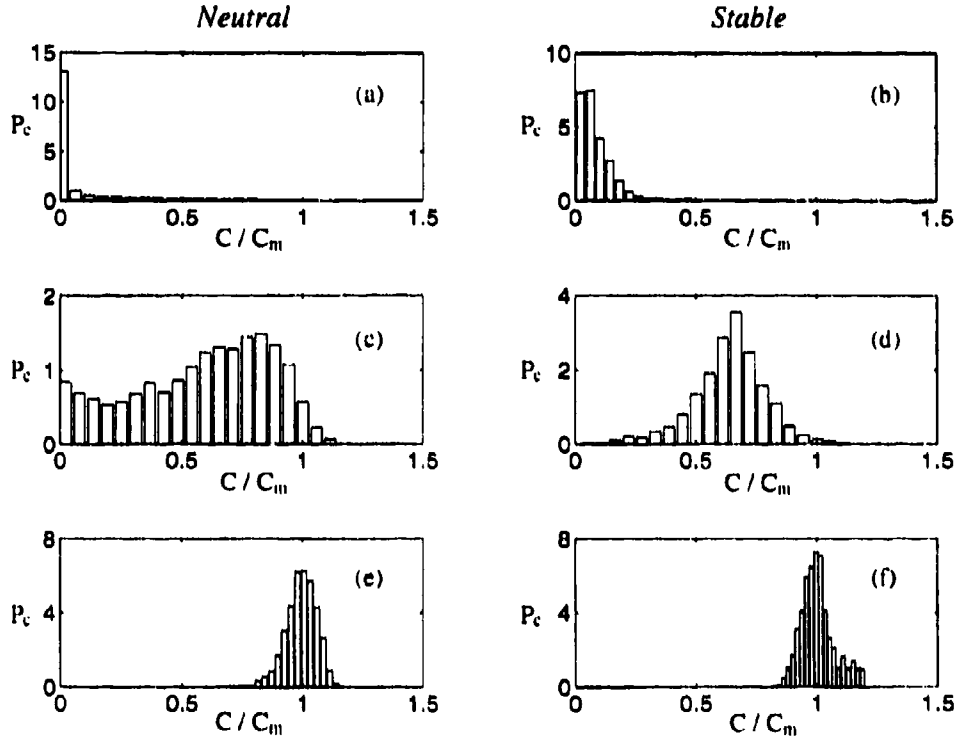
Figure 5: Time series of experimentally recorded instantaneous concentration. neutrally (a,c,e) and stably (b,d,f) stratified. Heights in the boundary layer: (a,b) – $y/\delta \approx$ 1.0;   (c,d) – $y/\delta \approx 0.6$;   (e,f) – $y/\delta \approx 0.05$.

of C_m (where C_m is the local maximum mean, and occurs at ground-level). The signal $C(t)$ becomes increasingly intermittent with distance from the wall, so that the probability density function (p.d.f.) becomes less Gaussian in shape — at $y/\delta = 0.6$ (figure 6c), the p.d.f. has a second peak at $C = 0$. At the boundary layer edge, the p.d.f. is near exponential in shape with a large peak at $C = 0$, reflecting the high intermittency of the signal.

For the stable data, two observations may be made: firstly, the maximum instantaneous concentrations are attenuated away from the wall; secondly, the intermittency is less pronounced. These effects cause the concentration p.d.f. to be less skewed and more Gaussian throughout most of the boundary layer. This is most noticeable when figures 5c & 5d and 6c & 6d are compared. Near the boundary layer edge, however, the signal remains intermittent as expected.

An explanation for the changes in the concentration p.d.f. may be gained by assuming that the inherent intermittent nature of the *neutral* $C(t)$ data is due to large-scale

Neutral   *Stable*

Figure 6: Probability density functions, P_c, of experimentally recorded instantaneous concentration, neutrally (a,c,e) and stably (b,d,f) stratified. Heights in the boundary layer: (a,b) – $y/\delta \approx 1.0$;   (c,d) – $y/\delta \approx 0.6$;   (e,f) – $y/\delta \approx 0.05$.

vertical motions, so that the FID probe samples either entrained free-stream fluid ($C = 0$) or rising fluid from the near-wall region ($C \approx C_m$). Small-scale mixing will give intermediate values of C, smearing the p.d.f. peaks at $C = 0$ and $C = C_m$. However, the time-scale of the large-scale motions is assumed short enough for these effects to be generally secondary in importance. This seems to be substantiated by the flow visualisation.

As we have seen from the previous section, a stable stratification suppresses large-scale vertical motions, so that in the middle of the boundary layer rising fluid parcels will not, in general, have come from the near-wall region, but from somewhere more local. The increased importance of small-scale mixing means that these parcels will have had time to mix locally, thus decreasing, on the whole, their concentration. This leads to a better mixed, more Gaussian concentration field, with less intermittency over most of the boundary layer, in agreement with measured stratified data.

5 Conclusions

A stably stratified turbulent boundary layer has been studied, using DNS and wind-tunnel experiments. Significant changes were observed in the entrainment into the boundary layer, and in the profiles of the vertical turbulent intensity and the turbulent shear stress. This was attributed to a suppression of large-scale vertical motions by the stable stratification.

Time series of instantaneous concentration were analysed, and remarks made on the variations in the concentration p.d.f. with both position in the boundary layer the level of stratification. These changes were also linked with the suppression of large-scale vertical motions.

We are grateful to Dr. Peter Voke for his help in setting up the simulations, and to Cambustion Ltd. for loan of the FID equipment.

6 References

ARYA,S.P.S. (1975). Buoyancy effects in a horizontal flat-plate boundary layer. *J. Fluid Mech.*, **68**, 321-43.

BRITTER,R.E. (1988). Laboratory experiments on turbulence in density-stratified fluids. in *Proc. 8th Symposium of Turbulence and Diffusion, San Diego, USA*.

COWAN,I.R. (1994). Density-stratified turbulent boundary layers. *PhD thesis, Department of Engineering, University of Cambridge, UK*.

COWAN,I.R. & BRITTER (1994). Direct numerical simulation of a stably stratified turbulent boundary layer. in *Proc. First ERCOFTAC Workshop on Direct and Large Eddy Simulations, Guilford, UK*.

GAO,S., LESLIE,D.C. & VOKE,P.R. (1991). Large eddy simulation of thermal impinging jets. *Report ME-FD/91.02, University of Surrey, Guilford, UK*.

McQUAID,J. & WRIGHT,W. (1973). The response of a hot-wire anemometer in flows of gas mixtures. *Int. J. Heat Mass Transfer*, **16**, 819-828.

STRETCH,D.D. (1986). The dispersion of slightly dense contaminants in a turbulent boundary layer. *PhD thesis, Department of Engineering, University of Cambridge. UK*.

VOKE,P.R. & GAVRILAKIS,S. (1993). Numerical study of a tripped boundary layer. *Technical Report ME-FD/93.10, Department of Mechanical Engineering, University of Surrey*.

Convection and Internal Waves
in a Stably Stratified Shear Flow

Patrick C. Gallacher
Naval Research Laboratory, SSC
Stennis Space Center, MS 39529-5004
(601) 688-5315 (Voice)
(601) 688-4759 (Fax)
p.gallacher (Omnet)
gallachr@nrlssc.navy.mil (Internet)

Hemantha W. Wijesekera
Applied Physics Laboratory
University of Washington
Seattle, Washington 98105

Wijesekera and Dillon (1991) hypothesized that internal
gravity waves could be generated just below the upper ocean mixed
layer as a result of convective plumes in the mixed layer.
Furthermore they demonstrated that these waves could propagate
downward and generate the secondary mixing events that are seen
in the equatorial thermocline. We have designed a series of Large
Eddy Simulations to test this hypothesis.

The domain for the Large Eddy Simulations consists of a
surface turbulent boundary layer overlying a stably stratified
region in the upper ocean. The boundary layer is forced by
surface cooling with no wind stress. The surface cooling has a
maximum value of 500 W/m^2 and the form of a double Gaussian with
a half width of 27 m in the x direction and is uniform in the y
direction. We impose a large-scale mean horizontal velocity field
in the ocean by continually nudging the velocity field toward a
prescribed vertical profile. The velocity profile varies in the
vertical and allows for the possibility of critical layer
absorption of the downward propagating gravity waves. The Cor-
iolis force is set to zero to simulate equatorial conditions.

The model domain is 200 meters square in the horizontal and
100 meters deep. The numerical grid consists of 75^3 points with
uniform spacing. The incompressible, Navier-Stokes equations are
solved spectrally in the horizontal and a finite difference
scheme is employed in the vertical. The diffusivity is variable
and depends on the magnitude of the subgrid scale energy. A
prognostic equation is solved for the subgrid scale energy. The
horizontal boundary conditions are periodic. The vertical bound-
ary conditions at the top of the model domain are the imposed
fluxes of heat and momentum, at the bottom the boundary condi-
tions radiate gravity waves out of the domain. The code is based
on the atmospheric Large Eddy Simulation code of Moeng (1984).

The imposed surface cooling generates convection in the
initially isothermal surface layer significantly increasing the

1

level of resolved scale turbulent kinetic energy. The energy is distributed among the normal Reynolds stresses as predicted by theory, the vertical component is the largest and the maximum value occurs at about mid-depth in the turbulent layer. The turbulent boundary layer deepens with time. The frequency spectra of the resolved scale fields have approximate -5/3 slopes in the boundary layer.

Below the boundary layer the results display a high frequency internal gravity wave field in the stratified region only when the mean shear is imposed on the flow. The wavelengths in the direction of mean shear are approximately 2-3 times larger than the wavelengths in the direction of no mean shear. The frequency spectra of the resolved scale fields peak near the buoyancy frequency in the stratified layer. There is a maximum in the resolved scale turbulent kinetic energy at the critical layer.

The resolved scale kinetic energy budget, heat-flux budget, and coherence and phase relations are calculated directly from the model data and will be used to further describe the physics of the wave field and the turbulent boundary layer.

References

Moeng, C-H., 1984: A large-eddy-simulation model for the study of planetary boundary-layer turbulence. *Jour. Atmos. Sci.*, 41, 2052--2062.

Wijesekera, Hemantha W. and Thomas M. Dillon, 1991: Internal waves and mixing in the upper equatorial Pacific Ocean. *J. Geophys. Res.*, 96, 7115-7125.

2

TURBULENT WAKES IN STRATIFIED FLUIDS: RESULTS OF NUMERICAL EXPERIMENTS

Chernykh G.G., Moshkin N.P., Voropayeva O.F.

Institute of Computational Technologies, Siberian Division of the Russian Academy of Sciences, 630090, Novosibirsk, RUSSIA

A hierarchy of second-order semi-empirical models of turbulence including modified $e - \epsilon$ models and the model with differential equations of transformation of a set of Reynolds stresses was used for the numerical simulation of turbulent wakes behind axisymmetrical bodies and generated by the wakes of internal waves in stratified fluids. In order to simulate above flow the three-dimensional parabolized systems of equations were used. The employed finite-difference algorithms are based on the method of splitting into physical processes and space variables. The numerical models of the far turbulent wakes were based on the assumption of independence wave motions and diffusion processes under large decay time. The agreement between the calculated characteristics of turbulent wakes and well-known experimental data obtained by Lin and Pao is sufficiently good. Simplified models of flow have been constructed. The calculation results for turbulent wake characteristics and internal waves generated by it in pycnocline are presented.

Turbulent wakes behind the axisymmetrical bodies in stratified fluids have been studied by several authors (for details see references). Shooley and Stewart [1] experimentally analyzed the turbulent wake behind a self-propelled body and demonstrated its collapse and wake-generated internal waves. The collapse of the momentumless wake in linearly stratified media was investigated by Merritt [2]. Lin and Pao carried out a detailed study of turbulence characteristics in turbulent wakes behind the bodies moving in a linearly stratified media [3,4]. Experimental analysis of internal waves generated by bodies moving in stratified fluids was performed by Gilreath and Brandt [5]. They also presented their theoretical estimates of internal waves including a case of the wake collapse in pycnocline. A series of studies carried out late [6-10] was concerned with the flow generated by a sphere moving in the stratified fluid. Different flow regimes have been studied versus Reynolds and Froude numbers in both near and far wakes. Bonneton, Chomaz and Hopfinger [10] experimentally and theoretically studied internal waves generated by a sphere moving in linearly stratified fluid in great detail. The wake wave component was considered associated with coherent wake structures. Voisin [11] carried out detailed analysis of the experimental data on turbulent wakes decay in stratified fluids and theoretically estimated the internal waves parameters.

Onufriev [12] theoretically studied the initial stage of the wake development. Donaldson, Lewellen and Teske [13] numerically modelled a turbulent wake behind a self-propelled body in a linearly stratified medium and the wake of collapse-generated internal waves. Hassid [4] numerically simulated the dynamics of turbulent wakes behind self-propelled and towed bodies. The obtained data on the changes in the characteristic sizes of the wakes and changes in velocity defect and turbulence energy on the wake axis versus the distance from the body proved to be in good agreement with the Lin's and Pao's experimental data. Danilenko and Tolstykh [14] have considered the turbulent wake behind a

self-propelled body as an example of the application of the stratified flows computation method. The construction of simplified mathematical models of the far turbulent wakes (and internal waves generated by it) behind the body in a linearly stratified fluid was discussed in [15].

Our analysis of the results obtained by the known to us researchers of the numerical modelling of turbulent wakes in stratified fluid, allowed us to conclude that the numerical models are not sufficiently complete. In particular, there are no numerical modelling results on anisotropic decay of the intensities of turbulent fluctuations of the vertical and horizontal velocity components in a far momentumless turbulent wake in linearly stratified medium experimentally obtained in [3]. We attempted to fill those gaps in this problem.

1.**Basic equations.** In order to describe the flow in the far turbulent wake behind an axisymmetric body in a stratified medium we used the following system of averaged equations of motion, continuity and incompressibility (in Boussinesq approach)

$$U_0\frac{\partial U_1}{\partial x} + V\frac{\partial U_1}{\partial y} + W\frac{\partial U_1}{\partial z} = \frac{\partial}{\partial y}\langle u'v'\rangle + \frac{\partial}{\partial z}\langle u'w'\rangle, \tag{1}$$

$$U_0\frac{\partial V}{\partial x} + V\frac{\partial V}{\partial y} + W\frac{\partial V}{\partial z} = -\frac{1}{\rho_0}\frac{\partial\langle p_1\rangle}{\partial y} - \frac{\partial}{\partial y}\langle v'^2\rangle - \frac{\partial}{\partial z}\langle v'w'\rangle \tag{2}$$

$$U_0\frac{\partial W}{\partial x} + V\frac{\partial W}{\partial y} + W\frac{\partial W}{\partial z} = -\frac{1}{\rho_0}\frac{\partial\langle p_1\rangle}{\partial z} - \frac{\partial}{\partial y}\langle v'w'\rangle - \frac{\partial}{\partial z}\langle w'^2\rangle - g\frac{\langle \rho_1\rangle}{\rho_0}. \tag{3}$$

$$U_0\frac{\partial\langle \rho_1\rangle}{\partial x} + V\frac{\partial\langle \rho_1\rangle}{\partial y} + W\frac{\partial\langle \rho_1\rangle}{\partial z} + W\frac{d\rho_s}{dz} = -\frac{\partial}{\partial y}\langle v'\rho'\rangle - \frac{\partial}{\partial z}\langle w'\rho'\rangle, \tag{4}$$

$$\frac{\partial V}{\partial y} + \frac{\partial W}{\partial z} = \frac{\partial U_1}{\partial x}. \tag{5}$$

In equations (1)-(5) $U_1 = U_0 - U$ stands for the defect of the averaged streamwise velocity component; U, V, W designate the velocity components of the averaged motion along the axes x, y, z; p_1 is the pressure deviation from the hydrostatic state due to the stratification $\rho_s(z)$; U_0 is the velocity of the incident nonperturbed flow; g is the acceleration due to gravity, $\langle \rho_1\rangle$ is the averaged density defect $\rho_1 = \rho - \rho_s, \rho_s = \rho_s(z)$ is the density of unperturbed fluid; $\rho_0 = \rho_s(0)$; primed symbols denote the fluctuating components, $(\ )$ is the averaging sign. The flow density is assumed a linear function of the temperature; stratification is assumed to be weak and stable. In the right-hand sides of Eqs. (1)-(4) the terms containing the derivative with respect to x have been omitted under the assumption of their smallness as well as co-factors in the form of the coefficient of the laminar viscosity or diffusion.

The system of equations (1)-(5) is non-closed, here 3 closed mathematical models of flow are considered. In the first of them (Model 1) in addition to equations (1)-(5) the equation of turbulence energy c balance are invoked as well as the equation of rate of energy dissipation ε into heat. The values of the tensor components of Reynolds stresses $\langle u_i'u_j'\rangle$ and the vector of density fluxes $\langle u_i'\rho'\rangle$ were determined making use of the model of locally-equilibrium approximation similar to that employed [4]. In Model 2 the tensor components of Reynolds stresses were found by employing approximations [16]

$$\langle u_i'u_j'\rangle = \frac{2}{3}\delta_{ij}c + \frac{c}{c_1\varepsilon}[(1-c_2)(P_{ij} - \frac{2}{3}\delta_{ij}P) + (1-c_3)(G_{ij} - \frac{2}{3}\delta_{ij}G)].$$

$$P_{ij} = -\langle u_i' u_k' \rangle \frac{\partial U_j}{\partial x_k} - \langle u_j' u_k' \rangle \frac{\partial U_i}{\partial x_k}, \quad G_{ij} = -\frac{1}{\rho_0} g_i \langle u_j' \rho' \rangle, \quad P = P_{ii}/2, \quad G = G_{ii}/2, \quad (6)$$

$$C_2 = 0.6, \quad C_3 = 0.3, \quad g_i = (0, 0, -g).$$

The components of the vector $\langle u_i' \rho' \rangle$ were sought in the same way as in Model 1. In Model 3 the following approximations were employed for the values $\langle u'v' \rangle$, $\langle u'w' \rangle$

$$\langle u'v' \rangle = C_s \frac{\langle v'^2 \rangle e}{\varepsilon} \frac{\partial U_1}{\partial y}, \quad \langle u'w' \rangle = C_s \frac{\langle w'^2 \rangle e}{\varepsilon} \frac{\partial U_1}{\partial z}, \quad C_s = 0.25. \quad (7)$$

The quantities $\langle u'^2 \rangle$, $\langle v'^2 \rangle$, $\langle w'^2 \rangle$, $\langle v'w' \rangle$ were determined by solving the corresponding differential transport equations [17, 16]. The values e and ε in Models 2,3 were obtained from the equations similar to those of Model 3 allowing for (6), (7). In all the models the quantity $\langle \rho'^2 \rangle$ was obtained from the algebraic relation of the local-equilibrium approximation

$$\langle \rho'^2 \rangle = -\frac{2}{C_T} \frac{e}{\varepsilon} \langle w' \rho' \rangle \frac{\partial \langle \rho \rangle}{\partial z}, \quad C_T = 1.25. \quad (8)$$

2.Statement the problem. Numerical algorithms.

Marching variable x in the considered problem plays the role of time. Initial conditions for the Models 1,2 at some $x = x_0$ were assigned in accordance with experimental data of Lin and Pao [3,4] similar to those taken in [4]. As for Model 3, it was applied only for the calculation of momentumless wake characteristics and as initial data it employed self-similar solution corresponding to the homogeneous fluid and in agreement with experimental data [3]. For the sake of symmetry, the problem solution was sought only in the first quadrant of the plane $Y \times Z$ with the corresponding symmetry conditions laid down on coordinate axes. The problem solution was sought in the sufficiently large rectangular area $0 \leq y \leq Y, 0 \leq z \leq Z$. At the boundaries of the rectangular $y = Y: z = Z$ laid down zero boundary conditions of the value of velocity and density defects, turbulence energy, dissipation and tensor components of Reynolds stresses. Variables of the problem can be rendered dimensionless on making use of the length scale D i.e. body diameter and the scale U_0 i.e. the velocity of unperturbed flow. Let us also introduce $\langle \bar{\rho}_1 \rangle = \langle \rho_1 \rangle / a D \rho_0$. As a result, in equations rendered dimensionless g will be substituted by the quantity $4\pi/Fr^2$ where $Fr = F_D = U_0 T/D$ is the density Froude number, $T = 2\pi/\sqrt{a g}$ is Väisälä-Brunt period, $a = -(1/\rho_0) d\rho_s/dz$ if $z = 0$. In numerical modelling of the flow in the wake two finite difference algorithms were employed. Algorithm 1 is based on explicit splitting into space variables for the equations (1), (4) and other similar equations and on the application of an implicit splitting into physical processes to the system of equations (2), (3), (5). The calculations showed the possibility to use a two-dimensional analogue of incompressibility equation (5) with the zero right-hand side. In this case, the stream function ψ can be introduced and the vorticity ω. The calculation algorithm using these variables (algorithm 2) is based on the methods of splitting into space variables. The stream function was obtained through the solution of the respective Poisson equation by means of an iterative scheme of stabilizing corrections. Both uniform and non-uniform grids were employed condensing towards the origin of coordinates. The algorithms were tested by calculations on a sequence of grids.

3.Calculation results.

Figs. 1-3 show the Model 1 calculation results versus experimental data obtained by Lin and Pao on the drag wake. The agreement with experimental data and Hassid's calculation results [4] can be considered satisfactory. Fig. 4 shows the

lines $\langle \rho_1 \rangle / aD\rho_0 = const$ for the time value $t/T = x/U_0 T = 1.5$. The lines are represented by the following levels 1 - $-.38 \cdot 10^{-1}$, 2 - $-.25 \cdot 10^{-1}$, 3 - 0.0, 4 - $.21 \cdot 10^{-2}$, 5 - $.90 \cdot 10^{-2}$, 6 - $.50 \cdot 10^{-1}$. The data of numerically modelled decay of the momentumless wake in linearly stratified medium are shown on Figs. 5-13. Calculation results on Fig. 5 are in sufficiently good agreement with experimental data. The better agreement can be achieved making use of Model 2. Fig. 7 shows the time variation of the values of total turbulence energy $\dot{E}$ and the wave energy in the wake $\dot{P}$ ($Fr = 120$, Model 3)

$$\dot{E} = \int\limits_0^\infty \int\limits_0^\infty \dot{e} \, d\ddot{y} d\ddot{z}, \quad \dot{P} = \int\limits_0^\infty \int\limits_0^\infty \Big(\frac{\ddot{V}^2 + \ddot{W}^2}{2} + \frac{2\pi^2}{Fr^2} \langle \dot{\rho}_1 \rangle^2 \Big) d\ddot{y} d\ddot{z}, \quad \dot{e} = e/U_0^2, \quad \ddot{y} = y/D, \quad \ddot{z} = z/D.$$

It is clear that as the total turbulence energy monotonously decreases, the quantity $\dot{P}(t/T)$ becomes actually constant at $t/T \geq 1.5$. Such behaviour of $\dot{E}, \dot{P}$ is the evidence of independence, as in the problem of dynamics of the turbulent fluid region [18], diffusion and wave processes. In this connection, in order to calculate the characteristics of the turbulent wake itself diffusion model can be used where $V = W = 0, g \neq 0$. The internal waves can be calculated by Euler equations. Making use of diffusion model significantly reduces the size of the grid region. In the case of pycnocline the simplified models can be employed at large t values. The numerically modelled turbulent wake characteristics for value $F_D = 120$ are compared with laboratory results obtained by Lin and Pao [3] on Figs. 8-12. Model 3 yields the satisfactory agreement of fluctuations intensities dynamics of the horizontal and vertical components. In Models 1,2 these values were obtained from the respective algebraic representations. It is possible that the deviations at $t/T \geq 5$ on Figs. 10,11 are caused by non-universal initial mathematical models with respect to turbulent numbers Rc and Pc.

The dynamics of the turbulent wake in the fluid with non-linear distribution $\rho_s(z) = \rho_0 - a\beta \tanh z/\beta, \beta = 0.3$ is illustrated by Figs. 13 - 15. Figs. 13 - 14 show the stream function lines $\psi/U_0 D = const$ for $t/T = 1.3$ represented by the following levels 1 - $-.4836 \cdot 10^{-5}$, 2 - $+.1251 \cdot 10^{-3}$, 3 - $+.2551 \cdot 10^{-3}$, 4 - $+.3851 \cdot 10^{-3}$, 5 - $+.5151 \cdot 10^{-3}$, 6 - $+.6451 \cdot 10^{-3}$, 7 - $+.7751 \cdot 10^{-3}$, 8 - $+.9050 \cdot 10^{-3}$, 9 - $+.1035 \cdot 10^{-2}$, 10 - 0.0. Fig. 15 shows the lines of equal energy $e/e(t,0,0) = const$ characterized by the following levels: 1 - 0.01, 2 - 0.01, 3 - 0.2, 4 - 0.3, 5 - 0.4, 6 - 0.5, 7 - 0.6, 8 - 0.7, 9 - 0.8, 10 - 0.9. Fig. 16-17 for the sake of comparison show the stream function lines distributions and turbulence energy for linear stratification with the same levels as Figs. 13-15. It can be seen that both the towed and self-propelled body the behaviour of internal waves in linear stratified fluid is in qualitative agreement with the behaviour of internal waves generated by local perturbation of the density field in stratified medium [19].

Therefore, the developed numerical models provide the satisfactory description of turbulent wakes dynamics in stratified medium. Turbulent diffusion processes are fairly interesting for the investigations of stratified flows. The experimental data of Lin and Pao can be considered a good test of mathematical models.
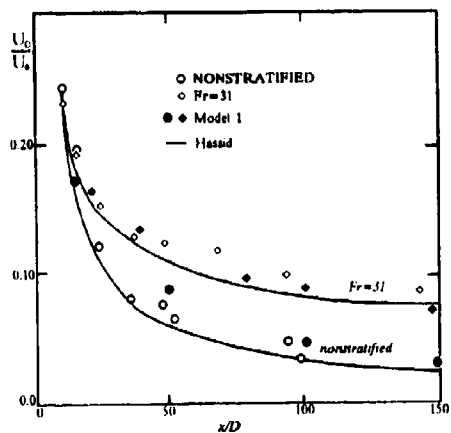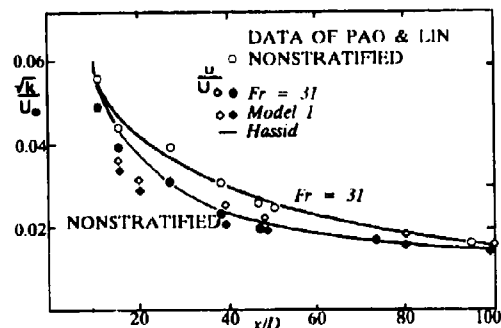
Fig.1 Centerline velocity defect in drag wakes.

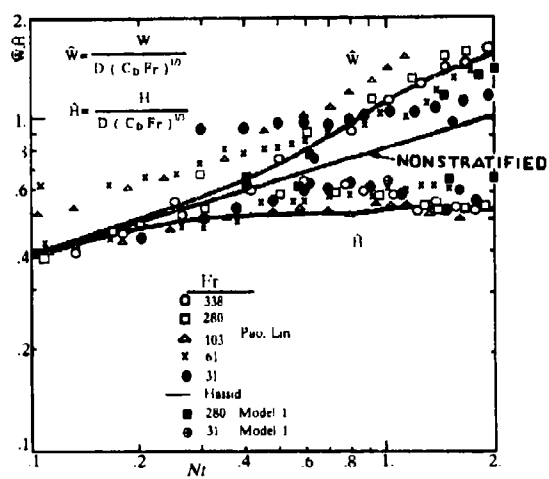Fig.2 Centerline turbulent energy in drag wakes.

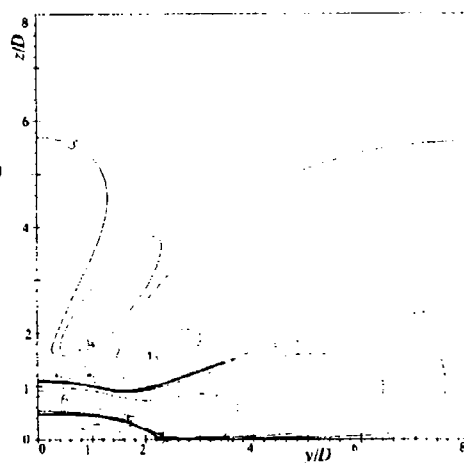Fig.3 Nondimensional width and height of a drag wakes.

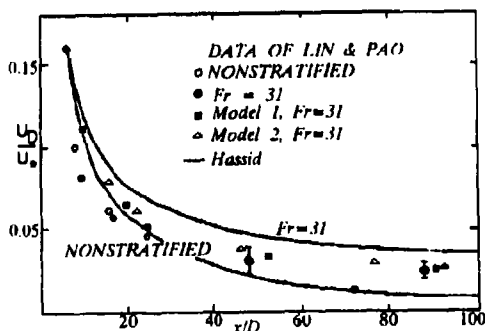Fig.4 Isolines $\langle \rho_1 \rangle / aD\rho_0 = const$ (Model 1)

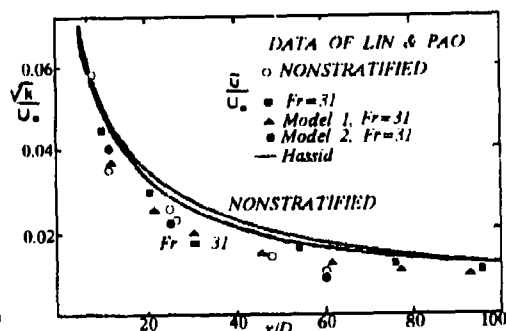Fig.5 Centerline velocity defect in momentumless wakes.

Fig.6 Centerline turbulent energy in momentumless wakes.

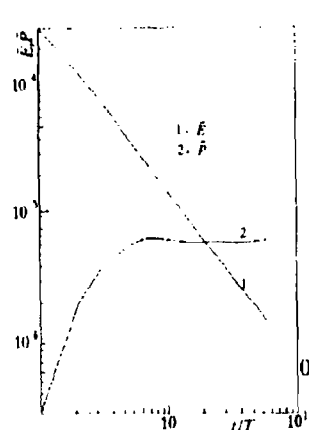
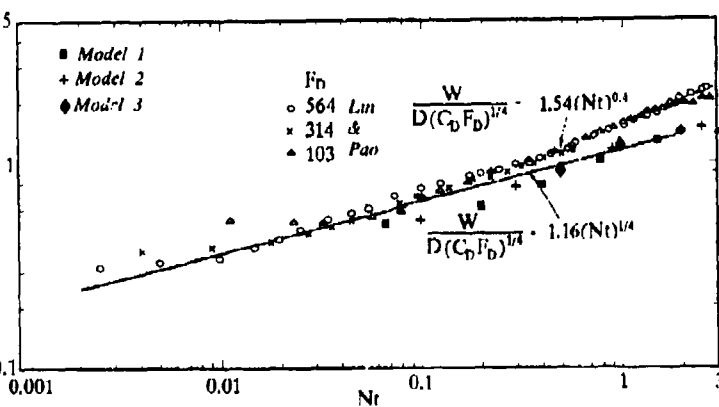Fig.7 Time variation of a total kinetic turbulent energy $\tilde{E}$ and energy of internal waves, $\tilde{P}$.

Fig.8 Nondimensional width of a momentumless wakes.

$$\frac{W}{D(C_D F_D)^{1/4}} = 1.54(Nt)^{0.4}$$

$$\frac{W}{D(C_D F_D)^{1/4}} = 1.16(Nt)^{1/4}$$
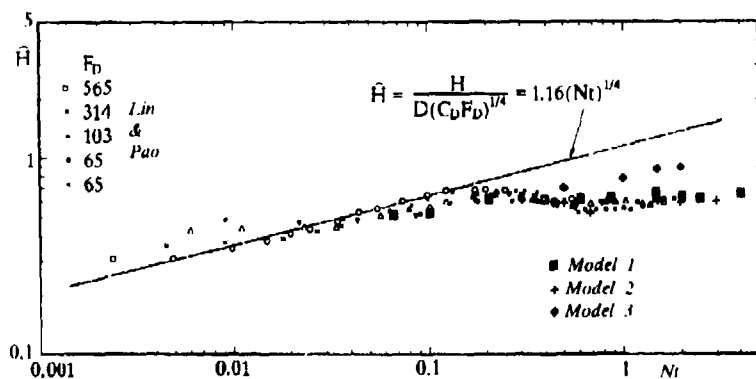
Fig.9 Nondimensional height of a momentumless wakes.

$$\tilde{H} = \frac{H}{D(C_D F_D)^{1/4}} = 1.16(Nt)^{1/4}$$
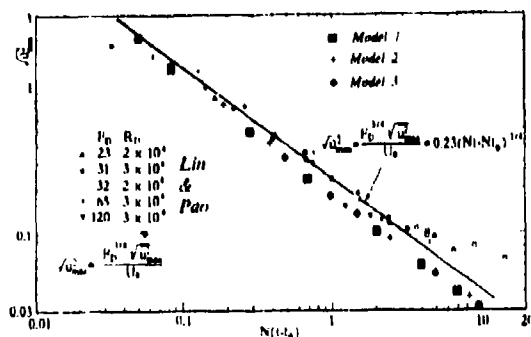
Fig.10 Decay of maximum velocity fluctuations $\sqrt{\bar{u}_{max}^2} = \sqrt{\langle u'^2 \rangle_{max}}$ in the momentumless wakes.
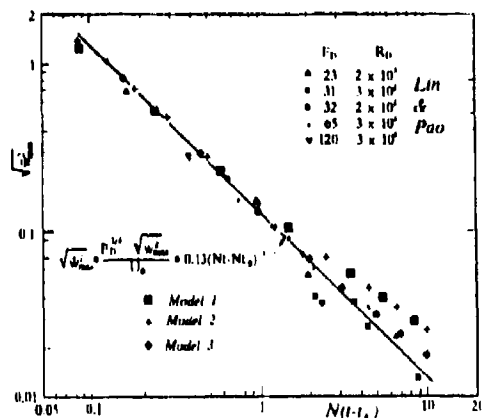
Fig.11 Decay of maximum velocity fluctuations $\sqrt{\bar{w}_{max}^2} = \sqrt{\langle w'^2 \rangle_{max}}$ in the momentumless wakes.
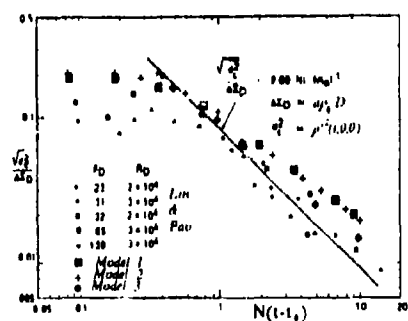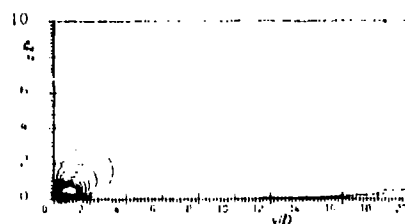

Fig.12 Evolution of centerline density fluctuations.

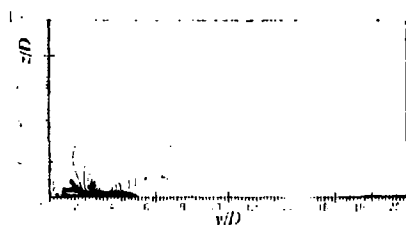Fig.13 Isolines $\Psi/U_0 D$, nonlinear stratification, $t/T = Nt = 1.0$.

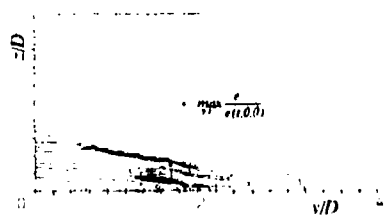Fig.14 Isolines $\Psi/U_0 D$, nonlinear stratification, $t/T = Nt = 3.0$.

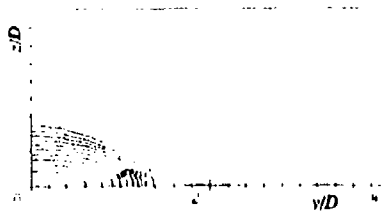Fig.15 Isolines $c/c(t,0,0) = const.$ $t/T = 3.0$, linear stratification.

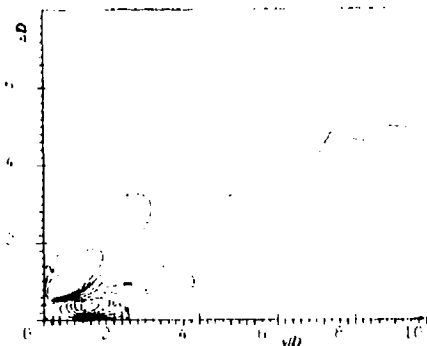Fig.16 Isolines $c/c(t,0,0) = const$, $t/T = 1.0$, linear stratification.

Fig.17 Isolines $\Psi/U_0 D = const$, $t/T = 1.0$, linear stratification

REFERENCES

1. A.H. Schooley, R.W. Stewart. J. Fluid Mech. 15 (1963), 83-96.
2. C.E. Merrit. AIAA J. 12 (1974), 940-949.
3. J.T. Lin, Y.H. Pao. Ann. Rev. Fiuid Mech. 11 (1979), 317-338.
4. S. Hassid. J. Hydronautics 14 (1980), No. 1, 25-32.
5. H.E. Gilreath, A. Brandt. AIAA J. 23 (1985), 693-700.
6. E.Y. Sysoeva, Y.D. Chashechkin. J. Appl. Mech. Tech. Phys. 27 (1986), 190-196.
7. E.J. Hopfinger, J.B. Flor, J.M. Chomaz, P. Bonneton. Exps Fluids 11 (1991), 255-261.
8. Q. Lin, D.L. Boyer, J.S. Fernando. Phys. Fluids A, 4 (1992), No. 8, 1687-1696.
9. J.M. Chomaz, P. Bonneton, A. Butet, E.J. Hopfinger. Phys. Fluids A, 5 (1993), No. 11, 2799-2806.
10. P. Bonneton, J.M. Chomaz, E.J. Hopfinger. J. Fluid Mech. 254 (1993), 23-40.
11. B. Voisin. PhD thesis, Paris 6 University, 1991.
12. A.T. Onufriev. J. Appl. Mech. Tech. Phys. 5 (1970), 68-72.
13. W.S. Lewellen, M.E. Teske, C. Dup. Donaldson. AIAA J. 14 (1976), 382-387.
14. A.Yu. Danilenko, A.I. Tolstykh. Numerical methods in dynamics of viscous fluid. Novosibirsk, Inst. Theoret. Appl. Mech. 1983, 110-114.
15. G.G. Chernykh, N.N. Fedorova, N.P. Moshkin. Russian J. Theor. Appl. Mech. 2 (1992), 295-301.
16. W. Rodi. J. Geoph. Res. 92 (1987), C5, 5305-5328.
17. M.M Gibson, B.E. Launder. J. Fluid Mech. 86 (1978), 491-511.
18. G.G. Chernykh, Y.M. Lytkin, I.V. Sturova. Proceed. Internat. Symp. Refined Modelling Flows, 7-10 Sept., 1982, Paris, 671-679.
19. J. Wu. J. Fluid Mech. 35 (1969), 531-541.

Modelling deep ocean convection events

by G. N. IVEY, M. J. COATES and J. R. TAYLOR[†]

Department of Environmental Engineering
Centre for Water Research
University of Western Australia
Nedlands, Western Australia

Abstract

To model deep convective processes in a stratified ocean, a laboratory experiment was constructed in which, for convenience, the problem was inverted and a convective mixed layer generated by a localised source of bottom heating in a rotating, thermally stratified fluid. Following the initiation of the heating, a column of heated and well-mixed fluid forms over the heated plate and steadily erodes the overlying ambient stratification. Rotation initially confines the heated fluid above the central plate but, as time progresses, the front separating the well-mixed heated fluid and the surrounding ambient stratified fluid becomes unstable, eventually generating a field of baroclinic vortices. While the heat transport process is complex, temperature and velocity measurements are used to describe the evolution of the flow field, and the development of the flow instabilities and heat transport.

1. Introduction

The mechanisms of deep water formation are a subject of considerable interest due to their important role in affecting deep ocean overturning rates and residence times, the oceanic heat transport and the rate of oceanic uptake of CO_2 (e.g. Maier-Reimer et al. 1993). The formation of deep water occurs primarily in a few high latitude locations (e.g. Gascard 1991) in which intense localized surface cooling generates fluid which is sufficiently dense to penetrate the underlying stable density stratification associated with the seasonal thermocline. Early work on deep convection has been reviewed by Killworth (1983), and more recently field studies in locations such as the Greenland Sea (e.g. Schott et al. 1993a) and the Golfe du Lion (e.g. Schott and Leamann 1991) have reported direct observations of deep ocean convection events. Such observations are difficult to make, however, and the available data remain sparse.

Recently Jones and Marshall (1993) have used a nonhydrostatic numerical model to study deep convection in a homogeneous ocean. In general, their numerical experiments supported the concurrent laboratory studies of Maxworthy and Narimousa (1994) in homogeneous fluids in showing the formation of a series of rotationally controlled plumes within the convective chimney which eventually go baroclinically unstable. Maxworthy and Narimousa (1994) extended the earlier work of Fernando et al. (1991) by examining the dynamics of convection in a rotating homogeneous fluid when the source of de-stabilizing buoyancy was applied over a finite circular portion of the upper horizontal boundary in a circular tank with salt as the de-stratifying medium. They confirmed the observations of Fernando et al. (1991) on the transition depth h_c when the flow field made a transition from fully 3D turbulence close to the source to a rotationally controlled turbulence field where quasi-2D vortex structures formed and characterised the flow for greater distances from the source of buoyancy. In applying their results to the field observations, Maxworthy and Narimousa (1994) noted that the transition depth h_c was usually large compared to the depth at which convective motions have been observed and, indeed, often

---

[†] Current address: Department of Physics, Australian Defence Force Academy, University of N.S.W., Canberra, Australian Capital Territory.

large when compared to the depth of the ocean. The implication for the homogeneous case is that rotation may more directly affect the outflow of convectively mixed fluid from a convection event rather than directly affect the small scale 3D turbulence itself.

Given these observations, we have designed an experimental program in which the experiments are conducted in a parameter range where rotation affects but does not control the turbulence (see below) and, given that field observations indicate that a stable background density stratification is typically present (e.g. Gascard 1991), our experiments focus on the case of a stably stratified environment.

2. Experiments

The experiments were conducted in a 1m diameter by 0.5m deep circular perspex tank, double walled to reduce the heat losses. The outer wall was octagonal to allow undistorted horizontal views through the inner circular sidewall of the tank. To model the surface cooling observed in the field, we heat from below in the laboratory accomplished by centrally mounting on the base of the circular cavity a 0.4m diameter copper plate which formed the upper surface of a heat exchanger. Thus the plate could be heated from below by pumping hot fluid through the heat exchanger. Measurements of the flow rates and temperature drop of the heat exchanger fluid allowed the heat flux into the working fluid to be determined. A false bottom in the tank could also be rotated to simulate the effect of pre-conditioning of the stratification. The entire assembly was mounted on a rotating turntable revolving at a constant rate.

The temperature changes induced by the heating were measured with a rack of six fast response thermistors which could be vertically traversed, enabling vertical temperature profiles to be obtained at a 1mm resolution. The thermistors were fixed in the rack at the six different radii of 0, 0.1, 0.15, 0.2, 0.3, and 0.4 m.

The velocity fields were obtained by the use of particle image velocimetry (PIV) as implemented by Stevens and Coates (1994). Here, the flow was seeded with finely ground Pliolite particles, and the tank was illuminated by a horizontal laser light sheet. From a laser mounted external to the rotating table, the light beam was passed through an optical slip ring and onto a pair of orthogonal X-Y scanning mirrors mounted at the edge of the rotating table. The sheet produced by the scanning mirrors was collimated by a Fresnel lens and deflected into the tank by a large 45° mirror. The scanning mirrors allowed the sheet to be located at any depth and for these experiments the horizontal 5mm thick light sheet was regularly traversed through the mixed layer. The experiments were recorded from a CCD camera onto video tape, and from this recording image pairs were extracted at the times for which velocities were required. The velocities were then determined by a cross correlation between the two images of the pair obtained a short time Δt apart, typically $\Delta t = 0.32$s. The necessity of being able to resolve the Pliolite particles limited the field of view of the CCD camera to approximately $210\,\text{mm} \times 300\,\text{mm}$.

3. Description of the experiments

We focus here on three runs, summarized in table 1, covering a range of buoyancy fluxes B and rotation rates $f = 4\pi/T$, where T is the rotational period. All experiments had similar initial linear stratifications. We describe a typical run (run 48) to demonstrate the sequence of events which occurs following the initiation of the buoyancy flux.

Table 1: *A summary of the experimental runs. The symbols are defined in the text.*

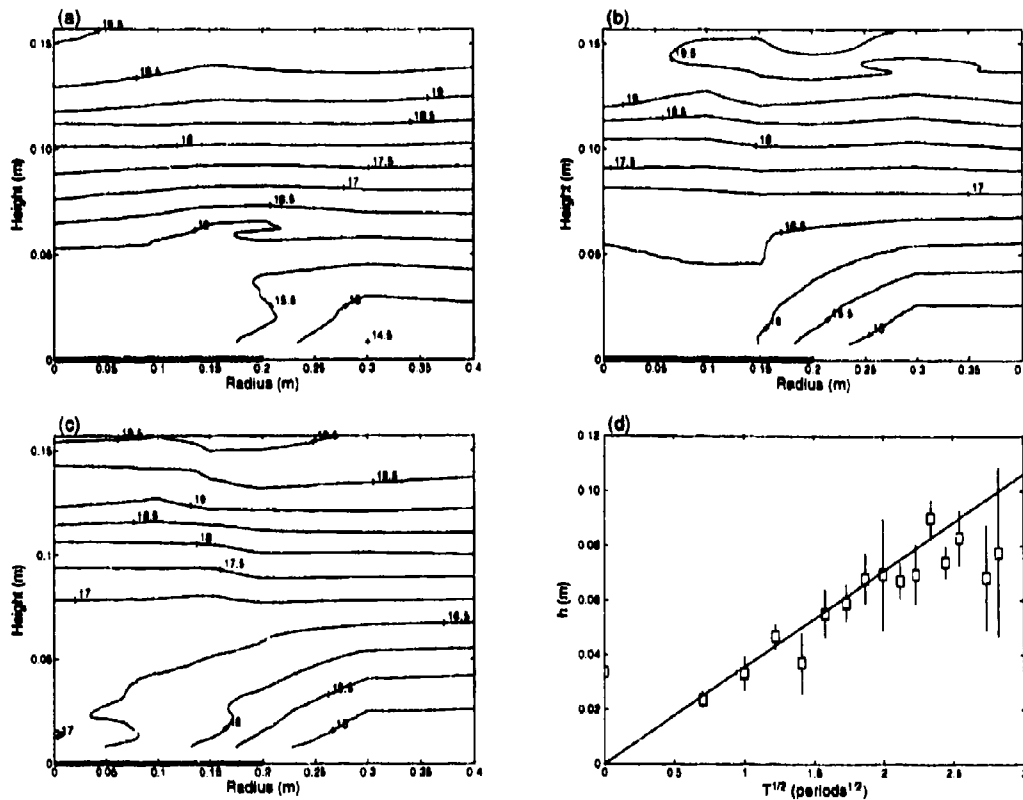| Run	f ($\text{rad}\,\text{s}^{-1}$)	T (s)	B (m^2s^{-3})	N (s^{-1})	λ_f (m)	L_R (m)	λ_f/L_R
42	0.42	30	1.87×10^{-6}	0.31	0.105	0.025	4.2
44	0.42	30	2.10×10^{-6}	0.25	0.089	0.027	3.4
48	0.21	60	0.97×10^{-6}	0.31	0.209	0.052	4.0

Figure 1: *The temperature structure for run 48 at (a) $1.5T$, (b) $3.5T$ and (c) $4.0T$, where T is the rotational period. The centre of the tank is located at $R = 0.0$ m and the outermost thermistor is at $R = 0.4$ m. The solid thick line from $R = 0.0$ m to $R = 0.2$ m marks the position of the heated plate. From the temperature data, the height of the mixed layer can be plotted (d) against time, where the solid line is from equation (3).*

After the commencement of the heating, convective plumes began to rise above the copper plate, eroding the overlying ambient stratification, and by $1.5T$ (fig. 1a) a mixed layer with thickness 5 cm has developed over the heated plate (the thick line on fig. 1). Initially, rotation therefore has the effect of confining the convective motions to the region directly above the heated plate. By $3.5T$, the mixed layer has thickened to approximately 8 cm (fig. 1b), but there has also been a partial incursion of ambient fluid over the heated plate and these lateral adjustments are driven by the lateral temperature gradients established between the mixed layer and the stably stratified ambient fluid. By $4.0T$ (fig. 1c), the mixed layer has reached its near maximum value.

The mixed layer height can be estimated by taking the average of the heights as measured by the three innermost profiling thermistors above the plate. The data for run 48 are plotted in fig. 1d, and show the steady increase of the mixed layer height with time with a maximum value at $t \approx 5T$. For longer times, the depth measurements are irregular due to the inhomogeneous nature of the layer as a consequence of strong radial motions and the identification of a mixed layer becomes difficult.

Fig. 2 shows the development of the horizontal flow field at four different times and heights over a 120° quadrant of the tank. The rim of the heated plate is marked by the dashed line. Three main regions of the flow can be seen in fig. 2. The first is a turbulent
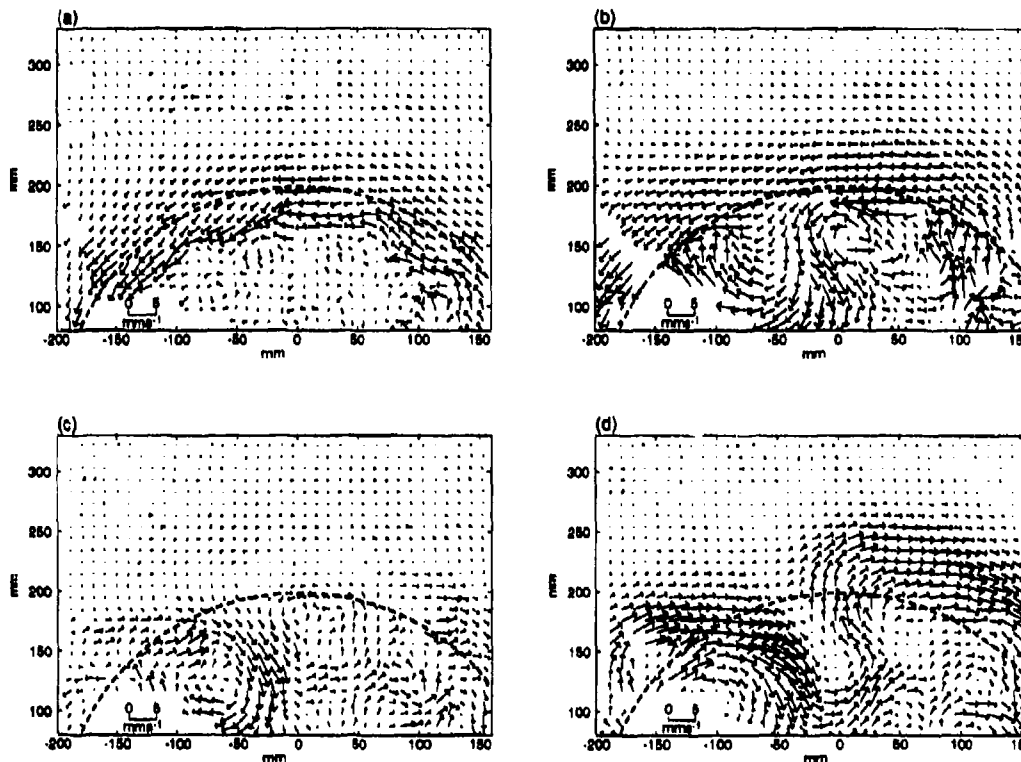
Figure 2: *The flow velocities at the times and heights of (a) 1.42T, 9 mm; (b) 3.47T, 10 mm; (c) 3.62T, 30 mm; and (d) 3.95T, 70 mm for run 48. Only a 120° quadrant of the tank is shown, with the rim of the heated plate marked as the dashed line. The table rotation is anticlockwise (cyclonic).*

region over the heated plate, where the small scale turbulent motion characteristic of the convective plumes can be seen. Well beyond the plate there is a quiescent far field, and between these two regions, there is a developing azimuthal flow or rim current. This current was rapidly established just above and at the edge of the heated plate by 1.42T (fig. 2a), flowing in a cyclonic direction (the same sense as the table rotation). By 3.47T (fig. 2b) the current has increased in strength and is already highly distorted by a relatively large scale wavelike instability in the current. Conversely, at mid-height of the mixed layer and only slightly later (fig. 2c at 3.62T), no rim current can be seen and only the turbulent convective motions above the plate are visible. Near the top of the mixed layer at 3.95T (fig. 2d), on the other hand, a well defined rim current is again visible, now flowing in the opposite (anticyclonic) direction, but distorted by a growing instability, with eddies beginning to form. For longer times the instability continues to grow in amplitude, eventually generating six eddies around the periphery of the heated plate.

4. Results

Rotation controls the turbulence when the Rossby number, based on velocity and length scales characterizing the turbulent scales of motion, is small. The available experimental

evidence (Hopfinger et al. 1983, Fleury et al. 1991, Fernando et al. 1991, Maxworthy and Narimousa 1994, Coates et al. 1994) suggests the critical Rossby number lies in the range $0.20 < Ro_c < 0.44$ and the corresponding critical length at which turbulence properties will deviate from their non-rotating values is in the range

$$13 \left(\frac{B}{f^3} \right)^{1/2} < h_c < 42 \left(\frac{B}{f^3} \right)^{1/2} . \tag{1}$$

As in the ocean, h_c is large compared to the depth of the stratified fluid in the present experiments and this is consistent with the observations of Coates et al. (1994) who showed the vertical and horizontal turbulent velocity scales and the integral scales of the turbulence in the mixed layer were independent of the rotation rate and given by

$$w = 0.5(Bh)^{1/3}, \quad u = 0.3(Bh)^{1/3} \quad \text{and} \quad l = 0.25h. \tag{2}$$

In the absence of rotational effects, when a constant de-stabilizing buoyancy flux B is applied at the horizontal boundary $z = 0$ of a fluid which has a constant density gradient N, a well mixed layer of thickness h will grow according to (e.g. Turner 1973)

$$h = 2^{1/2}B^{1/2}t^{1/2}/N \tag{3}$$

Ivey et al. (1993) demonstrated that the deepening law in (3) is valid, and the prediction in (3) is plotted in fig. 1d for comparison.

Consider now the case where the buoyancy flux B is applied over only a finite circular portion L of the horizontal boundary. The mixed layer will develop only over the segment L and its thickness h will grow according to (3). As the mixed layer deepens, a horizontal buoyancy anomaly is now developed between the mixed fluid and the ambient fluid of strength

$$g' \sim N^2 h. \tag{4}$$

The fluid will attempt to adjust horizontally under the action of the buoyancy forces in a time scale N^{-1} but rotation will limit the lateral adjustment scale to

$$L_R \sim Nh/f \tag{5}$$

i.e. the Rossby radius of deformation based on mixed layer height and the above will be valid provided $L_R < L$.

Assuming turbulent effects are unimportant in the mean momentum balance, a thermal wind balance prevails due to the maintained horizontal density gradient across the outer boundary of the convective region of the form

$$f\frac{\partial u}{\partial z} \sim \frac{\partial g'}{\partial r} \tag{6}$$

where u is the azimuthal or rim current that must develop around the periphery of the convective region, and r is the radial co-ordinate. Substituting (4) and (5) into (6) yields

$$f\frac{u}{h} \sim \frac{\partial g'}{\partial r} \sim \frac{N^2 h}{Nh/f} \tag{7}$$
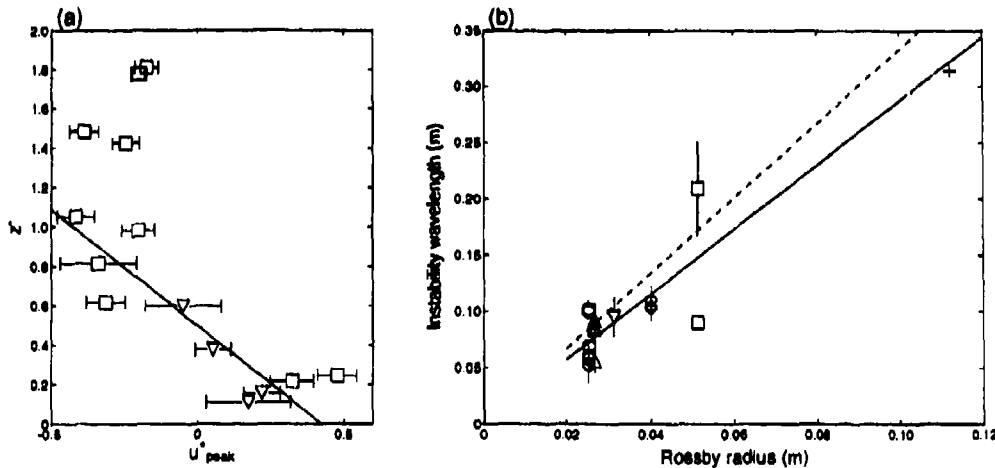
or

$$u \sim Nh. \tag{8}$$

Figure 3: *(a) The peak non-dimensional rim current plotted against the height $z^* = z/h$ for the two runs 44 (∇) and 48 ($\square$). Also shown is the line of best fit computed from the data within the mixed layer ($0 < z^* < 1$). (b) The instability wavelength plotted against the Rossby radius for runs 42 ($\diamond$), 44 (∇) and 48 ($\square$). Also shown are the data for runs 50 ($\bigcirc$), 51 ($+$) and 56 ($\triangle$) from Coates et al. (1994). The solid line $\lambda = 2.9L_R$ is the minimum instability wavelength from the analysis of Samelson (1993) while the dashed line is the estimated final value for the instability wavelength, given by $\lambda_f = 3.3L_R$.*

Thus the magnitude of the rim current is simply the local buoyancy velocity scale, and substituting for h from (3) yields

$$u \sim (Bt)^{1/2}. \tag{9}$$

A Gaussian curve was fitted to the azimuthal velocity components from runs 44 and 48, and the position and magnitude of the peak in the rim current were extracted (see Coates et al. 1994). These maximum velocity data, non-dimensionalized using (9), are plotted against the non-dimensional height $z^* = z/h$ in fig. 3a. The error bars for the peak velocities in fig. 3a were determined as the rms value of the deviation between the fitted Gaussian curve and the measured values. We did not attempt to compute rim velocities by the above procedures beyond about $t \approx 2.5T$ due to the distortion of the azimuthal swirl of the rim current caused by the growing long-wave instability for these runs. The standard deviation σ_W of the Gaussian fit also allows an estimation of the width of the rim current to be made. Defining the rim current width as $4\sigma_W$, the rim width is consistent with eq. (5) and is estimated to be $W \approx (1.7 \pm 0.7)L_R$.

As fig. 3a shows, the predicted magnitude of the rim current from equation (9) is in good agreement with the observations, especially considering that the velocity data are obtained over a wide range of depths h and times. If the radial density gradient in (6) is constant with height, then from (6) the rim current magnitude in fact varies linearly with height, as is the case shown in fig. 3a. The line of best fit to the data within the mixed layer ($0 < z^* < 1$) is in dimensional terms

$$u_{\text{peak}} = -0.85B^{1/2}t^{1/2}\left(\frac{z}{h} - \frac{1}{2}\right) \tag{10}$$

where h is given by equation (3).

The other feature clearly evident in fig. 3a is the apparent slow decay of the rim current velocity with height above the mixed layer, where the signature of the rim current can

in fact be detected up to $2h$ before it has decayed to zero. The momentum transport coefficient applicable above the mixed layer will not be simply the laminar viscosity, since firstly it is clear there are periodic incursions of mixed layer fluid above the mean height of the mixed layer and, secondly, there is very likely a radiation of inertial-gravity waves above the mixed layer into the overlying fluid which will effectively transport momentum into the stratified ambient at rates above molecular values.

The long wave instability can be readily identified as a growing along-front perturbation in the rim current. The scale of these instabilities was determined from the radial velocity components as, once the instability had reached a finite amplitude, the maximum excursion of the oscillation corresponded to the position where the radial velocity component went to zero. Measuring the distance between these zero crossings of the radial velocity data gave a measure of the wavelength of the instability. In each run the observed wavelength increases slowly with time, a result also observed by Narimousa and Maxworthy (1987) in a two layer model of the instability of upwelling fronts, and after about four periods the instability wavelength reached a maximum value. After this time, the excursions due to the instability became large enough to break off into independent eddies, and the general flow structure became very complex. The final value of the instability wavelength λ_f at long times for the experiments is (Coates et al. 1994)

$$\lambda_f = (3.3 \pm 0.6)L_R \tag{11}$$

where the Rossby radius L_R is defined in (5) and h is given by (3) evaluated at time $4\pi/f$ when the base geostrophic flow is established. This estimate of the final wavelength is shown on fig. 3b as the dashed line.

The stability analysis of Samelson (1993) predicts that the flow should be unstable to wavelengths $\lambda_f > 2.9L_R$, shown as the solid line in fig. 3b, with the fastest growing wavelength $\lambda_f = 5L_R$. The observed wavelengths are thus in the unstable range but are smaller than the wavelength of the fastest growing mode predicted by the linear instability theory. There are differences between the present configuration and the assumptions of linear stability theory. For example, linear stability theory assumes the initial disturbance is composed of a synthesis of waves each possessing the same initial (infinitesimal) amplitude and covering all possible wavenumbers. Conversely, the unsteady base flow in the experiments is perturbed by the small scale convective turbulence in the mixed layer which has a preferred length scale, the integral lengthscale of the 3D convective turbulence, and the amplitude of the perturbations is both finite and effectively distributed over a rather narrow band of wavelengths centred around this integral lengthscale.

In summary, while linear instability theory is not directly applicable, it is clear that theory and experiment are consistent in showing a similar dependence of the unstable wavelengths on the local Rossby radius. Considering the overall dynamics of deep convection, the most important point is that the rim current becomes unstable to baroclinic disturbances and this subsequently disrupts the convective deepening.

5. Discussion

Schott et al. (1993a) reported results from a current meter array moored in the central Greenland Sea in the winter of 1988/89. Vertical velocities of up to $3\,\mathrm{cms}^{-1}$ associated with plumes estimated to be of 350 m in horizontal extent and extending down to depths of 1400 m were reported during this deep convection event. The surface buoyancy flux B was estimated as $B = 6 \times 10^{-8}\,\mathrm{m^2 s^{-3}}$ and with $f = 1.4 \times 10^{-4}\mathrm{s}^{-1}$ equation (1) indicates the critical depth lies in the range $1.9\,\mathrm{km} < h_c < 6.2\,\mathrm{km}$. We conclude that the observations down to depths of 1400 m are thus not controlled by rotation and the observed vertical velocities are given by equation (2) yielding

$$w \approx 0.5(Bh)^{1/3} = 2.2\,\mathrm{cms}^{-1}, \quad l \approx 0.25h = 350\,\mathrm{m}$$

in agreement with the observations. Maximum rim current velocities after 5 days would be $7\,\mathrm{cms}^{-1}$ (from 10) at the top and bottom of the convecting region and, while the

event lasts longer, the current is likely to be baroclinically unstable after this time. As in the case of the laboratory experiments, the difficultly arises in choosing the appropriate vertical length scale to use in equation (3). Consistent with the methodology above, we estimate the appropriate mixed layer depth to be the sum of the initial depth of $350\,\mathrm{m}$ plus the deepening from equation (3) (using $N = 4.2 \times 10^{-4}\,\mathrm{s}^{-1}$ from Gascard 1991) after $t = 4\pi/f$, yielding a scale measured from the free surface of $h \approx 600\,\mathrm{m}$. The implied Rossby radius is $1.8\,\mathrm{km}$, and the predicted eddy scale is then $6\,\mathrm{km}$ (from 11), which seems plausible although no direct estimates were reported for comparison. Finally, it is important to note (e.g. Schott et al. 1993b) that the velocities in (2) are turbulent velocity scales and there is no mean vertical velocity associated with the deep convection.

References

COATES M. J., IVEY G. N. and TAYLOR J. R. 1994. Unsteady, turbulent convection into a rotating, stratified fluid: modelling deep convection. Submitted to *J. Phys. Oceanogr.*

FERNANDO H. J. S., CHEN R.-R., and BOYER D. L. 1991. Effects of rotation on convective turbulence. *J. Fluid Mech.* **228**. 513-547.

FLEURY M., MORY M., HOPFINGER E.J., and AUCHERE D. 1991. Effects of rotation on turbulent mixing across a density interface. *J. Fluid Mech.* **223**. 165-191.

GASCARD J.C. 1991. Open ocean convection and deep water formation revisited in the Mediterranean, Labrador, Greenland, and Weddel seas. In *Deep Convection and deep water formation in the oceans*. Edited by P. C. Chu and J. C. Gascard. Published by Elsevier. 157-182.

HOPFINGER E.J., GRIFFITHS R.W., and MORY M. 1983. The structure of turbulence in homogeneous and stratified rotating fluids. *J. Méch. Theoriq. Appl (Special Issue).* **44**. 21-82.

IVEY G. N., TAYLOR J. R., and COATES M. J. 1993. Convectively driven mixed layer growth in a rotating, stratified fluid. Submitted to *Deep Sea Res.*

JONES H. and MARSHALL J. 1993. Convection with rotation in a natural ocean: a study of open-ocean convection. *J. Phys. Oceanogr.* **23**. 1009-1039.

KILLWORTH P. D. 1983. Deep convection in the world ocean. *Rev. Geophys. Space Phys.* **21**. 1-26.

MAIER-REIMER E., MIKOLAJEWICZ U., and HASSELMANN K. 1991. Mean circulation of the Hamburg LSG OGCM and its sensitivity to the thermohaline surface forcing. *J. Phys. Oceanogr.* **23**. 731-757.

MAXWORTHY T. and NARIMOUSA S. 1994. Unsteady turbulent convection into a homogeneous, rotating fluid, with oceanographic applications. In press *J. Phys. Oceanogr.*

NARIMOUSA S. and MAXWORTHY T. 1987. Coastal upwelling on a sloping bottom: the formation of plumes, jets and pinched-off cyclones. *J. Fluid Mech.* **176**. 169-190.

SAMELSON R. M. 1993. Linear instability of a mixed-layer front. *J. Geophys. Res.* **98**. 10195-10204.

SCHOTT F. A. and LEAMANN K. D. 1991 Observations with moored acoustic doppler current profilers in the convection regime in the Golfe du Lion. *J. Phys. Oceanogr.* **21**. 558-574.

SCHOTT F. A., VISBECK M. and FISCHER J. 1993a. Observations of vertical currents and convection in the central Greenland sea during the winter of 1988/89. *J. Geophys. Res.* **98**. 14,401-14,422.

SCHOTT F. A., VISBECK M. and SEND U. 1993b. Open ocean deep convection, Mediterranean and Greenland Seas. To appear in *Ocean Processes on Climate Dynamics.* Kluwer.

STEVENS C. L. and COATES M. J. 1994. A maximized cross correlation technique for resolving velocity fields in laboratory experiments. In press *IAHR J. of Hydraulic Res.*

TURNER J. S. 1973. *Buoyancy effects in fluids.* Cambridge.

Penetrative convection in rapidly rotating flows
Sonya Legg*+ and Jim McWilliams+
+ National Center for Atmospheric Research,
Boulder, CO 80307, USA
* Joint Institute for Laboratory Astrophysics,
University of Colorado, Boulder, CO 80309, USA

1 Introduction

1.1 Penetrative convection

When a convective mixed layer forced by a surface buoyancy flux is bounded by a stably stratified region, convective elements may overshoot the level of neutral stability and penetrate into the region of stable stratification. The region into which this overshoot occurs, the penetration zone or entrainment layer, is characterised by a reverse buoyancy flux. In the atmospheric planetary boundary layer it is known that the ratio between the negative buoyancy flux and the surface buoyancy flux is typically -0.2 (Deardorff et al (69)). Penetrative convection typically results in a steepening of the density gradient the penetration zone, resulting in a strong pycnocline bounding the mixed layer. In parameterising convective mixing in both the atmosphere and the ocean, it is important to correctly represent the penetration zone, since it is through this region that properties are communicated between the surface mixed layer and the stably stratified region.

1.2 Influence of rotation on convection

If we define the convective Rossby number as the ratio of advective to inertial timescales: $Ro = w^*/(fh)$ where w^* is the convective velocity scale, h is the mixed layer depth, and f is the coriolis parameter, and $w^* \sim (Bh)^{(1/3)}$ where B is the surface buoyancy flux, we would expect rotation to strongly influence the convection when $Ro < 1$ (Fernando et al (91)). In the ocean the surface buoyancy flux is usually significantly less than that in the atmosphere, so that unlike atmospheric convection, ocean convection may be significantly influenced by rotation. Numerous studies of non-rotating penetrative convection have been made, but penetrative deepening of the mixed layer in the presence of rotation has received little attention, although there have been some recent studies of the entrainment of a mechanically forced turbulent mixed layer with strong rotation (Fleury et al (91)). Hence the following simulations will examine penetrative convection in the small Rossby number limit.

1.3 Experimental design

We present results of several simulations of convection into an initially uniformly stably stratified fluid. The simulations are distinguished by varying rotation. Our model does not include the effects of salinity, and density is linearly proportional to temperature. The flux Rayleigh number applied at the upper surface is held constant at $Ra_f = 1.4 \times 10^8$ and is defined by

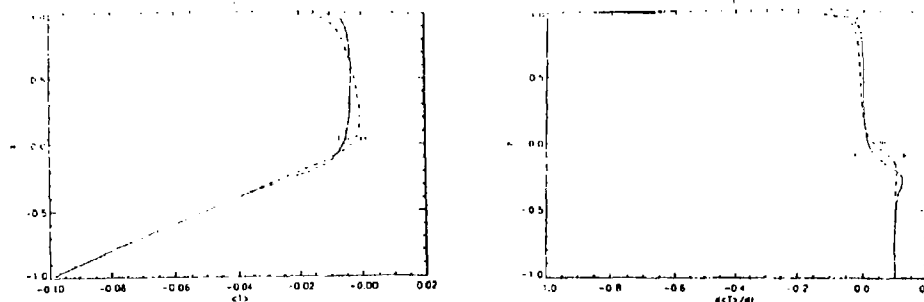$$Ra_f = \frac{g\alpha L^4}{\nu\kappa}\left(-\frac{\partial T}{\partial z}\right)$$

(1)

Figure 1: *(a) Horizontally averaged temperature $< T >$ (b) Horizontally averaged temperature gradient $d < T > /dz$, at $t = 0.05$. (i) No rotation, (ii) $f = 2500.0$, (iii) $f = 8000.0$ (non-dimensionalised). $Ra_f = 1.4 \times 10^8$ and initial stratification $(\partial T/\partial z)_0 = 0.1$.*

where g is the gravitational acceleration, α is the coefficient of thermal expansion, L is the length scale, ν is the viscosity, κ is the thermal diffusion and $\partial T/\partial z$ is the temperature gradient at the upper surface. The initial stratification, non-dimensionalised by the magnitude of the temperature gradient at the upper surface, is $(dT/dz)_0 = 0.1$, for all the simulations. The integration domain is a cuboid volume of aspect ratio 4x4x1, spanning a depth of $z = -1.0$, to $z = 1.0$ non-dimensional length scales, and integrations are carried out at a resolution of 128x128x65. Boundary conditions are stress-free at upper and lower surfaces and periodic at side walls, while flux boundary conditions are applied for temperature at the top and bottom ($(dT/dz)_{z=-1.0} = (dT/dz)_0$ and $(dT/dz)_{z=1.0} = -1.0$) (non-dimensionalised). Results of these simulations are examined after initial transients associated with the onset of convection have decayed away, and the mixed layer is deepening steadily.

2 Influence of rotation on statistics

2.1 Mean temperature profile

Figure 1 shows the instantaneous vertical profiles of (a) the horizontally averaged temperature and (b) its gradient, for the three simulations carried out at varying rotation. The control run, having no rotation, demonstrates many of the well-known features of penetrative convection. A negative temperature gradient is confined to a small boundary layer near the upper surface, while the mixed layer has a uniform temperature. Below the mixed layer is a region of enhanced temperature gradient. The two runs with strong rotation show significant differences from this control simulation. As the Coriolis parameter increases, an increasingly large negative temperature gradient is maintained in the convectively mixed layer. A similar negative temperature gradient has been observed in simulations of Rayleigh-Benard convection (Julien et al (94)) and laboratory experiments (Boubnov and Golitsyn (91)). Strong lateral mixing generated by the cyclonic vortices associated with convective plumes in rotating convection appears to inhibit the vertical mixing process. The enhancement of the stable stratification in the penetration zone observed in the non-rotating case is considerably reduced for strong rotation.
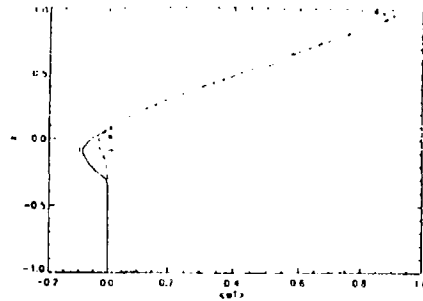
2

Figure 2: *Horizontally averaged convective buoyancy flux $< w'T' >$, at $t = 0.05$. (i) no rotation, (ii) $f = 2500.0$, (iii) $f = 8000.0$. Parameters as in figure 1.*

2.2 Negative buoyancy flux in penetration zone

Figure 2 shows the instantaneous buoyancy flux as a function of height for all three simulations. The positive buoyancy flux associated with the convectively mixed region is slightly reduced as rotation is increased, as is the depth at which this buoyancy flux tends to zero. However, much more significant changes are observed in the penetration zone, where significantly less negative buoyancy flux is observed for strong rotation. The width of the region of negative buoyancy flux is also considerably reduced at high rotation. The two rotating cases do not show much difference between them. It is to be noted that the magnitude of negative buoyancy flux in the non-rotating case is only about 50% of that observed in atmospheric convection, an indication that the Peclet number of these experiments is relatively low, where $Pe = w^*h/\kappa$. The relatively low resolution of these simulations means that κ is large. Higher Peclet numbers will require higher resolution simulations and are the focus of current work by the authors.

3 Time-dependance of mixed layer parameters.

3.1 Temperature gradient in the mixed layer

Figure (3) shows the temperature gradient in the center of the mixed layer as a function of time. For the non-rotating case, as an efficient turbulent convection is established, this temperature gradient quickly equilibrates near zero. Both the rotating cases are significantly non-zero, with the magnitude decreasing as mixed layer depth increases with time.

3.2 Vertical velocity scale

Figure (4) shows the maximum value of rms vertical velocity as a function of time, indicating that rotation significantly reduces the vertical velocity. The rotating cases show significantly smaller fluctuations than the non-rotating case, probably due to the greater number of plumes contained within the volume, over which the horizontal average is taken. In addition, the slope of the curve appears to be different for the two rotating experiments
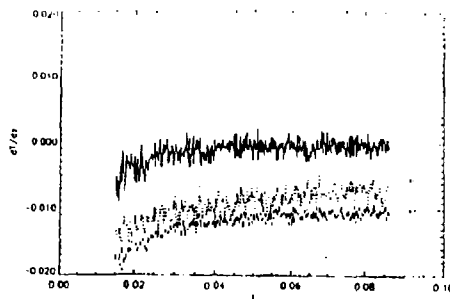
3

Figure 3: *Horizontally averaged temperature gradient in the centre of the mixed layer, as a function of time. (i) No rotation, (ii) f= 2500.0, (iii) f=8000.0. Parameters as in figure 1.*
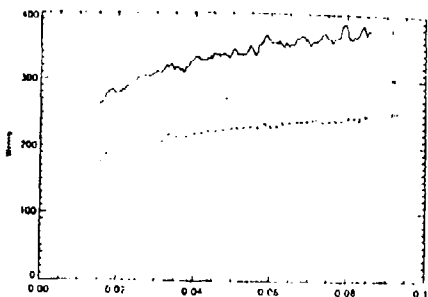

Figure 4: *Maximum value of rms vertical velocity as a function of time. (i) No rotation, (ii) f= 2500.0, (iii) f=8000.0. Parameters as in figure 1.*

as compared with the nonrotating experiment.

3.3 Mixed layer and penetration layer depths

We may define the mixed layer as either the depth at which the temperature gradient tends to a moderately stable value (one tenth of the initial stratification was chosen) or as the depth at which the convective buoyancy flux first passes through zero. Measurements of the mixed layer depth defined by both the above criteria are shown in figures (5a) and (5b) respectively. Also shown is the mixed layer depth calculated by assuming non-penetrative convection, in which $h = \sqrt{(2t(dT/dz)_{z=1.0}/(dT/dz)_0}$ (after non-dimensionalisation). We see that the depth at which the buoyancy flux passes through zero shows little variation with f, while the mixed layer depth predicted from the temperature gradient is slightly deeper for the non-rotating case. All are less than the non-penetrative prediction, but of similar tendency with time. The maximum depth of the penetration zone, defined either by the depth at which the temperature gradient tends to the background value (figure (6a)), or the depth at which the buoyancy flux and its gradient tend to zero (figure (6b)), is significantly less for the two rotating cases than for the non-rotating calculation. Hence
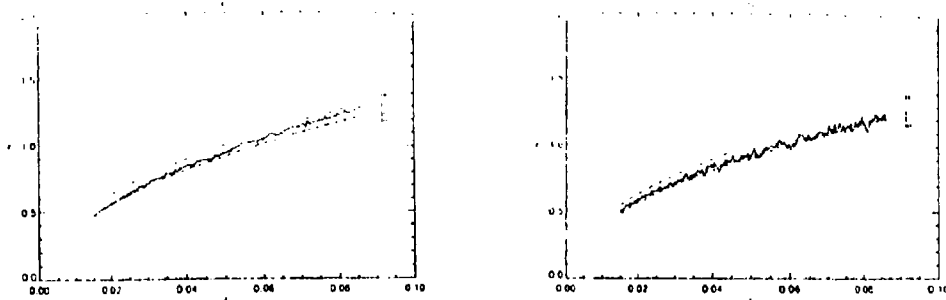
Figure 5: *The mixed layer depth as a function of time. (a) The depth at which the temperature gradient tends to 0.1 of its initial value. (b) The depth at which the convective buoyancy flux $< w'T' >$ passes through zero. (i) No rotation, (ii) $f= 2500.0$, (iii) $f=8000.0$, (iv) non-penetrative prediction. Parameters as in figure 1.*
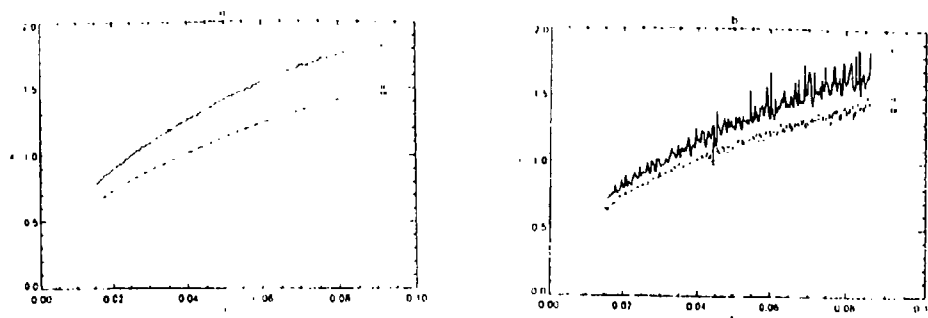

Figure 6: *The maximum depth of the penetration zone, as a function of time. (a) The depth at which the temperature gradient is within 10% of the initial value. (b) The depth at which the buoyancy flux is less than 10% of its maximum negative amplitude. (i) No rotation, (ii) $f= 2500.0$, (iii) $f=8000.0$. Parameters as in figure 1.*

the width of the penetration zone, defined by the difference between the maximum depth of penetration and the mixed layer depth is significantly reduced at strong rotation.

4 Discussion

The principle differences introduced by rotation in penetrative convection appear to be a reduction in the magnitude of the negative buoyancy flux and in the width of the penetration zone, a reduction in the velocity scale, and a significant negative temperature gradient in the mixed layer. All imply a less efficient transport of properties in the vertical. The reduction in the magnitude of the vertical velocity is reminiscent of experiments on unsteady convection into an intially homogenous fluid performed by Jones and Marshall (93). They suggest that the velocity scale for rotating convection is reduced compared to non-rotating convection because the horizontal expansion of the convecting cells as they

deepen is suppressed in accordance with the Taylor-Proudman theorem. It is possible that the reduction of the magnitude of the negative buoyancy flux is due to the lower Peclet numbers in the rotating cases, caused by the lower vertical velocities. However, the magnitude of the negative buoyancy flux is reduced by a much greater proportion than the vertical velocity scale. It is also possible that reductions in the horizontal scales of the convecting elements by rotation (as observed by Jones and Marshall (93) and Julien et al (94) for example) reduce the penetration depth of the elements, if the depth to which the plumes penetrate is a function of the length scale of the vortical circulation associated with the plume (eg Breidenthal (92)). The reduction in the efficiency of vertical transport of properties indicated by the temperature gradient would also imply less efficient vertical transport into the stably stratified region, and hence, reduced penetration. While further analysis and simulations will be necessary to resolve these questions, these preliminary experiments make it clear that rotation can significantly alter the mean properties of the convective mixed layer, and its effects should therefore be considered in ocean mixed layer models.

References.

Boubnov B.M., and G.S. Golitsyn, 1990 Temperature and velocity field regimes of convective motions in a rotating plane fluid layer. *J. Fluid Mech.*, **219**, 215-239.

Breidenthal, R.E., 1992 Entrainment at thin stratified interfaces: The efferts of Schmidt, Richardson and Reynolds numbers. *Phys. Fluids A*, **4**, 2141-2144.

Deardorff, J.W., G.E. Willis, and D.K. Lilly, 1969 Laboratory investigation of nonsteady penetrative convection. *J. Fluid Mech.*, **35**, 7-31.

Fernando, H.J.S, R-R Chen and D.L. Boyer, 1991 Effects of rotation on convective turbulence. *J. Fluid Mech.*, **228**, 513-547.

Fleury, M., M. Mory, E.J. Hopfinger and D. Auchrre, 1991 Effects of rotation on turbulent mixing across a density interface. *J. Fluid Mech.*, **223** 165-191.

Jones, H. and Marshall, J.M., 1993 Convection in a neutral ocean; a study of open-ocean deep convection. *J. Phys. Oceanogr.*, **23**, 1009-1039.

Julien K., S. Legg, J. McWilliams, and J. Werne, 1994 A statistical analysis of the influence of rotation in turbulent Rayleigh-Benard convection. In preparation.

The Interaction of Convection and Internal Waves

N. KALE AND L. G. REDEKOPP
Departments of Aerospace and Mechanical Engineering
University of Southern California
Los Angeles, California 90089-1191

Abstract

The instability and weakly nonlinear dynamics of convective motion in a horizontal layer heated from below is studied when the upper boundary is deformable and supportive of internal gravity waves. The linear stability is defined and weakly nonlinear evolution systems for specific modes are obtained. It is found that a strong coupling between a long gravity wave and convective motions exists leading to episodic mixing events.

1 Introduction

The phenomenon of thermal convection occurring in a horizontal layer heated from below has been studied extensively, both because of its relevance in physical contexts and its utility as a model for pattern-forming instabilities and transition to turbulence. In the present study the coupling between convection occurring as a result of thermal instability and wave motion in a contiguous layer is considered. This is motivated by the role of convective transport in mixing processes in the upper ocean or in the troposphere. In either case, the convective dynamics occurs in a layer adjoining a stably stratified medium. As a consequence, convective motions may "resonate" with internal waves leading to enhanced transport and even wave breaking. On the other hand, the action of waves in a region next to a convective layer may modulate the local Rayleigh number and, thereby, effectively inhibit convective activity, at least when the modulation time scale is sufficiently short. It appears, therefore, that off-setting effects exist and the nonlinear coupling between convection and internal waves can lead to some non-trivial dynamics which may have important practical implications. It is the understanding of these dynamics that is addressed here.

2 Problem Definition

In the present discussion we seek to clarify the basic features of the interaction of convection and internal waves and to assess the significance of the interaction in practical contexts. For this purpose, the prototypical model shown in Figure 1 containing the minimum structure is employed. It consists of a convecting mixed layer bounded from below by a non-deformable, stress-free, plane isothermal surface which is heated. Above the convecting layer is an unbounded domain of homogeneous fluid. The ambient medium is immiscible and separated from the convecting layer by a deformable interface across which a stable density change

$\delta\rho$ exists. To simplify the analysis, we invoke the Boussinesq approximation and, for consistency, assume the density anomaly $\delta\rho$ across the interfacial thermocline is small. An important dimensionless parameter δ, the ratio of the density anomaly to the magnitude of the (unstable) density change across the convecting layer, emerges which measures the deformability of the free interface. When δ is order one, the time-scale for convective motions is commensurate with the period of long gravity waves and a dynamical coupling is possible. When δ becomes large, the time scales are disparate and the deformability of the interface becomes negligible. This is the case, for example, at the air-water interface at the ocean surface. The formulation of this problem with specification of the interface matching conditions is provided by Pavithran & Redekopp [1994].

To isolate the essential aspects of the problem we focus on the special case where the ambient fluid contiguous with the convecting layer is perfect (i.e., inviscid and non-conducting). In this limit the ambient fluid is "passive", but the capacity to support an internal wave at the deformable interface exists. The parameter δ defined above then enters via the normal stress condition which, for motion in the (x, z) plane with respective velocity components (u, w), can be expressed as

$$\text{Ra}\zeta\left(\delta + \frac{1}{2}\zeta\right) + p + \frac{2}{1+\zeta_x^2}\{w_z - \zeta_x(u_z + w_x) + \zeta_x^2 u_x\} = 0, \tag{1}$$

where subscripts denote partial derivative with respect to the indicated variable. In writing this expression, where the Rayleigh number Ra appears in addition to δ, we have used dimensionless variables based on a length scale equal to the layer depth d and a time scale equal to the vertical diffusion time d^2/κ. The temperature anomaly θ is scaled by $\frac{\nu\kappa}{\alpha g d^3}$, where α is the coefficient of thermal expansion, and the perturbation pressure p is scaled by $\frac{\rho_1\nu\kappa}{d^2}$, where ρ_1 is a reference density equal to the static value at the lower, isothermal boundary. The x coordinate is in the plane of the lower, non-deformable boundary and z points upward from this boundary. The condition (1) is applied at the disturbed interface position $z = 1 + \zeta(x, t)$. A mixed thermal boundary condition is specified at the interface which allows for an interfacial (convective or radiative) heat flux so that an equilibrium, hydrostatic state attained by heating from below is possible. The thermal condition which is also applied at the deformable interface located at $z = 1 + \zeta(x, t)$, is given by

$$\theta_z - \zeta_x\theta_x = -\text{B}(\theta - \text{Ra}\zeta)\sqrt{1 + \zeta_x^2} - \text{Ra}\left(\sqrt{1 + \zeta_x^2} - 1\right). \tag{2}$$

The dimensionless parameter B appearing in this relation is the Biot number based on the heat transfer coefficient at the free interface. The left hand side is the conductive heat flux in the convecting layer evaluated at the position of the deformed interface. The right hand side gives the (convective or radiative) heat flux from the interface from above minus the equilibrium flux evaluated at the location of the deformed interface. As the Biot number becomes large, corresponding to very efficient heat transfer from the interface, the condition for an isothermal surface is approached. As the Biot number tends to vanish, the condition of an insulated boundary is approached. The use of the Biot number in this single-layer model is helpful for distinguishing the different modes of convective instability and clarifying

2

different limits. The remaining boundary conditions at the interface $z = 1 + \zeta(x,t)$ are the kinematic condition

$$w = \zeta_t + u\zeta_x,$$ (3)

and the vanishing of the tangential stress

$$\frac{1}{2}(1 - \zeta_x^2)(w_x + u_z) + \zeta_x(w_z - u_x) = 0.$$ (4)

The conditions at the lower non-deformable boundary correspond to those for an impermeable, stress-free, isothermal surface.

3 Summary of Linear Stability Results

The linearized problem for the convection model defined above admits two modes of instability for order-one values of δ and B. There is a short-wave mode which exhibits a stationary bifurcation at onset. There is also a long-wave mode with an oscillatory instability. The co-existence of these two modes was found by Benguria & Depassier [1987] who considered the linear problem of convection in a horizontal layer with an order one density change across the free surface. The critical Rayleigh numbers for these modes also vary with δ and B, and conditions exist where the short-wave mode can dominate over the long-wave mode and vice-versa. For example, the critical Rayleigh number for the long-wave mode is given by

$$Ra_c = 180\frac{(B + 1)^2}{B + 6}.$$ (5)

One observes that the critical Rayleigh number for this mode is independent of the interface parameter δ and approaches a value of $Ra_c = 30$ when the interface is an insulated boundary (i.e., $B = 0$). As the Biot number becomes large and the interface approaches an isothermal boundary, the critical Rayleigh number for this mode tends to infinity and the role of this oscillatory, long-wave mode of convection vanishes. At intermediate values of the Biot number a mode competition can occur.

On the other hand, the critical condition for the stationary short-wave mode depends strongly on δ. For asymptotically large values of δ and $B \to \infty$, the critical Rayleigh number approaches the well-known value $27\pi^4/4$ for convection between non-deformable, isothermal, stress-free boundaries computed first by Rayleigh (cf., Chandrasekhar [1961]). Pavithran & Redekopp [1994] derived the asymptotic results for convection with these boundary conditions

$$k_c \sim \frac{\sqrt{2}\pi}{2} - \frac{4\sqrt{2}}{9\pi 8} + O\left(\frac{1}{\delta}\right)^2,$$ (6a)

$$Ra_c \sim \frac{27\pi^4}{4} - \frac{10\pi^2}{8} + O\left(\frac{1}{\delta}\right)^2.$$ (6b)

As δ decreases, the critical condition for this mode moves to lower Rayleigh numbers and lower wave numbers. This is indicated by the bold arrow in Figure 2. The variation of the

3

critical Rayleigh number Ra_c and associated wave number k_c for the special case $B \to \infty$ is shown in Figure 3. One observes from this figure that the critical condition for this mode moves to the origin of the Ra-k plane at a finite, critical value of $\delta = \delta_c$. The critical value of δ for arbitrary Biot number is given by

$$\delta_c = \frac{B}{3(B+1)}. \tag{7}$$

With isothermal boundary conditions (i.e., $B \to \infty$), $\delta_c = 1/3$, the value indicated by the numerical results shown in Figure 3. For small values of B, the critical value approaches $\delta_c = B/3$.

4 Nonlinear Evolution Equations

Application of a consistent asymptotic approximation for the dynamics in the vicinity of the critical Rayleigh number for the onset of convective motion via a stationary bifurcation at finite wave number, assuming the Biot number is large so the long-wave mode is damped, leads to the scaled evolution system

$$A_t = -ik_c U A + \mu A - \gamma H A + A_{xx} - |A|^2 A, \tag{8}$$

$$H_t = -U_x + \alpha H_{xx} - \nu(|A|^2)_{xx}, \tag{9}$$

$$U_t = -\beta H_x + \sigma(|A|^2)_x + \lambda U_{xx}. \tag{10}$$

In this system $A(x,t)$ is the modulation amplitude of, say, the vertical velocity of local, convective motions with spatial periodicity $2\pi/k_c$. $H(x,t)$ is the slowly-varying or long-wave component of the interface deformation which has a corresponding, horizontal drift velocity $U(x,t)$. The first equation is consistent with that obtained by Newell & Whitehead [1969] in the case where $U = H = 0$. The Doppler-shift effect, under the condition $H = 0$ so that both boundaries are non-deformable, was shown by Zippelius & Siggia [1983] and by Coullet & Huerre [1986] to have an important dynamical role in the case of convective patterns. They demonstrated that the marginal, vertical-vorticity mode in cases with stress-free boundaries couples effectively via the Doppler term in the first equation. In the present case, a strong dynamical coupling occurs even for convection in the plane where the vertical vorticity mode is not active. When convection is absent (i.e., $A = 0$), the last two equations describe the linear, non-dispersive propagation of an interfacial gravity wave which is damped. The degree of freedom associated with the height field (or compressional mode) gives rise to a non-trivial coupling between convection and waves even for motion in a plane.

The system (8–10) describes convective rolls coupled with waves whose wave number is oriented in the same direction as that for the rolls. Strictly speaking, the vertical asymmetry of the present model implies that the planform of convective motion near onset is hexagonal (see, for example, Schluter, Lortz & Busse [1965]). However, at higher values of the supercriticality measured by the growth-rate parameter μ, rolls can become the stable configuration of convection. This has been confirmed in this case by Pavithran & Redekopp [1994]. Hence, it is believed that the above system has general validity. This can, in fact,

4

be established by appealing directly to the invariance properties of the underlying equations for the problem. The principal features of the coupling described by the above system are the generation of a drift current (for $\sigma \neq 0$) by spatial inhomogeneities in the amplitude of convection, the Doppler shift effect of the drift current on the phase of the roll amplitude $A(x,t)$, and the modulation of the linear growth rate (for $\gamma \neq 0$) through the variablity of the convective layer thickness associated with the concomitant wave field. Self-nonlinear and dispersive effects of the long-wave drift field would enter the latter two equations at higher approximations in the asymptotic sequence. Preliminary numerical simulations of the system (8–10) reveal that the convective activity can be · uite episodic. As convection ensues at super-critical conditions, energy is transferred to long waves which both modulate the local Rayleigh number and radiate away. As a consequence, the convection amplitude declines until a quasi-steady, super-critical state is re-established and a new burst of convection occurs. The nonlinear dynamics of this process, as well as the efficiency of internal wave generation, are under study.

A phase dynamics study of spatially-periodic, finite-amplitude roll solutions of (8) for $U = H = 0$ has been performed (cf., Redekopp [1994]) for the evolution system (8–10). The phase dynamics is third-order in time for the general system. The linear equation for the phase $\phi(x,t)$ in the long-wave limit is

$$\phi_{ttt} = a\phi_{xxt} + b\phi_{xxtt} + c\phi_{xxxx}. \tag{11}$$

The third-order dynamics arises through the simultaneous breaking of the Galilean invariance and the release of the large-scale compressional mode. When the parameters $\beta = \gamma = \sigma = 0$ in (8–10), both of these broken invariances are suppressed and $a = c = 0$ in (11). In this case (11) reduces to the diffusive phase equation familiar to the Eckhaus criterion (cf., Pomeau & Manneville [1979]). When $\beta = \gamma = 0$ in (8–10), the compressional mode is suppressed, but the Galilean invariance is preserved. In this case $b = c = 0$ in (11) and one obtains a propagative phase dynamics discussed by Coullet & Fauve [1985] and by Coullet & Huerre [1986] in the case of convection between non-deformable, stress-free boundaries at low Prandtl numbers.

Over a range of the parameters B and δ the onset of convection occurs through an oscillatory, long-wave mode. Considering only the nonlinear evolution of this mode, and after some scaling to balance the leading-order nonlinear and dispersive effects, one obtains a perturbed Korteweg-deVries equation which can be expressed as

$$h_\tau + nhh_\xi + mh_{\xi\xi\xi} = -g(\Delta h_{\xi\xi} - h_{\xi\xi\xi\xi}). \tag{12}$$

The parameter Δ measures the criticality of the mode (i.e., $\Delta > 0$ for Ra > Ra$_c$). In this case one can find equilibrium, propagating states which are driven by the release of potential energy through convection and damped by the dissipative processes. This equation is applicable when $\delta > \delta_c$ defined by (7) and is written in a coordinate system (ξ, τ) which is moving along a characteristic of the linear, non-dispersive system. This analysis reveals that propagating cells of convective motion are possible which are associated with finite-amplitude displacements of the interface.

5

Another long-wave limit exists for $\delta \simeq \delta_c$. In this case the critical condition for the short-wave mode approaches $k = 0$ and has a critical Rayleigh number below the minimum value for the long-wave mode. The dynamical evolution under these conditions can also be defined. It is described by a "damped" Boussinesq equation

$$h_{TT} - Sh_{XX} - \Gamma_1(h^2)_{XX} - \Gamma_2 h_{XXXX} = -\Delta_1 h_{XXT}. \tag{13}$$

We have not examined this limit in much detail as yet. However, based on earlier work on the Boussinesq equation by Hickernell [1983ab], who showed that a class of solutions exists which become singular in finite time, there may be conditions where the coupling between convection and waves can become quite violent.

Acknowledgment

References

Benguria, R. D. & Depassier, M. C. 1987. Oscillatory instabilities in the Rayleigh-Benard problem with a free surface. *Phys. Fluids*, **30**, 1678-1682.

Chandrasekhar, S. 1961 *Hydrodynamic and Hydromagnetic Stability*. Oxford University Press.

Coullet, P. & Fauve, S. 1985. Propagative phase dynamics for systems with Galilean invariance. *Phys. Rev. Lett.*, **55**, 2857-2859.

Coullet, P. & Huerre, P. 1986. Resonance and phase solitons in spatially-forced thermal convection. *Physica D*, **23**, 27-44.

Hickernell, F. J. 1983a. The evolution of large horizontal-scale disturbances in marginally stable, inviscid, shear flows. I. Derivation of the amplitude evolution equations. *Stud. Appl. Math.*, **69**, 1-21.

Hickernell, F. J. 1983a. The evolution of large horizontal-scale disturbances in marginally stable, inviscid, shear flows. II. Solutions of the Boussinesq equation. *Stud. Appl. Math.*, **69**, 23-49.

Newell, A. C. & Whitehead, J. A. 1969. Finite bandwidth, finite amplitude convection. *J. Fluid Mech.*, **38**, 279-303.

Pavithran, S. & Redekopp, L. G. 1994 The coupling of gravity waves and convection: amplitude equations and planform selection. *Stud. Appl. Math.*, accepted for publication.

Redekopp, L. G. 1994. Phase dynamics for the coupling of convection and waves—a natural co-dimension-three problem. (submitted for publication).

Schluter, D. A., Lortz, D. & Busse, F. H. 1965. On the stability of steady finite amplitude convection. *J. Fluid Mech.*, **23**, 129-144.

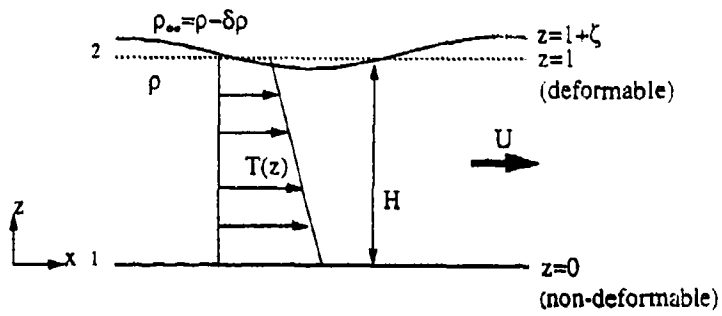Zippelius, A. & Siggia, E. D. 1983. Stability of finite amplitude convection. *Phys. Fluids*, **26**, 2905-2915.

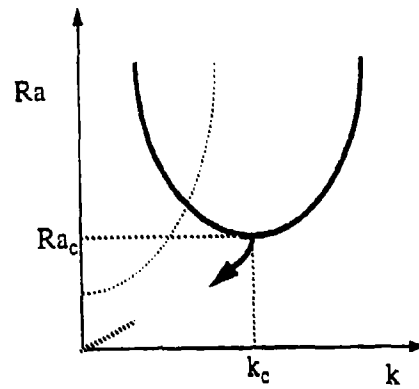Figure 1. Geometrical configuration of convection model

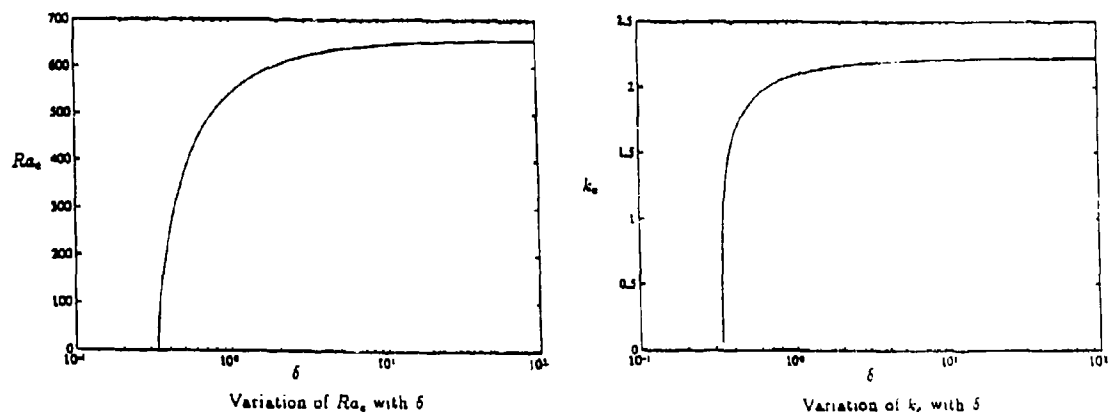Figure 2. Neutral curves for oscillatory and stationary modes.

Variation of Ra_c with δ

Variation of k_c with δ

Figure 3.

On the nature of multicell flow regimes observed in confined thermosolutal convection with lateral heating

N. Tsitverblit

Faculty of Engineering. Tel-Aviv University. Ramat-Aviv, Israel

March 23, 1994

Abstract

As has recently been uncovered by Tsitverblit & Kit (1993), the laterally heated thermosolutal systems are characterized by a great variety of the multiple steady flows. In this paper, the attention is focused on the the structure of steady solutions at a value of Ra_S larger than that broached in the above work. This structure is characterized by a number of additional limit points and symmetry-breaking bifurcation points, and apart from one-, two-, three-, and four-cell flows incident to the smaller Ra_S, five-cell symmetric and asymmetric flow patterns are also observed. Qualitative characteristics and stability of the multiple steady solutions are discussed from the standpoint of their possible relevance to the nature of the flow patterns observed in previous studies, performed at the very large Ra_S.

1   Introduction

Since the classical works by Thorpe, Hutt & Soulsby (1969) and Hart (1971). where the double-diffusive instability was established as the key mechanism causing the emergence of convective layers in an infinite laterally heated slot containing stably stratified brine, the behavior of the layers has been extensively studied in application to finite enclosures (see Chen. Briggs, and Wirtz 1971. Lee. Hyun & Kang 1990. Lee & Hyun 1991. and the references therein). Both the temporal evolution of the system of convective layers and the developed states were found to depend essentially on the ratio between the solute concentration and temperature gradients (the buoyancy ratio). In particular, when the value of this parameter was varied, the convective layers were found to form either successively from top and bottom of an enclosure towards its center or simultaneously throughout the entire cavity. flows possessing different numbers of cells with and without regions of almost motionless fluid between them were found. symmetric and asymmetric transient and steady, or quasi steady, flow patterns were observed.

Recently, Tsitverblit & Kit (1993) (subsequently TK) have emphasized the role of steady bifurcation phenomena in the formation of the convective layers. The multiplicity of the steady flows was then demonstrated by Tsitverblit (1994) (subsequently T) to derive from non-degenerate hysteresis points and isolas of asymmetric solutions. arising as the salinity Rayleigh number is increased from its critical value designating the commencement of the double-diffusive region (Hart 1971). Based on the results of TK and T, one can claim that the bifurcation phenomena at the large values of Ra_S, relevant to most previous studies. is expected to be so increasingly complex that the computational costs

1

needed for its exploration would probably be prohibitive. In view of this, the purpose of the present work has been to examine the types of steady flows and their stability at as large Ra_S as is allowed by reasonable computational costs. Such data would enable one to establish regularities in the traits of the steady solutions that could give an insight into the nature of various flow regimes observed in the previous studies, performed at the very large Ra_S.

2 Formulation of the problem

The problem considered is essentially the same as that described in TK. In particular, the aspect ratio $\gamma = H/d$ (H is the height of an enclosure, d its width) was set to $\gamma = 3$. The salt concentration Rayleigh number, however, was specified to be larger than that used in TK, $Ra_S = g\beta d^4(\frac{\partial c_0}{\partial z})/k_S\nu = 60000$ (in TK, $Ra_S = 30000$ was considered); g being the gravitational acceleration, β the coefficient of solutal expansion, $(\frac{\partial c_0}{\partial z})$ the imposed solute concentration gradient, k_S the diffusivity of salt, ν the kinematic viscosity. The Prandtl number $Pr = \nu/k_T = 6.7$; the Schmidt number $Sch = \nu/k_S = 677$. Here, k_T is the diffusivity of heat. The Boussinesq approximation of the steady two-dimensional Navier-Stokes equation in the conventional vorticity-stream function formulation, together with the energy and salinity diffusion equations have been discretized by central finite differences to obtain a finite-dimensional system of equations. The boundary conditions incorporated into these equations were as follows. The horizontal walls were assumed to have constant concentrations of salt and to be adiabatic. At the vertical walls, a temperature difference was specified at each step, and these boundaries were taken to be insulating to salt. All the walls were assumed no-slip.

The Euler-Newton continuation method was applied to trace out the solution of the finite-dimensional system of equations as thermal Rayleigh number $Ra_T = g\alpha\Delta T d^3/k_T\nu$ is varied. Here, α is the coefficient of thermal expansion, ΔT is the temperature difference between the vertical walls. During this procedure, the presence of limit points was detected by noticing the failure of convergence of the Newton method. Limit points were rounded using the Keller (1977) arclength continuation algorithm. Asymmetric solutions were reached as follows. First, a small asymmetry was introduced into the governing equations in the vicinity of a Jacobian sign alteration observed during continuation of the corresponding symmetric branch. Thereby, the unfolding of the symmetry-breaking bifurcation point associated with this sign change was achieved. Then, the solution of the asymmetric equations, continued through the unfolded bifurcation point away from it, was used as the initial approximation for the Newton-method iterations to arrive at the nearby asymmetric solution of the symmetric problem. Once such a solution was reached, it was continued away from the bifurcation point by the above continuation methods.

3 Results

The results of T are indicative of the presence of three qualitatively different scenarios of promotion of the solution multiplicity when the salinity Rayleigh number is increased. The first two of them are associated with the bending of a single branch and emergence either of a pair of limit points, via the formation of the corresponding non-degenerate hysteresis point (this mechanism is illustrated in fig. 1 a), or a single limit point on an asymmetric branch, changing the criticality of one of the associated bifurcation points in the quartic symmetry-breaking bifurcation (fig. 1 b). The third one is essentially due to the formation of the isolas of asymmetric solutions at the symmetric branches, from each of which, a pair of symmetry-breaking bifurcations is born (this is illustrated in fig. 1 c). Due to the action of these mechanisms, the structure of steady solutions eventually becomes extremely complex. In particular, the bifurcation diagram for $Ra_S = 60000$, computed in this work, is represented in fig. 2. For comparison, the full version of the

bifurcation diagram at $Ra_S = 30000$ (fig. 3) is also presented, part of which was already discussed in TK. Here, $\phi(x)$ stands for a functional capturing the variation of a measure of the symmetric component of solution vector x, and so, two asymmetric branches (the dashed lines), being the result of a symmetry-breaking bifurcation point, are depicted as one. For the clarity of the figures, $\phi(x)$ was intentionally made to increase whenever a limit point is passed irrespective of the real behavior of the functional chosen. In what follows, we will focus our attention primarily on the singularities and types of flows not having their analogues in the bifurcation diagram for $Ra_S = 30000$.

The symmetric solutions are represented in fig. 4. Like in the flows at the smaller values of Ra_S, convective motion is seen to have almost no effect on the temperature field, which remains very close to conductive due to the low intensity of convection at the small Rayleigh numbers. The changes in the salinity field, however, are a lot more tangible owing to the much smaller diffusivity of salt. As the steady solution is continued in the thermal Rayleigh number from zero along branches $S1, \ldots, S3$ (see fig. 2), two end cells gradually take up the entire enclosure (fig. 4 a), as is the case also at $Ra_S = 30000$ (see fig. 2 a,b,c in TK). The intensity of the cells at $Ra_S = 60000$, however, is slightly higher than that of their analogues at $Ra_S = 30000$ (fig. 2 c in TK), which is exhibited both by the more significant distortions in the constant-salinity lines and the larger undulations in the isotherms. Over branch $S4$, the two cells become cuddled together near the center of an enclosure, and as limit point $L4$ is passed, the formation of two additional cells is observed at the end walls (fig. 4 b). As Ra_T is increased along branch $S5$, the four-cell array is gradually built (fig. 4 c). With further increase of Ra_T, the intensity of each cell grows, which is reflected in the lines of constant salinity (fig. 4 d). The existence of limit point $L5$, however, brings a number of changes in the development of the four cell flow with respect to $Ra_S = 30000$. In particular, after this limit point has been passed, two central cells are found to be detached from each other (fig. 4 e) and start interacting with their end-wall counterparts. As a result of such an interaction, the end cells are progressively suppressed by the growing cells in the center (fig. 4 f,g). After limit point $L6$ is rounded, two central cells remain alone (fig. 4 h).

Thus at this stage, the effect of the increase in Ra_S from 30000 to 60000 on the symmetric-solution structure seems to be reduced to the emergence of the additional S-type structure consisting of limit points $L5$ and $L6$ in place of the interval of single branch $S5$ at $Ra_T = 30000$. In spite of the existence of the four cell flow along the associated branches, however, the pattern ultimately formed near $L6$ is of the two-cell type (fig. 4 h), like the one near limit point $L4$ (at the very outset of branch $S4$). These two cells remain alone within an interval of branch $S7$ above limit point $L6$, but as the thermal Rayleigh number is sufficiently increased along this branch, two other cells arise again. This time, the formation of the four-cell flow is associated with the peripheral parts of the streamlines of the cell pair starting to separate from the main bodies of the cells. These separating regions become almost detached from their parents manifesting themselves like small single cells (fig. 4 i). With further increase of Ra_T, the newly formed small cells grow in size reaching approximately the dimensions of the parent ones, their intensity also increases (fig. 4 j). In spite of the presence of the additional (with respect to the bifurcation diagram at $Ra_S = 30000$) S-type structure, associated with limit points $L7$ and $L8$, subsequent development of the four cell flow qualitatively resembles that along the branch $S5$ in fig. 3, due to the interaction between each of the central cells on one hand and its end-wall counterpart on the other, the whole array becomes weaker on the background of the arising surrounding streamlines (fig. 4 k). The cells ultimately fade away in the vicinity of limit point $L9$ at branch $S9$ (fig. 4 l). Unlike the events at $Ra_S = 30000$, however, it is the formation of a five- rather than a three-cell flow that is observed after rounding limit point $L9$. Not far from the outset of the five-cell flow, the arrangement of the cells in this flow reminds that in its four-cell predecessor with an additional cell in the center (fig. 4 m). Five cells arranged in an orderly manner are formed at the smaller values of Ra_T over branch $S10$ (fig. 4 n). Their mutual interaction results in that two end cells appreciably lose their intensity (fig. 4 o) and practically vanish as limit point $L10$ is approached (fig. 4 p). The three-cell flow formed in this way undergoes subsequent modifications along branches $S11, \ldots, S14$ and is replaced with one

cell after limit point $L14$ is passed. These changes, however, are qualitatively identical to the appropriate events at $Ra_S = 30000$, for which reason, they are not described here.

Like at the smaller values of Ra_S, the multiplicity of the symmetric flows described above is accompanied by a variety of asymmetric solutions, being the result of symmetry breaking bifurcation points $B1, ..., B18$. They are depicted by the dashed lines in fig. 2,3. In particular, like for $Ra_S = 30000$ (see fig. 2 h,i in TK), the onset of the first instability is caused by the breaking of the central symmetry between the end cells at symmetry breaking bifurcation point $B1$. The total number of the bifurcation points, however, has increased by eight compared to $Ra_S = 30000$ (fig. 3). Moreover, new asymmetric branches have emerged on account of the formation of limit points in the asymmetric branches at $Ra_S = 30000$, via the mechanism represented in fig. 1 (b). An essential common feature of all the asymmetric solutions at any $Ra_S \leq 30000$ (the corresponding bifurcation diagrams are presented in T), however, has been preserved also at $Ra_S = 60000$ — their pairs necessarily form a closed curve intersecting the symmetric branches in the corresponding bifurcation points (fig. 2, 3 illustrate only the projections of such curves on the symmetric plane). In this sense, the asymmetric branches can be regarded as the alternative scenarios of transformation of one of the symmetric flows into another skipping their modifications taking place in the symmetric plane. The examples of the streamline contours of asymmetric solutions at $Ra_S = 60000$ are presented in fig. 5.

Stability of the steady solutions has been studied by simulating the temporal evolution of the linearized system of the governing equations resulting from a disturbance introduced into its initial conditions. It is worth being noted that a minus sign in fig. 2,3 is indicative of the presence of the negative eigenvalue in the set of eigenvalues of the system of linearized governing equations. As a consequence, the solution is necessarily unstable within the corresponding interval of Ra_T. In spite of the formation of the five-cell flow and the appearance of many new multiple solutions as Ra_S is increased from 30000 to 60000, the set of the stable steady flows at $Ra_S = 60000$ has remained qualitatively the same as it was at $Ra_S = 30000$. In particular, besides asymmetric branch $A2$ and symmetric branches $S1$ and $S15$ at the small and the large Ra_T, respectively, the only stable steady flow is represented by the short interval between $L14$ and $B17$ of branch $S15$.

Thus for the thermal Rayleigh numbers between zero and that of limit point $L15$, the stable solution is unique, and it is characterized by two very weak end cells like the ones in fig. 2 (a) from TK. Two stable steady solutions coexist between limit points $L15$ and $L14$; the second is the asymmetric one-cell flow (see fig. 5 b). Between limit point $L14$ and bifurcation point $B17$, the set of the stable solutions comprises also the symmetric one-cell flow from the stable interval of branch $S15$ (this flow is similar to the slightly asymmetric one-cell pattern in fig. 5 r). The latter flow becomes unstable for Ra_T above $B17$, and so, only two stable solutions are present between $B17$ and $B1$. In the interval between $B1$ and $B18$ only the asymmetric one-cell flow (branch $A2$) is stable. When Ra_T is increased above $B18$, this solution exchanges its stability with the symmetric one-cell flow persisting up to the very large values of Ra_T (this flow is similar to the one in fig. 2 g from TK).

4   Discussion and conclusions

It is interesting that, in spite of the multiplicity of the flow patterns, there can nevertheless be distinguished generic features of these flows. In particular even based on the partial results presented here, it can be noticed that when the bifurcation parameter approaches its minimal value along a branch, the trend of the steady solution towards having some slow motion, almost stagnant, regions, either between a pair of cells or between a cell and the nearby end wall, can be clearly observed. Such regions can be identified either by the absence of the signs of cellular motion in the streamline patterns or by the absence of significant distortions in the constant-salinity lines. These trends are associated either with the gradual decay and vanishing of one of the end cells (or them both, in the symmetric

case), or with the shrinking of the existing cells either from one of the end walls (both of them) or from each other as Ra_T is decreased along the branch. As the thermal Rayleigh number is increased to its maximal values at a branch, however, the trend towards either giving rise to new cells or enlarging the existing ones on an entire enclosure, so that the whole space of the cavity be taken up by the cellular motion, is tangibly displayed. As a consequence of such a behavior, all the steady solutions at Ra_T above limit point $L3$ are characterized by the convective cells occupying the entire enclosure. The steady solutions possessing flow regions that either are practically stagnant or are characterized by the motion of the relatively very low intensity can be found starting from the value of the thermal Rayleigh number slightly smaller than that at $L3$, and below the Ra_T corresponding to approximately the middle of branch $S4$, such a region (or regions) are present in almost all the solutions. However, apart from the one-, two-, three-, and four-cell flows observed at $Ra_S \leq 30000$, the set of the solutions without the stagnant region comprises also the symmetric and asymmetric five-cell flow patterns.

The dependence of the presence of a stagnant flow region in a steady solution on whether Ra_T is below or above a critical interval (the one between the middle of $S4$ and $L4$) is reminiscent of the "successive" and "simultaneous" modes of layer formation observed in previous studies below and above an appropriately defined Rayleigh number, respectively. It is interesting that the stability results described above exhibited so large time scales of the instabilities that the steady flows could eventually be long (in application to the experimental set of Lee *et al.* 1990, for many hours) observed in the experiment. Thus, even allowing for possible qualitative changes in the steady solution structure and for variation of the growth rates of the instabilities as the salinity Rayleigh number is further increased up to the very large values used in the previous studies, it nevertheless appears that the features of unstable steady flows are of basic significance for the understanding of the nature of the "successive" and "simultaneous" flow regimes observed in the past.

References

[1] Chen, C. F., Briggs, D. G. and Wirtz, R. A. (1971) Stability of thermal convection in a salinity gradient due to lateral heating. *Int. J. Heat Mass Transfer* 14, 57-65.

[2] Hart, J. E. (1971) On sideways diffusive instability. *J. Fluid Mech.* 49, 279-288.

[3] Keller, H. B. (1977) Numerical solution of bifurcation and nonlinear eigenvalue problems. In *Applications of bifurcation theory*. (ed. Rabinowitz, P.H.). Academic Press: New York..

[4] Lee, J. W. and Hyun, J. M. (1991) Double-diffusive convection in a cavity under a vertical solutal gradient and a horizontal temperature gradient. *Int. J. Heat Mass Transfer* 34, 2423-2427.

[5] Lee, J. W., Hyun, M. T. and Kang, Y. S. (1990) Confined natural convection due to lateral heating in a stably stratified solution. *Int. J. Heat Mass Transfer* 33, 869-875.

[6] Thorpe, S. A., Hutt, P. K. and Soulsby, R. (1969) The effect of horizontal gradients on thermohaline convection. *J. Fluid Mech.* 38, 375-400.

[7] Tsitverblit, N. (1994) Bifurcation phenomena in confined thermosolutal convection with lateral heating: commencement of the double-diffusive region. Submitted.

[8] Tsitverblit, N. and Kit, E. (1993) The multiplicity of steady flows in confined double-diffusive convection with lateral heating. *Phys. Fluids A* 5(4), 1062-1064.
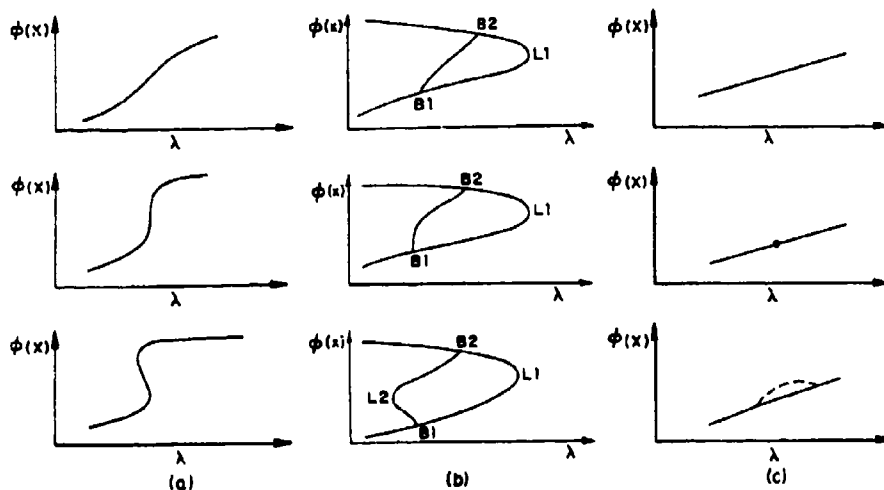
Figure 1: The mechanisms responsible for promotion of the solution multiplicity with the second parameter, Ra_S, being varied. (a) the emergence of two limit points via the formation of a non-degenerate hysteresis point; (b) the emergence of a single limit point due to the exchange of the criticality of a symmetry-breaking bifurcation point; (c) the emergence of a pair of symmetry-breaking bifurcation points via the formation of the isola of asymmetric solutions at a symmetric solution branch.
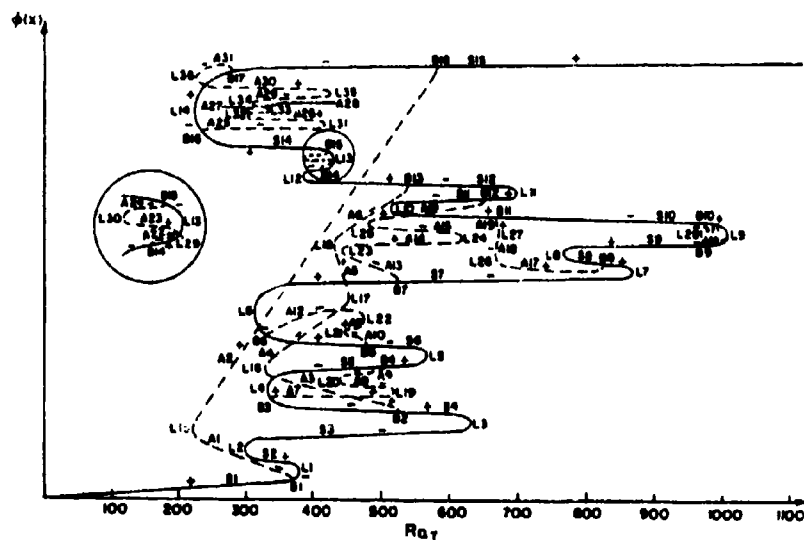

Figure 2: The schematic diagram of the variation of a measure of the symmetric component $\phi(X)$ of solution vector X with thermal Rayleigh number Ra_T; $Ra_S = 60000$. $S1, ..., S15$ (the solid lines) are symmetric branches. $A1, ..., A31$ (the dashed lines) are asymmetric branches. $L1, ..., L36$—limit points. $B1, ..., B18$—symmetry-breaking bifurcation points. The plus and minus signs designate the signs of the Jacobian determinant at the corresponding intervals.

6
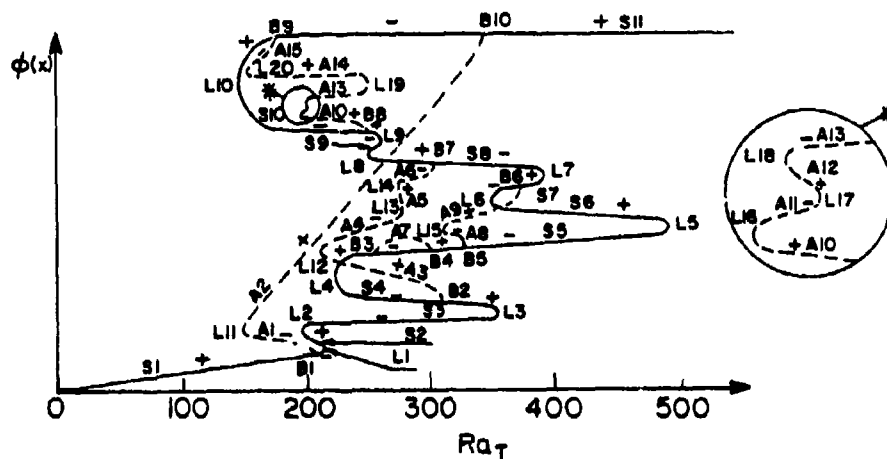
Figure 3: The schematic diagram of the variation of a measure of the symmetric component $\phi(X)$ of solution vector X with thermal Rayleigh number Ra_T; $Ra_S = 30000$. $S_1, \ldots, S11$ (the solid lines) are symmetric branches. $A1, \ldots, A15$ (the dashed lines) are asymmetric branches. $L1, \ldots, L20$—limit points. $B1, \ldots, B10$—symmetry-breaking bifurcation points. The plus and minus signs designate the signs of the Jacobian determinant at the corresponding intervals.
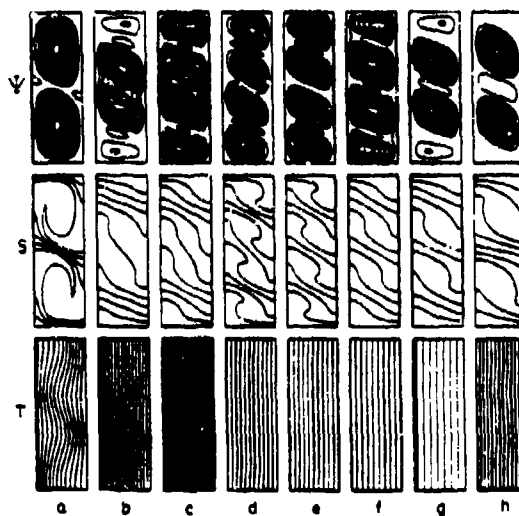
Figure 4: (a),...,(h) Symmetric steady solutions. $Ra_S = 60000$. ψ streamlines. S the lines of constant salinity. T isotherms. Left wall is at higher temperature. All the contours are equally spaced between their maximum and minimum values. (a) $Ra_T = 620$, branch $S3$; (b) $Ra_T = 378$, branch $S5$; (c) $Ra_T = 496$, branch $S5$; (d) $Ra_T = 560$, branch $S5$; (e) $Ra_T = 511$, branch $S6$; (f) $Ra_T = 451$, branch $S6$; (g) $Ra_T = 321$, branch $S6$; (h) $Ra_T = 323$, branch $S7$.
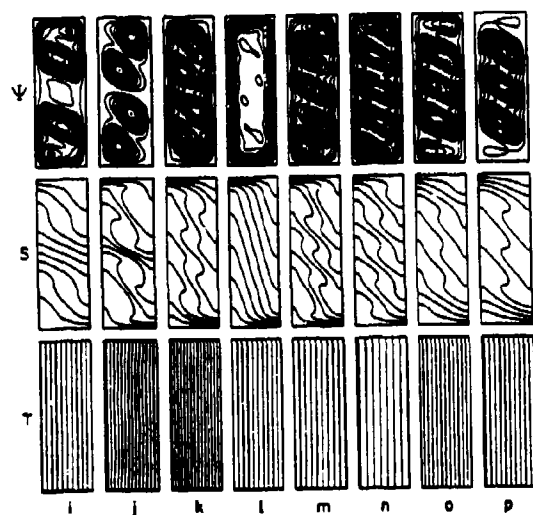
Figure 4: (i)....,(p). Symmetric steady solutions; $Ra_S = 60000$. Ψ: streamlines, S: the lines of constant salinity. T: isotherms. Left wall is at higher temperature. All the contours are equally spaced between their maximum and minimum values. (i) $Ra_T = 509$, branch $S7$; (j) $Ra_T = 729$, branch $S7$; (k) $Ra_T = 770$, branch $S8$; (l) $Ra_T = 1003$, branch $S9$; (m) $Ra_T = 900$, branch $S10$; (n) $Ra_T = 720$, branch $S10$; (o) $Ra_T = 590$, branch $S10$; (p) $Ra_T = 515$, branch $S10$
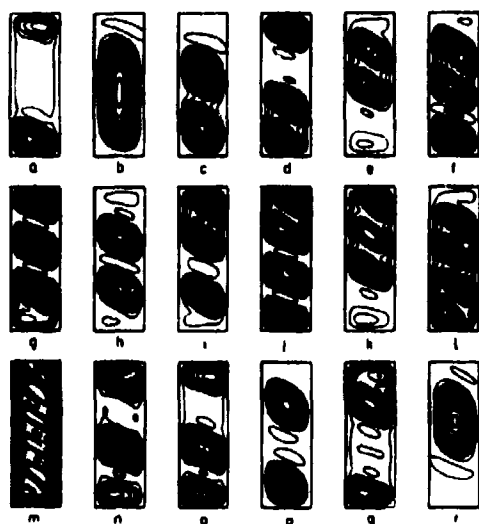
Figure 5. The streamline contours of asymmetric steady solutions; $Ra_S = 60000$. Left wall is at higher temperature. All the contours are equally spaced between their maximum and minimum values. (a) $Ra_T = 346$, branch $A1$; (b) $Ra_T = 406$, branch $A2$; (c) $Ra_T = 337$, branch $A3$; (d) $Ra_T = 433$, branch $A5$; (e) $Ra_T = 403$, branch $A7$; (f) $Ra_T = 440$, branch $A8$; (g) $Ra_T = 463$, branch $A11$; (h) $Ra_T = 340$, branch $A12$; (i) $Ra_T = 461$, branch $A13$; (j) $Ra_T = 518$, branch $A14$; (k) $Ra_T = 502$, branch $A15$; (l) $Ra_T = 678$, branch $A17$; (m) $Ra_T = 989$, branch $A20$; (n) $Ra_T = 386$, branch $A23$; (o) $Ra_T = 412$, branch $A25$; (p) $Ra_T = 310$, branch $A29$; (q) $Ra_T = 423$, branch $A30$; (r) $Ra_T = 244$, branch $A31$

BOUNDARY LAYER AND SCALING PROPERTIES
IN TURBULENT THERMAL CONVECTION

F. Chillá[(o)], S. Ciliberto[(*)], C. Innocenti[(o)], C. Laroche[(*)]

(*) Ecole Normale Supérieure de Lyon
Laboratoire de Physique, C.N.R.S. URA1325
46, Allée d'Italie
69364 Lyon, France

(o) C.R.T.B.T., 25 Avenue des Martyrs, 38042 Grenoble, France

(o) I.M.G.- L.E.G.I., B.P.53, 38041 Grenoble, France

Abstract: We describe an experiment which has been designed to measure both spatial and temporal features of turbulent thermal convection in a fluid layer heated from below. Specifically we have studied the dependence of the heat flow versus the Rayleigh number, the thermal boundary layer profile, the temperature probability distribution function, the frequency and wave number power spectra. Scaling exponent of temperature structure functions have been evaluated using the recently introduced method of Extended Self Similarity.

(1) Introduction

Many properties of thermal convection in a horizontal fluid layer heated from below are not yet well understood. One of the most important is the dependence of the Nusselt number, that is the non-dimensional heat flow, as a function of the Rayleigh number $Ra = \alpha g d^3 \Delta T / \nu \chi$, where α is the thermal expansion coefficient of water, g the gravitational acceleration, d the height of the cell, ΔT the temperature drop across the cell, ν the kinematic viscosity and χ the thermal diffusivity of the fluid under study. The dependence of Nu versus Ra is certainly induced by the boundary layer shape and from the characteristics of the large scale circulation [1,2,3]. The study of the boundary layer is not only important to determine Nu but also the statistical properties of the temperature field inside the bulk which are strongly influenced by the fluctuations near the walls[2,3,4]. Indeed it has been observed [1] that the probability distribution functions (P.D.F.) of temperature measured in the center of the cell presents, at $Ra > 10^7$, exponential tails which are related to a logarithmic dependence on z of the r.m.s. fluctuations closed to the boundary layer[2,3,4].

Finally an other important problem in turbulent thermal convection is the scaling of temperature and velocity fields. In the experiments of ref.5,6 it has been found that the measured scaling exponents were consistent with those predicted by Bolgiano and Obukhov[7] for turbulence in stratified media. However in several recent papers[8,9,10] it has been shown that this scaling could be possible also in

1

thermal convection. In contrast in ref.11 the standard Kolmogorov law $K^{-5/3}$ is predicted for the temperature wave-number power spectra and it has been argued that the exponent $-7/5$, found in the experiment [5], could be valid only for frequency spectra but not for wave-number spectra which should present the steeper power law at $K^{-5/3}$.

We have investigated all these effects in an experiment on turbulent Rayleigh-Benard convection. This experiment has been designed to measure both temporal and spatial features of turbulent regimes in a cell filled with water and heated from below. The description of the experiment can be found in ref.2,3,13. thus we remind here only the main features. The average temperature of the cell was $45°C$ corresponding to a Prandtl number, $Pr = \nu/\chi$ of about 4. By changing the height d of the cell from $6.5cm$ to $40cm$ and we were able to cover the interval of Rayleigh numbers Ra from 10^6 to 10^{10}. As the horizontal length of the cell was $40cm$, the aspect ratio L/d was changed from 6 to 1. Local temperature measurements were done with a small thermocouple whose position could be changed in order to test different regions of the flow. Spatial measurements were done with a laser beam sweeping technique described in previous papers (see ref.2,3 and reference therein) and by changing the thermocouple position.
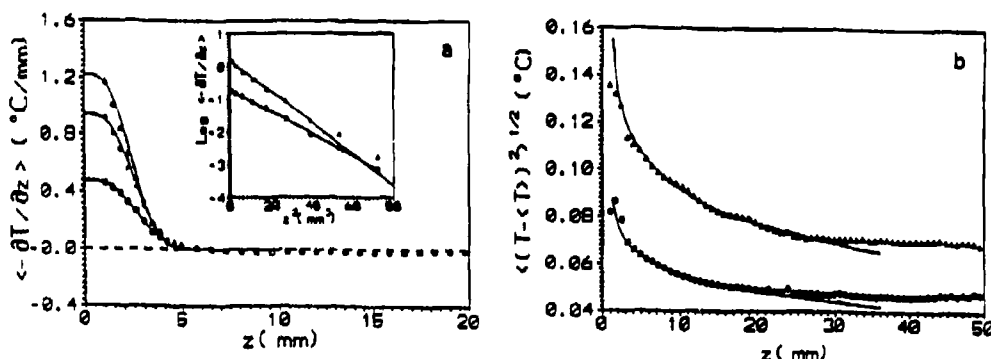

Figure 1: a) Dependence of $\partial_z \bar{T}$ on z for different values of Ra, $\circ$ $Ra = 5 \cdot 10^7$, $\star$ $Ra = 10^8$, $\triangle$ $Ra = 2 \cdot 10^8$. The continuous line correspond to best fits done with eq.1. Insert: dependence of $\log_{10} \partial_z \bar{T}$ on z^3, the straight lines show the accuracy of the fit.

b) dependence of the root mean square of the fluctuations of T as a function of z for two different values Ra, $\circ$ $Ra = 10^8$, $\triangle$ $Ra = 2 \cdot 10^8$. The continuos lines are logarithmic best fits for $z > z_v$.

(2) Boundary layer

From our optical measurements we can also compute

$\partial_z \bar{T}(z) = << \partial_z \bar{T}(x, z, t) >_x >_t$, that is the z component of the temperature gradient averaged on an horizontal plane , and the root mean square fluctuations $\delta \bar{T}(z) = << (\bar{T} - < \bar{T} >_t)^2 >_x >_t^{1/2}$, where $< . >_u$ stands for average on the variable u. These two fields $\partial_z \bar{T}$ and $\delta \hat{T}$ are reported in fig.1 as a function of z for

2

different values of Ra. Only the lower part of the cell is shown. Notice that, for $z > 5mm$, $\partial_z \tilde{T}$ is slightly negative and it reaches 0 once again at $z \geq 20mm$. This indicates that a small thermal inversion is present at $Ra \simeq 10^8$. The continuous lines in fig.1a are a best fit done with the boundary layer shape proposed in ref.11:

$$\partial_z T \propto \frac{B \exp[(-z^3/9\chi\tau x)]}{(\tau x)^{1/3}} \tag{1}$$

where B depends on boundary conditions and τ is a characteristic time such that $Nu \propto B\tau^{-1/3}$ [3]. The agreement between the measured temperature derivative and the fits is good. The accuracy of the fit is clearly seen, in the insert of Fig.1a, where $\log \partial_z T$ versus z^3 is shown. We realize that the fit deviates for $z > z_v$, where z_v is the viscous sublayer depth. More details about the implication of eq.1 can be found in ref.3.

In Fig.1b, where the r.m.s. of temperature fluctuations is shown, we see that the strongest fluctuations are close to the boundary layers as it should be expected because of the hot plumes coming out the boundary[1,2,3]. The continuous lines is a logarithmic best fit which is the reason for the exponential tails observed in the temperature P.D.F. observed at $Ra > 10^7$ [2,3,4].

The knowledge of $\partial_z \tilde{T}$ at the bottom plate of the cell is also useful to measure the heat flow with the optical technique in addition to the standard calorimetric one. The results are shown in ref.3.

(3) Scaling laws in turbulent convection

Several experiments [5,6] have shown that the temperature and velocity fields present scaling exponents which agree with those predicted by the Obukov-Bolgiano [7] arguments for turbulence in a stable stratified medium. This means that the temperature and velocity spectra should scale as $K^{-7/5}$ and $K^{-11/5}$ respectively.

However many experimental measurements are done just in a single point, thus it is important to study the relationship existing in thermal convection between frequency and wave number power spectra[13,3]. We found that when the mean recirculation flow, inside the cell, is stable, the frequency and wave number spectra coincide by simply using Taylor hypothesis. In contrast in the points of the cell where the mean flow does not exist frequency and wave number spectra are different. We have also noticed that, because of the instabilities of the mean flow, scaling is observed better in spatial measurements than in temporal ones. Thus the possibility of observing a scaling in time measurements is related to the mean flow stability. This feature has been also observed in recent numerical simulations [14].

All these problems and the fact that, at very high Ra, the standard Kolmogorov scaling could be indeed observed make a clear evaluation of the scaling laws in thermal convection rather difficult. Furthermore the distinction between the Kolmogorov and the Bolgiano scaling can be influenced also by the intermittent corrections. The best way to study this problem is to compute the temperature structure functions of order p, that is

$$<| \delta T(r)^p |> = < |T(x + r) - T(x)|^p >$$

and then to use Extended Self Similarity (E.S.S.)[15] which works very well even for very small Reynolds number, that is the case of our experiment. It has been

3

recently shown that E.S.S. works also in thermal convection[16]. E.S.S. consists in finding the scaling laws using structure functions of different orders:

$$< \mid \delta T(r) \mid^p > = < \mid \delta T(r) \mid >^{\xi(p)}$$

Specifically it has been shown[16] that $\xi(2)$ is 1.4 for the Bolgiano scaling and 1.7 for the Kolmogorov one.

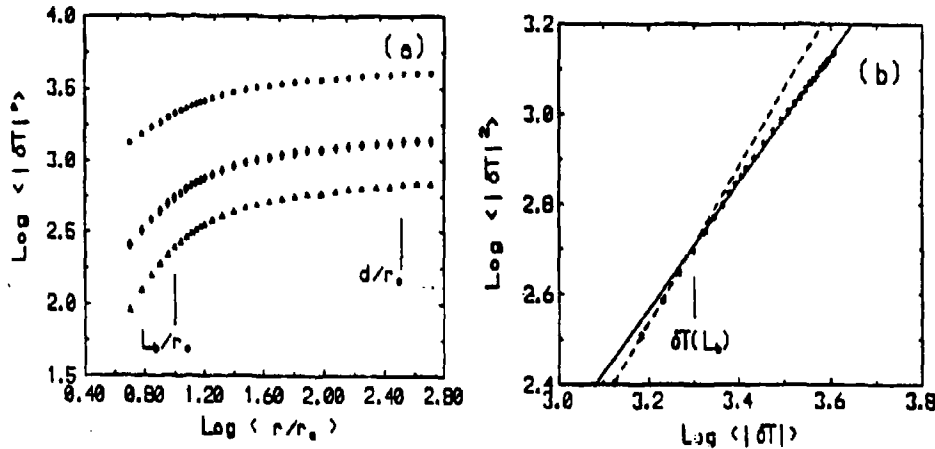**Figure 2:** Temperature structure functions at $Ra = 4 \cdot 10^8$ obtained from the thermocouple in a single point and uisng Taylor hypothesis.

a) Temperature structure functions $< \mid \delta T(r) \mid^p >$ as a function of r for p=1 *, p=2 ◊ and p= 3 △. The Bolgiano length L_b and the integral length scale d are also indicated. b) Extended self similarity between p=2 and p=1. Notice that the Bolgiano scaling indicated by the solid straight line, with slope 1.4, stops exactly at $< \mid \delta T(L_b) \mid >$ as expected. The dashed line has a slope of 1.7.

In Fig.2a) the structure functions for p=2 and p=1 are reported whereas in fig.2b) they are shown one against the other. A clear scale is observed with $\xi(2) = 1.4$. The structure functions of fig.2 have been computed using time measurements and then making used of Taylor hypothesis to transform them in spatial measurements. In fig.3 we show the structure functions directly measured in space by measuring the moments of the temperature difference between two points at a distance r changing the thermocouple position. A rather clear scaling is observed as a function of the distance r (fig. 3a) and when a structure function is drawn as a function of the other fig.3b. The results repported in fig.2 and 3 clearly show that the Bolgiano scaling is the correct one at least at small Ra. It could be not in this way at different Prandtl number and higher Ra see also ref.3.
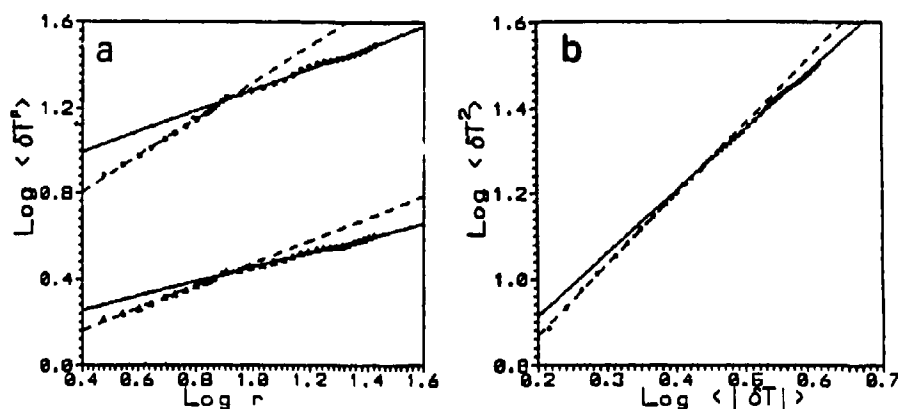
4

Figure 3: Temperature structure functions at $Ra = 10^{10}$ obtained by direct spatial measurements

a) Temperature structure functions $< |\delta T(r)|^P >$ as a function of r for p= 1 $\triangle$ and p=2 $*$.

b) Extended self similarity between p=2 and p=1. The Bolgiano scaling is indicated by the solid straight line, with slope 1.4. The dashed line has a slope of 1.7.

(4) Conclusions

Using an experiment on turbulent thermal convection which allows to measure both spatial and temporal features of the temperature field, we have shown that the conjectures of ref.5 on thermal boundary layer are correct. We have shown that the spatial P.D.F. of temperature fluctuations has an exponential tails which implies a logarithmic dependence on z of the fluctuations amplitudes. Finally using E.S.S. we have clearly show that in the range of Ra number used in our experiment the appropriate scaling is the Bolgiano one.

We acknowledge useful discussion with R. Benzi.

References:

[1]: F. Heslot, B. Castaing, A. Libchaber, Phys. Rev. A 36, 5870 (1987); B. Castaing, G. Gunaratne, F. Heslot, L. Kadanoff, A. Libchaber, S. Thomae, X. Z. Wu, S. Zalesky, G. Zanetti, J. Fluid Mech. 204, 1 (1989).

[2]: F. Chillá, S. Ciliberto, C. Innocenti, Europhysics Letters 22, 681 (1993).

[3]: F. Chillá, S. Ciliberto, C. Innocenti, E. Pampaloni Nuovo Cimento D 15, 1229 (1993).

[4]: R. Massaioli, R. Benzi, S. Succi, Europhysics Letters 21, 305 (1993).

[5]: M. Sano, X. Z. Wu, A. Libchaber, Phys. Rev. A 40, 6421 (1989); X. Z. Wu, L. Kadanoff, A. Libchaber, M. Sano, Phys. Rev. Lett. 64, 2140 (1990).

[6]: P. Tong, Y. Shen, Phys. Rev. Lett. 69, 2066 (1992).

[7]: R. Bolgiano, J. Geophys. Res. 64, 2226 (1959); A. M. Obukhov, Dokl. Akad. Nauk. S.S.S.R. 125, 1246 (1959).

[8]: V.S. L'vov, Phys. Rev. Lett. 67, 687 (1991); Physica 57 D, 85 (1992).

[9]: I. Procaccia, R. Zeltak, Phys. Rev. A42, 821 (1990).

5

[10]: V. Yakhot, Phys. Rev. Lett., 769 (1992).
[11]: B. Shraiman, E. Siggia, Phys. Rev. A 42, 3651 (1990).
[12]: T. Y. Chu, R. J. Goldstein, J. Fluid Mech. 60, 141 (1973).
[13]: F. Chillá, S. Ciliberto, C. Innocenti, E. Pampaloni Europhysics Letters 22, 23 (1993).
[14]: R. Benzi, L. Tripiccione private communication.
[15]: R. Benzi, S. Ciliberto, R. Tripiccione, C. Baudet, F. Massaioli, S. Succi, Phys. Rew. E 48, 29 (1993); R. Benzi, S. Ciliberto, G. Ruiz Chavarria, C. Baudet, R. Tripiccione, Europhysics letters 24, 275 (1993).
[16]: R. Benzi, L. Tripiccione, F. Massaioli, S. Succi, S. Ciliberto, Europhysics Letters, 25, 341 (1994).

Experimental Study of High-Rayleigh-Number Convection in Mercury and Water

S. Cioni, S. Ciliberto and J. Sommeria

Laboratoire de Physique
Ecole Normale Supérieure de Lyon (URA 1325 CNRS)
46, Allée d'Italie 69364 Lyon Cedex 07 France

May 4, 1994

Abstract

Preliminary experimental results of Rayleigh-Bénard convection in the strongly turbulent regime are presented. The liquids tested are mercury ($Pr = 0.025$) and water ($Pr = 7$). The experiment cover a range of Rayleigh numbers between $1.6 \times 10^7 < Ra < 6.3 \times 10^9$. The convective chamber consists of a cylindrical cell of aspect ratio $\Gamma = 1$ ($\Gamma = \frac{diameter}{depth}$). In the turbulent regimes it has been measured the heat flux, the temperature fluctuation spectra and the structure of the mean flow. For $Ra > 2 \times 10^9$ a transition to a new turbulent regime was observed with considerable increase of the Nusselt number. A decreasing of Nusselt with decreasing Prandtl number is observed.

1 Introduction

An horizontal layer of fluid subjected to uniform heating from below and cooling from above is a classical (unstably) stratified system. The strongly turbulent regime has been the subject of numerous recent investigations [1] [2]. These experiments have been performed at Prandtl number close to unity (in helium or water) and the influence of this parameter has been little explored. Convection at low Prandtl numbers has been carefully investigated near the onset of unsteady motions [3], [4], but the strongly turbulent regimes seem not to have been studied since Rossby [5] and Globe & Dropkins [6]. In the present investigation. we extend these results to a wider range of Rayleigh numbers, and compare them with experiments in water. Furthermore, we investigate the structure and dynamics of the mean flow which is spontaneously produced in such Rayleigh-Benard configuration.
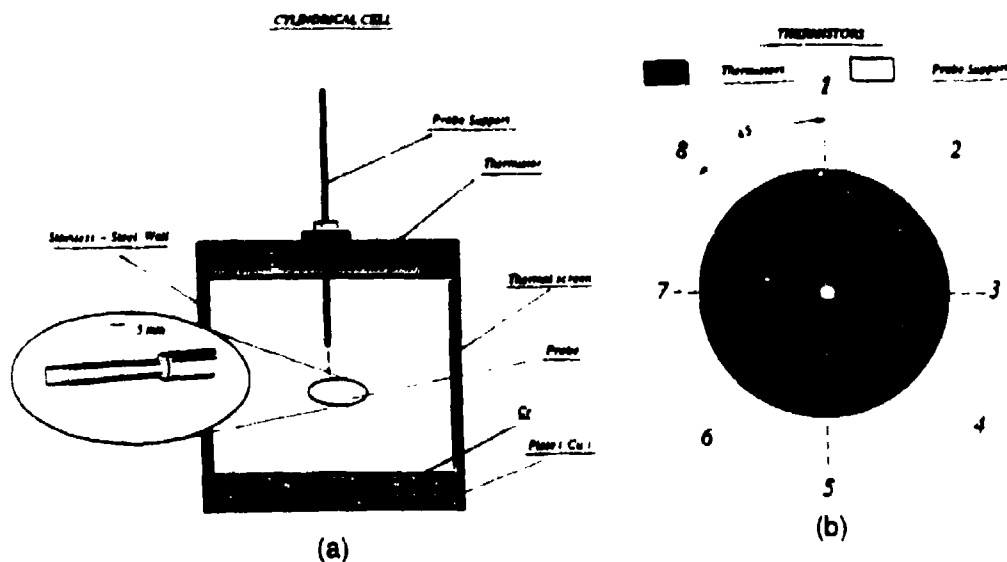
1

Figure 1: (a) Test apparatus. (b) Arrangement of nickel-teflon thermistors in the heater and cooler plate.

2   Apparatus and Experimental Procedure

A detailed description of the cell can be found in [7] and will be published. Here we give only its main characteristic. The test chamber is a cylindrical cell (Fig.1) of internal diameter and height 21.3 cm. Both plates are in copper 5 cm thick, coated with nickel ($50\mu m$ thick)to avoid amalgamation with mercury. The cell is thermally insulated from the outside by neoprene layers, and surrounded by a thermal screen to minimize heat losses. The bottom plate is heated with a constant power by electrical resistances, forming a double spiral to avoid magnetic effects on mercury flows. The upper plate is cooled and thermally regulated by a water circulation. For measuring the temperature at the upper and lower boundaries of the layer, boreholes are sunk radially into the copper plates and calibrated thermistors are inserted. The depth of the boreholes is $7cm$ and distance of the boreholes tips from the plate surface is 3 mm.

Three different sets of data have been obtained: the heating power, the temperature differences across the cell as function of time at six positions and local temperature fluctuactions inside the fluid. These are obtained from the resistance of a platinum film. $250\mu m$ long, coated on a small wire, of diameter $25\mu m$, electrically insulated from mercury by a thin quartz layer. (it is a T.S.I. hot film probe used with a small current, 10 mA, producing negligible overheating).

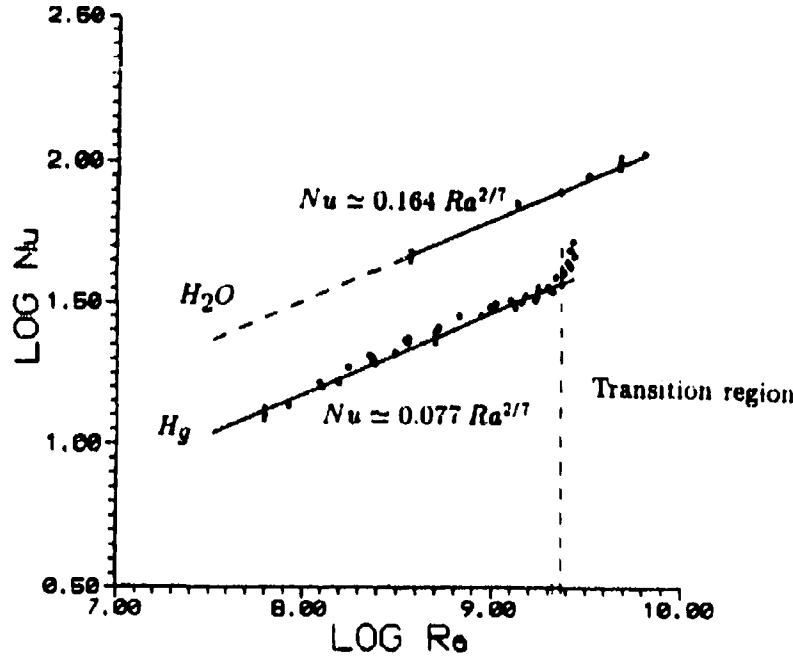We study the permanent flow regime for different values of the heating power.

2

Figure 2: Nusselt *versus* Rayleigh in water and mercury

3 Heat transfer measurements

We first determine the temperature difference ΔT between the bottom and top plates as a function of the heating power. This is represented in non-dimensional form by the Nusselt number ($Nu = \frac{total\ heat\ flux}{conductive\ heat\ flux}$) versus the Rayleigh number Ra. In fact the temperature in the top and bottom fluctuates in time with fairly large amplitude, especially in mercury (20% of ΔT), and a time average is performed (over several hours). Also a systematic horizontal temperature gradient appears in each plate, in relation with a big convective roll at the scale of the whole cell, as discussed in next section. Thus a spatial average in each plate is performed in order to get the mean temperature difference ΔT. The results are represented in Fig. 2 in the case of water ($Pr = 7$) and mercury ($Pr=0.025$). A good fit of the data is provided by the following formula

$$Nu_{H_2o} = 0.164 Ra^{\frac{2}{7}}$$

for water in the range $3.7 \times 10^8 < Ra < 7 \times 10^9$

$$Nu_{H_g} = 0.077 Ra^{\frac{2}{7}}$$

for mercury in the range $1.6 \times 10^7 < Ra < 2.7 \times 10^9$

Our results with water are in excellent agreement with precedent works [9]. Our values of Nu for mercury, extrapollated to lower Ra, are about 1.5 times lower than the result

3

of Globe & Dropkins [6] (obtained in a cell with aspect ratio 3.8 or 2). The range of Ra is not sufficient to distinguish between a 2/7 power, and the 1/3 power assumed in earlier theories. Nevertheless, the lower value of Nu for lower Pr is clearly established. This is in agreement with similar comparisons made at lower Ra [6][5]. However this result is in contradiction with the model of Shraiman & Siggia [8], which has been however successfull in several other predictions [9], [10]. By contrast, it agrees with the earlier theory of Kraichnan [11]. Further experimental measurements are needed to better discriminate between the different theories, and may be suggest new ones.

In the case of mercury, a very sharp increase of Nu is observed near $Ra \simeq 2.1 \times 10^9$. This could correspond to a transition expected when the viscous boundary layer becomes thinner than the thermal boundary layer [2]. Notice however that this transition is observed near the maximum Ra that we can reach with our apparatus, and we have difficulties in reproducing the data (by contrast the results at lower Ra are quite reproducible). Investigation is in progress to clarify this problem.

4   Dynamics of the mean flow

The spontaneous formation of a large convective roll, at the scale of the whole experimental cell, has been noticed by previous investigators, and is an important ingredient of the model by Shraiman and Siggia [8]. We show here that this so called mean flow has in fact a complex dynamics on a slow time scale. As stated earlier, the temperature distribution in the bottom and top plates is a convenient track of this mean flow. The temperature records at two locations at the bottom and tops plates, are shown as function of time in Fig. 3 at $Ra \simeq 1.2 \times 10^9$. We notice fluctuations on the time scale of several minutes, and switches between two regimes persisting during one or several hours. The fluctuations at two diametrally opposit locations (probes 2 and 6), are opposit, so that these switches can be interpreted as a reversal of the mean flow (The negative crosscorrelation is also an indication that the observed fluctuations are not linked with the thermal regulation system). The dipolar structure of the temperature distribution on each plate is confirmed by the crosscorrelations between the different probes (Fig.4a). Surprisingly enough, this correlation is not only verified for the major reversals, but also for more rapid fluctuations. It appears indeed in Fig.4b that the crosscorrelation strongly decreases for time intervals of a few minutes, so that a significant part of the crosscorrelation comes from fluctuations on that time. Therefore the "mean flow" undergoes a quite complex dynamics that has to be further investigated.

5   Temperature fluctuation spectra

The third objective of this study is to explore the scaling laws in temperature fluctuation spectra ($S_\Theta(k) \sim k^\xi$), once fully developed turbulence regime is established. All these spectra were made at the 1/4 of the total height from the bottom.
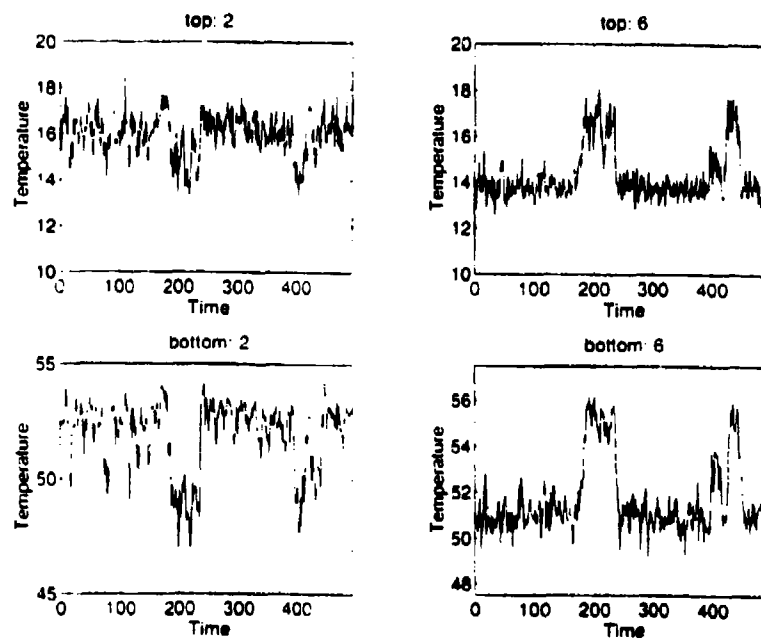
4

Figure 3: Temperature thermistor records *versus* time (in minutes).
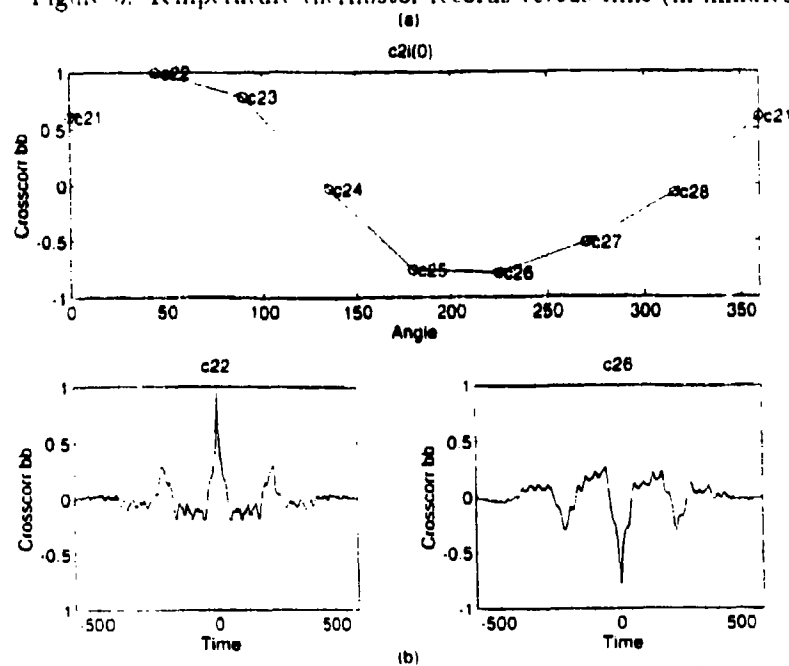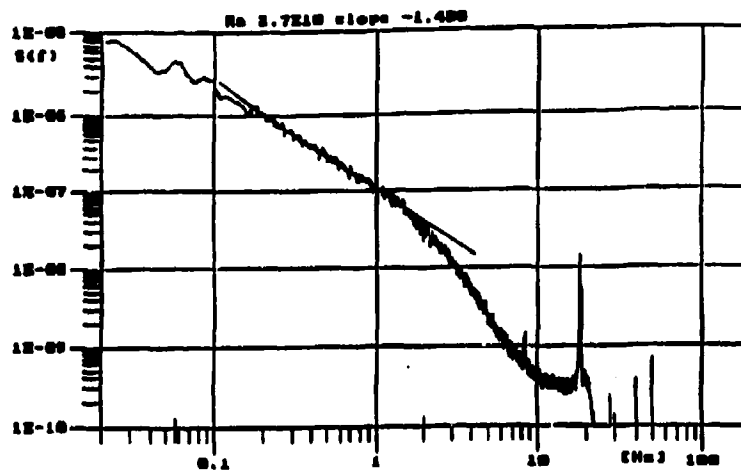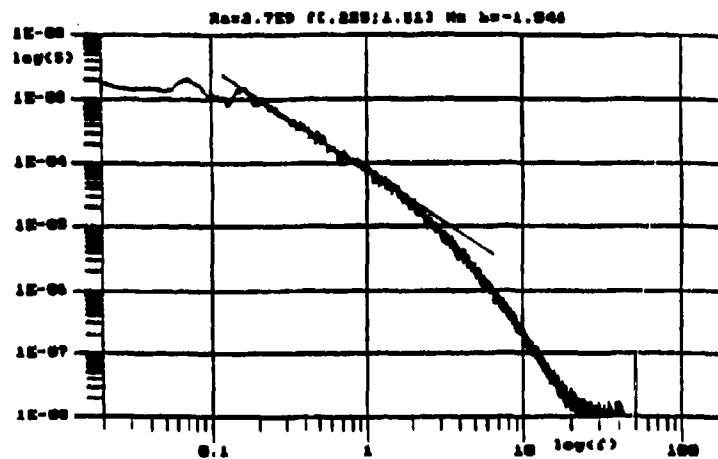

Figure 4: Crosscorrelation function of temperature thermistor records: (a) at $t = 0$ *versus* angle (in degrees); (b) C_{22}, C_{26} *versus* time (in minutes), where $C_{ij} = < b_i, b_j >$.

5

Figure 5: Temperature fluctuation spectra a)in water, b) in mercury.

The spectral data of the present work, show in water (see Fig. 5) a well defined 7/5 law, in agreement with the scaling of Bolgiano and Obukhov [13] [12]. This confirms previous experimental works. On the other hand, the experimental findings in mercury (see Fig. 5) don't show a very clear scaling law. The spectra are however closer to Kolmogorov scaling, as expected from an estimation of the respective fluxes of temperature and velocity fluctuations [9].

6   Summary

These preliminary experimental results show that convection at low Prandtl number, presents several interesting and differents feature with respect to convection in fluids with Prandtl number of order one, for example the transition of Nusselt *versus* Rayleigh in

6

mercury for $Ra > 2.1 \times 10^9$ (which remains to be confirmed).

Furthermore, the strong temperature fluctuations induced by the fully developed convection allow us to to show that the previously observed "mean flow" has a complex dynamics on long time scales, involving fluctuations and reversals.

Although, at the moment, we cannot determine the exponent of Nu versus Ra with high accuracy, we can affirm with confidence the observed dependence on the Prandtl number.

References

[1] CASTAING B., et al., 1989 "Scaling of hard thermal turbulence in Rayleigh-Bénard convection", J. Fluid Mech. **204**, 1.

[2] SIGGIA E.D. 1994 "High Rayleigh number convection", Annual Rev. Fluid Mechanics.

[3] CHIFFAUDEL A., FAUVE S. & PERRIN B. 1987 "Viscous and inertial convection at low Prandtl number: experimental study" Europhys. Lett. 4(5), 555-560.

[4] KEK V. & MULLER U. 1993 "Low Prandtl number convection in layers heated from below" Int. J. Heat Mass Transfer 36 (11), 2795-2804.

[5] ROSSBY H.T., 1969 "A study of Bénard convection with and witout rotation", J. Fluid Mech. **36**, 309.

[6] GLOBE S., DROPKIN D., 1959 "Natural-convection heat transfer in liquids confined by two horizontal plates and heated from below", Journal of Heat Transfer **31**, 24.

[7] CIONI S. Tesi di Laurea, Universitdi Firenze, 1993 (unpublished).

[8] SHRAIMAN B.I., SIGGIA E.D., 1990 "Heat transport in high-Rayleigh-number convection", Phys. Rev. A **42**, 3650

[9] CHILLA F., CILIBERTO S., INNOCENTI C., PAMPALONI E., 1993 "Boundary layer and scaling properties in turbulent thermal convection", J. Il Nuovo Cimento **15D**, 1229.

[10] BARTOLONI A., et al., September 1993 "LBE simulations of Rayleigh-Bénard convection on the APE100 parallel processor", International Journal of Modern Physics C,

[11] KRAICHNAN R. 1962 "Turbulent thermal convection at arbitrary Prandtl number", Phys. Fluids 5, 1374.

[12] OBUKHOV A.M., 1959 "Effect of Archimedean forces on the structure of the temperature field in a turbulent flow", Izv. Akad. Nauk. SSSR Ser. Georgr. e Geifiz. **125**, 1246.

[13] BOLGIANO R., 1959 "Turbulent spectra in a stably stratified atmosphere", *Journal of Geophysical Research* SSSR Ser. Georgr. e Geifiz. **64**, 2226.

8

Rayleigh-Taylor instability:
perturbations, boundaries and growth

Stuart B. Dalziel

Department of Applied Mathematics and Theoretical Physics
The University of Cambridge, Silver Street
Cambridge CB3 9EW, ENGLAND
Phone: (44)(223) 337840; Fax: 337918; E-mail: sd103@amtp.cam.ac.uk

ABSTRACT

One of the simplest experimental systems which exhibits Rayleigh-Taylor instability is that where a homogeneous layer of fluid overlies a similar layer of less dense fluid. Initially the two layers are separated by a horizontal barrier. The instability starts when the barrier is removed. Quantitative measures of the spatio-temporal velocity and density structure of the flow have been made using a range of image processing techniques. These data are then compared with theoretical and numerical predictions of the development of the instability.

This paper addresses the question of how closely these simple experimental flows relate to idealised numerical simulations. Such simulations predict growth rates significantly lower than those observed in experiments. Three-dimensional numerical simulations typically utilise a horizontally periodic domain and a spectrum of random initial perturbations. The destabilising acceleration is turned on at the same instant everywhere in the domain. In contrast, experiments are performed in a finite domain with solid sidewalls. The withdrawal of the barrier introduces strong, coherent perturbations to the initial state of the fluid and the finite time required to remove the barrier introduces a delay in the initiation of the instability across the tank. The structure and effect of these coherent perturbations, the delay in initiating the instability and the coupling of the flow with the boundaries of the tank are analysed and their influence on the subsequent evolution of the flow determined.

1. Introduction

Along with Kelvin-Helmholtz instability, Rayleigh-Taylor instability is one of the fundamental mechanisms through which mixing occurs in stratified flows. For miscible fluids the instability develops whenever fluid of a greater density overlies fluid of a lower density. Such unstable stratifications frequently occur in stratified flows due to gravity currents, breaking internal waves, buoyancy sources and a variety of other mechanisms. A thorough understanding of the instability in relatively simple situations will aid our understanding of the mixing events which occur in more complex flows.

Previous experiments have used a range of techniques to produce the initial unstable density stratification. At the high technology end rocket motors (e.g. Smeeton & Youngs, 1988) and linear electric motors (Dimonte et al., 1994) have been used to accelerate cells containing initially stable stratifications downward at $10^3 g$. Accelerations as high as $10^4 g$ (e.g. Zaytsev et al., 1994) have been achieved using pressurised gas. Attempts to simply invert a stable stratification (e.g. Voropayev et al., 1993) are hampered by Kelvin's circulation theorem requiring the body of the fluid to remain irrotational and so the initial unstable interface is not normal to the gravity vector.
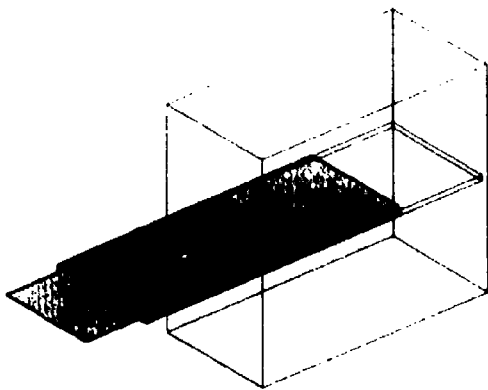
FIGURE 1: Schematic of experimental apparatus showing the original solid barrier.

In this paper we report on some results obtained using a simple barrier of novel design (Lane-Serff, 1989, p. A7; Dalziel 1993, 1994) to separate the two layers of fluid. Previous workers (Linden & Redondo, 1991) have seen that a simple, solid barrier leaves behind it a wake which has a long-term influence on the flow.

The barrier and tank used in the current experiments are sketched in figure 1. The barrier consists of two sheets of stainless steel (dark grey) separated along the edges by two strips of the same material to form a long, flat tube. Two pieces of nylon fabric (light grey) pass through the centre of this tube. At the inner end of the barrier one piece of the fabric is folded back on itself and laid on top of the barrier and fastened to the end wall of the tank through which the barrier passes. The second piece of fabric returns along the lower side of the barrier to be fastened to the end wall. As the barrier is withdrawn, any unsupported fabric is removed through the centre of the barrier. The net result of this arrangement is to eliminate any shear between the barrier and the fluid above and below. All the shear is confined between the barrier and the nylon fabric.

Unfortunately this barrier arrangement is not ideal. In section 2 we investigate details of the perturbation introduced by the barrier, while in section 3, we present a gross qualitative comparison between the experimental flow and numerical predictions of Youngs (1991,
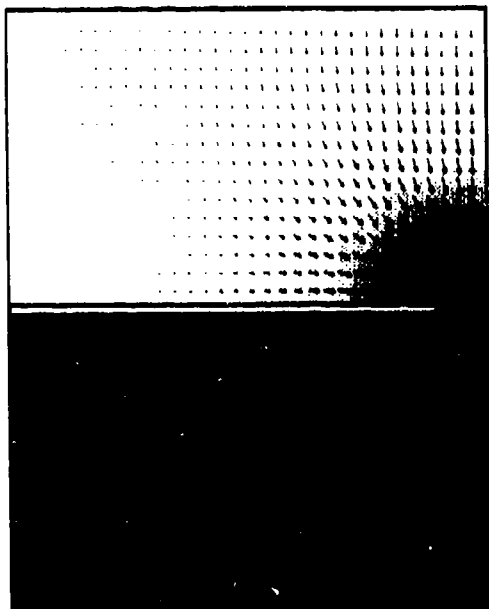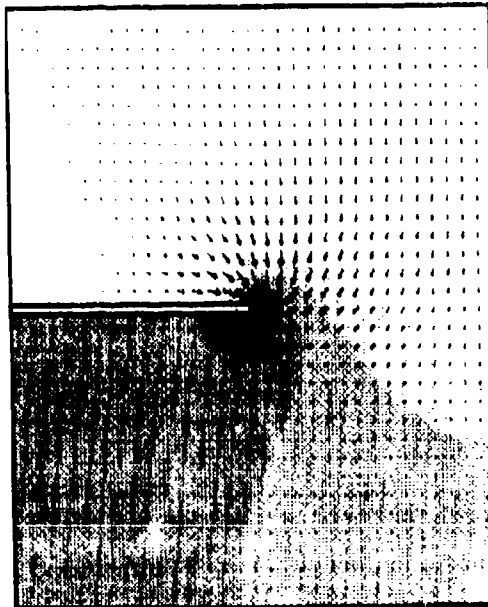
(a)   (b)

FIGURE 2: Velocity vectors (arrows) and velocity potential (grey scale) for model of barrier removal (a) 10% withdrawn. (b) 50% withdrawn.

1994). In section 4 we discuss some of the details of the structure of the concentration field and in section 5 the velocity fields. The main conclusions are highlighted in section 6.

2. Initial perturbations

While the novel design of the barrier outlined in the introduction removes most if not all of the shear between the barrier and the fluid above and below, it still introduces significant perturbations to the flow. The primary mechanism for these perturbations is the removal of a finite volume from the tank, and the associated need for fluid to move to replace the void left behind. As the working fluid (water stratified and refractive index matched with salt and alcohol) is essentially incompressible and the tank rigid, it is necessary to have a free surface which must move down as the barrier is removed. The barrier measures approximately 2.4mm thick (including the nylon fabric) and so the free surface must move down by this amount. Note that the potential energy released by the downward movement of the upper layer exactly balances the work done on the barrier by the hydrostatic component of the pressure during the removal process.

As a first approximation to the flow produced by the removal of the barrier we may assume two-dimensional, irrotational flow and utilise potential flow theory. For the present discussion we take the free surface to be flat and at constant pressure and the walls and barrier to be impermeable. At the end of the barrier the horizontal velocity is equal to the speed of withdrawal. With these boundary conditions time enters the problem only through the distance the barrier protrudes into the tank. We may thus replace the moving barrier by a fixed barrier and fluid sink.

This model for the flow induced by the barrier has been solved numerically using a multigrid technique for the velocity potential φ. Figure 2 plots the velocity (arrows) and velocity potential (grey scale) for the perturbation at two different barrier positions. Note that the vertical velocities near the trailing edge of the barrier are much stronger at early stages in the withdrawal process. This results in an overall tilt to the interface as the barrier is withdrawn.

If the fluid were unstratified and truly irrotational then the motion would stop once the barrier was fully withdrawn. However rotational flow will exist, particularly in the vacinity of the trailing edge of the barrier where the nylon fabric is pulled around the corners of the stainless steel sheets. These rotational aspects to the flow introduce additional fine-scale motions plus enable the tilting process to continue even after the barrier withdrawal is complete.

The fine-scale rotational perturbations are at a length scale an order of magnitude greater than that associated with the linearly most unstable mode. They also contain significant energy, swamping the linear growth phase of the instability in a stratified run. Coupling between the tank walls and the large scale tilt due to the removal of a finite volume draws energy from the stratification to set up a large scale overturning motion. The direction of this large scale overturning is always the same and is consistent with the potential flow model.

3. Qualitative comparison

Figure 3 presents a qualitative comparison of the present experiments and the numerical simulations of Youngs (pers. comm.). In the experiments the lower layer is dyed using a combination of food colour, textile dyes and fluorescent dye (sodium fluorescein) to produce an opaque, shiny interface between the upper and lower layers. The results of Youngs are from a direct numerical simulation of the compressible Euler equations. The simulations were run

at low Mach number to minimise compressibility effects. An attempt was made to model the time lag between one end of the tank and the other as the barrier was withdrawn. While white noise and a wave-like perturbation comparable with the experimental fine scales was introduced to trigger the instability, the barrier was assumed to be infinitely thin and shear free.
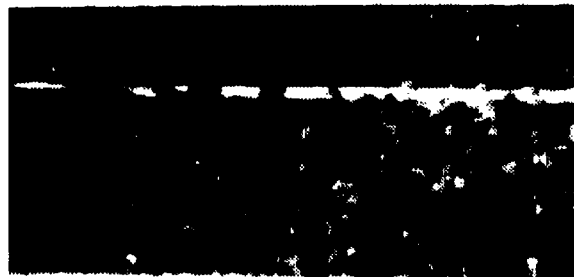
The experimental and numerical flow are clearly similar. While the length scales achieved differ (for the numerical flow they depend partly on the spectrum of the noise introduced to trigger the instability), the individual structures are very similar and follow the same general development.

4. Concentration field

4.1 LIF IMAGES

Figure 4 shows the evolution of the instability as a sequence of LIF (Light Induced Fluorescence) images of the lower half of the tank. In these experiments sodium fluorescein dye was added to the upper layer and the flow illuminated (from below) by a sheet of light approximately 1mm thick (over the entire depth of the tank) from a 300W mercury arc lamp. The flow was imaged using a high resolution monochrome video camera equipped with a mechanical shutter

(a)

(b)
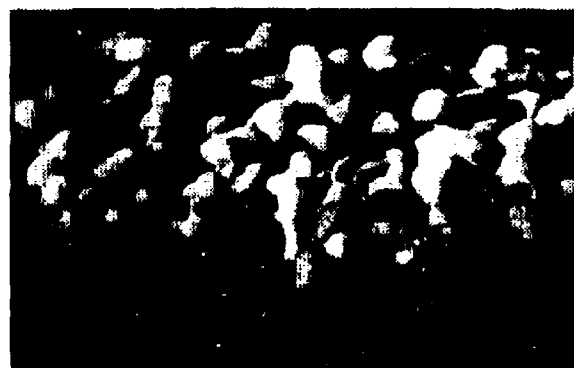
(c)

(d)

FIGURE 3: Perspective view of the early evolution of the instability for experimental and numerical flows. Times are measured from the start of the withdrawal process. Experiments: (a) *t*=2s, (b) *t*=3s, (c) *t*=4s. Numerical simulation: (d) *t*=5s.

4

FIGURE 4: Corrected LIF images showing the evolution of the instability. Times as indicated.

(to ensure simultaneous acquisition of the even and odd video fields). The video signal was recorded on a Super VHS video recorder for later processing using DigImage, an image processing system developed in DAMTP over the last five years.

Image processing of the raw images was necessary for three reasons: the intensity of the illuminating sheet was not uniform along the length of the tank, the individual light rays attenuated due to absorption by the fluorescent dye, and the light rays were not parallel. The intensity at the edges of the light sheet used for the experiment in figure 4 was only approximately 20% as bright as that in the middle. As a result, the image correction procedure has apparently enhanced the noise content of the images in these regions.

In the very early stages (figure 4, $t=2s$) the fine scale perturbation introduced by the nylon fabric at the end of the barrier is visible as rapid roll-up on a length scale of approximately 10mm. In comparison, the linearly most unstable mode (e.g. Chandrasekhar, 1961, p. 447) for this density ratio $(\rho_{upper}/\rho_{lower} = 1.006)$ is approximately 2mm. There is up/down some asymmetry of these structures, presumably due to the net downward motion of the upper layer. Perspective views such as those in figure 3 suggest that these initial structures are three-dimensional in nature. The structures rapidly interact and combine to produce successively larger scales, a process which continues until the flow

FIGURE 5: Ensemble mean LIF image at $t=12s$.

extends through the entire depth of the tank (*t*=12s).

The large scale effect of removing a finite volume can be seen as the more rapid growth of the structure at the right-hand wall of the tank. The growth of this structure leads eventually to a clockwise overturning motion on the scale of the tank. This feature is consistent throughout these experiments as can be seen from figure 5 which represents the ensemble mean LIF field from 25 individual experimental runs at *t*=12s.

4.2 GROWTH RATE

It is possible to calculate a wide range of concentration statistics from the LIF images presented in the previous section. Here we shall limit ourselves to the growth rate and fractal dimension.

Figure 6 plots the ensemble mean (25 runs) temporal evolution of the penetration of the upper layer into the lower half of the tank. The penetration depth is defined as the depth where there is at least 5% upper layer fluid in the central 50% of the tank. From dimensional analysis we expect self-similar penetration with the penetration depth *h* scaling as

$$h = \frac{1}{2}\alpha\frac{\Delta\rho}{\rho}gt^2 + h_0,\tag{1}$$

where $\Delta\rho = \rho_{upper} - \rho_{lower}$, $\bar{\rho} = \frac{1}{2}(\rho_{upper} + \rho_{lower})$, g is gravity, h_0 is the effect of the small scale perturbations and α is some constant of proportionality. This scaling law is plotted as a solid line on figure 6 with $\alpha = 0.05$. This is in broad agreement with the earlier experiments of Linden & Redondo (1991) who were restricted to density ratios of greater than 1.06 (*i.e.* density differences ten times greater than the present experiments) due to the wake from their simple barrier. The current growth rates also compare well with the $\alpha = 0.06$ found in the rocket experiments of Smeeton & Youngs (1988) and fall within the range of values found in direct numerical simulation ($\alpha = 0.03 \sim 0.05$).

If we select only the experiments we thought were the best in the sense that everything ran smoothly and there were no other undesirable influences, then our estimate of the growth rate could be reduced to around $\alpha = 0.04$. On the other hand, if we were to look at the growth rate over the entire length of the tank, we would find that it was dominated by the rapid growth down the right-hand boundary due to the flow imparted by removing a finite volume. Clearly then there is still some doubt about the true value of α for these experiments.

FIGURE 6: Penetration depth of mixing region for ensemble of experiments (x) and similarity law (line).

There is also uncertainty about the growth rate calculated from numerical simulations. With gradual improvement of the numerical codes and increase in resolution, the *best estimate* for the growth rate has dropped from 0.05 (Youngs, 1991) to 0.03 (Youngs, 1994).
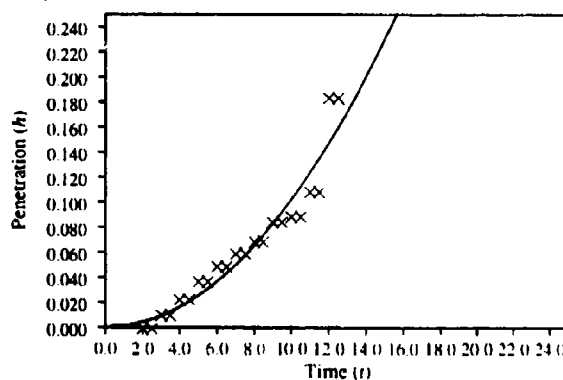
4.3 FRACTAL DIMENSION

It is still a subject of debate as to how useful a knowledge of the fractal dimension of a material surface is in understanding the dynamics of the flow. We shall not enter this debate in this paper other than to note that the fractal dimension is a useful measure of the degree of self similarity of the fine scales in the flow.

Figure 7 plots the temporal evolution of the fractal dimension of the 50% concentration contour for an ensemble of 25 experiments. The three key features of this evolution are the initial growth phase for $t<5s$, the self similarity maintained up until $t=14s$ and finally the gradual increase in the dimension at later times. Comparison with the LIF images presented in figure 4 shows the initial phase corresponds to the distortion to the initially planar interface $(D=1)$ due to perturbations introduced by the barrier gradually interacting with each other and
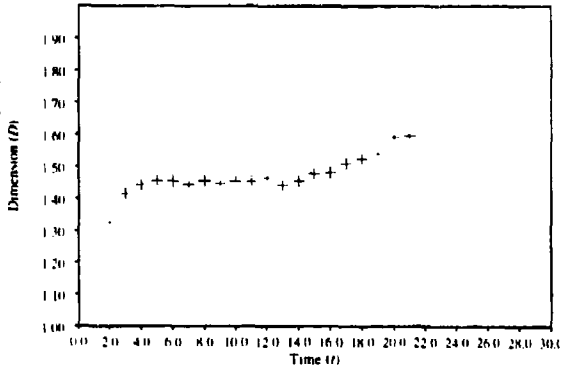
FIGURE 7: Evolution of fractal dimension.

the unstable stratification. From approximately $t=4s$ the self similar development described by (1) is established. While the boundaries of the tank start to be important by $t=12s$, it is not until somewhat later that we see a response and the development of more highly folded concentration contours. The numerical work of Youngs (1994) shows a similar time lag before the onset of self similarity (in this case characterised by the growth rate following equation (1)).

In the absence of molecular diffusion of dye and salt, the fractal dimension would continue to increase towards $D=2$ as the internal wave field continues to break. With diffusion, the increase in dimension due to folding will eventually be balanced by diffusion, with the dimension then slowly decreasing towards unity (the final state will be a continuous density stratification with the 50% concentration contour corresponding to a horizontal surface).

6. Conclusions

In this paper we have shown broad qualitative agreement between a series of simple laboratory experiments and sophisticated direct numerical simulations of classical Rayleigh-Taylor instability. While the quantitative comparison is less favourable, we have shown that the discrepancy between the predicted and observed development may be explained in terms of the initial perturbations to the flow produced by removing the barrier initially separating these two layers. For these perturbations to have their full impact on the flow, it is necessary to consider the coupling between them and the tank walls.

We have demonstrated that the flow achieves a self similar growth phase despite these initial perturbations. In addition to the t^2 growth rate and the constant fractal dimension presented in this paper, concentration fluctuation power spectra and the evolution of the velocity field also show self similar behaviour.

Acknowledgements

their invaluable discussions and contributions to this work.

References

Chandrasekhar, S. (1961): *Hydrodynamic and Hydromagnetic Stability*; Oxford University Press, 652 pp.

Dalziel, S.B. (1993): Rayleigh-Taylor instability: experiments with image analysis; *Dyn. Atmos. and Oceans* **20**, 127-153.

Dalziel, S.B. (1994): Perturbations and coherent flow in Rayleigh-Taylor instability; in *4th International Workshop on the Physics of Compressible Turbulent Mixing*, ed. P.F. Linden, D.L. Youngs & S.B. Dalziel; 32-41.

Dimonte, G., Remington, B., Stry, P., Burke, G. Crowley, P., Hawke, R., Morrizon, J. & Susoeff, A. (1994): Turbulent hydrodynamic mix experiment; in *4th International Workshop on the Physics of Compressible Turbulent Mixing*, ed. P.F. Linden, D.L. Youngs & S.B. Dalziel; 42-49.

Lane-Serff, G.F. (1989): *Heat flow and air movement in buildings*; PhD thesis, University of Cambridge, Cambridge; 131 pp.

Linden, P.F. & Redondo, J.M. (1991): Molecular mixing in Rayleigh-Taylor instability. Part 1: global mixing; *Phys. Fluids A* **3**, 1269-1277.

Smeeton, V.S & Youngs, D.L. (1988): *Experimental investigation of turbulent mixing by Rayleigh-Taylor instability*; AWRE Rep. 002/84, Ministry of Defence.

Voropayev, S.I., Afanasyev, Y.D. & van Heijst, G.J.F. (1993): Experiments on the evolution of gravitational instability of an overturned, initially stably-stratified fluid; *Phys. Fluids A* **10**, 2461-2466.

Youngs, D.L. (1991): Three-dimensional numerical simulation of turbulent mixing in Rayleigh-Taylor instability; *Phys. Fluids A* **3**, 1312-1320.

Youngs, D.L. (1994): Direct three-dimensional numerical simulation of mixing by Rayleigh-Taylor instability; in *4th International Workshop on the Physics of Compressible Turbulent Mixing*, ed. P.F. Linden, D.L. Youngs & S.B. Dalziel; 167-177.

Zaytsev, S.G., Chebotareva, E.I. & Titov, S.N. (1994):The study of Rayleigh-Taylor instabiling in continuous interface; in *4th International Workshop on the Physics of Compressible Turbulent Mixing*, ed. P.F. Linden, D.L. Youngs & S.B. Dalziel; 178-187.

Rayleigh-Taylor Stability of a Two-Fluid System
Under a General Rotation Field

by

L. A. Dávalos-Orozco
Instituto de Investigaciones en Materiales
Universidad Nacional Autónoma de México
Apartado Postal 70-360, Delegación Coyoacán
04510 México D. F., México

Abstract

In this paper we investigate the Rayleigh-Taylor instability of a two-fluid layer system under a general rotation field. Gravity is always perpendicular to the two layers. It is found that, in an unstable situation, an increase in the densities difference increases the stable angular area of wave propagation, measured with respect to the horizontal component of rotation. However, it is found that the vertical component of rotation decreases not only this stable angular area but also the range in which the horizontal component stabilizes the system, according to a previous research by Dávalos-Orozco (1993). This decrease in stable area comes along with a decrease in the growth rate. It is shown, by numerical analysis of the eigenvalue equation, that the stable angular area disappears after the non dimensional vertical component of rotation attains the value .33, approximately. Exact and approximate analytical results are calculated to understand the physics of the numerical results.

1. Introduction

The Rayleigh-Taylor instability (RTI) has been the subject of recent research due to its importance in stratified systems among which planetary and stellar atmospheres are two examples. In order to describe realistic situations, different properties of the fluid have been included in theoretical investigations. For instance, Chandrasekhar (1955) included the effect of viscosity and Reid (1961) the effects of both viscosity and surface tension. The fluid can also be supposed as being made of a number of layers or as being continuously stratified. For a review see Chandresekhar (1961). Recently, important advances have been attained from the theoretical point of view by Yiantsios and Higgins (1989). A new and original experiment has being done by Fermigier et al. (1992) which gives a light in the development of the RTI not seen before.

The effect of external forces has importance mainly in planetary and stellar systems. Coriolis and centrifugal forces are the more common in these systems and play an important role in determining many phenomena including RTI. The effect of rotation making an angle with gravity was first investigated by Hide (1956a) and gave a detailed analysis only for the case of rotation parallel to gravity Hide (1956b). Bjerknes et al. (1933) were the first to

include the effect of vertical rotation in a two-fluid layer system In a recent research, the RTI of a continuously stratified fluid in a general rotating field has been investigated by Dávalos-Orozco and Aguilar-Rosas (1989a). They found the upper bound of the growth rate of instability and, by means of an example, they found that, for large values of the wave number, a bifurcation occurs in the plane of the angle of maximum growth rate against the wave number for vertical component of rotation comparable in magnitude with the horizontal component. This angle of maxima is measured with respect to the horizontal component of rotation.

A continuously stratified horizontal magnetic field has been included by Dávalos-Orozco and Aguilar-Rosas (1989b) who obtained the upper bound for the growth rate of the instability in a continuously stratified fluid under a general rotation field. See also Dávalos-Orozco (1991).

Dávalos-Orozco (1993) investigated the RTI of two superposed fluids under a horizontal rotation field and also under the simultaneous action of horizontal rotation and magnetic fields.

In this paper we investigate the RTI in a two-fluid layer system under a general rotation field. Viscosity is ignored. The results obtained here are an extension of those given in the paper by Dávalos-Orozco (1993). Here, we clarify the importance the horizontal component of rotation has in RTI and how the vertical component of rotation can not eliminate the effect of the former until a fixed magnitude, obtained numerically, is reached. Exact and approximate analytical results will be calculated to help in the understanding of the physics of the problem and to identify the correct numerical results.

The structure of the paper is as follows. In section 2 the perturbed equations of motion are presented using normal modes along with the boundary conditions. In section 3, a discussion of the proper value equation obtained in section 2 is given and one exact and one approximate solutions are calculated to help in the numerical analysis discussed in section 4. The conclusions are given in section 5.

2. Equations of motion

We consider that the two fluids composing the stratified layer are non-dissipative and that the Euler's equations govern the system under rotation. We suppose that at the onset the system is in static equilibrium but in an unstable situation with a fluid of density ρ_2 over another of density ρ_1, where $\rho_2 > \rho_1$. The gravity force is perpendicular to the two layers. After a perturbation is given to the system, the variables satisfy a system of linear equations, where we suppose that all dependent variables have the form $\exp[i(k_x\ x + k_y\ y) + n\ t]$. Then, a combination of those equations leads to an equation of motion satisfied in each medium:

$$n^2(k^2 - D^2)w - 4(i\Omega^+ + \Omega_z D)^2 w = 0 \quad \ldots \ldots \ldots \ldots \ldots \ldots \ldots \ldots \quad (1)$$

2

This equation is solved trying a solution w $\propto \exp(\gamma z)$ and using the condition of continuity of the vertical component of velocity w at the interface and the jump condition at the interface, that is, $w_1 = w_2$ and

$$w_0(2n\Omega^- + ik^2g)\Delta\rho + i(n^2 + 4\Omega_z^2)\Delta(\rho D w_0) - 4\Omega^+\Omega_z[\Delta(\rho w_0) + \rho\Delta w_0] = 0 \quad \ldots \quad (2)$$

Here, $\Delta G = G_2 - G_1$, is the jump of a quantity, k_x and k_y are the x and y components of the wave vector where k is its magnitude and n is a complex number whose real and imaginary parts are the growth rate of the perturbation and the frequency of the oscillation, respectively. $\Omega^+ = k_x\Omega_x + k_y\Omega_y$ and $\Omega^- = k_x\Omega_y - k_y\Omega_x$ where Ω_x, Ω_y and Ω_z are the x, y and z-components of the rotation vector. All this leads us to the following eigenvalue equation in non dimensional form:

$$\{N^4 + N^2[F_z^2 + F^2\cos^2(\theta - \alpha)]\}^{1/2} = [1 - 2iNF\sin(\theta - \alpha)]A \quad \ldots\ldots\ldots\ldots (3)$$

where $N = n/(gk)^{1/2}$, $F_z = \Omega_z/(gk)^{1/2}$, $F = \Omega/(gk)^{1/2}$ and Ω is the magnitude of the horizontal component of rotation. $A = (\rho_2 - \rho_1)/(\rho_1 + \rho_2) > 0$ represents the densities difference, θ is the angle of propagation of the perturbation with respect to the x-axis and α is the angle of the horizontal component of rotation with respect to the x-axis. From now on, α will be made equal to zero. This has no influence in the results. For more details in the derivation see Dávalos-Orozco (1993).

3. Approximate and Exact solution

Squaring both sides of Eq.(3) we obtain a forth order nonlinear polynomial equation with complex coefficients. This leads us to a problem because when squaring, we lose the information given by the non dimensional densities difference A. This information is important because, as we will see, the stability of the system under study is not only determined by A, but also by the vertical and horizontal components of rotation. Only in the case of vertical rotation A determines the stability. In this circumstances, it is necessary to know in advance which two solutions, of the four obtained from the forth order polynomial, are the correct. To this end, we obtain an approximate solution. Note that the eigenvalue equation has a solution purely imaginary, that is, $N = iI$. Then, the condition $I^4 > I^2[F_z^2 + F^2\cos^2\theta]$ is obtained, which lets us obtain the following approximations of the two solutions, if we suppose that N satisfies a similar inequality (Dávalos-Orozco (1993)):

$$N = i\ AF\sin\theta \pm \{A - 2F_z^2 - F^2(A^2\sin^2\theta + 2\cos^2\theta)\}^{1/2} \quad \ldots\ldots\ldots\ldots (4)$$

3

From this equations we obtain a critical F for stability:

$$FSc^2 = (A - 2F_z^2)/(A^2 \sin^2\theta + 2\cos^2\theta) \dots\dots\dots\dots\dots\dots\dots (5)$$

This approximation is valid for small F and F_z and for θ near to 90°, as shown by numerical analysis. Numerical analysis shows that an increase in F leads to FSc, that is, the system stabilizes, but also it shows that, after a further increase, the system destabilizes. In order to show this analytically we looked for an exact solution to this new critical value. To this end, we suppose again that N is purely imaginary. Then, two inequalities from both sides of the eigenvalue equation are obtained. One is that shown above. The other is $1 \geq 2IF \sin\theta$. See Dávalos-Orozco (1993) for the conditions necessary to preserve the signs of the inequality in order to be able of squaring both sides of it. Then, after squaring both sides of this inequality and multiplying member to member with the first inequality, a condition for stability is obtained which at criticality for instability gives the following value for the critical horizontal component of rotation:

$$FIc^2 = .5\cos^2\theta\{-F_z^2 + [F_z^4 + .25\cot^2\theta]^{1/2}\} \dots\dots\dots\dots\dots\dots\dots (6)$$

This result is exact in the sense that no approximation has been made in its calculation and it is a direct result from the eigenvalue equation, in contrast to the method used to obtain FSc. Note that the value of FIc is independent of the A. The two critical values obtained in this section will be very useful in determining the correct solutions of the eigenvalue equation.

4. Numerical Analysis

The numerical solution of the forth order polynomial eigenvalue equation corroborated the results obtained for FSc and FIc when F_z and θ are small enough. Results were obtained for different values of A, but here only two values $A = .4$ and 1 are presented combined with two values of $F_z = .01$ and .15, in a plot of F against θ. In Fig. 1 , graphs of log F against θ are shown for $F_z = .01$. First, lets investigate the case $\theta = 90°$. An increase in F leads the system to FSc, point after which there is stability. With a further increase it reaches FIc, point after which the system becomes unstable increasing the growth rate again until a maximum FM is reached. Later the growth rate decreases monotonically. It is important to note that in the absence of the vertical component of rotation (see Dávalos-Orozco (1993)) there were no FIc at $\theta = 90°$. In other words, the value of FIc $= \infty$ at $\theta = 90°$ when $F_z = 0$. This may be shown by means of Eq.(6) for FIc taking the limit for $\theta = 90$ adequately. Another way is to calculate FIzc instead of FIc. This last procedure gives $FIc^2 = 1/16F_z^2$ for $\theta = 90°$. For the case of Fig.1, $F_z = .01$, which gives log F $= 1.3979$. That is, a very small value of the vertical component of rotation reduces considerably the stable range of F $\theta = 90°$. After the crossing of the lines FSc and FIc, a line of minimum of growth rate

4

appears as a remnant of the former stable area. It disappears after the crossing with FM. This behavior is similar to that in the absence of F_z. Note that an increase in A increases the stable angular area along with an increases in the growth rate in the unstable angular areas. The contrary is valid too when A decreases. Therefore, there are no contradictions about the meaning of stability. Fig.2 shows curves of F against θ for $F_z = .15$. Here, the stable angular areas are considerably reduced but again an increase in A increases this area. Notice that this increase is due exclusively to a decrease in the value of FSc.

The limit angle for stability may again be calculated analytically as in Dávalos-Orozco (1993). However, this angle is approximate because use is made of Eqs.(5) and (6) obtained above, one of which is an approximation. As seen in Fig.(1) and (2), FSc and FIc cross just at the end of the stable angular area. Use of this idea, equating FSc to FIc, gives:

$$\tan^2\theta_L = R^2/\{1 - 4F_z^2 R\} \quad \dots \dots \dots \dots \dots \dots \dots \dots \dots \dots \dots \dots \dots \quad (7)$$

where $R = \{2+(2)^{1/2}\}/A$. Note that in the absence of F_z this equation reduces to that obtained by Dávalos-Orozco (1993). The figures show that the larger limit angle is attained for $A = 1$. Then, from the denominator and for $A = 1$, we find that $F_z = [1/4\{2 + (2)^{1/2}\}]^{1/2} = .2705$ is the approximate value at which the stable angular area must disappear. Numerical analysis shows that this area disappears at $F_z = .33$. Fig.3 presents graphs of θ_L against F_z for different values of A using the approximate Eq.(7). The approximation is good for small values of F_z, fair for values a little larger than .1 and bad for larger values.

5. Conclusions

We have shown that a two-fluids system under a general rotation field presents a more complicated behavior compared to the cases in which the vertical and horizontal components of rotation are present alone. The densities difference parameter A increases the stable angular area as in the case of horizontal rotation alone but even a small magnitude of the vertical component of rotation works to eliminate, considerably, the stable angular region decreasing, at the same time, the growth rate. The angular region disappears when Fz = .33 . Note that, to complete the stability analysis for all the 360° angular region, the graphs shown in Figs.(1) and (2) must be reflected every 90°. The growth rate in the figures is larger at the lower left side and smaller at the upper right side.

References

Bjerknes, V. J. Bjerknes, H. Solberg and T. Bergeron (1933) **Physicalische Hydrodynamics** (Springer-Verlag).

Chandrasekhar, S. (1955) The character of the equilibrium of an incompressible heavy viscous fluid of variable density, *Proc. Camb. Phil. Soc.* **51**, 162.

Chandrasekhar, S. (1961) **Hydrodynamic and Hidromagnetic Stability** (Claredon Press, Oxford).

Dávalos-Orozco L. A. and J. E. Aguilar-Rosas (1989a) Rayleigh-Taylor instability of a continuously stratified fluid under a general rotation field. *Phys. Fluids A* 1, 1192.

Dávalos-Orozco L. A. and J. E. Aguilar-Rosas (1989b) Rayleigh-Taylor instability of a continuously stratified magnetofluid under a general rotation field. *Phys. Fluids A* 1, 1600.

Dávalos-Orozco L. A. (1991) Reply to comments of Chakraborty and Tuteja. *Phys. Fluids A* 3, 3127.

Dávalos-Orozco L. A. (1993) Rayleigh-Taylor instability of two superposed fluids under imposed horizontal and parallel rotation and magnetic fields. *Fluid Dynamics Research* 12, 243.

Fermigier, M., L. Limat, J. E. Wesfreid, P. Boudinet and C. Quilliet (1992) Two dimensional patterns in Rayleigh-Taylor instability of a thin layer, *J. Fluid Mech.* 236, 349.

Hide, R. (1956a) The character of the equilibrium of a heavy, viscous, incompressible rotating fluid of variable density. I. General theory, *Q. J. Mech. Appl. Math.* 9, 22.

Hide, R. (1956b) The character of the equilibrium of a heavy, viscous, incompressible rotating fluid of variable density. II. Two special cases, *Q. J. Mech. Appl. Math.* 9, 35.

Reid, W. H. (1961) The effect of surface tension and viscosity on the stability of two superposed fluids, *Proc. Camb. Phil. Soc.* 57, 415.

Yiantsios, S. G. and B. G. Higgins (1989) Rayleigh-Taylor instability in thin viscous films, *Phys. Fluids A* 1, 1484.
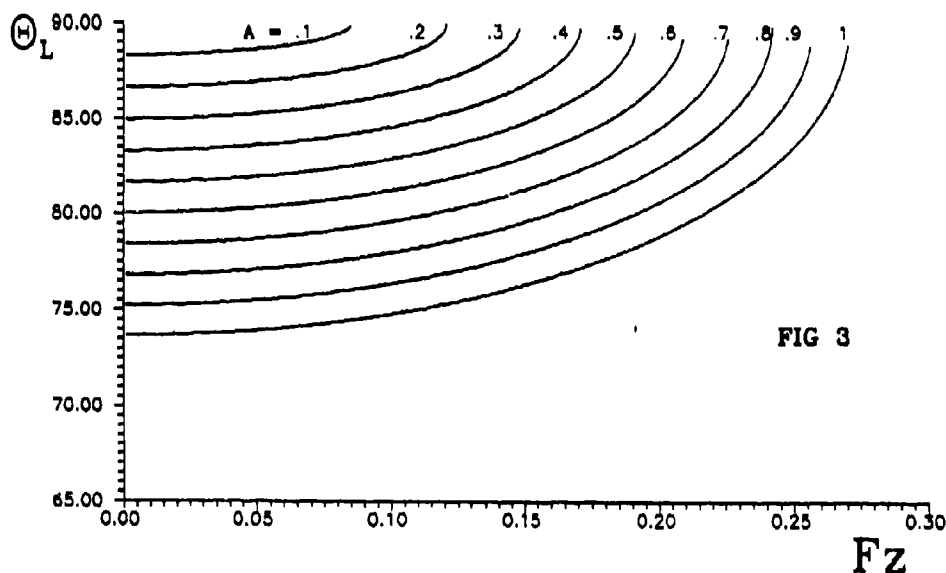
Fig 3. Limit angle for stability. Good approximation for Fz less than .1. Numerical analysis shows that after Fz = .32 all angles are unstable.
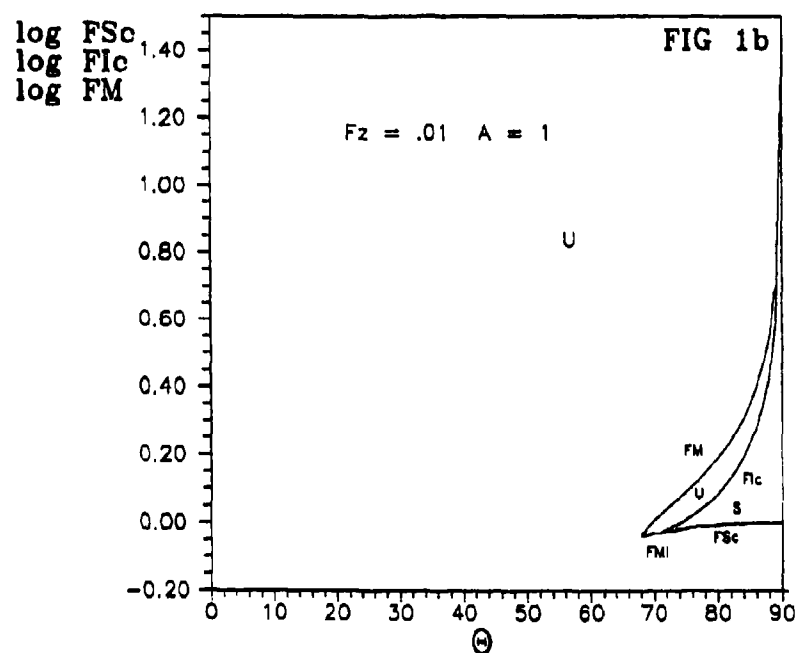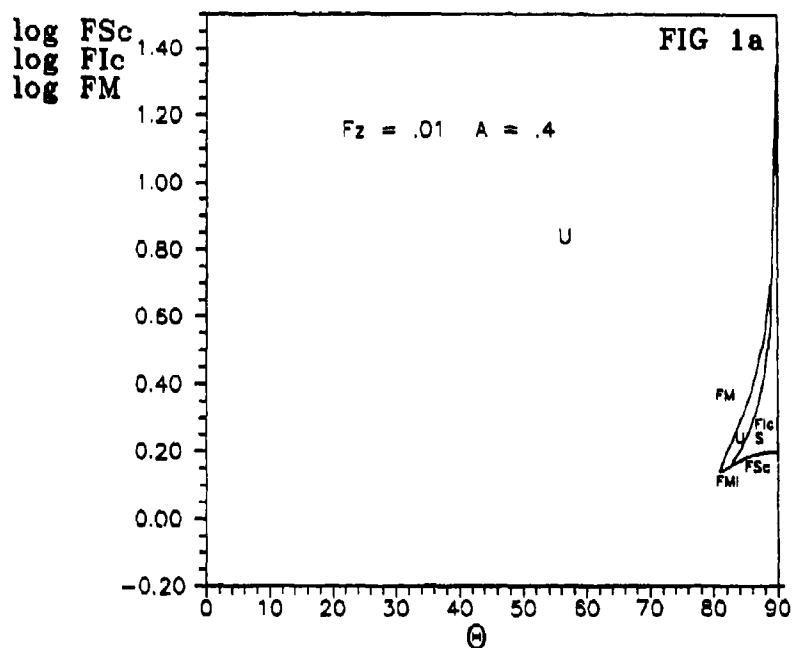
FIG 1a

log FSc
log FIc
log FM

1.40
1.20
1.00
0.80
0.60
0.40
0.20
0.00
-0.20

$Fz = .01$ $A = .4$

U

FM
FIc
U S
FMI   FSc

0   10   20   30   40   50   60   70   80   90
Θ

FIG 1b

log FSc
log FIc
log FM

1.40
1.20
1.00
0.80
0.60
0.40
0.20
0.00
-0.20

$Fz = .01$ $A = 1$

U

FM
FIc
U   S
FMI   FSc

0   10   20   30   40   50   60   70   80   90
Θ

FIG 1. F vs. Θ. The growth rate and stable area increase with the density difference. FIc extended to infinity at $\Theta = 90$ for $Fz = 0$. Here, it is finite. (U) S = (un)stable.
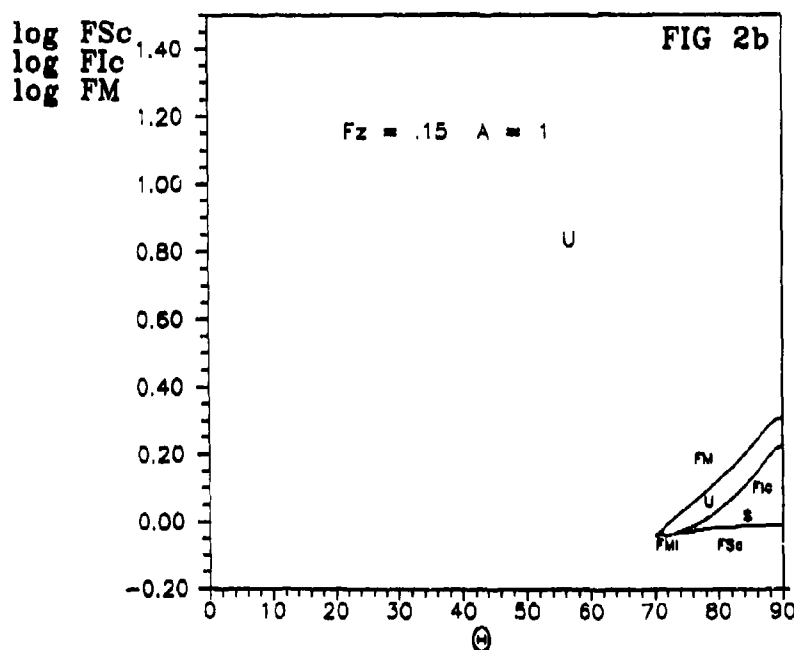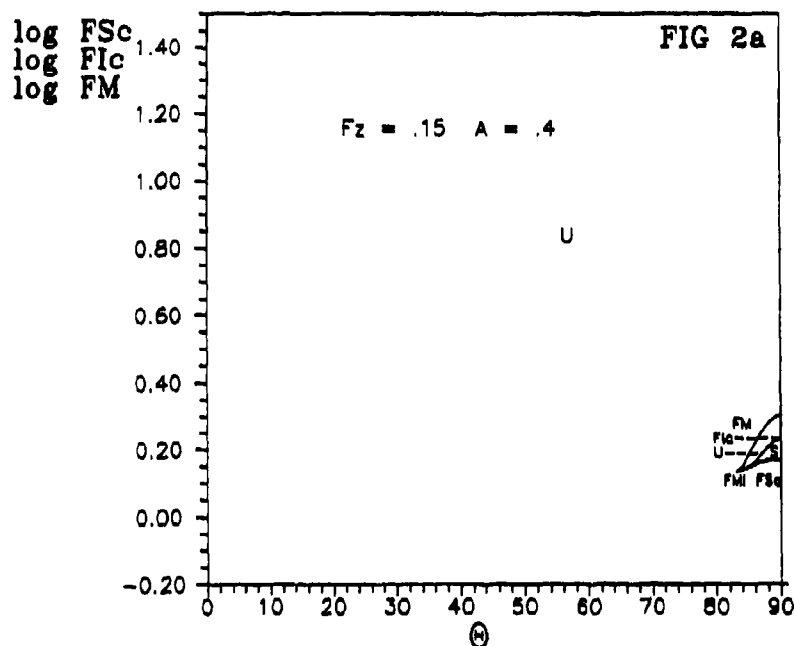
7

Fig 2. F vs. θ. An increase in Fz decreases the stable area while the density difference increases it with the growth rate.

8